UNIVERSITY OF CALIFORNIA, SAN DIEGO

Steel Baseplate Connections with Ductile Anchors for the Improved Seismic Performance of Structural Systems

A dissertation submitted in partial satisfaction of the requirements for the degree of

Doctor of Philosophy

in

Structural Engineering

by

Christopher Anderson Trautner

Committee in charge:

Professor Tara Hutchinson, Chair
Professor Joel Conte
Professor José Restrepo
Professor David Sandwell
Professor Peter Shearer

2016

The Dissertation of Christopher Anderson Trautner is approved, and it is acceptable in quality and form for publication on microfilm:

_____

_____

_____

_____

_____
Chair

University of California, San Diego

2016

DEDICATION

This dissertation is dedicated to my fiancée, Alanna, and to my parents, Ellen and Chris.

TABLE OF CONTENTS

LIST OF FIGURES

LIST OF TABLES

NOTATION

This section defines the acronyms, variables, subscripts, and selected nomenclature used in this dissertation.

Notation

Acronym/ Abbreviation	*Meaning*
Ann	Annealed (bonded anchor all-thread steel)
AR	As-Received (bonded anchor all-thread steel)
B	Bonded (adhesive) anchor
CI	Cast in
CL	Centerline
CW	Cold-worked
CW-A	Cold-worked, subsequently annealed (same as Ann)
HR	Hot-rolled
ID	Inside diameter
MDF	Medium-density fiberboard
OD	Outside diameter
UC	Undercut

Variables	*Meaning*
b	Length/width of square baseplate
d	Depth of W-section member
d	Distance from anchor to extreme compressive fiber (Chapter 5)
d_1	Minor diameter of internal thread (Chapter 2)

e	Eccentricity (=M/P)
f'_c, f'_g	Compressive strength of concrete and grout, respectively
h	Height of hollow structural section (HSS) member
h_{act}	Height of application of lateral load to column, measured from top of slab
h_b	Height of base slab
h_c	Total height of the column, measured from bottom of baseplate to top
h_s, h_j	Height of spreader beam in test S3S1, height of axial load application jacks (including spreader beam) in test
l_D	length of thread chamfer (per ASME B1.1, Chapter 2)
n	Johnson-Cook exponential paramter (Chapter 2)
s_N, s_M	Spacing of corner anchors in the x-direction, y-direction
t_b, t_g	Thickness of baseplate, thickness of grout
A, A_g	Anchor area, gross area of column
A	Johnson-Cook linear parameter (Chapter 2)
B	Johnson-Cook hardening parameter (Chapter 2)
D	Anchor diameter
D_{bsc}	Basic thread diameter given by ASME B1.1
D_2	Pitch diameter of internal thread
DR	Drift Ratio
E_g, E_s, E_t	Elastic modulus of grout, elastic modulus of steel, tangent modulus of steel
EL	Elongation (%)

F	Measured applied lateral load
F_a	Applied axial force in test S3S1
F_h	Applied lateral force from 50-kip actuator
F_y	Yield strength or stress (of steel or anchor component)
F_u	Ultimate strength or stress (of steel or anchor component)
H	Story height
$L_{i,e}$	Distance along anchor axis from the center of thread to thread edge (i=internal thread, e=external thread, Chapter 2)
L_f, L_g, L_s	Free length, gage length, and stretch length (see definitions below)
M, M_u, M_n	Moment, required moment, and nominal strength
M	Width of the baseplate in the y direction, perpendicular to the column web for W section. Not to be confused with moment, above (definition should be clear based on context)
M_c	Moment corrected for axial force component, i.e. moment carried by the connection only (test S3S1 only)
M_{uc}	Moment calculated directly from actuator load cell including axial load component (test S3S1)
N	Length of baseplate in the x-direction (parallel with column web)
P	Axial load on connection (Chapter 3)
P	Pitch distance (Chapter 2)
T	Period of structure
W	Weight of structure or lumped weight (Chapter 5)
W_c	Cockcroft-Latham damage parameter
Y	Distance over which constant compressive stress is assumed to act (Fischer and Kloiber 2006)

ε_{pl}	Effective plastic strain
ϕ	Strength reduction factor
Δ	Displacement of various components, subscripts used to indicate direction
ΔL, ΔL_u	Anchor elongation, anchor elongation capacity
θ	Rotation of various components
Ω	Overstrength factor (ASCE 2010)

Subscripts	*Meaning*
c, b	Column, baseplate
i, o	Initial
h,v	*Horizontal, vertical*
u	Ultimate
x, y, z	Coordinate directions

Nomenclature	*Definition*
Exposed length	In a baseplate connection, the distance from the top of the concrete or epoxy adhesive to the bottom of the top washer/nut assembly. Equal to the stretch length if there is no strain penetration (see below)
Free length	Same as exposed length. See Figure 2-2
Gage length	Length over which a quantity of interest is measured in a tensile test. May or may not be equal to the stretch length and/or the free length
Strain penetration	The phenomenon of plastic strain occurring within the substrate in an embedded material. In the case of the current dissertation,

	this refers to plastic strain occurring in embedded anchors in tension below the level of the concrete
Stretch length	In a baseplate connection, the length over which significant plastic strain occurs. This may be equal to the *exposed length*, or may be greater if *strain penetration* occurs.

ACKNOWLEDGEMENTS

This research was funded partly by Hilti Corporation through the auspices of the *Hilti Seismic Project (HSP)*. Material and technical assistance was provided by Hilti North America. The program managers of the HSP were Dr. Philipp Grosser and Dr. Roberto Piccinin. Technical oversight of the project was provided by Dr. Ulrich Bourgund, Mr. John Silva, and Mr. Robert Bachman. The financial and technical support of these organizations and individuals is gratefully acknowledged. Opinions, findings, and conclusions are those of the author, and do not necessarily reflect the views of the sponsoring organizations.

I would like to thank my doctoral committee for their support and guidance. Professors José Restrepo and Joel Conte were two of the most excellent teachers I have had in my career, and I appreciate their openness in discussing technical challenges throughout my time at UCSD. I was fortunate enough to have Professors Peter Shearer and David Sandwell for my out-of-department seismology coursework. I particularly enjoyed their classes as background and foundation for my work within the Structural Engineering Department at UCSD.

I would like to express my particular gratitude to the Hilti Corporation and the individuals involved in the technical oversight of the program, particularly Mr. John Silva, who was always taken time from his busy schedule to help with reports and papers. Though we occasionally disagreed on technical matters, my discussions with him have been some of the most instructive of my time at UCSD. I have appreciated the opportunity to work on a multi-national research project; I have learned a great deal from working with Hilti engineers around the world.

Much of the work presented herein was performed in the Powell Structural Laboratories and would not have been possible without the help of the world-class staff there. I would like to thank Dr. Christopher Latham, Noah Aldrich, Mike Sanders, and Paul Greco for their help during the various phases of the experimental work. In particular, I am grateful for the assistance of Darren McKay, who directed the control of the actuators and shake table. His willingness to be invested in the project, work demanding hours, and keep all project participants safe is much appreciated. I would also like to gratefully acknowledge the undergraduates and high school students who assisted me at various stages of the work. Undergraduates YJ Yoo and Arthur Nguyen, as well as PhD student Gloria Faraone, were extremely helpful in various mechanical and instrumentation setups. Guillermo Fernandez and Elizabeth Moreno, high school students from Mexico at UCSD for summer internships, were very helpful in preparing the shake table specimen. Albert Liang was instrumental in processing dynamic test data and video clips during the final phase of testing. Finally, I would like to thank Matteo Copellini for performing much of the tensile testing presented in Chapter 2. This particular portion of the research would not have been possible without his diligence.

I would like to thank my advisor, Professor Tara Hutchinson, for her advice and unwavering support throughout my time at UCSD. She has been an outstanding mentor, advocate, and friend. She supported me on a single, coherent topic for the duration of my PhD; for that I am immeasurably grateful. I have very much appreciated her guidance in technical writing and the visual display of quantitative information. Through her, I have also gotten my first exposure to academic grant and proposal

writing, which I am sure I will use throughout my future career. Through her recommendations and the support of Professor Ahmed Elgamal, I was able to teach an upper-division undergraduate class, Earthquake Engineering (SE 180). This has been a personal goal of mine for at least 10 years, and I could not have taken advantage of this without their help.

Finally, I would like to thank my family: my parents, who have supported me without question in everything I have undertaken in the last 30 years, and my fiancée, who is the kindest and most supportive person I know.

Chapter 2 contains material published in the following journal paper: Trautner, C., Hutchinson, T., Copellini, M., Grosser, P., Bachman, R., and Silva, J. (Accepted). "Developing Ductility using Concrete Anchorage," American Concrete Institute Structural Journal. The dissertation author was the primary author on this paper.

Chapter 3 contains material published in the following journal papers: Trautner, C., Hutchinson, T., Grosser, P., and Silva, J. (2015). “Effects of detailing on the cyclic behavior of steel baseplate connections designed to promote anchor yielding.” ASCE Journal of Structural Engineering, *10.1061/(ASCE)ST.1943-541X.0001361, 04015117*. Trautner, C., Hutchinson, T.C., Grosser, P, and Silva, J. (Accepted), "An Investigation of Steel Column Baseplate Connection Details Incorporating Ductile Anchors," ASCE Journal of Structural Engineering. The dissertation author was the primary author on these papers.

Chapter 4 contains material submitted for publication in the following journal paper: Trautner, C. and Hutchinson, T., (In Review). "Development, Verification, and

Design Application of a Parametric Finite Element Model for Typical Steel Moment Frame Column Baseplate Connections," ASCE Journal of Structural Engineering. The dissertation author was the primary author on this paper.

Chapter 5 contains material submitted in the following journal papers, of which the dissertation author is the primary author: Trautner, C., Hutchinson, T., Copellini, M., Grosser, P., Bachman, R., and Silva, J. (Accepted). "Developing Ductility using Concrete Anchorage," American Concrete Institute Structural Journal. Trautner, C. and Hutchinson, T., (In Review). "Shake-Table Testing of a Miniature Steel Building with Ductile-Anchor, Uplifting-Column Base Connections for Improved Seismic Performance," Earthquake Engineering and Structural Dynamics. The dissertation author was the primary author on both papers.

VITA

EDUCATION

2007	B.S. in Civil Engineering, Summa Cum Laude, Lehigh University, Bethlehem, Pennsylvania
2009	M.S. in Structural Engineering, Lehigh University
2016	Ph.D. in Structural Engineering, University of California, San Diego

SCHOLARSHIPS AND AWARDS

2007 the	American Society of Civil Engineers, Lehigh Valley Chapter Student of Year
2008-2009	Lehigh University Presidential Scholarship Ben T. Yen Graduate Fellowship
2012-2016	Structural Engineering Departmental Fellowship Hilti Fellowship

EXPERIENCE

2004	Intern, Engineering Department, City of Aspen, Colorado
2005-2006	Engineering Technician, Engineering Department, City of Aspen, Colorado
2007-2008	Research and Teaching Assistant, Lehigh University
2009-2012	Staff Engineer, Simpson Gumpertz & Heger, Waltham, Massachusetts
2012-2016	Research and Teaching Assistant, University of California, San Diego
2015 (fall)	Graduate Student Teaching Associate for SE 180 - Earthquake Engineering, University of California, San Diego
2014-2016	Research and Development Specialist Comtech Manufacturing, Huntington Beach, CA
2016-present	Launch Vehicles Structures Engineer, SpaceX, Hawthorne, CA

PROFESSIONAL LICENSURE

Professional & Structural Engineer: MA Structural PE #50013, CA Civil PE #C82210, IL SE #081.007462

PUBLICATIONS

Peer-reviewed journal articles:

Trautner, C. and Hutchinson, T., (In Review). "Shake-Table Testing of a Miniature Steel Building with Ductile-Anchor, Uplifting-Column Base Connections for Improved Seismic Performance," Earthquake Engineering and Structural Dynamics.

Trautner, C. Zheng, Y., McCartney, J., and Hutchinson, T., (In Review). "Improvements in Frictional Characteristics and Earthquake Motion Fidelity from Repairs to a Servo-Hydraulic Shake Table," Earthquake Engineering and Structural Dynamics.

Trautner, C. and Hutchinson, T., (In Review). "Development, Verification, and Design Application of a Parametric Finite Element Model for Typical Steel Moment Frame Column Baseplate Connections," ASCE Journal of Structural Engineering.

Trautner, C., Hutchinson, T.C., Grosser, P, and Silva, J. (Accepted), "An Investigation of Steel Column Baseplate Connection Details Incorporating Ductile Anchors," ASCE Journal of Structural Engineering.

Trautner, C., Hutchinson, T., Copellini, M., Grosser, P., Bachman, R., and Silva, J. (Accepted). "Developing Ductility using Concrete Anchorage," American Concrete Institute Structural Journal.

Trautner, C., Hutchinson, T., Grosser, P., and Silva, J. (2015). “Effects of detailing on the cyclic behavior of steel baseplate connections designed to promote anchor yielding.” ASCE Journal of Structural Engineering, *10.1061/(ASCE)ST.1943-541X.0001361, 04015117.*

Trautner, C., and Ojdrovic, R. (2014) "Comparison of Directional and Envelope Wind Load Provisions of ASCE 7," Journal of Structural Engineering, 140(4) , American Society of Civil Engineers, Reston, VA.

Trautner, C., McGinnis, M., and Pessiki, S. (2011) "Application of the Incremental Core-Drilling Method to Determine In-Situ Stresses in Concrete," Materials Journal, 108(3) 290-299, American Concrete Institute, Farmington Hills, MI.

Trautner, C., McGinnis, M., and Pessiki, S. (2010) "Analytical and Numerical Development of the Incremental Core Drilling Method of Non-destructive Determination of In-situ Stresses in Concrete Structures," Journal of Strain Analysis for Engineering Design, 45(8), 647-658.

Magazine articles:

Trautner, C., Ojdrovic, R., Schafer, B., and Jones, N. (2013) "Anatomy of a Collapse," *Civil Engineering*, April 2013, pp 66-71.

Refereed conference papers:

Trautner, C., Hutchinson, T., (Accepted) "Seismic Response of a Model Moment-Frame Steel Building with Ductile-Anchor Uplifting Baseplate Connections," 16th World Conference on Earthquake Engineering, Santiago, Chile, January 9-13 2017.

Trautner, C. and Ojdrovic, R. (2016). "Analysis of Large-Diameter Knife Gate Valve Performance," Pipelines Conference, July 17-20 2016, Kansas City, Missouri. American Society of Civil Engineers, Reston, Virginia.

Trautner, C., Hutchinson, T., and Grosser, P. (2014) "Cyclic Behavior of Structural Base Plate Connections with Ductile Fastening Failure: Component Test Results," 10th US National Conference on Earthquake Engineering, Anchorage, Alaska, July 21-25. Earthquake Engineering Research Institute, Oakland, California.

Trautner, C., Ojdrovic, R., Schafer, B, and Jones, N. (2012) " An Investigation of the Collapse of the Dallas Cowboys Practice Facility," 6th Congress on Forensic Engineering, San Francisco, California, October 31 - November 3. American Society of Civil Engineers, Reston, Virginia.

Trautner, C., McGinnis, M., and Pessiki, S. (2011) "The Incremental Core Drilling Method to Determine In-Situ Stresses in Concrete," Conference and Exposition on Experimental and Applied Mechanics, Uncasville, Connecticut, June 13-16 2011. Society for Experimental Mechanics, Bethel, Connecticut.

ABSTRACT OF THE DISSERTATION

Steel Baseplate Connections with Ductile Anchors for the Improved Seismic Performance of Structural Systems

by

Christopher Anderson Trautner

Doctor of Philosophy in Structural Engineering

University of California, San Diego, 2016

Professor Tara Hutchinson, Chair

Baseplate connections, typically consisting of a steel baseplate welded to the terminus of a structural member, concrete anchors, and grout, are common features in buildings and nonbuilding structures. Incorporation of yielding anchors in these critical connections has received increased attention due to good performance observed during recent earthquakes. Such a strategy is attractive as a design approach, as the connections can provide a fuse at the location of seismic input, add to overall system ductility, and may elongate the system period. However, neither a systematic study of connection details that permit robust performance with yielding anchors, nor an investigation of the potential benefits of using such connections to reduce system-level seismic demands has been performed to date.

To these ends, a suite of baseplate component and system-level tests, as well as complimentary high-fidelity numerical simulations, was undertaken to systematically investigate detailing options to help advance the innovative concept of yielding-anchor base connections. First, a program of pseudo-static testing of a typical exposed steel column baseplate connection was executed to understand the details that may influence connection performance, including the anchor type, constituent materials, anchor stretch length, and connection setting arrangement. The impacts of these details on connection strength and rotation capacity are quantified. A novel categorization scheme of connection limit states was developed to track the evolution of damage in the connection. A 3-D, fiber-section numerical model was developed and verified against the results of this test program and several others available in the literature, providing a robust, generalized predictive method for the response of connections with parameters outside the current test program.

Subsequently, dynamic shake table testing of a miniature steel building was undertaken to probe the beneficial system-level effects that ductile, uplifting baseplate connections may have versus traditional "strong anchor" connections and superstructure fuses. These benefits were readily observed in testing and found in numerical analyses including reductions in total base shear of up to 50% and the virtual elimination of residual drift when compared to traditional systems. These results, combined with the ease of post-earthquake repair, demonstrate the usefulness of the ductile-anchor approach in improving overall seismic performance.

Chapter 1: Introduction

1.1 Background

Baseplate connections are ubiquitous in many different structural types: in building structures at the bottom of columns, in nonbuilding structures such as tanks, silos, and equipment at the bottom of steel plate walls, and in nonstructural components where they are anchored to structural elements such as concrete floors and slabs. Regardless of the particular application, baseplate connections generally share some common features: a concrete foundation, a base plate welded to the terminus of a primary structural member, concrete anchors, and grout. Optional features include shear studs or shear keys, "chairs" to increase the anchor stretch length, baseplate stiffeners, and leveling components such as shim plates or leveling nuts. Examples of baseplate connections in building and nonbuilding structures are shown in Figure 1-1. In general, the research in this dissertation is focused on baseplate connections in building structures, however the issues explored in this research are also applicable to other structural types and extensible to other types of connections.

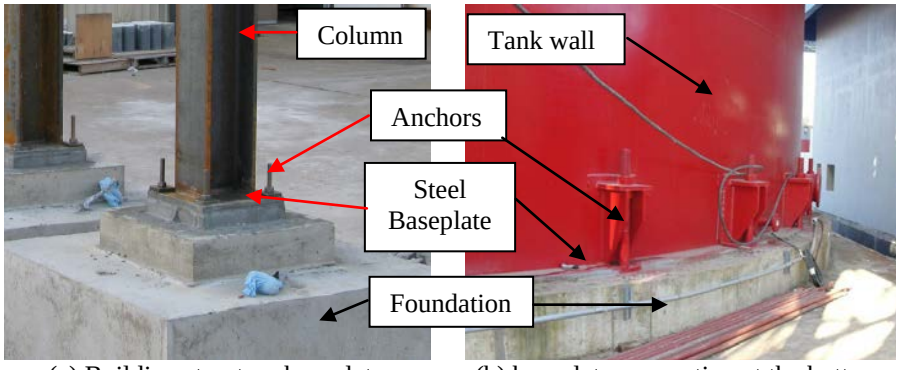

(a) Building structure baseplate connection (from Gomez et al. 2010)

(b) baseplate connection at the bottom of a steel tank (from Soules et al. 2016)

Figure 1-1: Examples of various types of baseplate connections

Within the broad category of "building-type" baseplate connections, connections may be further classified according to the type of seismic force resisting system (SFRS) they support. The connection shown in Figure 1-1(a) is an example of a moment-frame connection, the primary focus of this work. This type of connection resists lateral loads primarily through flexure, as opposed to braced-frame connections which may resist significant shear. Moment frame connections may be designed as either exposed or embedded (Figure 1-2(a)). Embedded connections have the advantage that when used to connect the SFRS, the strength of the slab may be utilized to resist shear demands that must otherwise be taken by the anchors, friction, or a shear key. However, the flexible nature of moment frames often means that the total shear is less than in braced frames, negating some of the need for embedded connections. Moreover, exposed connections have great advantages in terms of simplicity and ease of construction, and as a result they represent a large portion of current construction (Fisher and Kloiber 2006). Exposed connections may be further classified as having flexible, semi-rigid, or rigid baseplates, depending on the fraction of the total connection rotation θ due to deformation of the anchors versus the plate (Figure 1-2(b)). This dissertation focuses on the latter classification, i.e. connections which are dominated by the behavior of the anchors.

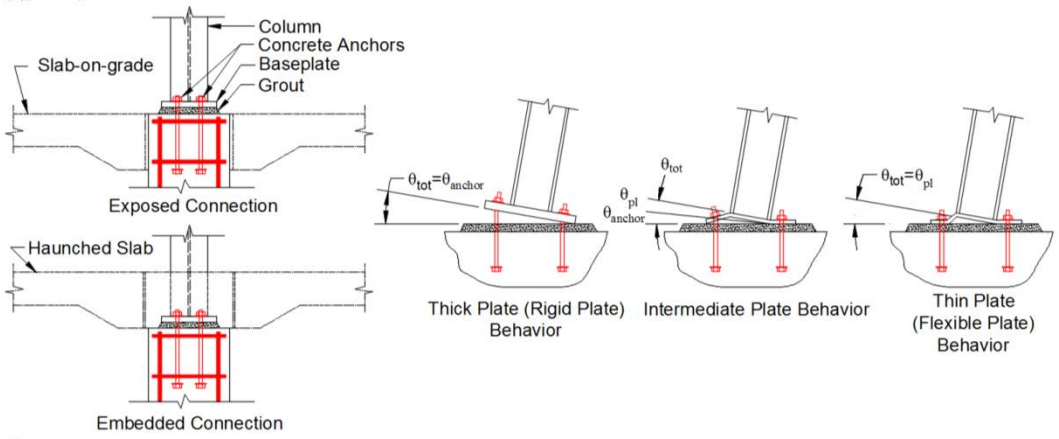

(a) exposed versus embedded (b) "rigid-plate" versus "flexible plate" behavior (after Astaneh et al. 1992)

Figure 1-2: Classification schemes for moment-frame steel column baseplate connections

1.2 State of the Art

The behavior of baseplate connections has long been recognized to play a critical role in the seismic performance of structures. In the last 40 years or so, design of these connections in the United States has emphasized a "strong connection" approach, forcing nonlinear behavior into the superstructure to a large degree, and favoring linear or nearly-linear behavior of the connections under seismic loads. For example, a special moment frame (SMF), as defined by AISC (2010), is expected to dissipate energy during seismic excitation via yielding in the beams near the beam-column connections. The beams may have a reduced section in this region (a detail known as the Reduced Beam Section, or RBS). Unfortunately, the plastic deformation of the superstructure in these regions often leads to sizable residual drifts that may require significant repairs and/or building replacement.

Force-based procedures for the design of baseplate connections in moment frames have been promulgated to the design community based on the results of

extensive testing (e.g. DeWolf 1978, DeWolf and Sarisley 1980, Picard and Beaulieu 1985). Foremost among design guides in current use is the American Institute of Steel Construction (AISC) Steel Design Guide 1, "Base Plate and Anchor Rod Design" (Fisher and Kloiber 2006)[1]. At the time of its publication, this design guide incorporated the building code requirements from the 2005 AISC *Seismic Provisions for Structural Steel Buildings* and the 2002 ACI *Building Code Requirements for Structural Concrete* (AISC 2005c, ACI 2002). At that time, these codes required that anchors for moment-frame SFRSs be designed to resist 110% of the plastic moment of the attached column, or be designed for the amplified seismic load, virtually precluding any anchor or baseplate plasticity.

However, in the last few years, there has been a shift in this paradigm. Impetus for this shift has come partly from observations following the 2010 Maule, Chile earthquake. In that event, anchorages incorporating shear lugs and mild steel anchors with a well-defined stretch length, or region over which plastic deformation is designed and expected to occur, performed very well. Such connections exhibited substantial inelastic deformation without failure (Soules et al. 2016). In some cases, particularly for tanks and other vessels, inelastic behavior in the structure was minimal and the structures were returned to use very quickly by shimming underneath the elongated anchors (Figure 1-3(a)). For connections without a well-defined stretch length, anchor fracture and connection failure were often the result (Figure 1-3(b)).

[1] This document is referred to as AISC DG1 throughout this dissertation

(a) Chimney base connection with ~2 in. of anchor stretch (shims placed after event)

(b) Building column connection with fractured anchor (no stretch length)

Figure 1-3: Comparison of connection performance with and without stretch length in Maule Earthquake (from Soules et al. 2016)

The stretch length provided in well-detailed connections ranged from 8 to as much as 16 bolt diameters (*D*). While many of the cases documented involved anchorage of tanks, vessels, and chimneys, it was noted that similar detailing was routinely used for column bases in steel braced frames and moment frames, wherein a welded anchor chair is provided on either side of the column web. Many of these structures exhibited not only good connection performance, but also good system-level performance. In several cases, rocking motion associated with significant connection uplift was observed. Previous research, described in detail in the following section, has associated such rocking motion with reduced system-level seismic demands.

1.3 Design Code Approach in the United States

In the current building code requirements governing concrete anchor design, ACI 318-14 (Section 17.2.3.4), tension-loaded anchors in structures assigned to high

seismic zones (Seismic Design Categories C, D, E, and F) must satisfy at least one of four pathways for verifying the robustness of the connection to resist seismic tension demands[2]. The first of these (option *a*) is intended to provide ductility in the steel anchor element. The other three options (options *b*, *c* and *d*, respectively) involve development of the yield strength of the attached component, development of the limiting strength of a non-yielding component (e.g., wood), or design for an amplified seismic demand, in accordance with previous editions of the code. The ductile anchor option often yields the lowest required strength and is attractive to designers. The specific requirements of option *a* are[3]:

- The nominal characteristic concrete strength must be equal to or greater than 1.2 times the nominal steel strength of the anchor element (yield criterion).
- To avoid premature fracture of threaded connections, where connections are not threaded over their entire length, the ratio of ultimate to yield stress (f_u/f_y) must be at least 1.3, unless the threaded portions of the anchor are upset.[3]
- To ensure that sufficient yield deformation is developed in the anchor (rod) element, it must satisfy the requirements for a *ductile steel element* and must be provided with a length over which uniform yield strain can develop (*stretch length*) of at least 8 anchor diameters (8D), unless otherwise determined by analysis.

Ironically, this shift to allow an option to provide a ductile anchor with a well-defined stretch length has historical antecedents. Connections with a large, well-defined stretch length were part of widely-used design references dating to the 1960s (Blodgett 1966). The idea of providing ductility in concrete anchorage initially emerged in the mid-1970s in nuclear design provisions, specifically ACI 349 (ACI 1976), although no

---

[2] Components comprising less than 20% of the total seismic force are exempt from this requirement.
[3] Note that the ratio of f_u/f_y is also practically limited to a maximum of 1.9 to prevent yielding at service loads. See ACI 318-14 Section 17.4.1.2.

specific limits were placed on the minimum length over which yield strains could develop. In the 1997 Uniform Building Code, an anchor embedment (rather than stretch length) of 8 diameters delineated an anchor as either ductile or non-ductile, a distinction that was manifested in the form of penalties on the required design force (ICBO 1997). The current stretch length requirement is also consistent with Chilean industrial design practice dating to at least the early 2000s (INN 2003).

1.4 Motivation and Problem Statement

The observed good performance of baseplate connections incorporating a well-defined anchor stretch length in the 2010 Maule, Chile earthquake has started to influence building codes in the United States to allow, and indeed encourage, such a design approach. The same observations suggest that such an approach could be leveraged to reduce overall seismic demands by encouraging rocking motion and energy dissipation at the connection. However, neither a systematic study of "traditional" connection details which permit robust performance, nor an investigation of the potential benefits of using such connections to reduce system-level seismic demands has been performed to date. Therefore, the overarching hypothesis of this research is that that ductility and energy dissipation may be realized through the structural concrete fastening, and features of the design of the connection may be exploited to promote these behaviors. The main objectives of this research are threefold:

1. To investigate common connection details that may contribute to desirable connection behavior in the context of "traditional" connections, i.e. connections that are not specifically designed to undergo uplift or very large rotations in the aim of reducing system-level seismic demands. Such details include anchor type, anchor constituent materials, anchor stretch length, and connection setting arrangement.

2. To develop base connections capable of undergoing uplift and/or very large rotations. These connections include ductile anchors with a large, well-defined stretch length and the ability to be easily repaired and/or replaced following a seismic event.

3. To investigate potential reductions in system-level demands by utilizing ductile, uplifting base connections incorporating the features investigated in (1) and (2) as a part of an overall strategic distribution of ductile elements throughout the structure.

The overarching outcomes of this effort include the improvement of the state of practice with regard to traditional baseplate connections designed for conventional buildings, as well as scientific support in the form of experimental data and numerical simulations validating the benefits of building structures incorporating uplifting connections with ductile anchors. The research is focused primarily on exposed, moment-frame type connections similar to those shown in Figure 1-2(b).

1.5 Summary of Previous Research

1.5.1 Research on Traditional Baseplate Connections

There is a substantial body of work related to the general subject of column baseplate connections in buildings, dating back over 60 years. Salmon et al. (1957) was one of the first papers to give systematic consideration to the analysis and design of such connections, pioneering an analysis procedure for moment loads considering the relative strength of the anchors and grout/concrete system, and a concrete compression resultant located based on rational principles. Such procedures are still in widespread use in design guides such as AISC DG 1, and are discussed throughout this dissertation. Following this effort, allowable grout bearing pressures and allowable anchor rod stresses were used for connection design in the AISC specifications. However, these pressures did not have an experimental basis until the work of DeWolf (1978) and DeWolf and Sarisley (1980). Together, these two studies performed approximately 35 tests on moment-frame type connections, with the primary goal of evaluating the AISC allowable stress provisions and new ultimate stress design methods. While these tests were invaluable as the first exploration of the different failure mechanisms possible in baseplate connections, they were small-scale. The largest column tested was an HSS4x4 square section, far smaller than sections typically used for main column members in building structures.

In the following years, there were a large number of follow-up investigations performed using large- or full-scale column sections. The current research is related primarily to the full-scale seismic behavior of exposed, moment-frame baseplate connections. Therefore, similar experimental work under lateral loads was of primary

interest. Grauvilardell et al. (2005) provides an extensive summary of many of the papers that have been published on this subject, including excellent synopses of much of the experimental work that has been performed. Of the studies reviewed as part of that work, those considered to be most pertinent to the current work were selected for more detailed study and consideration. Such studies included those that included lateral loads, used column sizes that could be considered at least half scale (based on the author's judgment), and consisted of at least two tests. These studies are summarized in Table 1-1, below. It should be noted that the majority of these tests incorporated mild steel baseplates and steel structural sections. The yield stress of the anchors varied from about 36 ksi to over 100 ksi. Individual studies of particular import to the present work are shaded in the table and discussed below.

Table 1-1: Summary of previous large-scale research efforts on exposed, moment-frame steel column baseplate connections under lateral loads

Citation	Number of Tests	Anchor Types	Anchor Diameter, in.	Base Plate Thickness Range, in.	Load protocol	Major Experimental Variables
Akiyama et. al. (1984)	25	Cast-in -anchor block -deformed round anchor rods	0.79 - 1.42	0.47 - 2.36	Cyclic	-End detail and depth of rod embedment -Shape of column and base plate
Picard and Beaulieu (1985)	15	Cast-in (threaded both ends)	0.75	0.43 - 1.14	Monotonic	-Column section -Number of anchor rods
Sato (1987)	6	Cast-in -Standard -Pre-tensioned	1.18 - 1.65	1.26-2.40	Unknown	-Size of base plate -Column axial load -Yield ratio
Hon and Melchers (1988)	26	Cast-in (different sizes)	0.79 - 0.94	0.47 - 1.18	Monotonic and Cyclic	-Base plate thickness -Anchor rod size
Astaneh et al. (1992)	6	Cast-in	0.75	0.25 - 0.75	Cyclic, with Axial	-Amount of axial load -Base plate thickness
Igarshi et al. (1992)	4	Cast-in (4 types, different levels of pretension)	1.18	1.42	Cyclic	-Anchor type (hooked, threaded, pretensioned, etc.)
Melchers (1992)	10	Cast-in (different sizes, yield strength)	0.47 - 0.63	0.24 - 0.47	Cyclic	-Base plate thickness -No. and size of rods -Anchor rod yield strength
Targowski et al. (1993)	12	Unknown (assume cast-in)	0.63	0.24 - 0.39	Monotonic and Cyclic	-Column section -base plate thickness
Wald et al. (1994)	14	Unknown (assume cast-in)	0.94	0.39 - 0.78	Monotonic, with Axial	-Baseplate thickness

Table 1-1: Summary of previous large-scale research efforts on exposed, moment-frame steel column baseplate connections under lateral loads (continued)

Citation	Number of Tests	Anchor Types	Anchor Diameter, in.	Base Plate Thickness Range, in.	Load protocol	Major Experimental Variables
Akiyama et al. (1998)	2	Cast-in	1.3	1.18 - 2.36	Cyclic	-Baseplate thickness
Burda and Itani (1999)	6	Cast-in	1.5	0.75 - 1.25	Cyclic	-Baseplate area -Baseplate thickness
Fahmy (1999)	3	Cast-in	1.25 - 2.0	2.75	Cyclic	-No. of anchor rods -Weld material
Adany et al. (2000)	5	Cast-in	Unknown	0.47 - 0.98	Cyclic	-Baseplate thickness -Pretensioning
Li et al. (2000)	7	Cast-in (into cast steel base)	1.18	2.16	Cyclic, with Axial	-Column section -Anchor rod strength
Lee et al. (2001)	4	Cast-in	1.25 - 2.0	2.25	Cyclic	-No of anchor rods -Weld material
Miyasaka et al. (2001)	8	Cast-in	Unknown	0.79 - 2.36	Monotonic	-Base plate thickness -Location of anchor rod
Somiya et al. (2002)	12	Cast-in	0.87	1.42 - 1.77	Cyclic, with Axial	-Axial load and load rate -Plate and tube thickness
Gomez et al. (2010)	7	Cast-In Place	0.75 - 1.25	2	Cyclic, with Axial	-Imposed gravity load -Anchor size -Anchor configuration

Picard and Beaulieu (1985):

This study, performed in Canada, was one of the first systematic experimental investigations into the behavior of exposed moment frame baseplate connections under lateral loads. In this study, the authors performed 15 pseudo-static tests incorporating column sizes between HSS 6x6x12 and W6x25, baseplate sizes between about 7/16 and 1-1/4 in., and 3/4 in. diameter mild steel anchors. Loading conditions included only monotonic concentric axial loads, eccentric axial loads, and lateral-only loads. The authors back-calculated fixity factors for each test, and found that axial compression greatly increases the flexural stiffness of the connection. In addition, they evaluated contemporary methods of determining connection strength, and found them to be reasonable and conservative.

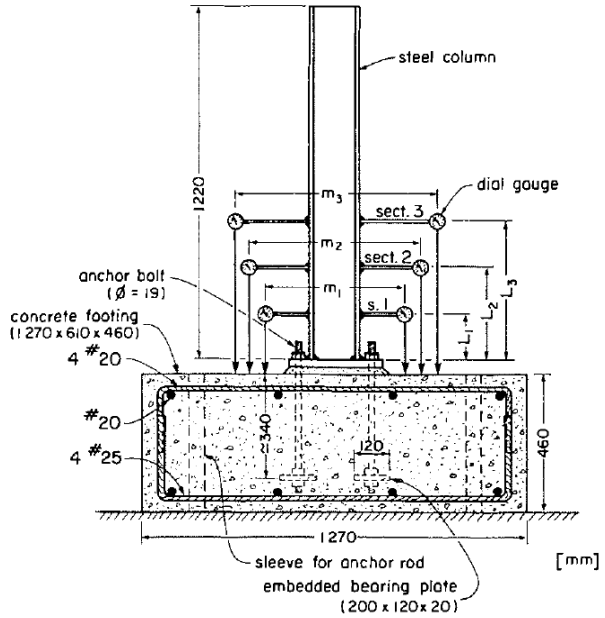

Note: units in [mm]

Figure 1-4: Diagram of experimental specimen of Picard and Beaulieau (1985)

Astaneh et al. (1992):

Astaneh, Bergsma, and Shen performed six pseudo-static tests under cyclic lateral load. The column was a W6x25 stub, and the anchor size was 3/4 in. for all tests. The baseplate thickness was varied between 0.25 and 0.75 in., with a test with and without axial load for each thickness tested. Interestingly, this is one of the few tests programs that explicitly stated the setting method used for the tests. In this case, setting nuts and washers were used below the baseplate. The test setup and applied rotation history are shown in Figure 1-5. The loading protocol is of particular interest in this study, as it represents the first time a gradually-increasing, repeated cyclic load protocol was used for the testing of baseplate connections.

This study found that existing design guidelines were sufficient for connections with relatively thick baseplates; however this study was the first to categorize baseplates according to the relative strength and stiffness of the constituent parts. The authors also gave a detailed description of the limit states observed, however the connection rotations at which each limit state was observed was not recorded and no formal categorization scheme of limit states was proposed.

The authors recommend different design formulas depending on the thickness of the baseplate under consideration, as shown in Figure 1-6. This approach is attractive versus the design methods that were available at the time, due to the potential increases in accuracy from more detailed considerations of the bearing stress distribution. However, it is practically difficult to say *a priori* which way a baseplate will behave due to the interplay of the baseplate thickness, baseplate plan dimensions, and the types and

locations of yield lines that will eventually develop, therefore this approach was not widely adopted. The authors note that the "thin plate" behavior (far right in Figure 1-6) has a reduced chance of achieving non-ductile limit states such as anchor fracture, although weld fracture was not observed during this testing. In their summary, the authors postulate that more flexible base connections are a plausible way to reduce overall structural demands and their use should be recommended for high-seismic areas.

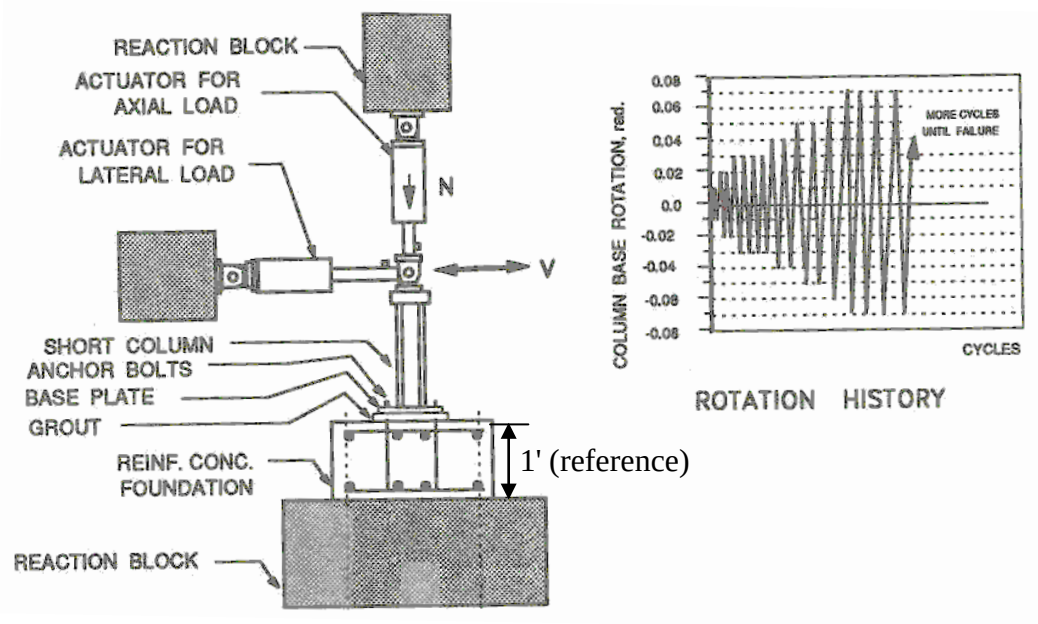

Figure 1-5: Diagram of experimental specimen (from Asteneh et al., 1992)

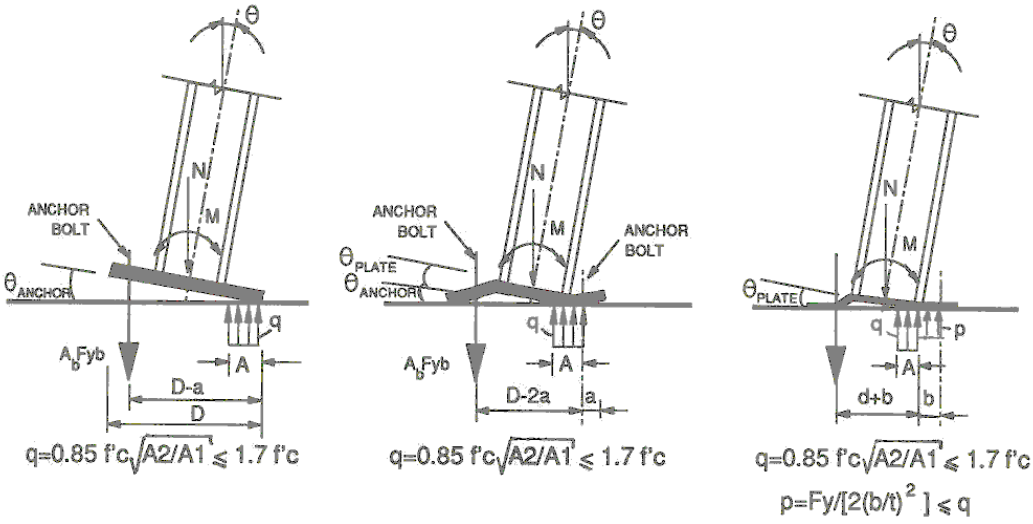

Figure 1-6: Proposed behavior-dependent model for baseplate connection design (from Asteneh et. al., 1992)

Fahmy 1999:

The relatively small experimental portion of this work was part of a larger project related to the analysis of steel column baseplate connections. Although only three tests were carried out, these tests are unique in that they are both full-scale and relatively large, utilizing a W10x77 column with a 2-3/4 in. baseplate, and anchors up to 2 in. nominal diameter. The tests conducted as part of this work used a relatively tall column stub, and were subjected to cyclic lateral load only. This testing program was the first to use the now-common SAC[4] steel testing protocol as applied to steel column baseplate connections (Clark 1997). In addition to the anchor- and grout-related failure mechanisms observed in other tests, one of the tests conducted underwent sudden and catastrophic weld fracture at a fraction of the rotation of the other tests. A second test underwent

[4] An acronym for the joint venture of organizations responsible for the development of this protocol: Structural Engineers Association (SEA), Applied Technology Council (ATC), and the Consortium of Universities for Research in Earthquake Engineering (CUREE).

limited weld cracking. The cause of this was believed to be weld electrode with poor toughness and poor weld detailing. Although the research program as a whole concluded that existing methods for the design of these connections were generally adequate, this study brought attention to detailing-related limit states that may significantly hinder the ability of the connection to develop large rotations that may be otherwise expected.

Gomez (2010):

This primarily experimental program involved testing of seven specimens. Primary experimental variables included: the type of loading (monotonic and cyclic lateral loading with and without axial load), the number of anchors (4 and 8 anchor patterns), and the anchor grade (ASTM F1554 Gr. 36 and Gr. 105 anchors were tested). The column size, constant for all tests, was a W8x48. The test setup used a long-stroke hydraulic actuator to impart lateral loads at the approximate inflection point of a typical story, estimated to be 2/3 of the story height. A spreader beam was used to apply vertical loads for several of the tests. A schematic of the test setup is shown in Figure 1-7. The primary purpose of this testing was to determine the effect that the experimental parameters had on the strength and stiffness characteristics of these connections. A companion study by one of the co-authors used the data from this study and the data from the Picard and Beaulieu study to develop a method for determining the stiffness associated with first connection yield (Kanvinde et al. 2012).

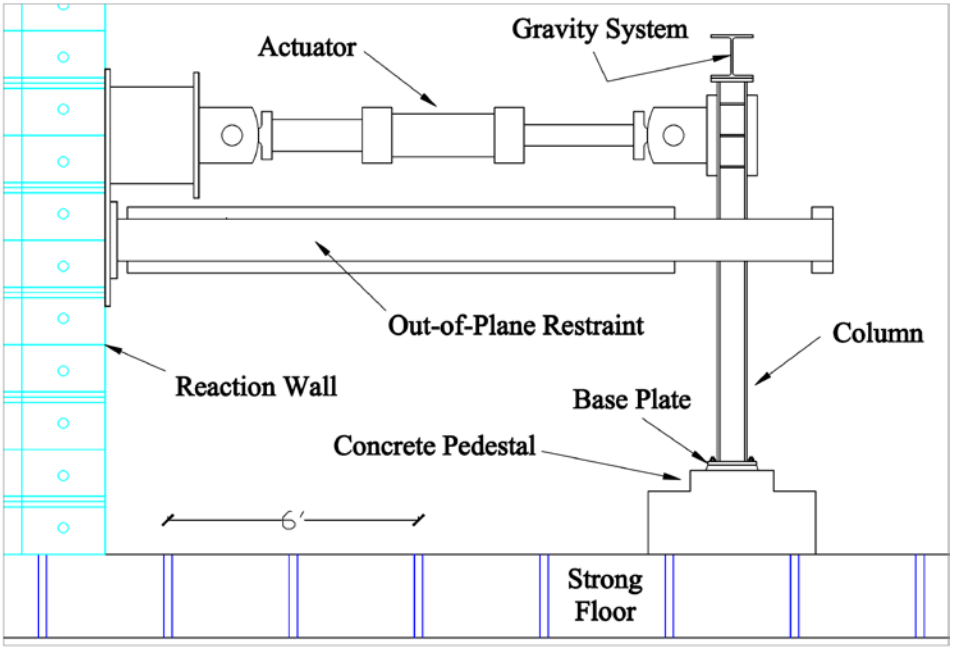

Figure 1-7: Diagram of lateral and vertical loading system used for W8x48 connection tests (from Gomez et. al., 2010)

1.5.2 Research on Ductile Baseplate and Rocking Systems

The tests discussed in the previous section were primarily intended to improve design and analysis procedures for column baseplate connections for typical SFRSs with energy dissipating features located in the superstructure. In contrast to this paradigm, there has been a limited amount of work done on systems that leverage uplifting and/or rocking behavior as a method to reduce overall seismic demands.

Clough and Huckelbridge (1977):

This study represents the first large-scale experimental investigation into steel moment frame systems with columns allowed to uplift. The test building consisted of a three- three-story moment frame at approximately half-scale. The test building was three-dimensional, although horizontal excitation was in one direction only. The excitation

records used for this testing program were not time-compressed for exact dimensional similitude, meaning that this test is an example of the "miniature building" approach that has been subsequently used for the economical testing of earthquake engineering structures (Restrepo et al. 2014). An elevation of the test structure is shown in Figure 1-8. The structure was tested in configurations where the columns were and were not allowed to uplift. In the cases where uplift was allowed, the base connections consisted of relatively complex "vertical roller" systems, as shown in the figure. These connections provided the required shear resistance, but did not prevent uplift or rotation.

The results of this testing indicated that inertial forces were reduced up to about 30% for the configurations where uplift was allowed versus otherwise identical tests with fixed bases, although this was somewhat dependent on the exact motion characteristics. Maximum strain ductility demands in the superstructure were reduced from approximately 5 to less than unity. However, maximum story drifts increased significantly for the cases where uplift was allowed. The authors concluded that allowing column uplift could allow more economical designs for building structures, and pursued the larger-scale test program described in the following section.

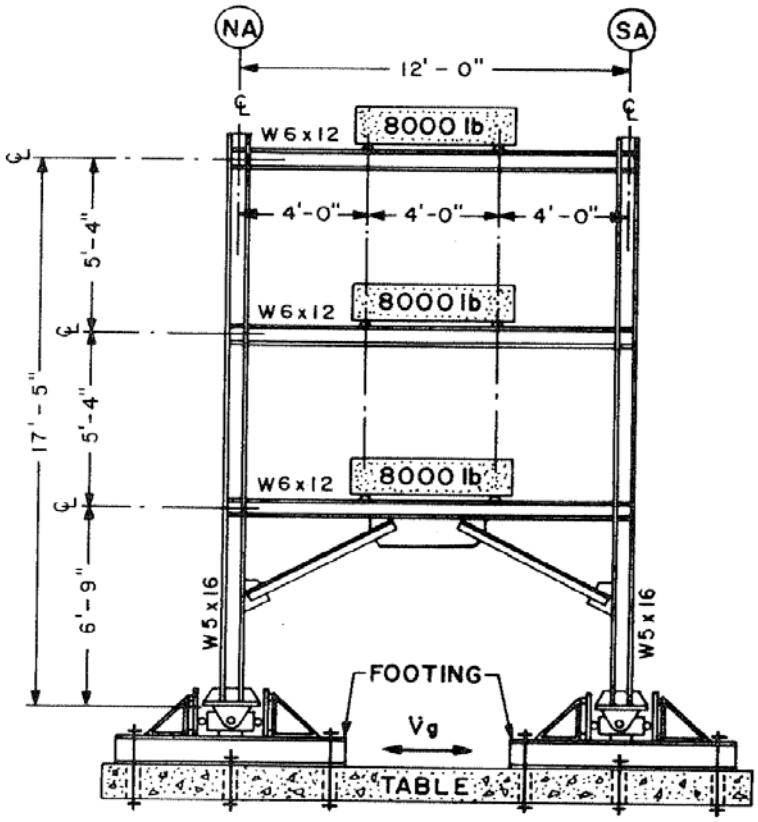

Figure 1-8: Elevation of test structure showing roller-type base supports (from Clough and Huckelbridge 1977)

Huckelbridge (1977):

Hucklebridge tested a 1/3 scale, 9-story, 3-bay structure under a variety of different earthquake motions. In contrast to the previous study, the uplifting connections tested here were relatively simple, consisting of a single, long, thin plate connection welded to the column base on one end and bolted to the shake table on the other. Flexure in this plate allowed the columns to uplift while restraining sliding-type motion by opposing the direction of the plates throughout the structure. The overall structural dimensions and a detail of the connection are shown in Figure 1-8. This structure was designed to be relatively "stocky", under the assumption that if rocking-type motion

could be beneficial for structure, it would almost certainly be beneficial to structures with more tall and narrow aspect ratios.

The structure was tested under almost 70 different motions, although data was reduced and presented for only about 11 of these motions. Internal forces were reduced for the uplifting configurations in almost all cases. The authors concluded that the rocking paradigm was desirable for a number of different reasons, most importantly that a rocking system establishes a "ceiling" over which increased motion may result in increased displacements but not increased internal forces. The authors present a number of design guidelines as part of the work. Chief among these is suggesting that the restraint to uplifting motion should be relatively weak, but that some energy dissipation device could be considered for this location.

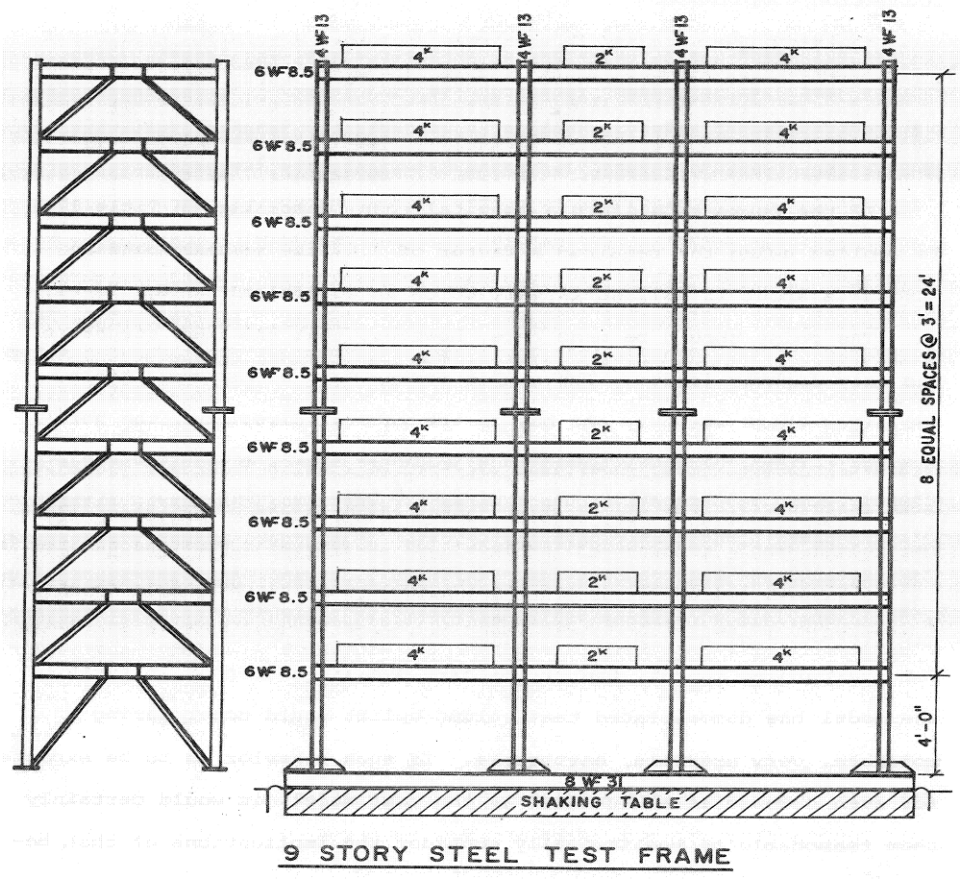

(a) Elevation view

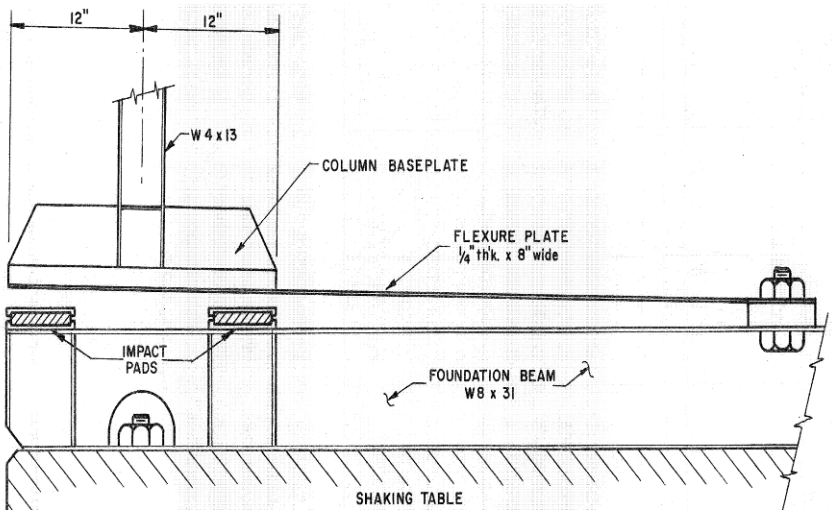

(b) Detail of uplifting connection

Figure 1-9: Schematics of test structure of Hucklebridge (1977)

Midorikowa et al. (2006, 2008):

This work involved testing of a 1/2 scale, 3-story, 1-bay braced-frame structure in two configurations: fixed-base and with columns allowed to uplift. The uplifting mechanism was similar to that used by Hucklebridge (1977), and consisted of a cruciform-shaped, very thin baseplate attached securely to the shake table structure. The overall structural dimensions and uplifting mechanism are shown in Figure 1-10. In contrast to Clough and Hucklebridge (1977), the motion for this test was time scaled by $1/\sqrt{2}$ in an effort to maintain experimental similitude. The authors found that peak base shear could be reduced up to about 50%, depending on the maximum amplitude of the motion. The thin-baseplate approach was noted to give good performance and restrain sliding motion effectively. However, the authors note that there were high strains achieved in these components.

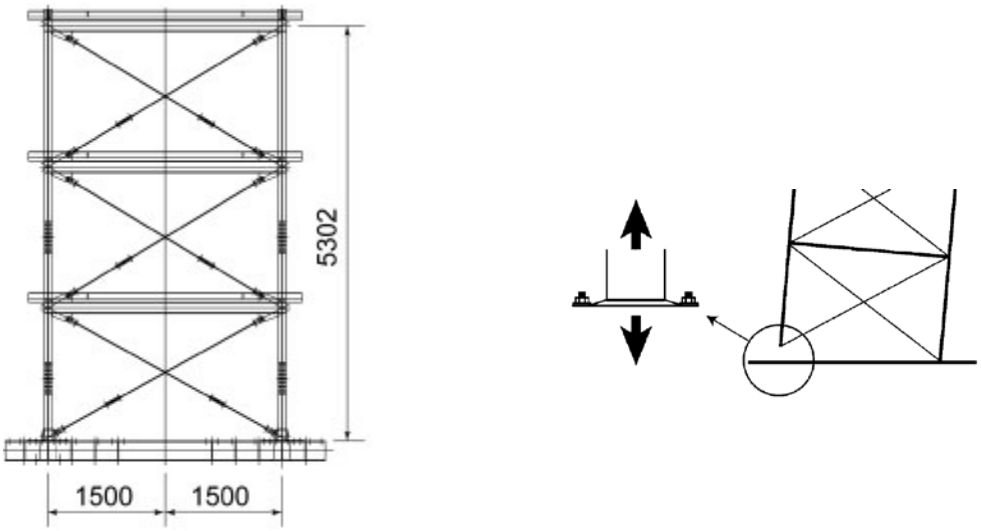

(a) overall structure dimensions for SFRS system in direction of shaking [dimensions in mm]

(b) baseplate uplift mechanism

Figure 1-10: Rocking concept of Midorikowa et al. (2006)

1.6 Synthesis of Existing Studies

From the preceding sections, it is apparent that there is significant research regarding the improved performance of rocking and uplifting-column frame systems versus traditional "fixed-base" systems. The observations from the 2010 Maule, Chile earthquake strongly indicate that base connections with anchors designed to yield (particularly those with a well-defined stretch length) are conducive to desirable connection and system-level behavior. To the author's knowledge, no research has been performed to date specifically regarding uplifting-column or rocking systems incorporating ductile anchors as part of the base connection design. There are a number of potential advantages to such a ductile-anchor uplifting-column system, but there are also significant technical challenges that have not been addressed in the existing literature. In particular:

- As noted by Hucklebridge, (1977), the base connection is an ideal place for an energy-dissipating element, owing to its location at the point of seismic input and the potential for stable rocking motion to develop. A ductile anchor loaded in tension provides such an element. However, it is not clear what the mechanical properties or stretch length of such anchors must be to perform this function.
- Concrete anchors are easily replaced as a sacrificial element when properly designed, allowing fast, economical repair of the structure when compared to plastic behavior in the superstructure. A potential process for replacing concrete anchor inserts in removable anchors is shown in Figure 1-11. To date there has been no research on the design of such anchors.

- In contrast to other methods of seismic building protection such as base isolation, supplemental dampers, or even other rocking systems such as those presented by Clough and Hucklebridge (1977) or Midorikowa (2006), the use of ductile anchors requires a minimum departure from current design and construction practice. However, there has been little study performed on connection details which will allow robust performance of such connections.

Each of these challenges is addressed within the scope of the objectives of this dissertation identified in Section 1.4 .

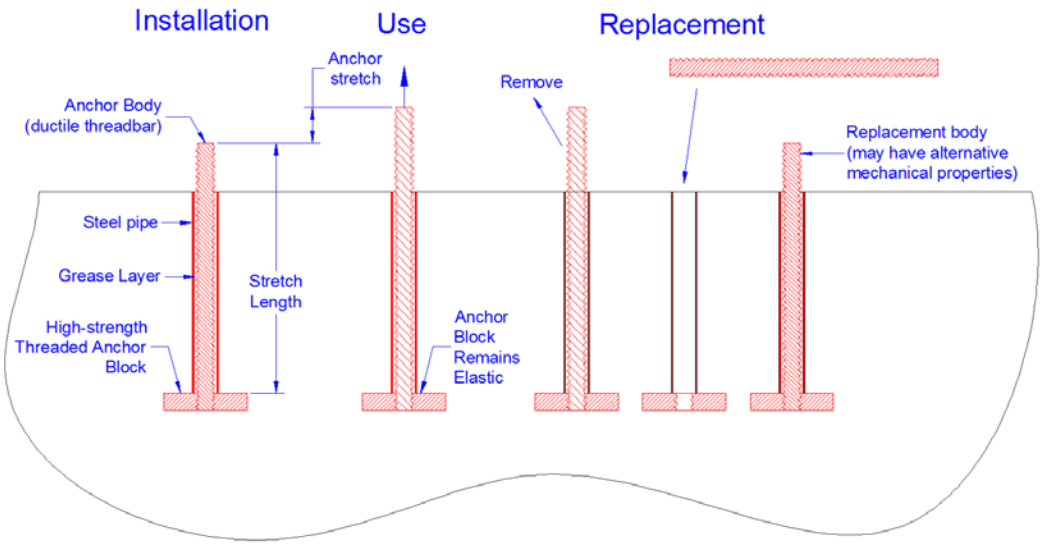

Figure 1-11: Repair of removable concrete anchors using replaceable inserts

1.7 Scope and Organization of Dissertation

This dissertation is divided into six chapters, as follows: Chapter 1 provides an introduction to the problem and clearly defines the objectives of the work. Chapter 2 describes monotonic tension testing and modeling of concrete anchor materials, as well as tension testing of reference anchors in free-field, uncracked concrete. Chapter 3

presents data from component-level experiments on "traditional" steel column baseplate connections, i.e. connections that attempt to promote desirable connection performance by preventing anchor fracture, but are not specifically designed or expected to improve overall system-level structural performance. This chapter also presents a systematic analysis of the experimental data presented in Chapter 3. Chapter 4 includes the development of a numerical model that is verified against the experimental work presented in Chapter 3, as well as several the results of other large-scale testing programs. Chapter 5 describes the design, development, dynamic testing, and analysis of a miniature steel building incorporating ductile, uplifting base connections designed to reduce system-level seismic demands. A summary of significant findings, conclusions from the overall work, and impacts on design practice are presented in Chapter 6. Finally, three appendices are included, providing the design and construction drawings of the component tests and miniature steel building, as well as a listing of the keywords used in the numerical models of the anchor tension tests, component connection tests, and miniature building.

Chapter 2: Anchor Reference and Anchor Material Tensile Testing

2.1 Introduction

Anchor reference and tensile testing was performed in parallel with the pseudo-static baseplate connection component testing described in the following Chapter. Herein, "reference tests" refer to tensile loading of anchors embedded in reinforced concrete until failure. "Tensile tests" refer to testing of anchors or anchor constituent parts (mainly allthread used for adhesive anchors) in a universal testing machine.

2.2 Tensile Test Series

2.2.1 Background and Purpose

To be effective, stretch length must be specified in conjunction with some measure of anchor ductility; i.e., an unyielding element would not benefit from the provision of stretch length. ACI 318-14 defines a *ductile steel element* as "an element with a tensile test elongation of at least 14 percent and a reduction in area of at least 30 percent", where the tensile test elongation "should be measured over the gauge length specified by the appropriate ASTM standard for the steel" (ACI 2014). Anchors meeting the requirements of American Society for Testing and Materials (ASTM) A307-12 are specifically considered by ACI 318 as ductile steel elements. ASTM A193 B7 all-thread is also often used in conjunction with adhesive systems to form bonded anchors (ASTM 2009). However, the preeminent specification for concrete anchors in the US is ASTM F1554, which provides requirements for concrete anchor bolts, all-thread, and hooked bars (ASTM 2007).

Clearly, there is an essential interplay between the stretch length requirements of ACI 318 and the anchor material specifications in ASTM standards. However, methods for measuring the tensile test elongation vary. For example, ASTM A193 B7 uses a free length of 4D when evaluating elongation, F1554 uses 8 in., and A307 lacks specific elongation requirements unless machined specimens are tested. This means that anchors conforming to different standards may provide different levels of performance in terms of preventing anchor fracture, particularly when used in conjunction with a finite stretch length prescription such as that contained in ACI 318. A more fundamental problem is that ASTM F1554 elongation requirements currently apply only to the hot-rolled raw material and not the finished product[5]. When F1554 all-thread is produced, cold drawing of the rod is often (though not always) performed in an effort to maintain thread tolerances over long stick lengths. Cold working may increase the strength and decrease the ductility of the finished product beyond the ostensible requirements of the standard, as demonstrated by the testing presented below.

Limit states applicable in the context of concrete anchorage design include anchor yielding and anchor fracture. Anchor fracture may be described as the ultimate limit state, since in the context of the current discussion; failure of an anchor may precipitate catastrophic failure of other parts of the structural system. A second type of limit state is related to anchor serviceability. It is well known that prior to fracture of an anchor or bolt, sufficient plastic deformation of the threads may render the part non-functional, as

---

[5] ASTM F1554 requirements were recently changed to enforce ductility measurements on the basis of the finished product, partly on the basis of the work presented herein. Depending on when these changes formally take effect, the problems with the standard identified herein may or may not still be relevant.

the thread deformation will cause nuts to bind. This limit state is particularly important for anchors that are designed to have controlled yielding over a defined stretch length. One may easily imagine that when confronted with anchors that have plastically deformed, two issues are of concern, namely: 1) How much of the anchor deformation capacity remains, i.e. will subsequent loading cause anchor fracture? 2) Are the anchors still serviceable? That is, are the anchors still capable of accepting new nuts and sufficiently serving their purpose as fasteners? The answers to these questions will determine whether anchor replacement is necessary. Reliable answers to these questions have important economic implications, as anchor replacement at industrial facilities was a significant source of cost following the 2010 Maule, Chile earthquake (Soules et al 2016).

Considering these limit states, the goals of the tensile testing program were to:

1. Determine whether material provided under current, common ASTM standards is consistent with ACI's definition of a "ductile steel element",
2. Determine the effectiveness of the 8D requirement by examining the relationship between stretch length and elongation at fracture for several materials, and
3. Determine the elongation associated with nut binding on threaded parts (i.e. the serviceability limit state).

To accomplish these, all-thread and headed anchors between 3/4 and 1-1/2 in. (19 - 38 mm) diameter from three different manufacturers were tested at a number of different stretch lengths below, at, and above 8D. Specimens were tested in a tensile test machine monotonically, as shown in Figure 2-1. Special fixtures, consisting of a welded, threaded

attachment were placed in the machine grips designed to ensure that the stretch length was as close to the measured free length as practicable. Data recorded during the test included head displacement, force, and strain from an extensometer. Additionally, an ASTM A563 heavy hex nut was spun up and down each specimen continuously during testing, and the instance at which the nut could no longer be spun by hand was recorded. Testing was displacement-controlled, and displacement rates were well below that required by standards such as ASTM F606 to ensure pseudo-static behavior (ASTM 2011).

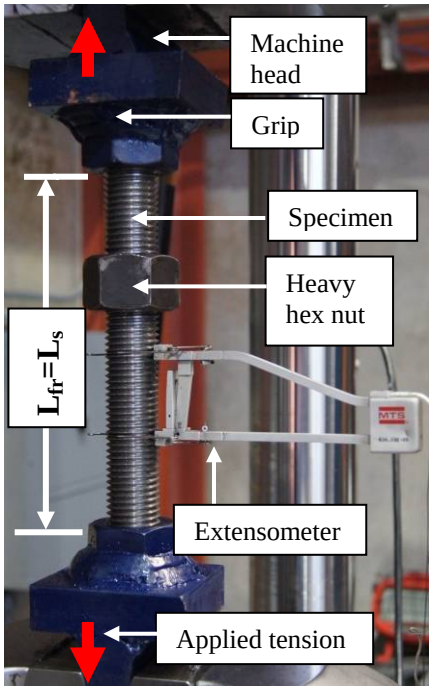

Figure 2-1: Photograph of typical tension test setup showing well-defined free length

It is important to recognize the relationship between the defined lengths in the tensile tests and actual anchors embedded in concrete. *Stretch length* L_s is specifically defined by the commentary of ACI 318-14 as "the length of an anchor over which

inelastic elongations are designed to occur for earthquake loadings" (ACI 2014). If plastic deformation of the anchor occurs beneath the concrete, stretch length may not be the same as the *free length* L_{fr}, herein defined as the length of the anchor above the concrete. This phenomenon, illustrated in Figure 2-2, is known as strain penetration, and is the subject of discussions later in this chapter and elsewhere in the dissertation. In these tension tests, L_{fr} is assumed to be the same as L_s, given that strain penetration into the threaded grips was observed to be minimal.

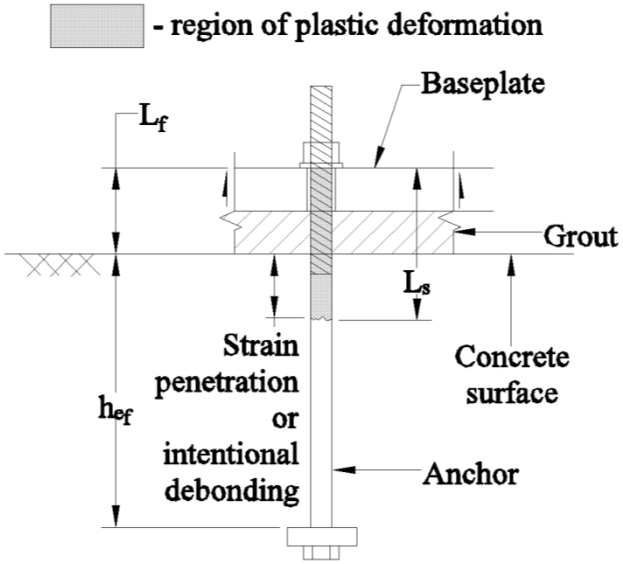

Figure 2-2: Definition of free length L_f and stretch length L_s

2.2.2 Scope of testing

More than 90 tension tests on all-thread and headed anchors of four different diameters at stretch lengths ranging from 2D to 16D were conducted (Table 2-1). In general, 2-3 tests were performed for each test configuration, except for the ASTM F1554 Gr. 55 and ASTM A193 B7 materials, where only one sample was available for

each free length. It should be noted that the behavior of the HR F1554 Gr. 36 headed anchors from Supplier 1 was very similar to that of Supplier 3 HR F1554 Gr. 36 all-thread. The behavior of other headed anchors and hooked anchors are expected to be similar, given like materials and manufacturing methods. Note that the ASTM F1554 material tested would also conform to ASTM A307 under the conditions tested.

Table 2-1: Tensile test matrix

Material short name[a]	Supplier	Finished material[b]	ASTM standard (from supplier)	Additional standard compliance	Diameter tested, in.[c]	Approx. range of L_s tested
CW Gr 36	1	Cold-worked mild carbon steel AT	F1554 Gr 36	A307	0.75, 1.0, 1.25, 1.5	2D-11D
HR Gr 36	1	Hot-rolled carbon steel HA (no cold work)	F1554 Gr 36	A307	0.75	10.7D
CW-A Gr 36	1	Cold-worked, annealed mild carbon steel AT	F1554 Gr 36	A307	0.75, 1.0, 1.25	2D-11D
CW Gr 55	1	Cold-worked Gr 55 modified mild steel AT	F1554 Gr 55	--	0.75, 1.25	2D-11D
CW Gr 36	2	Cold-worked mild carbon steel AT	F1554 Gr 36	A307	0.75	10.7D
CW A307	3	Cold-worked mild carbon steel AT	A307	--	0.75	10.7D
HR Gr 36	3	Hot-rolled carbon steel AT (no cold work)	F1554 Gr 36	A307	0.75, 1.0, 1.25, 1.5	2D-16D
A193 B7	4	Quenched and tempered Cr-Mo steel AT	A193 B7	--	1.0	3D-8D

NOTES: a) CW: cold worked, CW-A: cold worked, annealed, HR: hot-rolled (no cold working performed) b) AT = all-thread, HA=headed anchor with upset threads c) 1 in. = 25.4mm

2.2.3 Test results

Mechanical behavior

Tension test data are presented with two pairs of axes: force – displacement (lower left), and stress – elongation (upper right). It is important to note that the elongation *EL* of the top x-axis represents the *equivalent uniform strain* on the bar over a gage length equal to the stretch length, and not the actual distribution of strain in the bar,

which may be highly non-uniform, particularly as the bar approaches fracture. Elongation is obtained by dividing the measured anchor deformation by the stretch length:

$$EL\ (\%) = \Delta L/L_s*100 \qquad \text{Eq. 2-1}$$

The shape of the curves, as well as the relative locations of critical points such as yield strength, ultimate strength, and fracture were generally similar for all diameters tested, as typified by data from the 1 in. (25 mm) diameter bars at an 8 in. (203 mm) stretch length (Figure 2-3). The cold-worked, annealed (CW-A) and hot-rolled (HR) F1554 material as well as the A193 B7 material exhibited well-defined yield plateaus, whereas the cold worked (CW) material, regardless of nominal grade, did not. The A193 B7 material generally had elongation at fracture between that of the CW and HR mild steel material. Fracture surfaces for these four materials were consistent with typical characteristics of the observed behavior (Figure 2-4). CW-A and HR fracture surfaces were generally cup-and-cone, typical of mild steel plasticity. The CW fracture surfaces were generally jagged and flattened, consistent with significantly work-hardened mild steel, whereas A193 B7 surfaces were generally very jagged with several intersecting failure planes, typical of quenched and tempered alloy steels. The length over which large plastic deformation occurred, as inferred by a reduction in area of at least 10%, was generally short for the CW and A193 B7 steels (1-2 diameters on either side of the fracture surface), while significantly longer for the HR and CW-A steels (3-4 diameters or more from the fracture surface).

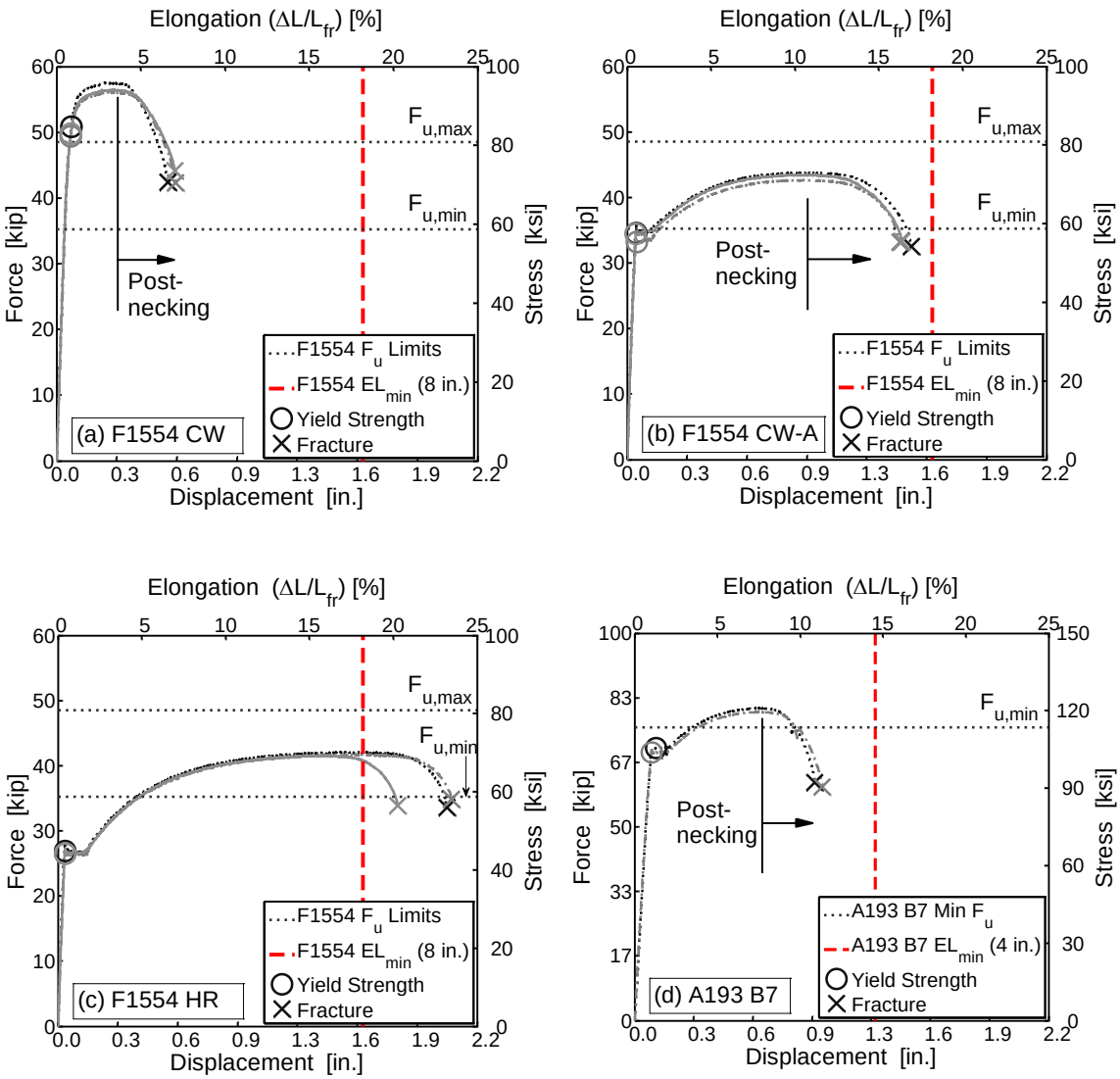

NOTES: 1in.=25.4mm, 1kip=4.448 kN, 1ksi=6.895MPa. Y-axes in (d) varies from (a)-(c)

Figure 2-3: Typical force-displacement and stress-elongation response for 1 in. (25mm) diameter samples, L_s =8 in. [203mm]: (a) F1554 Gr. 36 CW, (b) F1554 CW-A, (c) F1554 HR, (d) A193 B7

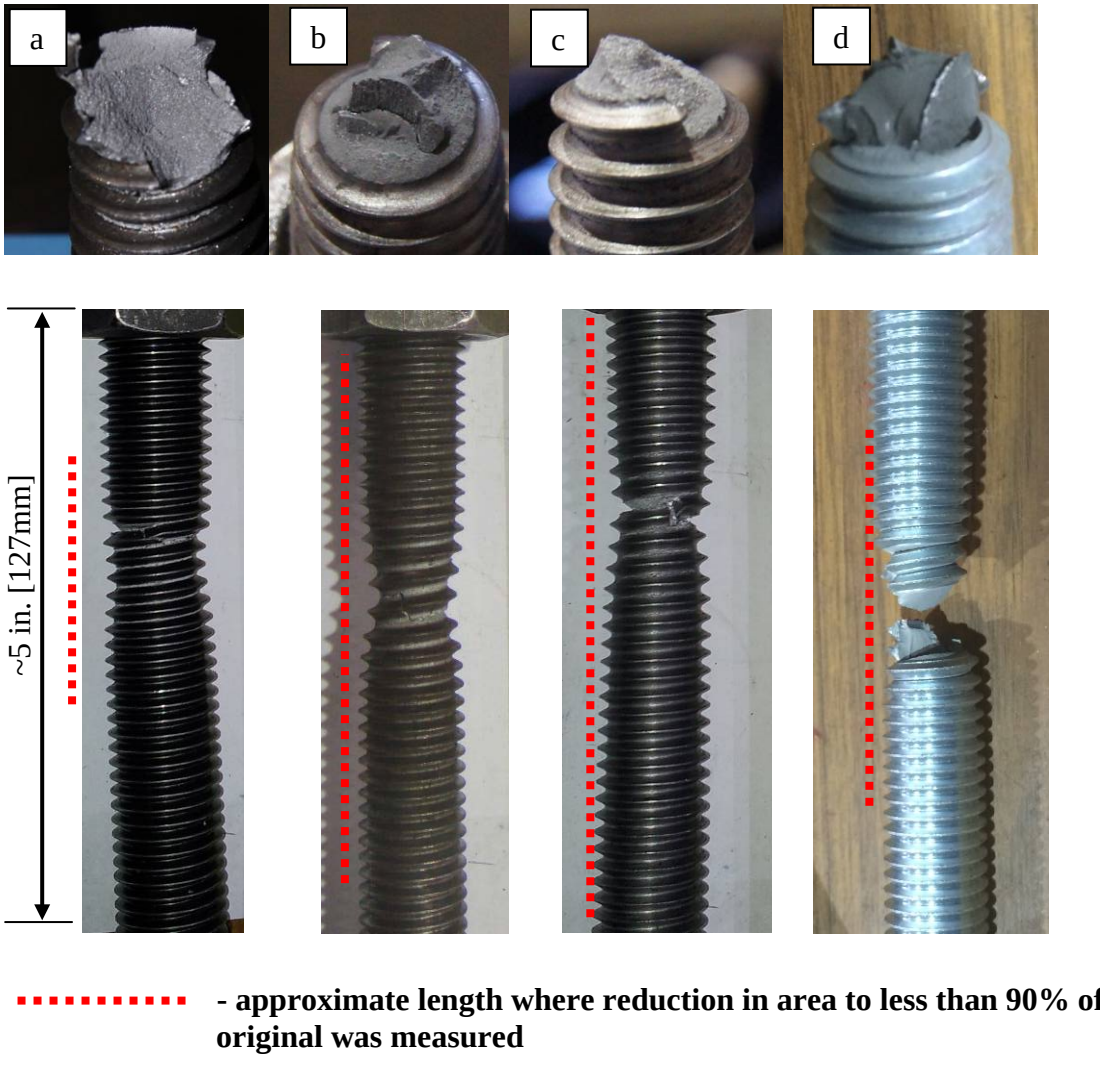

Figure 2-4: Typical fracture surfaces and regions of significant plastic flow: (a) F1554 Gr. 36 CW, (b) F1554 CW-A, (c) F1554 HR, and (d) A193 B7

The data in Figure 2-3 highlight three problems with the ACI 318 definition of a "ductile steel element" without regard to a specific ASTM standard. First, ASTM A193 B7 has a requirement for 16% minimum elongation, but this applies for tests with a free length of 4D, in this case 4 in. (102 mm)[9]. At the 8 in. (203 mm) stretch length (8D for this diameter), the measured elongation was about 12%. Relying on the minimum elongation of 14% as stated by ACI, which ASTM A193 B7 provides at a stretch length

other than 8D, would result in an unconservative overestimate of the deformation capacity at an 8D stretch length. This problem would likely become more pronounced at larger diameters. Second, the ASTM F1554-07 standard has only an ostensible elongation at fracture requirement. As currently stated, it pertains only to the raw material from which the anchors are made, but it does not apply to the finished product. This results in a large and uncontrolled range of elongation at fracture of the final F1554 product, as evidenced by Figure 2-3(a)-(c). Additionally, the CW products exceeded the maximum allowable strength allowed by the standard in almost all cases. Third, the automatic exemption of A307 is problematic, given that some products that met A307 had elongations at fracture of less than 7% (Figure 2-3(a)). Note that the behavior in these curves is indicative of the expected behavior from all-thread and headed anchors with upset threads, in which the body minor diameter is essentially constant along the length of the anchor[6]. Anchors with cut threads usually exhibit a "kink" in the yield plateau as yielding transitions from the smaller-diameter to the large-diameter region.

The average measured elastic modulus, yield strength, ultimate strength, and the measured elongation in 8 in., EL_8, is provided in Table 2-2. Although not directly measured during the testing program, necking was assumed to initiate at the peak of the engineering stress-strain curve, in accordance with generally accepted theory of the behavior of ductile steels. Post-necking deformation is calculated as the deformation between peak stress and fracture, as shown in Figure 2-3. Material characteristics, which do not conform to the strength requirements or ostensible deformation requirements of

[6] Commonly produced for Gr. 36 headed anchors up to about 1-1/4 in. diameter.

ASTM F1554-07 are highlighted in gray. In general, the cold-worked products were found to have higher ultimate strengths than allowed by F1554. The ratio of f_u/f_y was found to be as low as 1.16 for the cold-worked Gr. 36 AT, indicating this materials' extreme unsuitability for cut threading over only a portion of the anchor's length, a practice which is disallowed by current ACI requirements. The higher f_u/f_y ratios were associated with the carbon-steel products with the largest elongation capacity.

Table 2-2: Average tensile yield and ultimate strength and elongation at fracture with Ls=8 in. (EL8)

Material short name[a]	Supplier	Dia. D, in.	Yield strength f_y, ksi (MPa)[b]	Ultimate strength, f_u, ksi (MPa)[c]	Ave. f_u/f_y	Modulus E, ksi (GPa)[d]	Elongation in 8 in. EL_8 (%)	Fraction of post-necking elong. (% of EL_8)
CW Gr 36 AT	1	0.75	74.5 (514)	92.2 (636)	1.16	26,500 (182.7)	9.4	44.4
		1.0	83.7 (577)	94.6 (577)			6.9	51.5
		1.25	80.0 (552)	93.9 (552)			9.8	52.0
		1.50	82.8 (571)	89.6 (571)			10.2	49.3
CW-A Gr 36 AT	1	0.75	51.5 (355)	69.5 (355)	1.30	24,800 (171.0)	22.7	25.4
		1.0	56.6 (390)	72.4 (390)			18.0	36.0
		1.25	58.1 (401)	74.1 (401)			19.1	35.5
CW Gr 55 AT	1	0.75	74.6 (514)	98.8 (514)	1.39	29,200 (201.3)	12.5	30.0
		1.25	63.3 (436)	92.3 (436)			16.4	35.6
HR Gr 36 HA	1	0.75	16.5 (114)	26.3 (181)	1.59	28,800 (198.6)	24.3	32.6
CW Gr 36 AT	2	0.75	21.2 (146)	29.3 (202)	1.38	N/A	15.9	26.5
CW A307 AT	3	0.75	24.7 (170)	30.5 (210)	1.23	N/A	10.2	42.0
HR Gr 36 AT	3	0.75	44.0 (303)	69.2 (303)	1.59	31,000 (213.7)	27.3	23.3
		1.0	44.2 (305)	70.0 (305)			24.5	24.2
		1.25	44.2 (305)	71.5 (305)			22.7	31.3
		1.50	44.8 (309)	70.5 (309)			24.6	28.8
A193 B7 AT	4	1.0	114.9 (792)	133.3 (792)	1.16	28,900 (199.3)	12.5	34.4
				Average:	1.35			

NOTES: a) AT=all-thread, HA=headed anchor. b) Strength values calculated on the basis of stress area. c) F1554 materials, which exceeded the maximum strength allowed by the standard, are hatched in gray. d) Modulus values are calculated on the basis of stress area, as given by ASTM F1554. Tests for which strain data was not taken via extensometer are marked N/A.

Many of the cold-worked products exhibited deformation at fracture about half of the 20% requirement for Gr. 36 raw material. Importantly, the measured elongation at fracture was also less than the 14% required by ACI 318, even though this material would also conform to ASTM A307. Annealing was found to restore the ductility of the cold-

worked material, i.e., the cold-worked, annealed material behaved similar to the hot-rolled, although with marginally lower elongation at fracture and higher yield strength. The post-necking fraction of total deformation was markedly higher for the Gr. 36 CW material. With the exception of the 3/4" (19mm) material from Supplier 2, this fraction was nearly 50%, while the post-necking deformation of the HR and CW-A was between about 20 and 35% of total. Therefore, not only is the CW material more brittle, but it also has a negative slope in the force-deformation response for a much larger portion of the total available deformation. This is an important characteristic when considering the potential for overload in an anchor.

Nut function and serviceability

The serviceability limit state is generally defined as a failure in which the part or structure is unable to serve its intended purpose. Binding between the anchor and the nut threads will cause serviceability failure in anchors. A lower-bound estimation of nut failure can be predicted by considering the thread geometry as the anchor undergoes plastic strain (Figure 2-5a). Calculation of first contact is a lower bound estimation of nut failure, as contact does not necessarily imply immediate failure. As suggested by the figure, the contact between the parts will depend on the amount of plastic strain in the part and the initial gap between the teeth.

To determine the range of strain at which contact will first occur, the maximum and minimum major diameter of the internal thread, D_{max} and D_{min} must be calculated based on dimensions and tolerances given by ASME B1.1[18] (Figure 2-5(b)):

$$D_{max,min} = D_{2max,min} + \frac{2(0.25P - 0.5l_{Dmax,Dbsc})}{\tan(30°)} \quad \text{Eq. 2-2}$$

where P is the thread pitch, D_{2max} and D_{2min} are the maximum and minimum pitch diameters for the internal thread, and l_{Dmax} and l_{Dbsc} are the lengths of chamfers at the maximum and minimum major diameters of the internal thread. Note that in all equations, the subscripts *min* and *max* are consistent among all terms in the equation, i.e. to obtain D_{max} in Eq. 1, D_{2max} and l_{Dmax} are required. The minimum and maximum distances along the axis of the anchor from the center of a internal thread to the edge of the thread at the pitch diameter, defined as L_i, is:

$$L_{imax,min} = 0.5l_{Dmax,Dbsc} + 0.5(D_{max,min} - D_{2bsc}) \tan(30°) \quad \text{Eq. 2-3}$$

Similar calculations can be performed for the minor diameter of the internal thread:

$$d_{1max,min} = d_{2max,min} - \frac{2(0.25P - 0.5l_{Dbsc})}{\tan(30°)} \quad \text{Eq. 2-4}$$

where d_{2max} and d_{2min} are the maximum and minimum pitch diameters for the external thread. In this case, only l_{Dbsc} is utilized because no maximum chamfer dimension is given for external threads. The thread-center to edge of thread distance for the external thread L_e is then:

$$L_{emax,min} = 0.5P - 0.5l_{Dbsc} - 0.5(D_{2bsc} - d_{1max,min}) \quad \text{Eq. 2-5}$$

Once these dimensions have been calculated, the strain at which first contact is expected is the total gap between the internal and external threads, divided by the thread pitch (the length over which this gap is taken up):

$$\epsilon_{max,min} = \frac{2(L_{imax,min} - L_{emin,max})}{P} \quad \text{Eq. 2-6}$$

It is noted that this derivation assumes that there is no diameter change as the anchor strains plastically. This assumption is justified based on the relatively small plastic strains at which nut failure was observed (well before significant necking) and also conservative,

in that it should provide a lower bound to actual failure. Theoretical estimates using Eq. 2-6 are compared with the nut serviceability test results in Figure 2-6. Material types are denoted with different shades, while symbols differentiate stretch lengths. Several trends are apparent from the analysis of these results. First, all data presented fall within the bounds of the predicted first contact; moreover, 80% of the data falls within the middle 50% of the predicted range. This suggests that the prediction method is reasonable, as one would expect that the thread tolerances would be near the mean allowed by ASME B1.1. Second, there are no obvious trends regarding material type or stretch length, meaning that the thread geometry is the critical parameter, and the functional dependence of the relationships presented previously of nut failure on strain only is reasonable. Lastly, the majority of the test data falls between 2% and 6% strain, suggesting that the majority of threaded parts would be expected to lose functionality in this range of strain.

Current Chilean industrial design practice is to reject fasteners that have undergone more than 5% strain (Soules et al. 2016). Using elongation as an acceptance criterion is somewhat problematic for the ultimate limit state, as discussed below (Figure 2-12). However, elongation at nut failure was generally observed before necking and strength loss for even the most brittle material, as shown by comparing the data in Figure 2-6 to the curves shown in Figure 2-3. This means that the strain over the bar is nearly uniform at the serviceability limit state. The data suggest that 5% is a reasonable lower bound for serviceability failure, given that approximately 95% of the fasteners were found to be non-functional at this level.

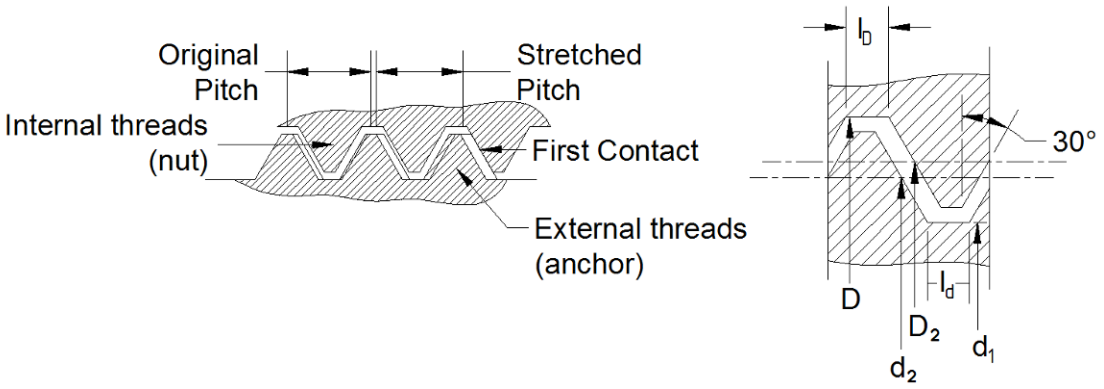

(a) Geometry (b) Dimensions

Figure 2-5: Undeformed and deformed threads

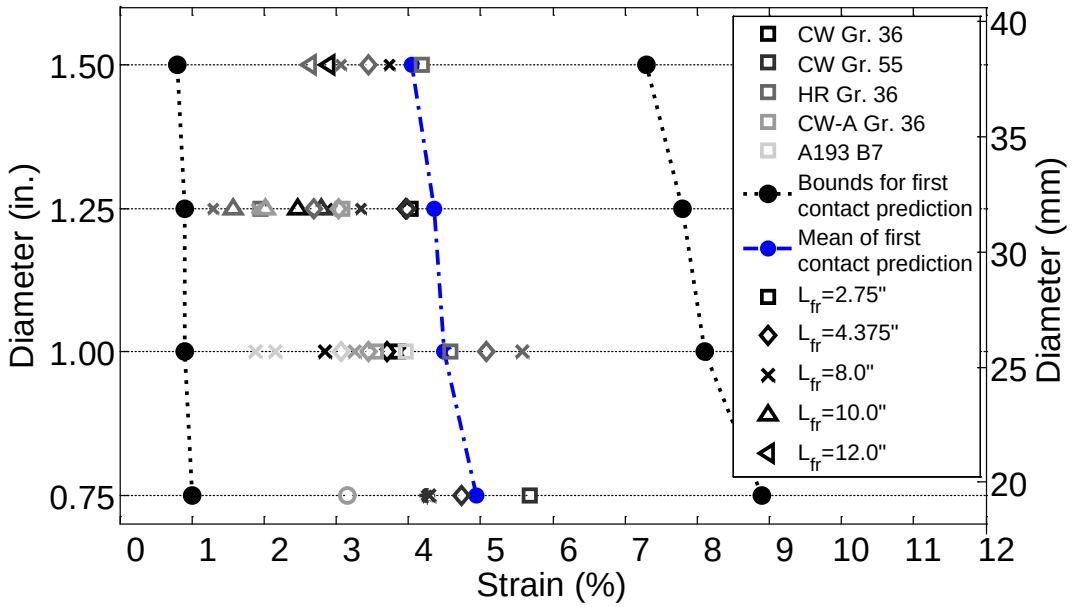

Figure 2-6: Nut failure data with bounds of prediction of first contact

2.2.4 Numerical Modeling and Analysis

A numerical model was developed in LS-DYNA (LSTC 2013) and verified against the test results in order to predict the behavior of anchors with characteristics

outside of the range of the testing program. The model consisted of an axisymmetric representation of the anchor body, which allows reduction of the problem to 2-D (Wilson 1965). A typical model is shown in Figure 2-7(a). Four-node, volume-weighted axisymmetric elements were used throughout the model (LS-DYNA shell *SECTION formulation 15). The diameter of the anchor representation was selected to match that of the anchor body (in the case of anchors with a smooth shank) and the minor diameter for all-thread anchors. The models used between 15 and 35 elements over the radius, for a maximum element size of less than 0.05in (1.3mm) in the largest models.

Nodes located within the boundaries of the grips shown in Figure 2-1(a) were fixed (bottom) or slaved to a master node (top) allowing application of the measured tension test displacement history. Only nodes on the external surface of the model were constrained, representing the support of the fixture nuts around the circumference of the anchor. To capture the nonlinear behavior of the anchor, a simplified version of the Johnson-Cook plasticity rule was implemented (Johnson and Cook 1983). The Johnson-Cook criterion, as implemented in LS-DYNA, compares stress in the element to a plastic flow stress to determine nonlinear deformations. Neglecting strain rate and heating effects, this rule may be expressed as:

$$\sigma_y = A + B\varepsilon_p{}^n \qquad \text{Eq. 2-7}$$

where σ_y is the flow stress, ε_p is the equivalent plastic strain, A controls the constant value of flow stress, B modulates the linear relationship with the plastic strain exponential term, and n is the plastic strain exponent. This material rule is implemented in LS-DYNA as MAT017 (LSTC 2013). Because anchor elongation was an important variable in the

current study, a method to model anchor fracture was also desired. Several damage evolution models are implemented in LS-DYNA, allowing element deletion and progressive fracture to be simulated. Of these, the Cockcroft-Latham damage model was selected due to its simple functional form and accuracy for the current problem. In this model, the damage measurement, which is used to evaluate whether an element has "fractured" and lost the ability to carry load, is dependent on strain rate and the total plastic work for that element. In LS-DYNA, this rule is implemented as (LSTC 2013):

$$\dot{D} = \frac{D_c}{W_c} \max(\sigma_1, 0)\dot{p} \qquad \text{Eq. 2-8}$$

where $\dot{D}$ is the rate of damage evolution, $\dot{p}$ is a normalized equivalent plastic strain rate, D_c is a damage parameter (which was consistently taken equal to 1 in the current simulations), and W_c is a plastic work per volume. When the normalized damage value D (integral of $\dot{D}$) reaches 1, the element is eroded from the calculation. With these two models, the entire range of plastic behavior, including bar facture, may be simulated, as shown in Figure 2-8. This simulation approach is attractive because it requires the selection of only four parameters: A, B, and n for the plasticity model, and W_c for the damage model.

A parametric analysis was conducted in which each of these parameters was adjusted to determine a best fit to the measured force-displacement response of the 1in. (25 mm) diameter specimens presented previously by minimizing the square-root-sum-of-squares (SRSS) error with respect to the calculated versus measured force at three points in the nonlinear range of response. These points were strategically chosen to constrain the fit of the curve around the yield strength, ultimate strength, and near

fracture. These best-fit parameters, summarized in Table 2-3, were then used to simulate the response of tests at other diameters in the test program for verification, which were evaluated by comparing the key points of ultimate strength and elongation at fracture. Typical results from one 1 in. (25 mm) diameter "calibration" model and one 1.5 in. (38mm) "verification" model are shown with corresponding test results in Figure 2-7(b). The model was found to give stable results for the mesh sizes used in a mesh refinement study.

In addition to examining the match between the measured and simulated force-displacement data, the model was also evaluated on its ability to calculate the plastic flow in the area around the fracture surface. This evaluation was performed by comparing the measured reduction of area of the specimen after fracture to the area of the finite-element model at the termination of the analysis. Diameters were measured at up to 23 points along the length of the specimen, as shown in Figure 2-9. Reduction of area measurements were taken on many different specimens. For brevity, the full set of reduction of area measurements in not included herein, but is available in Trautner et al. (2015a). Typical comparisons of the measured data to the model, in this case for D=1 in., L_s=8 in. are shown in Figure 2-10. Although a quantitative comparison of the data is not undertaken, the qualitative match of the measured versus simulated reduction in area is quite good. The model correctly predicts a very localized reduction in area for the CW material, as well as relatively longer regions of reduction in area with pronounced "notches" at the fracture surface for the CW-A and HR materials.

It should be noted that this type of analysis does not explicitly consider the stress localization that occurs at the thread root. However, a sensitivity study suggests that the effect of the threads is negligible for the diameters and material types under consideration. This study considered the three different material types, comparing D=1 in. models with and without the threads included as axisymmetric elements. This approach is not ideal, as the threads are helical, not strictly axisymmetric; however, this approximation is necessary due to the very large number of elements that would be required to represent the true helical geometry with sufficient element size in a 3-D model. The threads appear not to play a large role in the response for two reasons. First, the threads are not large enough versus the diameter of the part to affect the stress flow significantly. The stress contours shown in Figure 2-11(a) indicate that significant axial stress is confined to the main body of the anchor. Secondly, the thread "notches" are neither sharp enough nor deep enough to cause significant stress concentrations which could cause premature fracture of the part prior to what would be expected for a smooth rod. Differences in the force-deformation response between the models were found to be very small, less than 5% in terms of maximum force and less than 10% in terms of elongation, as shown in Figure 2-11(b). Therefore, smooth-shank modeling was deemed to be acceptable, and used throughout the numerical simulation program.

The axisymmetric modeling approach and best-fit parameters presented herein resulted in good agreement with test results and reasonable extrapolations in the current study. However, application of this approach to significantly different material types, geometries, or anchor sizes may require additional investigation.

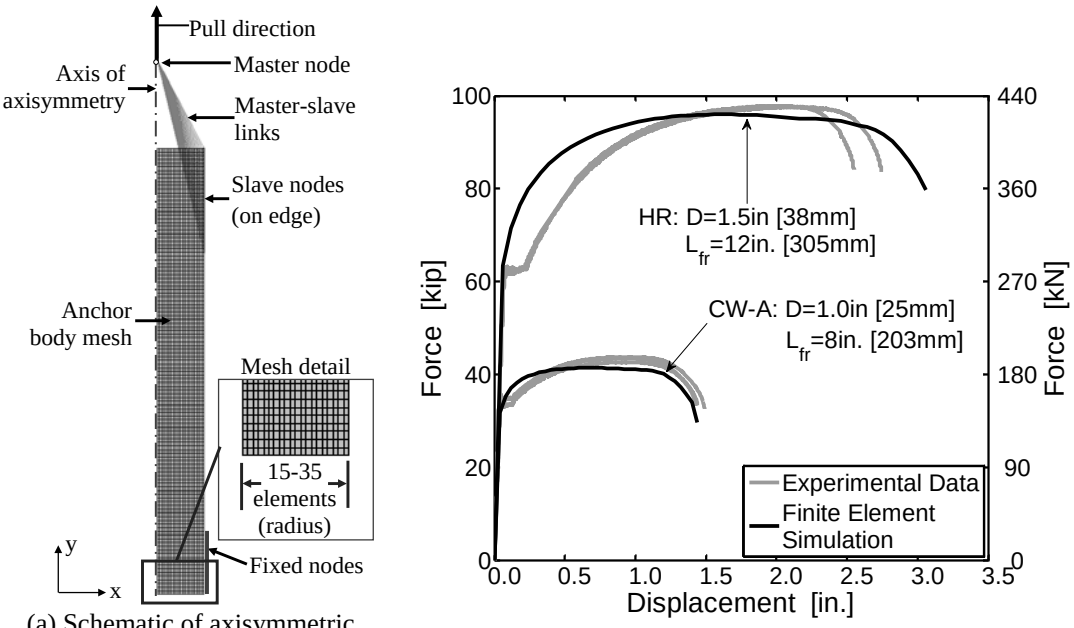

(a) Schematic of axisymmetric model

(b) typical comparison of model results to test data for two diameters and material types

Figure 2-7: Axisymmetric model of anchor tension tests

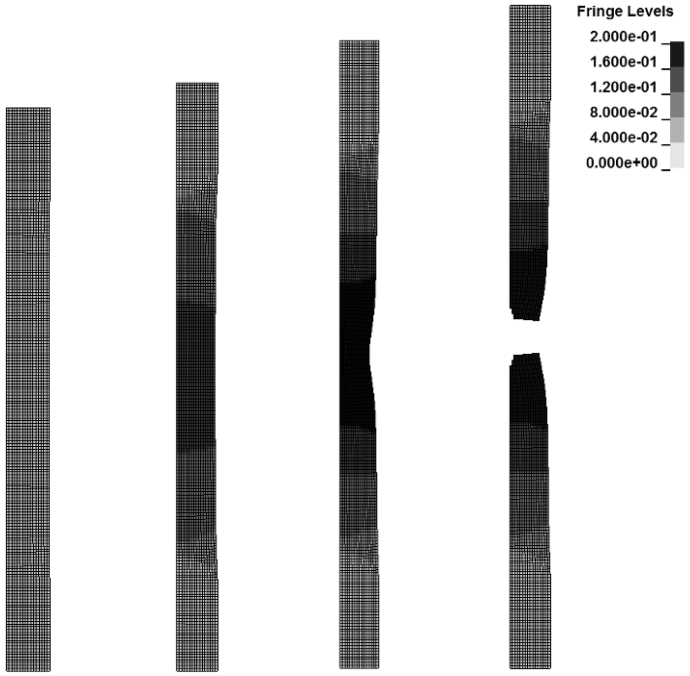

Figure 2-8: Simulation of tensile test through fracture (contours show magnitude of local plastic strain)

Table 2-3: Best-fit Johnson-Cook metal plasticity and Cockroft-Latham damage parameters based on 1 in. (25 mm) diameter tests

	Modified Johnson-Cook Parameters				Average Misfit (avg. of all stretch lengths tested)	
Type of Material	A, ksi (MPa)	B, ksi (MPa)	n	W_c, kip-in (kN-m)	F_u	ΔL_u
F1554 Gr 36 CW	55.5 (382)	81.0 (558)	0.09	55 (6.2)	0.7%	2.5%
F1554 Gr 36 HR	23.0 (159)	123.0 (848)	0.27	72 (8.1)	3.8%	8.1%
F1554 Gr 36 CW-A	8.0 (55)	130.0 (896)	0.158	65 (7.3)	4.4%	6.7%

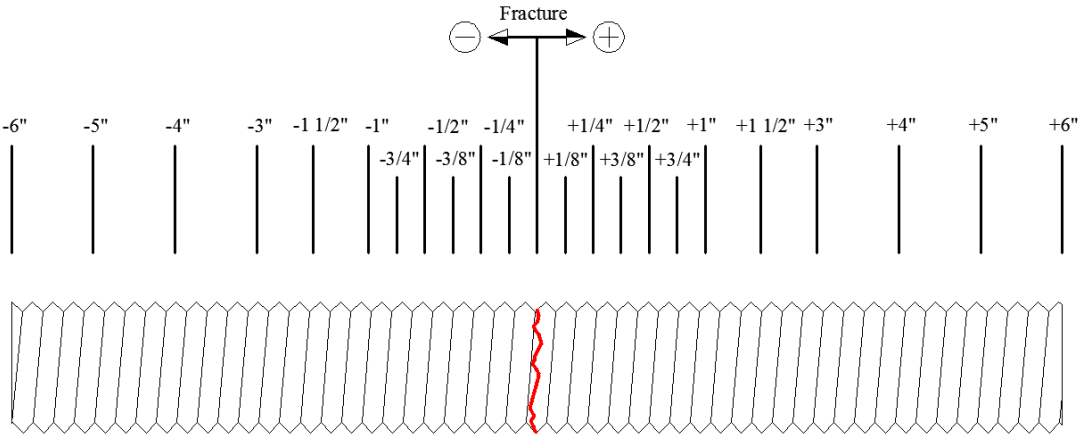

Figure 2-9: Location of reduction of area measurements

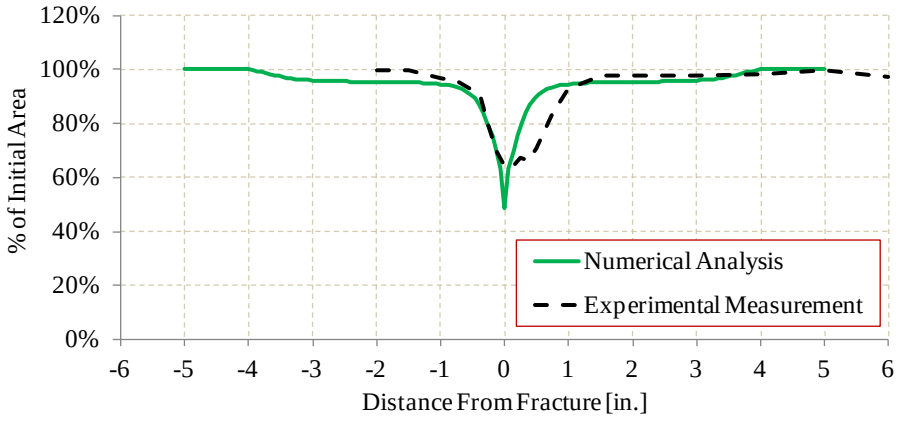

(a) CW

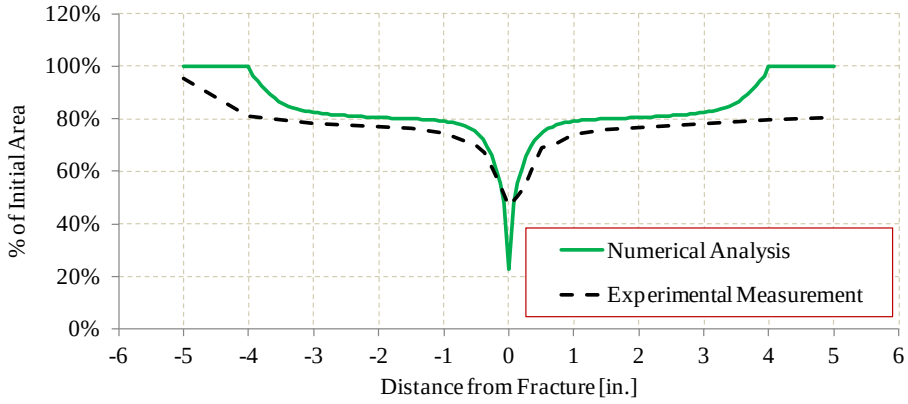

(b) HR

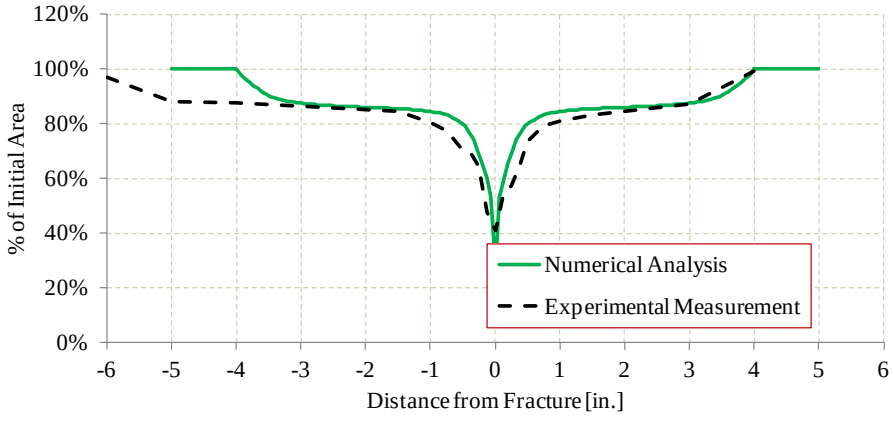

(c) CW-A

Figure 2-10: Measured versus simulated reduction of area for D=1", L_s =8" bars

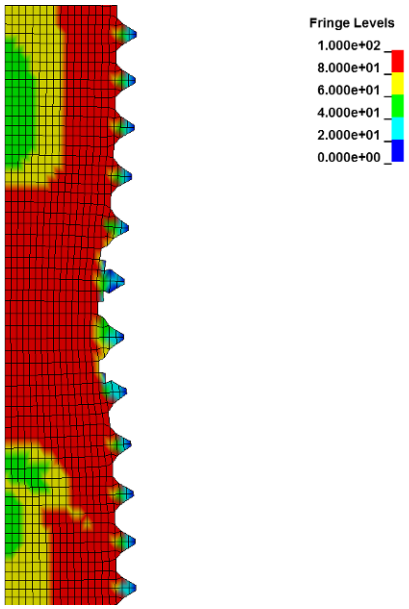

(a) Axial stress in threaded model at load step near fracture

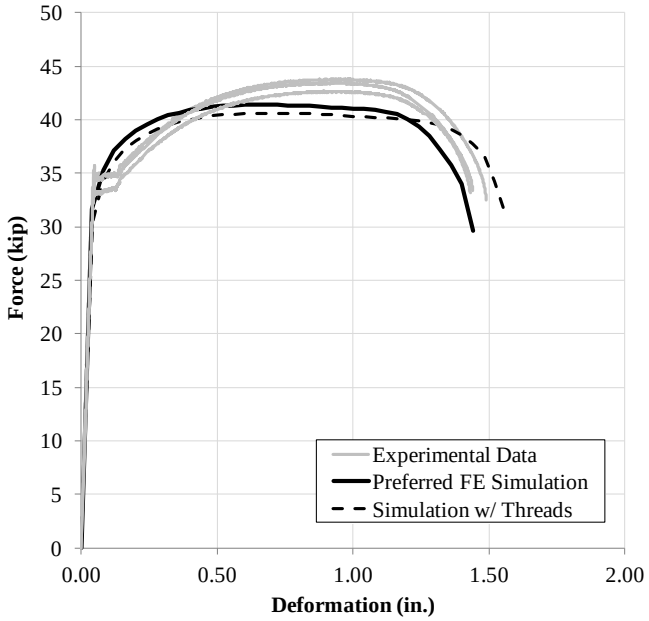

(b) Comparison of model results with and without threads

Figure 2-11: Results of thread sensitivity study for D=1" CW-A model

The validated numerical model was used to study the relationship between stretch length and deformation capacity for the various materials tested. Both the measured and simulated elongations at fracture for each of the material types and diameters considered are presented in Figure 2-12. Note that this data is applicable only to all-thread and partially threaded anchors that have upset threads. Partially cut-threaded anchors could be simulated using the Johnson-Cook material properties, but the model geometry would need to be adjusted. The gray lines represent simulation results. Note that the elongation at fracture is marked in boxes for the smallest and longest stretch lengths considered. Simulation of the A193 B7 material was not performed, as insufficient test data was available to calibrate and verify the model.

Several interesting patterns are evident in these results. Importantly, the elongation at fracture is not directly proportional to increases in stretch length. That is, a

doubling of the stretch length (e.g., from 4D to 8D) is not associated with a doubling of the available anchor deformation. In contrast, the percent elongation at fracture reduces with increasing stretch length. This highlights the need for elongation requirements to be expressed in engineering length units rather than as a percentage. The available elongation at fracture is not a significantly dependent on diameter for a given stretch length. For example, for HR material at L_s = 8 in. (25 mm), available elongation is about 2 in. (51 mm) or 25%, regardless of diameter. This means that connection strength and deformation capacity may be considered independently in design.

Perhaps most importantly, although elongation is not directly proportional to stretch length, the relationship is roughly linear. The slope of a best fit line drawn through data for several different stretch lengths can be used to determine how "efficient" a material type is in providing additional elongation capacity for a given increase in stretch length. This phenomenon has important practical implications, most notably that if elongation data from at least two points is known for a given material type, elongation at a third stretch length can be reasonably predicted using linear interpolation or extrapolation. The testing program included stretch lengths down to 2.75 in., which is about as small as would likely be encountered in practice. Extrapolation to larger stretch lengths can either be accomplished using the finite element modeling technique introduced herein, or may be approximated by the linear extrapolation formula:

$$\Delta L_{u,new} = \Delta L_u + (L_{s,new} - L_{s,\max})s \qquad \text{Eq. 2-9}$$

where $\Delta L_{u,new}$ is the new elongation at fracture, ΔL_u is the elongation at fracture corresponding to the longest tested stretch length $L_{s,max}$, $L_{s,new}$ is the new stretch length, and s is the slope of the stretch length/elongation at fracture line. The parameter s was determined for each of the different diameters tested, as shown in Table 2-4. Note that these values were calculated using only the test results; the simulation results shown in Figure 2-12 were not included. This parameter describes the "efficiency" of additional stretch length in providing additional deformation capacity. In this context, F1554 Gr. 36 HR material is the most efficient with an average s of about 0.20, followed by F1554 Gr. 36 CW-A, F1554 Gr. 55, A193 B7, and finally CW Gr. 36 with an s of about 0.05. It seems probable, therefore, that in many cases providing an anchor fabricated from ductile material with a reasonable stretch length may provide greater elongation capacity than a comparatively long stretch length and a less ductile material.

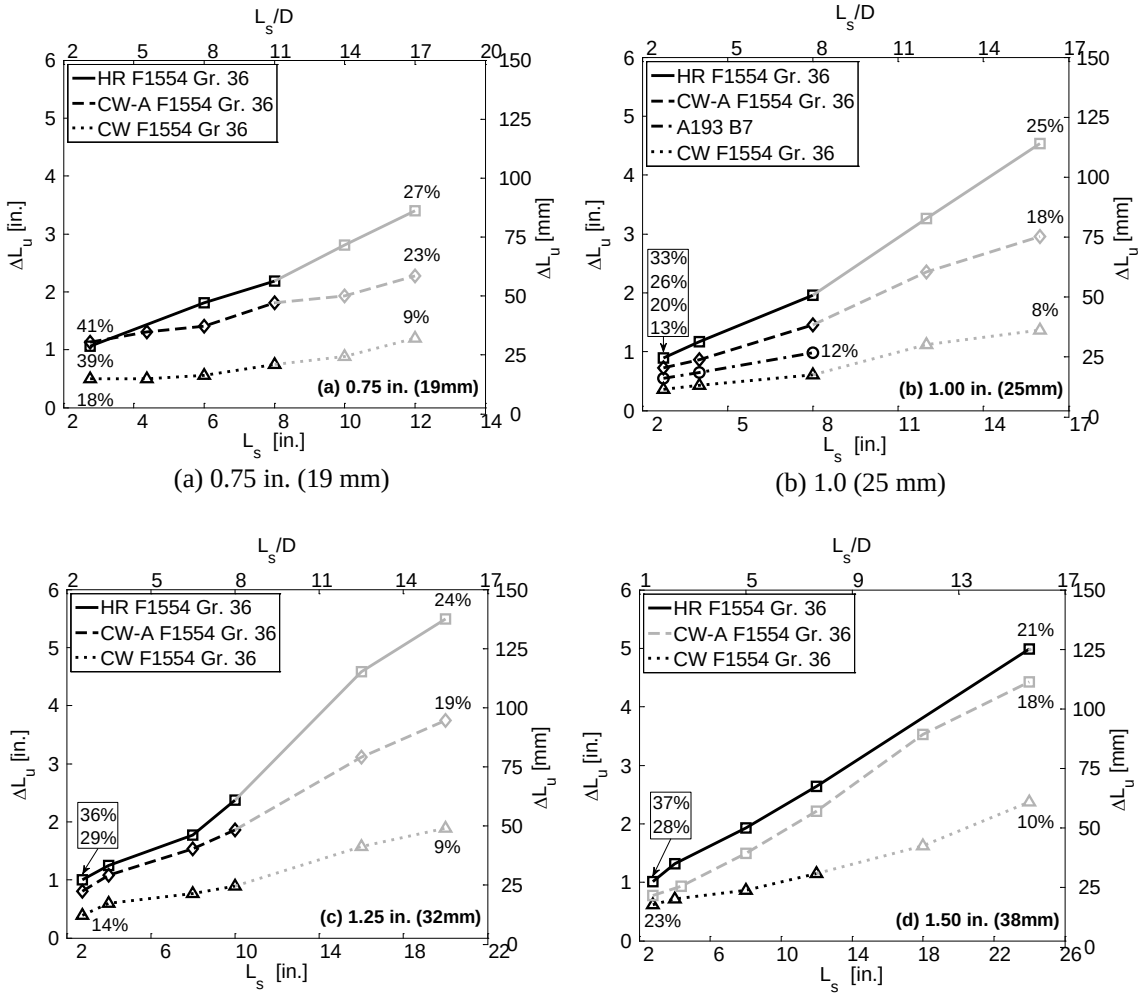

(a) 0.75 in. (19 mm)

(b) 1.0 (25 mm)

(c) 1.25 (32 mm)

(d) 1.5 in. (38 mm) diameter

NOTES: 1) x-axis is different for each figure. 2) Black represents test data, gray represents simulation results. 3) Boxed values represent elongation at fracture over L_s.

Figure 2-12: Relationship between deformation at fracture and stretch length for different material types and diameters

Table 2-4: Factor *s* calculated from test data for all material types and diameters

Material Type	D=0.75 in.	D=1 in.	D=1.25 in.	D=1.5 in.	Average
F1554 Gr. 36 HR	0.215	0.203	0.190	0.187	0.199
F1554 Gr. 36 CW-A	0.130	0.139	0.145	-	0.138
F1554 Gr. 36 CW	0.048	0.048	0.069	0.057	0.056
F1554 Gr. 55	0.090	-	0.120	-	0.115
A193 B7	-	0.083	-	-	0.083

2.3 Reference Test Series

The reference test series consisted of monotonic tension testing of single anchors embedded into reinforced concrete. In general, the anchors tested in this series were the same type used in connection tests described in this next chapter. The anchor embedment and geometry are shown in figures of the connection tests described in the next chapter (see Figure 3-2). The primary purpose of the reference testing was to:

1. Verify of proper anchor performance, particularly that of the adhesive anchor systems, prior to use in the connection tests.
2. Establish force-displacement data for the anchors used in the component connection tests. This data was used for subsequent modeling of the connection tests, described in Chapter 4.
3. Evaluate the anchor performance, particularly on the basis of how strain penetration may affect elongation capacity.

The reference testing was performed in three stations located on each face of the experimental slabs used for the component connection testing, described in the following chapter. Each test was performed with a free length (i.e. distance between bottom of nut/washer to top of concrete) of 4 in. This distance was selected as a reasonable

expected exposed length for anchors of this size, and identical to the actual exposed length in the connection tests (2.75 of nominal exposed length + 1.25 in. thickness of instrumentation). Because incorporating a load cell in the load path of the pullout tests was not possible (due to the need for an extension rod), the preload in the anchors was torque-controlled. Installation torque matched that used in the connection tests. The loading rate was controlled by limiting the amount of oil reaching the jack, by manipulating the needle valve at the pump manually. Load rates at the end of the test were highest, where the relatively high pump pressure coupled with decreasing strength of the rod made oil flow control difficult. Load rates during the end of the tests often approached 0.5 in/min, for the rest of the test the rate was on the order of 0.2 in/minute.

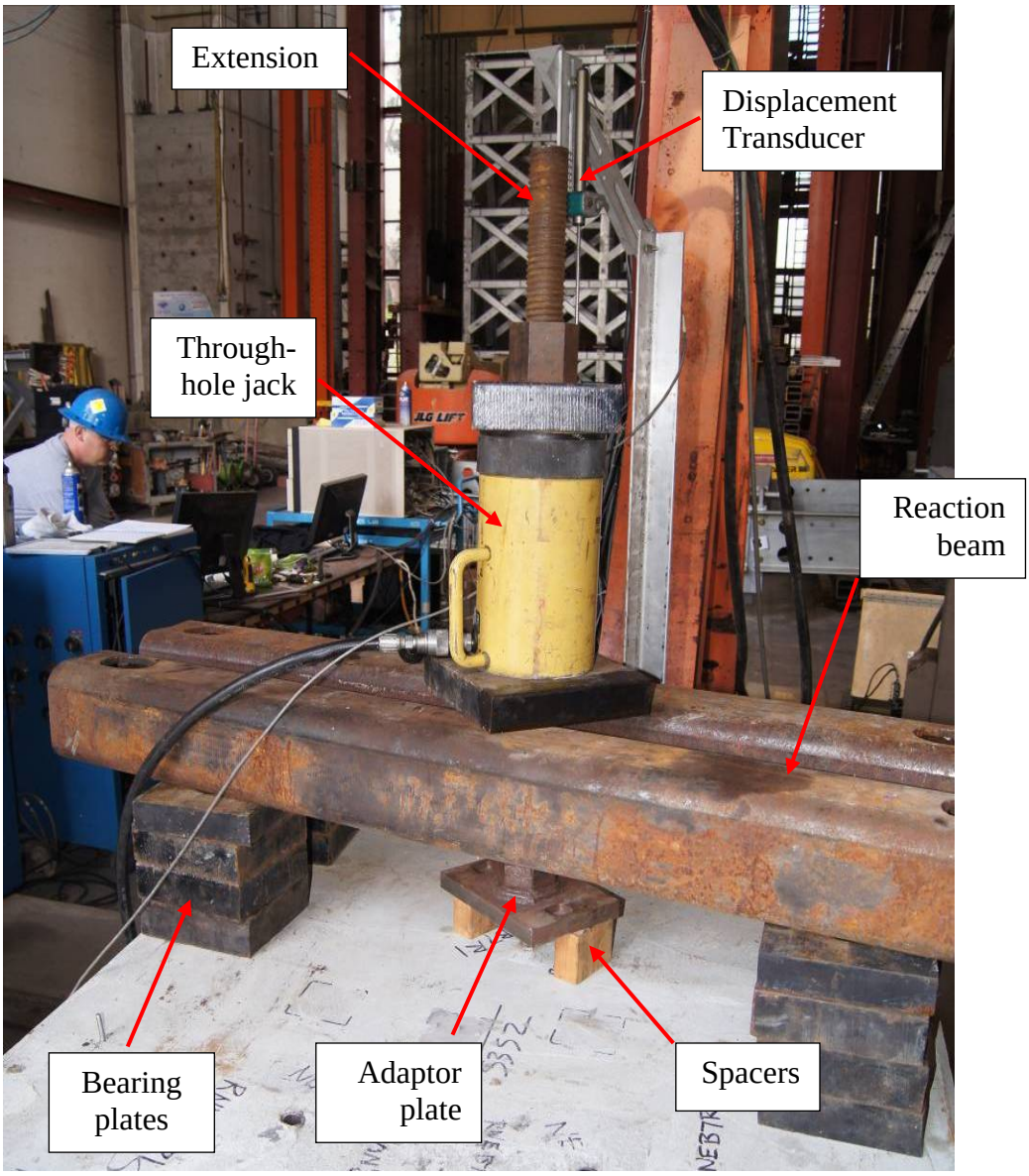

Figure 2-13: Typical reference test setup

In total, ten different types of reference tests were conducted (Table 2-5). The specific purpose, explanation of the acronym, and a description of each test type is given below:

- CI (**C**ast-**I**n): these three tests were performed with cast-in ASTM F1554 Gr. 36 (HR) headed anchors. The purpose of this test series was primarily determination

of the force-displacement response, as this anchor type was used in several different connection tests.

- BAnn (**B**onded anchors, **Ann**ealed steel): these three tests were performed with CW-A allthread anchors bonded with epoxy-type adhesive. The purpose of this test series was verification of the adhesive performance and anchor strength prior to use in connection tests, as well as establishing force-displacement data for later numerical modeling.
- UC (**U**nder**c**ut): these three tests, performed with M20x250/100 undercut anchors, were performed primarily for verification of anchor performance and establishing force-displacement data for later numerical modeling.
- BAR (**B**onded, **As-R**eceived cold-worked): these three tests were performed with CW allthread anchors bonded with epoxy-type adhesive. The purpose of this test series was primarily establishing force-displacement data for later numerical modeling. These tests were also compared to the BAnn test series to quantify the differences in anchor performance attributable to insert steel type.
- CIB7 (**C**ast-**I**n A193**B7** allthread): these two tests were performed with ASTM A193 B7 all-thread fitted with a nut, washer, and fender washer for pullout resistance. The purpose of this test was a comparison with the CIT and CI test sequences, to evaluate how material selection and the presence of threads affects the amount of strain penetration and concrete surface damage during loading. These anchors were not used in any of the connection tests described in Chapter 3.

- UCS (**U**nder**c**ut, **S**mall): these three tests were performed with "standard" M16x190/40 undercut anchors (ISO 8.8 cone bolts). The purpose of this test was twofold: first, to obtain force-displacement data for future modeling of baseplate connections with standard M16 undercut anchors and second, to evaluate the performance of the "standard" HDA versus the "ductile" HDA anchors. These anchors were not used in any of the connection tests described in Chapter 3.
- UCSD (**U**nder**c**ut, **S**mall, **D**uctile): these six tests were performed with "ductile" M16x190/40 undercut anchors (ISO 4.6 cone bolts). The purpose of these tests were essentially identical to the UCS series: force-displacement data for further numerical analysis and comparison to the "standard" HDA anchor. However, one important difference was that tests 1,4, and 5 were performed with an unmodified anchor -- that is, the bolt extension was not cut off and coupled with an extension like the ductile undercut anchors used in the connection tests were (as described previously). The other tests (2, 3, and 6) were performed with anchors identical to those used in the connection tests. This provided a point of comparison to verify that the force-displacement characteristics of the undercut anchors were not significantly affected by the extension modification.
- CIT (**C**ast-**I**n, Fully **T**hreaded): these four tests were performed with headed, hot-rolled anchors which had been manually threaded for their entire length (in their manufactured condition, these anchors had 6 inches of threading and 10 inches of smooth shaft). Two of these tests (CITR2 and CITR3) were cast directly into the concrete. The others were debonded along the embedded length via the use of

duct tape speared with grease. Together, these two sets of tests will help determine whether the threading exposed to the concrete directly is effective in limiting the amount of strain penetration that occurs.

- R-series (**R**emovable anchors): these two tests were performed after the completion of test S3S2. The purpose of these tests was to demonstrate that the permanent anchor body of the removable anchors was capable of accepting a new anchor insert and being loaded without a significant loss in performance. Test RNWAnnR1 was performed with an insert identical to what was used in the removable anchors to begin with (annealed all-thread) in the north-west (NW) anchor station. Upon successful completion of that test, test RNEB7R1 was conducted with a piece of A193B7 all-thread in the north-east (NE) anchor station, in order to find out what the ultimate capacity of the removable anchor body was, and what the failure mechanism would be.
- BAnnR4-BAnnR5 (**B**onded, **Ann**ealed allthread): these three tests were performed with a hybrid epoxy-cementitious adhesive. These tests were otherwise identical to the other BAnn tests performed with epoxy-only adhesive. These tests were performed to obtain force-displacement data for future numerical simulations, and to provide a point of comparison to determine whether strain penetration effects are different between the two types of epoxy.

Table 2-5: List of reference tests

Test Designations (Test Number)	Anchor Type	Anchor Steel	Slab #
CIR1, CIR2, CIR3	Cast-In	F1554 Gr. 36 (HR)	1
BAnnR1, BAnnR2, BAnnR3	Bonded	F1554 Gr. 36 (CW-A)	2
UCR1, UCR2 UCR3	Undercut (20mm)	Undercut	2
BARR1, BARR2, BARR3	Bonded	F1554 Gr. 36 (CW)	1
CIB7R1, CIB7R2	Cast-in, allthread, washer and nut	A193 B7	3
UCSR1, UCSR2, UCSR3	Undercut (16mm)	ISO 8.8	2
UCSDR1 - UCSDR6	Undercut (16mm ductile)	ISO 4.6	3
CITR1, CITR2, CITR3, CITR4	Cast-in, headed, fully threaded	F1554 Gr. 36 (HR)	3,4
RNWAnnR1, RNEB7R1	Removable	F1554 Gr. 36 (CW-A) and A193 B7	3
BAnnR4, BAnnR5, BAnnR6	Bonded (HIT HY-200)	F1554 Gr. 36 (CW-A)	4

NOTE: all anchors were 3/4 in. diameter, except for undercut anchors (manufacturer's metric sizes reported)

For brevity, the full set of measured force-displacement data is not presented herein, but it is given in Trautner and Hutchinson (2014a and 2015a). Typical force-displacement curves for a few anchor types used for numerical modeling later in this dissertation, as well as comparisons between a few different test series are presented and discussed below. The average yield force, ultimate force, and elongation at fracture for each test series is given in Table 2-6.

Table 2-6: Average yield force, ultimate force, and elongation at fracture for reference test series

Test series or designation	F_y, kip	F_u, kip	Δ_{max}, in.
CI	18.0	27.2	2.50 (2.25[a])
BAR	27.6	32.2	0.70
BAnn	17.6	24.6	1.41
UC	46.3	50.7	0.81
CIB7R	39.0	46.0	0.79
UCSR	15.5	31.3	0.60
UCSD (unmodified)	10.2	15.1	1.18
UCSD (modified)	9.0	14.5	1.23
CITR (unbonded)	16.5	25.1	2.06
CITR (fully bonded)	17.2	25.2	2.08
RNWAnnR1	18.2	24.2	2.41
RNEB7R1	37.5	43.4	0.38
BAnn (hybrid)	18.4	24.1	1.34

NOTES: [a] corrected for paste crushing (see text).

The smooth-shank, cast-in headed anchors were found to be the most ductile of all anchor types. The relatively high elongation at fracture of the CI anchors is believed to be due to two factors: 1) The anchors were roll-threaded directly from hot-rolled rounds, and 2) The smooth shank of the anchor permitted de-bonding over the entire embedded length, resulting in a much greater stretch length than for other anchor types. The anchors were 16 in. total length, with 6 in. of threading and 10 in. of smooth shank, meaning that elongation contributed by the embedded portion of the anchor was quite significant. The de-bonding behavior was verified by taking reduction of area measurements along the length of the anchor by coring and removing it from the concrete after the reference tests. A photograph of a removed anchor is shown with typical measurements in Figure 2-14. The average area reduction was about 16% (diameter reduction of almost 10%), indicating significant plastic flow along the entire length of the anchor.

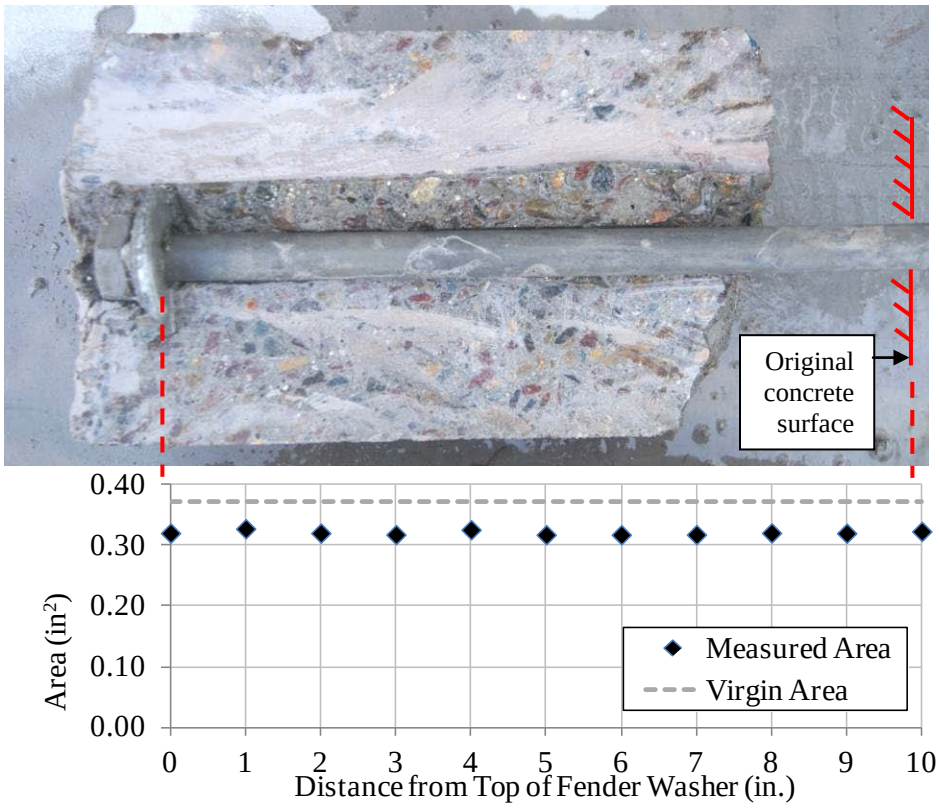

Figure 2-14: Photograph of cored & removed cast-in, smooth shank headed anchor with measurements of reduction of area indicating de-bonding

Following the CI test series, similar anchor types were tested to explore the role that strain penetration may have on the behavior of anchors of this type. Four identical headed, F1554 Gr. 36 anchors were hand-threaded along their entire length and then two were directly cast in the concrete, while two were wrapped in duct tape and greased in order to debond the full embedded length (test series CITR). The CIB7R tests were also similar, consisting of A193B7 allthread, heavy hex nuts and washers and cast directly in the concrete. The results from all the tests are shown in Figure 2-15 and the key vales are summarized in Table 2-6. As shown in the figure, CITR series test results were nearly identical, regardless of whether the shaft was deliberately unbonded from the concrete.

This suggests that very significant strain penetration (up to the full embedded length of the anchor) may be expected, even for fully threaded anchors. Unfortunately, the test data from the unmodified anchors (CIR test series) cannot be directly compared, due to the presence of "kinks" in the elastic portion of the curves. These kinks were caused by crushing of paste between the washer and head of the anchor, which intruded because the washer was not fastened to the anchor head (Figure 2-16, see Trautner and Hutchinson 2014a for more information). However, this data can be approximately corrected by subtracting the "extra" displacement caused by the crushing (identified in the figure). This was performed by subtracting the difference in the displacement from the apparent "real" yield kink in the smooth shank data from the kink in the fully threaded data. This approach makes the assumption that all of the "extra" displacement due to the paste crushing occurs prior to yield. This assumption is somewhat justified, however, by the fact that the yield force is much greater than the difference between yield and ultimate strength, meaning the additional post-yield force demand (which would lead to more paste crushing) is relatively small. The ultimate strength and elongation at fracture for each anchor type (including the corrected elongations for the smooth shank tests) are summarized in Table 2-6.

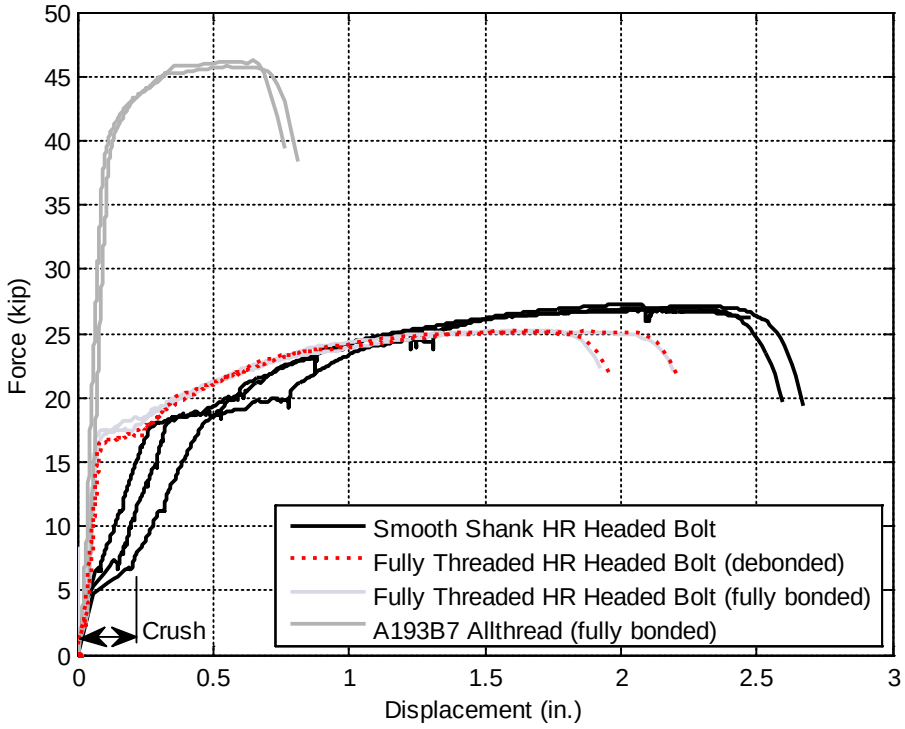

Figure 2-15: Force-displacement curves - all cast-in reference tests

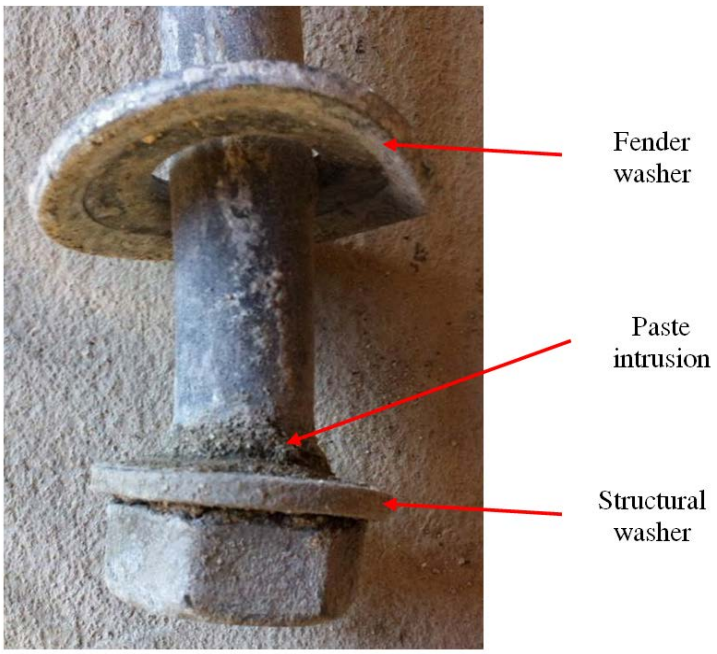

Figure 2-16: Paste Intrusion Between Fender Washer and Structural Washer – Test CIR1

Considering only the F1554 Gr. 36 anchors, the ultimate strength is slightly lower for the fully-threaded anchors. This was somewhat expected, given that all specimens were found to fracture in the smooth shank portion of the anchor, and the fully-threaded specimens have a reduced cross-sectional area in the shank. It is believed that all anchors fractured in the shank due to the cold-work of the roll-threading, which increases the strength of this portion of the anchor. Interestingly, the elongation at fracture for the hand-threaded anchors was within 7% of that of the smooth bar. Most importantly, the difference in elongation between the bonded and unbonded threaded anchors was less than 5%. This suggests quite strongly that for this anchor size and grade, the stretch length may be considered to be much greater than the free length, defined as the length above the concrete surface. Because the total elongation at fracture was so similar for the threaded anchors, this suggests that strain penetration and length of debonding occurred in the threaded anchors (i.e. similar to what was measured in Figure 2-14).

In fundamental terms, strain penetration will be prevented if the strength of the paste (or other material, such as epoxy) within the threads of the anchor over a given length is equal to the current force in the anchor. This situation is analogous to rebar development length, with the exception that threaded anchors are not specifically designed to create this type of effect (as rebar deformations are). A hypothetical force balance is shown in Figure 2-17. The shaded region shows an assumed distribution of the shear stress intensity, with the highest intensity (darkest) nearest the surface of the concrete. If the intensity of this stress exceeds the shear strength of the concrete paste (or

epoxy, for bonded anchors) at some given depth, some plastic deformation will occur in the anchor at this depth as the forces are redistributed lower in the anchor.

The actual interplay of these forces is complex, but a simplified explanation of why the CIT anchors may debond over their entire length may be made by considering the geometry of the anchor threads. Among individual anchors, the actual diameter of the inside and outside of the threads may vary somewhat. However, ASME B1.1 (ASME 2003) provides tolerances for several different diameters for externally threaded and internally threaded parts (i.e. anchor/bolt and nut threads, respectively), as shown in Figure 2-18. In the case of an anchor placed in concrete, there is no internally threaded part to mate with. However, it can be reasonably assumed that the concrete paste forms a nearly-perfect negative of the external threads. This negative was observed in examinations of anchors removed by coring in the current testing program (similar to the core shown in Figure 2-14). Therefore, the development of shear in the concrete must be based on a helix that has major and minor diameters that match those of the anchor itself. However, during plastic flow, the diameter of the anchor shrinks. Therefore, one may imagine that if sufficient plastic flow could develop, the anchor could fully pull away from the threaded concrete "negative", no shear would develop between the anchor threads and the concrete, and the unbonded region could extend to the bearing device at the bottom of the anchor. For the case of the 3/4 in. anchors considered in this study, the major external diameter stipulated to be between 0.7482 and 0.7353 in., and the minor diameter is stipulated to be a maximum of 0.6291 in. Although it does not represent a worst or best case scenario, using the average of the major diameter tolerances and the

maximum minor diameter represents a realistic situation that is likely not too far from extremes in thread tolerances that may occur. Taking these diameters, a uniform reduction in diameter of 1-0.6291/0.7418=15.2 % would allow the anchor to fully "clear" the inside of the concrete negative while undergoing plastic strain. The anchor measured in Figure 2-14 was measured to have a diameter reduction of nearly 10%. Even if the anchor does not undergo sufficient diameter reduction to completely disengage the surrounding concrete, it is very likely that even a modest reduction would greatly reduce the shear strength of the engaged threads, resulting in failure of the concrete at the molded thread negative and the same end result.

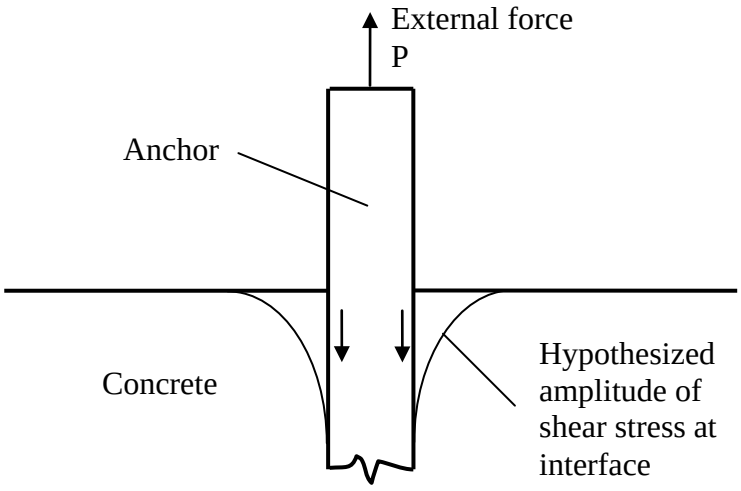

Figure 2-17: Force balance - development of shear in anchor threads

No direct analysis of the strain penetration that occurred in the cast-in A193B7 allthread can be made. However, the A193 B7 standard specifies a minimum elongation at fracture of 16% over a stretch length of 4D, which in this case would be 3 in. The pullout test was

performed with an exposed (out of concrete) length of about 5 in., therefore the equivalent % elongation at fracture would be expected to be less than 16%. However, taking the "best case" scenario of 16% elongation and a stretch length of 5 in., one would expect an elongation at fracture of about 0.8 in., which is very close to what was measured. Therefore, it may be concluded that for this material type and diameter, the exposed length and stretch length are the same (i.e. sufficient plastic flow does not develop to disengage the anchor from the concrete). The authors note that bond stress distributions have been of practical research interest for concrete reinforcing bars and concrete anchorages for at least 50 years (i.e. Salmon 1957). However, to the authors' knowledge, a comprehensive study of the bond stress distribution in embedded, threaded anchors has not been performed, and may provide a fruitful avenue for future research.

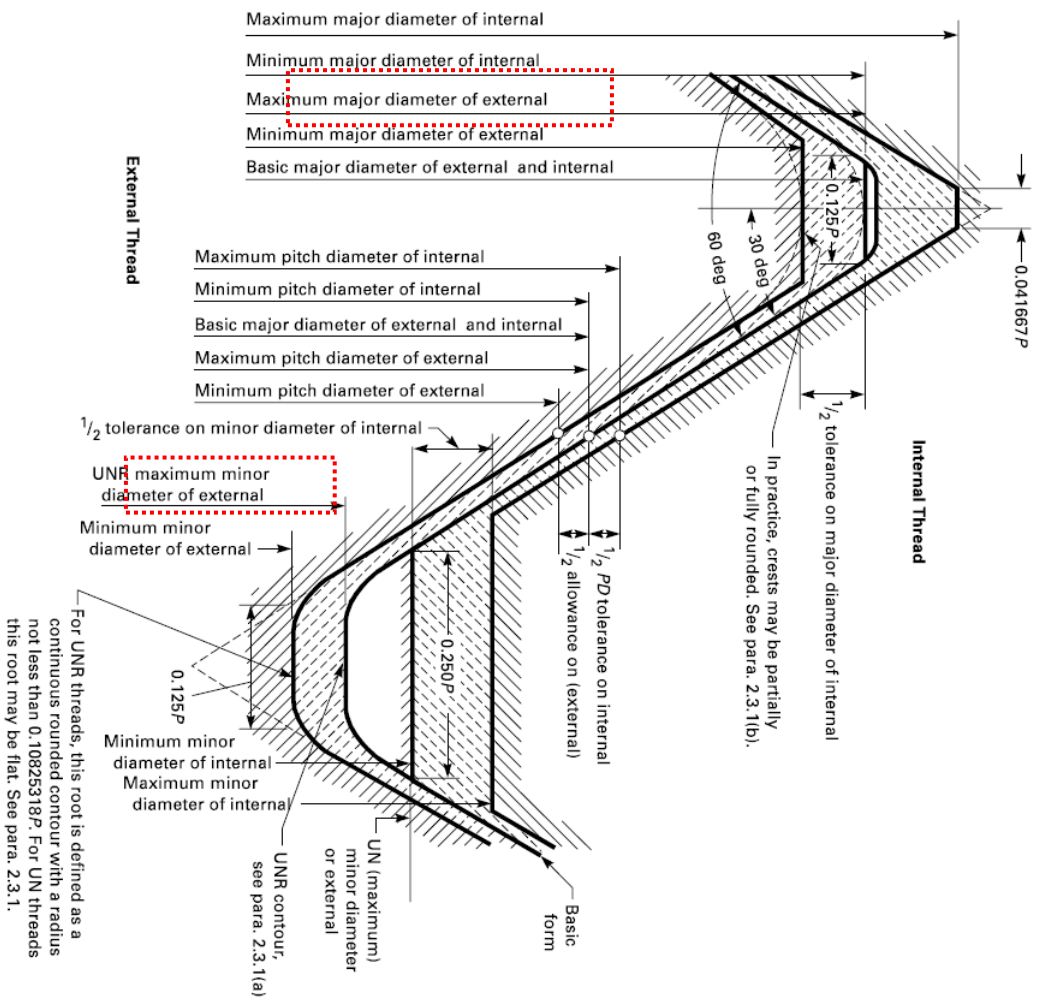

Figure 2-18: Diagram of UNC thread contours (from ASME B1.1 2003)

2.3.1 Removable Anchors

Removable anchor reference tests were performed as a "verification of concept" to the anchor inserts could be removed, replaced, and then the anchor assembly loaded again following a connection test (see Chapter 3). Two tests were performed, one in the NW anchor slot used the same material as used in the connection test (ASTM F1554 Gr. 36 annealed allthread), and another in the NE anchor slot with A193 B7 allthread, intended to determine the actual capacity of the anchor body. The force-displacement data from the two tests is shown superimposed over the fully-threaded, cast in anchor data in Figure 2-19. The ultimate strength and elongation at fracture were very similar to the cast-in anchors for the annealed F1554 insert, while the capacity of the anchor body itself was approximately 44 kips. The anchor body failed due to stripping of the bottom nut. The bottom nut was an ASTM F594 Standard Hex nut, which would ordinarily not be used with A193 B7 allthread[7]. These results indicate that the removable anchors have the potential to provide elongation capacity equal to or greater than that of the best "traditional" fastening solution, with a large margin against undesirable failure modes (nearly 2 to 1 against nut strip, and this margin could be improved by use of a ASTM F594 Heavy Hex nut, or a higher grade nut).

---

[7] ASTM A193 B7 stipulates ASTM F594 Heavy Hex nuts, minimum

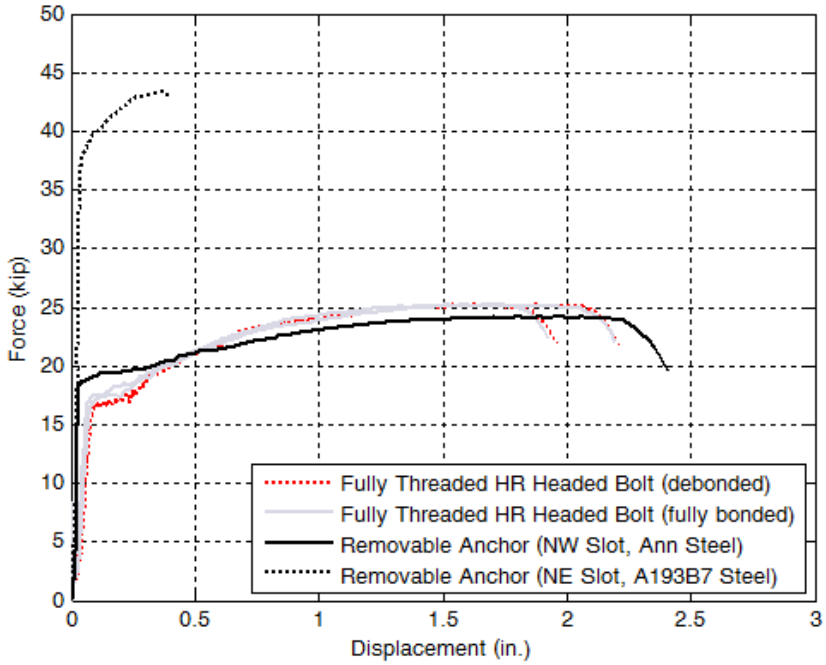

Figure 2-19: Force-displacement data from cast-in and removable anchor reference tests

2.3.2 Bonded Anchors

The force-displacement data for all of the bonded anchors are shown in Figure 2-20, and the ultimate strength and elongation at fracture are summarized in Table 1-1. Both sets of data show clearly that the behavior of the anchors is similar regardless of adhesive type. The average elongation at fracture for the two adhesive types was within about 1/16 in. This seems to make sense relative to the small failure cones observed after the tests, shown in Figure 2-21. The cones were observed to be a similar size for all tests (on the order of 6-8 in. in diameter), and do not suggest that strain penetration is any different for either of these two epoxies.

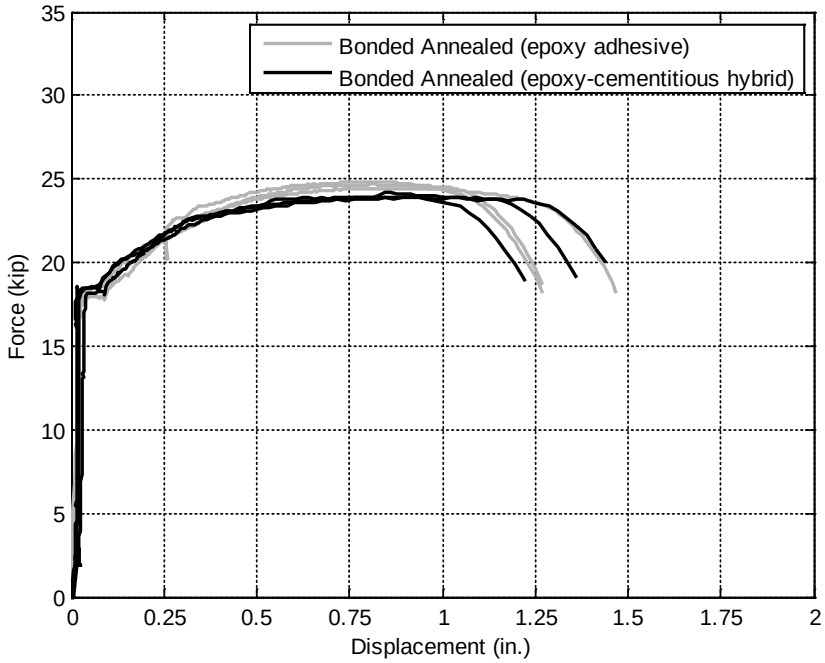

Figure 2-20: Force-displacement data from all bonded anchor reference tests (CW-A, cold-worked annealed steel)

(a) bonded anchor test, epoxy adhesive

(b) bonded anchor test, hybrid epoxy-cementitious adhesive

Figure 2-21: Comparison of typical concrete surface condition following reference tests

2.3.3 Undercut Anchors

Reference tests on three distinct types of 16mm nominal diameter undercut anchors were performed. Three "standard" undercut M16 anchors were tested as a control. Additionally, three unmodified and three modified "ductile" M16 anchors were tested. The modification consisted of removing approximately the top 3/4 in. of the anchor, and adding a coupling and approximately 2-1/2 in. of A193 B7 threaded rod as an extension. This modification was necessary to accommodate the grout and plate thickness required for connection tests (see Chapter 3).

The force-displacement data for the nine tests is shown in Figure 2-22. The ultimate strength and elongation at fracture are summarized in Table 2-6. The strength of the "standard" anchors was approximately double that of the ductile anchors, while the elongation was approximately halved. Among the ductile anchors, there was no significant difference found in the shape of the load-deflection curve. Therefore, it is concluded that modifying the ductile anchors did not affect the performance, and the modified anchors were used in the connection test S3S3 described in Chapter 3.

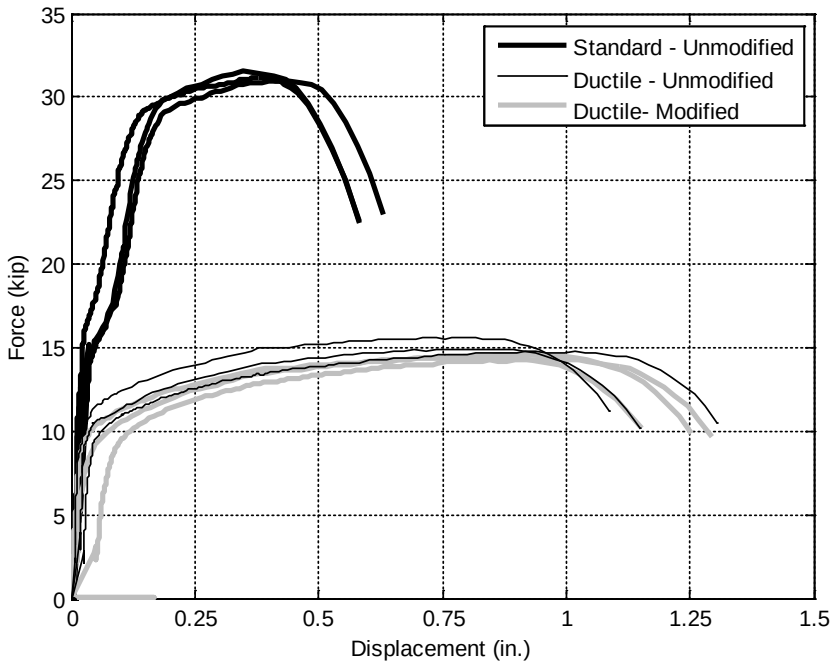

Figure 2-22: Force-displacement data from all 16mm undercut anchor reference tests

2.4 Summary Remarks

This chapter presented tension testing of anchor products, primarily allthread, reference testing of anchors in reinforced concrete, and related numerical analysis. The following are the primary results and conclusions from this work:

- From tension testing of allthread and headed anchor products, more ductile material experienced larger increases in deformation capacity when the free length was increased. This phenomenon is embodied in the parameter *s*, which may be determined from the slope of the stretch length/elongation at fracture curve. The parameter s was found to vary between about 20% for ASTM F1554 HR mateiral to about 5% for ASTM F1554 CW material. Using this parameter, the materials may be ranked from most to least ductile as follows: hot rolled

ASTM F1554 Gr. 36, cold-worked annealed F1554 Gr. 36, cold-worked F1554 Gr. 55, ASTM A193 B7, and cold-worked F1554 Gr. 36.

- The relationship between elongation at fracture and free length was found to be nearly linear for all of the materials within the range of free lengths tested, up to 16D. 16D represents a large free length compared to what is often provided in many types of connections. Therefore, a practical, reasonably accurate prediction of elongation at fracture for anchors with free lengths up to 16D could be made if elongation at fracture data from two bounding free lengths is available (i.e. if the parameter *s* can be reliably defined).
- "Nut functionality" was generally lost between about 2% and 6% elongation. Larger diameters generally failed at lower strains, as predicted by a geometric calculation based on the thread dimensions and tolerances of ASME B1.1. However, there was very significant scatter in the data, and certain combinations of materials and sizes were found to exhibit lower failure strains than expected. It is hypothesized that surface finish may play a role in this phenomena, but this was not verified as part of the current work.
- The numerical model calibrated on the basis of test results from the 1 in. diameter allthread was capable of very accurate predictions of yield and ultimate strength for other diameters. Prediction of elongation at fracture was generally good, but errors up to almost 30% were observed for the largest diameters and most extreme diameter/length ratios. Therefore, although this model has the capability to predict mechanical behavior outside the range of parameters tested, its use should be

limited for critical design situations and verified with test data wherever possible. Based on engineering judgment, it is likely that this model would give reasonably accurate results up to anchors of 2 or perhaps 2-1/2 in. diameter and free lengths up to 16D for products with similar manufacturing processing.

- The difference between the exposed length and the stretch length for all types of anchors is an extremely important issue for practicing engineers attempting to comply with building code requirements regarding stretch length (ACI 318-14). This issue is important because adding anchor stretch length via steel chairs on the topside of the baseplate or via an additional unbonded embedment depth is expensive, and difficult to accommodate in many situations. Currently, the code does not provide any type of guidance about what the stretch length should be considered to be, however it seems to suggest that the stretch length should be assumed equal to the exposed length. Based on the reference testing performed this assumption appears to appropriate for bonded anchors. However, this assumption appears to be unnecessarily conservative for cast-in anchors, especially those that are smooth-shank but also for those that are fully threaded in the cast-in portion. This conclusion is limited to a single anchor size (3/4 in.), therefore, additional research should be carried out to determine the relationship between exposed length and stretch length for common anchor types and sizes. Additionally, theoretical calculations should be carried out to determine an analytical relationship between matrix strength, matrix bond, thread geometry, and strain penetration (and resulting anchor deformation capacity).

2.5 Acknowledgement of Publications

Chapter 2 contains material published in the following journal paper: Trautner, C., Hutchinson, T., Copellini, M., Grosser, P., Bachman, R., and Silva, J. (Accepted). "Developing Ductility using Concrete Anchorage," American Concrete Institute Structural Journal. The dissertation author was the primary author on this paper.

Chapter 3: Component Testing of Steel Column Baseplate Connections

3.1 Introduction and Motivation

One of the overarching themes of this research is the hypothesis that ductility and energy dissipation may be realized through the structural concrete fastening, and features of the design of the connection may be exploited to promote these behaviors. As noted in Chapter 1, there have been efforts to investigate the behavior of moment frames with uplifting columns, but none have incorporated anchors as part of the uplifting mechanism. Using anchors in this fashion is an attractive approach, as it would require a minimal deviation from traditional construction practice, in contrast to some of the more exotic uplifting connections that have been tested to date (Clough 1977, Midorikowa 2006). In addition, there are a number of situations that commonly arise in "traditional" construction that have not been systematically studied. These include the following issues:

- Cast-in headed anchors typically consist of partially-threaded bolts conforming to ASTM F1554, equipped with washers and nuts to secure the baseplate. However, post-installed anchors, both mechanical and adhesive-type, are regularly used in baseplate connections to correct errors in construction, for light metal buildings, nonbuilding structures, and for the attachment of nonstructural components.
- Leveling nuts, placed below the baseplate, are a commonly-employed method for plumbing the column. However, their effect on connection behavior is unknown. In practice, the column leveling procedure is often left to the

discretion of the steel erector and does not enter into the analysis or design of the connection, a critical assumption that has never been formally tested.

- An assumption of bolt yield in design is generally only useful when associated with a defined length over which yield strain can develop. Anchor design procedures for seismic loading have historically included requirements associated with bolt yielding (e.g. ACI 2002, 2011). However, there has been increasing interest in using stretch length to provide ductile connection behavior, largely stemming from confirmation of the generally good performance of baseplate and tank anchorages employing a defined stretch length in the 2010 Maule, Chile earthquake (Soules et al. 2016). As a result, ACI 318-14 (2014) now includes specific design guidance for anchor stretch length where yielding is desired, as discussed in Chapter 1.
- All of the published literature on baseplate connections has used either monotonic or reversed cyclic loading following the SAC steel protocol (Clark 1997) or a similar symmetric protocol. Potential differences in behavior caused by different types of loading, specifically near-fault loading, has not been studied.
- Various other detailing considerations such as the baseplate hole size and the use of smooth-shank versus fully-threaded cast-in anchors are subjects of ongoing debate among code writers. The effects of such details have not been the subject of systematic testing.

The testing presented in this Chapter was carried out partly to evaluate characteristics of highly ductile connections which could be used in uplifting-type systems, and partly to investigate the behavior of traditional column baseplate connections that fall into one of more of these categories.

3.2 Experimental Design and Procedure

3.2.1 Background

The behavior of these types of connections may be broadly classified as "rigid-plate", "flexible plate", or "intermediate", depending on whether the thickness and configuration of the baseplate permits the formation of a plastic hinge in the plate before or after the anchors yield (see Figure 1-2, after Astaneh 1992). There is general consensus that current and historical design requirements and guidelines in the United States, including the AISC *Seismic Provisions for Structural Steel Buildings* (AISC 2005c, AISC 2010) and AISC DG1 (Dewolf and Ricker 1990; Fisher and Kloiber 2006), will result in intermediate-plate behavior (Grauvilardell et. al 2005), possibly tending toward rigid-plate behavior (Lee and Goel 2001). Because of this, and due to the fact that probing the effects of anchor selection was an underlying test objective, the column-baseplate assembly was designed to remain elastic throughout the testing program. This had the added advantage that the fixture could be re-used in subsequent tests. It should be noted that the research presented herein is applicable primarily to exposed moment-dominated base connections such as those supporting moment frames. Connection details common to all tests (grout thickness, concrete reinforcement, etc.)

were selected to be representative of typical construction practice for baseplate connections in the United States.

3.2.2 Specimen design

The seventeen tests were performed on sixteen stations located on four identical concrete slabs with a size of 3ft 9 in by 10 ft 9 in. in plan by 2 ft 9 in tall (Figure 3-1a). A 18 in. square, 1-1/4 in.-thick ASTM A36 baseplate with a 13 in. square 2 x 2 hole pattern was stiffened with 3/4 in.-thick ribs and welded to a W8x48 ASTM A992 steel column stub (Figure 3-1(b), top). This stiffened baseplate (SB) was used for most tests; however for two of the tests the baseplate was modified with larger 33mm dia. holes (condition LH, Figure 3-1(b), middle), or with the larger holes and no stiffeners (condition US, Figure 3-1 (b), bottom). The LH condition represents the baseplate (BP) hole size recommended by AISC Design Guide (DG) 1 for ease of construction (Fisher and Kloiber 2006). Schematics of each of the seventeen tests are shown in Figure 3-2. The features of each of these tests, including the different anchor types, are discussed in subsequent sections. Each test was given a designation consisting of a slab number and a test number. For example, test S2S4 was the fourth test on slab 4. The tests described herein were performed in two phases, with Phase I consisting of slabs 1 and 2 and Phase II consisting of slabs 3 and 4. Full drawings and design calculations for the tests are given in Trautner and Hutchinson (2014a, 2015a).

A photograph of the test setup is shown in Figure 3-3(a). Out-of plane bracing was provided by greased guide beams just below the level of the actuator. Baseplate condition SB is shown in Figure 3-3(a). In one instance, this configuration was

modified with plates on the stiffeners to create a "chair" for an increased stretch length, as shown in Figure 3-3c. This baseplate condition is referred to as SC herein (stiffened, with chair). The column extension was about 7 ft 5 in. to the level of the actuator and about 8 ft 9 in. to the bearing plate at the top of the column. Where required, axial load was applied to the specimen utilizing a spreader beam and a pair of approximately 1 in. diameter post-tensioning bars. The post-tensioning bars were loaded using through-hole jacks reacting against the underside of the laboratory floor.

Instrumentation consisted of a load cell and string pot extensometer at the level of the actuator, load washers and displacement pot extensometers on all anchors, inclinometers on the bottom of the column near the baseplate, and two displacement pots on targets mounted on the baseplate. For the one test where significant baseplate plasticity was expected, strain gages were placed near the edges of the column flanges two inches above the baseplate connection, and at six selected locations on the baseplate.

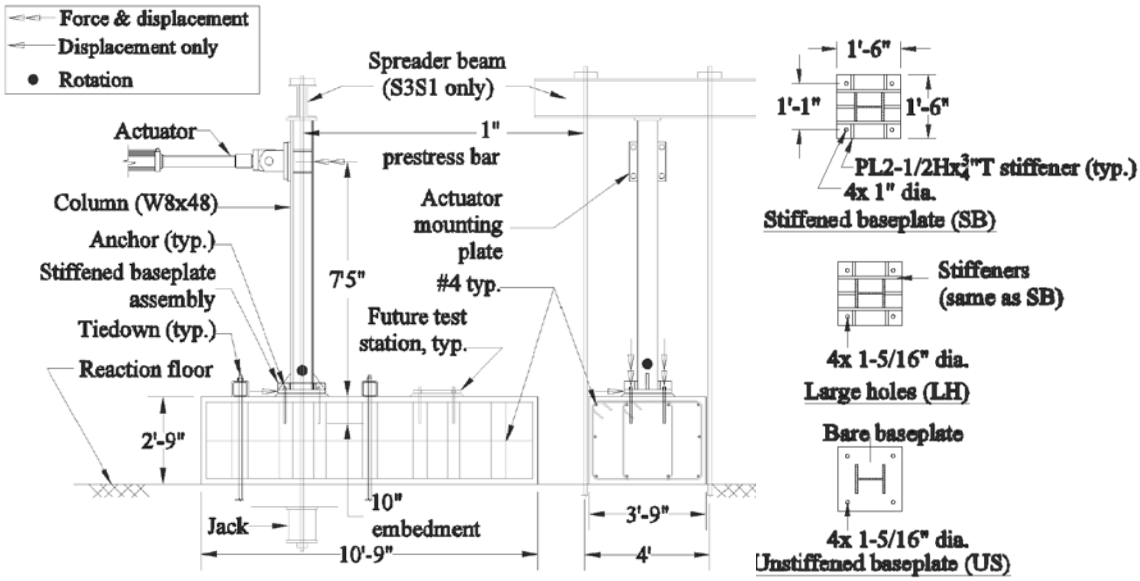

(a) Test specimen and general instrumentation layout (b) baseplate configurations

Figure 3-1: Connection test specimen drawings

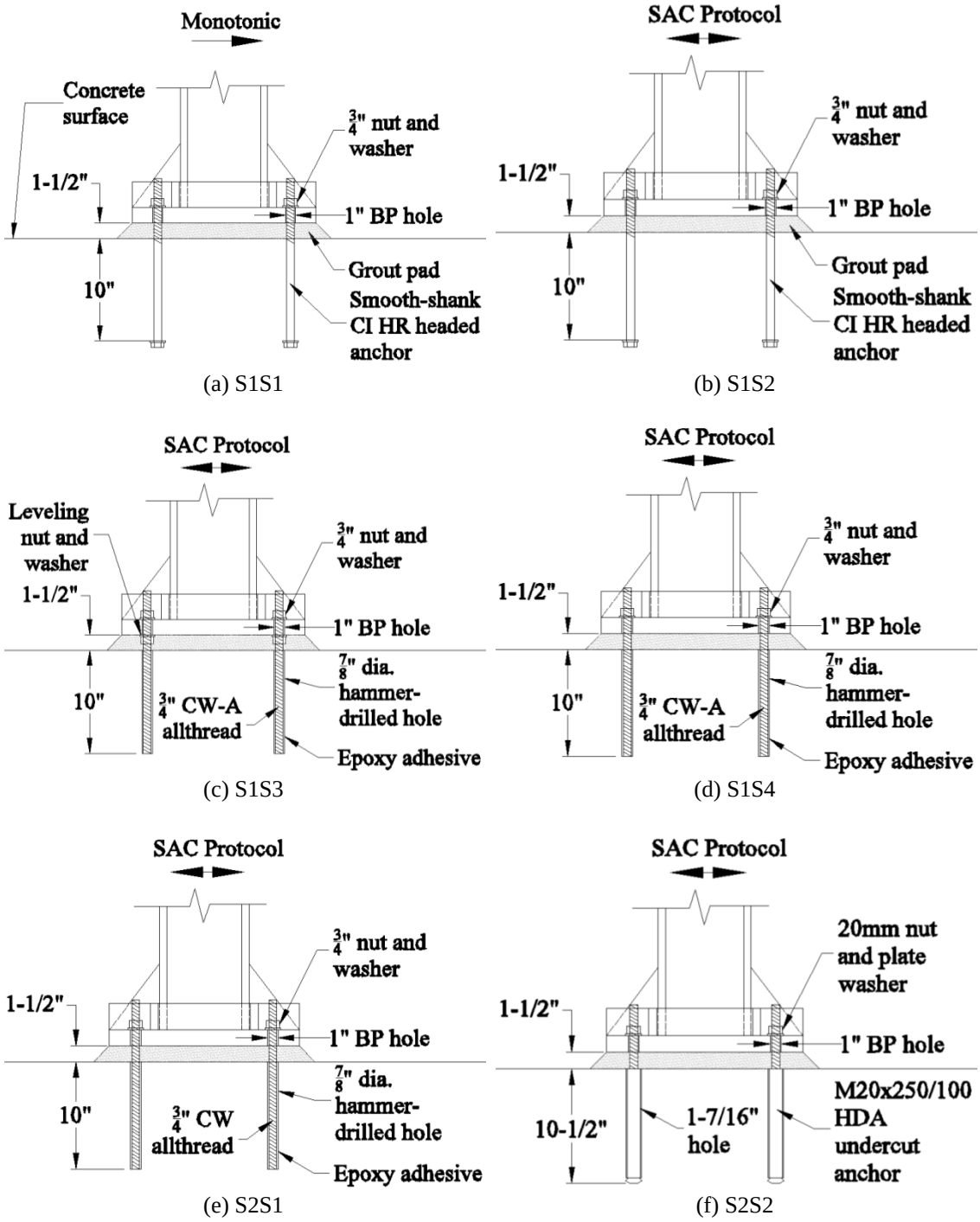

Figure 3-2: Individual elevation diagrams of connection tests

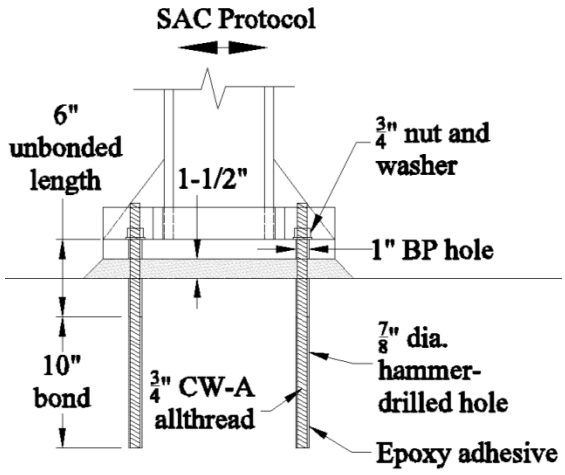

(g) S2S3

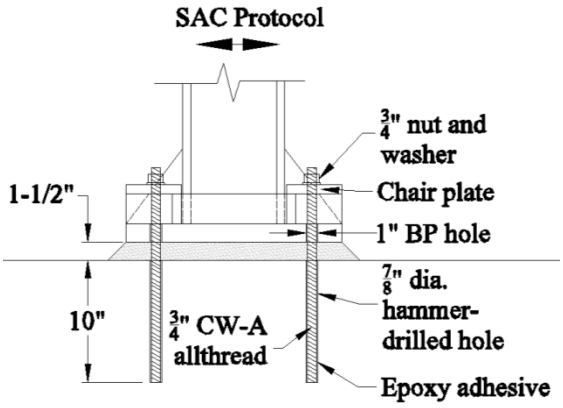

(h) S2S4

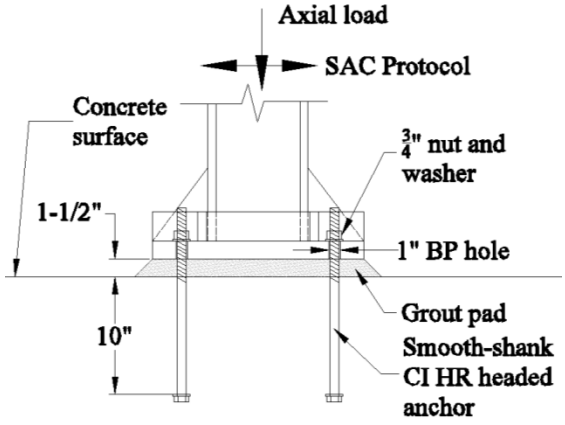

(i) S3S1

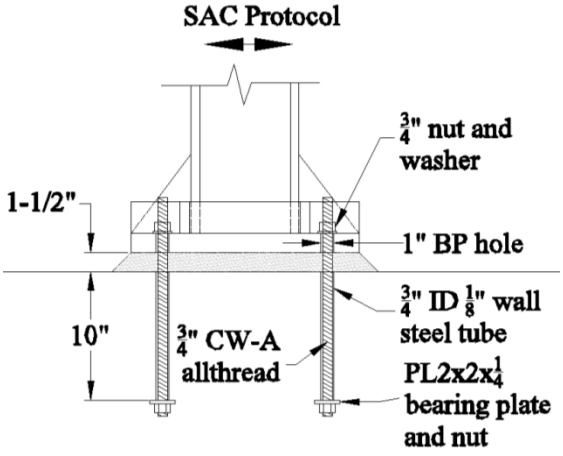

(j) S3S2

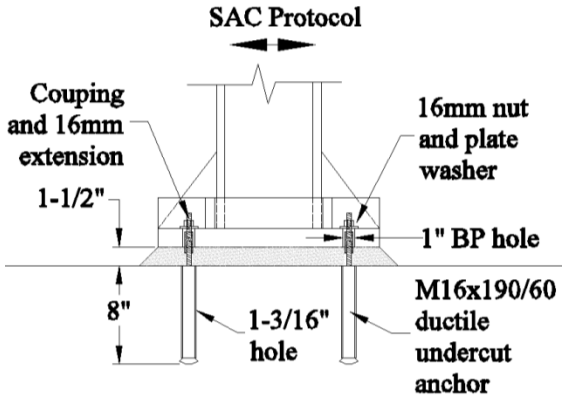

(k) S3S3

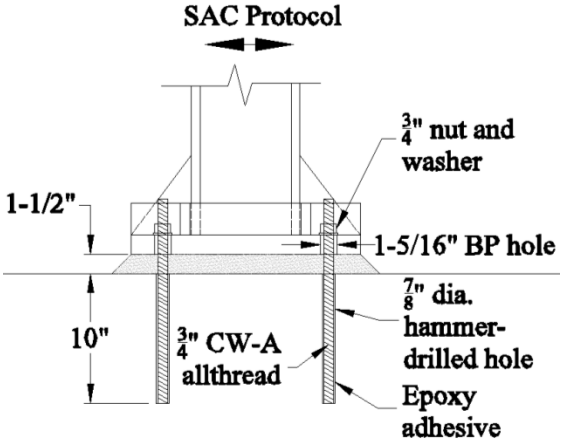

(l) S3S4

Figure 3-2: Individual elevation diagrams of connection tests (continued)

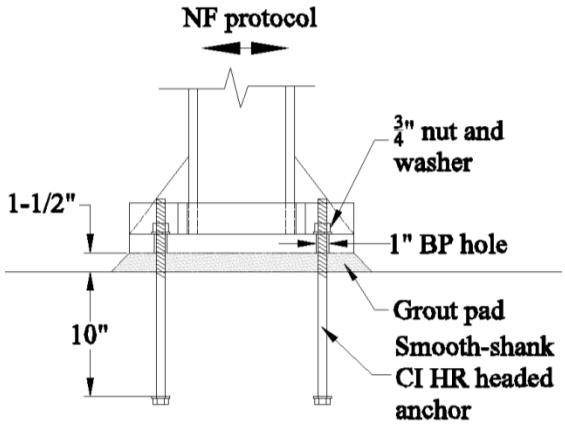

(m) S4S1

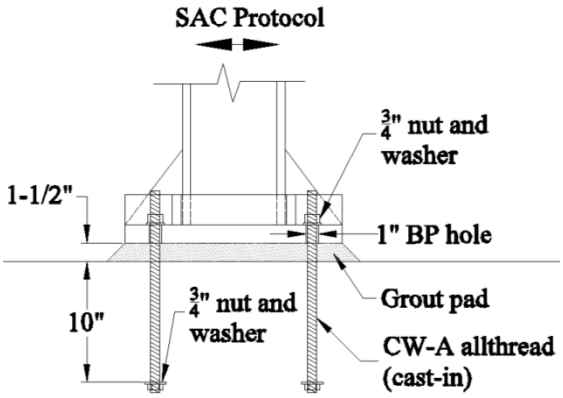

(n) S4S2

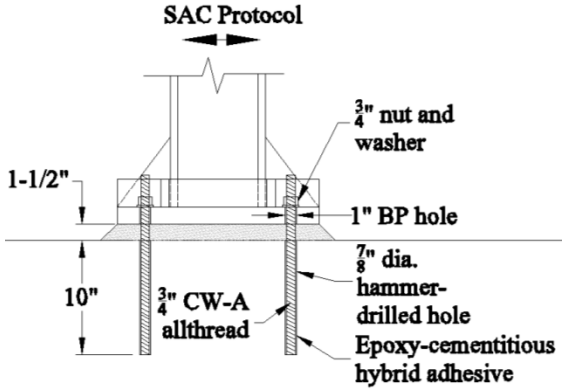

(o) S4S3

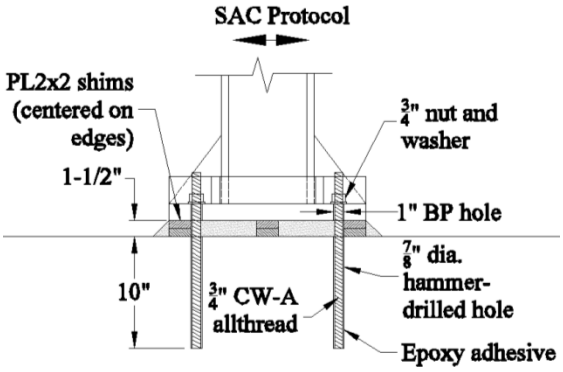

(p) S4S4

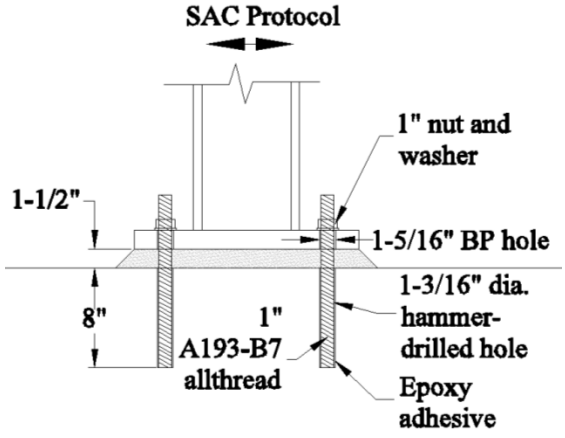

(q) S3S5

Figure 3-2: Individual elevation diagrams of connection tests (continued)

(a) Isometric view of column stub, and details of column base with variable stretch length

(b) Standard

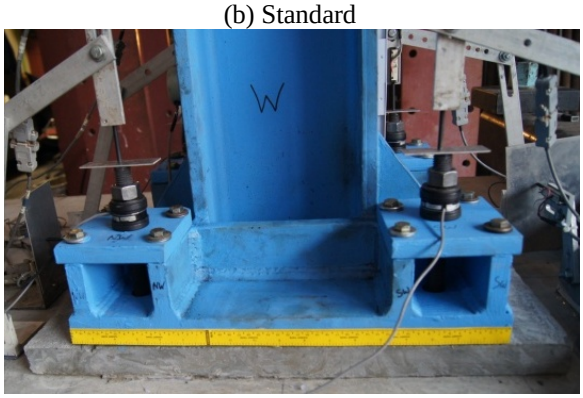

(c) Chair assembly providing 8 diameters (8D) stretch length

Figure 3-3: Photographs of connection test setup

The design of the connections was carried out using the methodology of AISC DG 1 (Fisher and Kloiber, 2006). The intent of the design was to promote ductility of the connection via steel yielding of the anchors with sufficient margin against other failure modes. The anchor embedment (10 in. in most cases, or approximately 13 bolt diameters) was chosen to provide a concrete-governed strength of the anchors (5% fractile) of at least 1.5 times the bolt nominal ultimate strength, consistent with the requirements of ACI 318-11 for seismically-loaded anchors in tension.

3.2.3 Material selection and properties

The material properties of different anchor types are discussed at length in Chapter 2. The connection tests presented herein contained a total of 8 different anchor types/configurations. The mechanical properties of these anchors were determined as part of the tensile and/or reference test series described in Chapter 2, as listed below. Mechanical properties (F_y, F_u and ΔL) for anchors tested as part of the tensile and reference test series are given in Table 2-2 and Table 2-6, respectively.

1. 3/4 in. diameter, cast-in, hot-rolled headed anchors conforming to ASTM F1554 Gr. 36. These anchors were tested as part of the tensile test series of Chapter 2 (Supplier 1 HR Gr. 36 HA) and as part of the reference tests (test series CI)
2. 3/4 in. diameter, cast-in, threaded anchors manufactured from the CW-A allthread from Supplier 1, described in Chapter 2. These anchors were not tested as part of the reference test series.
3. 3/4 in. diameter bonded anchors consisting of epoxy-type adhesive and CW-A allthread from Supplier 1. This anchor type was tested in the BAnn reference test series (BAnnR1-BAnnR3).
4. 3/4 in. diameter bonded anchors consisting of epoxy-type adhesive and CW allthread from Supplier 1. This anchor type was tested in the BAR reference test series.
5. 3/4 in. diameter bonded anchors consisting of a hybrid cementitious/epoxy adhesive and CW-A allthread from Supplier 1. This anchor type was tested in the BAnn reference test series (BAnnR4-BAnnR6).

6. 20-mm nominal diameter, ISO 8.8 undercut anchors. This anchor type was tested as part of the UC reference test series.
7. 16-mm nominal diameter, ISO 4.6 "ductile" undercut anchors. This anchor type was tested as part of the UCSD reference test series.
8. 1-in. diameter bonded anchors, consisting of an epoxy-type adhesive and ASTM A193 B7 allthread inserts from Supplier 4 . This allthread was tested as part of the tensile testing program.

Examples of some of the cast-in anchor types are shown in Figure 3-4. All anchors were provided with ASTM F436 washers and ASTM A563A standard hex nuts, except for anchor types 6-8, above. These anchors were provided with higher-grade heavy hex nuts and washers consistent with the higher mechanical properties of these types.

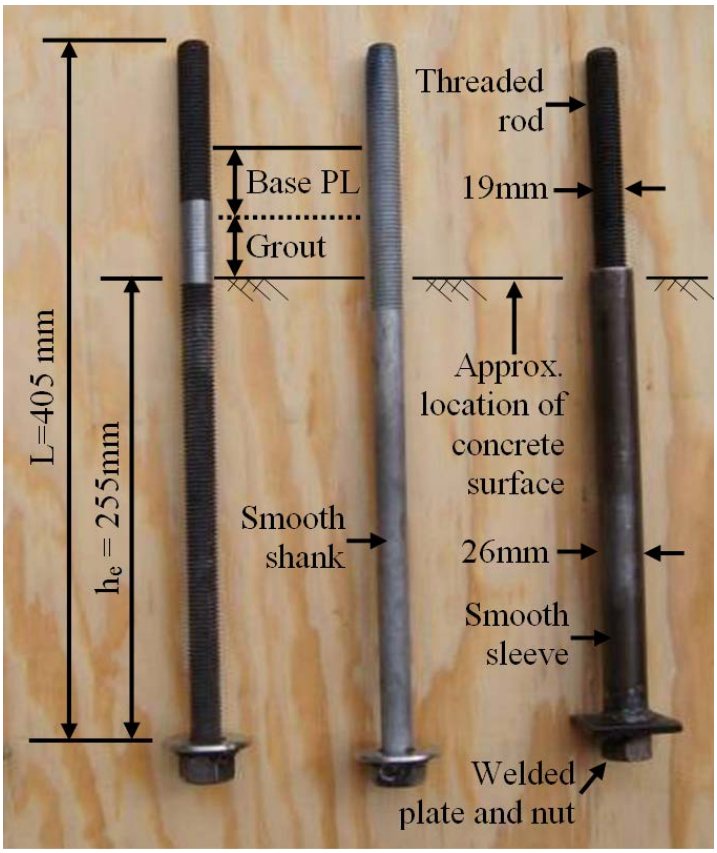

Figure 3-4: Examples of cast-in anchors used in the test program (from left to right): cast-in (fully threaded), cast-in (headed with smooth shank), and removable

Design of the connections was based on a minimum concrete compressive strength of 35 MPa. The concrete in the specimens achieved a 28-day compressive strength of about 41 MPa, and a day-of test range of between 47 and 51 MPa. Although the concrete had a higher strength than desired, this served to increase the margin against concrete breakout failure, and did not otherwise affect the test results. The baseplate grout used for the tests had an average day-of-test compressive strength of 71MPa, and a range between 61 and 81 MPa. This is estimated to be typical for the long-term strength of typical baseplate grouts, and was consistent with tested grout strengths from other published sources (e.g. Fahmy 1999, Gomez et al. 2010).

3.2.4 Test stations

Connection stations were tested sequentially, with cast-in locations performed first. Each test was given a designation with the slab and station number, i.e. test S2S1 was the first test station on slab 2 (Table 3-1). Slabs S1 and S2 comprised the Phase I testing program and S3 and S4 comprised the Phase II testing program. Four tests each were conducted using slabs S1, S2, and S4. Five experiments were conducted on Specimen 3 (S3S1 through S3S5, with one station being used twice). For each test, parameter(s) which were major experimental variables or were compared to previous tests are shaded. Note that the connections are characterized in terms of their *free length*, L_f, defined as the distance from the top of adhesive or concrete to the bottom of the nut (Figure 2-2). This distance is consistent with previous definitions of free length (e.g. Salmon et al. 1957), although occasionally the term *exposed length* has been used. Note that this length is distinct from, and may or may not be equal to, the *stretch length* L_s, the length over which significant plastic strain actually occurs. The stretch length is typically more relevant for the behavior of the connection than the free length. The total anchor length is the free length plus the embedment depth, $L_f + h_{ef}$.

Test S1S1 and S1S2 included cast-in anchors and were identical except for the loading protocol: monotonic for S1S1 and reversed cyclic for S1S2. The baseline test configuration consisted of a stiffened baseplate (SB) set on a pre-formed grout pad without setting nuts or shims (GP), loaded using the SAC drift-controlled steel cyclic protocol (Clark et al. 1997, see description in next section). Test S1S4 incorporated bonded anchors with epoxy adhesive and CW-A inserts. This test provided a control for

several other cases. Test S2S1 was identical to S1S4, except that CW inserts were used. Test S1S3 was identical to S1S4, except that setting nuts were used. Tests S2S3 and S2S4 were identical to S1S4, except that additional stretch length (8D) was provided by unbonding and via the use of a chair, respectively (Figure 3-3(c)). Test S2S2 incorporated self-undercutting anchors.

Test S3S1 was identical to test S1S2, except for the application of a constant axial load of about 70 kips (=10% AF_y, where A is the cross-sectional area of the column) via the spreader beam shown in Figure 3-1. Test S4S1 was loaded with zero axial load, but a loading protocol intended to reflect near-fault effects was utilized (Krawinkler et al. 2000). This protocol, referred to as the cyclic near-fault (NF) protocol herein, is designed to include some of the features which are commonly observed at near-fault sites and is described in the following section. Tests S3S2, S3S3, S4S2, S4S3, and S4S4 were all similar to S1S4, except they utilized different anchor types or anchor adhesive. The 16mm diameter undercut anchors utilized in test S3S3 were modified for increased ductility compared to the 20mm diameter undercut anchors used in test S2S2. Test S3S2 utilized a removable/replaceable anchor. This anchor consisted of a body with a smooth sleeve welded to a bearing plate and nut (Figure 3-4). The body was cast into the concrete, and a threaded rod that could be replaced following a seismic event or other overload was threaded into the bottom nut.

Test S3S4 was otherwise identical to test S1S4, except that the baseplate holes were enlarged to 1-5/16 in. (the LH configuration shown in Figure 3-1). This value was chosen as the diameter recommended by AISC DG 1 (Fisher and Kloiber 2006) to

prevent erection tolerance issues during construction. This value is significantly larger than the values for oversize holes typically used in steel connections (AISC 2005a). Test S3S5 was conducted with 25mm-diameter ASTM A193 B7 (ASTM 2009) anchors bonded with epoxy adhesive. The larger size and high yield strength of these anchors (nominally 105ksi) was used in conjunction with an unstiffened baseplate in an attempt to elicit significant baseplate yielding and connection failure via a concrete-dominated mechanism. This test was conducted in the same station used for test S3S3 by removing the undercut anchors and re-using the holes. The diameter of the concrete holes required for the undercut anchors used in that test were the same as required for 1-in. diameter bonded anchors with threaded inserts for test S3S5, per the manufacturers printed installation instructions. The test was performed last, following modification of the baseplate for larger holes for test S3S4.

Table 3-1: Connection test matrix

Test designation[1]	Fastening[2]	Setting method[3]	BP type[4]	Load protocol[5]	Free length, in. (xD)	Anchor preload/F_y (kN)
S1S1	CI HA	GP	SB	Mono	2.75 (3.7)	5.0/16.4
S1S2	CI HA	GP	SB	Cyclic	2.75 (3.7)	5.0/16.4
S1S3	Bonded (CW-A)	LN	SB	Cyclic	2.75 (3.7)	5.0/17.3
S1S4	Bonded (CW-A)	GP	SB	Cyclic	2.75 (3.7)	5.0/17.3
S2S1	Bonded (CW)	GP	SB	Cyclic	2.75 (3.7)	5.0/17.3
S2S2	Undercut	GP	SB	Cyclic	12.5 (15.9)	16.0/46.3
S2S3	Bonded (CW-A, UB)	GP	SB	Cyclic	6.0 (8)	5.0/17.3
S2S4	Bonded (CW-A, C)	GP	SB	Cyclic	6.0 (8)	5.0/17.3
S3S1	CI HA	GP	SB	Cyclic, AL	2.75 (3.7)	5.0/16.4
S3S2	Removable	GP	SB	Cyclic	12.75 (12.8)	5.0/17.3
S3S3	Undercut	GP	SB	Cyclic	10.25 (16.3)	8.3/9.0
S3S4	Bonded, Epoxy (CW-A)	GP	LH	Cyclic	2.75 (3.7)	5.0/17.3
S3S5	Bonded, Epoxy (A193)	GP	US	Cyclic	2.75 (3.7)	10.1/69.0
S4S1	CI HA	GP	SB	Cyclic, NF	2.75 (3.7)	5.0/16.4
S4S2	CI threaded anchor	GP	SB	Cyclic	2.75 (3.7)	5.0/17.3
S4S3	Bonded, Hybrid (CW-A)	GP	SB	Cyclic	2.75 (3.7)	5.0/17.3
S4S4	Bonded, Epoxy (CW-A)	SS	SB	Cyclic	2.75 (3.7)	5.0/17.3

[1]Designation is SxSy, where x is the slab number and y is the station number.
[2]CI - cast in, HA - headed anchor, CW - cold-worked, CW-A - cold-worked, annealed, A193 - ASTM A193 B7, UB - 8D stretch length via unbonding, C - 8D stretch length via chair (Figure 3-3c)
[3]Baseplate types: GP = grout pad, LN=leveling nut, SS = shim stack
[4]SB = standard (stiffened), LH = large anchor holes, US = unstiffened
[5]Mono - monotonic, NF - near-fault protocol, AL - axial load (P=310 kN=0.10AF_y)

3.2.5 Loading protocol

With the exception of S1S1, which was loaded monotonically, the SAC[8] steel protocol (Figure 3-5) was used for the majority of the tests. This testing protocol was selected because it is the preeminent testing protocol for steel sub-assemblies, and has been used by several other research efforts into the behavior of steel column baseplate connections (Fahmy 1999, Gomez 2010). In order to determine whether load protocol has a significant effect on the performance of baseplate connections, a single test was run with an alternative cyclic load protocol. A protocol with near-fault effects was

[8] An acronym for the organizations responsible for the development of the protocol. See Chapter 1.

desired, as near-fault effects are widely recognized to elicit significantly different behavior and load histories. There are essentially only two near-fault protocols which are widely accepted: the CUREE near-fault protocol and the SAC near-fault protocol (Krawinkler 2009). Although the shape of the CUREE protocol would produce the desired failure sequence in the current tests (i.e. anchor fracture in a monotonic push at the end of the test), the overall shape of the protocol is based on the response of wood-frame structures and does not make sense in the context of the current tests.

The SAC near-fault protocol is designed to include some of the effects which are commonly observed at near-fault sites, namely, a smaller number of larger-amplitude cycles caused by a “pulse” of relatively strong motion (Krawinkler et. al 2000). In contrast to the SAC steel protocol, the SAC near-fault protocol is also directionally biased. This means that there are a greater number of cycles in one direction versus the other, and the protocol does not return to zero after every displacement excursion. The drift history of the near-fault protocol is plotted in Figure 3-6. In the event that the connection did not fail after the completion of the protocol, a monotonic push was added in order to achieve anchor fracture.

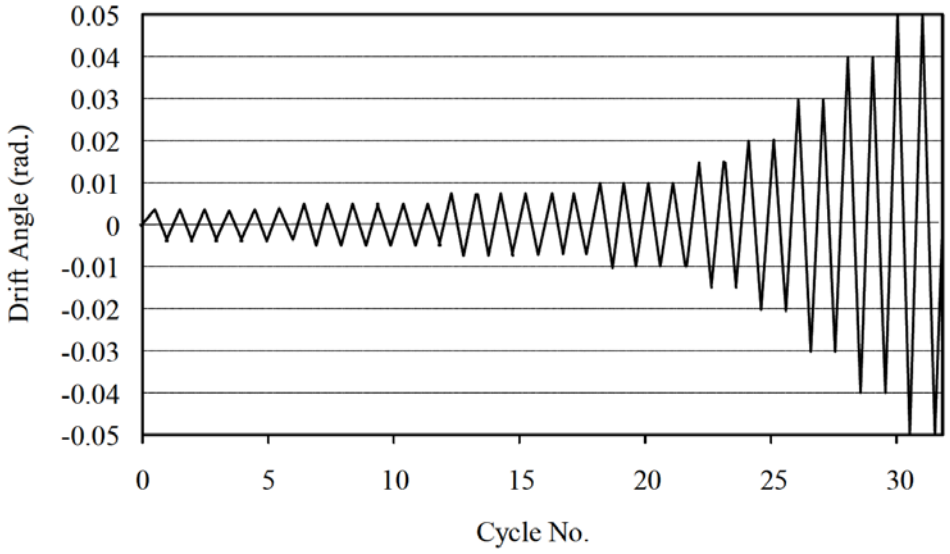

Figure 3-5: Displacement history of SAC Steel Protocol (from Krawinkler 2009)

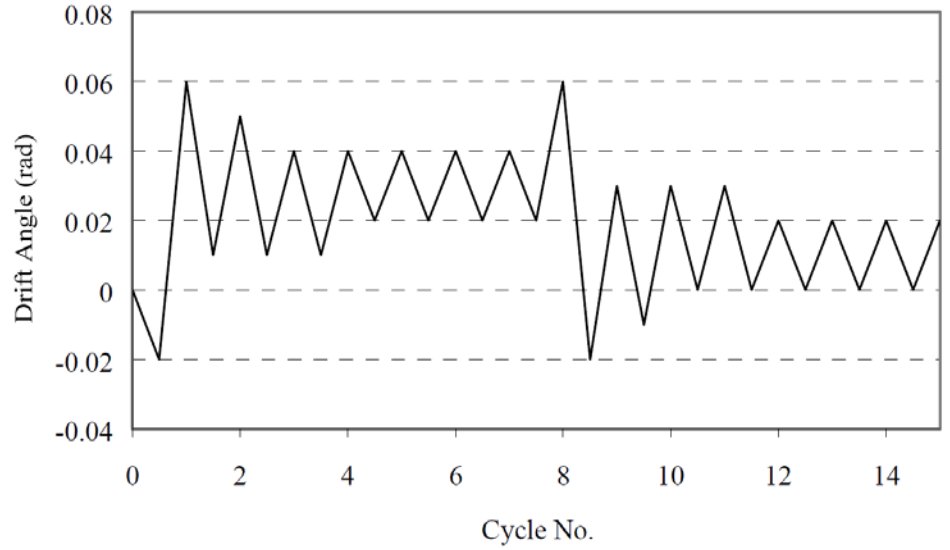

Figure 3-6: Displacement history of SAC Near-Fault Protocol (from Krawinkler 2009)

3.3 Damage Evolution and Limit States

To the author's knowledge, there does not exist a standardized hierarchy of connection damage states for column baseplate connections. To aid in the analysis and discussion of the current tests and to facilitate comparisons with other tests in a performance-based framework, damage states were developed to describe the "health" of the connections during testing. In general, connection damage and eventual failure is caused by damage to any of the connection components, including the grout and/or concrete, anchors and/or shear lugs, or the baseplate and/or column (e.g. Picard and Beaulieu 1984, Fahmy 1999, Gomez 2010). Damage to each of these components may be categorized as minor, moderate, or severe. Minor damage is generally more cosmetic and will have a limited impact on connection stiffness, severe damage compromises the connection's stiffness and/or strength significantly, and as a result will cause connection failure. To facilitate tracking of the damage states, damage to each component was assigned a prefix: "CG" for concrete or grout, "A" for anchors, and "B" for the baseplate. The severity is expressed by a number, ranging from 0 for none/very minor to 3 for severe damage. The proposed limit states relevant to the current tests are summarized in Table 3-2.

The observed connection rotations corresponding to each damage state are summarized in Table 3-3. For the tests with the cast-in anchors in Phase I of the work (S1S1 and S1S2), softening of the connection was observed around 2-3millirads. Post-test coring and recovery of the anchors revealed localized crushing around the anchor head, due to concrete paste intrusion between the provided structural washer and bolt head, identical to what was found for the CIR reference test series (Figure 2-16). This

was prevented in subsequent tests with CI headed anchors by tack-welding the bearing washer to the anchor head. Anchor yielding was observed in all tests between 2 and 9 millirads. This limit state was determined by examining the load-displacement data from the fasteners. The relatively tight bunching of this limit state makes sense from a kinematic point of view - anchors with similar yield strengths are undergoing an essentially identical forced connection rotation would be expected to yield at approximately the same time.

Connections that were dominated by anchor plasticity in the nonlinear range of response attained limit state A-1, corresponding to the yield stiffness, at a rotation of less than 10 millirads. Limit states A-2 and A-3 were variable, and were strongly dependent on the yield strength and elongation capacity of the anchor steel, as might be expected. Limit state CG-2 was generally associated with extensive cracking and crushing of the grout at the compression toe of the connection, followed by anchor fracture (A-3), as shown in Figure 3-7(a) and (b). Connection failure caused by anchor fracture (damage state A-3), generally occurred at connection rotations between 37 and about 150 millirads, although this was highly dependent on the variables of the particular test.

Initial grout cracking for the baseplate dominated test S3S5 occurred at a similar rotation as the anchor-dominated cases. Baseplate yield occurred at a rotation of approximately 10 millirads followed relatively quickly by cracking of the flange/baseplate welds at about 19 millirads (Figure 3-7c). This finding was in line with the observations of Fahmy (1999), who found that cracking and eventual fracture

may occur prior to the attainment of any other limit states, and concluded that proper weld detailing and fracture-toughness requirements may be necessary for proper connection function. Although this connection eventually failed due to anchor bond/breakout failure (Figure 3-54), it seems likely that given the very early development of weld cracks, weld fracture may have been a controlling limit state given even slightly higher anchor strength.

Table 3-2: Proposed damage states and descriptions

State	Description and criteria	Consequences
CG-1	Initial cracking of grout or concrete, localized around compression toe and/or anchor holes	Minimal reduction of connection bending stiffness. Damage is cosmetic, repair unnecessary.
CG-2	Widespread cracking of grout and/or concrete	Additional softening of connection. Grout and concrete may require chipping and replacement to assure bearing is not compromised in future loading.
CG-3	Extensive grout or concrete cracking and crushing	Significant loss of connection stiffness. May be associated with maximum connection strength, depending on relative strength of grout and anchors. Possible loss of shear capacity. Grout will require extensive repair and/or replacement.
A-0	Initial softening	Caused by localized crushing around anchor head. Applicable only to cast-in anchor types
A-1	Initial yield	Significant softening of connection. Anchor bolts may require re-tightening.
A-2	Elongation at half of that required for fracture	Anchor bolts may require replacement, depending on thread tolerance, anchor ductility, and total anchor elongation.
A-3	Fracture	Failure of connection, sudden loss of connection capacity. Replacement of anchors, additional drilling of baseplate to accommodate post-installed anchors may be necessary.
B-1	Initial yield in baseplate	Softening of connection bending stiffness. Degree of reduction in stiffness will depend on configuration of connection and location of initial yield.
B-2	Development of baseplate plasticity	Development of maximum connection strength. Baseplate may need repair or replacement. Column-BP welds may begin to fracture.
B-3	Baseplate fracture	Development of fractures in the baseplate or in the baseplate-column or baseplate-stiffener welds. Associated with sudden loss of capacity. Baseplate connection will require extensive repair or replacement

Damage variables: CG: grout and/or concrete, A=anchor, B=baseplate; 0: very minor, 1: minor, 2: moderate, 3: severe

Table 3-3: Summary of observed damage states, observed yield strength, observed and predicted connection strengths, and secant stiffnesses

	Connection rotation corresponding to damage state, millirad								Connection strength, M_u (kip-in)		Yield strength, M_y (kip-in)	Secant yield stiffness β_y (kip-in/mrad)	
Test	CG-1[a]	CG-2	CG-3	B-1/B-2	A-0	A-1	A-2	A-3	Observed	Predicted[b]	Observed	Observed	Predicted[c]
S1S1[d]	P	28	-	-	2	8	-	-	894.8	847.0	415.6	52.0	74.0
S1S2	2	15	-	-	3	7.5	65	149	828.5	847.0	442.8	59.0	74.0
S1S3	2	12	-	-	-	2.5	35	68	715.2	711.6	440.3	176.1	92.1
S1S4	12	35	-	-	-	4	46	93	747.9	711.6	368.2	92.1	92.1
S2S1	P	15	-	-	-	3.5	19	37	998.4	945.3	511.1	146.0	128.3
S2S2	P	21	-	-	-	9	25	51	1560.4	1637.4	1378.1	153.1	137.2
S2S3	3	91	-	-	-	4	58	125	749.7	711.6	389.4	97.4	86.0
S2S4	1	37	-	-	-	5	60	122	739.9	711.6	424.8	85.0	86.0
S3S1	P	17	73	-	-	3	72	152[e]	739.1	809.0	425.6	141.6	72.6
S3S2	P	21	-	-	-	10	85	161+	697.5	711.6	507.3	85.0	77.9
S3S3	P	28	-	-	-	5	46	93	446.1	442.6	239.1	79.7	70.8
S3S4	15	31	-	-	-	7	47	97	694.8	711.6	497.7	99.1	92.1
S3S5	5	21	27	10/19	-	26	-	31[f]	1554.2	1597.6	569.1	75.2	72.6
S4S1	19	54	-	-	-	8	75	153	840.0	847.0	595.3	70.8	74.3
S4S2	14	39	-	-	-	8	66	140	703.7	711.6	560.4	59.3	92.1
S4S3	15	40	-	-	-	9	52	109	700.1	711.6	488.9	80.5	92.1
S4S4	9	35	-	-	-	3	48	100	684.2	711.6	1341	162.9	92.1

Notes: Dark gray indicates slight over prediction of moment strength, light gray indicates significant over- or under-prediction of rotational stiffness.

[a] "P" indicates damage state was attained during anchor preloading.
[b] Prediction per AISC DG 1 method
[c] Prediction per Kanvinde et al. (2012) method
[d] Direct rotation measurement not made, all rotations estimated from drift measurements accounting for elastic flexibility of the column. Test not run to failure.
[e] Failure after removal of axial load.
[f] Failure by concrete breakout/bond failure of anchors; all others by anchor steel fracture.

(a) Test S3S1: damage state CG-2

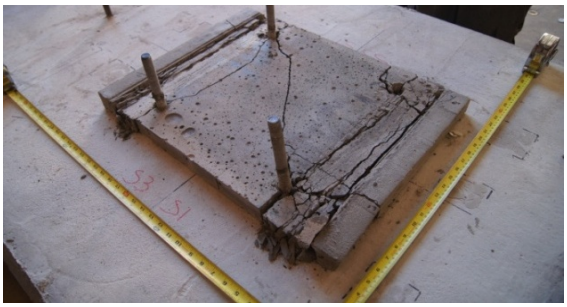

(b) Test S3S1: damage state A-3/CG-3

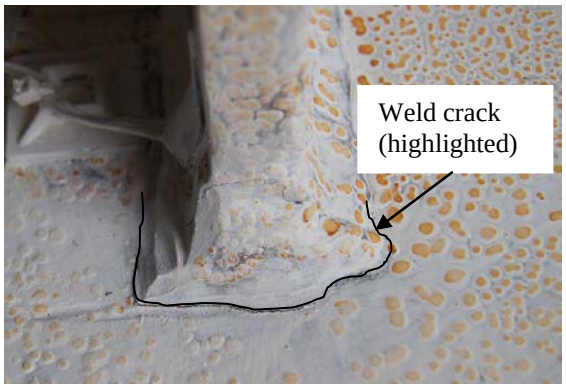

(c) Test S3S5: damage state B-2

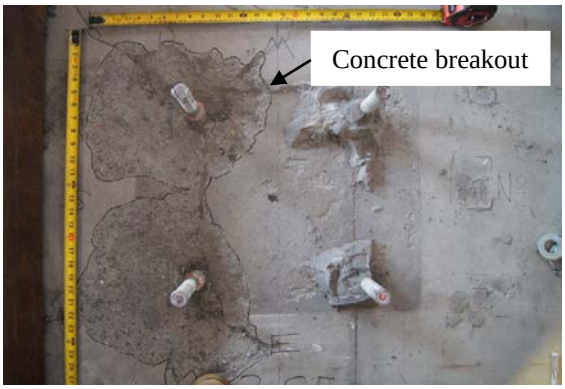

(d) Test S3S5: damage state A-3

Figure 3-7: Prominent damage states

The predicted strength of the connection was calculated using the AISC DG 1 methodology, which assumes a uniform compressive bearing stress q is distributed over an area that is the width of the plate *B* by some fraction *Y* of the total length of the plate N (Figure 3-8), where:

$$Y = \left(f + \frac{N}{2}\right) \pm \left[\left(f + \frac{N}{2}\right)^2 - \frac{2P_r(e+f)}{q_{max}}\right] \qquad \text{Eq. 3-1}$$

In this equation, *f* is the distance from the tension side anchor to the application of force and moment, P_r is the applied axial load, and q is the maximum bearing stress, as shown in Figure 3-8. The ultimate strength of the connection is then calculated as:

$$M_n = \frac{1}{2} F_u (N + d_a - Y) \qquad \text{Eq. 3-2}$$

where F_u is the sum of the ultimate anchor strengths on the tension side (two times the values given in Table 2-2 for the current test setup) and d_a is the distance between the anchors. In design situations, it is desirable that the calculated ultimate strength be equal to or slightly less than the observed ultimate strength to support an accurate, but conservative design methodology. In general, the agreement between the calculated and observed strength was excellent, with predictions within about 5% of observed values for all but three cases, including S3S1. In this case, the predicted strength was about 10% higher than the observed strength. This difference is believed to be due to the axial load combined with the large number of cycles imposed on the connection by the time ultimate strength was achieved. The combined effects resulted in extensive grout damage, particularly near the edges of the baseplate (Figure 3-7b). This likely lead to a smaller distance between the tensile and compressive resultants than assumed by the AISC DG 1 methodology, which is an implicitly monotonic analysis procedure and does not consider the accumulation of cyclic damage to the grout. However, a 10% difference in predicted and achieved connection strength would likely not be of significant concern for typical design situations. The predicted connection strength for test S3S5 was calculated using the expected strength of the anchor group versus ACI 318-14 (ACI 2014), and was within about 4% of the observed value.

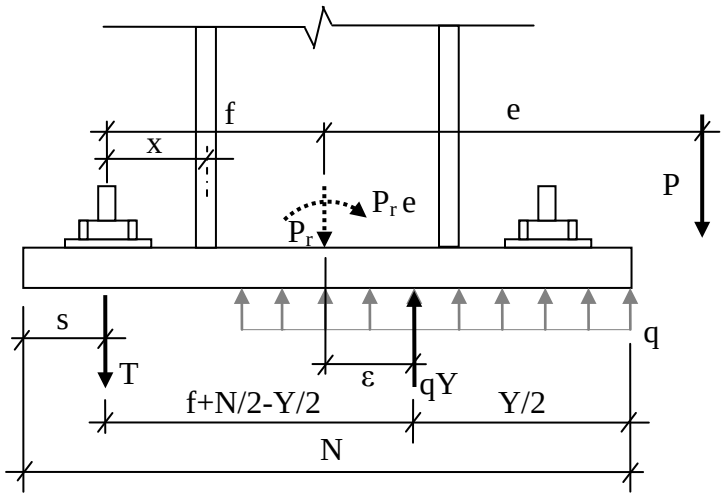

Figure 3-8: Assumed baseplate force distribution with large moment (after Fisher and Kloiber 2006)

Although the predicted strength was within about 5% for tests S1S1 and S4S1, these tests indicate a potential issue with the AISC DG 1 methodology. This issue is related to the anchors that are effective in tension at different levels of rotation. For this particular connection, when loaded monotonically or asymmetrically in one direction, both pairs of anchors are engaged in tension as the connection is rotated. Conversely, when loaded cyclically, both anchor pairs accumulate plastic deformations at small rotations. Therefore, when the maximum connection strength is attained at a relatively large rotation, only the extreme tensile anchor pair is effective. This mechanism is discussed in greater detail in the next section. Although this phenomenon had a relatively minor effect on the tests presented herein, connections designed with multiple rows of fasteners could be more severely affected if anchors that sustain plastic deformation in both directions are included in the moment strength. The potential for this occurrence should be identified in future revisions to the standard.

The data in Table 3-3 also include the stiffness associated with the first yield of the connection, β_y, according to the method of Kanvinde et al. (2012). This method is was formulated based on tests with cast-in anchors (Picard and Beaulieu 1985, Gomez et al. 2010). This method uses many of the same concepts and notation as the AISC DG 1 method for determining connection strength. For the case of high eccentricity (i.e. when the plate is expected to uplift on the tension side, as is the case for the current tests), the rotation associated with first yield is determined by the addition of component deformation associated with first yield of the connection:

$$\theta = (\Delta_{rod} + \Delta_{plate}^{tension} + \Delta_{plate}^{compression} + \Delta_{concrete})/(s + N/2) \qquad \text{Eq. 3-3}$$

where s is the anchor edge distance, Δ_{rod} is the upward elastic deformation associated with the anchor bolts, Δ_{plate} is the downward and upward deformation associated with the plate on the compression- and tension-side flaps extending outward from the column faces, and $\Delta_{concrete}$ is the downward deformation associated with elastic deformation of the footing (as defined in Fig. 6 of Kanvinde et al. 2012). Anchors of all types were cored and examined after testing, and significant reductions in diameter were measured over the full anchor length for cast-in and undercut anchor types, and only over the exposed length for the adhesive anchors. Therefore, the length of the anchor considered in the calculation of Δ_{rod} was the full embedded length of the anchor for the cast-in and undercut connections, and the exposed length of anchor for the adhesive connections. The method produces substantial agreement in most of the tests (within about 15%) with a few notable exceptions, shaded in Table 3-3. First, the connections incorporating cast-in anchors with un-welded bearing washers (S1S1 and S1S2) had significantly lower

observed stiffnesses than predicted. This is most likely due to the paste crushing around the anchor head noted previously, which served to soften the anchors at lower loads. The second exception is the test incorporating leveling nuts and shim stacks (S1S3 and S4S4, respectively). These two tests exhibited a secant stiffness nearly double that predicted. The reason for this is likely twofold. In the case of S1S3, the pretensioning of the anchor clamps the baseplate between these two nuts, resulting in direct bending of the anchors during baseplate rotation, therefore increasing overall rotational stiffness. Secondly, in both cases, it is likely that the baseplate compression is carried at least partly by compression on the setting nut through the anchor at small rotations. This is a stiffer load path than direct bearing on grout assumed in the method by Kanvinde et al.

3.4 Data analysis and comparisons of hysteretic behavior

3.4.1 Axial Load Comparison

Test S3S1 was identical to test S1S2 except for the applied axial load, F_a, of approximately 70 kips and the condition of the bearing washers at the bottom of the CI anchors. In test S1S2, the bearing washers were loose on top of the anchor head, which allowed paste to intrude between the anchor head and the washer (Figure 2-16). In test S3S1, the washers were tack welded to the anchors prior to insertion into the concrete, preventing this problem. The observed initial stiffness was significantly higher than the initial stiffness observed in test S1S2 (Table 3-3). Unfortunately, it cannot be ascertained how much of the difference in the stiffness prior to yield is due to the difference in the anchor head condition versus the stiffening effect of the axial load. The moment presented in Figure 3-9 for test S3S1 is simply the raw actuator force multiplied by the

vertical distance between the connection and the actuator connection. The spikes in the data due to sudden stops of the test have been removed.

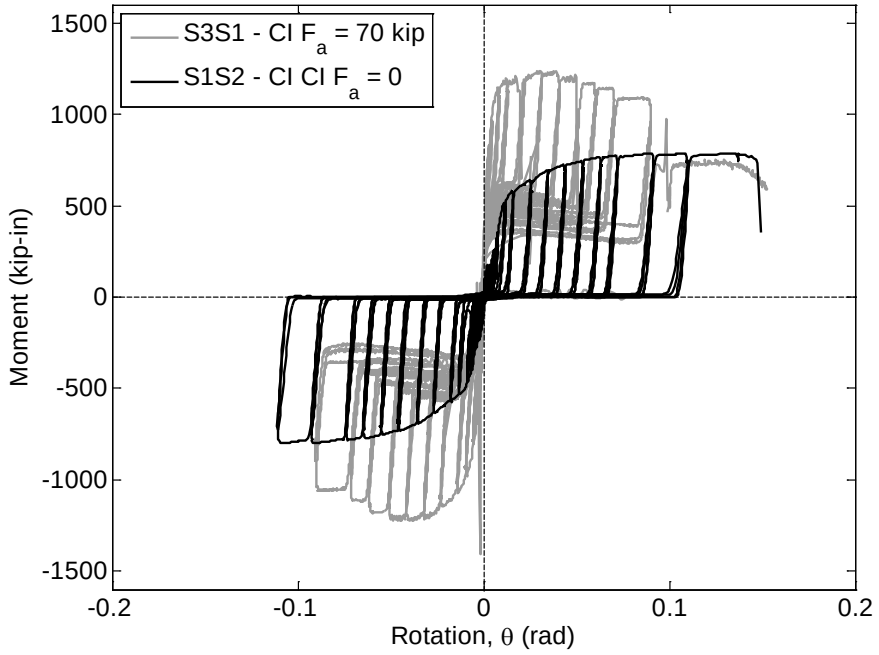

Figure 3-9: Moment-rotation comparison: with and without axial load (no correction to moment calculated using actuator force only)

In all other tests, the moment experienced by the connection is simply the measured lateral actuator force multiplied by the vertical distance to the connection. The moment shown in Figure 3-9 for test S3S1 is not equal to the moment resisted by the connection due to the application of the axial load, which causes an additional moment about the base of the connection. This additional moment must be removed to determine the moment actually carried by the connection. In the undeformed configuration, the axial load has no eccentricity about the base and does not impart an additional moment to the system (Figure 3-10). Here, the horizontal measured force on the actuator is denoted F_h, the measured axial load is F_a, the compression force from the grout on the baseplate is C,

and the shear resisted by the anchors and grout is lumped together in V_c. Because the friction force from the grout is assumed to be much larger than the shear resisted by the anchors, this force is co-located with the grout compressive force *C*. As the system is deformed, both the lateral and vertical components of the measured axial force F_a create a moment about the base, as shown in Figure 3-11. When the connection is engaged, as at the beginning of the test and at each excursion of the hysteretic loop, the anchors exert a tensile force T at the bottom of the connection. The required correction can be found by calculating the moment from the axial force about the point of contact of C.

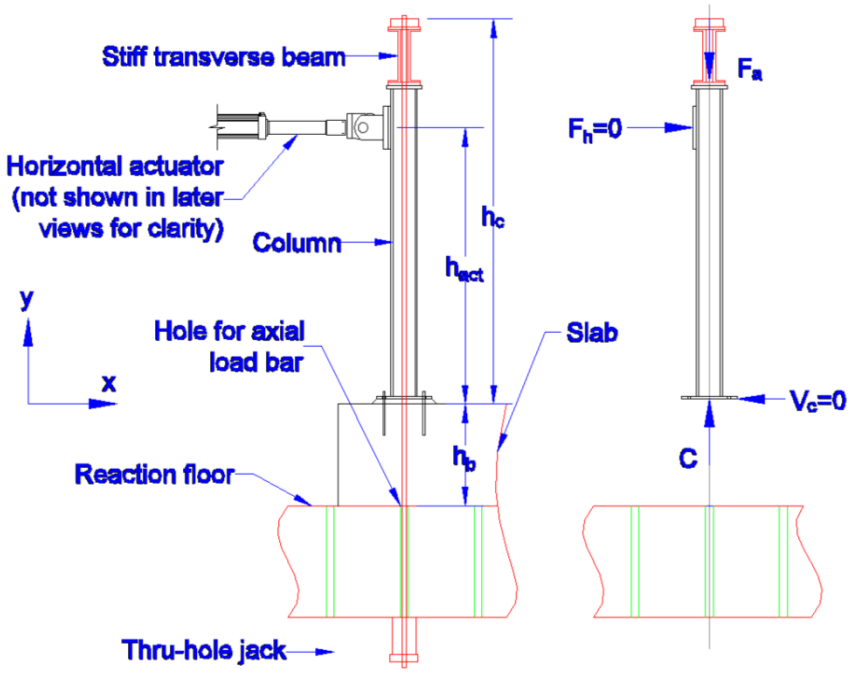

Figure 3-10: Diagram of test S3S1 and free-body diagram of column in undeformed configuration

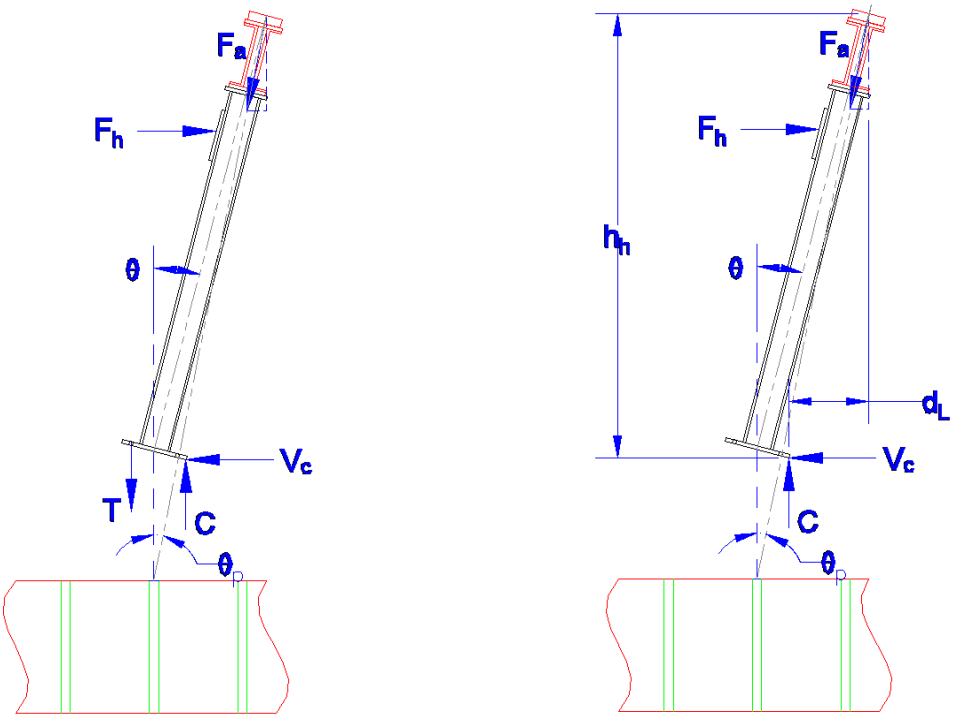

(a) With connection engaged

(b) with connection disengaged after anchor yielding (right)

Figure 3-11: Free-body diagrams of column assembly

As shown in Figure 3-11, it is assumed that the post-tensioning bar rotates about a point where it enters the floor. The rotation of the bar measured from vertical, θ_p, is not equal to the connection rotation, but may be calculated by the measured actuator deformation. The variation of the bar rotation as a function of connection rotation is shown in Figure 3-12. With this, the horizontal and vertical components of the applied axial force F_a may be calculated using Eq. 3-4 and 3-5. There were several emergency stops which caused sudden drops in the applied axial load due to the rapid movement of the column (Trautner and Hutchinson 2015a, 2015b). However, other than these points, the axial load varied a maximum of about +/- 5% from the average value of 72 kips

(Figure 3-13). Therefore, throughout the following calculations, the average value of F_a=72.0 kips was used.

$$F_{ah} = F_a sin(\theta_p) \quad \text{Eq. 3-4}$$

$$F_{av} = F_a cos(\theta_p) \quad \text{Eq. 3-5}$$

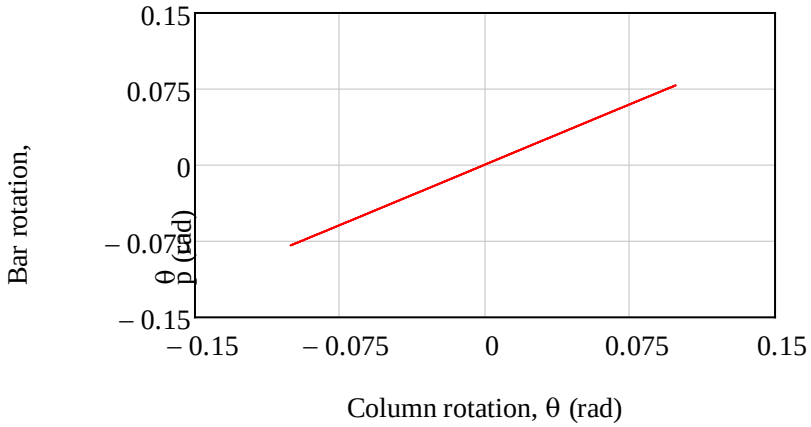

Figure 3-12: Variation of bar rotation θ_p as a function of column rotation θ

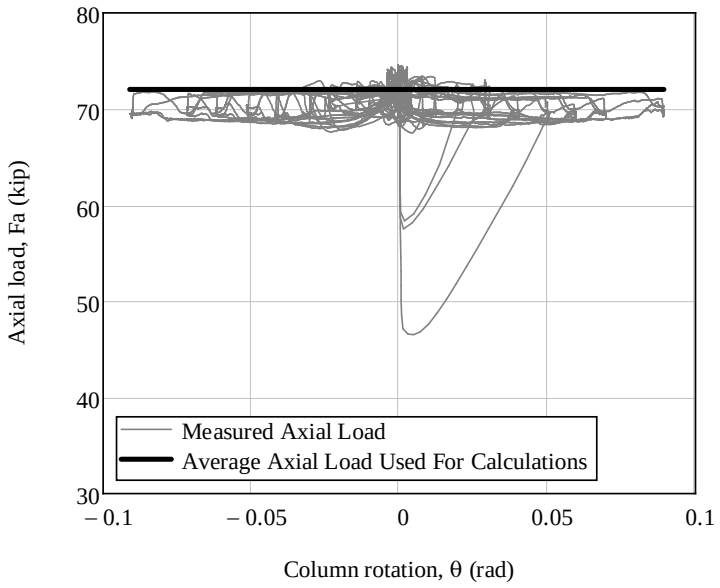

Figure 3-13: Applied axial load as a function of column rotation and average axial load used for calculations

The variation of these forces with connection rotation is shown in Figure 3-14. Note that under large deformations, the vertical force becomes very slightly smaller. The vertical distance from the connection to the horizontal component is essentially constant. However, the horizontal location of the compression resultant changes, depending on the direction of loading. That is, it is on the south side of the baseplate when loading is to the south, and the north side of the baseplate when loading is to the north. This movement is further complicated by the warping of the baseplate (Trautner and Hutchinson 2014a, 2014b). In previous analysis, idealization of the baseplate bottom surface as a semi-circular arc with a maximum edge gap of 1/16 in. gave good agreement with observed test results. Using the same idealization, the horizontal distance from the undeformed column centerline to the contact point, denoted d_{cc}, can be calculated based on the rotation of the baseplate arc (Figure 3-15). However, the compression resultant does not travel to the extreme edge of the baseplate, due to the fact that the grout crushes over a finite distance near the edge of the plate. In previous design and analysis calculations (Trautner and Hutchinson 2014a, 2014b), the region of grout crushing was assumed to impart a constant bearing stress in accordance with the design procedure of AISC DG 1 (Fischer and Kloiber 2006). Calculations performed under this assumption showed excellent agreement with test data. Therefore, for the current test, the compression resultant was assumed to travel to a maximum distance of Y away from the edge of the baseplate. With these assumptions, d_{cc} was calculated using Eq. 3-6 and Eq. 3-7. Equation 3-6 is applicable when $\theta < \theta_{con}$, where θ_{con} is the connection rotation associated

with movement of *C* to the maximum distance of *b/2 - Y*, calculated to be 0.0069 rad for the assumed baseplate profile.

$$d_{cc} = \left(\frac{b}{2} - Y\right) sin\left(\frac{\theta}{\theta_{con}}\right) \quad \text{Eq. 3-6}$$

$$d_{cc} = \left(\frac{b}{2} - Y\right) signum(\theta) \quad \text{Eq. 3-7}$$

The distance d_{cc} calculated with these equations is shown in Figure 3-16, along with the total distance from the compression resultant C to the axial load application point on the top of the column assembly d_L (see the right side of Figure 3-11 for definition of d_L). The distance from the horizontal component of axial force F_{ah} to the bottom of the baseplate h_h (shown in Figure 3-11) stays nearly constant but drops some at large deformations, as shown in Figure 3-17. Using these distances, and the vertical and horizontal components of axial force given in Figure 3-14, the total correction moment M_c can be calculated as:

$$M_c = F_{av}d_L - F_{ah}h_h \quad \text{Eq. 3-8}$$

The final corrected moment M_f is then calculated as:

$$M_f = M_m - M_c \quad \text{Eq. 3-9}$$

where M_m is the moment calculated from the measured actuator force. The correction moment M_c is shown superimposed on M_m in Figure 3-18. The correction moment follows the bottom of each hysteretic loop as the connection is unloaded following each peak. Therefore, the corrected moment M_f, is zero at each of these points. This provides a check on the correction, as the moment should be zero at points at which the connection is not engaged. The test data from subsequent cycles falls significantly below the correction moment because significant grout damage occurred during successive,

repeated cycling at each excursion amplitude. A photograph of the extensive observed grout damage is shown in Figure 3-22. The grout damage moved the compressive resultant closer to the neutral axis than the position that is assumed in the forgoing development, therefore making the correction moment too large for all but the first cycle. This is because the location of contact is calculated based on the compression block location of the AISC DG 1 design procedure, which does not consider the effects of cyclic loading. Unfortunately, no additional data is available to quantify how much the compressive resultant moves due to this phenomenon. The final corrected moment M_f is shown in Figure 3-19.

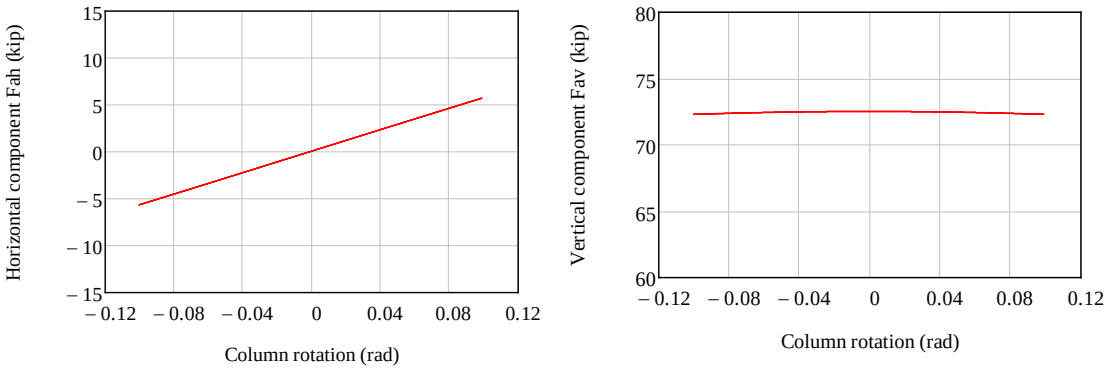

(a) Vertical

(b) Horizontal

Figure 3-14: Components of applied axial force

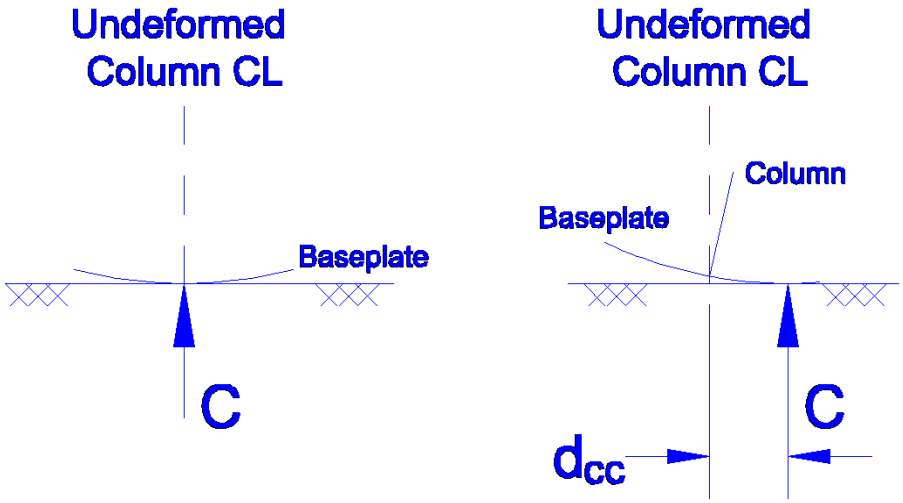

Figure 3-15: Horizontal distance from original column centerline to compression resultant, d_{cc} (deformation of baseplate exaggerated)

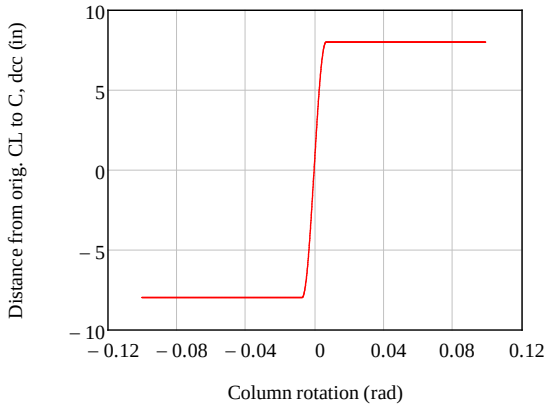

(a) Distance from original column centerline to compression resultant, d_{cc}

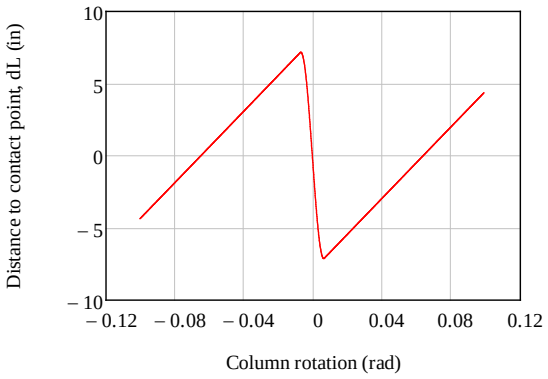

(b) total distance from point of axial load application to compression resultant, d_L

Figure 3-16: Distances calculated for P-Δ correction

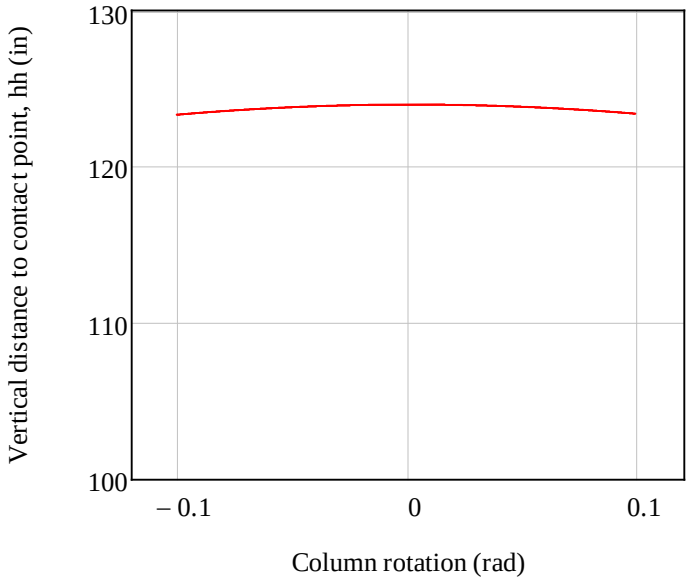

Figure 3-17: Distance from the horizontal component of axial force to the bottom of the baseplate, h

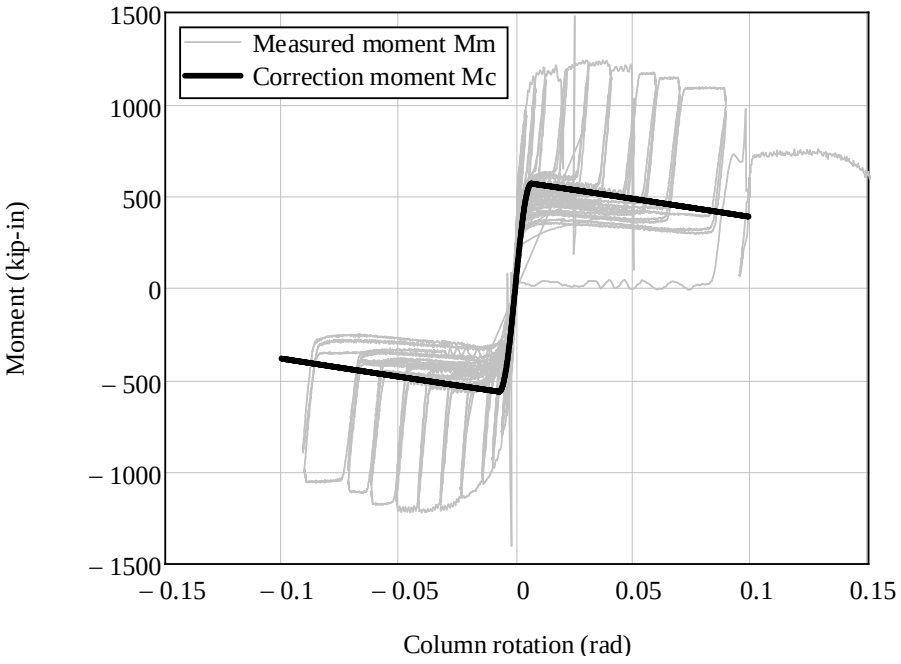

Figure 3-18: Raw test data and correction moment

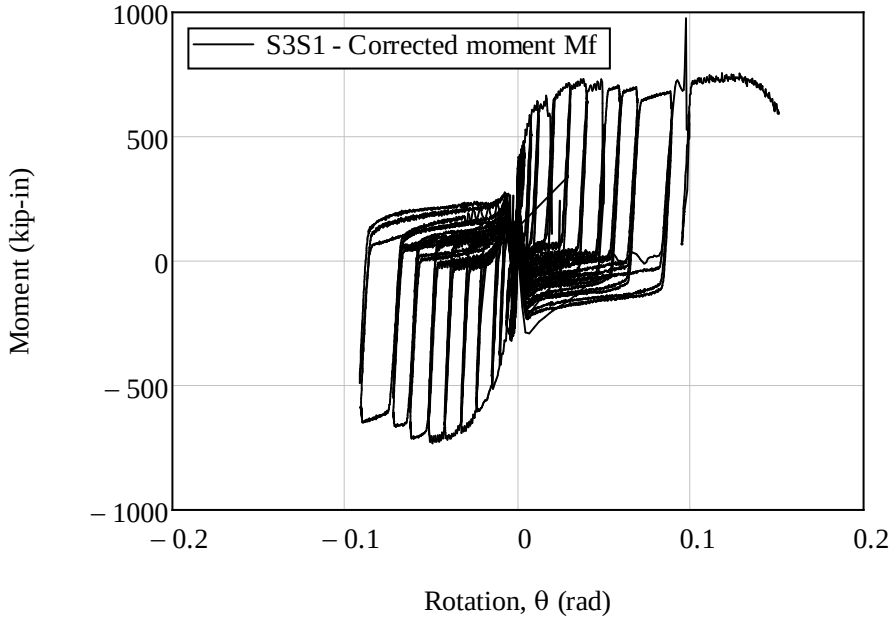

Figure 3-19: S3S1 measured, corrected moment-rotation response

The corrected data appears to be reasonable, as the general shape of the curve is consistent with test S2S1, which would be expected based on the fact that this is a very similar, anchor-dominated connection. The maximum strength of the connection during the axial load phase is about 733 kip-in, which is about 20% lower than for test S2S1, but is within about 10% of the predicted strength of 809 kip-in (using the methodology of AISC DG 1). The fact that the predicted strength is lower than the measured strength is somewhat expected, as the development of maximum strength did not occur until a connection rotation of about 0.05 rad, at which time significant cycling had occurred, crushing more grout than would be assumed in a single monotonic push, as is assumed in the design method of AISC DG 1.

Correction of the moment-rotation response due to friction of the column on the bracing structure was also considered. Relative deformations of the bracing system of up

to approximately 1/8" were measured during the test (Figure 3-20). Note that these deformations were measured at the level of the bracing guides, as shown in Figure 3-21. This was approximately double the observed deformation in the identical test without applied axial load (S1S2). The reason for the increased deformations is believed to be slight, unavoidable eccentricity of the axial load rig, which caused a lateral overturning moment that was resisted by the bracing structure. This force equilibrium is shown in Figure 3-21. However, friction is believed not to have affected the test results significantly, based on an inspection of the raw moment-rotation behavior shown in Figure 3-9. At the origin, every pass of the hysteretic curve passes very nearly through the origin. Because friction always opposes the direction of motion and the testing was not paused while passing through the origin, there would be a vertical offset and the curves would not pass through the origin if friction were significant. Therefore, it may be concluded that the friction force from the bracing structure is negligible. Given that the deformations of the bracing system were significant, the small friction force must be attributed to a low coefficient of friction due to careful greasing of the guide beams.

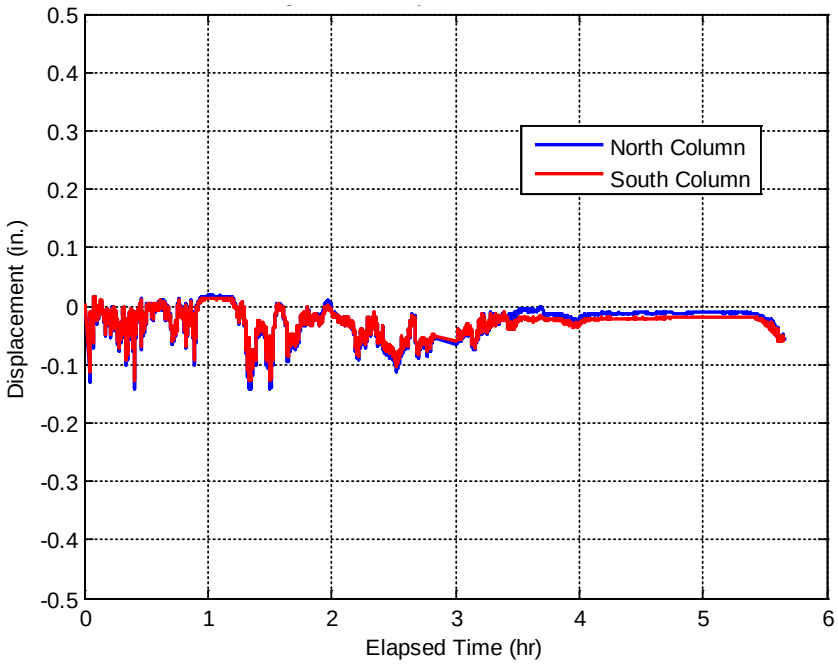

Figure 3-20: Relative deformation of bracing columns during test S3S1

Figure 3-21: S3S1 specimen equilibrium showing accidental overturning moment and lateral bracing reaction force

In terms of physical damage, test S3S1 sustained grout damage generally earlier than test S1S2. Cracking of the grout was observed after axial load application and before lateral loading. After testing, significant grout crushing was observed at both toes, extending all the way to the center of the anchor holes, as shown in Figure 3-22. Grout crushing extended about 2-1/2 inches in test S3S1, and less than an inch in test S1S2. This amount of grout crushing is reasonable compared to the values of *Y* used in the correction to the moment-rotation curve, above. There was essentially no damage to the concrete in either test, as shown in Figure 3-23.

(a) S1S2, no axial load (b) S3S1, axial load

Figure 3-22: Post-failure grout pad condition comparison - axial load

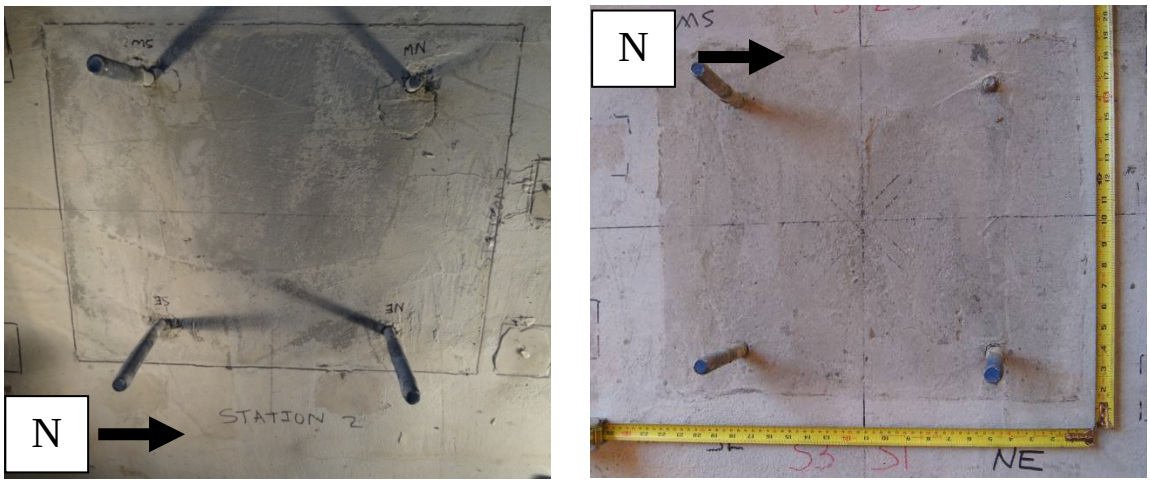

(a) S1S2, no axial load (b) S3S1, axial load

Figure 3-23: Post-failure concrete condition comparison - axial load

The earlier and more extensive grout damage is thought to be responsible for an important difference in observed behavior between this test and test S1S2. A comparison of the corrected S3S1 data and the S1S2 data is shown in Figure 3-24. Note that this data has been edited to remove spurious spikes caused by the test stoppages. The point at which the axial load was removed is identified with an arrow. Prior to about 0.05 rad, the salient hysteretic characteristics are very similar. After about 0.05 rad, the test S3S1 data dips significantly below the S1S2 curve. As the grout near the extreme fibers is continually damaged due to repeated loading under the significant axial load, the compression resultant cannot "travel" as far away from the anchors, resulting in a smaller moment arm and a smaller resisting moment. It should be noted that 0.05 rad is beyond the rotation that most connections would be expected to undergo, even under extreme lateral loadings.

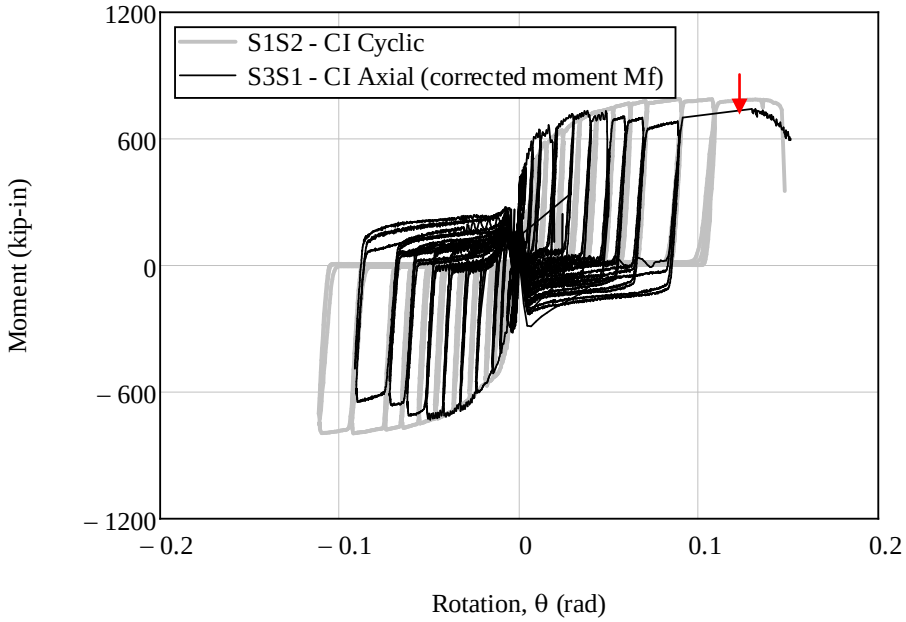

(a) Hysteretic behavior

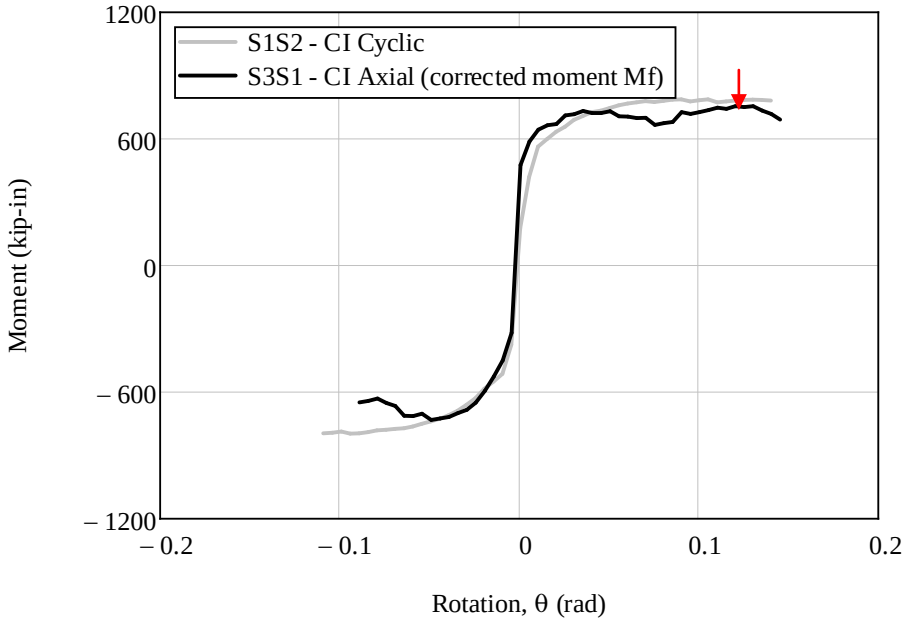

(b) Backbone of response

Figure 3-24: Comparison of corrected S3S1 and S1S2 data

3.4.2 Stretch Length Comparison

As discussed previously, ACI 318-14 includes an option for the design of fasteners subjected to seismic loads without the use of an overstrength factor so long as a prescribed stretch length of 8D is provided, where D is the diameter of the fastener (ACI 2014). Tests S2S3 and S2S4 incorporate identical free lengths intended to allow anchor stretch (8D), however this free length was implemented using two different designs, as suggested by ACI 318-14. S3S3 utilizes an increased embedment depth and a section of the anchor unbonded from the concrete in the top 8D. S2S4 incorporates a chair welded to the baseplate to increase the stretch length of the exposed portion of the anchor (Figure 3-2(g)-(h), Figure 3-3(c)). For most of the test, the global behavior of the connections with these two methods was practically indistinguishable, as shown in Figure 3-25. Test S2S3 sustained load to a very slightly larger drift ratio at failure. Additionally, the initial stiffness was significantly higher and damage state A-1 was attained sooner in test S2S3, as shown in the inset.

The condition of the grout pad after testing was observed to be significantly different in the two tests (Figure 3-26). There were no differences observed between the two grout pads prior to testing, except that in test S2S4, the anchors were embedded directly in the grout. In test S2S3, the anchors were wrapped in a layer of twine, duct tape, and grease as they penetrated the grout pad. The increased grout damage observed in test S2S4 is may be partly due to the relatively small holes utilized in the construction of the anchor chair (1 in. diameter). The relatively tight tolerance of the holes in the upper chair results in more bending in the anchor, which coupled with the direct embedment of

the anchors within the grout makes damage more likely. Conversely, the layer of twine wrapped around the anchors in S2S3 makes grout damage less likely, as the twine would need to compress prior to hard contact between the anchor and the grout (Figure 3-27). Although the grout damage did not result in a significant difference in behavior between the two tests, the grout used in the current tests was of relatively high strength and axial load was minimal, meaning that the grout pad was able to develop the necessary compression resultant even when fragmented. Weaker grouts or larger applied axial loads may result in connection behavior more sensitive to grout damage.

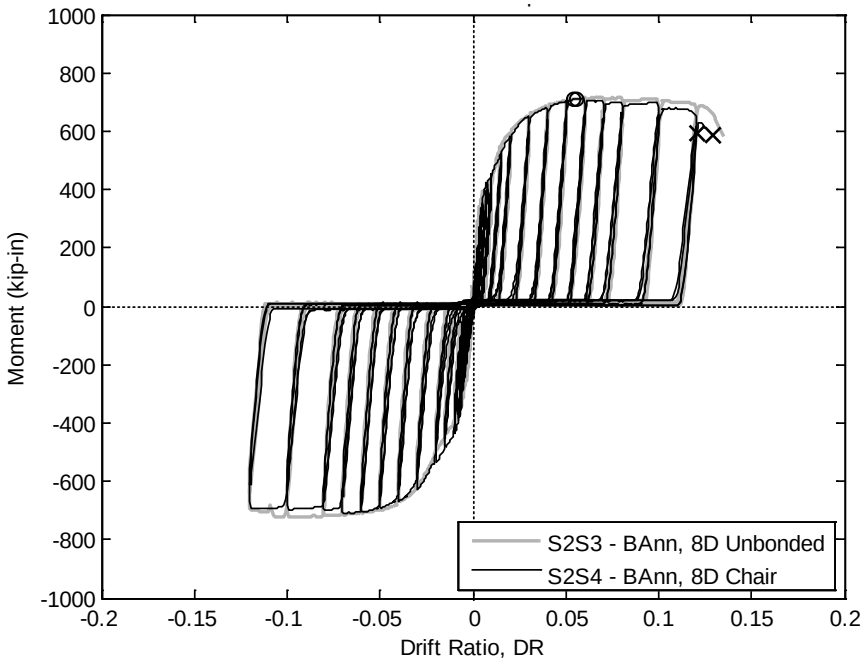

(a) Global moment-drift measurements

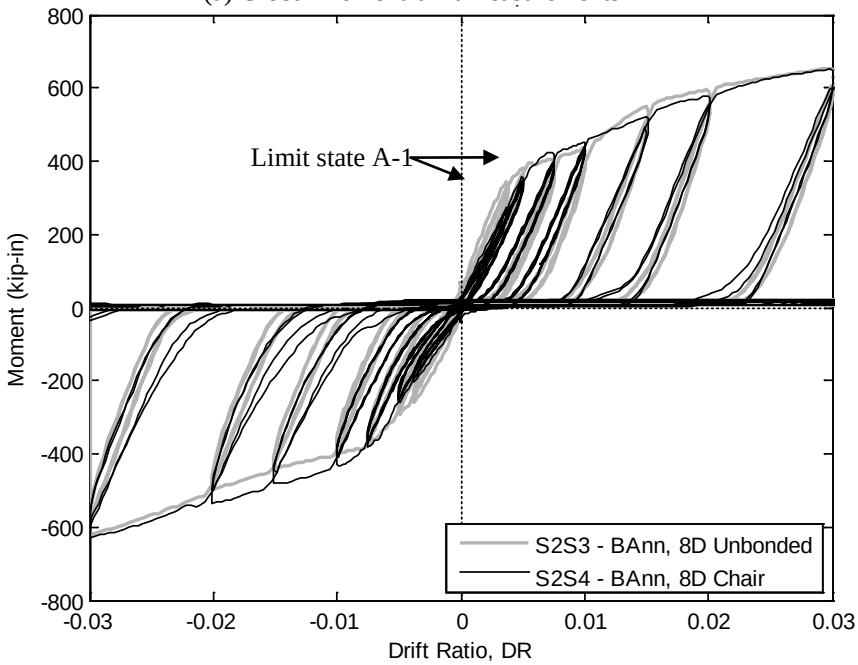

(b) Initial behavior comparison

Figure 3-25: Global response comparison, S2S3 and S2S4

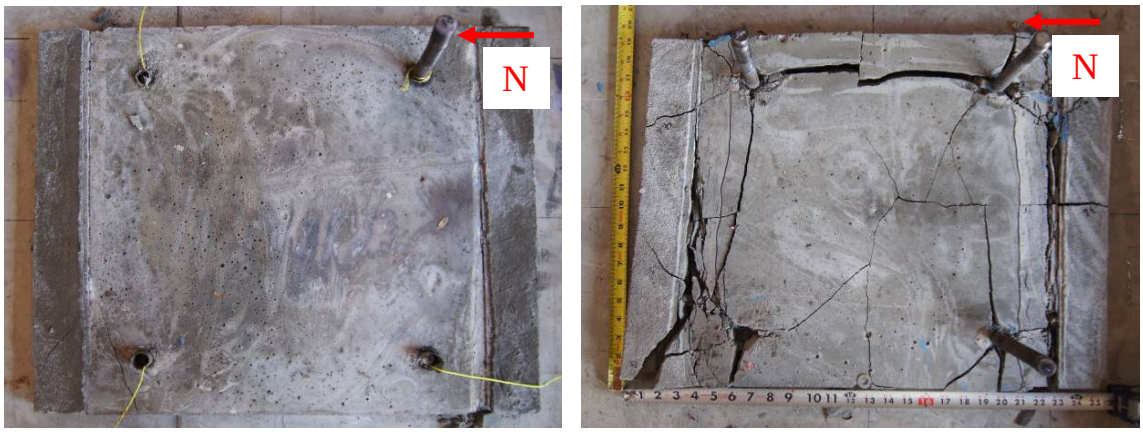

(a) S2S3 (b) S2S4

Figure 3-26: Grout pad condition after testing

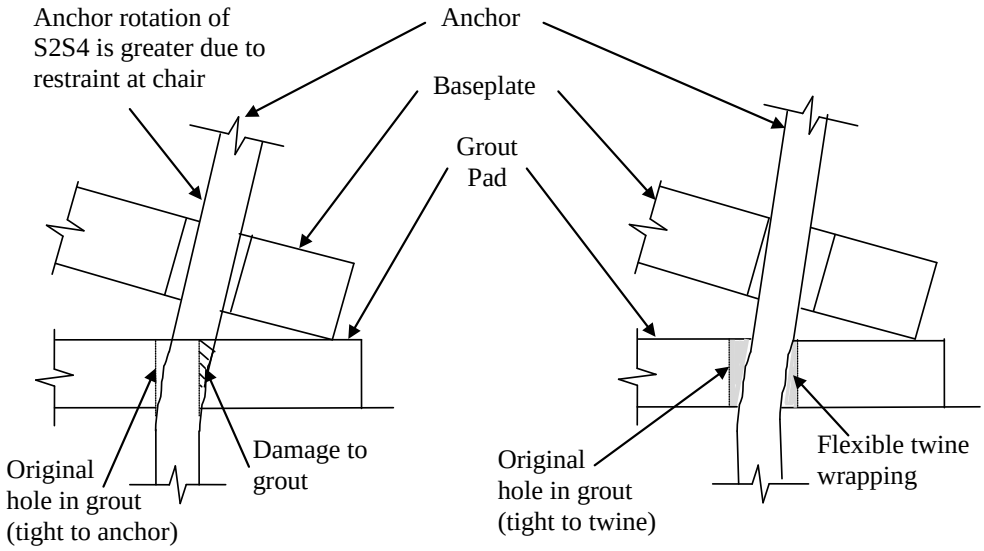

(a) Test S2S4 (b) Test S2S3

Figure 3-27: Influence of anchor wrapping on grout damage

Tests S2S3 and S2S4 were identical to test S1S4 except for the implementation of stretch length. Therefore, a comparison between these tests provides a direct assessment of the increase in ductility afforded by increasing stretch length. The global behavior of

S2S3 and S2S4 is compared to S1S4 in Figure 3-28. As shown in these figures, the ultimate strength of all tests is very similar. Examining the initial portions of both plots, it is evident that damage state A-1 is reached at a lower drift ratio, and the initial stiffness of S2S3 is significantly higher than both S1S4 and S2S4 (Table 3-3). The fact that the test without stretch length (S1S4) exhibits a lower initial stiffness and that the two tests with stretch length exhibit significantly different initial stiffnesses suggests that other factors have a greater influence on the initial stiffness of the connection. Most importantly, the rotation at fracture is only about 30% greater for tests S2S3 and S2S4 for the 80% increase in stretch length relative to S1S4. This phenomenon is directly related to the efficiency parameter *s* discussed in Chapter 2, where it was found that for every 1 in. increase in stretch length, the CW-A material provided about 0.14 in. additional elongation at fracture. This relatively small change in rotation at fracture due to a potentially costly change to the design of the connection is contrasted with the very dramatic change when comparing S2S1 and S1S4, which involved a change in anchor material from relatively brittle to ductile anchor material (see Table 3-3). This result strongly suggests that material selection, rather than modest stretch length changes, may prevent anchor fracture contributing to connection failure.

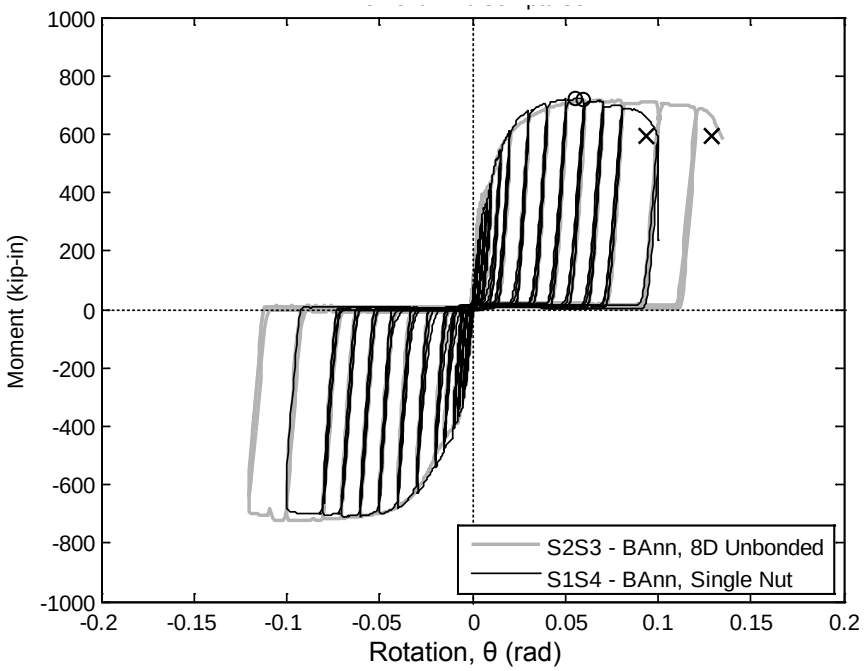

(a) Global moment-drift measurements

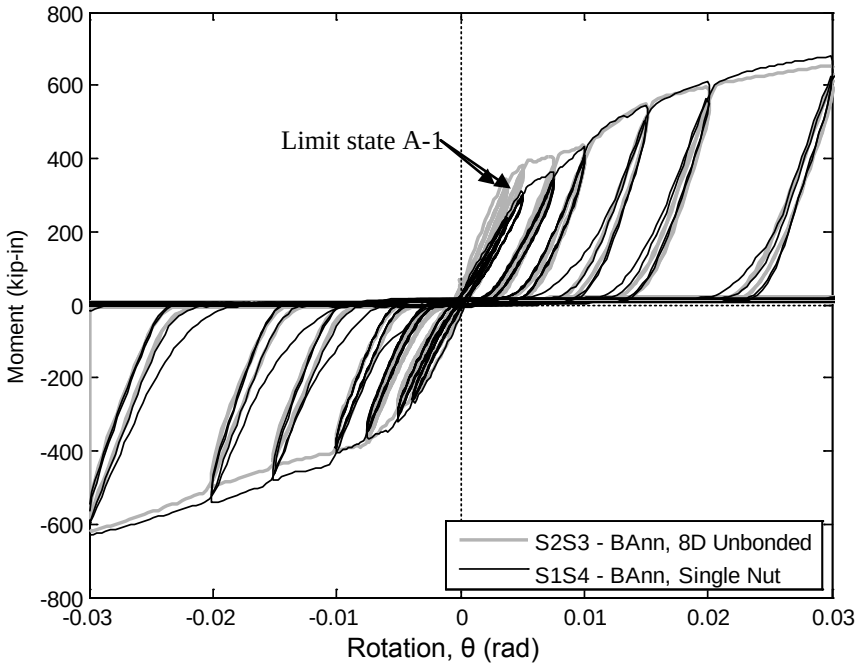

(b) Initial behavior comparison

Figure 3-28: Global response comparison, S1S4 and S2S3 (a) for S1S4 and S2S3

3.4.3 Cast-In Anchor Shank Condition

To determine the role of strain penetration in the rotation capacity of the connection, test S4S2 was designed to be nearly identical to test S1S2, except that the cast-in anchors were fabricated of annealed all-thread. The elongation at fracture of this all-thread was measured to be nearly identical to that of the headed bolts used in test S1S2 at the 8 in. stretch length required by ASTM F1554 (see Chapter 2). Therefore, differences in the rotation capacity may be reasonably attributed to differences in the strain penetration between the two anchor configurations.

The moment-rotation curves from the two tests are overlayed in Figure 3-29. The test with CI headed bolts (test S1S2) achieves approximately 15% higher ultimate strength, which makes sense given that the ultimate strength of the headed bolt is approximately 15% higher than the annealed allthread (see Chapter 2). Overall, the shape of the two curves is similar. However, the stiffness to yield is significantly higher in test S4S2. Unfortunately, it is not possible to determine whether this is due to differences in anchor type, or due to the paste intrusion in test S1S2, which softened the anchor response. However, the initial stiffness of both tests, highlighted with an arrow in Figure 3-30, is very similar. This suggests that the early response of the connection is not sensitive to the anchor shank condition (threaded or smooth).

The rotation capacity of test S4S2 was only about 5% less than that of test S1S2. It was observed that for tests with bonded anchors, such as S1S4, the rotation capacity was consistent with an effective stretch length about equal to the exposed length of the anchor (Trautner and Hutchinson 2014b). However, this result is somewhat unsurprising,

given that the elongation capacity of single-anchor tests in tension were very similar in fully cast-in and debonded configurations (Table 2-6). The result of test S4S2 indicates that significant plastic strain must develop beneath the surface of the concrete despite the shank of the anchor being fully threaded. This result is especially significant considering that stronger concrete would be expected to more effectively resist strain penetration. The concrete compressive strength at the time of testing was about 6,750 psi, in the upper range of what would be expected for concrete foundations in practice. The explanation for the strain penetration in this test appears to be that the shear developed between the threads of the anchor and the concrete is greater than the breakout strength of the near-surface concrete and/or the shear strength of the concrete embedded within the threads, particularly considering the tendency for plastic flow to reduce the diameter and engagement of the threads with the concrete (see Figure 2-17 and related discussion). This behavior is in contrast to test S1S2, where strain developed in the cast-in portion of the smooth shank without damaging the concrete. These mechanisms are consistent with pictures of the concrete surface taken after each test, shown in Figure 3-31. It is hypothesized that as the anchor was loaded, progressively larger failure surfaces were developed, such that plastic strain progressed towards the bottom of the anchor. Although this could not be verified directly, this hypothesis is consistent with the fracturing observed on top of the final failure cones, shown in Figure 3-32. The well-developed cracking, highlighted with arrows, is consistent with multiple progressive failures.

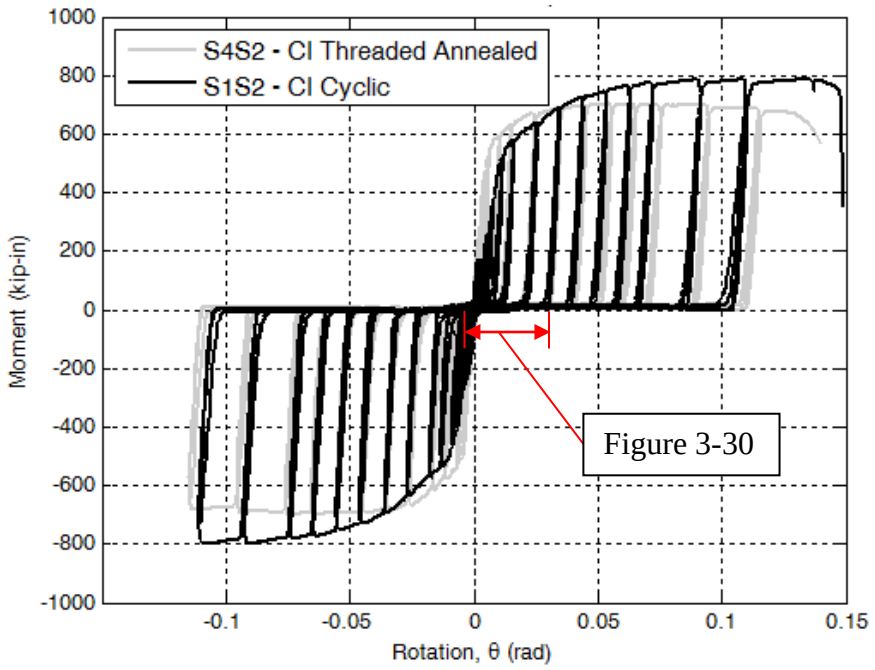

Figure 3-29: Moment-rotation comparison: cast-in anchor types

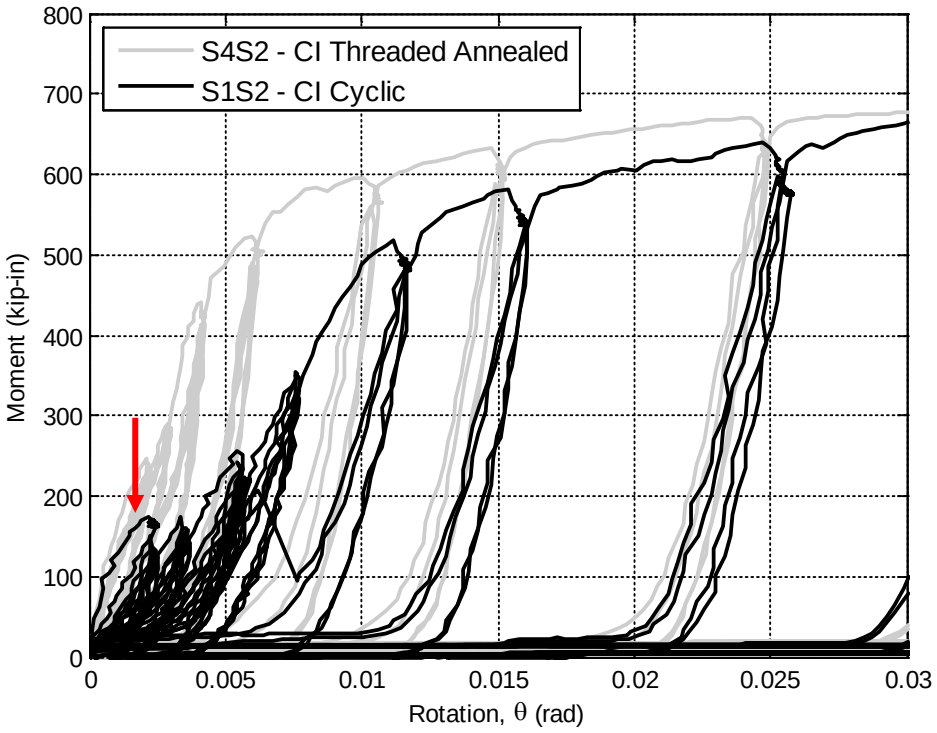

Figure 3-30: Early-stage moment rotation curve showing similar initial stiffness

(a) Cast-in smooth shank

(b) cast-in threaded shank

Figure 3-31: Post-test condition of concrete surface

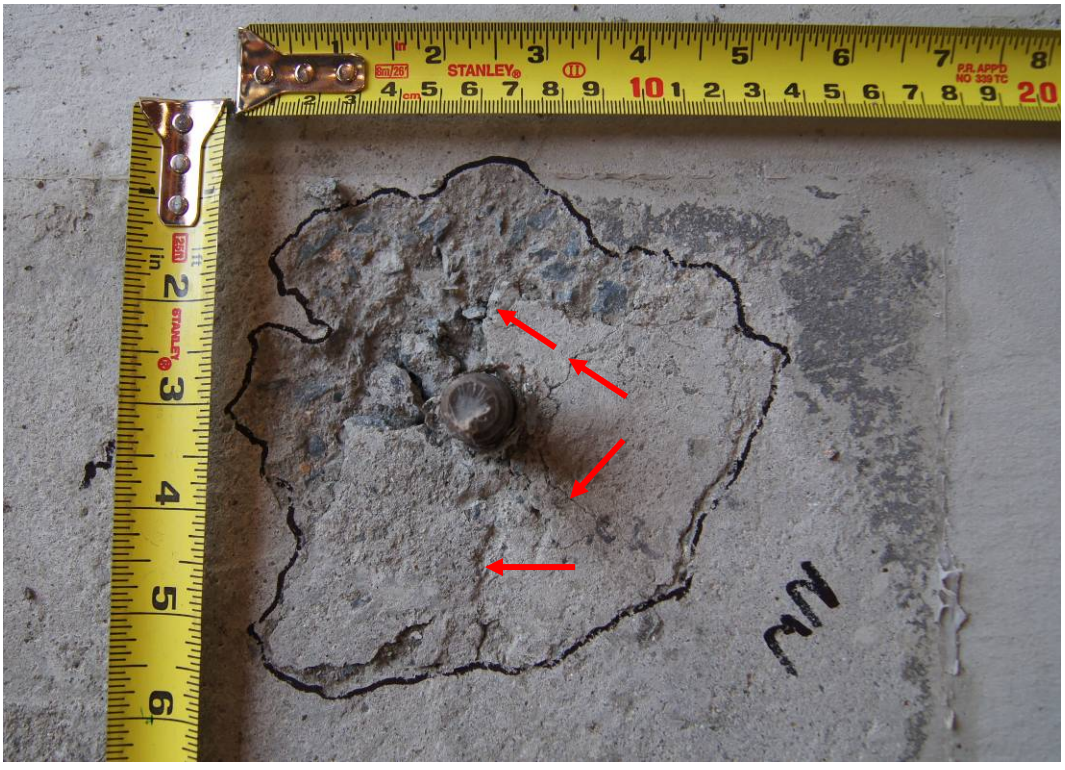

Figure 3-32: Post-test condition of S4S2 NW anchor

3.4.4 Removable Anchor Connection

The removable anchors created for this testing program were designed to provide a connection that could be easily replaced after a hypothetical seismic event or other damage. The anchors consisted of a body made from tube steel with a welded bearing washer/nut assembly at the bottom to accept a 3/4-in allthread insert. For connection test S3S2, the insert consisted of annealed allthread. The most similar connection to S3S2 tested in Phase I was test S1S2. This comparison is most relevant because the mechanical properties of the cast-in headed anchors of test S1S2 and the annealed allthread are very similar.

The moment-rotation curves from these two tests are presented together in Figure 3-33. The ultimate strength of test S3S2 was about 15% lower, which makes sense as the ultimate strength of the annealed allthread was about 15% lower than that of the cast-in headed bolts (See Chapter 2). The removable anchor connection was not run to failure due to actuator stroke limits. However, it is believed that the connection was near failure, based on the fact that elongation at fracture of the cast-in headed bolts and annealed allthread was similar and the effective stretch length of the two tests was identical. Interestingly, the initial stiffness of the connections (prior to the anchor softening associated with test S1S2), was nearly identical. It is assumed that the stiffness of the connection is directly proportional to the stiffness of the anchors (a reasonable assumption for the stiff-baseplate configuration considered herein). The elastic stiffness of the anchors may be estimated to be $k_a=AE/L$, where A is the cross-sectional area, E is Young's modulus, and L is the free length over which elastic deformation may be

assumed to occur. A and E may be assumed to be identical for the two tests, therefore, it may be concluded that the smooth-shank anchor debonds from the concrete at very low load levels, such that the stretch length becomes the full embedded length immediately upon loading.

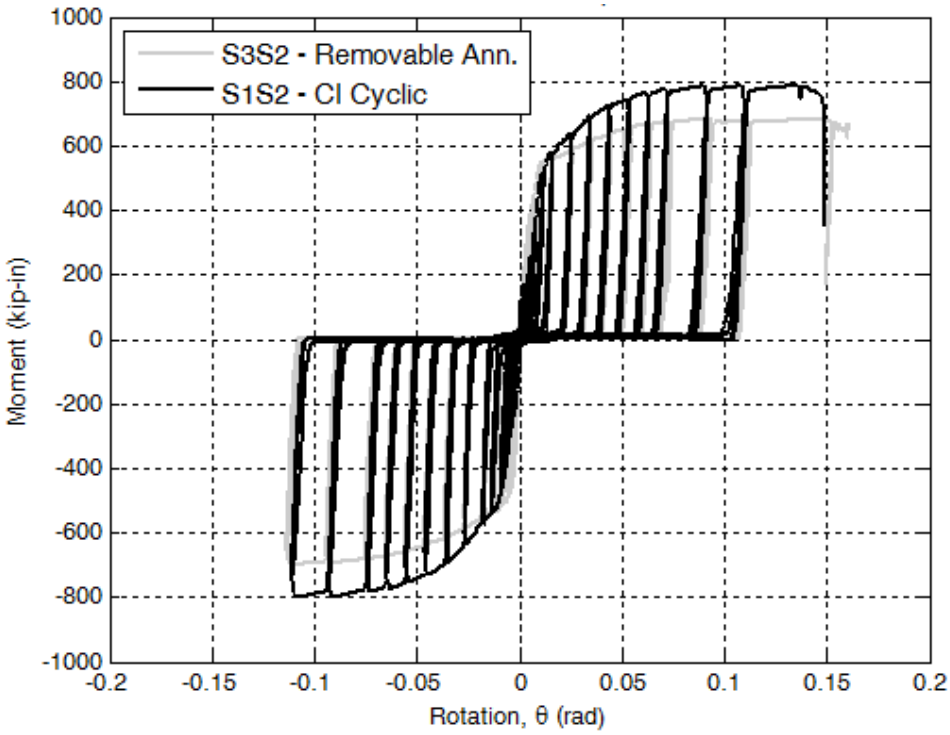

Figure 3-33: Moment-rotation comparison: removable anchor (S3S2) vs. smooth-shank cast-in (S1S2)

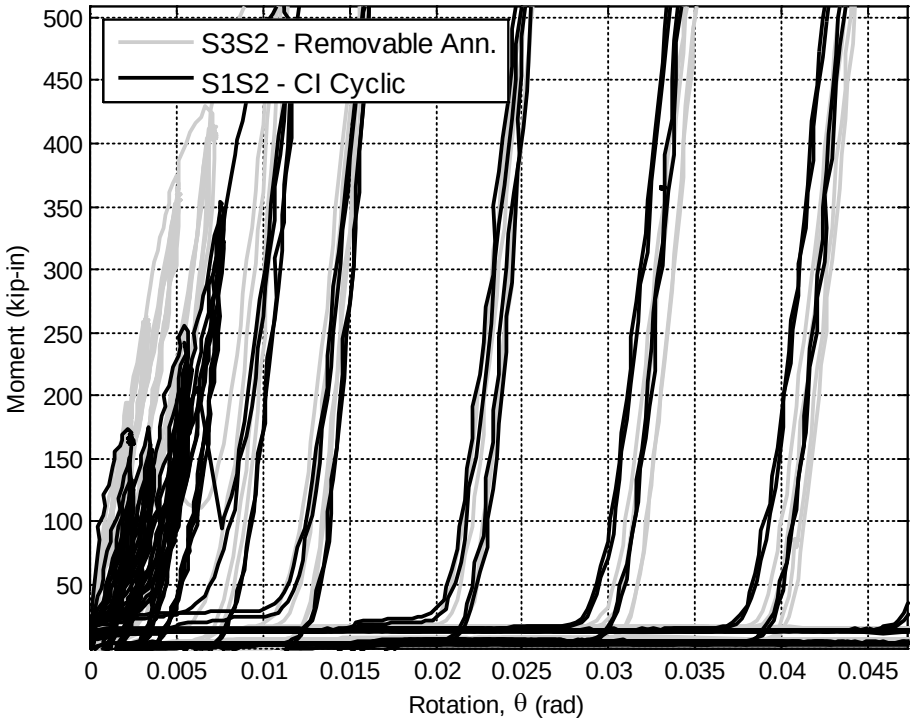

Figure 3-34: Initial stiffness comparison: removable anchor (S3S2) vs. smooth-shank cast-in (S1S2)

Physical damage to the concrete in test S3S2 was essentially negligible, even less than that observed in test S1S2 (Figure 3-35). This aspect of the anchor system is critical, as damage to the concrete would complicate the replacement procedure and lessen the usefulness of such a system. This aspect would likely be more important in a shear-dominated connection, because local crushing of the concrete near the top of the anchor is often observed prior to failure in anchors highly loaded in shear. However, the removable anchors have an advantage in this respect over cast-in or bonded anchors in that the bearing area of the body of the anchor is larger than the diameter of the anchor. This should reduce bearing stresses and the magnitude of local crushing. Further research should be conducted to determine the effectiveness of such anchoring systems in shear-dominated applications, however, based on the good performance of this anchor type

observed in this test, a similar removable anchor system was used in the dynamic testing of uplifting-column systems presented in Chapter 5.

(a) Cast-in smooth shank (b) Removable

Figure 3-35: Post-test condition of concrete surface – shank condition comparison

3.4.5 Adhesive Comparison - Bonded Connections

The S4S3 connection included bonded anchors constructed with a hybrid adhesive. In contrast to the epoxy-only adhesive used for all other tests, the hybrid adhesive incorporates both epoxy and cementitious bonding agents to reduce the amount of hole cleaning required prior to anchor placement. However, this adhesive has somewhat lower bond strength than the epoxy-only adhesive, although in this application the strength was still sufficient to have a significant margin against bond failure versus anchor fracture. The moment rotation curve of test S4S3 is presented in Figure 3-36 along with test S1S4, which was otherwise identical to S4S3 except for the adhesive type. As expected, the ultimate strength of the two connections was nearly identical, as identical annealed allthread inserts were used.

The rotation capacity of test S4S2 was approximately 15% greater than test S1S4. This is somewhat surprising, as there was no discernible difference in the elongation at

fracture of reference tests performed with the epoxy versus hybrid adhesives (see Figure 2-20). Moreover, the small concrete failure cones observed at the termination of both tests were approximately the same size and depth, as shown in Figure 3-37. However, greater rotation capacity should be possible only with increased damage to the epoxy. A possible explanation of this behavior is that the hybrid epoxy is more prone to damage under combined tensile/shear loading than epoxy, although no testing or evidence exists to support this assertion. The amount of increased stretch length to account for the increased rotation capacity of this connection is discussed in the context of parametric numerical analyses in the next Chapter.

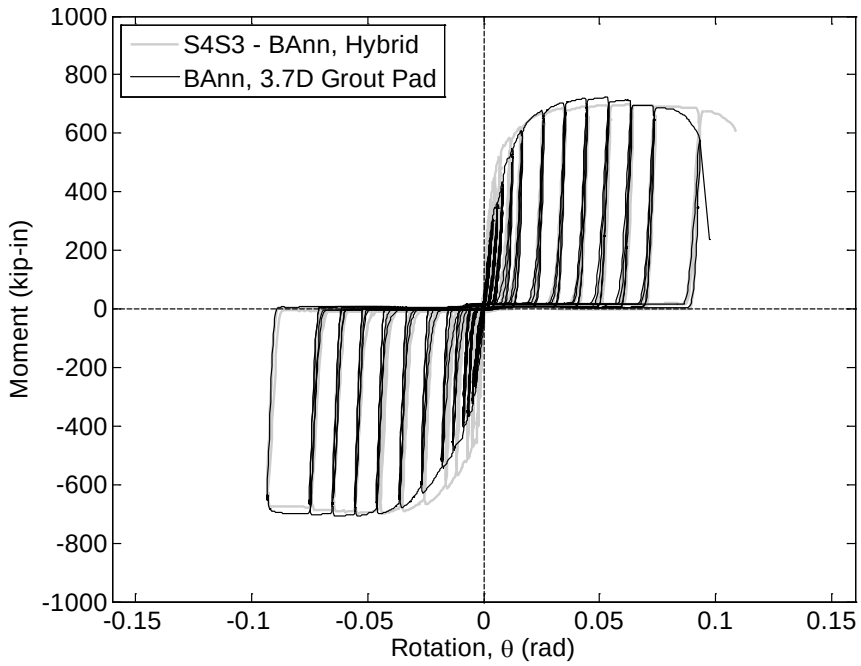

Figure 3-36: Moment-rotation comparison: adhesive types

(a) Test S1S4 (b) Test S4S3

Figure 3-37: Post-test condition of concrete surface – adhesive type comparison

3.4.6 Load Protocol Effect

Test S1S1 and S1S2 were identical except for loading protocol -- test S1S1 was loaded monotonically up to an actuator displacement of approximately 12 in. while test S2S2 was loaded cyclically using the SAC protocol. The moment-rotation response of these two tests are shown in Figure 3-38. As shown in the figure, the S1S1 test has a similar initial stiffness and measured response up to rotations of approximately 0.025 rad. At larger drifts, the S1S1 curve attains higher loads. The maximum difference between the two curves is approximately 75 kip-in at the drift corresponding to the termination of the S1S1 test, or about 10% of the ultimate strength of the connection.

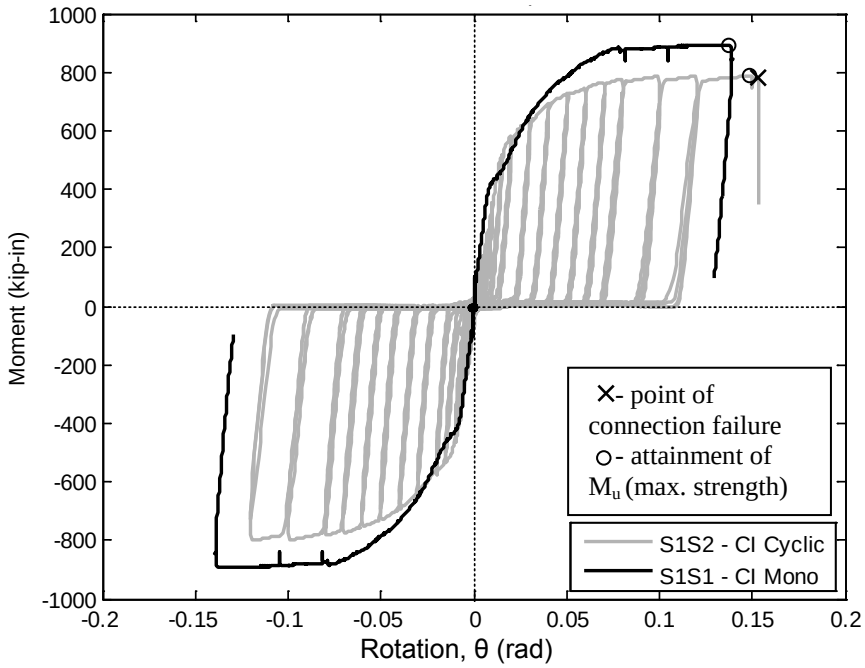

Figure 3-38: Comparison of S1S1 and S1S2 Global Moment-Rotation Measurements

It is not uncommon to observe a lower ultimate strength in a component when loaded cyclically versus monotonically. However, similar behavior was observed for test S4S1, which was identical to test S1S2 except that test S4S1 was performed with the SAC near-fault protocol. Additionally, the bearing washers used for test S4S1 were tack-welded to the anchor shanks, similar to test S3S1, as described previously. The moment-rotation data from these two tests is presented in Figure 3-39. The effect of the tack-welded washers appears to be significant in the pre-yield stiffness of the connection, as test S4S1 does not have the drop associated with anchor softening seen in test S1S2 (highlighted with solid arrows in the figure). Regardless of these features, the shape and rotation capacity of S4S1 is very similar to that of S1S2, except that ultimate strength of test S4S1 is about 7% higher than S1S2. The reason for the slightly higher connection strength in tests S1S1 and S4S1 than S1S2 can be traced to the contribution of the near-

side anchors. That is, the anchor pair nearer to the compression toe of the connection is in tension as the connection reaches its ultimate strength, as shown in Figure 3-40. In test S1S2, because the protocol is fully reversed, all anchors always have enough accumulated plastic strain to prevent engagement when the loading is reversed. However, when the anchor does not have accumulated plastic strain, the near-side anchors form part of the tensile resultant and overall strength is reduced.

There are two anomalies in the moment-rotation data for S4S1, consisting of small spikes in the measured moment where the connection should be unloaded. These are identified in Figure 3-39 with dashed arrows and numbers. The points at which these spikes occurred during the loading procedure are identified in Figure 3-41. Spike 1 occurred after the first excursion to the south, on the reversal to the first excursion to the north just prior to passing through zero displacement. This load spike appears to be due to the grout pad becoming unbonded but staying intact as it was lifted on the first excursion. As the connection returned to zero displacement, the pad contacted the concrete first and allowed the development of some compression before cracking, developing some positive moment. Spike 2 seems to have a similar cause. As the connection returned to zero displacement, a large piece of unbroken grout bound on the anchors that were most recently tension-side, allowing development of a compression resultant through the unbroken grout and down the anchors. The grout appears to have cracked and fallen down off the anchors relatively quickly, accounting for the relatively low amplitude of the peak. It is likely that similar peaks were not observed in other tests due to the fact that the SAC protocol has 6 excursions at lower amplitudes, which would tend to fracture and

damage the grout around both pairs of anchors, preventing them from binding. This hypothesis seems to be supported by the comparison of the end-of-test grout condition shown in Figure 3-42. There is a significant amount of powered and spalled grout near the anchors in test S1S2 that is absent in test S4S1. Additionally, there is much more cracking and fragmentation of the grout at the compression toes of S2S1, suggesting that this type of grout damage is associated with a large number of smaller amplitude cycles.

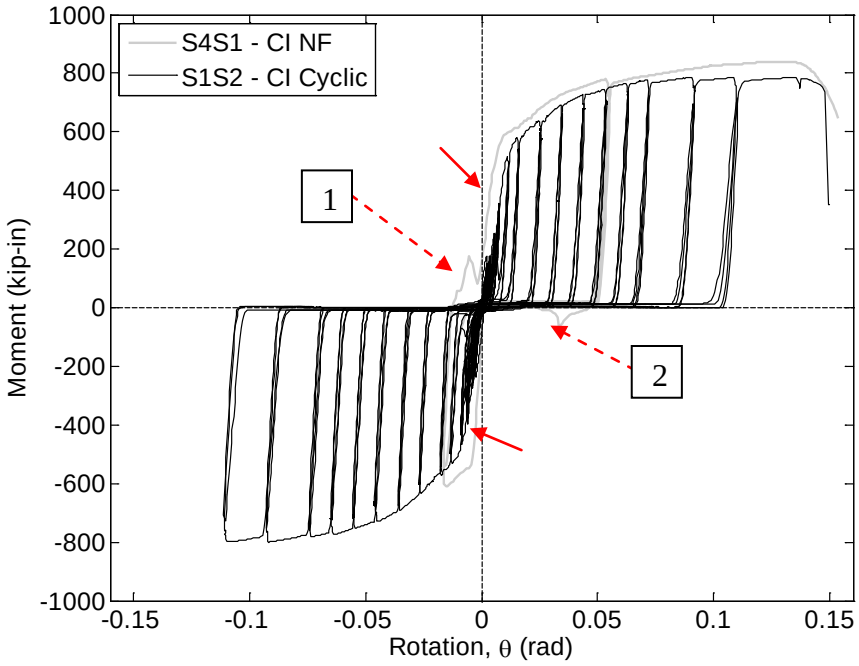

NOTE: Dashed arrows denote load spikes, see Figure 3-41

Figure 3-39: Moment-rotation comparison: loading protocol

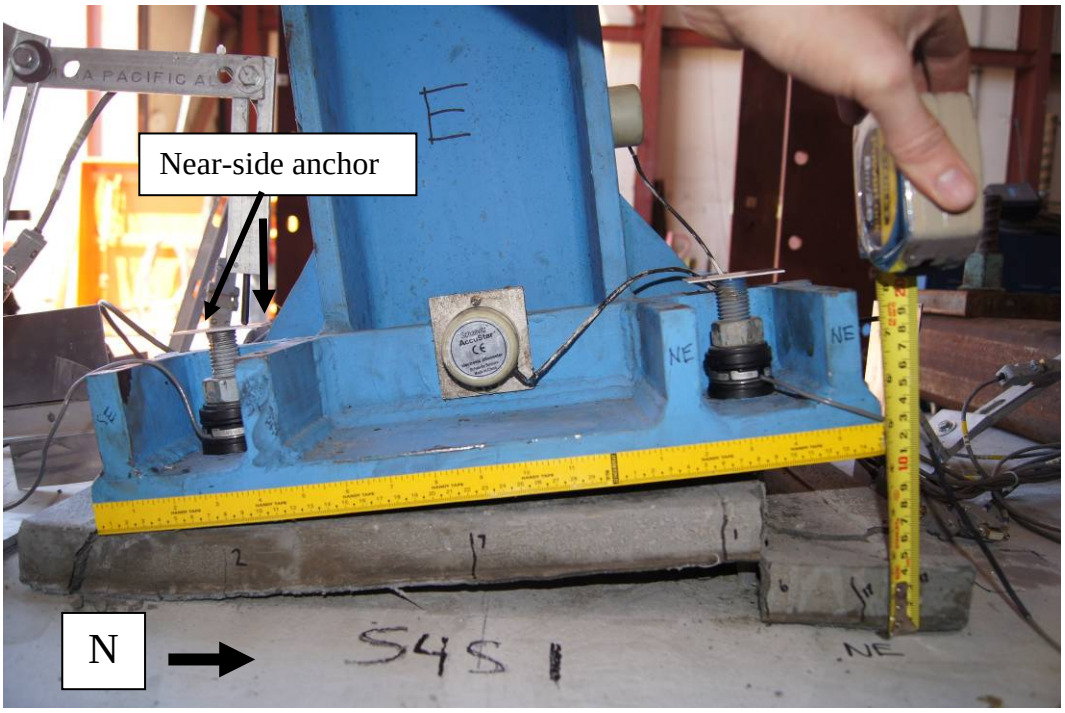

Figure 3-40: Test S4S1 at failure showing near-side anchor engagement

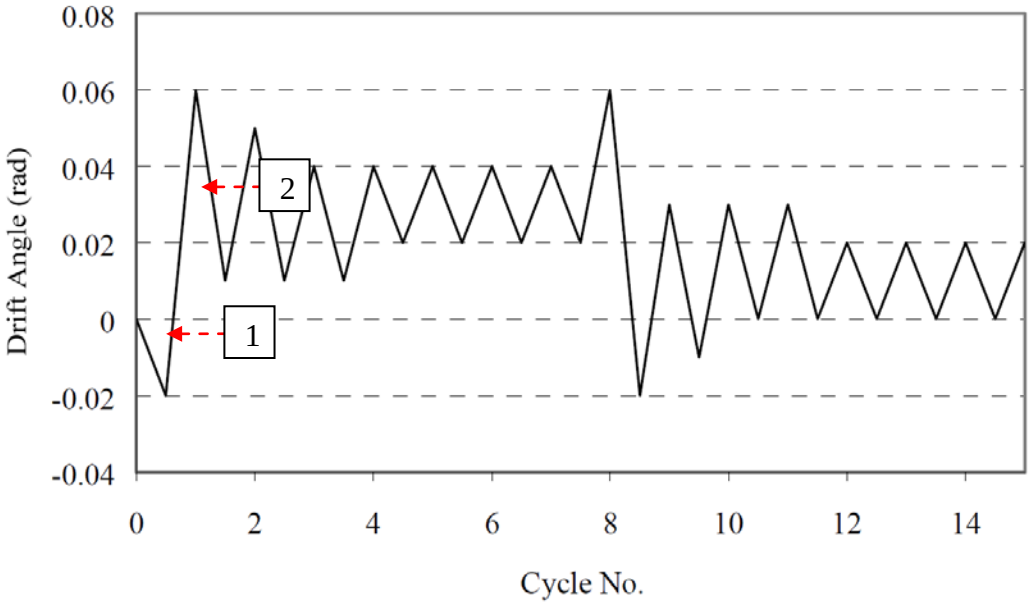

Figure 3-41: Test S4S1 loading protocol with approximate locations of load spikes

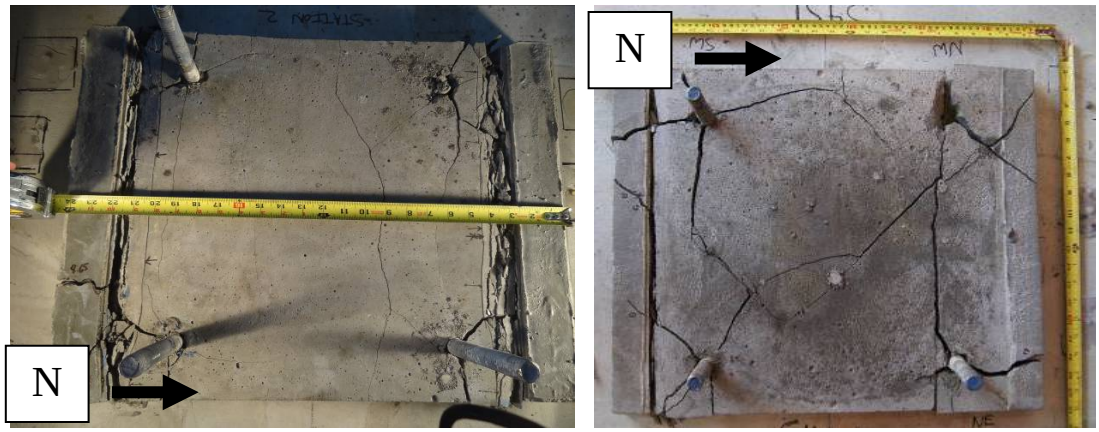

(a) Test S1S2 (SAC) (b) Test S4S1 (NF)

Figure 3-42: Comparison of grout pad after testing – load protocol effect comparison

3.4.7 Column Setting Method Comparison

Three different column setting methods were tested on identical connections. Test S1S4 was performed with bonded anchors incorporating epoxy adhesive, and was set directly on a pre-formed grout pad. This condition is unlikely to occur in practice, as it does not provide a mechanism for leveling the column, however this provides a baseline to evaluate the setting method effect. Tests S1S3 and S4S4 were otherwise identical, but incorporated setting nuts and steel setting shims, respectively. The moment-rotation data from the three tests, shown in Figure 3-43, indicates that the steel shim method is essentially indistinguishable from the direct-on grout method. The ~10% increase in rotation capacity between S1S4 and S4S4 is attributable to inherent variability in the elongation capacity of the anchors and there is no compelling evidence that this difference is due to any differences in the connection behavior.

The behavior of test S1S3 is significantly different from the other two tests. Test S1S3 displayed pinched hysteresis atypical of any other tests, and significantly impaired

rotation capacity. The reason for this is that the baseplate can essentially slide on the bottom setting nuts and shear the anchors after plastic strain brings the level of the setting nuts above the level of the grout pad, as shown in Figure 3-45. Compared to test S4S4, test S1S3 had 32% less rotation capacity and approximately half of the dissipated energy (area under the hysteretic curve). This result indicates a strong need for further research in this topic, as previous research has not included setting method as a variable and this is not an aspect of construction which typically receives any design attention. Interestingly, both test S1S3 and S4S4 had significantly higher yield tangent stiffnesses as shown in Figure 3-44 (values are given in Table 3-3). This behavior makes sense, as these two tests had a direct steel-to-concrete bearing mechanism, the steel shims for S4S4 and the setting nuts to the anchors for test S1S3. Of these, one would expect higher stiffness from test S4S4 as observed, where the bearing steel is closer to the extreme fiber (Figure 3-2).

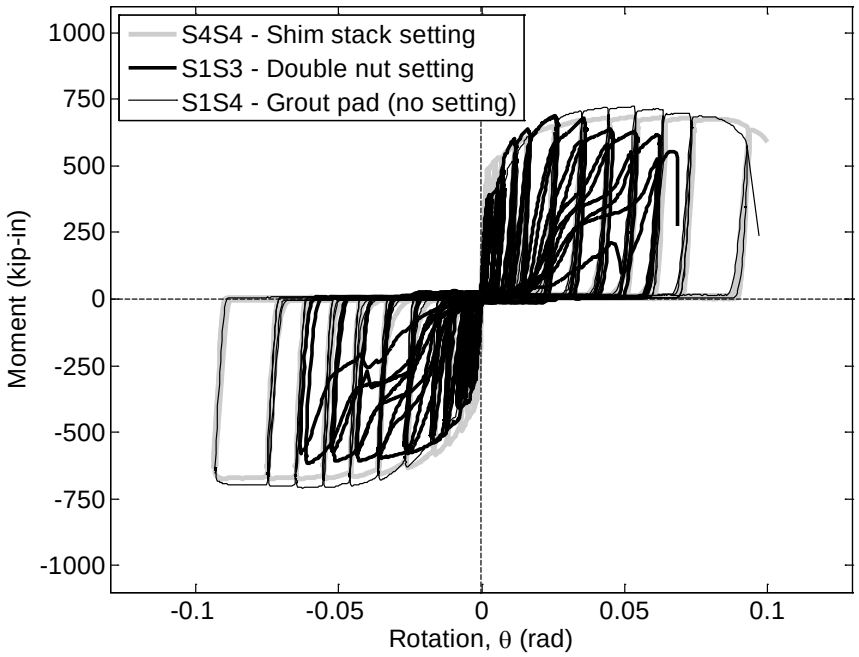

Figure 3-43: Moment-rotation comparison: setting methods

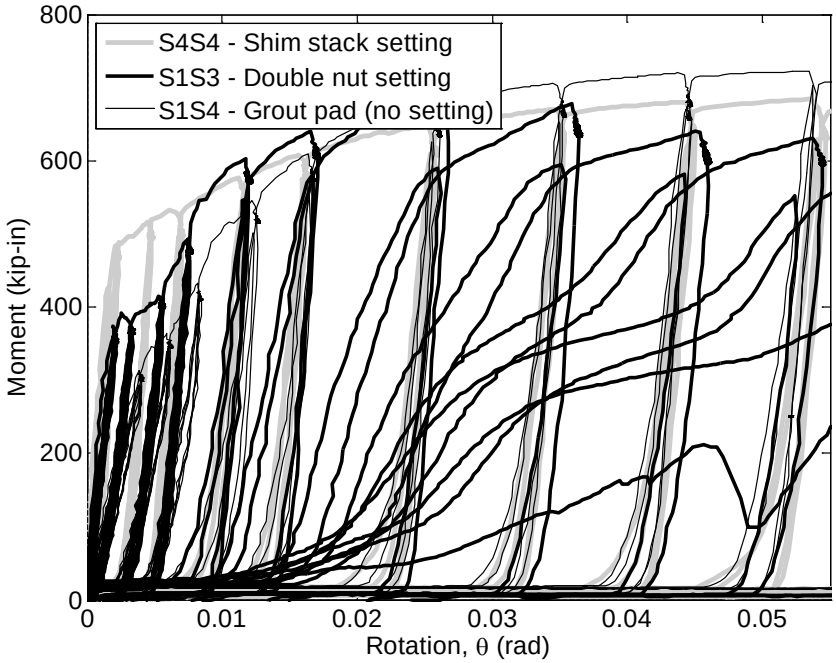

Figure 3-44: Initial stiffness comparison: setting methods

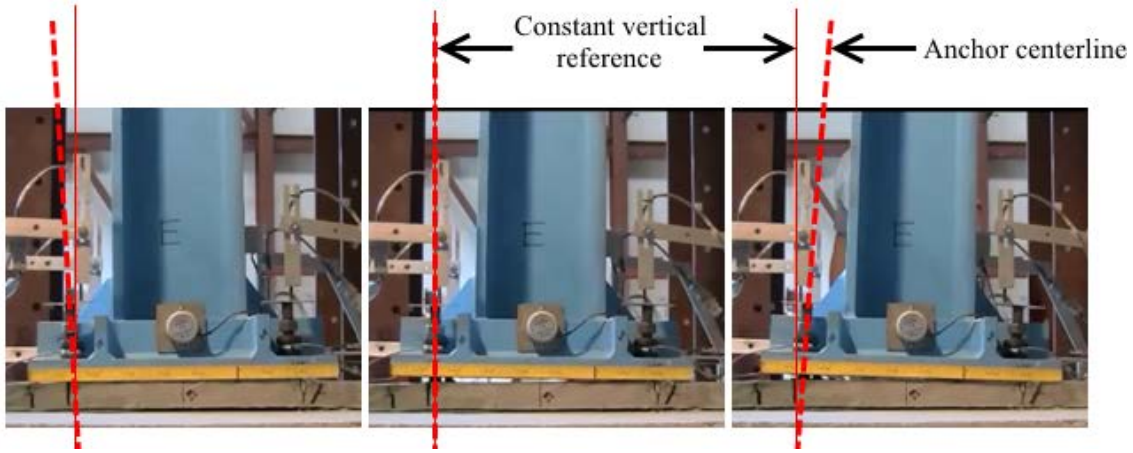

Figure 3-45: Specimen sliding and anchor shearing in test S1S3 (three photos from the 0.02 imposed drift cycle)

3.5 Anchor Hole Size Effect

Typical steel-to-steel connections in steel buildings use either "standard" or "oversize" holes. Depending on the size of the bolts in question, oversize holes are between 1/8 and 5/16 in. larger than the nominal diameter of the bolt, with larger oversizing for larger bolts. In contrast, AISC DG 1 (Fisher and Kloiber 2006) recommends that the holes for steel column baseplate connections be drilled between 9/16 and 1-1/4 in. larger than the nominal diameter of the anchor. As stated in the design guide, "These hole sizes originated in the first edition, based on field problems in achieving the column setting tolerances required for the previous somewhat smaller recommended sizes" (Fisher and Kloiber 2006). This motivation is counter to most other recommendations given in AISC documents regarding structural components, which are generally based on meeting required strength and serviceability requirements, with constructability as a secondary consideration. This is particularly unusual, as bolt holes

used elsewhere in the SFRS are strictly controlled, and larger sizes are not permitted without the approval of the engineer of record (AISC 2010).

To determine the effects of the relatively large holes permitted by AISC DG 1, a test (S3S4) was run that was otherwise identical to test S4S1 except that the baseplate holes were enlarged to 1-5/16 in. (the full amount recommended by AISC DG 1) from 1 in. Plate washers were used to cover the larger holes as recommended in the standard. The moment-rotation curves from the tests were essentially identical, as shown in Figure 3-46. The condition of the grout after testing is shown in Figure 3-47 for the two tests. There is perhaps slightly more fragmentation of the grout at the extreme corners of the pad and slightly wider separation of the grout fragments in the middle of the pad for the test performed with larger holes, but the differences do not seem to be significant. Overall, it may be concluded that the size of the anchor hole does not appear to have a significant effect on connection performance. However, it should also be noted that these tests have a high moment-to-shear (M/V) ratio. If the amount of shear in the connection were increased (say, as a result of a braced-frame configuration), it is possible that increased anchor hole size could result in more connection movement.

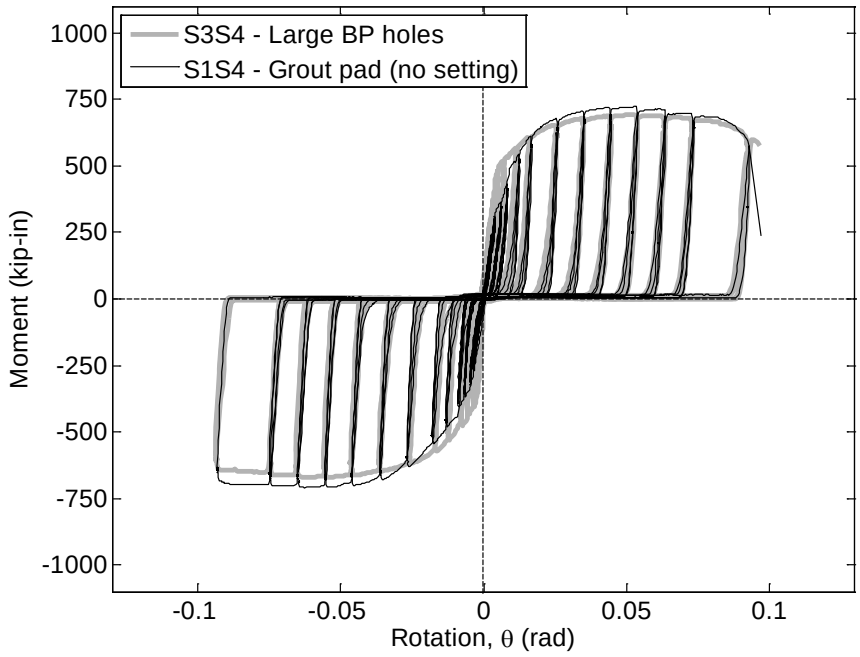

Figure 3-46: Moment-rotation comparison - baseplate hole size

(a) 1 in. holes (b) 1-5/16 in. holes

Figure 3-47: Post-test grout damage comparison – hole size comparison

3.6 Relative Connection Component Strength Effect

Test S3S5 was the only test performed where the failure mechanism was not anchor fracture. Because significant baseplate and column plasticity was expected, the

test was instrumented with 16 strain gages, with the locations as shown in Figure 3-48. Because of the uniqueness of this test, there is no specific "comparison" test as there was for most other of the tests performed. As a reference, the S1S2 moment-rotation data is presented with the S3S5 data in Figure 3-49 and Figure 3-50. There are a number of interesting comparisons that can be made between these two tests based on these figures:

- The strength of test S3S5 was just over 1500 kip-in, tied for the strongest of all connections tested. The strength of the connection was a consequence of not needing to provide a margin between brittle failures, such as breakout and bond failure, and anchor fracture, as was required for all other tests including S1S2.
- Interestingly, test S2S2 (incorporating "standard" M20 undercut anchors) had essentially the same ultimate strength as S3S5, but failed via anchor fracture. This may be in part due to the fact that cracking of the concrete occurred during testing of S3S5 due to the use of hold-down locations that were farther from the test station. Cracking was not observed in test S2S2. It is well-known that cracking in concrete may significantly lower the strength of bonded anchors, and may have caused failure at a lower load than would have otherwise been achieved. This hypothesis is supported by the fact that the connection acheived 4% imposed drift when loaded to the south when the northern, uncracked anchors were in tenstion, yet failed at a lower imposed drift when loaded to the north. However, the failure load on the connection was accurately predicted by the ACI 318-11 Appendix D equations (see Table 3-3).

- The initial stiffness of S3S5 is nearly identical to that of S1S2 prior to anchor head paste crushing, as shown in Figure 3-50. This suggests that the effect of an unstiffened baseplate in S3S5 was counteracted by larger anchors and a shorter effective stretch length.
- Connections where the nonlinear response is governed by the behavior of the anchors and setting nuts are not used, such as S1S2, have zero residual rotation at zero imposed moment. This was true even for relatively brittle connections such as S2S1 and connections with less desirable hysteretic characteristics such as S1S3. In contrast, as shown in Figure 3-49, test S3S5 has significant residual rotation at zero moment. Prior to failure, the greatest rotation achieved by the connection was approximately 32.4 millrad. When brought to zero moment, the residual rotation was approximately 16.4 millirad, approximately 50% of the maximum. This result indicates that anchor-dominated connections can be self centering. If not designed to stay completely elastic, strong-plate connections may contribute to permanent deformations in the structure.

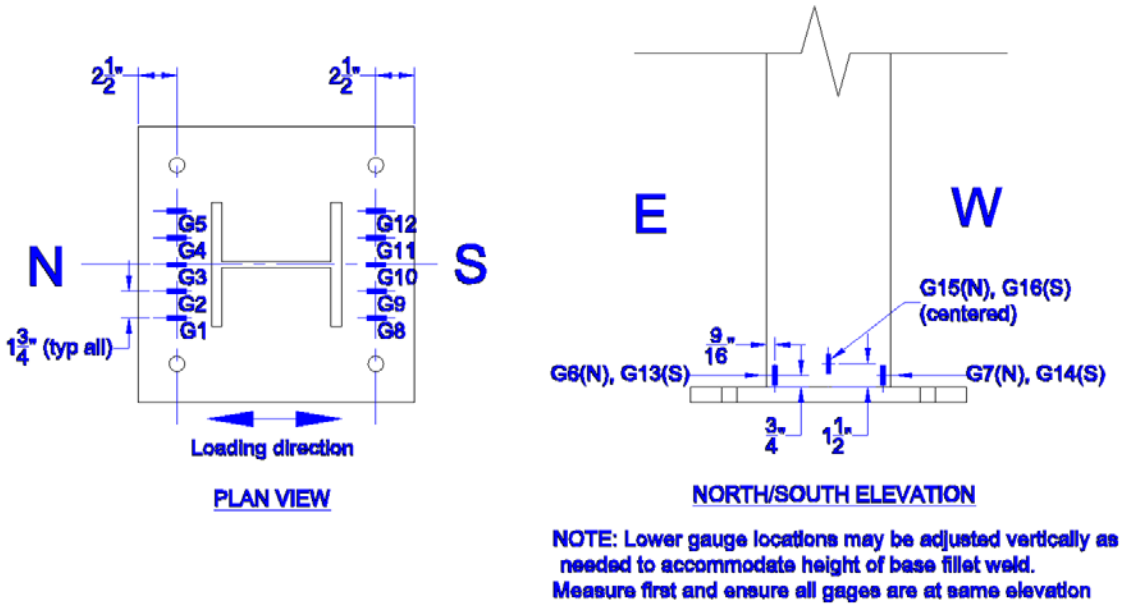

Figure 3-48: Layout of strain gages in test S3S5

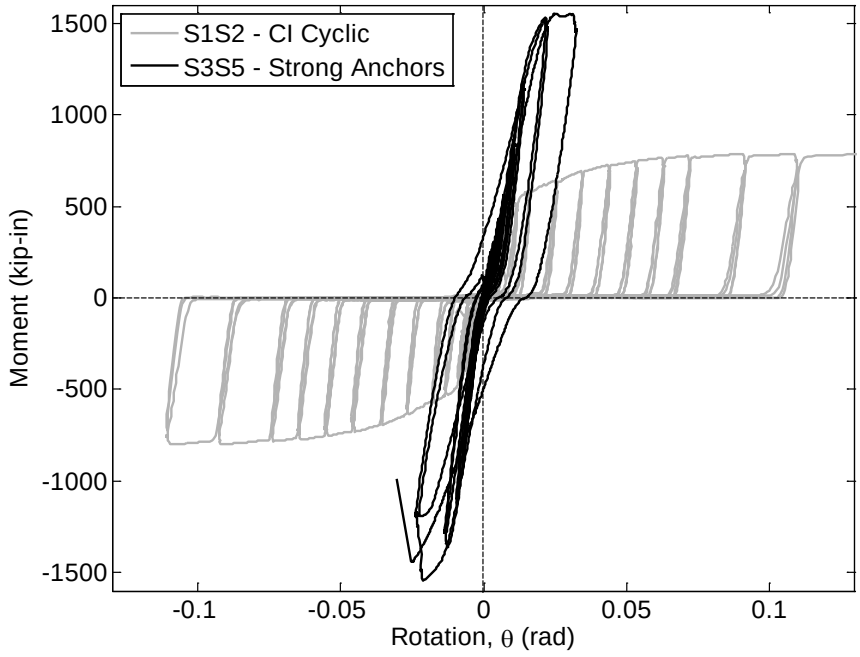

Figure 3-49: Moment-rotation comparison: relative component strength

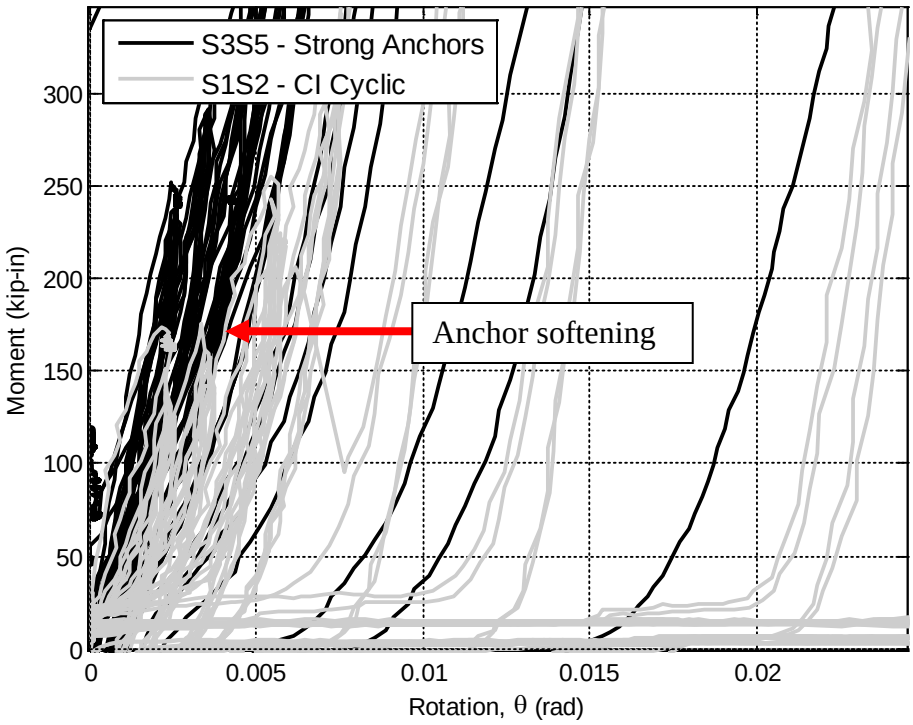

Figure 3-50: Initial stiffness comparison: relative component strength

The distribution of plastic strain within the baseplate was found to be very nonuniform, as indicated in the top portion of Figure 3-51. Note that these strains are plotted relative to normalized top displacement, which describes the fraction of the total distance in the loading protocol the specimen has undergone (Trautner and Hutchinson 2014a). The connection rotation is plotted with respect to normalized top displacement in Figure 3-52 for reference. The middle gage on the south side (G10) experienced a significant "baseline" strain that was static throughout testing, on top of which the strain due to horizontal loading is discernible. The reason for this is that the anchor preloading imparted significant bending on the baseplate, which was known to be warped approximately 1/16 in. on each edge, with a somewhat random distribution (Trautner and Hutchinson 2014b). Exact measurements of the baseplate warpage were not made.

However, the SE anchor was the last to be tightened in sequence, such that the measured static strain in this location is reasonable. It should be noted that the magnitude of this strain is nearly half the yield strain. Once other areas of the baseplate are at or near yield, at a normalized top displacement of approximately 0.7 (connection rotation of about 0.02 rad), this strain measurement falls in line with the others. This behavior makes sense, as plasticity at other locations in the plate should serve to relieve the elastic pretensioning strain. On the column, the outside strain gages (6, 7, 13, and 14) are consistently higher than those centered on the column (15 and 16), as shown in the bottom of Figure 3-51. These measurements are consistent with stress concentrations that may be expected near the flange-baseplate welds, as discussed in the next chapter. These measurements are also consistent with cracking observed a the baseplate-flange welds at the edges of the flanges, discussed below.

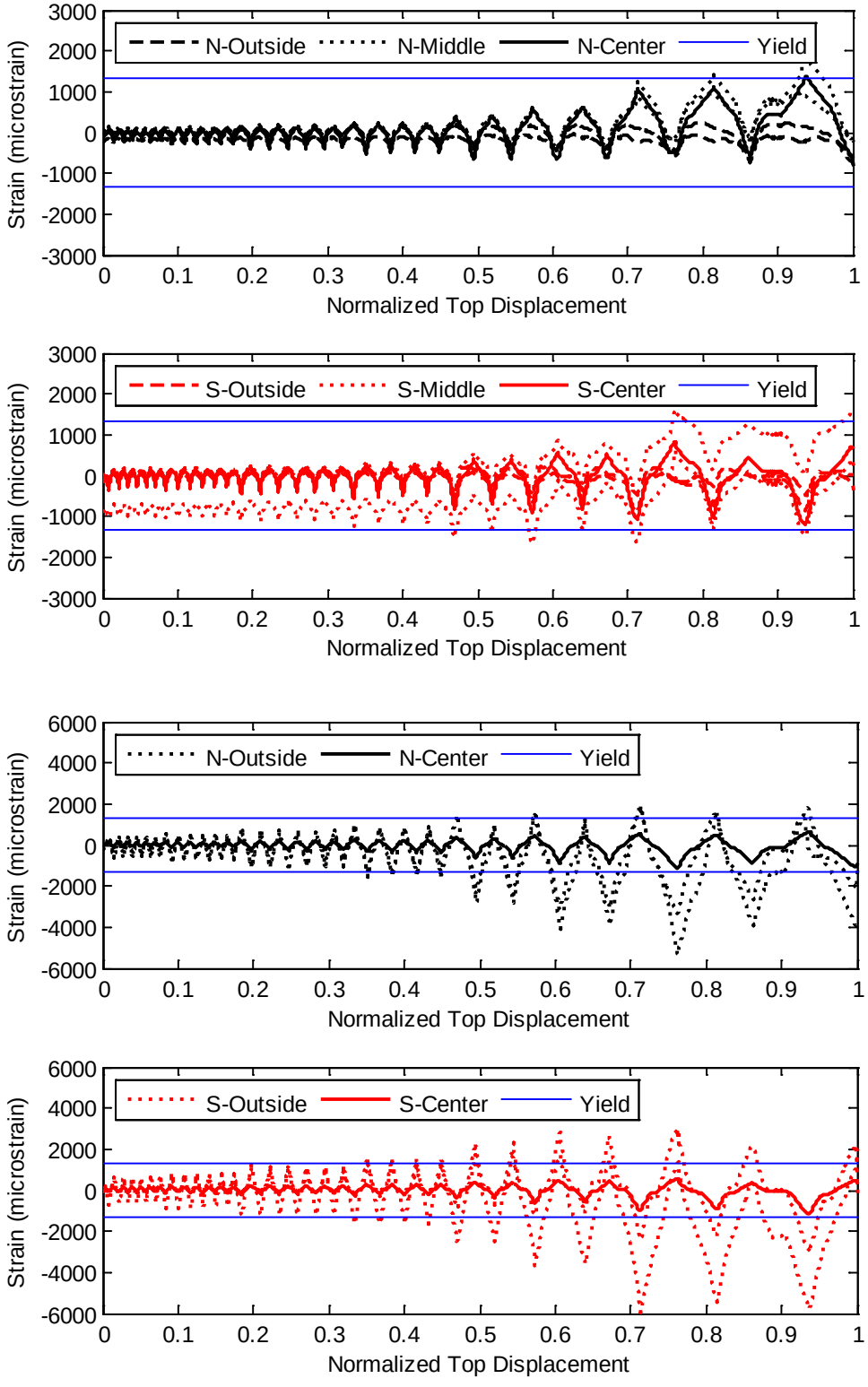

Figure 3-51: Strain gage measurements - baseplate (top) and column (bottom)

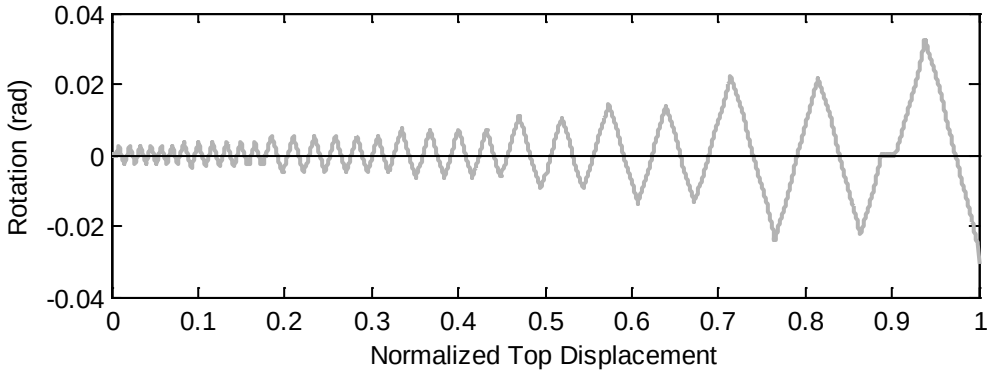

Figure 3-52: Imposed connection rotation versus normalized top displacement (S3S5)

In terms of physical damage, connection S3S5 qualitatively suffered more damage associated with undesirable limit states than any other connection. Cracking of the column-baseplate welds was observed at all four flange corners starting at approximately 3% imposed drift, as shown in Figure 3-53. During the second cycle of displacement to the N and S at 3% imposed drift, as well as the first excursion to the S at 4% drift, the cracks were observed to lengthen, suggesting that total fracture of the welds would be a possibility at increasing load, depending on the fracture toughness of the weld material. At 4% imposed drift to the N, bond failure was experienced by the SE anchor. The loading protocol was paused in-place, and failure of the SW anchor occurred shortly thereafter. As visible in Figure 3-54, the failure cones from the two anchors did not overlap significantly. Both of these findings are significant, as the design calculations for these connections (Trautner and Hutchinson 2014a), assume the simultaneous failure of both anchors with a shared breakout cone.

Interestingly, the grout damage in this test was much less severe than in other tests. The post-test grout condition is shown in Figure 3-55 for test S1S4 (left) and test S3S5 (right). The southern portion of the grout pad is fragmented due to the sudden

failure of the anchors on this side associated with uplift of the concrete; this damage did not occur during testing. On the north side, the grout pad is essentially pristine. This is interesting, as the moment applied to the S3S5 connection was over 40% larger than connection S1S4, suggesting that significant grout damage is more associated with load cycling, rather than the magnitude of the load applied. As a consequence of little grout damage occurring during testing, the grout remained adhered to the concrete surface and could not be removed with reasonable effort, as shown in Figure 3-54.

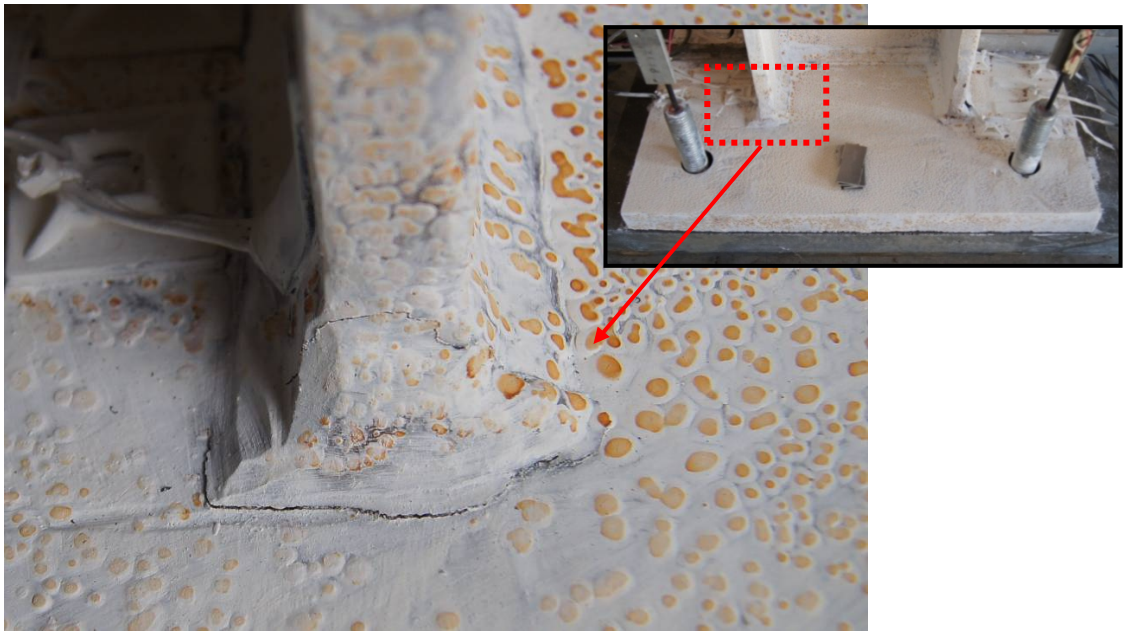

Figure 3-53: Cracking at NW flange weld, 3% imposed drift (first excursion to the south)

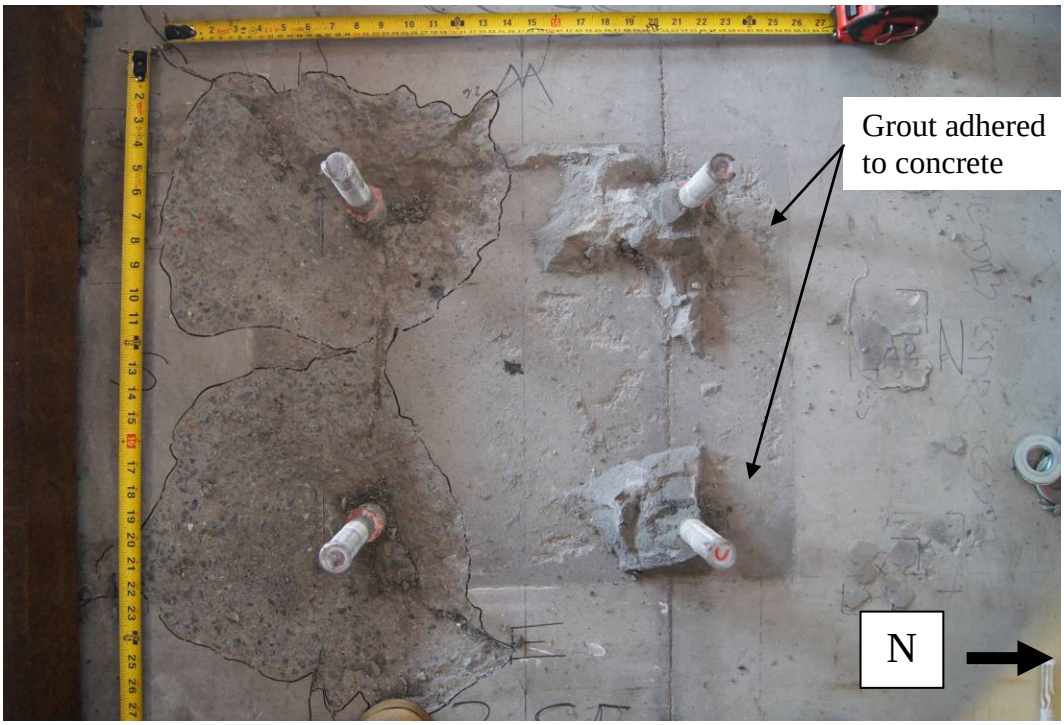

Figure 3-54: S3S5 Post-test concrete surface condition

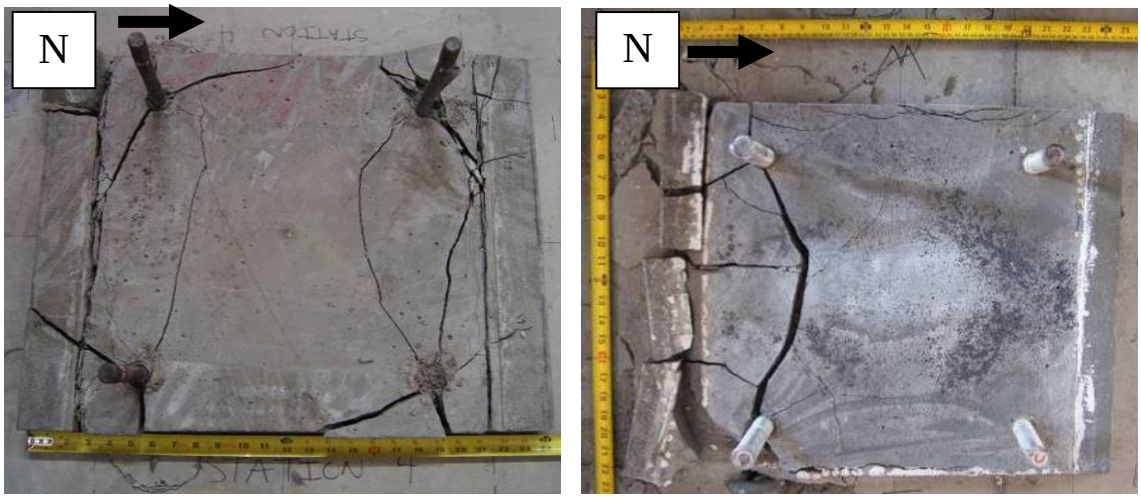

(a) S1S2 (b) S3S5

Figure 3-55: Grout damage comparison – relative anchor strength comparison

3.7 Overall test program comparisons

As summarized in Table 3-3, the approximate ranges for critical connection parameters were:

- Yield strength (M_y): 400 to 1400 kip-in
- Ultimate strength (M_u): 450 kip-in to 1550 kip-in.
- Yield stiffnesses (β_y): 50 to 175 kip-in/millirad
- Rotation capacity (θ_f): 30 to 160 millirad

These bounding values for these four key characteristics provide context to comparisons between tests. Ultimate strength/rotation capacity pairs for each test are plotted in Figure 3-56. From these values, a number of interesting comparisons can be made:

- The tests performed with undercut anchors, S2S2 and S3S3, vary nearly the entire range of all tests in terms of both ultimate strength and rotation capacity. It must be noted that the "standard" undercut anchors in test S2S2 were 20mm nominal diameter (nominal area of 0.487 in^2), while the ductile undercut anchors used in test S3S3 were only 16mm nominal diameter (nominal area of 0.312 in^2). Based solely on the ratio of nominal areas, one would expect approximately 36% lower strength from test S3S3, however the measured strength was approximately 70% lower. The mechanical properties for these two anchors are proprietary, and are not intended to conform to any particular US standard, however, the "ductile" undercut anchors are similar to ASTM F1554 Gr 36 tested as part of the current

research program, while the "standard" anchors are similar to ASTM F1554 Gr. 105 in terms of yield strength.

- Removable anchors (test S3S2) provide extremely robust rotation capacity in this connection geometry. This was the only test not run to failure due to insufficient actuator stroke. This test provided similar strength performance to the more traditional cast-in connections, and significantly higher rotation capacity. The rotation capacity that was achieved in this test, approximately 160 millirad, is far beyond what would be expected for any reasonable level of seismic demand in a "traditional" connection of this type. Reference testing on this anchor type performed in Chapter 2 suggested that the connection could accommodate more than 2-1/4 in. of direct uplift (Table 2-6). Based on this level of performance, a similar anchor type was utilized in dynamic testing of a structure with uplifting columns, as described in Chapter 5.
- All weak-anchor connections tested as part of the current program provided significantly larger rotation capacity versus the sole strong-anchor test S3S5. Even the next least-ductile connection (S2S1), constructed with bonded anchors with as-received allthread, had approximately 20% greater rotation capacity. The more ductile connection designs, such as S2S1, had about 5 times greater rotation capacity. As noted in the previous section, the relatively early connection failure was due to the fact that connection failure occurred suddenly, relatively early in the test due to anchor bond failure. However, development of significant cracking at all four corner flange welds (i.e. Figure 3-7) suggests that had anchor breakout

not occurred, weld fracture would likely have occurred relatively shortly thereafter. This exposes a particular advantage of providing connection ductility through a weak-anchor configuration - the anchors themselves are not welded components and have none of the well-known hazards of providing ductility in welded, moment-resisting components.

- The selection of anchor steel has a much more pronounced effect on the rotation capacity than increases in stretch length, as evidenced by a comparison of tests S1S4 (annealed steel), S2S1 (as-received steel), and S2S3/S2S4 (annealed steel, 8D stretch length). Annealed steel had over twice the rotation capacity of as-received steel, while an increase in stretch length from 2.75D to 8D (nominal) was associated with about a 25% increase in rotation capacity. The anchors with a measured elongation at fracture over a gage length of 8 in (EL_8) of less than 10% were associated with particularly large strength but low rotation capacity (see Chapter 2 for mechanical properties of anchors).
- The connection setting method has a pronounced effect on the behavior of the connection. The rotation capacity of test S4S4 (steel shims) was found to be nearly identical to the connection incorporating direct-on-grout setting (S1S4), and there were no discernible differences in overall behavior. In comparison, test S1S3 had a nearly 30% reduction in rotation capacity. It should be noted that the undesirable behavior associated with setting nuts would likely be exacerbated in connections with an increased stretch length, particularly if this stretch length was provided via unbonding. The reason for this is that this configuration would

provide additional length over which plastic strain could tend to move the bottom nut above the top of the grout, allowing the sliding and shearing behavior observed (Trautner and Hutchinson 2014b).

Yield strength/yield rotation pairs from each test are plotted in Figure 3-57. In this case, the majority of tests are in a relatively tight group, which makes sense from a kinematic/imposed rotation standpoint. The majority of tests were performed with anchors that have similar yield strength, therefore, at a given imposed rotation the majority of connections would be expected to yield. Note also that the four cast-in tests are tightly grouped together at a slightly higher rotation than the rest of the group. This also seems to make sense as these anchors have a longer effective stretch length than the bonded anchors. The points outside the group appear to have reasonable physical explanations:

- Test S2S2 was performed with undercut anchors that have significantly higher yield strength than any of the other tests, except for test S3S5. Therefore, this test may be expected to yield at a slightly larger rotation, but a significantly higher strength than others.

- The ductile undercut anchors used in test S3S3 were significantly smaller than any other anchors used in the testing program, having approximately 30% less nominal area than the 3/4 in. anchors used for the majority of the tests. As discussed previously, the yield stress for these anchors was similar to F1554 Gr 36. Therefore, it would be expected that the yield moment would be about 30% lower than other 3/4 in. Gr. 36 tests, which appears to be approximately what was observed.

- Test S3S1 was performed with applied axial load, which tends to have a stiffening effect on connections. Additionally, this test used welded bearing washers. Therefore, the yield secant stiffness for this test is expected to be higher than other tests with CI anchors (via a lower yield rotation, as shown in the figure).

First connection yield in the "strong-anchor" test S3S5 was associated with baseplate bending and weld cracking rather than anchor yielding. Therefore, it is unsurprising that this test has a significantly higher yield rotation and strength than all other tests. The overall performance of this connection (high yield strength, large yield rotation, high ultimate strength, and relatively low rotation capacity) would be acceptable, perhaps even desirable, in situations that do not require ductile lateral load performance, such as in the gravity framing system of a building or other structure.

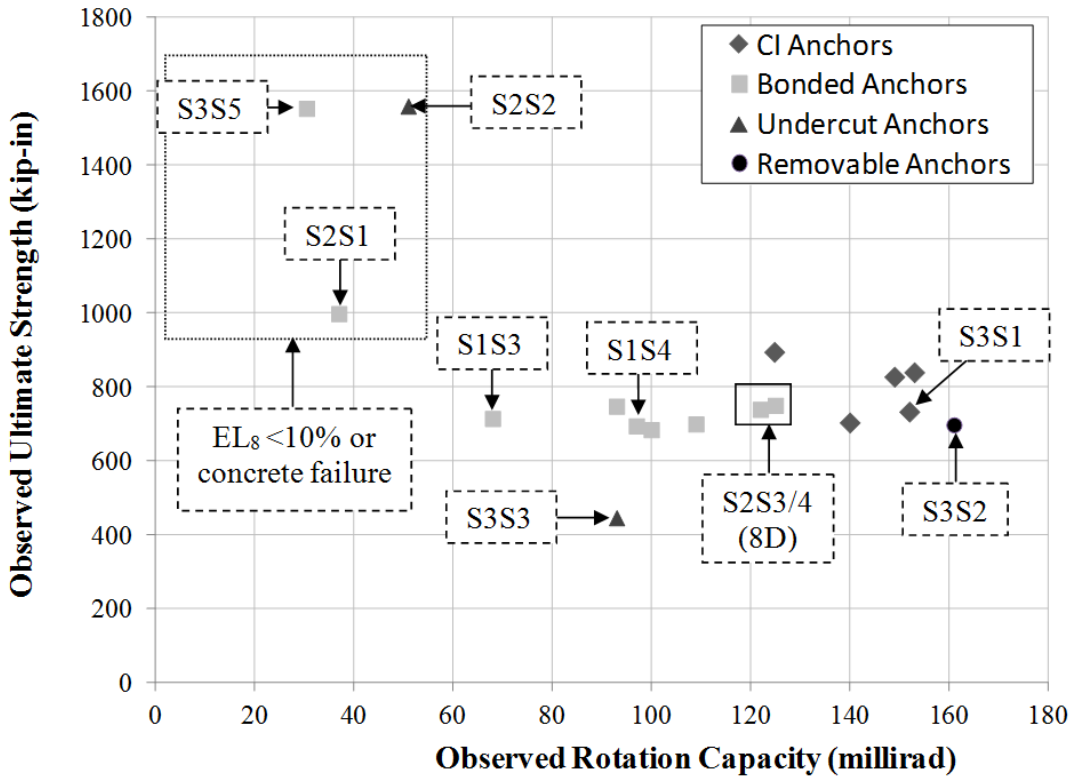

Notes: 1) rotation capacity and ultimate strength did not generally occur at the same instant. 2) Tests identified by name in figure are significant in some way relative to other like connections. See discussion in text.

Figure 3-56: Summary of ultimate strength-rotation capacity pairs for entire test program

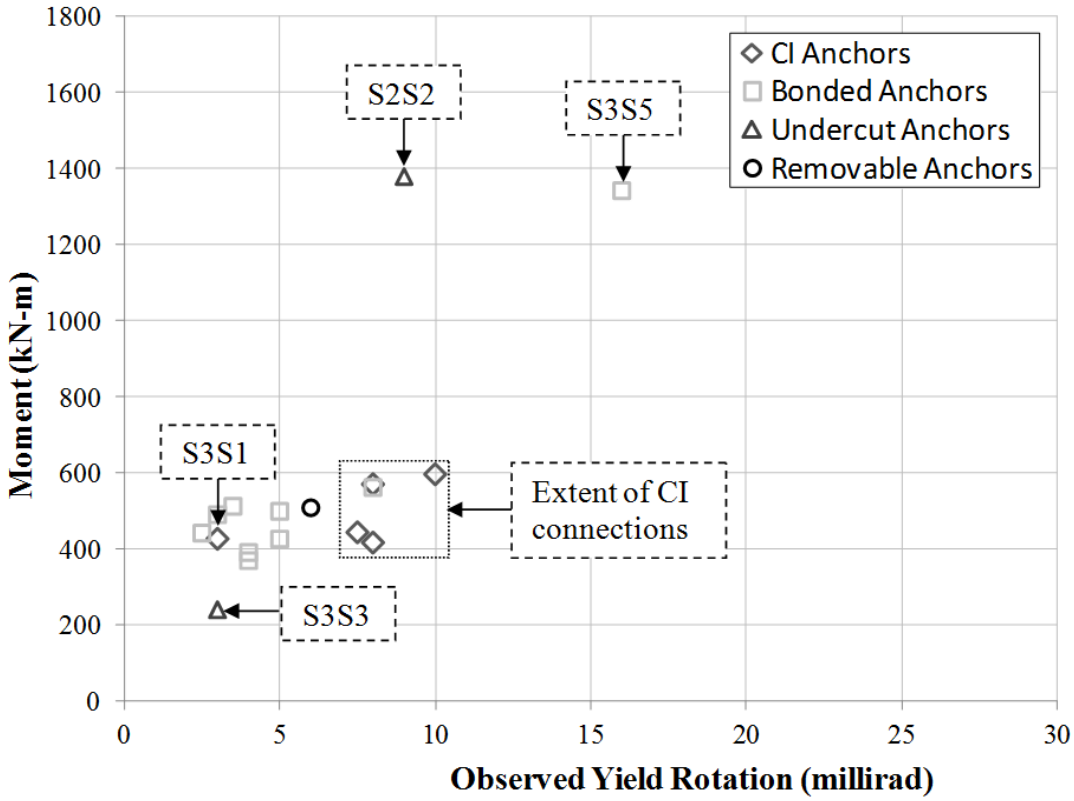

Figure 3-57: Summary of yield strength-yield rotation pairs for entire test program

3.8 Summary Remarks

This chapter presented the results of an experimental investigation into the behavior of steel column baseplate connections. Specifically, the investigation included tests intended to determine the effects of anchor type/material selection, setting method, stretch length, and other common detailing considerations on the overall behavior of the connection. The following summarize the major findings and conclusions of the work:

- Baseplate connections incorporating cast in, adhesive, and undercut anchors are capable of broad, stable hysteresis under cyclic moment loading. The rotation capacity of the connections was generally very robust, with a minimum approaching 0.04 radians for the connection incorporating adhesive anchors with relatively brittle, cold-worked all-thread, up to about 0.15 radians and above for connections incorporating hot-rolled cast-in anchors or removable anchors with annealed inserts.
- Existing predictive methods for ultimate strength and yield stiffness were found to be reasonable and generally conservative. The methodology for calculating connection strength under large moments given by AISC Design Guide 1 predicted connection strengths that were within about 6% of observed values not only for connections incorporating cast-in anchors, but also adhesive and undercut anchors. Extension of this method to cyclically loaded connections that have multiple rows of fasteners should be performed with care, however, because plastic strains in one direction of loading may prevent these anchors from being effective if the maximum rotation demand occurs in

the other direction of loading. The methodology proposed by Kanvinde et al. (2012) to determine the secant rotational stiffness associated with first yield of the connection was found to be accurate within about 15% for the majority of the tests performed. The method was found to be less accurate for connections incorporating direct-to-steel bearing elements, such as shim packs and setting nuts.

- Base connections exhibited slightly higher ultimate strength when loaded monotonically compared with otherwise identical, cyclically loaded counterparts. This was found to be due to the engagement of anchors on the compression side of the baseplate under monotonic loading that were not effective in resisting load when subjected to load reversal. Although for the current tests the difference in ultimate strength was only about 10%, this effect may be amplified in connections with multiple rows of anchors. Further study regarding optimal anchor layout and mechanical characteristics for resisting cyclic loading may prove useful in this regard.
- Increased stretch length was found to lead to incremental increases in connection rotation capacity. However, strain penetration was found to be highly variable depending on the type of anchor, and definition of the anchor stretch length proved to be problematic for some cases. Anchors bonded directly to concrete with epoxy adhesive were found to exhibit essentially no strain penetration, smooth-shank cast-in anchors were found to de-bond over their entire length at even relatively low strain levels, and cast-in anchors

consisting of threaded rod with a nut and bearing plate were found to de-bond over part of their embedment. This finding highlights the need for further work to develop guidelines to ensure the assumed stretch length is actually available to the connection. Effective detailing (e.g., grease, taping, or sleeves) as required to ensure a reliable, well-defined stretch length, should be further investigated.

- The choice of setting method (i.e., the use of baseplate shims vs. setting/leveling nuts) can have a pronounced effect on the behavior of connections. In cases where the setting method provides a more rigid path for compressive bearing than the grout pad under the baseplate, the secant stiffness associated with first yield of the connection is larger than that predicted by analysis methods that assume grout/concrete flexibility. The use of setting nuts in connections with anchor yielding may cause significantly degraded behavior due to "ratcheting" of the anchors as they elongate below the setting nut. This mechanism was found to lead to pinched hysteresis and premature anchor failure due to shear deformations. Given the paucity of data regarding yielding-anchor connections assembled with setting nuts, future analyses and test programs should consider their influence in developing design and detailing guidance.

3.9 Acknowledgement of Publications

Chapter 3 contains material published in the following journal papers: Trautner, C., Hutchinson, T., Grosser, P., and Silva, J. (2015). “Effects of detailing on the cyclic behavior of steel baseplate connections designed to promote anchor yielding.” ASCE Journal of Structural Engineering, *10.1061/(ASCE)ST.1943-541X.0001361, 04015117.* Trautner, C., Hutchinson, T.C., Grosser, P, and Silva, J. (Accepted), " An Investigation of Steel Column Baseplate Connection Details Incorporating Ductile Anchors," ASCE Journal of Structural Engineering. The dissertation author was the primary author on both papers.

Chapter 4: Component-Level Numerical Analysis of Steel Column Baseplate Connections

4.1 Motivation and Scope

The theoretical analysis of exposed steel column baseplate connections has been investigated since the 1950s. Salmon et al. (1957) published one of the first detailed analyses of such connections, concentrating on methods for predicting the moment-rotation behavior of exposed baseplate connections in unbraced structures. In this paper, a constant concrete bearing stress distribution was assumed at ultimate strength, and the overall nonlinear response of the plate, anchors, and concrete were considered. Since this seminal work, many researchers have attempted to compare similar analytical methods predicated on assumed or observed behavior to test results. Notable examples include those developed by Kanvinde et al. (2012) used in the previous chapter to predict the connection yield stiffness, a method developed by Targowski et al. (1993) to predicted yield-line patterns, rectangular stress block methods for the prediction of overall connection strength currently implemented in AISC Design Guide (DG) 1 (Fisher and Kloiber 2006), and methods currently used by the Eurocode (2009) to predict both strength and stiffness. These hand-based, analytical methods are attractive because of the relatively small number of required parameters and ease of use, facilitating their application in design situations. In concert with the development of such analytical methods, many researchers have developed finite-element numerical models suitable for the analysis of such connections. Such models generally fall into one of two categories, relatively simplistic linear or nonlinear spring models intended for system-level sensitivity analysis of buildings (e.g. Kawano and Matsui 1998, Aviram et al. 2010) or

relatively detailed shell- or solid-element models of particular test programs (e.g. Targowski et al. 1993, Fahmy 1999, Trautner et al. 2014b, Trautner 2015b). Recently, automated parametric analysis of such connections has been implemented by commercial programs such as Risa Base (Risa Technologies 2013). These models use the shell-element modeling approach integrated with design checks for anchors and baseplates. In such commercial software, connection analysis and system-level analysis may be partially integrated, with the system-level model providing demands for the design of the connection. In the future, closer integration of the two models is likely, with the connection model providing a moment-rotation or force-displacement curve for use in the global model, or the level of detail in the sub-model becoming practical for direct use in the global model.

There are limitations to both currently-available analytical and numerical techniques, however. In general, the analytical techniques are predicated on a certain type of behavior, and are often verified using a small number of experiments. Therefore, the techniques are not readily extensible to connections that do not behave in a similar manner or fall within the scope of the tests used for validation. For example, considering the techniques introduced earlier, the stiffness-prediction method of Kanvinde et al. (2012) and the yield-line pattern strength prediction method of Targowski et al. (1993) produce excellent results when compared to 4-anchor connections, but may not be readily adapted to 6- or 8-anchor configurations. The method of designing baseplate thickness contained in AISC Design Guide 1 (referred to herein as AISC DG 1) is similarly limited (Fisher and Kloiber 2006). In contrast, while finite-element models can be quite accurate, the effort required for the development of such models is usually excessive for a typical

design or analysis setting. Commercially-available programs incorporate a number of assumptions regarding anchor behavior, and have not been explicitly verified against test results in the open literature, to the authors' knowledge (Risa Technologies 2013). A rigorous, well-verified method of analysis which combines the ease of use of analytical methods with the accuracy and versatility of finite element analysis is needed.

This Chapter presents the development and verification of a finite element modeling approach for exposed baseplate connections in moment frames. The connections considered are subjected to combined axial and cyclic moment loads. The model utilizes an automatic mesh generation and postprocessing procedure developed specifically for this type of connection, in order to make parametric modeling economical. The parametric script allows control of baseplate size, column type and size, anchor layout, mesh parameters, loading, and other parameters. The script draws from a database of anchor test results available in the literature to accurately calibrate the anchor force-deformation response.. This paper discusses the general approach, input data sources, model limitations, and the results of a comprehensive verification program that includes a broad range of commonly-encountered connection sizes and configurations. Analysis of a design example from AISC DG 1, which illustrates the usefulness of the parametric modeling capability, is presented.

4.2 Model description

The finite element model presented herein is intended to predict the behavior of unstiffened, exposed baseplate connections subject to large moments in the presence of axial load, as would be expected in the lateral loading of an unbraced moment frame (Figure 4-1(a)). The model meshing and creation procedure is handled by a specialized

preprocessor as described in the next section, but features common to all models created with this approach include explicit representations of the column, baseplate, anchors, and grout and/or concrete (Figure 4-1(b)). The baseplate and column extension near the baseplate are modeled using shell elements, with a minimum of 9 through-thickness integration points. The column is transitioned from shell elements to beam elements using a kinematic coupling at a distance of at least one characteristic dimension (column section depth or flange width). This distance is required to allow local stress effects from the baseplate to dissipate, and is justified generally by St. Venant's principle and specifically by examination of the stress field in many different simulations. The anchors and grout are modeled using nonlinear springs. The model considers an $N \times M \times t_b$ baseplate[9] with 4, 6, or 8 anchors with a total center-to-center spacing of s_M and s_N, and a grout height of t_g (Figure 4-2). For typical applications, the total model height may be taken as 2/3 the height of the building story. This approach attempts to co-locate the zero-moment boundary condition of the top of the model with the approximate location of the inflection point in a laterally-loaded moment frame. The total column extension height may be varied to account for specific circumstances, such as matching the height of column extensions used in experiments, as described below.

All nodes attached to the bottom of the grout and anchor elements are fixed in all directions. This neglects the flexibility of the concrete in the vertical direction beneath the level of the grout, although this effect can be lumped into the nonlinear behavior of the

[9] M is also used to refer to moments. The use of the N × M nomenclature for baseplate size is consistent with practice in the United States, as exemplified in AISC DG1 and other AISC codes and standards. The exact meaning of M in this paper should be clear from context.

grout springs if desired. In a planar analysis, movement of the model out of the plane of the frame (y-translation) and twisting about the long axis of the column (rotation about the z-axis) are prevented by imposing boundary conditions at the top of the column stub. Loading typically consists of a vertical force *P* and imposed x-displacement at the top of the stub[10] (Figure 4-2(b)). This approach allows the application of displacement-based experimental test protocols (Clark 1997, Krawinkler 2009), monotonic pushover loading, or other displacement based loading.

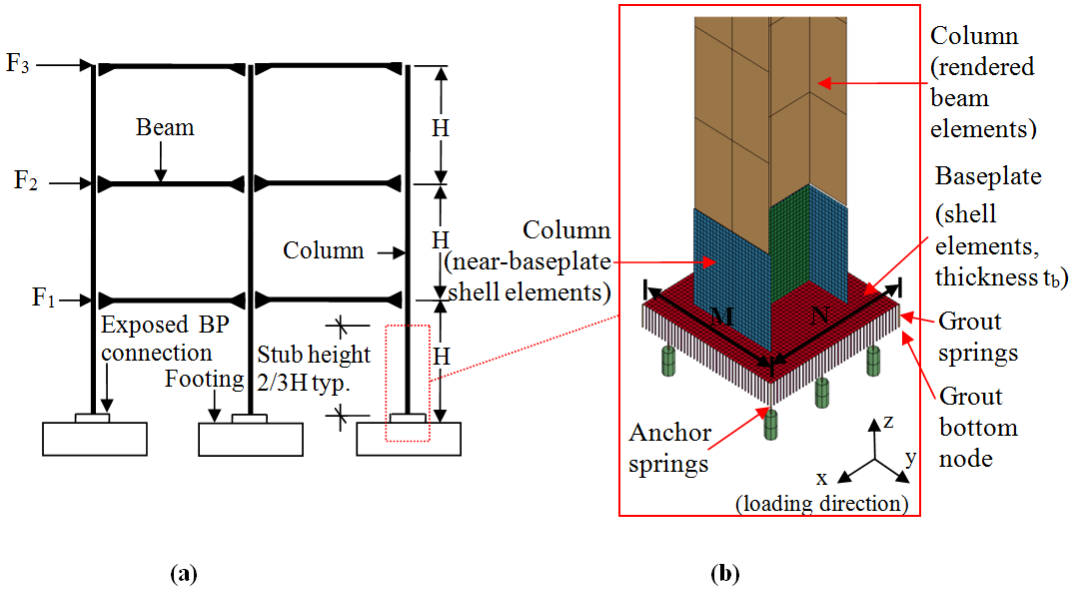

Figure 4-1: (a) Laterally-loaded frame, (b) finite-element model features and extents

[10] It should be noted that although only strong-axis loading is considered herein, bi-directional lateral loading can be accommodated. If only unidirectional loading is considered, further computational savings can be realized through the use of symmetry boundary conditions, although this approach is not taken in the current paper.

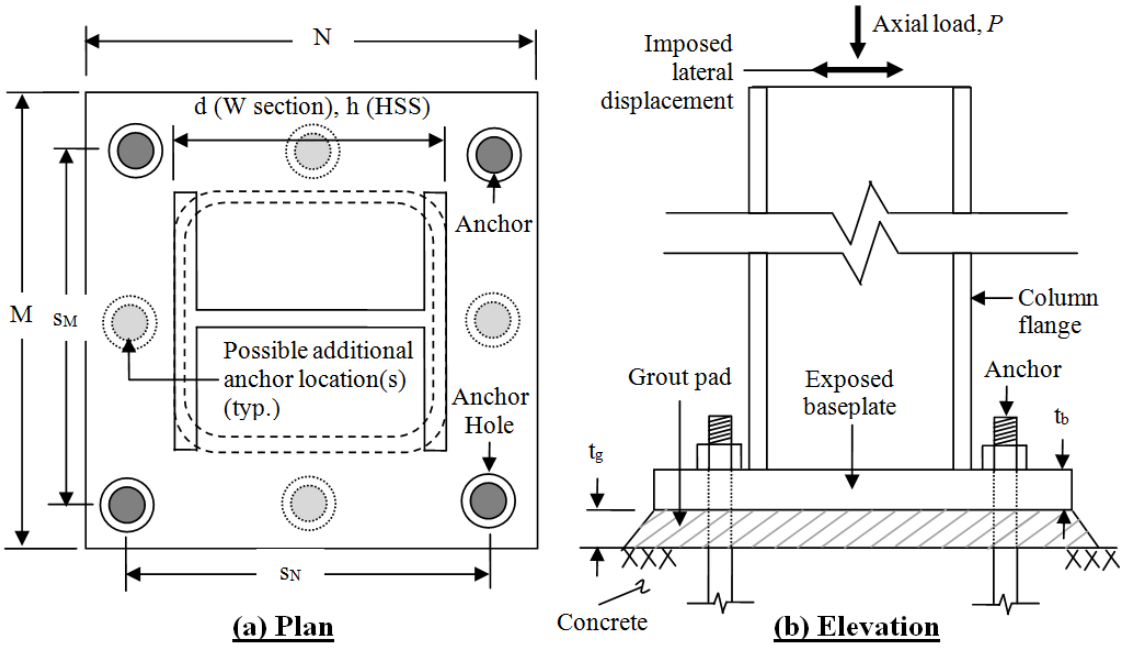

Figure 4-2: Key connection dimensions and parameters for use in numerical model

The anchors are modeled using nonlinear springs, calibrated using the results of the large testing program of anchor materials presented in Chapter 2. In this program the anchor diameter *D* ranged from about 5/8 in. to 1-1/2 in. The stretch length L_s, the distance over which plastic strain was expected to occur, was between 2D and 16D. The tests included anchors fabricated from four distinct types of steel, supplied from commercial sources under four common anchor specifications. The material types, specifications, and short names used to refer to each of the anchor types in the current work are summarized in Table 4-1. The ASTM F1554-07a Gr. 36 (CW) material type was not used in the current work, and is included only for completeness. Recent changes to the F1554 standard will preclude the manufacturing of cold-worked material without subsequent annealing (ASTM 2015).

Table 4-1: Summary of anchor types tested as part of Chapter 2, including similar specifications and short names used here

General Steel Type	Specification(s) tested	Similar specifications	Additional processing	Short name*
Low-carbon	• ASTM F1554-07a Gr. 36 • ASTM A307-12	-	Hot rolled (virgin)	HR
			Cold-worked	CW
			Cold-worked, annealed	CW-A
High-strength low-alloy	• ASTM F1554-07a Gr. 55	-	-	HSLA
Quenched and tempered alloy	• ASTM A193-09 Gr. B7	• ASTM F1554-07a Gr. 55 • ASTM F1554-07a Gr. 55	-	A

*Used in the current Chapter for reference

The typical behavior of the remaining three material types is shown in Figure 4-3(a). The F1554 Gr. 36 mild steel curve, in both the CW-A and HR forms, is distinguished by relatively low strength, a relatively long yield plateau, and very large displacement ductility. The F1554-07a Gr. 55 HSLA curve is distinguished by moderate strength, the absence of a yield plateau, and moderate post-yield hardening. The A193 B7 quenched and tempered alloy steel has relatively high strength, a small yield plateau, and a relatively high hardening modulus. These steel types cover the most commonly-supplied materials used for cast-in headed anchors and allthread used in post-installed bonded anchors. Other specifications with similar mechanical and chemical requirements include ASTM A345-11 BC and ASTM F1554-15 Gr. 105, two other quenched and tempered alloy steel specifications sometimes used for anchor bolts (ASTM 2011, 2015). These material types were adequately modeled using the results from the ASTM 193-B7 material, as discussed below.

For use in the current model, the appropriate force-displacement data was discretized into vectors F_i and D_i, where i is an integer index for each point. Chapter 2

presents methods to extend the applicability of the test results, including scaling relationships to determine the force-deformation relationship as well as elongation at fracture as a function of material type, diameter and free length. In the current work, extrapolation of force-deformation relationships to larger diameters was accomplished via scaling of the existing discretized force data F by the ratio of the anchor stress areas (as reported by ASTM F1554-07 for Class 2 threads) using the formula:

$$F_{i,model} = F_i \frac{A_{model}}{A_{test}}$$

where $F_{i,model}$ is the discretized force vector used in the model, A_{model} is the stress area of the (larger) anchor of interest for the model, and A_{test} is the stress area of the existing test data. For example, to scale data from a 19mm to 25mm diameter, the conversion factor would be $391mm^2/216mm^2=1.81$. To determine elongation at failure ΔL_u for a stretch length L_s that is outside the testing program, the following formula was used:

$$\Delta L_{u,new} = \Delta L_u + (L_s - L_{s,max})s$$

where $L_{s,max}$ is the maximum stretch length available in the testing program, and s is an "efficiency factor" that describes the gain in elongation capacity with added stretch length. The parameter *s* is the slope of a stretch length versus elongation at fracture curve, and ranges from 20% for hot-rolled mild steel anchors to about 5% for heat-treated alloy steel (see Chapter 2).

The general shape of the load-displacement behavior of the grout elements was developed based on compressive testing of 2 in. high-performance cementitious grout cubes reported in Chapter 3 per ASTM C109 (ASTM 2012c). These grout cubes had compressive strengths between 55 and 85 MPa, which is consistent with grout strengths

reported by others (e.g. Fahmy 1999, Gomez et al. 2010). The initial elastic modulus is assumed to be $500f'_g$, in accordance with ACI 530 recommendations (ACI 2013). The grout is considered to have linear, softening, peak, and residual regimes, consistent with observed behavior. The idealized force stress-strain curve is compared to 12 grout tests with similar ultimate strengths in Figure 4-3(b). The post-failure force is intended to account for two observed phenomena: 1) interlock between grout fragments, which allows development of some residual force, and 2) direct bearing between the baseplate and concrete through fractured grout pieces, as observed during baseplate connection testing (see Chapter 3). It should be noted that this approach does not account for any confinement effects that may affect the load-displacement behavior at the center of the grout pad. However, this approach is considered to be satisfactory as nearly all grout failures due to moment loading, even in connections with relatively high axial loads, initiate at the edges of the connection, where the behavior of the unconfined grout cubes is likely representative (e.g. Picard and Beaulieu 1985, Gomez et al. 2010). The model was found to be relatively insensitive to the exact grout modeling approach used, so long as a cap on the maximum grout force corresponding to attainment of f'_g was included.

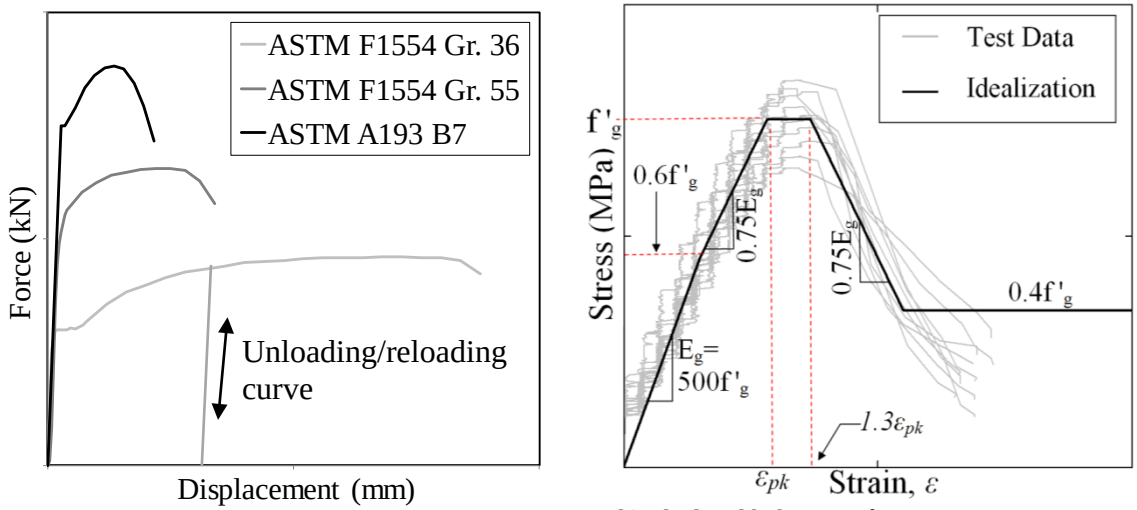

(a) Typical axial force-displacement behavior of ASTM F1554 Gr. 36 hot-rolled, Gr. 55 Cold-Worked, and ASTM A193 B7 alloy steel anchor materials

(b) Idealized behavior of grout in compression overlaid with test data

Figure 4-3: Force-displacement behavior of anchor steel and grout

The model is limited to connections in structures where the behavior is dominated by axial loads and/or flexure. The model does not account for shear slip between the baseplate and the grout, shear deformation of the grout itself, or shear deformations of the anchors. However, the magnitude of these deformations has been observed to be very small for these types of connections in many test programs (e.g. Picard and Beaulieu 1985, Fahmy 1999, Gomez 2010). As a result, the model should be limited to cases where flexure is the dominant component of the overall load - for the reasons discussed above, the grout modeling approach will likely give unrealistic results when failure is caused by large, uniform axial load.

4.3 Scripting for Parametric Analysis

Parametric analysis is accomplished through the use of meshing and postprocessing scripts which automate the model creation process. The input script,

implemented in Python 2.7 (2015), takes a limited number of input parameters and generates an input deck for LS-DYNA 6.1 (LSTC 2013). Although the deck is currently set up for LS-DYNA, any general-purpose finite element code could be used with minimal modification. The parameters needed for model creation are summarized in Table 4-2.

Table 4-2: Summary of input parameters for mesh generation script

Geometric parameters	Material properties	Mesh parameters	Loading
• Baseplate dimensions: N, M, t_b, d_{hole}, s_N, s_M, thickness of grout t_g (Figure 4-2) • AISC section name (section dimensions are taken from AISC electronic resources) • Number of anchors (4-, 6-, and 8-anchor patterns are supported)	• E_s, F_y, and and E_t for the baseplate steel and column steel • Force-deformation relationship for anchors* • Grout strength, f_g	• Number of baseplate elements (x and y directions) • Number of beam elements in the column	• Vertical axial load, P • Anchor preload • Lateral loading protocol (monotonic or cyclic)

* If the force-deformation relationship is not known from testing, one of the archetypical force-deformation response curves shown in Figure 4-3(a) may be used with known or estimated F_y, F_u, and elongation at fracture value to synthesize an approximate curve of reasonable accuracy

The input script first generates a baseplate mesh on a rectangular grid. The grid is slightly modified based on the exact dimensions of the column, which are determined using the AISC electronic database (AISC 2005a). Elements within the anchor hole diameter are assigned an artificially high stiffness, such that the anchor spring can be directly attached. Nodes and elements for the grout and anchors, associated with the appropriate nonlinear anchor force-deformation curve (Figure 4-3) are then created. The column stub is then meshed to a height of one characteristic dimension of the column (d for W-sections, h for HSS sections). A maximum element aspect ratio of 1.5:1 is allowed for the shell meshes. Mesh refinement studies performed as part of the current work have indicated that a characteristic shell element size of about 10mm is acceptable for most cases, giving a solution that changes by less than 10% for important output parameters of

interest with increasing refinement. A beam-shell coupling connects the stub to the column beam-element mesh. The loading is applied, and solution parameters and output requests are calculated automatically depending on the nature of the load, either monotonic or cyclic. After submission to the finite element program, an automated output postprocessing script uses the node and element numbering generated during input to collect all grout and anchor forces, element strains and stresses, and other key outputs for data analysis, plotting, and further postprocessing.

4.4 Model Verification

4.4.1 Description of Test Programs Used for Verification

Previous researchers have categorized steel column baseplate connections based on several characteristics. Among the most widely used and broadly applicable of these categorizations are: 1) Embedded-plate versus exposed-plate (e.g. Grauvilardell et al. 2005), 2) Large versus small eccentricity (Fisher and Kloiber, 2006), 3) fixed versus flexible, and 4) plate-dominated versus anchor-dominated (Astaneh et al. 1992). Categorization (1) is self explanatory, and only exposed-plate type connections are considered herein. Categorization via eccentricity (2) is somewhat arbitrary. However, AISC DG 1 defines large eccentricity or "large moment" as the case in which the compressive resultant cannot be resisted by bearing alone, i.e. when the eccentricity, *e,* the ratio of moment to axial load (*e=M/P)* falls outside the kern of the baseplate. For rectangular baseplates, this occurs when the eccentricity $e>N/3$, where N is the length of the baseplate in the direction of loading. Categorization based on fixity (3) is also somewhat subjective, however previous researchers have used criteria such as a limited percentage decrease in the flexural buckling resistance of a frame versus a theoretical

kinematically fixed connection to define "fixed" baseplate connections (Wald and Jaspart 1998). The plate-dominated versus anchor-dominated distinction (4) was first used by Astaneh et al. (1992) and used by several other researchers to distinguish connections where plastic behavior of the connection is dominated by yielding of the anchors or by plastic deformation of the baseplate. Connections having contributions from both plate and anchor plasticity are denoted as intermediate connections.

To be generally useful, a numerical model must be able to reasonably predict behavior for connections in any of these categorizations. Additionally, from a practical point of view, the model must be able to accurately predict behavior of connections with column, baseplate, anchor sizes, and anchor arrangements within common ranges used in practice. Ideally, the model should be able to capture failure mechanisms that have been observed in previous test programs, including baseplate yielding, column yielding, grout and/or concrete crushing, anchor yielding and fracture, anchor concrete limit states such as breakout and pullout, and weld fracture. The current model is capable of automatically predicting all but the last two, as any of the other failure mechanisms introduce a rigid body mode that will automatically terminate an implicit solution procedure. Concrete-related anchor limit states cannot be predicted by the model, as there is no explicit representation of the concrete. However, anchor forces from the model may be used to design against these limit states. Similarly, although a fracture criterion is not included in the material definitions of the current model, prediction of fracture in weld elements is discussed in the context of test results and in a hypothetical design scenario in subsequent sections.

Based on the preceding criteria, five distinct test programs were selected to verify the accuracy of the numerical model, namely: Picard and Beaulieu (1985), Fahmy (1999), Gomez et al. (2010), and Trautner et al (2015b, 2016b). The anchor patterns, anchor types, loading types, and behavior categories for these tests are summarized in Table 4-3. These 30 tests include connections in each of the behavioral categorizations discussed previously, and include baseplate sizes between 11 and 70mm, 4- 6- and 8-anchor patterns, three different anchor materials, and steel sections ranging from HSS 6x6x1/2 to W10x77. Both monotonic and cyclic loading cases Other large experimental studies of baseplate connections, such as Astaneh et al. (1992) and Burda and Itani (1999) were considered for additional verification, but were ultimately rejected as the general geometry, test parameters, and failure mechanisms were already included in the verification program. To the authors' knowledge, this verification program represents the largest systematic verification of a numerical model performed to date.

Table 4-3: Summary of test programs used for numerical model verification

Test program[a] (year)	Number of tests used	Column sizes	t_b (in.)	Anchor type and dia.(in.)[b]	Anchor pattern (total)	Lateral load type[c]	Applied axial load[d]	Behavior category[e]
1 (1985)	4	HSS 6x6x1/2 W6x25	1.125	CW (0.75)	2x2 (4)	m	0	I
2 (1999)	2	W10x77	2.75	A (1.25-2.0)	2x2 (4) 3x2 (6)	c	0	PD
3 (2010)	7	W8x48	1.0 - 2.0	HR, A (0.75)	2x2 (4) 3x2x3 (8)	m & c	0-0.22	I
4 (2015b)	8	W8x48	2.50[f]	HR, CW, A (0.75-0.79)	2x2 (4)	m & c	0	AD
5 (2016b)	9	W8x48	1.25-2.50[f]	HR, CW, A (0.625-1.0)	2x2 (4)	c & c(nf)	0-0.10	AD, PD, I
Total:	30							

[a]References: [1]Picard and Beaulieu (1985) [2]Fahmy (1999) [3]Gomez et al. (2010) [4]Trautner et al (2015b), [5]Trautner et al (2016b)
[b] See Table 4-1
[c] m - monotonic, c - cyclic (Clark 1996), c(nf) - cyclic, near-fault (Krawinkler 2000)
[d] As fraction of column compressive yield strength A_gF_y
[e] Observed plastic mechanisms, AD: anchor-dominated, PD: plate-dominated, I: intermediate (both)
[f] Stiffened baseplate used. Equivalent elastic thickness of solid baseplate reported

4.4.2 Selection of Verification Parameters and Sources of Uncertainty

The general geometry and anchor layout for the model was taken directly from the published studies. Yield strength for the baseplate and column steel, as well as grout compressive strength were also available for all test programs. The column and baseplate steel were assumed to be elastic-plastic with kinematic hardening. The hardening modulus E_t was assumed to be 250 ksi for all cases. For test programs 4 and 5, force-deformation relationships were available for the exact anchors used in the connection testing. All other test programs published the anchor embedment, specification and grade of anchor material, yield strength, and ultimate strength. However, complete force-deformation responses were not available. As seen in other analyses (i.e. Trautner et al. 2015b), the exact anchor force-deformation relationship, including the length of the yield plateau, may have a pronounced impact on the hysteretic behavior of the connection.

Therefore, in the present analyses, an effort was made to match the stretch length, anchor size, material type and grade to similar anchor properties that were tested in Chapter 2. In the case of test program 2 and 3, ASTM A193 B7 data was substituted for the A354 and ASTM F1554 Gr. 105 bolts used, as they are both quenched and tempered alloy materials[11] (Table 4-1).

4.4.3 Comparison of calculated and measured connection response

Comparisons between the numerical model and test data were made based on moment-rotation (M-θ) response where available, and on the basis of moment-drift ratio (M-DR) response otherwise. Comparisons between local-level responses (e.g. baseplate stress and strain and anchor deformation) were generally not possible as this information was not available in the literature. Model moment-rotation or moment-drift results are shown with test data from four of the test programs without significant axial load in Figure 4-4. These particular tests were selected for comparison to show typical model performance for a range of general connection features, including anchor pattern, behavior type, and controlling connection failure mechanism(s). In general, the salient hysteretic response is captured well, regardless of the particular features of each test. The data in Figure 4-4(a) is from an HSS connection with zero axial load and intermediate behavior. Only a relatively brief description of this test is available, therefore there was significant uncertainty in steel and anchor material properties, accounting for the relative

[11] Removal of the yield plateau from the A193 B7 curve, (similar to the F1554 Gr. 55 curve) was implemented for Test Program 3 to more closely match the reported post-yield behavior.

mismatch in response around the yield strength of the connection. Despite the material property uncertainty, the overall match to the specimen response is good.

Figure 4-4(b) is from a test of a W8x48 column with an 8-anchor pattern and intermediate baseplate behavior. This figure illustrates the parameters used for numerical comparisons between the test data and model calculations, discussed later. Although the unloading path is overly stiff, the match to other salient hysteretic features, especially the overall shape of the backbone curve, is excellent. Figure 4-4(c) shows a comparison to a baseplate-dominated connection with a relatively large W10x77 column, very thick 70mm baseplate, and a 6-anchor configuration. Although the match to the hysteretic curve was one of the best in the verification program, this example serves to illustrate an important limitation of the model. Weld fracture was a controlling limit state in this test, a limit state which is not captured by the model. However, the model can predict plastic strain demands in the vicinity of the baseplate welds These can then be used to approximately evaluate potential weld details, as discussed later in this paper. The data and analysis results from Figure 4-4(d) are for a W8x48, anchor-dominated connection performed by the authors. The mechanical properties of the anchors and grout were known with a high degree of certainty for this test, likely accounting for the accuracy of this simulation. Additional test-model comparisons are shown in Figure 4-5. Note that in the case of test program 5, test S3S5, the model is shown terminated at the point at which the total force in the tensile anchor pair is approximately that required for concrete breakout, which is the limit state this test attained.

The model is compared to tests with two different amplitudes of applied axial load in Figure 4-6. In these cases, the model again overpredicted the slope of the

unloading curves, however this particular region of the model response was found to be sensitive to the hardening modulus assumed for the baseplate steel, which is not known with certainty for this test. These cases may have had some variation in the baseplate properties, as other predictions of tests with axial load were relatively accurate. Taken as a whole, these comparisons illustrate the general success of the modeling approach in capturing the hysteretic moment-rotation response for a wide range of connection parameters.

To evaluate the accuracy of the model numerically, three parameters were compared (Figure 4-4(b)):

1. The yield stiffness β_y,
2. The secant stiffness at ultimate strength β_u,
3. The area under the monotonic response up to 0.04 rad rotation, or within the complete hysteretic loop with extreme points nearest 0.040 rad ($A_{0.04}$). Because the cyclic protocols used in all tests were drift-based (rather than rotation based), very few of the loops used for comparison actually terminated at exactly 0.04 rad (40 millirad). The loops varied between about 35 and 48 millirad (see Figure 4-4(b)), with some additional variation between the positive and negative values.

Note that because rotation measurements were available for only some test programs/parts of test programs, the units of these comparisons may be inconsistent. The yield stiffness and secant stiffness at ultimate strength are attractive parameters to base comparisons on because they include information about yield strength, yield rotation, and ultimate strength, common parameters of interest in design. The yield stiffness, β_y, was defined as the point at which there was a significant (>15%) drop in stiffness relative to

the initial stiffness associated with yielding of one or more connection components, significant grout failure, or both. The secant stiffness at ultimate strength, β_u, was compared to the test data at the rotation or drift ratio at which the maximum moment occurred in the test data. This approach was required because in some cases, particularly baseplate-plasticity dominated cases, the moment from the simulation is monotonically increasing. In tests with weld failure (i.e. Figure 4-4(c)) or other failure limit states not well-captured by the model, the simulation never achieves a "final" ultimate strength. It is reasonable, therefore, to use the point at which the test data achieved its ultimate strength as the point of comparison. However, this also shows that the simulation results cannot be used blindly to predict ultimate strength, and must be analyzed carefully to assess when limit states such as weld fracture may occur (as discussed later in this paper). Additional comparisons are plotted in Figure 4-5, as an illustration of the typical accuracy of the model. Note that in Test S3S5 of test program 5 (Figure 4-5(c)), a similar phenomenon to Figure 4-4(c) may be observed, i.e.

The area under the hysteretic curve is a useful point of comparison for two reasons: first, it is a measure of the energy dissipation and thus an indicator of overall connection behavior. Second, this measure indicates how well the connection captures the hardening or softening behavior of the connection, something that β_y and β_u cannot. A rotation of approximately 40 millirad was selected as the point of comparison for this area because it represents a relatively large, but still realistic deformation level that was achieved in all test programs.

The average, minimum, and maximum misfit for each of these parameters is given in Table 4-4. The overall average misfit was about 3% for the yield stiffness, 1%

for the ultimate stiffness, and 5% for the hysteretic area, indicating very accurate prediction in the mean sense. Individual maximum and minimum errors were up to 45%, although the number of cases with such relatively large errors were very small. The test and model results used for the comparison are also shown graphically in Figure 4-7. These plots do not indicate obvious systematic errors relative to the magnitude of β_y, β_u, or $A_{0.04}$, nor relative to any particular test program. Overall, the results indicate that the model is capable of accurate prediction over a wide range of connection types, sizes, loadings, and behaviors.

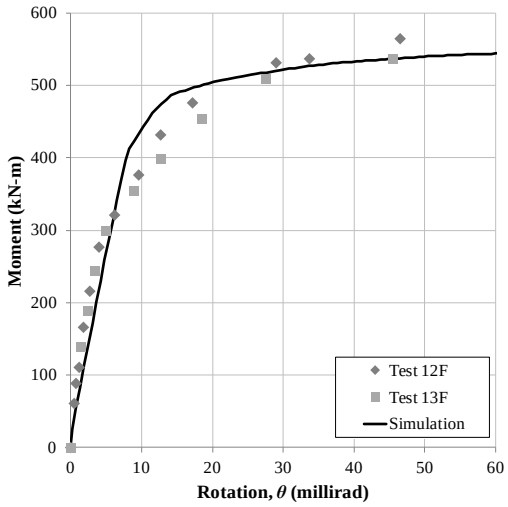

(a) HSS6x6x1/2, 4-anchor connection with anchor and baseplate yielding (Test program 2, Test 8F & 9F)

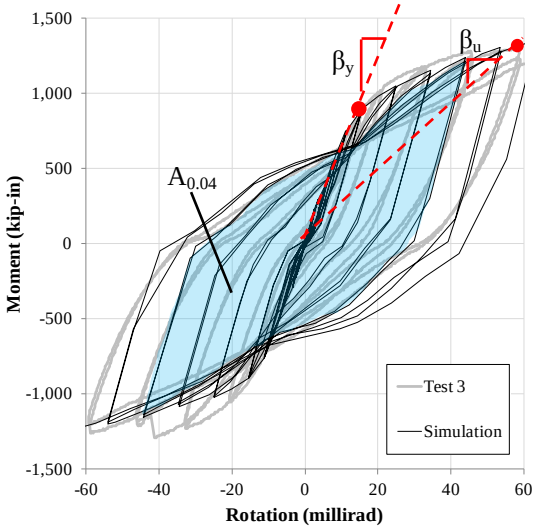

(b) W8x48, 8-anchor configuration with baseplate and anchor yielding (Test program 3, test 3)

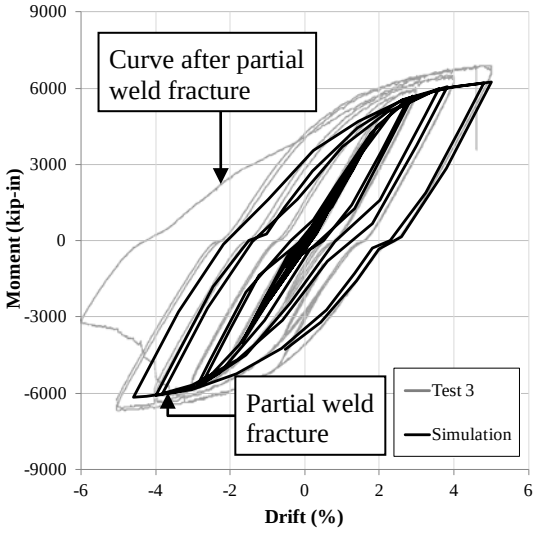

(c) W10x77, 6-anchor baseplate-plasticity dominated connection (Test program 3, test 3)*

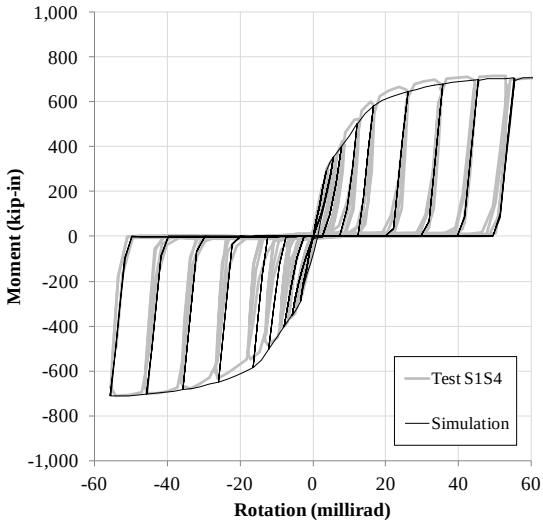

(d) W8x48, 4-anchor, anchor plasticity dominated connection (Test program 4, test S1S4)

NOTE: *Drift shown; rotation data unavailable.

Figure 4-4: Typical hysteretic response predictions for cases without significant axial load

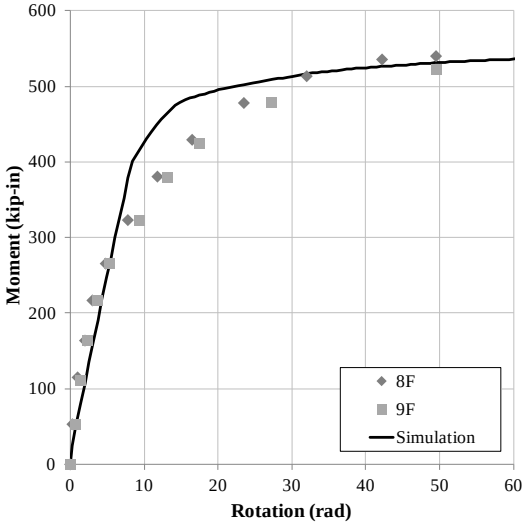

(a) W6x25, 4-anchor connection with anchor and baseplate yielding (Test program 2, Test 8F & 9F)

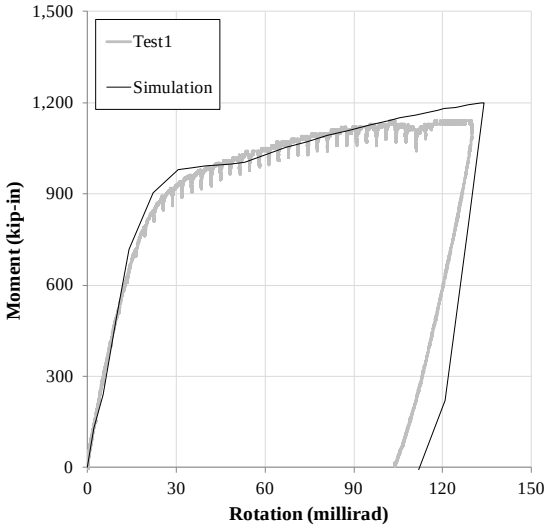

(b) W8x48, 8-anchor configuration with baseplate and anchor yielding (Test program 3, test 1)

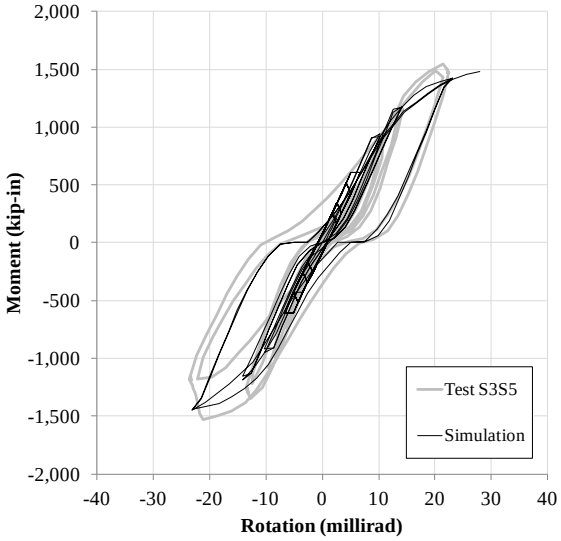

(c) W8x48, 4-anchor configuration with baseplate yielding only (Test program 5, test S3S5)*

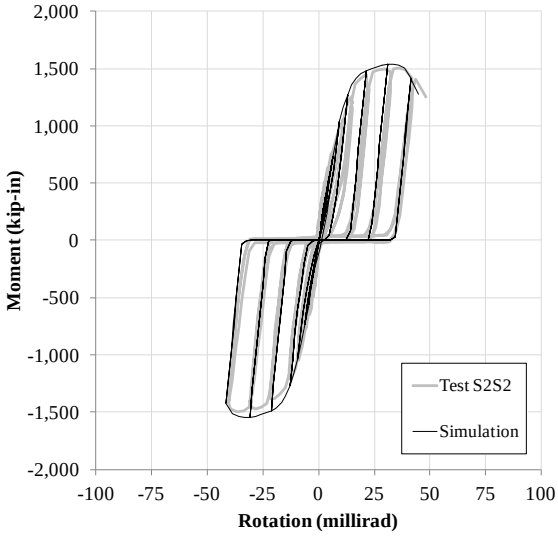

(d) W8x48, 4-anchor configuration with baseplate yielding only (Test program 4, test S2S2)

*Note: model terminated at approximate concrete breakout capacity of anchors

Figure 4-5: Additional hysteretic response predictions for cases without significant axial load

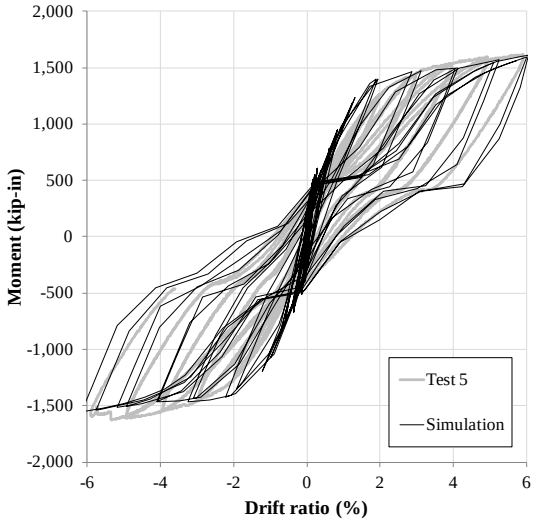

(a) W8x48, 4-anchor configuration with $P=0.13AF_y$ with baseplate and anchor yielding (Test program 3, test 5)

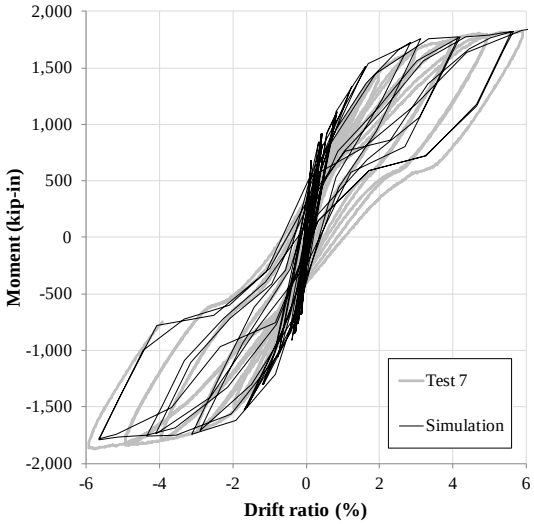

(b) W8x48, 4-anchor configuration with $P=0.22AF_y$ with baseplate and anchor yielding (Test program 3, test 7)

NOTE: results shown are uncorrected for large-deformation axial load effects (P-Δ), i.e. the moment shown is larger than the actual moment resisted by the connection.

Figure 4-6: Hysteretic response predictions for cases with significant axial load

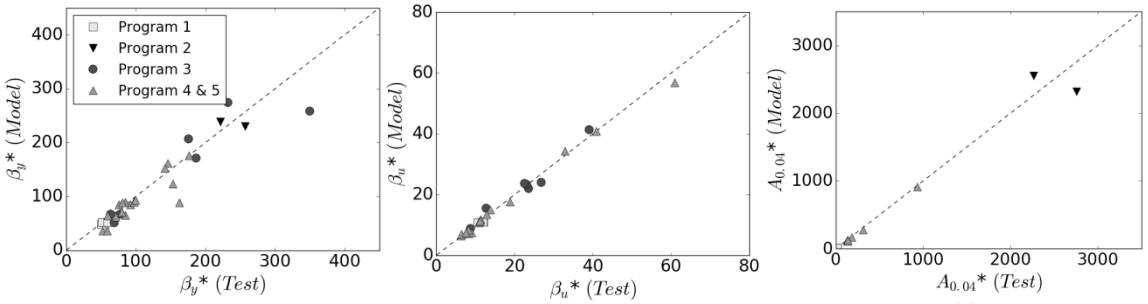

(a) (b) (c)

*Units for β_y, β_u, and $A_{0.04}$ are kip-in/millirad, kip-in/millirad, and kip-in-rad, respectively, for points where comparison was made on the basis of rotation, omitting the rad unit for drift-based data

Figure 4-7: Hysteretic response predictions for cases with significant axial load

Table 4-4: Summary of error between model predictions and test data

Test program	Number of tests used	Average, minimum, and maximum of the misfit within each test program (%)*								
		β_v			β_u			$A_{0.04}$		
		Avg.	Min.	Max.	Avg.	Min.	Max.	Avg.	Min.	Max.
1	4	-7.1	-13.2	0.2	-3.4	-9.6	3.2	-6.2	-10.7	-2.1
2	2	3.0	-4.9	10.8	10.3	5.8	14.9	1.4	-12.8	15.7
3	7	0.8	-18.0	26.0	-2.7	-21.5	10.7	8.4	-18.5	40.1
4	8	12.3	-11.2	38.3	-0.6	-5.9	12.7	10.1	1.8	21.2
5	9	6.1	-12.8	45.2	0.2	-9.7	16.4	7.1	-21.9	22.5
Overall avg. misfit (%):		**3.0**			**0.8**			**4.2**		

* Positive error indicates that the test data are larger than the model results

4.5 Model Application and Design Examples

4.5.1 Discussion of Parameter Variability and Sensitivity

As shown in Table 4-2, the model has over 25 different inputs that may be varied, leading to a prohibitively large number of potential simulations if all inputs were considered variable for a particular design scenario. However, for practical purposes, parameters may be qualitatively grouped into high, medium, and low variability (Table 4-5). In this context, variability means the control that the designer can exert over a particular parameter. For example, the column shape and size is likely dictated by the overall building design. Similarly, the global loads will have low variability because they cannot be changed by the analyst (although there may be some dependence on the final connection design). The steel modulus and hardening modulus may be considered constant for mild steel materials commonly used for the baseplate and column. The yield strength of the baseplate and column will be dictated by common material specifications for the region in which the building is built. In addition, select detailing considerations, such as the anchor hole size and grout thickness are defined by local standards of practice, but typically fall within relatively narrow bounds.

In contrast, the designer will likely have some control over the baseplate plan dimensions, although this is limited by overall building layout and practicality. Common baseplate sizes vary by the size of the column, with the sizes listed in Table 4-1 providing a reasonable starting point. AISC DG 1 recommends that 3/4 in. ASTM F1554 Gr 36 anchors be specified wherever possible from an economic point of view, with increased strength supplied by increasing diameter up to approximately 50mm before higher anchor grades are considered. ACI currently allows the design of connections for non-amplified seismic forces if a stretch length of 8D is provided, therefore a designer may want to consider this option if it is practical (ACI 2014). The designer will typically have the most control over the anchor pattern, baseplate thickness, and anchor size.

Table 4-5: Summary of input parameters with low, medium, and high practical variability

Low	Medium	High
Modulus and hardening modulus: E_s=200GPa E_t=1.7 GPa Yield strength: F_{yc}= 380MPa F_{yb}= 276MPa Grout thickness: 25-50mm Anchor hole size: Per AISC Design Guide 1 Loads: Fixed from building design Section type and size: W: commonly W8 to W14 HSS: commonly HSS8 to HSS18	Baseplate size and anchor spacing: Approximate size of typical plates: N=M=(d or h[1]) + 225mm $s_n = s_m$ = (d or h) + 100mm Anchor type: ASTM F1554 Gr. 36 (common) ASTM F1554 Gr. 55 or 105 ASTM A193 B7 Anchor stretch length: Small: $t_g + t_b$ Large: $t_g + t_b$ + 8D Anchor preload: Full for regions of high seismicity (AISC DG 1), reduced elsewhere	Anchor patterns: 4 (2x2 pattern) 6 (2x3 pattern) 8 (square 3x2x3 pattern) Baseplate thicknesses: Variable by column size. Commonly 19mm to over 75mm Anchor size: Variable by column size. Commonly 12mm to 50mm
NOTE: 1) d for W-sections, h for HSS		

4.5.2 Design example: Verification and detailed analysis of hand design including stretch length

Applications of parametric finite element analysis include verification, calculation of moment-rotation behavior (useful to inform nonlinear springs in global structural models), and improvement of connections designed with traditional hand calculations. AISC DG 1 (Fisher and Kloiber 2006) provides a large-moment design example with the following specifications:

- Column size: W12x96
- Axial load and strong-axis bending moment (LRFD): P_u=376 kip, M_u=3,600 kip-in
- Baseplate yield strength: F_y=36 ksi, unconfined concrete strength: 4ksi

Using the hand-analysis procedure outlined in the design guide, the solution shown in Figure 4-8(a) is determined. Using Table 4-5 as a guide, the designer may wish to evaluate some alterations to the design in terms of number of anchors and/or provided stretch length. The example notes that in medium to high seismic regions, ACI requires

that the steel strength must be increased by 33%, unless a stretch length of eight anchor diameters (8D) is provided (ACI 318-14 17.2.3.4.3 and 17.2.3.4.4). If stretch length is provided, this increase need not be considered. If no special steps are taken, the minimum stretch length in a baseplate connection may be taken as the distance from the top of the plate to the top of the concrete surface. In this case, the thickness of the plate (2 in.) plus a reasonable grout thickness (2 in.), for a total of 4 in. (2.6D). However, the example suggests an anchor embedment depth of 18 in., which could be utilized as stretch length in its entirety if appropriate measures to de-bond the anchor were taken, such as the use of anchor sleeves (resulting in total L_s=22 in. or 14.7D). Therefore, first cases to consider in a parametric analysis are: 1) the initial proposed solution with L_s=4 in., 2) the proposed solution with L_s= 18 in., and 3) a connection with L_s=4 in. and 33% higher anchor steel strength (provided by 4x 2in. diameter anchors). The moment-rotation response of each of these configurations are shown in Figure 4-8(b).

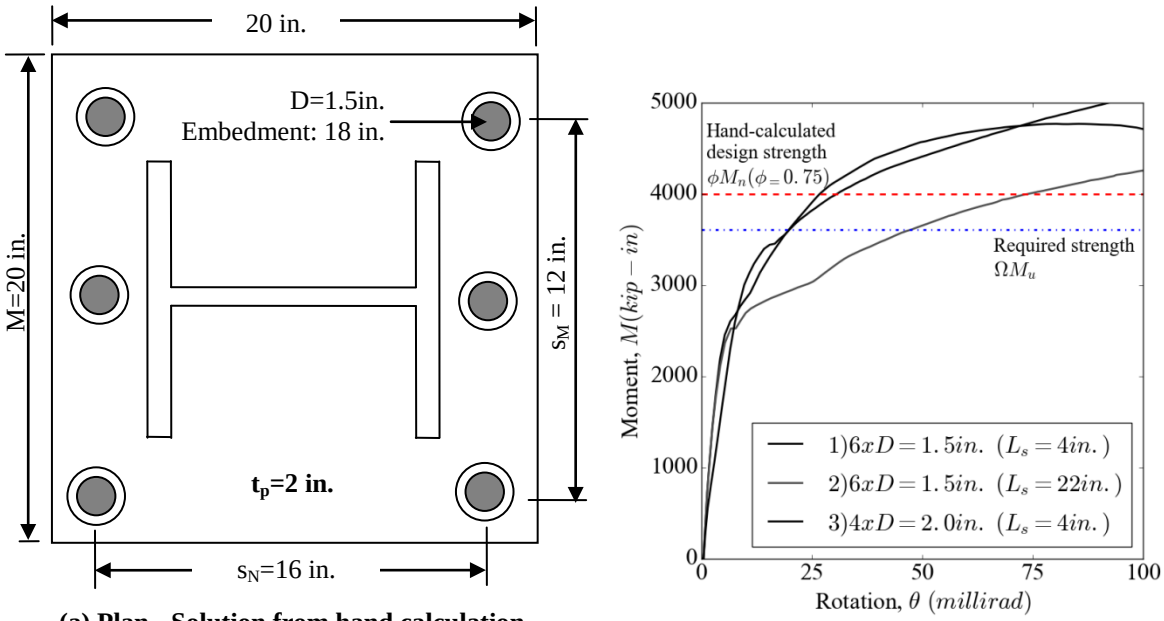

(a) Plan - Solution from hand calculation

(b)M-θ: initial parametric analysis

Figure 4-8: (a) Solution for AISC DG 1 example from hand calculations, (b) corresponding moment-rotation curve from analysis

As shown in the figure, the addition of significant stretch length greatly changes the post-yield behavior, including some kinks around yield due to different grout failure mechanisms. The L_s=22 in. connection achieves ultimate strength at larger rotations, due to the later development of hardening in the anchor. The eventual ultimate strength in both analysis cases is within 10% of the hand-calculated expected strength. Somewhat surprisingly, the use of four 2 in. anchors does not provide a large increase in strength at rotations less than 0.1rad. Additionally, this configuration has a significantly smaller yield stiffness. The cause of these two behaviors are related: the greater distance between the corner anchor positions and the column flanges versus the six anchor configuration mean that the plate is more flexible, and develops significant flange and plate plasticity at large rotations. This difference in behavior is illustrated in Figure 4-9, which shows

contours of equivalent plastic strain, ε_{pl}, defined as the integral of the plastic deformation tensor D_p (LSTC 2013):

$$\epsilon_{pl} = \int \sqrt{\frac{2}{3}\left(D_p\right)_{ij}}\, dt$$

These three analyses provide the nonlinear moment-rotation curves as direct output, which could be incorporated in a nonlinear time-history analysis of the structure to determine more accurate design loads[12].

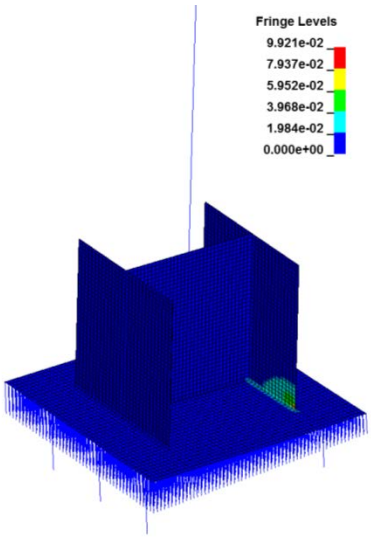

(a) linear plate behavior for the six-anchor pattern [case 1 above]

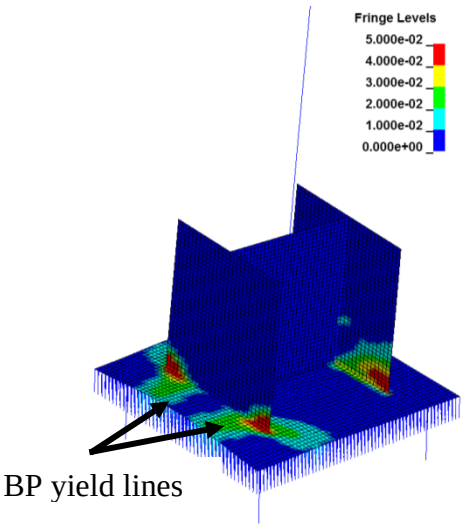

(b) yield lines for the four anchor pattern [case 3]

Figure 4-9: Contours of plastic strain, ε_{pl}

[12] In general, axial load will not be constant throughout the course of a nonlinear time history analysis. However, several analyses run with variable levels of axial load can be used to attempt to bracket the moment-rotation response.

Parametric analysis can provide a further benefit to the design process. As noted previously, weld fracture has been observed in several previous testing programs as a controlling or near controlling limit state, both in test S3S5 and in several other testing programs (e.g. Fahmy 1999, Gomez 2010). This limit state is particularly undesirable, as fracture of the flange welds may occur suddenly before any appreciable connection plasticity develops (Fahmy 1999). The stress state of the weld is affected by many different factors, including the flexibility of the baseplate, section type, and strength and positioning of the anchors, as well as the type of weld used (CJP, PJP, or fillet). Unfortunately, traditional hand design methods do not provide a method for evaluating connection configurations which may cause high weld demands leading to fracture, even in a qualitative way. However, the effective plastic strain introduced previously, ε_{pl}, is a convenient scalar value that may be used to quantify ductility demands in metal which may lead to rupture.

The parametric analysis may be expanded with several combinations of anchor pattern, spacing s_M, and stretch length were run, as summarized in Table 4-6. Note that cases 1-3, bolded in the table, correspond to the runs previously discussed, above. Case 4 and 5 are identical to case 2, except that Case 4 has closer spacing of the anchors in the y-direction, and Case 5 has a higher spacing. Case 6 and 7 are identical to case 3, except Case 6 has a slightly larger M dimension and Case 7 has a smaller s_M dimension.

Table 4-6: Summary of parametric analysis cases (bolded: cases plotted above)

Case #	Number of anchors	D (in.)	L_s (in.)	M (in.)	s_M (in.)
1	**6**	**1.5**	**4**	**20**	**12**
2	**6**	**1.5**	**22**	**20**	**12**
3	**4**	**2.0**	**4**	**20**	**12**
4	6	1.5	22	20	10
5	6	1.5	22	20	16
6	4	2.0	4	24	12
7	4	2.0	4	20	10

The moment-rotation behavior and effective plastic strain at the interface at a rotation of 40 millirad are plotted in Figure 4-10. 40 millirad was chosen for a basis of comparison because it represents a large, but not unrealistic rotation for a connection of this type under seismic excitation. All configurations exceed the required strength significantly, and would be acceptable from a strength standpoint ($\phi M_n > \Omega M_u$). The moment-rotation behavior of the six-anchor configurations (1,2,4, and 5) does not significantly dependent on the transverse spacing of the anchors, but is highly dependent on stretch length. The strength of the 4-anchor configuration with the wider baseplate (Case 6) is slightly higher, due to the larger compressive area, but this difference is also not significant. Somewhat counter-intuitively, the post-yield stiffness of Case 4 is significantly higher. This is due to the much smaller plastic strains in the flanges of the column, shown in Figure 4-10 (right) at 40 millirad rotation. The four-anchor configurations with $s_M = s_N$ (3 and 6) have very high plastic strain demand near the flange edges, up to about 10% (off the top of the graph). This indicates these configurations and would be at relatively high risk for cracking and fracture of the welds located there. Case 4 provides some improvement, but still results in about double the plastic strain demand

of the 6-anchor configuration with a narrow y-direction spacing[13], Case 4. This result strongly indicates that the six-anchor configuration is more likely to provide good rotation ductility necessary for robust connection performance. As a next step in the design process, the modeling procedure could then be expanded to include cases that provide the 33% increase in anchor steel in a six-anchor configuration, as well as additional anchor spacing options to determine a robust, optimized connection design.

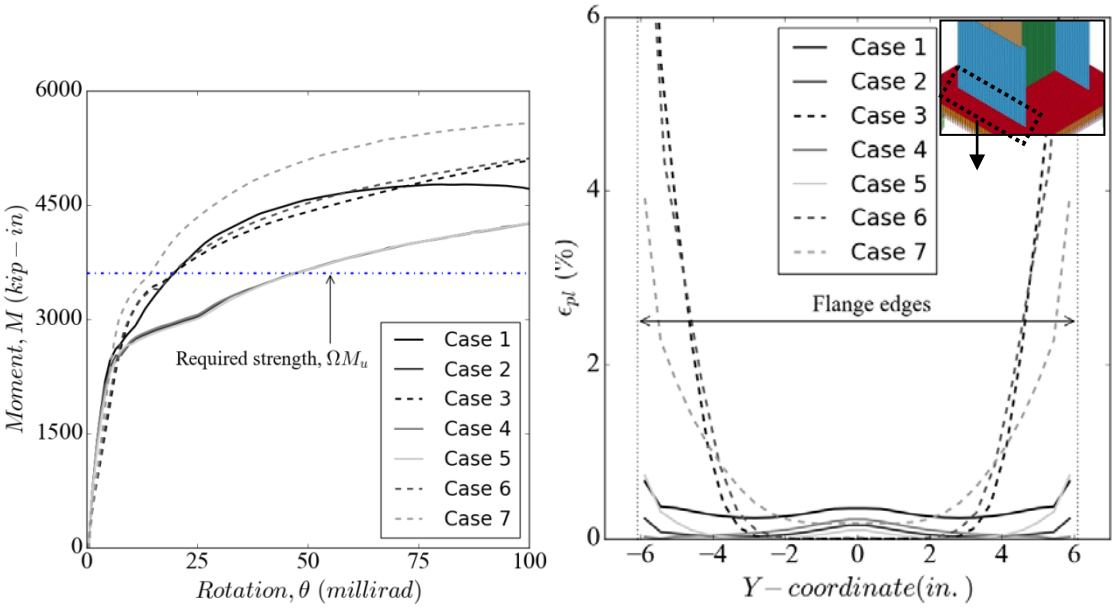

(a) Moment-rotation behavior (b) strain at flange-plate weld at 40 millirad rotation

Figure 4-10: Parametric analysis cases for AISC DG 1 example

4.5.3 Analysis of Stretch Length

Another practical application of the model involves the determination of the effective stretch length for a connection where this cannot be established *a priori*. Test S4S2 from Chapter 3 is such an example, where the concrete-anchor interface is such that

[13] Spacing in this direction must be checked to provide adequate concrete breakout strength. For the assumptions of uncracked, normalweight concrete, this spacing is adequate for this application.

a stretch length cannot be reliably determined from existing predictive methods. To establish the stretch length for this connection, a series of parametric models may be run with anchor data from tensile tests with successively longer stretch lengths (using data from Chapter 2). The rotation at failure may then be plotted against stretch length, as shown in Figure 4-11. Other connection tests known to have well-defined stretch length equal to the free length (i.e. those with epoxy-bonded anchors) plot very close to this line, validating this approach. Extrapolating to the observed rotation of test S4S2, an effective stretch length of about 280mm may be inferred (Figure 4-11 (a)). No slippage of the cast-in anchor plate or nut was observed in a recovered anchor, therefore, it may be concluded that strain penetration was very significant in this test. The total free length for this test, including instrumentation, was approximately 4 in. (Table 3-1, see footnote). Therefore, there was approximately 180mm of strain penetration, or about 70% of the embedment depth h_{ef}. Stated alternatively, the stretch length was approximately 80% of the total length of the anchor $L_f + h_{ef}$, which was about 13.75in. As shown in Figure 4-11(b), this behavior is therefore intermediate between bonded anchors and smooth-shank anchors, which were found to debond over their entire length, even at relatively low strains (See Chapter 3). Interestingly, this test had greater rotation capacity than S2S3 and S2S4, tests performed as part of the prior sequence with a well-defined 8D stretch length. However, strain penetration should not be relied upon for design, as reliable prediction methods do not currently exist. Although methods for determining bond stress and strain distributions of smooth and deformed concrete reinforcing bars have been developed (e.g. Abrishami and Mitchell 1996), they are not intended for the particular geometry of headed anchors or threaded rod, nor have they been validated for the high strains that can develop in

common anchoring applications. This result points to the need for more rational methods to determine the optimal stretch length in a connection of a given geometry, material type and configuration.

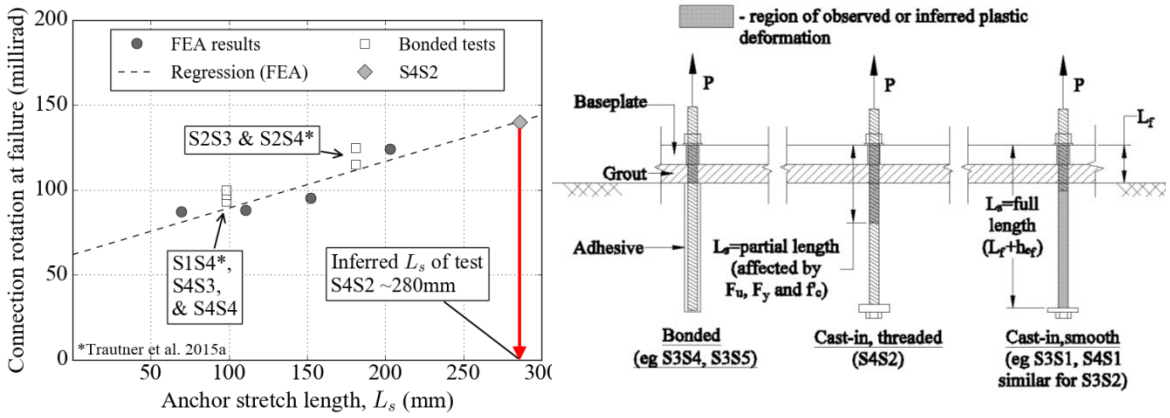

(a) Test results and regression from FEA modeling

(b) schematic illustrating the range of stretch lengths observed or inferred during tests

Figure 4-11: Parametric finite element model used to infer effective stretch length from experimental results

4.6 Summary Remarks

This Chapter presented a parametric finite element modeling procedure for the analysis of exposed, unbraced steel column baseplate connections subjected to moment and axial loads. This procedure uses shell and beam elements to represent the column and baseplate and a fiber-section representation of the anchors and grout. The main results and conclusions from this effort include:

- A preprocessor developed specifically for column baseplate connections was used to develop models based on a limited number of parameters of typical interest, allowing rapid parametric analysis. The model is unique in the amount of experimental data used to inform and verify the model; the mechanical behavior

of the anchors, grout, and steel was informed by a large data set from material testing, some of which is presented in Chapter 2.

- The calculated moment-rotation results from the model compared very favorably to the tests presented in Chapter 3, as well as published experimental results experimental programs available in the literature, using metrics of yield stiffness, secant stiffness at ultimate strength, and area under the hysteretic curve at moderate rotations. To the authors' knowledge, the verification program is the largest ever undertaken for unbraced, exposed baseplate connections.
- Average misfit for each of the evaluation parameters was between 5% and 20%. The usefulness of the procedure was illustrated in a design example that explored the differences in moment-rotation behavior and maximum plasticity in the welded region as a function of anchor size, layout, and stretch length. The general modeling approach presented in this Chapter was used for system-level modeling in Chapter 5.

4.7 Acknowledgement of Publications

Chapter 4 contains material submitted for publication in the following paper: Trautner, C. and Hutchinson, T., (In Review). "Development, Verification, and Design Application of a Parametric Finite Element Model for Typical Steel Moment Frame Column Baseplate Connections," ASCE Journal of Structural Engineering. The dissertation author was the primary author on this paper.

Chapter 5: Dynamic Testing and Numerical Analysis of Systems Incorporating Uplifting-Column, Ductile-Anchor Baseplate Connections

5.1 Introduction

This Chapter describes the testing of a miniature structural steel building on a shake table. The building was designed to have replaceable components such that several distributions of structural stiffness and strength were possible, ranging from strong-anchor/weak-superstructure to weak-anchor/strong superstructure. In addition, the structure could be changed from a moment-frame to a braced frame configuration. The main objectives of this work are:

- Basic research into the dynamic behavior of steel column baseplate connections. Previous research into the behavior of these types of connections has been overwhelmingly pseudo-static in nature (e.g. Grauvilardell et al. 2005, Gomez et al. 2010, Trautner and Hutchinson 2014a, Trautner and Hutchinson 2015a).

- A general comparison of the behavior of ductile-anchor design to "traditional" superstructure beam/column plastic hinge design

- Investigating the potential for reduction of global structural demands, specifically maximum drift, residual drift, maximum floor accelerations, in-structure response spectra, and maximum total base shear, via a ductile-anchor dominated design

- Providing system-level dynamic response data documenting the distribution of demands from service to extreme earthquakes for use in numerical model validation

In this dissertation, configurations are referred to by the building type and the portion of the building that is expected to undergo the greatest plastic deformation (e.g. base-dominated moment frame, or BD MF for a weak-anchor/strong superstructure moment frame). In total, five different configurations were tested. Each of these configurations

was assigned a Configuration Number between 1 and 5 based on the order in which testing was performed, as well as a descriptive acronym:

1. Base Connection-dominated Moment Frame (BD MF)
2. Structure-Dominated Moment Frame (SD MF)
3. Distributed Design Moment Frame (DD MF)
4. Single-degree-of-freedom Distributed Design Moment Frame (1DD MF)
5. Single-degree-of-freedom Base Connection-dominated Braced Frame (1BD BF)

The SD MF configuration was representative of current "traditional" seismic design practice, where plasticity in the structure is designed and expected to occur within well-defined regions in the superstructure. The details of all of the configurations are described. Each configuration was subjected to at least three different motions, which were given names and single-letter abbreviations for brevity: Service (S), Design (D), and Maximum (M), with some configurations tested under additional aftershock (A) and Extreme (E) motions. The performance objectives of the various structures were tied to the motion intensities. Data collection consisted of accelerometers and string pots at each floor level, strain gages located in areas subject to local plasticity, and other displacement transducers located strategically to recover anchor deformations and overall building movement. Data processing and extensive data analysis are also presented.

A substantial numerical analysis program was conducted in parallel with the test program. Initial numerical models were used to guide design and motion selection. Verification of more refined analysis models was performed using system identification techniques and the results of strong motion excitation. Modeling techniques for potential future expansion the results of the experimental program are presented and discussed.

5.2 Experimental Setup and Construction

5.2.1 Shake table description

The testing program was carried out at the South Powell Laboratory shake table. This table is dynamic testing facility with the purpose of studying the behavior of structures under simulated seismic action. The system consists of a single degree of freedom shake table with a 16x10 ft, 5/8 in. thick deck plate (Magenes 1989). The deck plate has 5/8 in. threaded holes on a 10-inch grid. The table is recessed in the floor to allow access to specimens on the table. A picture of the shake table with a mounted frame specimen is shown in Figure 5-1. The table has a maximum payload of 80 kips and moment capacity of 310 kip-ft. The table slides horizontally on two stationary shafts driven by a hydraulic actuator with a total dynamic stroke of 12 in., a static capacity of 110 kips, and a dynamic capacity of 91.5 kips. The bearing system consists of eight 0.125 m Garlock DU cylinders. The system operates on closed-loop displacement or acceleration control using an external command signal. Flow rate of the hydraulic system allows a peak sinusoidal velocity of 1 m/s. The actuator can induce peak accelerations of 9g on the bare table, and 1g on a fully-loaded table.

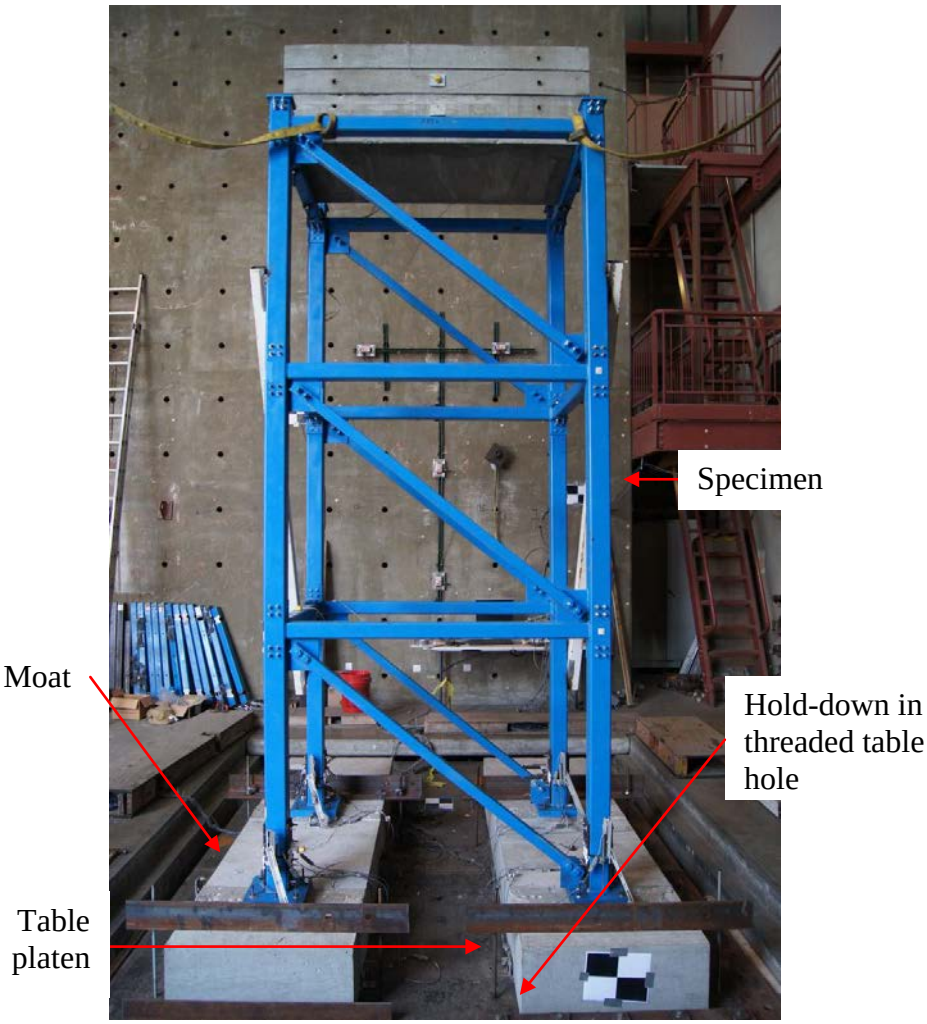

Figure 5-1: Picture of shake table with mounted specimen (picture taken along axis of shaking)

5.2.2 Design of specimen, foundations, and connections

Design Criteria

The overall design criteria were established in order to fulfill the research objectives stated in the introduction. The most important of these objectives was a comparison of the behavior of a traditional frame-fuse dominated structure versus a structure with ductile-anchor base connections allowed to uplift. These two structural configurations, therefore, became the bounding cases for the research program, and design criteria were established based on the intended behavior of these two cases. Based on preliminary work and practical considerations, the following criteria were established.

- The structure was designed as a “miniature building” – an approach that attempts to elicit the basic physical responses without providing exact time, force, and geometric similitude. This approach was rendered necessary by the size of the available shake table, and the need to economize the cost of components that could not be re-used, i.e. beams that would develop plastic hinges in some of the various structural configurations. This approach has been used successfully in the past to investigate the response of buildings with replaceable components (Restrepo et al 2014).
- The structure was designed to be a 1x1 bay, 3-D representation. This basic layout was chosen based on preliminary work which indicated that the out-of-plane support structures required for a 2-D frame would be too costly. Larger 3-D structures consisting of multiple bays were also considered, but were also rejected due to cost and complexity of the test setup.

- The structure incorporated a braced frame system in the direction perpendicular to shaking. This structural type was selected in order to force the natural frequencies of the perpendicular and torsional modes to be significantly higher than the fundamental natural frequency in the shaking direction.
- The lateral force resisting system of the structure in the direction of shaking was designed as a moment frame for structural configurations 1-4, and a braced frame for structural Configuration 5.
- The structure was chosen to have three "stories", with a total height of about 12 ft. This size was considered reasonable in terms of overall cost and fit within the available envelope on the shake table. In this context, "story" does not mean a habitable, finished floor, but may be defined as "elevation at which a lumped mass is present". Having three stories allowed significant flexibility in the total weight of the structure, and allowed evaluation of a multi-modal response.
- Although the structure was designed as a miniature building, the research program objectives are most strongly demonstrated as they relate to real structures if the fundamental frequency of the miniature building similar to those of real buildings. ASCE 7 (ASCE 7-10) suggests that the fundamental frequency of typical structures can be approximated as:

$$T_1 = 0.1N \qquad \text{Eq. 5-1}$$

where T_1 is the fundamental period and N is the number of stories. Therefore, T_1 should be approximately 0.3s (f_1 of about 3.3Hz) for the current structure. This constraint provided approximate ranges for the total structural mass and stiffness.

Design of the structure, particularly the design of the fuse elements, was intimately connected to the selection of test motions. In theory, any combination of strong and weak superstructure and base fuses could be tested with any intensity of motion, so long as the particular combination did not cause total collapse of the structure, and the preceding design criteria were met. However, the following criteria served to constrain both structural design and motion selection, which is discussed in detail subsequently:

- Maximum drifts and residual drifts in Configuration 2 (SD MF) that are consistent with typical values encountered during real earthquakes were desired. This design criterion was critical because it establishes the point of comparison to determine whether configurations with yielding anchors could provide improved performance. The target drifts are shown in the upper part of Table 5-1. Definitions for the motion intensities given in this table are given in Section 5.3.5
- For Configuration 1 (BD MF), anchor strains that are reasonable for the intensity of each motion were desired. This design criterion was necessary to ensure that undesirable anchor behavior (i.e. fracture, shear deformation) was prevented at each motion level. The elongation limits were established based on previous research on the maximum elongation of common anchor materials (See Chapter 2). Target anchor strains are given in the lower part of Table 5-1.

Table 5-1: Target maximum/residual drifts and anchor strains

		Motion Intensity Level			
Configuration	Criterion	Service	Design	Maximum	Aftershock
SD MF	Maximum roof drift	<0.5%	1-2%	2-3%	>1-2%
	Residual roof drift	<0.25%	0-1%	1-2%	>0-0.5%
BD MF	Anchor yielding	None to slight (<2x yield)	Moderate (~5%)	Substantial >5%	<5% (incremental)

5.3 Specimen Description and Design

A drawing of the general structure configuration, developed based on the design criteria discussed in the previous section, is given in Figure 5-2. Design calculations for the structure are included in Appendix B. The plan size of the building is 4 ft in the direction of shaking by 5 ft in the perpendicular direction. The structure has a story height of 4 ft., measured c-c of the beam members. Modular concrete floor slabs were used to provide mass at the floor levels, and could be rearranged to provide different mass configurations. Member sizes and material grades are summarized in the schedule shown in Table 5-2. The anchor pattern was 8 in. square.

Table 5-2: Member size and material grade schedule

Member	Member size	Material grade
C	HSS 4x4x3/16	ASTM A500 Gr. B
B1	HSS 3x3x3/16	
B2		
SB		
Br	HSS 2x2x1/8	
AB	L4x4x5/16	ASTM A36
Baseplate	PL 11x11x1-1/2	ASTM A36

The two end-frames consisting of members C, B1, and Br were designed to be constructed as a unit and were kept as assemblies throughout the testing program. Since

disassembly of these units was not required, the connection between member B1 and C was made by fillet welds all around the B1 member on the flat face of the C member. The connection of the Br bracing members was made with a 3/8 in. thick standard rectangular gusset plate and 2x 3/4 in. SAE Gr. 5 bolts on each end of the brace.

The balance between structure plasticity and anchor plasticity was elicited by cutting material away from member B2 for Configurations 2-4. Therefore, a bolted connection at the C-B2 joint was required to change out the different B2 members. To accommodate the HSS beam sections, double clip-angle connections incorporating four 3/8 in. SAE Gr. 5 diameter through-bolts were used (Figure 5-3). This type of connection was chosen as a compromise between expected rotational stiffness and simplicity of construction. To allow the full development of a structural mechanism with plastic hinges, part of each of the B2 beams was cut away for Configurations 2-5. The cutout geometry is shown in Figure 5-4. Similarly, the baseplate and a small amount of the column stub were cut off of the columns (member C), and were re-attached with a notched side plate. A typical cutout shape and hole pattern for this connection is shown in Figure 5-5, and the dimensions of the cutouts are shown for each Configuration in Figure 5-6. The connection was made with four 3/8 in. SAE Gr. 5 bolts extending through both side plates and the column. Photographs of each of the five completed specimens are shown in Figure 5-7 and Figure 5-8. Note that the addition of member SB was performed only for the final configuration (Configuration 5). The relationship between the design strength of the beam fuses, column fuses, and anchor fuses is summarized in Table 5-3. Note that full drawings and design calculations are provided in Trautner and Hutchinson (2016).

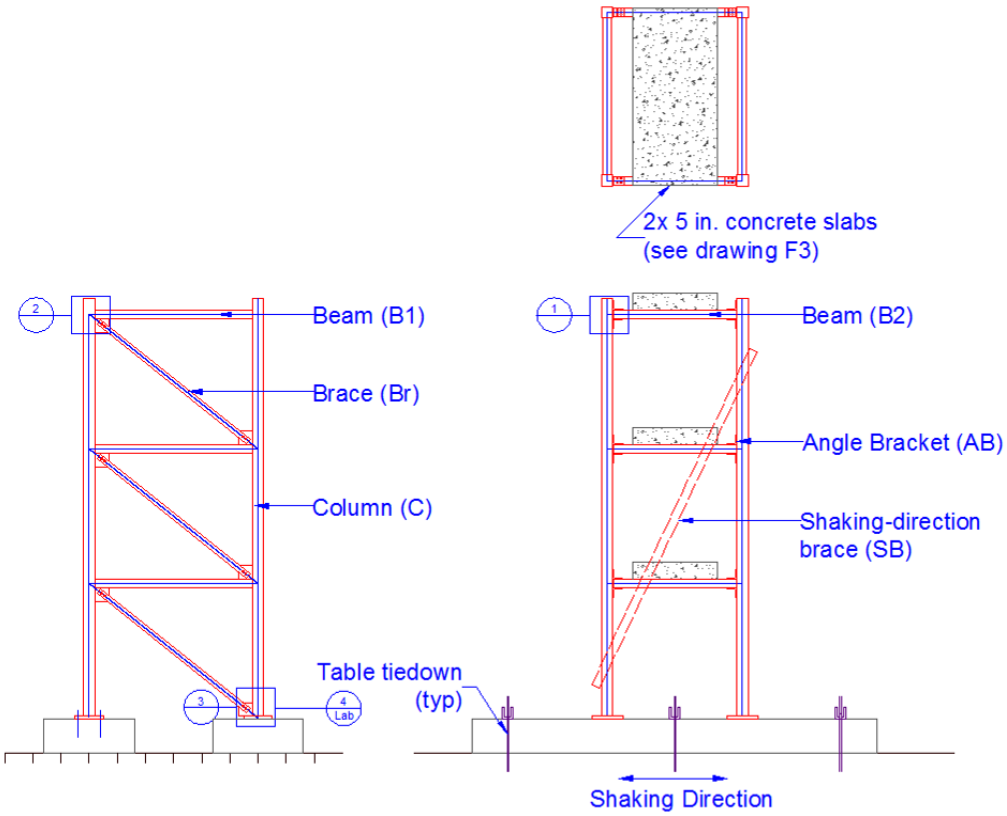

Figure 5-2: Overall structure configuration, plan view (upper right), N elevation (lower left), and E elevation (lower right)

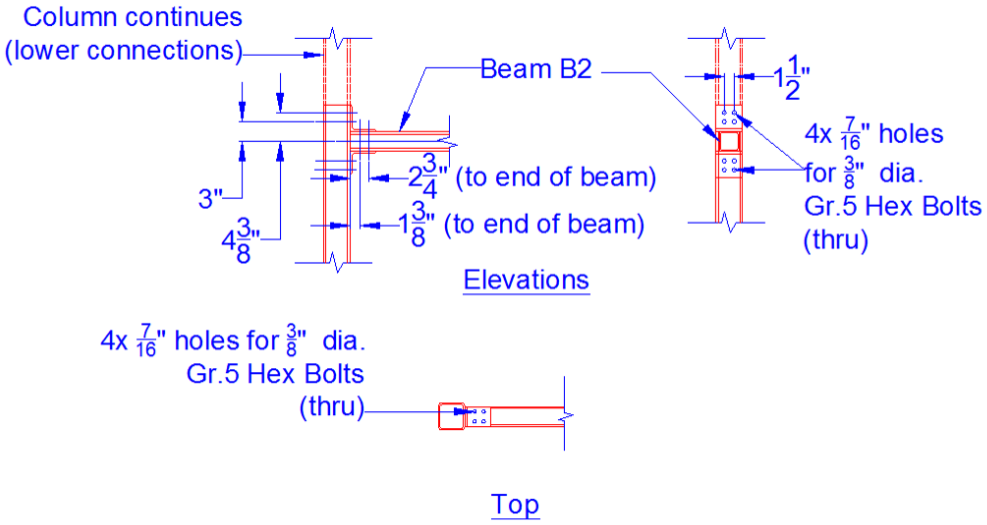

Figure 5-3: Drawings of C-B2 moment-resisting connections

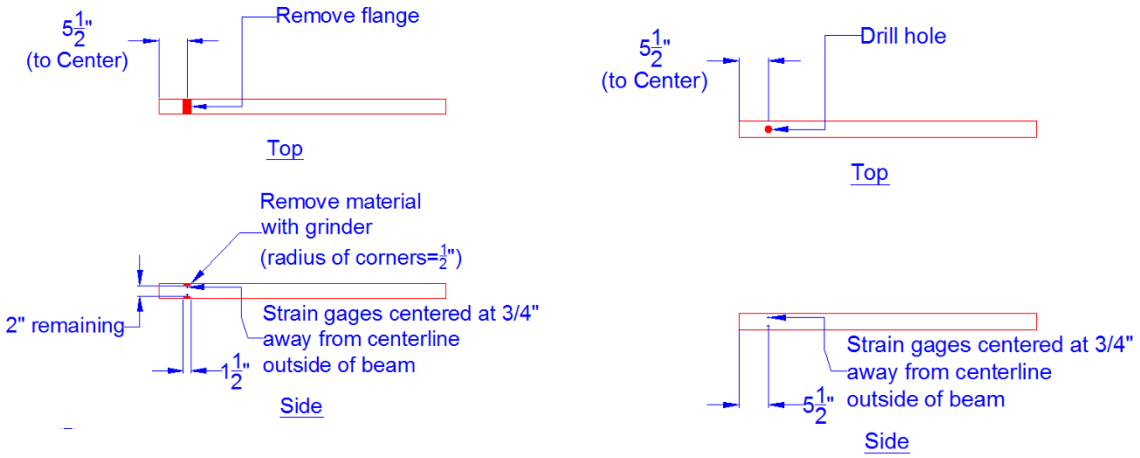

(a) Configuration 2 (SD MF)

(b) Configuration 3-5

Figure 5-4: Drawing of B2 moment fuses

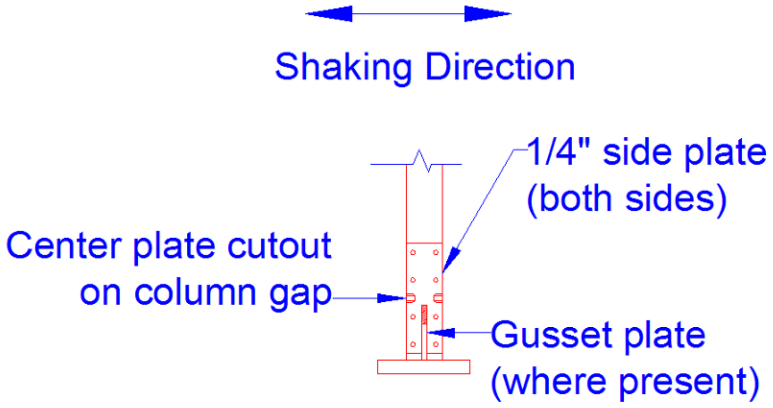

Figure 5-5: Drawing of base hinge side plate connection

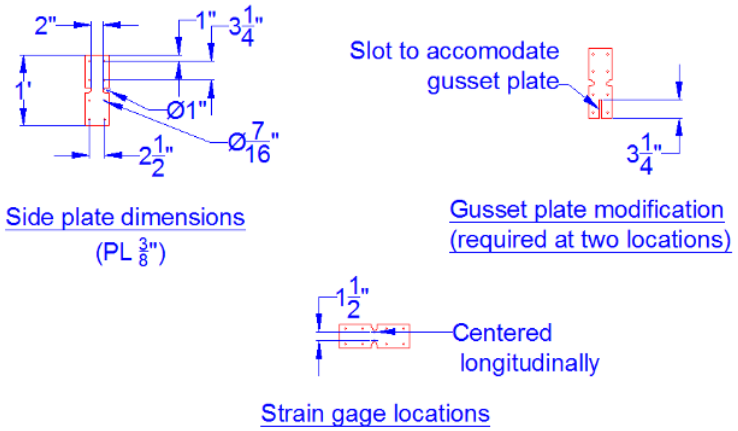

(a) Configuration 2 (SD MF)

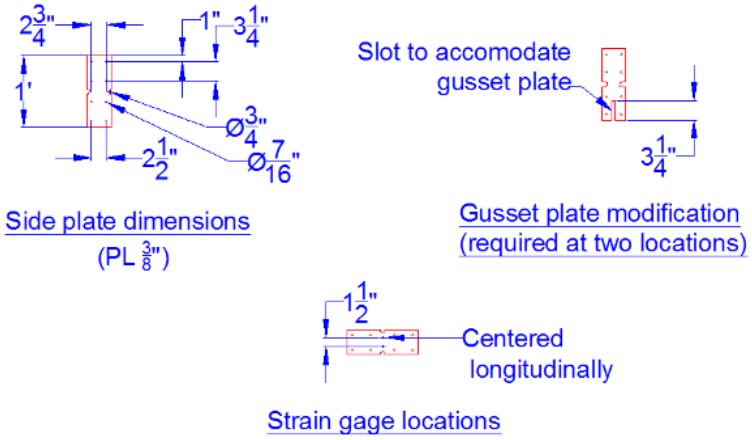

(b) Configuration 3-5

Figure 5-6: Drawing of column hinge notch

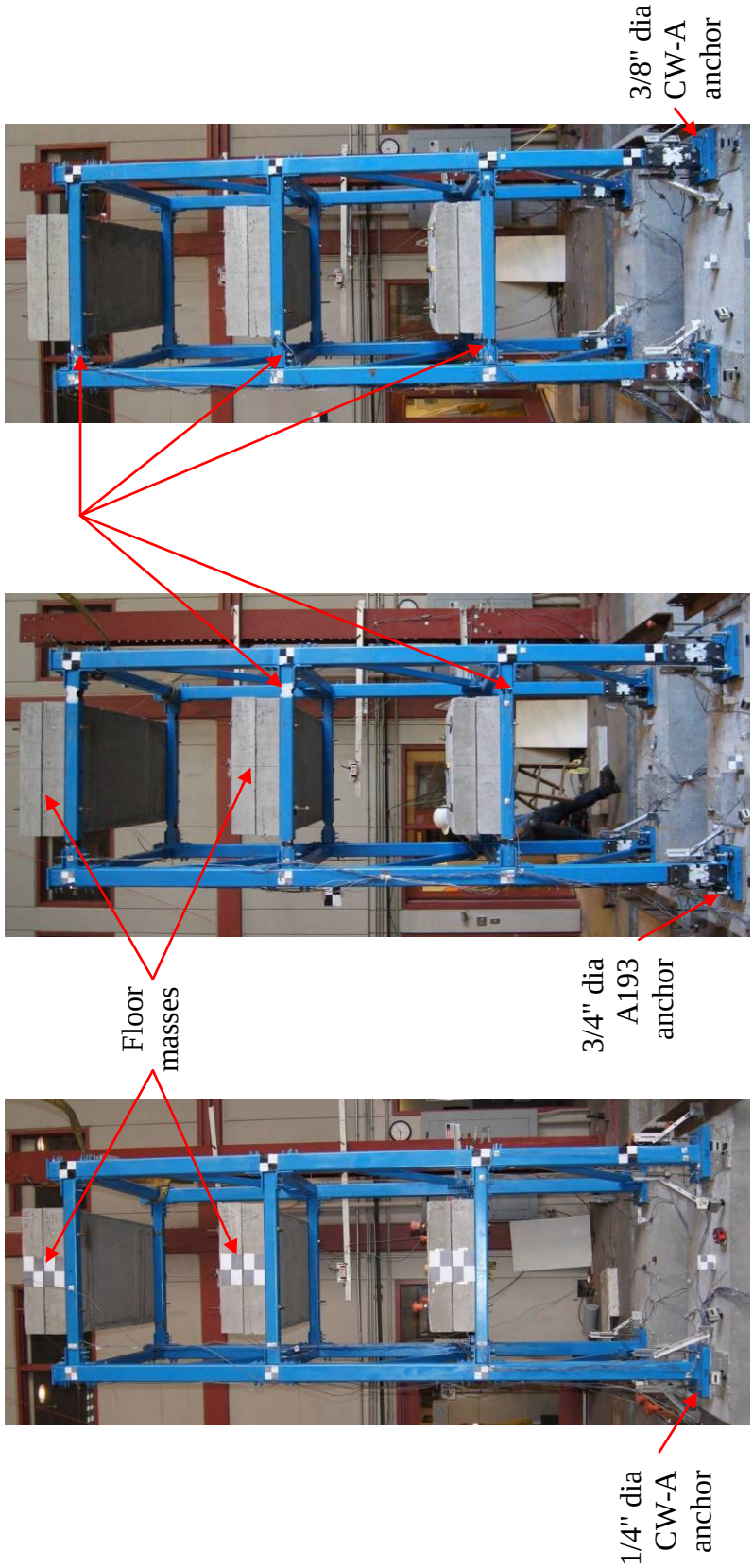

Figure 5-7: Specimen comparison, BD MF, SD MF, and DD MF (left to right)

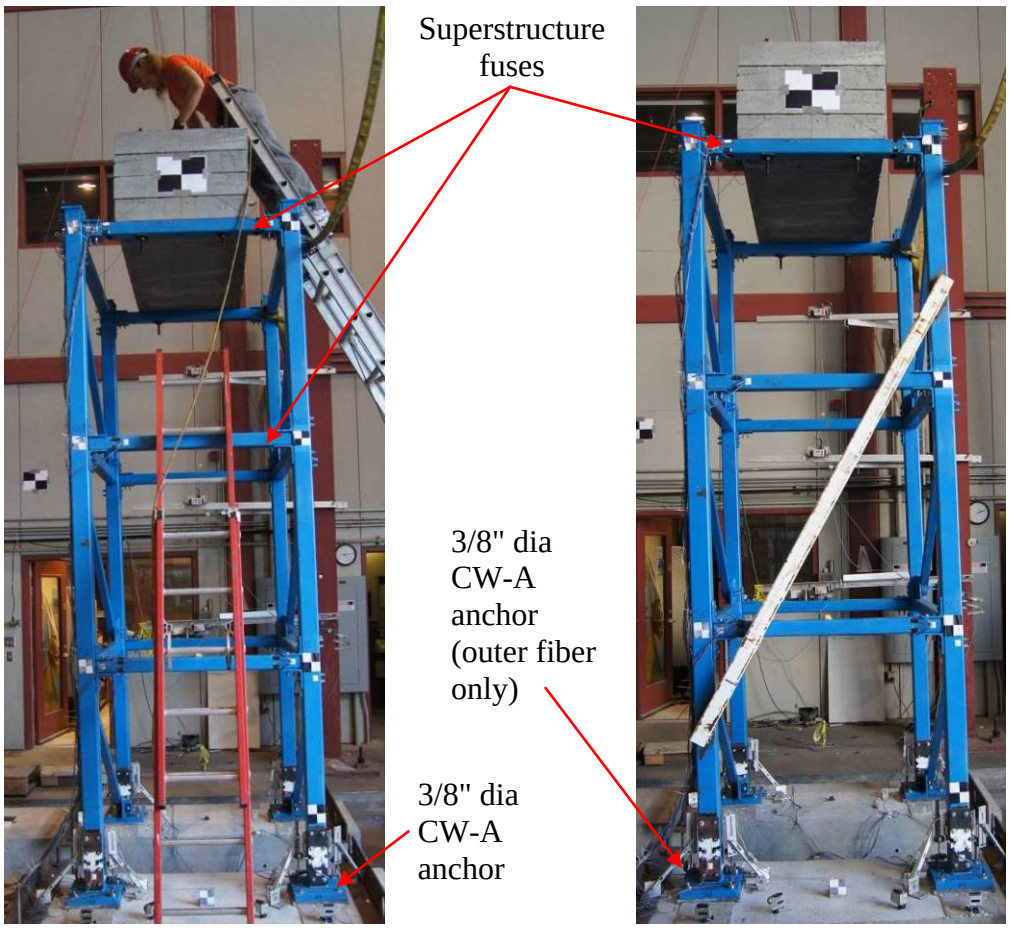

Figure 5-8: Specimen comparison, 1DD MF (left) and 1BD BF (right)

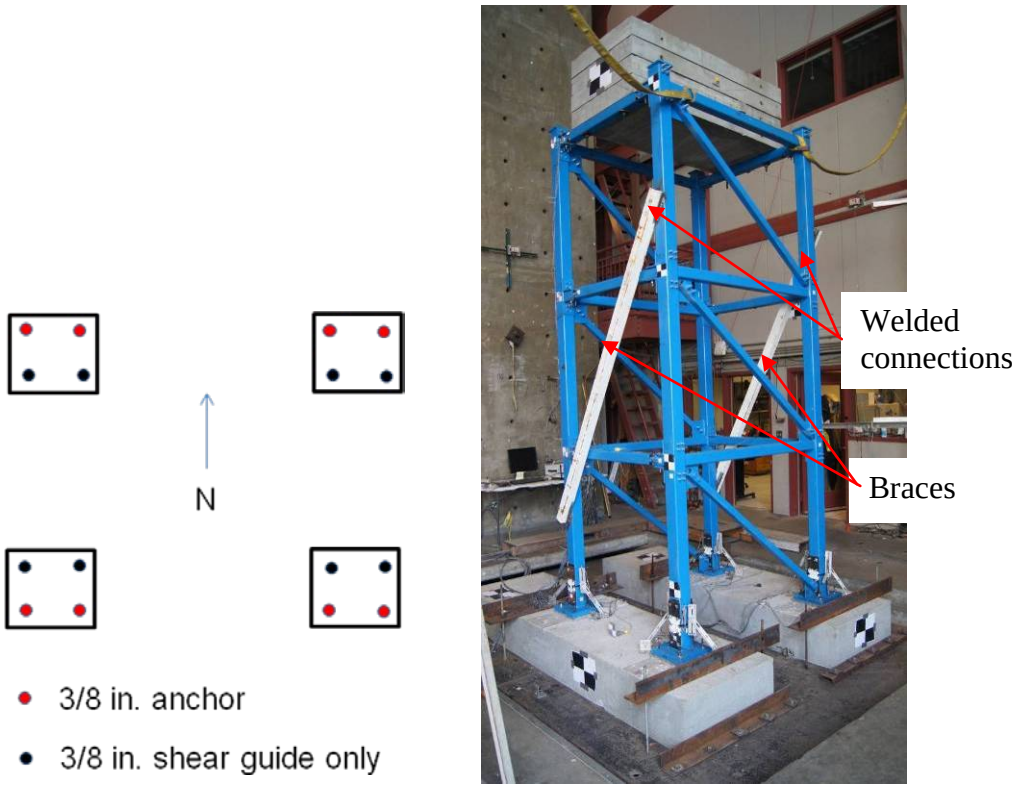

Figure 5-9: Anchor layout (left) and brace locations, Configuration 5 (TBD BF)

Table 5-3: Summary of design fuse strengths

Configuration	Description	Beam Fuse Yield Moment, kip-in (% of virgin)	Column Fuse Yield Moment, kip-in (% of virgin)	Anchor Group Plastic Moment kip-in (% of Column Fuse)
1	Base dominated	77.2 (100%)	165.5 (100%)	27.0 (16%)
2	Building dominated	11.8 (15%)	26.7 (17%)	701.4 (2500%)
3	Balanced design	49.9 (65%)	50.5 (32%)	57.0 (110%)
4	SDOF MF base dominated	49.9 (65%)	50.5 (32%)	57.0 (110%)
5	SDOF BF base dominated	N/A*	50.5 (32%)	N/A (see Figure 5-9)

*Beam contribution to lateral strength in this case is negligible

Foundation and base connection design

The foundations were designed in accordance with ACI 318-11 (ACI 2011). The foundations were designed for the maximum shear and moment from two potential limiting load cases: 1) transportation/placement and 2) reaction loads from the structure during testing. Conservatively, it was assumed that at some point during transport/placement/storage, the slabs might be simply supported at their ends. Reinforcement was provided to resist this self-weight simply-supported bending moment with an impact factor of 4. Even with this relatively large impact factor, minimum bending reinforcement was found to control. The moment from the structure uplift reaction was found to be relatively small due to the close placement of the foundation tiedowns. To provide minimum reinforcement, six #4 bars were provided on the top and bottom face, and one additional bar was placed at mid-height on the sides. Shear reinforcement was found to be unnecessary, however supplemental reinforcement was placed near the anchors to increase strength against undesirable failure modes such as anchor breakout. The basic foundation reinforcement is shown in Figure 5-10, and complete foundation and reinforcement drawings are included in Appendix B.

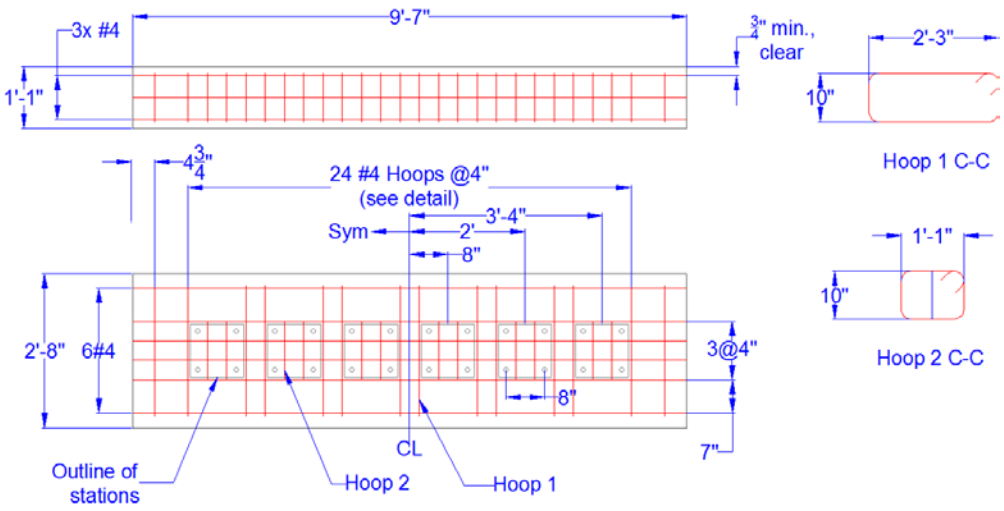

Figure 5-10: Diagram of foundation reinforcement

The base connections were designed in parallel with the superstructure components to provide the ratio between the various fuse strengths listed in Table 5-3. The baseplate plan size was selected purely on the basis of practicality and typical sizing for the column member size (4x4). The anchor spacing of eight inches square was selected to give adequate thickness between the anchor holes and the edge of the plate to develop a well-defined compression resultant along the edge of the plate. Because final motion selection was not complete during design, and anchor demands could not be calculated exactly, 3/4 in. diameter ASTM A193 B7 anchors were selected as being able to develop the nominal plastic moment capacity of the column members for the SD MF case (Configuration 2). Therefore, the base connection would not yield prior to the development of a plastic hinge even in the virgin column section. The anchor embedment for the bonded anchors was designed on the basis of having at least 1.15 times the nominal steel strength for the next-closest limit state (concrete breakout). The sizes of the anchors for the base-dominated and balanced configurations (1, 3, 4, and 5)

were selected based on the desired ratio of the base connection strength to the column strength. The embedment for the cast-in anchors was selected based on a conservative estimate of the anchor deformation capacity needed, based on a spectral analysis of the building considering global rocking as the only deformation mechanism. Design calculations for the baseplate connections are included in Appendix B.

Foundation and Shake Table Tiedown Design

The limit states of sliding and uplift were considered in the design of the connection to the shake table. Design of the connection was performed assuming that the maximum acceleration of the slabs would be at the PGA of the most intense input motion, and the maximum spectral acceleration of the structure would be at the maximum spectral acceleration in the neighborhood of the approximate period of the structure. Based on preliminary motion selection, these values were assumed to be 1.5g and 3.5g, respectively. Based on these values, the maximum total shear transferred to the foundations was about 16 kips and the maximum overturning moment was approximately 120 kip-ft.

Shear transfer from friction was conservatively not considered. Shear transfer to the slabs was provided by shear cleats at both ends of each slab. The shear cleats were fastened to the table using 5x 5/8 in. ASTM A307 bolts each (Figure 5-11, left). A307 bolts were used such that if accidental overload of the structure were to occur, failure would occur in the bolt body and would not damage the threaded shake table platen. The shear cleats were pre-compressed against the foundation slab using a hydraulic jack prior to bolt installation to ensure that no movement of the slab could occur between the cleats.

Two pairs of hold-downs were provided to prevent overturning. L4x4x3/8 angles were placed across each slab and low-grade 5/8 in. diameter carbon steel allthread was placed through holes cur on each side of the angle and threaded into the shake table platen (Figure 5-11, right). Calculations supporting the design of these elements are provided in Appendix C.

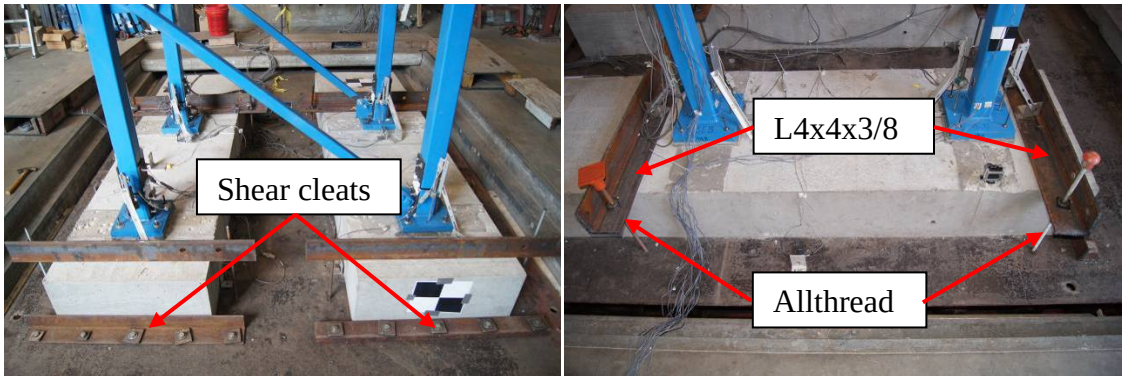

(a) Foundation tie-downs (b) Shear cleats

Figure 5-11: Table attachments and shear cleats

5.3.1 Construction of foundations and floor slabs

The concrete elements of the building (foundation and floor slabs) were formed and poured together. The floor slabs were formed with 5 in. tall 2x material. Because of the small height of the concrete for this element, the form sides were not supported other than with connections to each other at the form corners. The foundations were formed using plywood and 2x4 forms. The forms were supported with cleats fastened to the laboratory floor. The forms were tied in the short direction with strips of plywood that served as anchor holders for the slabs which received cast-in anchors (see next section for a description of the cast-in anchors). The slabs were fitted with four T-type coil inserts to allow lifting. The foundations were fitted with four larger "egg beater" type inserts. The

formwork, reinforcing, and lift inserts for the slabs and foundations are shown in Figure 5-12.

(a) Floor slab (b) Foundation

Figure 5-12: Photographs of reinforcement

The foundations and floor slabs were poured on July 15, 2015, starting at approximately 2pm. The concrete for both elements was delivered in a single truck. The slump of the concrete was measured to be 4.5 in. A total of 24 6x12 in. concrete cylinders were poured. The concrete was placed using a crane-mounted bucket to allow faster access to all forms, which were spread out over a significant area. The floor slab forms were filled in a single lift, and vibrated as needed to spread the concrete over the full area. The floor slabs were finished with steel trowels; however the surface was intentionally left somewhat rough to increase interface friction when two slabs were mounted in the structure. The foundation slabs were filled in two lifts, and vibrated after each lift. The forms were slightly overfilled (Figure 5-13(a)) to allow screeding. The

foundation slabs were finished using steel trowels. Unfortunately, the height beneath the anchor mounting plates was insufficient to allow for trowel manipulation. Therefore, the area underneath the plates was left unfinished (Figure 5-13(b)). This resulted in a raised, roughened surface when the plates were removed. The roughness and height of this surface was variable, depending on the flow of the concrete underneath the plate (Figure 5-14).

(a) Foundation form filling (b) Finish at cast-in anchor locations

Figure 5-13: Photographs of concrete placement

Figure 5-14: Uneven raised surface at cast-in anchor locations

5.3.2 Anchor fabrication and grout pad placement

Two types of anchors were used in the testing program: replaceable anchors and bonded anchors. Two different sizes of replaceable anchors were used, 1/4 in. dia./6 in. nominal embedment and 3/8 in. dia./8 in. nominal embedment. The first type was used for configuration 1, the second was used in configurations 3, 4, and 5. The basic construction of the anchor bodies was identical for the two sizes, consisting of a welded steel and stainless steel body that was cast into the concrete, and a threaded insert which can be removed and replaced (Figure 5-15, left). Stainless steel tubing was used in lieu of carbon steel tubing because stainless steel tubing is commonly available sized based on the inside diameter, which could be matched closely to the nominal diameter of the insert. This close fit was essential to allow shear transfer between the insert and the anchor body. The joints between the tubing/bearing plate and bearing plate/nut were tack welded at least 3 different locations and then sealed with silicone to ensure that concrete paste did not enter the anchor body during pouring. These joints were not welded all around as

with previous removable anchor prototypes (Trautner and Hutchinson 2015a) because of the relatively thin wall of the stainless tubing available in these diameters. The bonded anchors consisted of Hilti HAS-B 3/4 in. threaded inserts and Hilti RE-500 SD adhesive (Hilti 2011). Holes for the anchors were drilled with a hammer drill with a 7/8 in. dia. carbide-tipped bit to a nominal embedment of 10 in. The holes were cleaned with a brush and compressed air per the anchor manufacturer instructions. To ensure that the baseplate and anchors were aligned, the baseplate/column stub assemblies were removed from the structure and the anchors were bolted to the baseplate as the anchors were set in the adhesive (Figure 5-15, right).

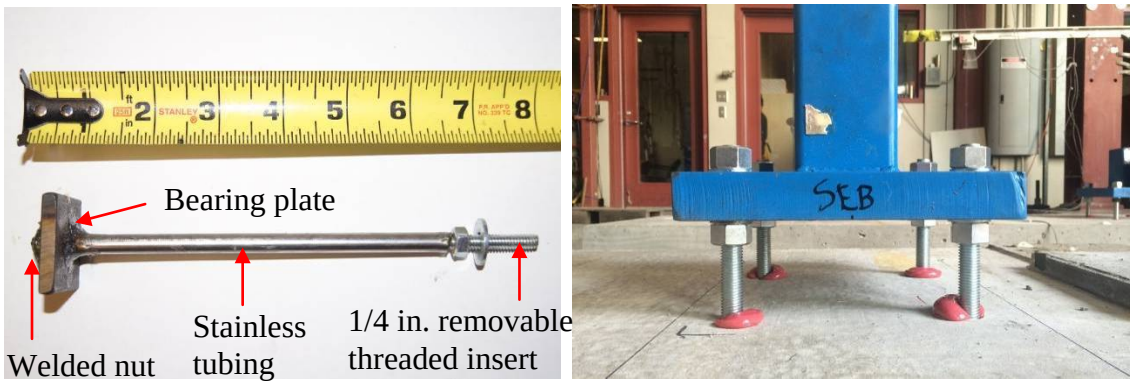

(a) Cast-in, removable anchor, 1/4 in. size (b) 3/4 in. bonded anchors

Figure 5-15: Comparison of anchor types used in test program

The grout pads were cast directly on the concrete slabs using wooden forms. The pads were cast prior to the placement of the specimen, which eliminated the need for setting nuts or steel shims that might affect the mechanical behavior of the connection. Wooden top plates cut with the precise hole pattern of each individual baseplate were placed over the forms to provide a level, smooth finish to the surface of the grout. The

raised concrete regions near the cast-in anchors (Figure 5-14) necessitated cutouts for the forms to ensure a uniform thickness of the pads, as shown in Figure 5-16. Fifty pound batches of Hilti Precision grout were mixed to a "flowable" consistency using four quarts of water. The surface of the concrete was brought to a saturated, surface-dry condition prior to grout placement, in accordance with the product instructions. The grout was placed directly into the forms with the top plate removed. Once the grout was brought to a relatively uniform level, the top plate was place. The grout was allowed to cure for at least 24 hours prior to removal of the forms. The grout was wet-cured for at least two days after the removal of the forms by placing wet rags over the area.

Figure 5-16: Grout forms for cast-in anchor stations with cutout (left) and post-installed anchor stations showing unfastened top plate (right)

5.3.3 Specimen construction and instrumentation

Mechanical Setup

All parts for the specimen were fabricated by Westech Metal Fabrication of San Diego, CA. The specimen was delivered in several parts: 1) two complete braced end frames, 2) 19 virgin beam members, 3) angle brackets and bolts. For Configuration 1, the

parts were assembled off of the foundations without the concrete mass slabs, and then the structure was lifted into place on the foundations as a unit. Special care was taken to ensure that the anchors and anchor holes were aligned, to avoid damage to the pre-set anchors. The structure was then checked for overall dimensional conformance to the drawings and was subjected to preliminary "bare frame" system identification tests. Following this, the masses were attached to the structure in preparation for testing.

Setup for Configurations 2-5 required several extra steps. removing the beam members individually. The beam members were delivered pre-drilled with the double-angle connection bolt holes, but were modified at the Powell labs to have the reduced section sizes listed in Table 5-3 for Configurations 2-5. The column fuse elements were fabricated completely at the Powell Labs. Photographs of the completed, in-place beam and column fuses are shown in Figure 5-17.

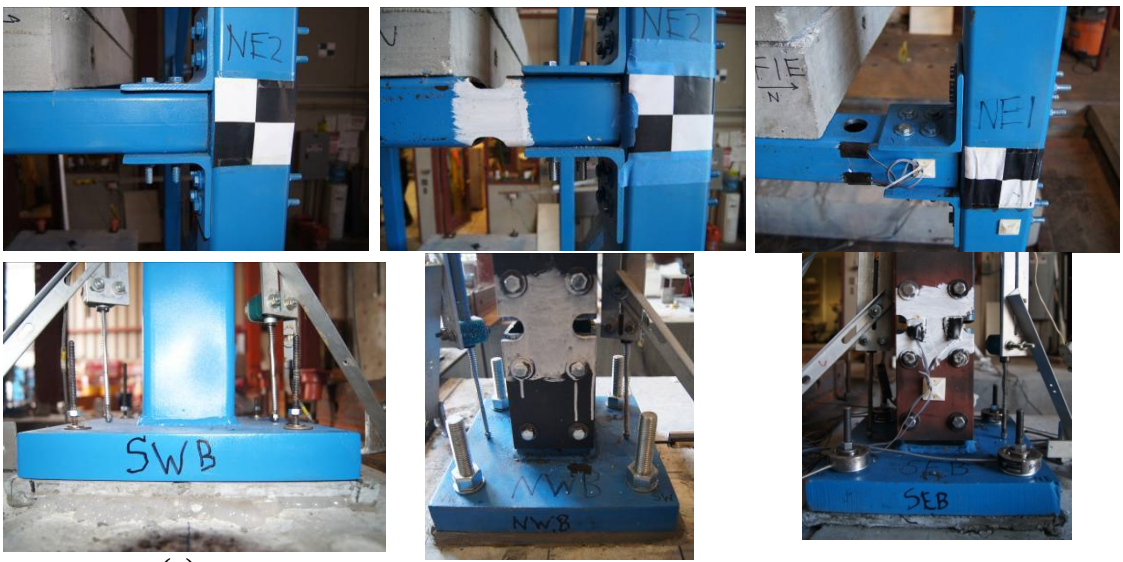

(a) (b) (c)

Figure 5-17: Finished in-situ beam and column fuses: (a) Configuration 1, (b) Configuration 2, (c) Configurations 3-5

Instrumentation and data acquisition

The structure was instrumented with a variety of sensors including accelerometers, string pots, displacement pots, and strain gages. A general instrumentation plan is shown in Figure 5-18. The various unique instrument names, used throughout this dissertation, are shown in Figure 5-19, Figure 5-20, and Figure 5-24. The prefix "D" was used to denote a sprung displacement pot, "S" was a strain gage, "SP" was a string pot, and "A" was an accelerometer. Additionally, the table control displacement "TD" and acceleration "TA" measurements were recorded (regardless of the control mode of the table). Although all floors were equipped with at least one accelerometer in the direction of shaking, the three accelerometers at floors 1 and 3 was sufficient to allow full resolution of the 2-D floor kinematics (two translations and a rotation). The three string pots at floor 3 (SP5, SP6, and SP7) provided fully-redundant displacement measurement at this floor. Vertical accelerometers were mounted on the tops of the B1 members on the third floor to resolve vertical structure motion and rocking (A4 and A5).

Displacement pots at the base level (D1-D12) were set up to resolve baseplate translation and rocking. Five accelerometers were mounted on the surface of the shake table, which were sufficient to provide redundant measurement of longitudinal (N-S) motion of the table, measure rotation about the vertical axis, transverse translation, vertical translation, and rotation about the N-S axis, assuming that the table behaves as a rigid body. No redundant measurement of table displacement was made.

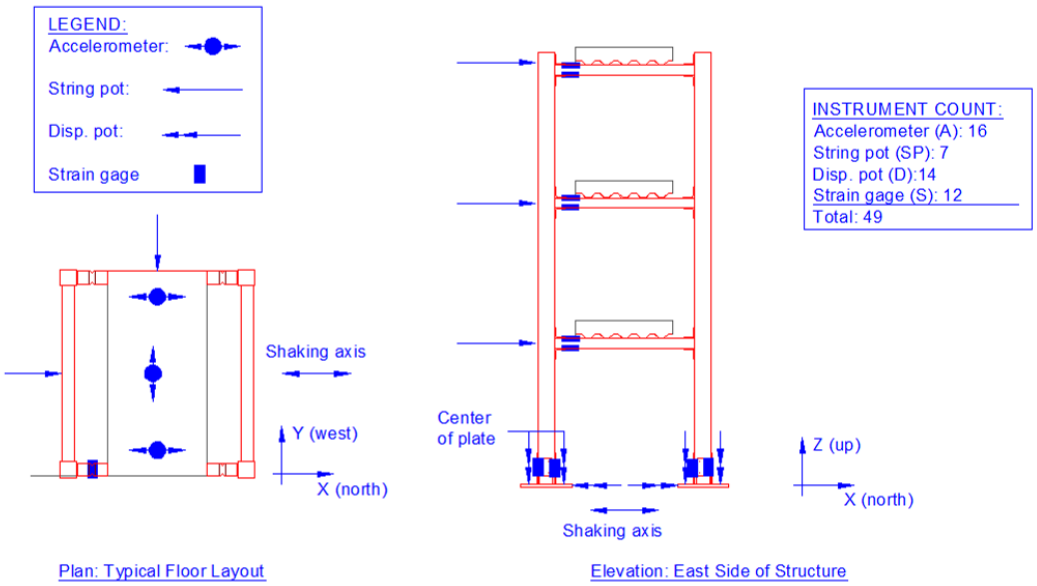

Figure 5-18: Basic instrumentation plan, typical floor plan and East elevation

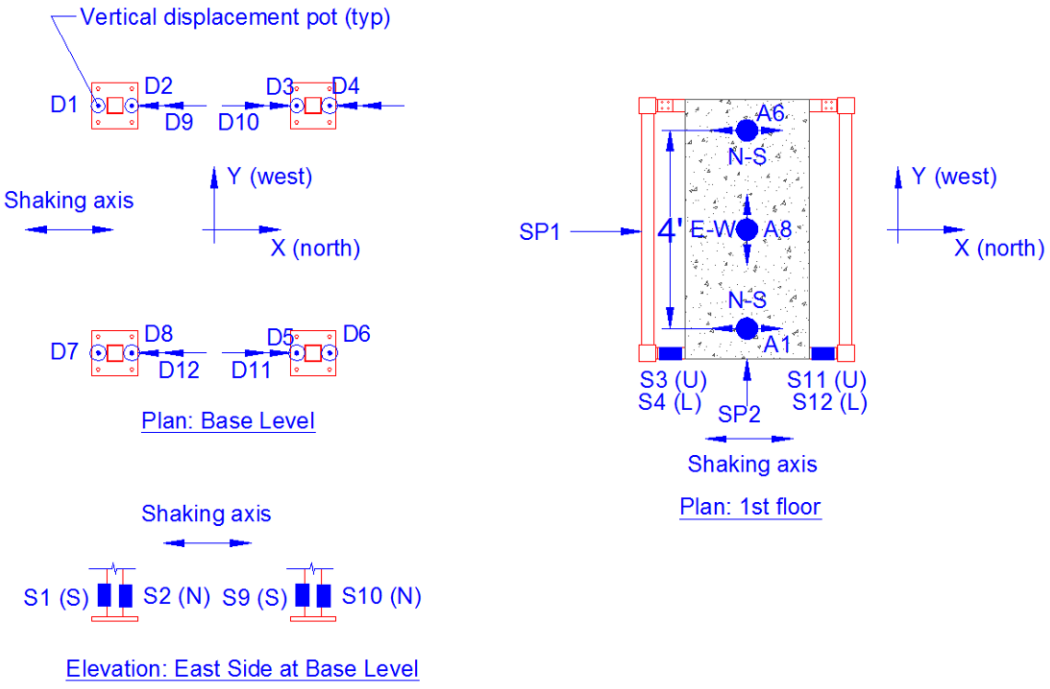

Figure 5-19: Instrument names for base connections, column fuses, and first floor

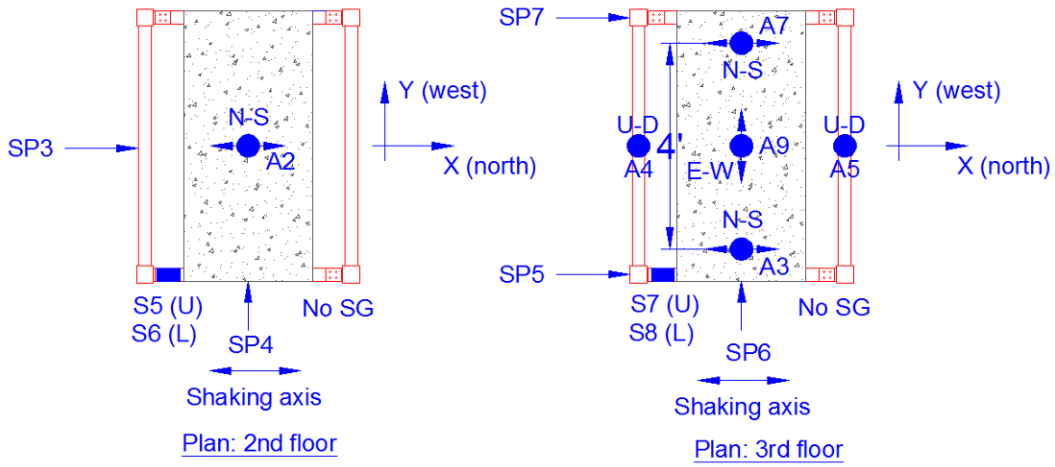

Figure 5-20: Instrument names for second and third floors

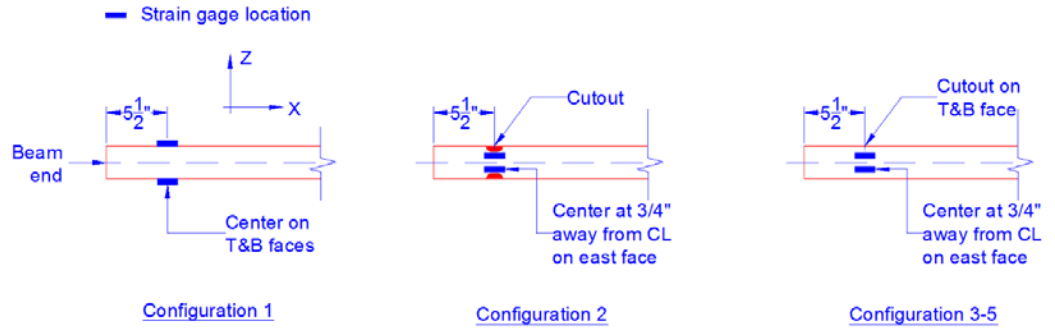

Figure 5-21: Detailed strain gages location: Configuration 1, Configuration 2, and Configuration 3-5 (left to right)

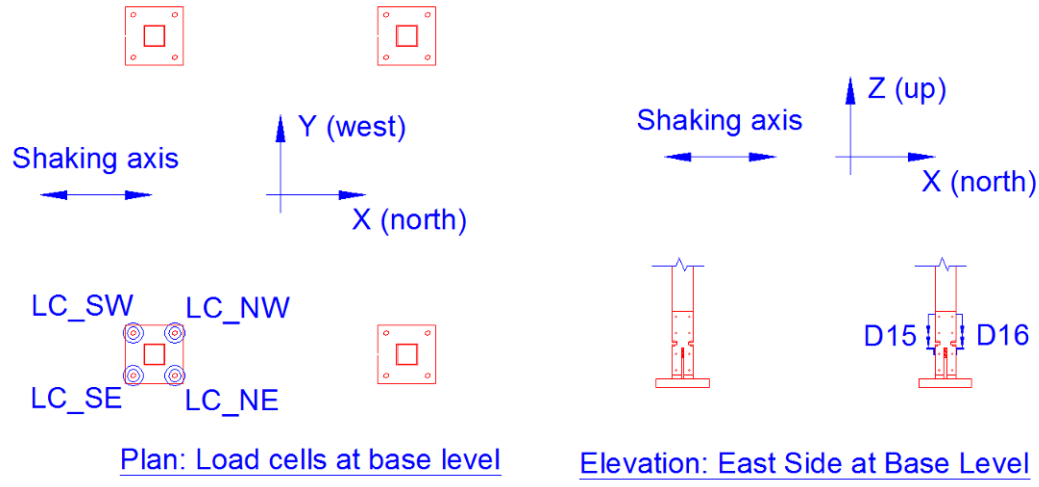

Figure 5-22: Instrument names for supplemental instrumentation

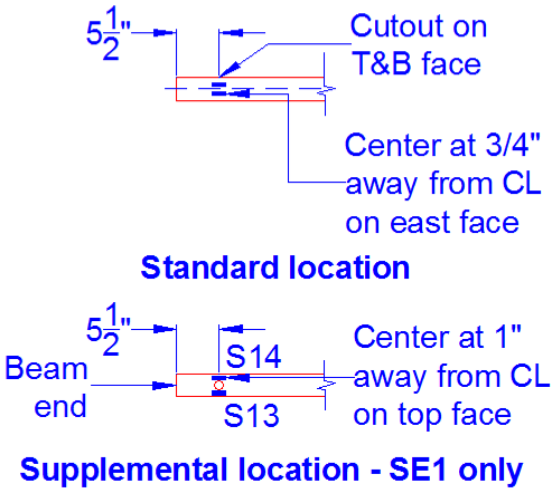

Figure 5-23: Instrument names for supplemental instrumentation: strain gages on Configurations 3-5 only

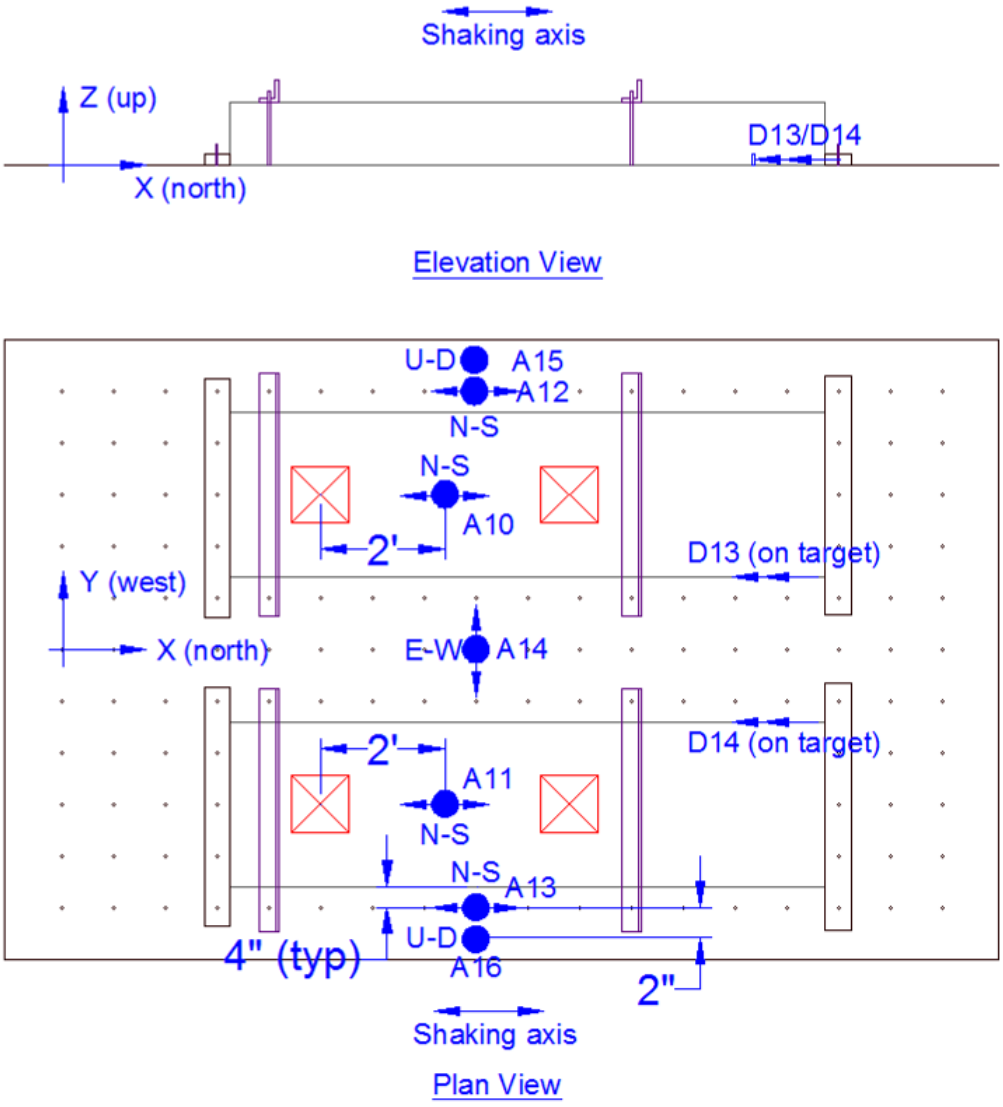

Figure 5-24: Foundation/shake table instrumentation, elevation (top) and plan (bottom)

a) Longitudinal string pots

(b) Baseplate displacement pots

(c) Floor-mounted accelerometers

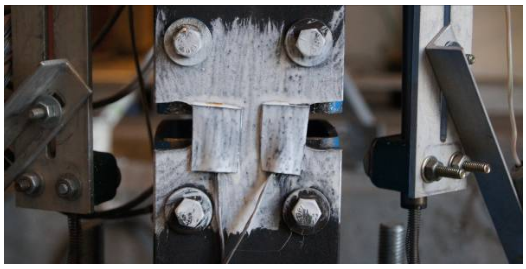

(d) Strain gages (Configuration 3)

Figure 5-25: Photographs of instrumentation on specimen

5.3.4 Specimen weight and weight distribution

The floor masses were slightly larger than intended, with the two-mass assemblies at each floor having an average thickness of approximately 10.75 in, instead of the intended 10.0 in. The dimensions of all other components were as-specified on the design drawings. An accounting for all of the components in Configuration 1-3 (the distributed-mass, moment-frame structures) is shown in Table 5-4. Total structural weight was about 6.7 kips, with the majority of this (nearly 80%) coming from the concrete floor masses. Tributary regions and floor-level lumped masses, such as would be appropriate for a multi-degree-of-freedom analysis of the structure, are shown in Figure 5-26. The magnitudes of the lumped masses, the total of which is equal to the total weight of the structure listed in Table 5-4, are shown in the figure. Masses were rounded to the nearest 10 lbf. Note that this accounting does not include the weight of the foundation slabs, which is estimated at 4.15 kips per slab.

The SDOF configurations (4 and 5) have the same components except that there are four floor slabs at the top level, for a total weight of about 4,885 lbf (including the 5% allowance for connections, etc.). Configuration 5 is slightly heavier due to the presence of the x-direction braces, but this additional weight (estimated at about 80 lbf) was neglected, as it is a trivial amount of the total structure weight. The mass distribution for these configurations is shown in Figure 5-27.

Table 5-4: Total structural weight calculation

Component	Total size per (various units)	Unit weight (various units)	Number of components	Subtotal (lbf)
Floor slabs	5.87 ft^3	150 pcf	6	5,283
Columns	12.38 ft	9.40 lbf/ft[1]	4	466
Beams (y-dir)	4.67 ft	6.85 lbf/ft[1]	6	192
Braces (y-dir)	5.67 ft	3.47 lbf/ft[1]	6	118
Beams (x-dir)	3.65 ft	6.85 lbf/ft[1]	6	150
Baseplates	0.105 ft^3	490 pcf	4	206
			Subtotal:	6,415
			Misc. hardware, welding, instrumentation, cabling, etc: 5%	320
			Total:	6,735

[1] AISC 2005

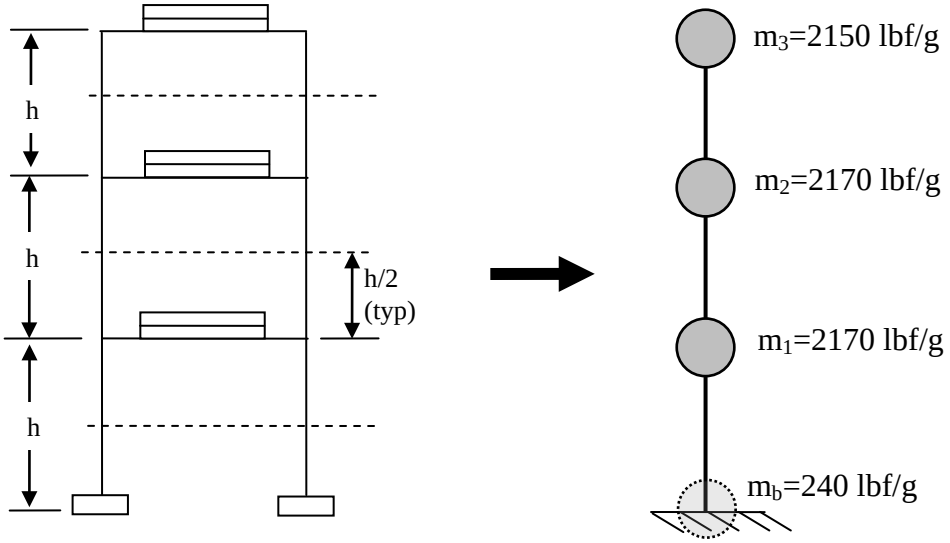

Note: figures shown are schematic only. Actual mass height from base is used for calculation of overturning moment in later chapters.

Figure 5-26: Tributary height and MDOF mass idealization (Configurations 1, 2, and 3)

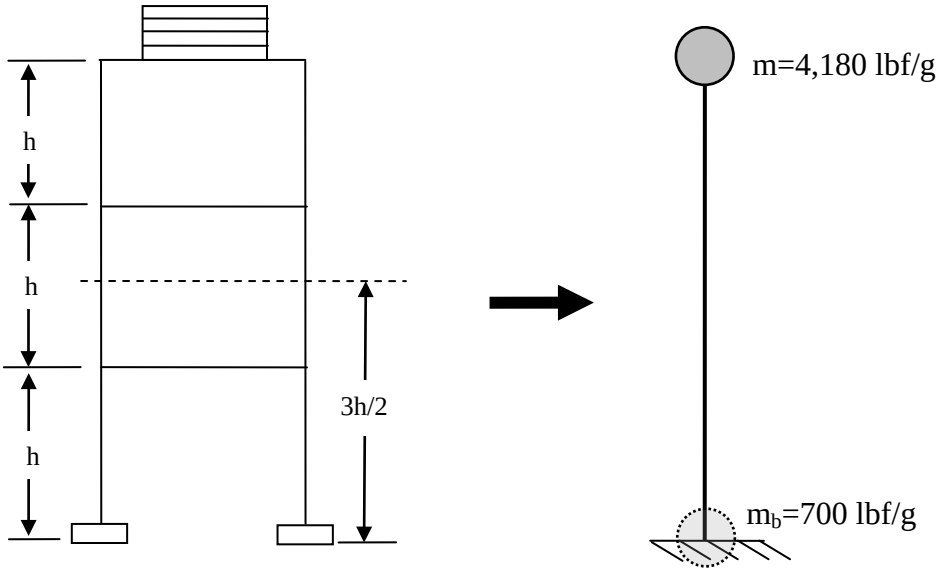

Note: figures shown are schematic only. Actual mass height from base is used for calculation of overturning moment in later chapters

Figure 5-27: Tributary height and mass idealization for SDOF structures (Configurations 4 and 5)

5.3.5 Motion selection, Characteristics, and Run Identification

In the United States, most seismic design is predicated on the response spectrum concept, as exemplified by the procedure given in ASCE 7-10 (ASCE 2010). The selection of earthquake motions to match the probabilistically-developed response spectra for any given site may be performed in a variety of different ways. Some popular methods include:

1. Selection of a suite of time histories that have a mean or other statistical distribution characteristic above the design response spectrum for a particular site for a range of period values of interest. This procedure is allowed by ASCE 7 for both linear and nonlinear time history analysis.

2. The use of spectrally-matched time histories, wherein a "seed" time history is modified, either in the frequency or time domain, to closely match the shape of a design response spectrum for a particular site. This procedure is often used in the nuclear industry, and is embodied in several nuclear codes (ASCE 43-05, ASCE 4-98).

3. The selection of a time history to elicit a desired response from the structure. This approach is often used with low-frequency structures, base isolated or otherwise, where a target spectral displacement may be an important design characteristic.

The current test structure is not intended to correspond to any real-world structure or site, and is only intended to probe the basic concepts of structures with yielding base connections. In this context, the development of a design response spectrum in the traditional sense was not necessary or desired. Therefore, approach 3 was utilized in the current work. The selection of motions was made primarily based on analysis of the SD-MF configuration (Configuration 2). This configuration was of primary interest for the selection of ground motions because it served as a control for the other experimental configurations. Therefore, any beneficial or detrimental effects in the configurations with ductile anchorages could be judged based on motions for a particular desired behavior in the control specimen.

The seismic hazard is often expressed using nomenclature corresponding to either the recurrence frequency of the nominal event associated with the probability of exceedance of spectral parameters, or the probability of collapse within a structure's lifetime. For example, ASCE 7-10 (ASCE 2010) expresses requirements for buildings and other structures in terms of a risk-targeted Maximum Considered Event (MCE_R) spectrum, which is associated with a nominal probability of collapse of 1% in 50 years. The "Design" spectrum is then taken as 2/3 of the MCE_R spectrum. Other classification systems have similar classification schemes, with an additional "Service" level defined as a relatively frequent earthquake with a nominal return period less than 50 years (SEAOC 2016). Although the motions selected for this research program do not have a

probabilistic basis, the names "Service", "Design", and "Maximum" were used to denote increasing severity for three demand levels. Because investigating the feasibility of repair of the base connections was a critical part of the research program, an additional motion denoted "Aftershock" was also added to the test program. This motion was intended to follow the Maximum-level motion and have a severity somewhere between the "Service" and "Maximum" motions. To select motions for each of these demand levels, the following criteria were used:

1. Eliciting desired maximum and residual drifts in the SD-MF structure, consistent with the expected performance of moment frame steel buildings for the variety of different demand levels. Due to the nature of this structure, this criterion involves a substantial amount of experience and engineering judgment. At the Design level, an approximate maximum drift for typical steel structures can be established utilizing code-required drift limitations. Table 12.12-1 of ASCE 7-10 requires that steel structures be limited to between 2 and 2.5% maximum drift for Design-level demands, depending on the structure height, structure importance, and interior detailing.

2. Peak ground accelerations within reasonable limits for motions associated with the levels of damage in (1). Again, because the structure is not intended to represent a particular building or site, the reasonableness of the motion with respect to PGA was evaluated based on judgment.

3. A range of different earthquake event types and distances was desired. This criteria stems from the desire to evaluate the structure under events that are common in different types of the world (i.e. subduction events in Japan versus shallow strike-slip events in the western United States)

The ranges used to evaluate criteria (1) and (2) are shown in Table 5-5. Note that the criterion for Design-level maximum drift was somewhat larger than the range suggested by Table 12.12-1 of ASCE 7, given the difficulty of accurately predicting drift in numerical models.

Table 5-5: Criteria used for motion selection

Motion short name (target performance)	Target maximum drift, residual drift, and anchor plastic elongation	Target PGA
Service	See Table 5-1	<0.5g
Design		0.5-0.75g
Maximum		>1.0g
Aftershock		<0.5g

To evaluate candidate motions, a numerical model was utilized, as described later in this Chapter. To differentiate between the relatively crude model used for motion selection, and the relatively detailed analysis models used subsequently, the earlier, less sophisticated model is referred to as the "design model" and the later model is referred to as the "analysis model". The design model was used to evaluate a suite of over 20 candidate motions with a variety of scaling factors. Those that met the selection criteria listed in Table 5-1 & Table 5-5 were selected for use and are listed in Table 5-6. For the remainder of this dissertation, the motions are referred to using the short names corresponding to each demand level which are given in this Table. Note that one additional motion level (short name), "Extreme", was added. This motion was run only once in the final structural configuration (5) to evaluate the remaining capacity and the structure's tolerance for extreme demands.

As shown in the table, the motions include two different events and three different recording stations. The epicentral distances ranged from about 80 km to less than 5 km. The scaling factors used to meet the selection criteria in Table 5-5 are listed with basic recording characteristics in Table 5-7. All of the strong-motion recordings utilized in the test program had a timestep of 0.005s (Nyquist frequency of 100Hz). The total motion

duration was between 40 seconds for the Loma Prieta event and 140 seconds for the Maule event. All motions were pre-filtered with the corner frequencies listed by the agency responsible for the recordings, either PEER (Loma Preita recordings) or Strong Motion Center (Maule).

Table 5-6: Summary of motion short names

Motion short name	Original recording file name	Event	Station* (Component)	Fault Type [Epicentral Distance to recording station]
Service	concepcion1002271.v2	2010 Maule (Chile)	Concepcion Centro (000)	Thrust [82.4 km]
Design	G01090.AT2	1989 Loma Prieta (Calif.)	Gilroy Array (090)	Oblique [9.6 km]
MCE	CLS000.AT2	1989 Loma Prieta (Calif.)	Corralitos (000)	Oblique [3.9 km]
Aftershock	G01090.AT2	1989 Loma Prieta (Calif.)	Gilroy Array (090)	Oblique [9.6 km]
Extreme	CLS000.AT2	1989 Loma Prieta (Calif.)	Corralitos (000)	Oblique [3.9km]

*Loma Prieta motions from PEER NGAWest2 database. Maule record from USGS Strong Motion Center (strongmotioncenter.org)

Table 5-7: Summary of basic recording characteristics

Motion short name	Scaling (Target PGA or RMS, g)	Time step (s)	Total motion duration (s)	Filtering corners (Hz)
Service	0.70 (0.28g)	0.005s	141.69	0.15 - 25.0
Design	1.50 (0.71g)	0.005s	39.945	0.20 - 50.0
Maximum	1.60 (1.03g)	0.005s	39.945	0.20 - 40.0
Aftershock	1.00 (0.47)	0.005s	39.945	0.20 - 50.0
Extreme	2.10 (1.35)	0.005s	39.945	0.20 - 40.0

Plots of acceleration, velocity, and displacement, as well as the 5/95% Arias Intensity for each of the selected target motions are shown in Figure 5-28. PGA, PGV,

PGD, predominant period, and the strong motion duration from the 5/95% Arias Intensity are listed in Table 5-8. These values are compared to the achieved values subsequently.

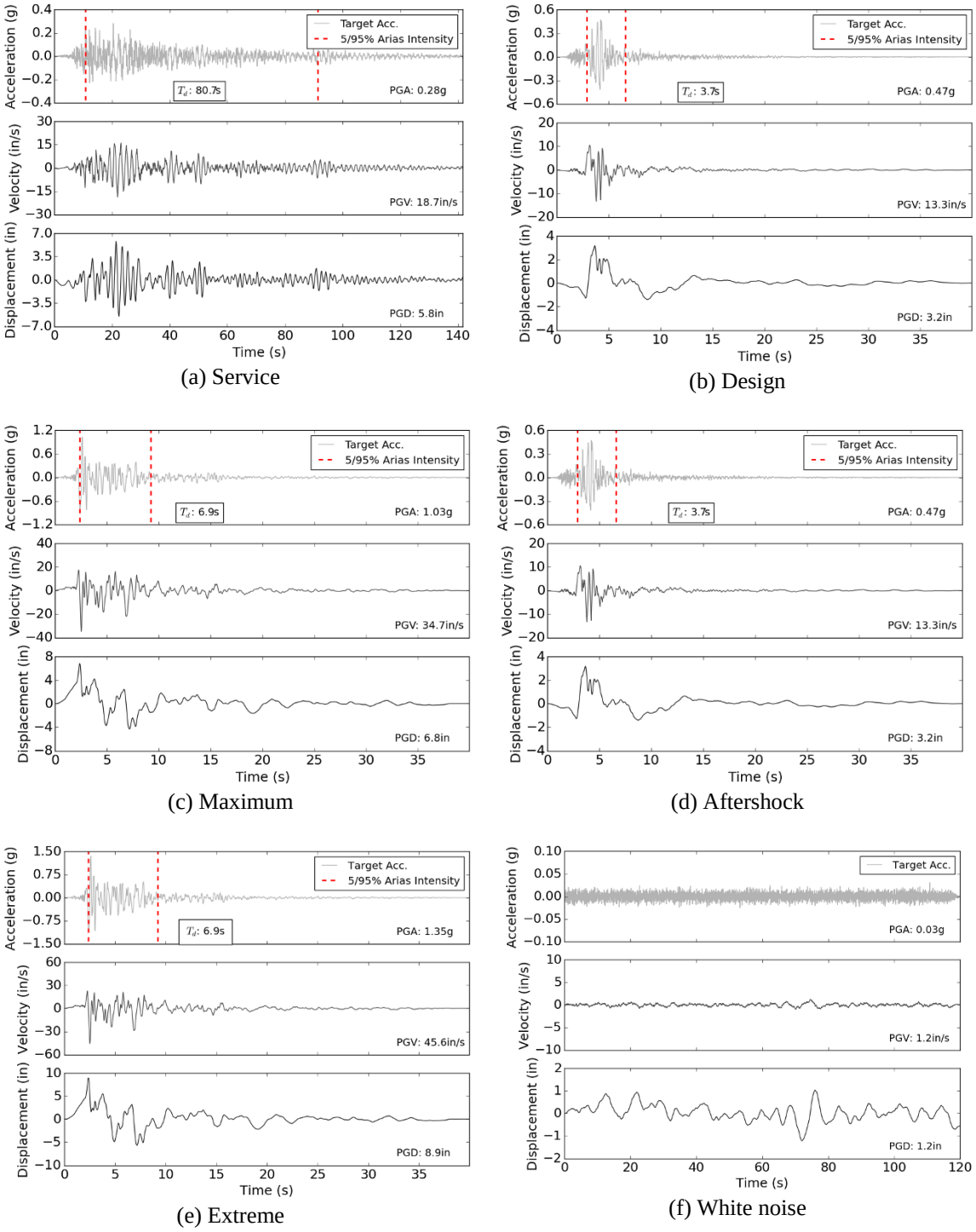

(a) Service (b) Design

(c) Maximum (d) Aftershock

(e) Extreme (f) White noise

Figure 5-28: Scaled acceleration, velocity, and displacement histories of the target motions with 5% and 95% Arias intensity and duration for strong motion runs

Table 5-8: Summary of key parameters for target motions

Characteristic	Service	Design	Maximum	Aftershock	Extreme	WN
PGA (g)	0.28	0.71	1.03	0.47	1.35	0.03
PGV (in/s)	18.7	20.0	34.7	13.3	45.6	1.2
PGD (in)	5.8	4.8	6.8	3.2	8.9	1.2
Predominant Period, s (from S_a)	0.23	0.39	0.31	0.39	0.31	--
Strong motion duration, T_d (s)	80.7	3.7	6.8	3.7	3.7	--

5.3.6 Test Procedure and Run ID Log

In general, the test procedure consisted of the following steps for each structure configuration:

1. Preparation of the test specimen: installation of beams, anchors, and column fuses appropriate for the particular configuration. The grout pads were prepared approximately one week before the start of the test.

2. Installation of all instrumentation: strain gages, accelerometers, string pots, and other displacement transducers. This step was carried out 1-2 days prior to the start of testing.

3. Instrumentation check: string pots and displacement transducers were verified to be functional immediately prior to the start of testing. Because they could not be directly tested by hand, accelerometers and strain gages were verified to be functional after the first white-noise motion.

4. Initial documentation: photographs of the instrumentation locations and the condition of all of the important structural features, including the beam-column connections, beam fuses, column fuses, anchors, and grout.

5. Video cameras (discussed earlier in this chapter) were set up to run for the duration of each of the planned strong motion and white noise runs.

6. White noise excitation: prior to any strong motion runs, the structure was subjected to white noise excitation, described in more detail in the following chapter, to ensure proper instrument function, to verify the structure natural frequency, and to check for any other mechanical or instrumentation problems.

7. Strong motion and additional white noise runs: for Configurations 1, 2 and, 3, the structure was subjected to "Service", "Design", "Maximum" and "Aftershock" motions, as described previously.

8. For the structures with yielding anchors, each strong motion run was preceded by a white-noise run with the anchors tightened and followed by a white noise run without any repair or replacement of the anchors.

9. Strong motion run documentation: following each strong motion run, the structure was inspected for visible damage. Photographs of all the structural features documented as part of Step 4 (Initial Documentation) were taken.

Some departures from the planned test procedure were made. For example, to determine whether there was a change in natural frequency associated with increased motion intensity, a series of increasing-amplitude white noise tests were run on Configuration 1 which were not part of the original test program. Several other departures also occurred, as discussed in the next chapter. For consistency, each test run is given a number, as listed in the Run identification (Run ID) log, given in Appendix D.

5.4 Test Results and Observations

5.4.1 Ancillary material test results

Concrete and grout compressive test results

Three 6"x12" concrete cylinders were tested at approximately 7,14, and 28 days. The dynamic test program was started approximately 42 days after the concrete was poured. Compressive testing was performed primarily to ensure that the design strength of the concrete was achieved. Because no concrete-influenced failure mechanisms (such as breakout or pullout) were expected or observed during the test program, no additional concrete cylinder testing was performed during the test sequence. The average concrete strengths are summarized in Table 5-9.

Table 5-9: Summary of tested concrete strengths (per ASTM C39-12a)

Concrete age (days)	Average concrete compressive strength, f'_c (ksi)
7	5.1
15	5.6
28	6.2

Three 2" grout cubes were tested on the first day dynamic testing for each of the configurations. The grout used develops a high early strength and does not undergo large strength gains after the first few days (Trautner and Hutchinson 2014a, 2015a). Therefore, the strength of the grout is expected to be approximately the same throughout the multiple tests which occurred on each grout pad. The grout testing is summarized in Table 5-11. Although there was a significant spread in the average compressive strengths, the values found were reasonable compared to previous tests on similar grout (Trautner and Hutchinson 2014a, 2015a).

Anchor material and structural member coupon tests

Prior to testing of the full structure on the shake table, tensile testing of the anchor inserts and coupons from the main structural members was conducted. It was not possible to procure 1/4 in. or 3/8 in. carbon steel allthread that was not cold-worked. Therefore, the allthread was annealed at 1200^{o} F for two hours, a procedure that has been used previously to increase ductility and restore nearly the mechanical properties of the virgin material (Trautner and Hutchinson 2014a). Testing of the anchor inserts was conducted using a free length of 8 in., in accordance with ASTM F1554-07 (ASTM 2007). The force-displacement curves from the anchor inserts are shown in Figure 5-29, with the minimum/maximum ultimate strength values and minimum elongation of ASTM F1554

shown for reference. Although conformance with this standard was not required, this standard provides a "reasonableness" comparison for the material used in this work as it relates to commonly available anchor products. Both anchor samples met the minimum yield strength and minimum elongation requirements, however the 3/8 in. sample was approximately5% below the minimum required ultimate strength. This result is not expected to influence the outcome of the dynamic testing of the structure significantly. The force-deformation relationships shown in these graphs were used for all analysis and modeling efforts described in Chapter 4.

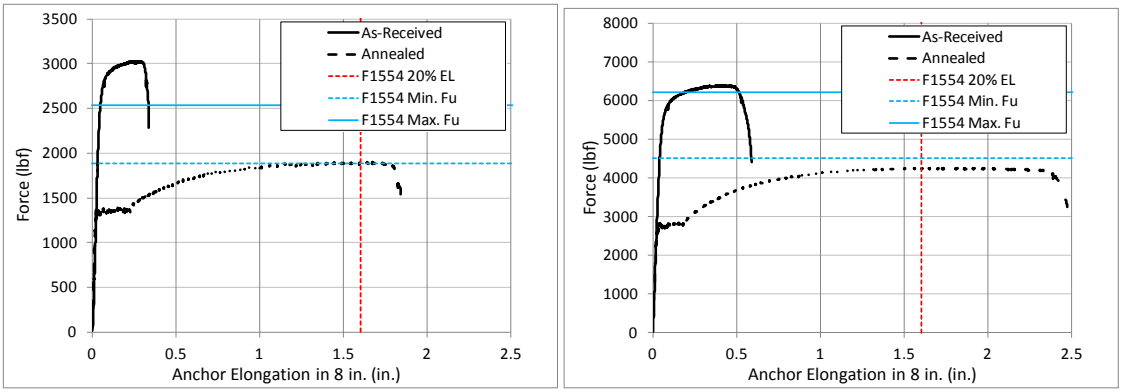

(a) 1/4 in. diameter (b) 3/8 in. diameter

Figure 5-29: Force-displacement response of the anchor inserts (8 in. stretch length)

Extra material from the main structural members (C, B1, and B2) was obtained from the fabricator to allow tensile coupon testing. Dog-bone coupons were cut from the "flat" area of each member, as well as from the plates used to make the column hinges. Tensile testing of these coupons was performed to establish the stress-strain behavior for later structural modeling. The stress-strain curves from each coupon are shown in Figure 5-30. Interestingly, the 3x3 material exhibited a significantly lower ultimate strength as well as a much greater total elongation versus the 4x4 coupon. Because square HSS is

typically bent from flat plate and then welded, one would expect a somewhat larger available elongation from the larger-width HSS because of the smaller total strain demands from the bending process. However, the ultimate strength of the smaller HSS should also be larger due to a greater amount of work hardening. The exact causes for the significant strength and elongation discrepancies are unknown. Because the material did not exhibit a well-defined yield plateau, the 0.2% strain offset criterion was used to identify the yield stress (Figure 5-31). The plate material exhibited classical mild steel plasticity with a well-defined yield plateau. The yield and ultimate stresses from each sample, which were used for all analysis and modeling of the test structure, are summarized in Table 5-10. The yield strain, assuming a modulus of elasticity of 29,000ksi, is also listed.

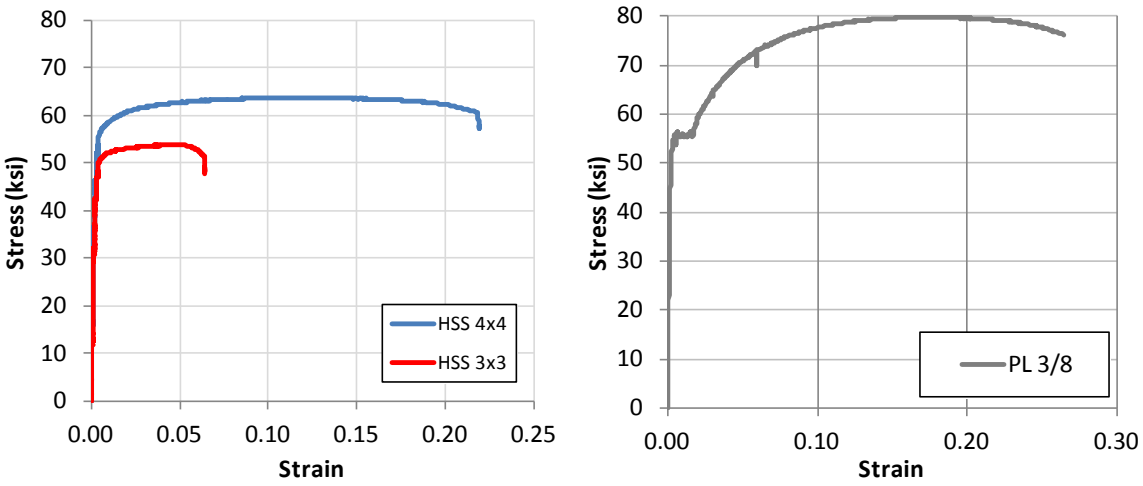

(a) HSS coupons (b) 3/8 in. thick plate coupon

Figure 5-30: Stress-strain response of steel used in experimental specimen

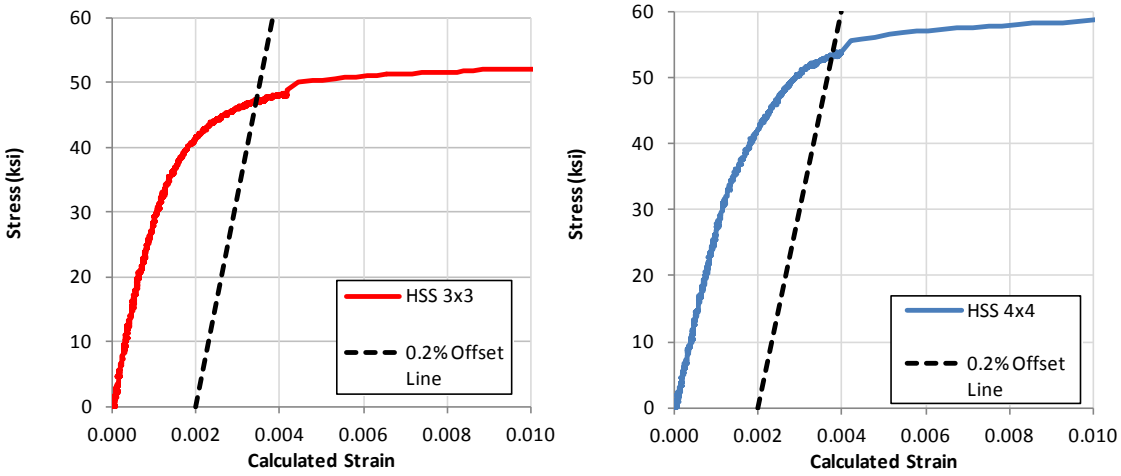

(a) HSS3x3x3x3/16 (b) HSS4x4x3/16 (right)

Figure 5-31: 0.2% offset yield strains from HSS coupons

Table 5-10: Yield and ultimate stresses from coupon testing

Section	Nominal Grade	F_y	ε_y ($\mu\varepsilon$)	F_u
HSS 3x3x3/16	A500 Gr. B	47.1	1620	53.9
HSS 4x4x3/16	A500 Gr. B	53.4	1840	63.8
PL 4x3/8	A36	55.3	1910	79.9

Table 5-11: Summary of tested grout strengths

Configuration	Average grout compressive strength, f'_g (ksi)
1	13.1
2	10.6
3/4/5	9.1
Average:	10.9

Hinge Concept Tests

To ensure that the proposed beam and column cutouts would provide smooth, stable hysteretic moment response, proof-of-concept tests were carried out on prototype beam and column members. These tests involved welding a cantilever HSS section to a plate mounted on the lab strongwall, then loading the tip and monitoring the response

with a displacement pot and strain gages mounted in the hinge area. The overall test setup is shown schematically in Figure 5-32. The specimen was tested in one direction, then unloaded, flipped vertically, then tested in the other direction. In this way, test data from the two parts of the test ("up" and "down") could be spliced together to determine the moment-rotation behavior under reversed cyclic loading. The rotation on the reduced section was calculated via small rotation theory as:

$$\theta = \frac{\Delta - \Delta_e}{L_H} \qquad \text{Eq. 5-2}$$

where Δ is the measured displacement at the point of load application and Δ_E is the elastic deformation of a cantilever beam over the distance from the hinge location to the point of load application (L_H, as shown in Figure 5-32).

The beam section and column section tested were similar, but slightly different than those eventually selected for dynamic testing (Figure 5-4 and Figure 5-6). The prototype beam section consisted of removing 2 in. of the corners of a 4x4x3/16 HSS, as shown in Figure 5-33.Strain gages were mounted at the center of the top and bottom flanges. The concept provided smooth moment-rotation behavior, and achieved the plastic moment calculated based on typical plastic beam section analysis of the smallest section (Figure 5-34). The lack of hardening (which would tend to increase the moment above M_p) is consistent with the stress-strain behavior of HSS steel used in the rest of the program (see Figure 5-30). However, this prototype section was rejected based on the inability to resolve the applied moment based on measured strains. As shown in Figure 5-35(a), the unsupported flanges buckled severely during loading. Unfortunately, this behavior was observed at relatively low rotations, about half that required for

attainment of the expected plastic moment. This meant that the global bending strain needed to calculate the applied moment was overwhelmed with a local strain associated with buckling of the cross-sectional element. The departure from the "expected" strain occurred relatively early in the loading process, at about $0.60M_p$ (Figure 5-35(b)). For this reason, the hinges used in the dynamic testing were designed without slender unsupported cross sectional elements, and strain gages were mounted on the side of the member.

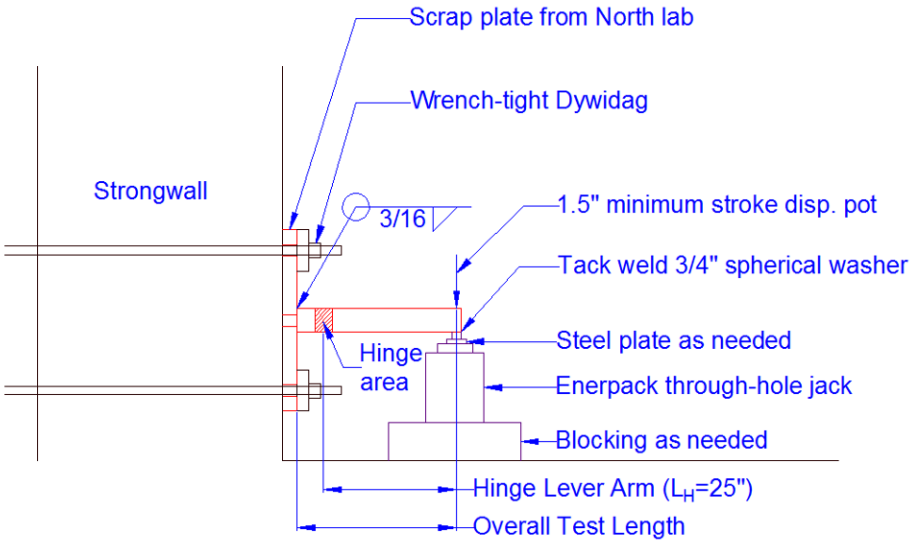

Figure 5-32: Setup for proof-of-concept beam and column hinge tests

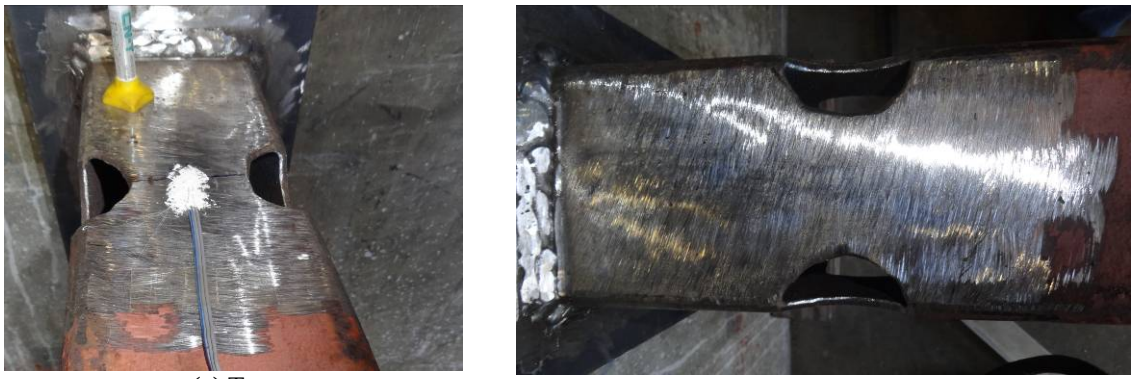

(a) Top (b) Side

Figure 5-33: Photographs of the concept beam test

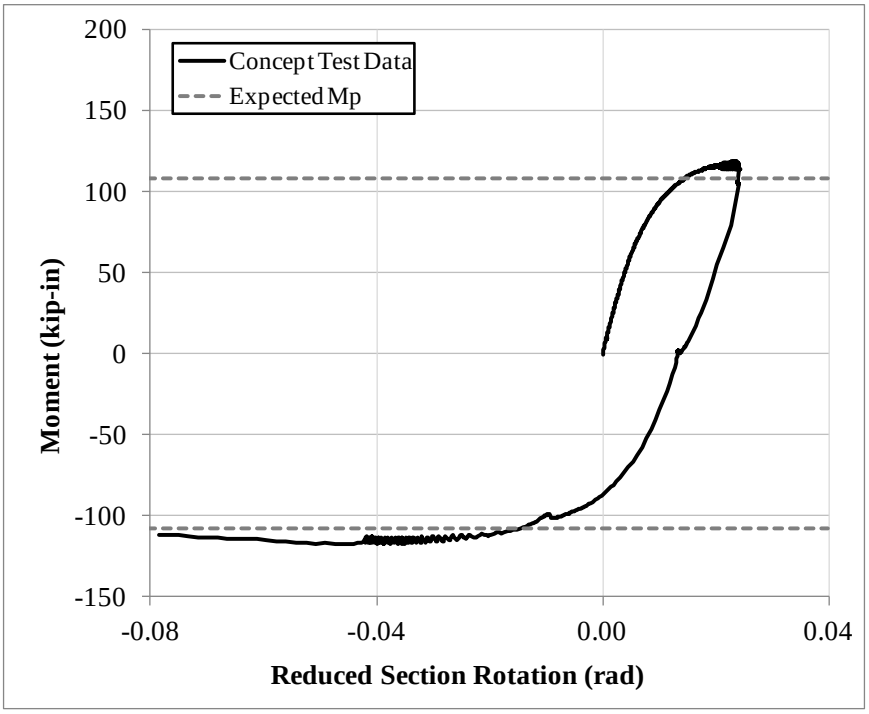

Figure 5-34: Moment-rotation behavior of beam concept test with calculated expected M_p

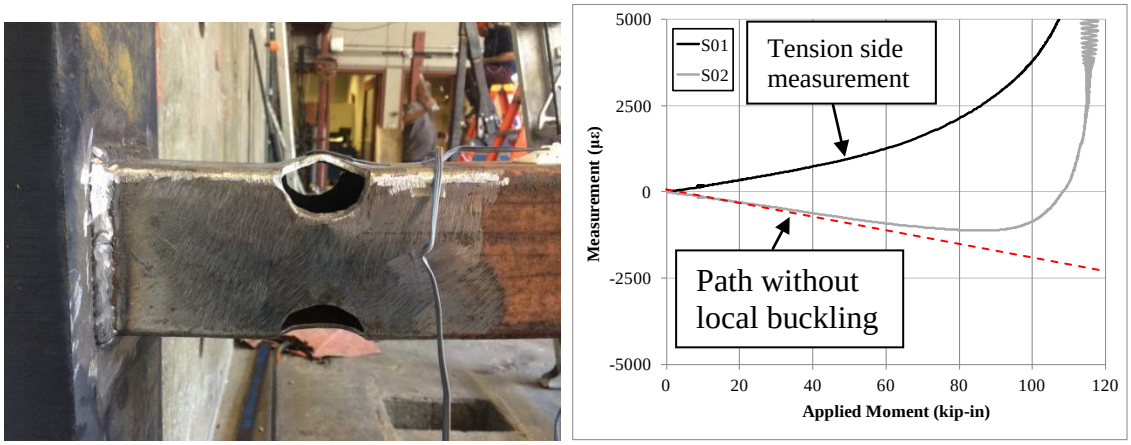

(a) (b)

Figure 5-35: Beam concept test results: (a) Observed buckling, (b) measured strain

The column concept test was identical to the eventual column fuse for Configuration 2 (Figure 5-6), expect that the side plates were 1/4" thick instead of 3/8", and the distance between the notches was 2.5 in. Strain gages were mounted 2 in. apart, centered on the centerline of each of the side plates. The measured moment-rotation response is shown in Figure 5-36. Although not as smooth as the beam concept test, the moment-rotation response achieves the expected M_y and M_p values at reasonable rotations. Because of the hardening behavior of this particular plate steel, significant strength beyond M_p was observed. Some minor drops in the moment, highlighted with arrows in the figure, are indicative of minor slip between the side plates and HSS. However, the installation torque on this connection was not tightly controlled. To prevent this, the side plates on the actual specimen were installed with full pretension on all installation bolts.

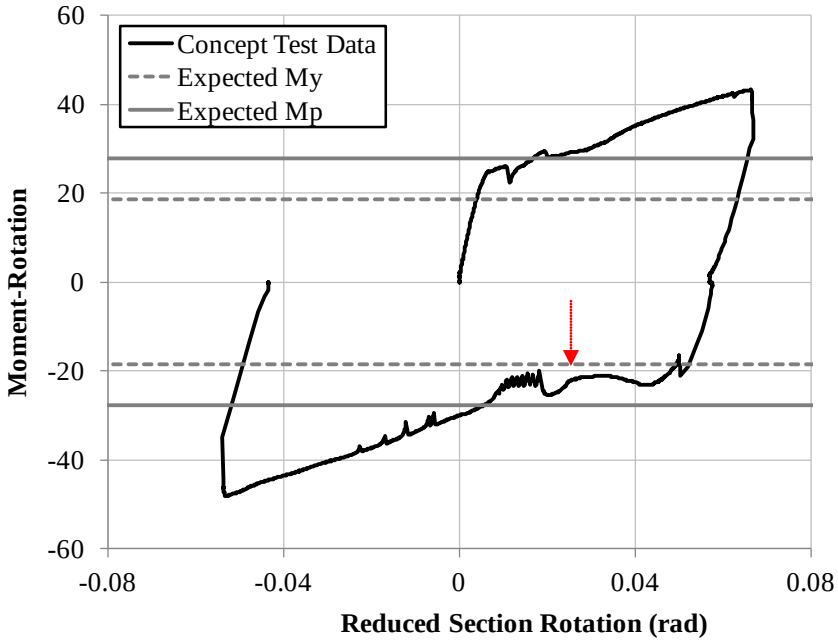

Figure 5-36: Moment-rotation behavior of column fuse concept test with calculated expected M_p

5.4.2 Dynamic Test Result Presentation and Typical Data Processing

Two distinct types of test were run on each specimen configuration: white-noise excitation and earthquake strong motion. The white-noise tests were used to determine the dynamic properties of the system, namely, the natural frequencies of the system. White-noise tests were run at critical points between strong-motion runs to determine whether any changes in the dynamic properties of the system had occurred. The target white noise motion is shown in black in Figure 5-38f. The white noise motion record was 120 seconds long, had a target root mean square (RMS) of 0.75%g, and was tapered at the start and end to prevent high-frequency motion spikes during start-up and run-down.

The natural frequencies were estimated using the transfer function *TF*, which was estimated as the quotient of the cross spectral density P_{yx} and power spectral density P_{xx}, where the subscripts *x* and *y* denote input and output, respectively:

$$TF_{xy}(f) = P_{yx}(f) / P_{xx}(f) \qquad \text{Eq. 5-3}$$

The cross-spectrum and power spectrum were calculated using Welch's method, as implemented in NumPy Version 1.10.1 and SciPy Version 0.15.1 (van der Walt 2011, Jones et. al 2015). The length of segments was 16384, overlapped by 50%. With the sampling frequency f_s=256 Hz used for all tests, the frequency resolution for the transfer function was approximately 0.004Hz. To estimate peaks, the transfer function estimate was smoothed using a 3-point moving average, which is often used in estimations of the peaks of power spectral density plots in earthquake engineering applications (ASCE 1998). This procedure was used on data collected from a variety of places on the structure, however the time-coherent average of the top accelerometers A7 and A3 were

often used, as they contained the clearest signal for the modes of interest. Typical results of this processing are shown in Figure 5-37. Establishing peaks as clear natural frequencies was performed using a degree of engineering judgment; however peaks that protruded more than 5dB above the surrounding features were generally considered to represent major modes of the structure.

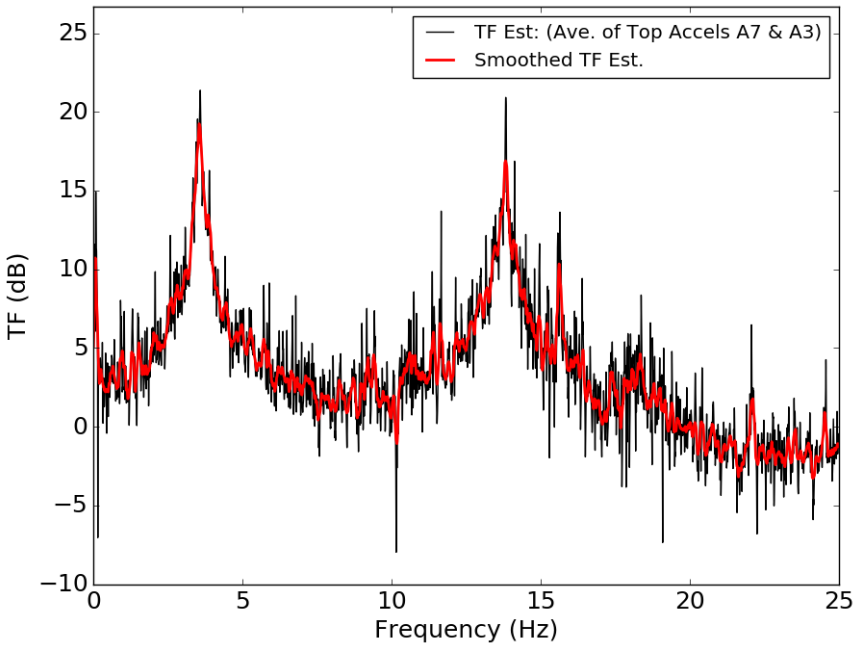

Figure 5-37: Typical transfer function estimate with raw and smoothed transfer function estimates

Data from the strong motion tests was processed using the following steps:

1. Data was split into "pre-test" and "test" portions. The "pre-test" portion was not subject to further postprocessing, and was only used to determine the effects of anchor pre-tensioning.

2. The "test" portion of the data was trimmed to have a small lead-in to the start of strong motion input to the shake table, and to conclude at the end of the input.

The acceleration data in the trimmed portion was filtered. The filter corners were set at 0.5Hz and 30 Hz, except where specifically noted otherwise. Justification for the filter parameters is provided in Appendix D.

5.4.3 Typical Shake Table Performance and Achieved Motions

The performance characteristics of the shake table used for the current work are discussed in a previous chapter. Recent previous studies (i.e. Trautner et al. 2016c) have indicated that the difference between the input and achieved motion on this table may be significant, depending on the particular motion characteristics. Part of the observed difference may be attributed to the error inherent in the feedback system, and some of the difference may be attributed to friction in the shake table bearings. Regardless of the exact sources, it is well-understood that the achieved motion will have some significant differences to the input motion. For the current work, the shake table was run in acceleration control. On-line iteration (OLI), a method which attempts to modify the source record to account for the finite mass of the table and response of the system in order to improve the match of the achieved motion, was not used for the current work based on the recommendation of laboratory staff. This decision was made considering that the mass and stiffness of the structure were expected to change throughout the test program, and uniform achieved motions were desired throughout.

Typical target and achieved acceleration time histories for each of the five strong motions used in the test program, as well as the target 0.75%g RMS white noise used for system identification are shown in Figure 5-38. There were only small differences in the achieved motion between the various runs for the different structure configurations. The achieved strong-motion plots in this figure have been filtered with a 4-th order Butterworth filter with corner frequencies at 0.05 and 30Hz, consistent with filtering performed for the rest of the structural accelerations. In contrast to the strong-motion

runs, the white-noise motion had broad-band power by design, therefore it is low-pass filtered only at the input frequency of 50 Hz. In all cases, the PGA of the achieved motion was significantly greater than the target motion, with the exceedance between about 10% and 50%. Corresponding pseudo-acceleration response spectra for the strong motion runs, shown for 2% and 5% damping in Figure 5-40, are shown with the range of fundamental periods observed throughout the testing program (period determination is discussed in the following sections). These plots indicate that within the period range of primary interest, response to the target and achieved motions was very close, generally within 10% or less. The target and achieved power spectral density (PSD) of the white noise for the x-direction is shown in Figure 5-41. The PSD is reasonably flat, as desired, until approximately 20 Hz, with a peak at the table foundation frequency of about 25Hz. There were significant peaks in the PSD measured at the table in the other two directions (Y: A12/A13 and Z: A15/A16). These were caused by feedback of the structural modes into the table in these directions. Transfer functions for the structure are discussed in the next sections.

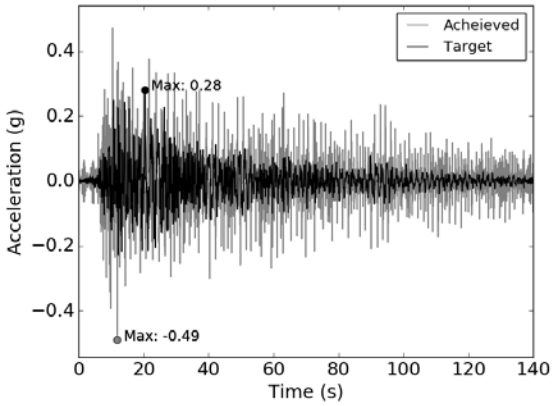

(a) Service

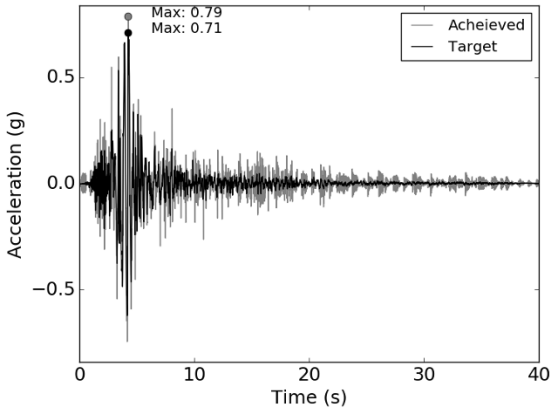

(b) Design

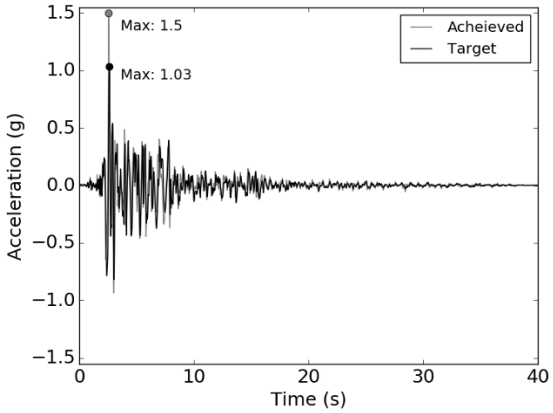

(c) Maximum

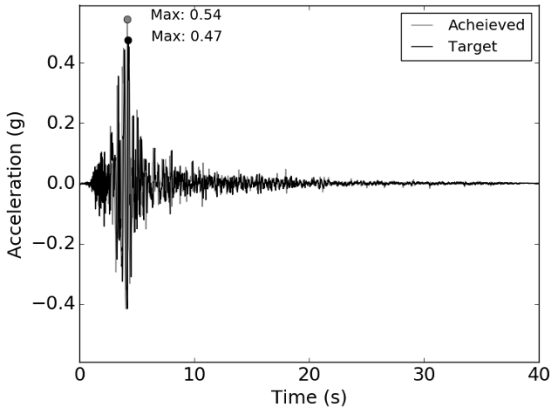

(d) Aftershock

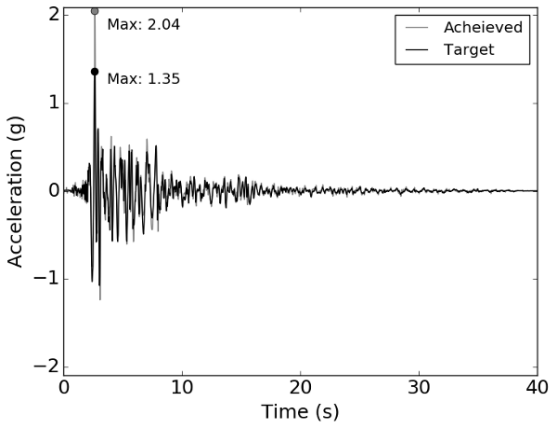

(e) Extreme

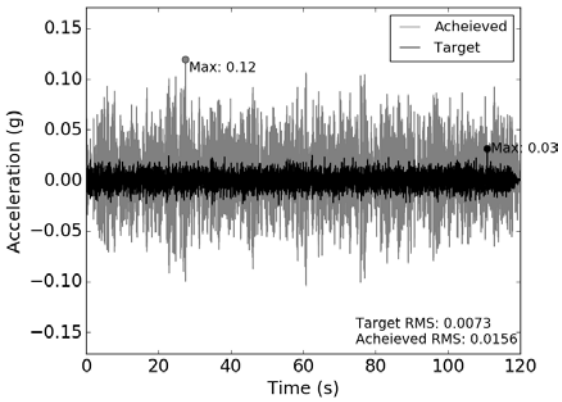

(f) White noise

Figure 5-38: Target versus achieved, filtered acceleration time histories of the target motions

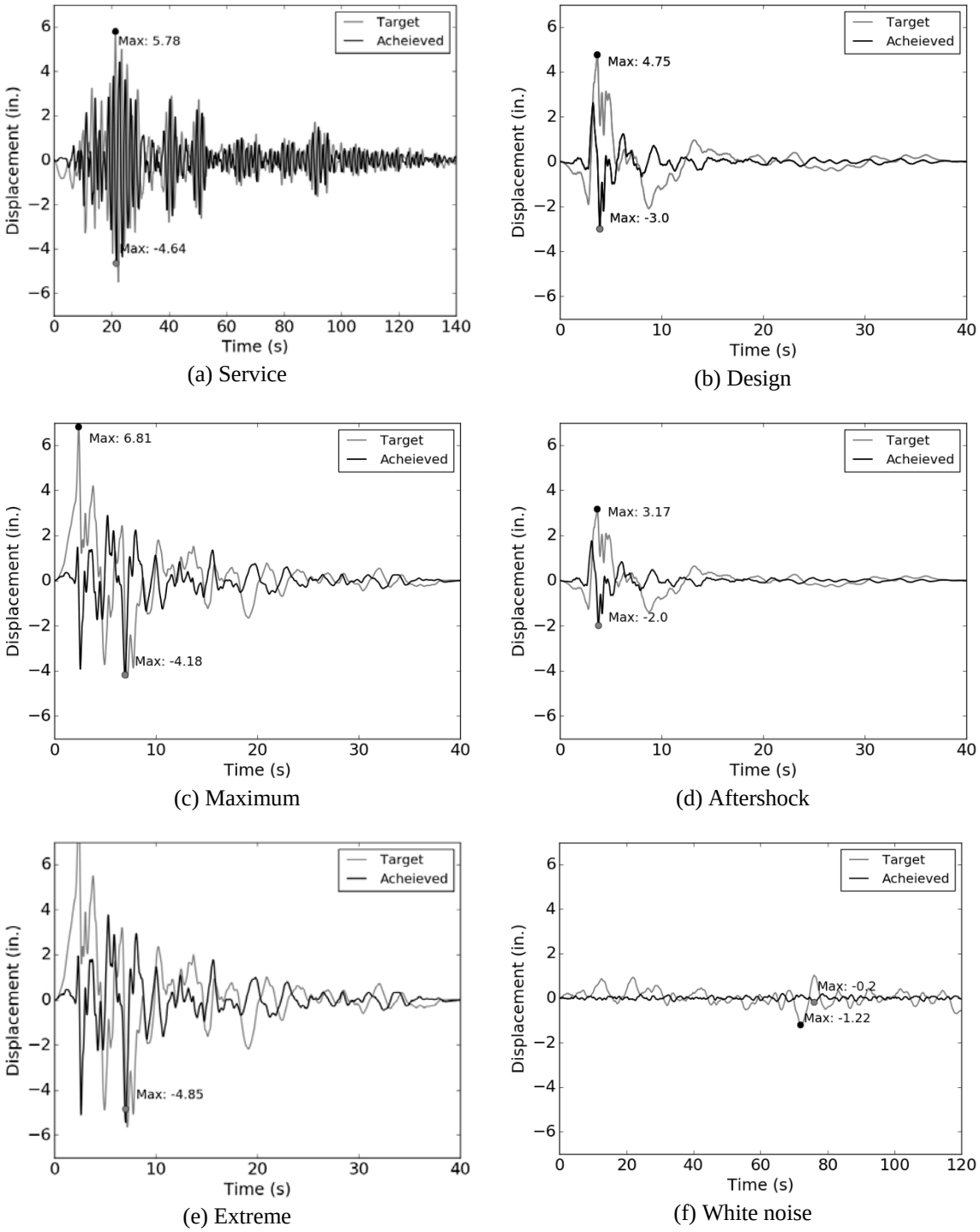

Figure 5-39: Target versus achieved, measured displacement time histories of the target motions

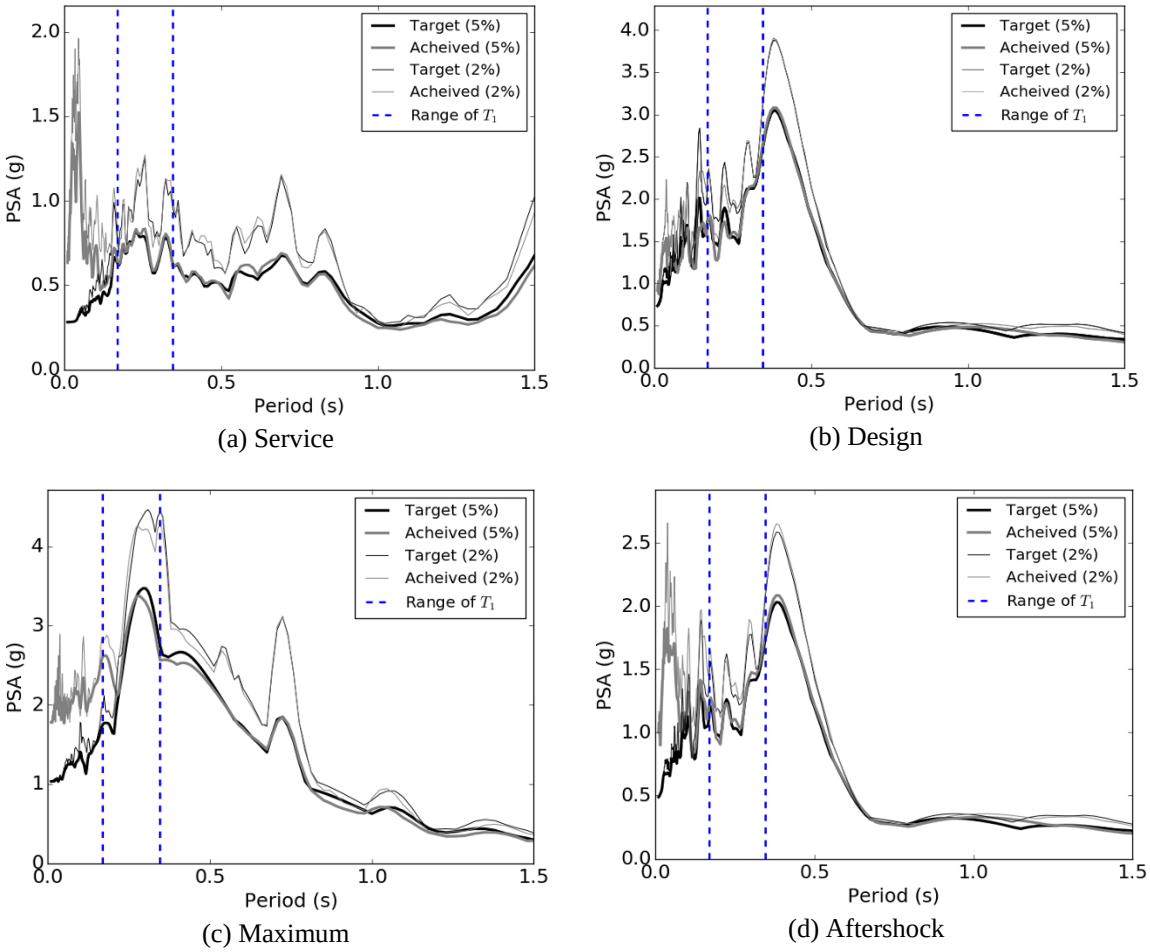

(a) Service

(b) Design

(c) Maximum

(d) Aftershock

Figure 5-40: Target versus achieved 2% and 5%-damped pseudo-acceleration response spectra for strong motion runs

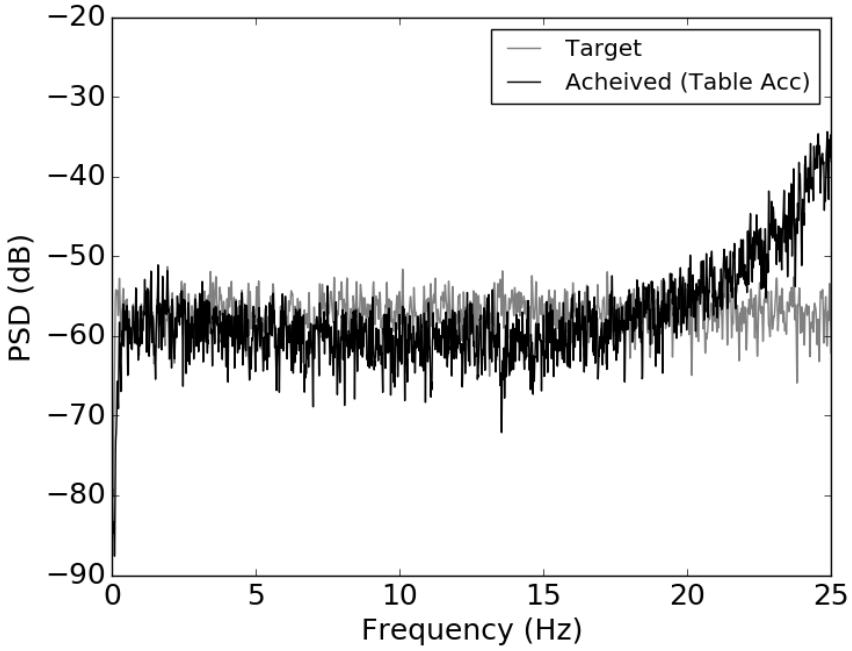

Figure 5-41: Target versus achieved power spectral density for white noise

Table 5-12: Summary of target vs. achieved motion characteristics

			Target, (achieved)		
Motion name	Service	Design	Maximum	Aftershock	Extreme
PGA (g)	0.28 (0.49)	0.71 (0.79)	1.03 (1.5)	0.47 (0.54)	1.35 (2.04)
PGV (in/s)	18.7 (16.1)	20.0 (18.4)	34.7 (29.6)	13.3 (12.8)	45.6 (37.7)
PGD (in)	5.8 (4.6)	4.8 (3.0)	6.8 (4.2)	3.2 (2.0)	8.9 (4.8)
T_d (s)	80.7 (103.2)	3.7 (12.0)	6.8 (11.7)	3.7 (11.4)	3.7 (11.4)
Average % difference in S_a within period range of interest (5% damping)	1.9	-1.8	7.9	1.9	6.8

5.4.4 Test Results and Physical Damage Summary

This section presents the measurements and observations made during the testing of each of the five structure configurations. Comparisons of relative structure performance and overall analysis are presented in the following section.

General Observations and Ancillary Measurements

As described in Chapter 2, the shake table and foundation slabs were equipped with an array of accelerometers in order to fully characterize the motion imparted to the structure. A15 and A16 measured vertical acceleration and were mounted on the east and west edges of the shake table platen. Typical time histories from the Design motion, in this case from Configuration 1, are shown in Figure 5-42. Two time histories are shown in each plot: the raw measurements and the measurements processed with a low-pass 4th order Butterworth filter with a corner frequency of 20 Hz. This corner frequency was selected as a conservative upper bound of structural frequencies that are of interest in the current work (as discussed below). The maximum measured vertical acceleration was on the order of 0.2g, however the maximum value in the filtered data drops to below 0.05g. This behavior was typical for all structural configurations and all motions, with the peaks slightly higher and lower for the Maximum and Service/Aftershock motions, respectively. Because the magnitude of the maximum vertical acceleration was low relative to the applied horizontal acceleration and because the vertical motion had very little content in the range of structural frequencies of interest to the current work, the vertical shake table acceleration was not subjected to further postprocessing and was not used for any subsequent work.

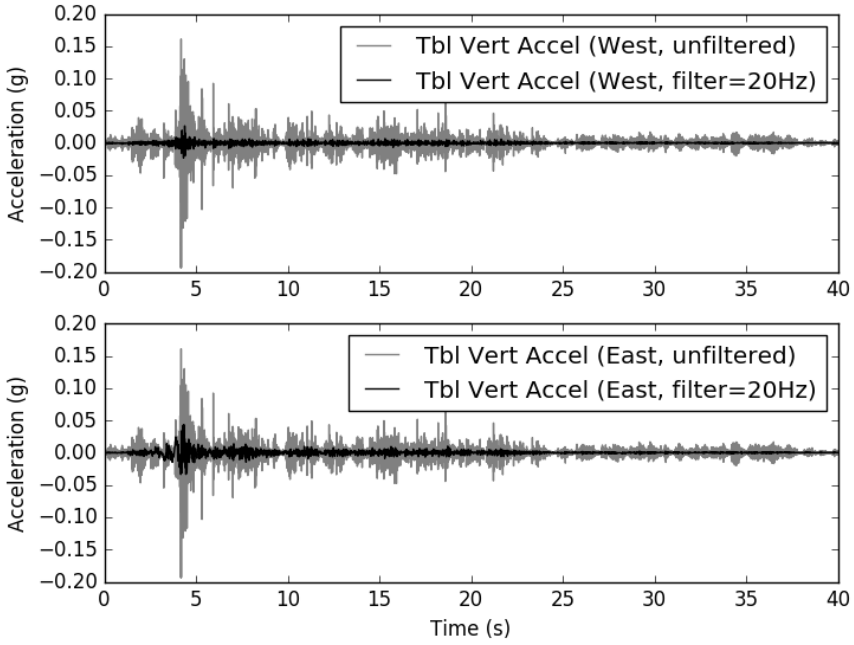

Figure 5-42: Time history of vertical motion measured on the east and west edges of the shake table platen from Design motion (A16 and A15, respectively)

In addition to the accelerometer mounted on the table that is used for feedback and control, two pairs of accelerometers were mounted on the table edges (A12 and A13) and on the footings themselves (A10 and A11). These accelerometers were used to evaluate whether there were any differences in the motion achieved by the table and imparted to the foundation and structure. The motion measured by the table accelerometer is compared to the motion measured by A10 and A11 in Figure 5-44. The measured table acceleration was very similar to the acceleration at the footing level. Therefore, measurements from the table accelerometer were utilized to make comparisons in this dissertation, for example establishing the amplification factor from the ground acceleration to a given floor acceleration. Accelerations form A10 - A13 are not postprocessed or utilized further.

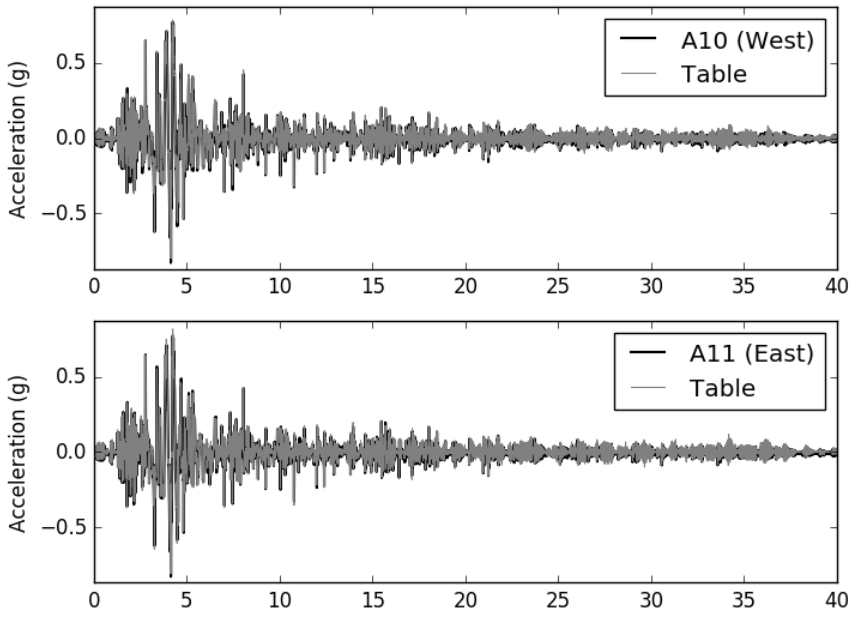

Figure 5-43: Time history of measured longitudinal footing accelerations (A10 and A11) versus table-mounted accelerometer

The specimen was attached to the shake table platen using a combination of tiedowns and shear keys. Displacement pots (D13 and D14) were mounted to the sides of the slab to determine whether any differential movement occurred during testing. For configurations 1-4, the maximum differential movement for either slab was less than 0.0005 in., even during the Maximum motion (Figure 5-44(a)). During the "Extreme" motion run for Configuration 5 only, there was some relative displacement recorded, up to about 0.006 in. However, this level of relative motion is still extremely small, and is not expected to affect the test results significantly. Therefore, differential movement of the slab and the table is assumed to be zero, and readings from these instruments are not discussed subsequently.

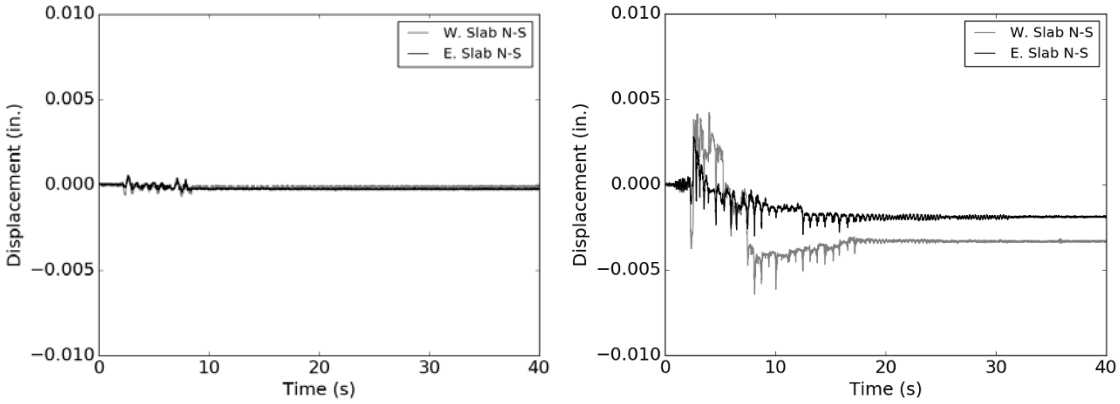

(a) Typical movement during "Maximum" motion

(b) highest recorded slab motion from "Extreme" motion, Configuration 5

Figure 5-44: Time histories of N-S movement of slabs during testing

Several pieces of instrumentation were strategically positioned to evaluate the torsional response of the structure. As shown in Figure 5-19 and Figure 5-20, string pots SP5 and SP7 were positioned such that the differential displacement could be used to calculate the rotation about the vertical z-axis (θ_z) at the top floor. For all configurations and strong motion runs, this quantity was negligibly small. A typical time history of θ_z, in this case from Configuration 1 subjected to the Design motion, is shown in Figure 5-45. Typical maximum values of θ_z were less than 0.1°. The maximum value observed was approximately 0.5° for Configuration 5 under the Extreme motion. This value was significantly larger than for any other test.

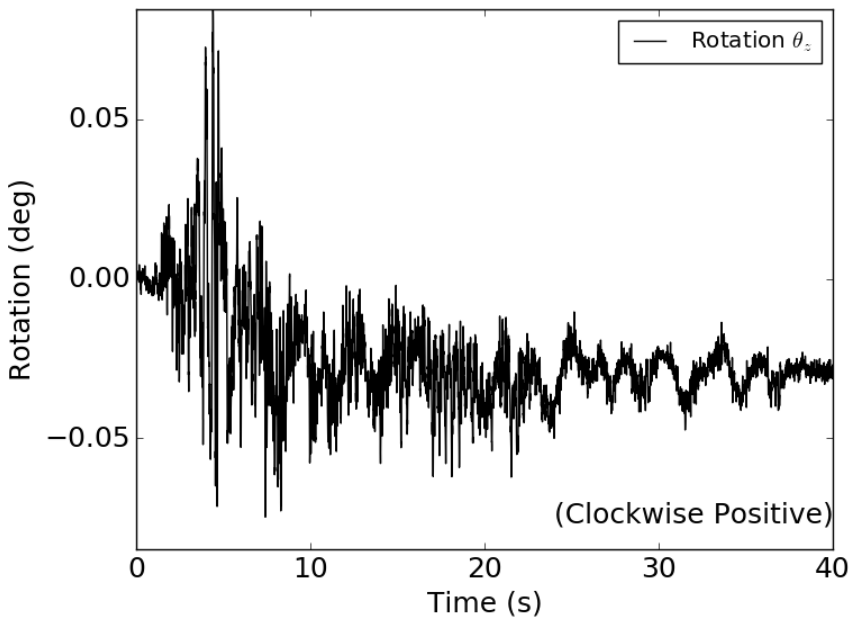

Figure 5-45: Typical time history of top floor rotation about the vertical axis, θ_z (Configuration 1 Design Motion)

Configuration 1 (BD MF)

Configuration 1 was the first configuration tested. During the testing program, there was no observed damage to the beams, columns, or braces. Photographs of the beam-column connections taken after the full test sequence are shown in Figure 5-46. The connections remained straight and square, and there was no visible damage to the clip angles or bolts after the entire motion sequence was complete. However, review of the test videos indicated that some deformation of the connections occurred, even though the connection apparently returned to its original state after shaking. The connection bolts were checked and re-tightened after each motion; however, only a few individual bolts required a minimal re-tightening.

Some minor grout cracking was observed following the Service motion, shown in Figure 5-47(a). Based on the localized nature of this cracking, it is believed that this

cracking was due to minor construction flaws at this location, and not indicative of any global tendency for the grout pads to sustain damage at this load level. At the service level motion, the anchor nuts were found to have loosened, but the plastic elongation of the anchor was barely visible to the naked eye. However, from the design motion onward, plastic anchor elongation was visible and measurable, as shown in Figure 5-47(b-d). Although there was some variability among the four baseplates, visible anchor elongation was about 1/4 in. following the Design motion, about 3/8 in. after the Maximum motion, and about 1/8 in. following the Aftershock motion.

(a) Side view (b) Top view

Figure 5-46: Configuration 1 - condition of beam-column connections at end of strong motion sequence

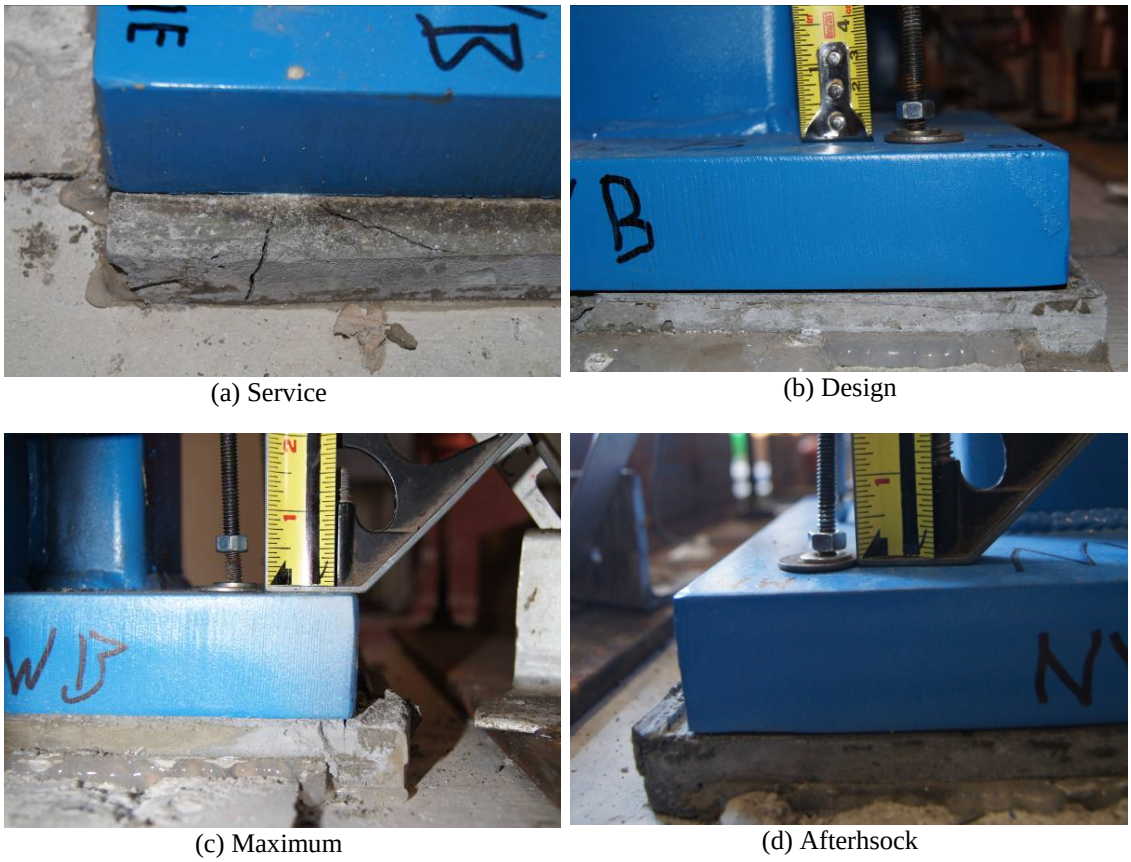

(a) Service (b) Design

(c) Maximum (d) Afterhsock

Figure 5-47: Configuration 1 - prominent anchor and/or grout damage after each of the strong motion tests

Time histories of the measured vertical baseplate displacements are shown in Figure 5-49. Note that the baseplate may be assumed rigid for the current tests, such that the anchor elongation of the north and south anchor pairs may be taken equal to the measured vertical displacement. Under this assumption, anchor elongations of up to 0.56 in. were measured during the maximum motion. The observed residual anchor elongations (Figure 5-47) were found to fit well with the maximum values measured during the test, identified with solid circles in the traces. The maximum measured anchor deformation correspond to an elongation of approximately 6.6%. Interestingly, following the Maximum motion, the NE and SE anchors on the NE baseplate could not be re-

tightened due to the nut binding on the threads, and were therefore replaced prior to the Aftershock motion. Nut failure at this level of elongation corresponds fairly well to the work presented in Chapter 2, which found that serviceability failure due to nut malfunction generally occurred between 2 and 6% elongation for larger allthread (see Figure 2-6).

Uplift at the column centerline and rotation were calculated using the kinematics shown in Figure 5-48. The uplift at the column centerline, Δ_z, and rotation of the baseplate, θ_y were calculated based on the measured north and south vertical displacements Δ_n and Δ_s as:

$$\Delta_z = (\Delta_n + \Delta_s)/2 \qquad \text{Eq. 5-3}$$

$$\theta_y = atan[(\Delta_n - \Delta_s)/s_n] \qquad \text{Eq. 5-4}$$

where s_n is the spacing of the anchors in the x-direction, which in the current work is the same as the spacing of the sensors. The uplift and rotation are plotted in Figure 5-50 for the Design and Maximum motions. The maximum column uplift for the Design case was less than 1/4 in., while for the maximum case it was nearly 1/2 in. Rotation demands under the Maximum motion were up to 3.4 degrees (0.06 rad). This level of rotation and column uplift is substantial for a connection of this type.

Strains in the beam and column were measured at the locations identified in Figure 5-21. A typical time history of the measured strains, in this case for the Design motion, is shown in Figure 5-51. Referring to the yield strains in Table 5-10, the maximum strains were less than half of yield in both cases. The maximum strain under the Maximum motion was approximately half of yield.

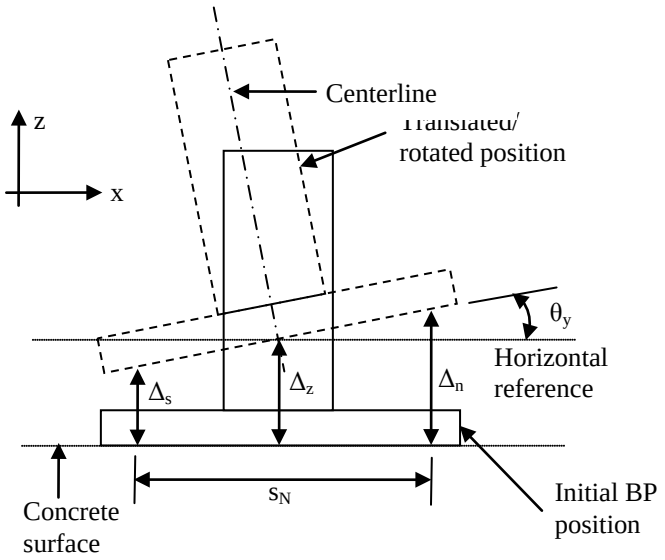

Figure 5-48: Schematic of baseplate rotation and uplift at column CL

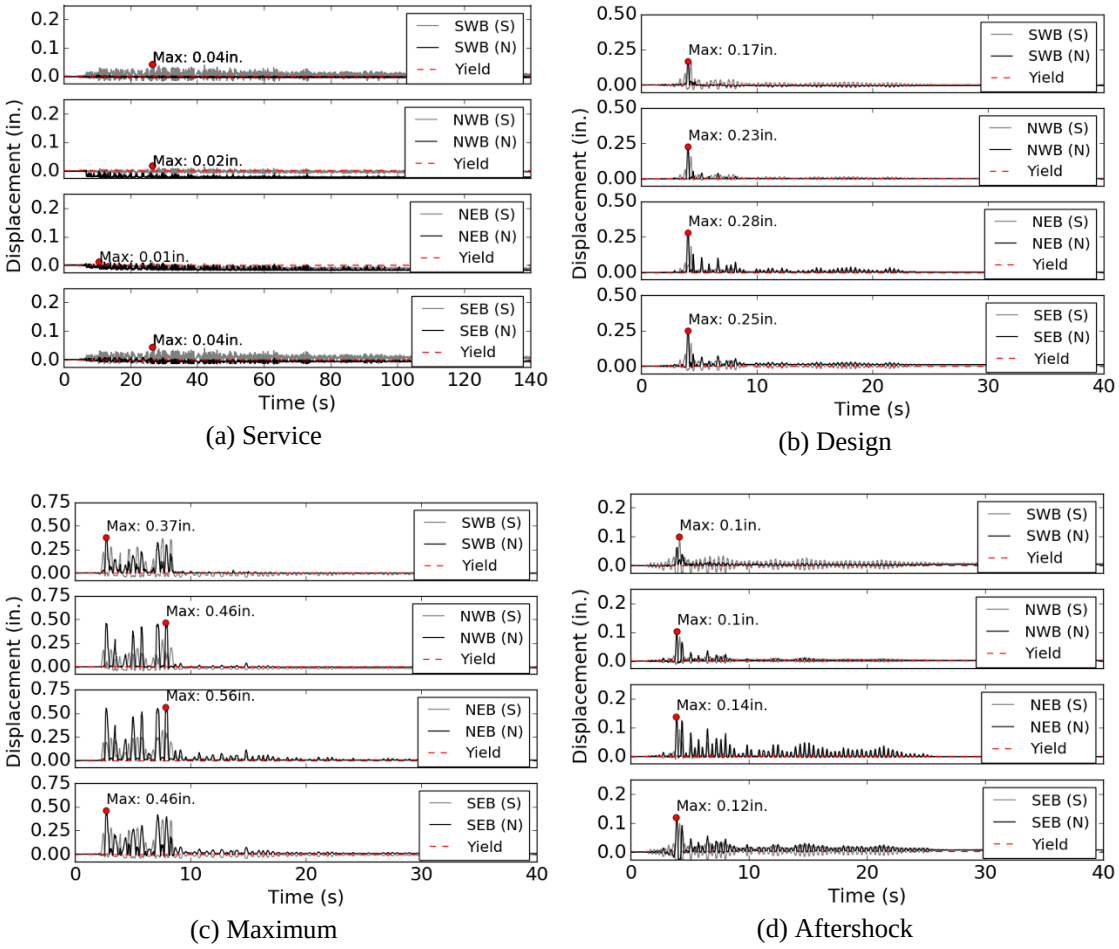

(a) Service (b) Design

(c) Maximum (d) Aftershock

Figure 5-49: Configuration 1, time history of measured vertical baseplate displacements at anchor locations under different motions

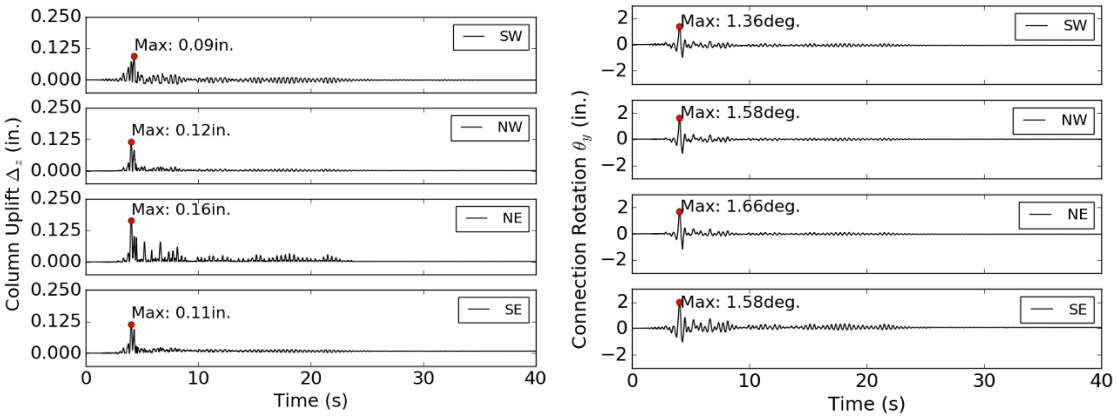

(a) Design

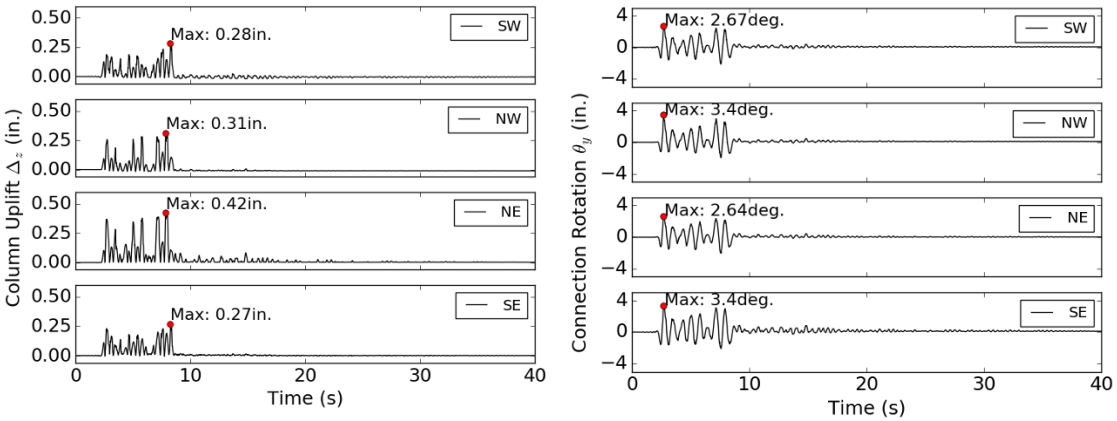

(b) Maximum

Figure 5-50: Configuration 1, time history of column uplift and baseplate connection rotation under most intense motions under most intense motions

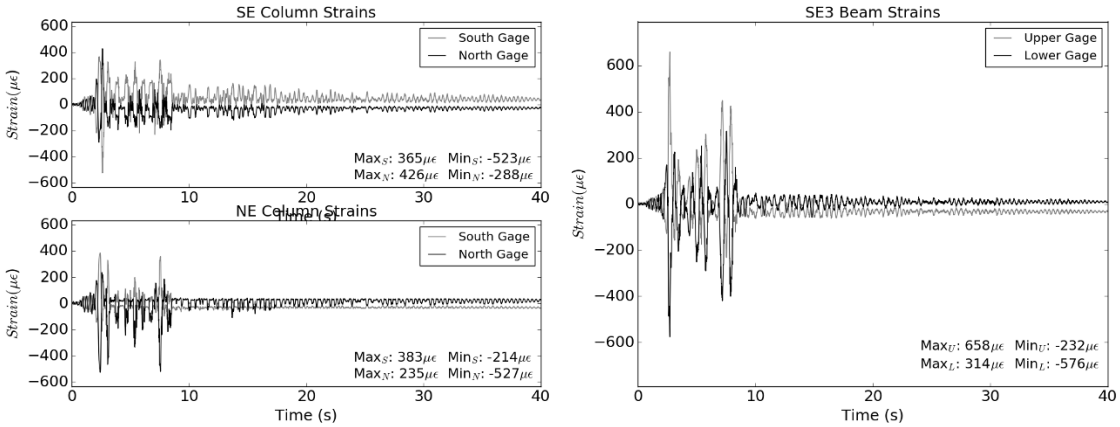

(a) SE column strains

(b) 3rd-floor beam strains (NE corner of structure)

Figure 5-51: Configuration 1, time history of strains in superstructure under design motion

Time histories of the measured horizontal baseplate displacements relative to the foundation slabs are shown in Figure 5-52. Maximum anchor displacements of up to 0.35 in. were measured during the Maximum motion, however, residual displacements were essentially negligible, indicating that the structure "came back" to its original position, which agrees with observations of the anchors and baseplate made during and after each test (Figure 5-47).

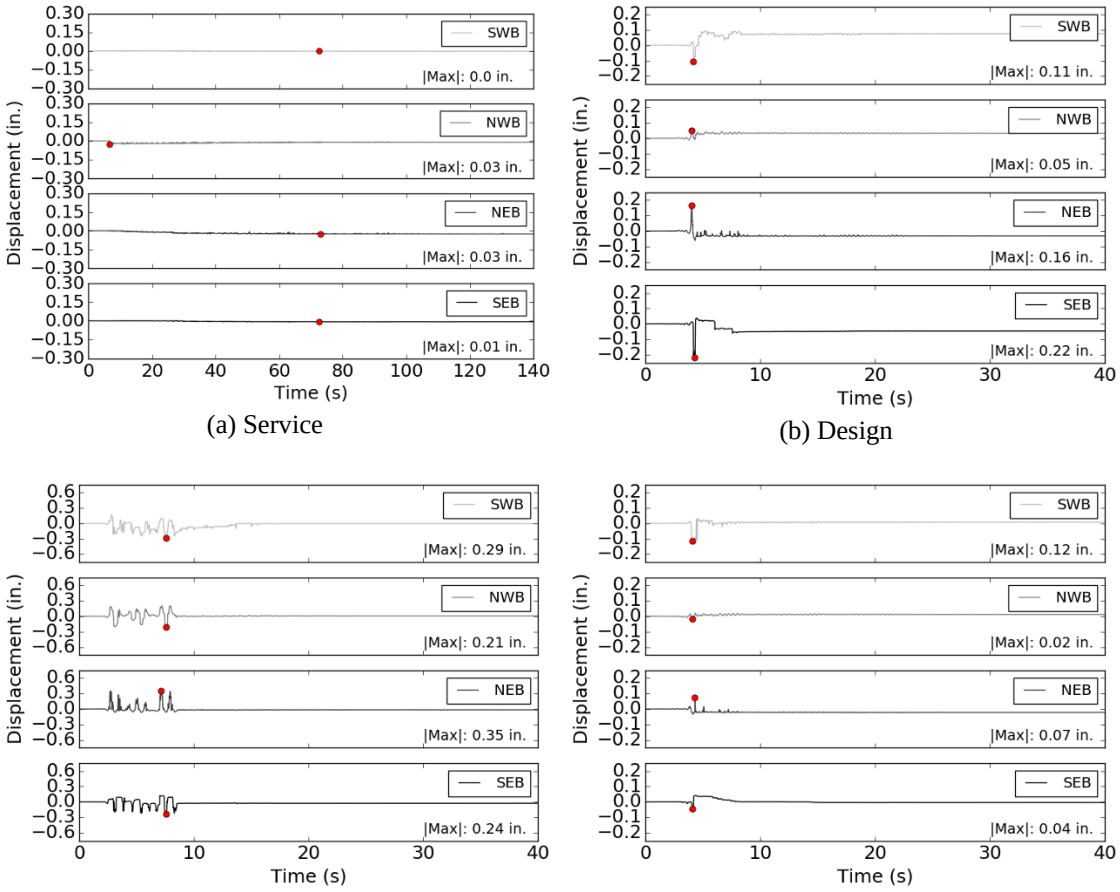

(a) Service (b) Design

(c) Maximum (d) Aftershock

Note: positive direction is north on longitudinal displacement plots

Figure 5-52: Configuration 1, time history of horizontal (x-direction) baseplate displacements

Table and floor level acceleration histories are shown in Figure 5-53. As may be expected, accelerations at the higher floors were generally higher, although there was substantial variation in the amplification that occurred depending on the motion. There was also no clear pattern regarding the direction of the maxima; for example, under the service motion all floor maxima were in the same direction and opposed to the input maximum, and under the Design motion only the top two maxima were aligned with the input peak. Under the design, maximum, and aftershock motions, the floor-level maxima were clearly correlated with a high-frequency spike in the input motion. The

consequences of this in terms of total base shear are discussed in a subsequent section. In-structure response spectra (ISRS) for each of the three floors are presented in Figure 5-54. These response spectra were generally bi-modal or tri-modal, with one peak corresponding to the peak in the input motion, one peak corresponding to the natural frequency of the fundamental mode of the structure, and one peak corresponding to high-frequency "noise" caused by table friction, as discussed previously.

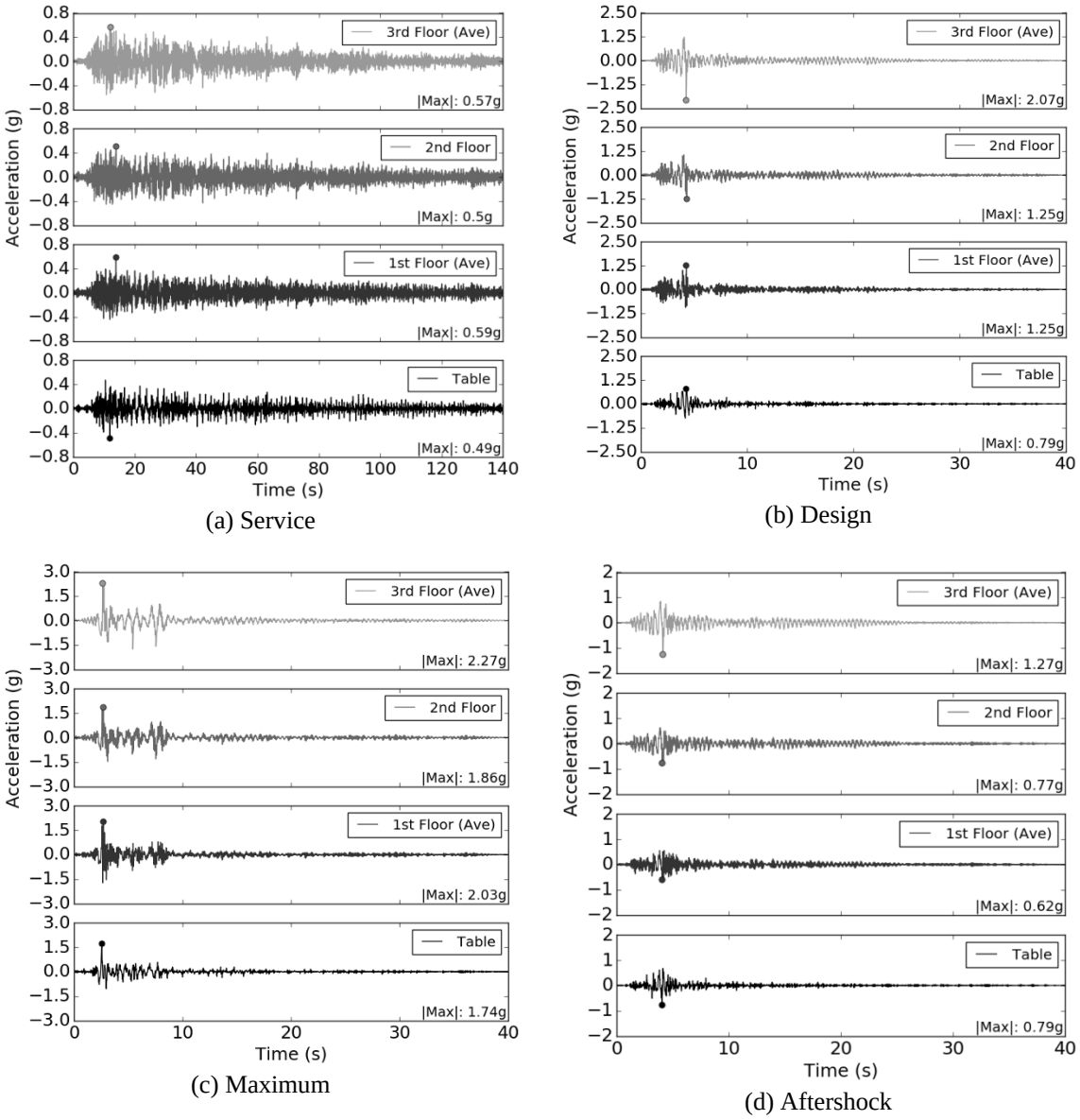

Figure 5-53: Configuration 1, ground and floor acceleration time histories for different motion cases

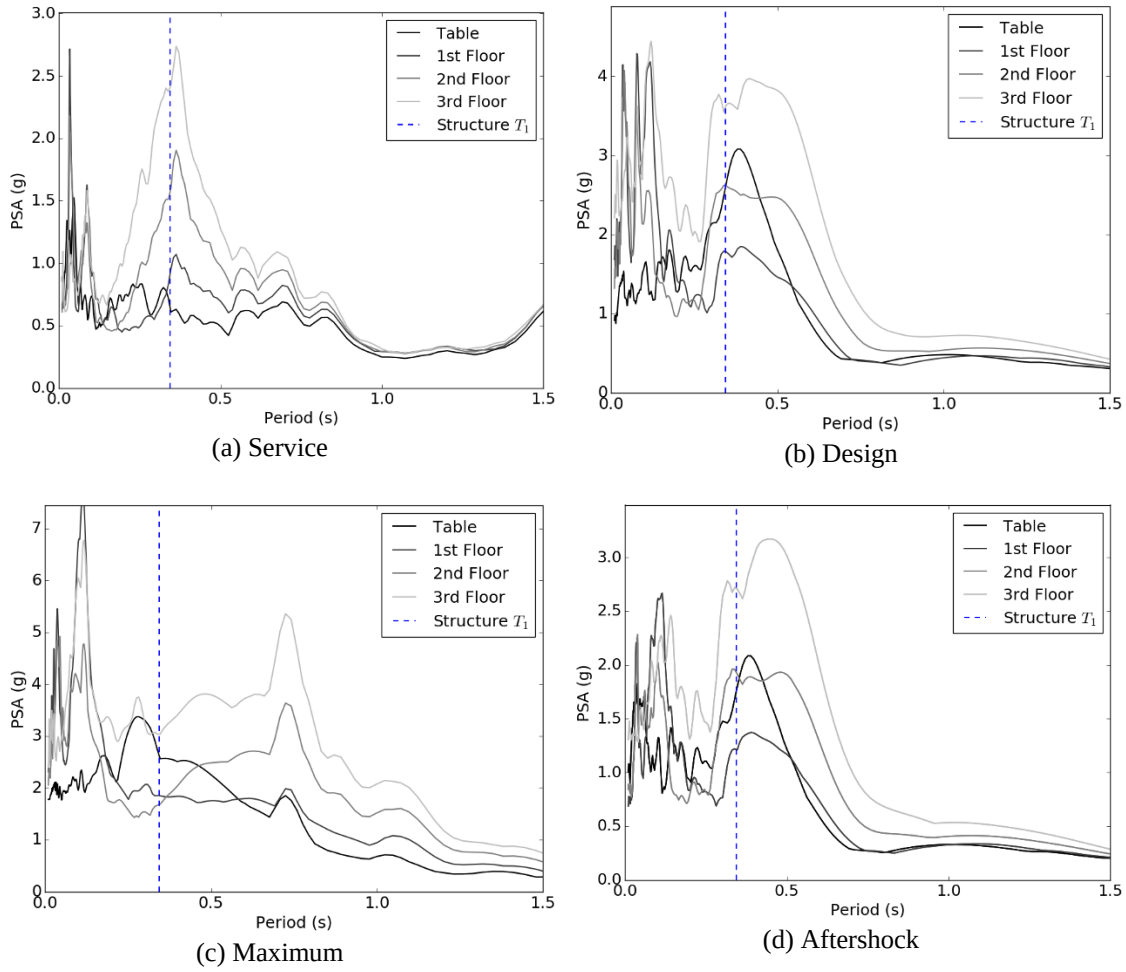

Figure 5-54: Configuration 1, 5%-damped response spectra at ground and floor levels for different motion cases

Time histories of interstory drift are presented in Figure 5-55. In all cases except for the Aftershock motion, the peak drift in the first story is on the order of 20-40% higher than the other two stories. In all cases except for the Service motion, the maximum drifts in each story occurred within a very small time window. In the case of the maximum motion, there were several cycles of large, nearly-constant drift during the strongest portion of the motion (refer to Figure 5-53 for the base acceleration time history). Based on video of the test, these large cycles were due to a global rocking mode

associated with significant baseplate uplift. Residual drifts were generally very small, with maximum values for the Service, Design, Maximum, and Aftershock motions of 0.11%, 0.06%, 0.2%, and 0.03%, respectively.

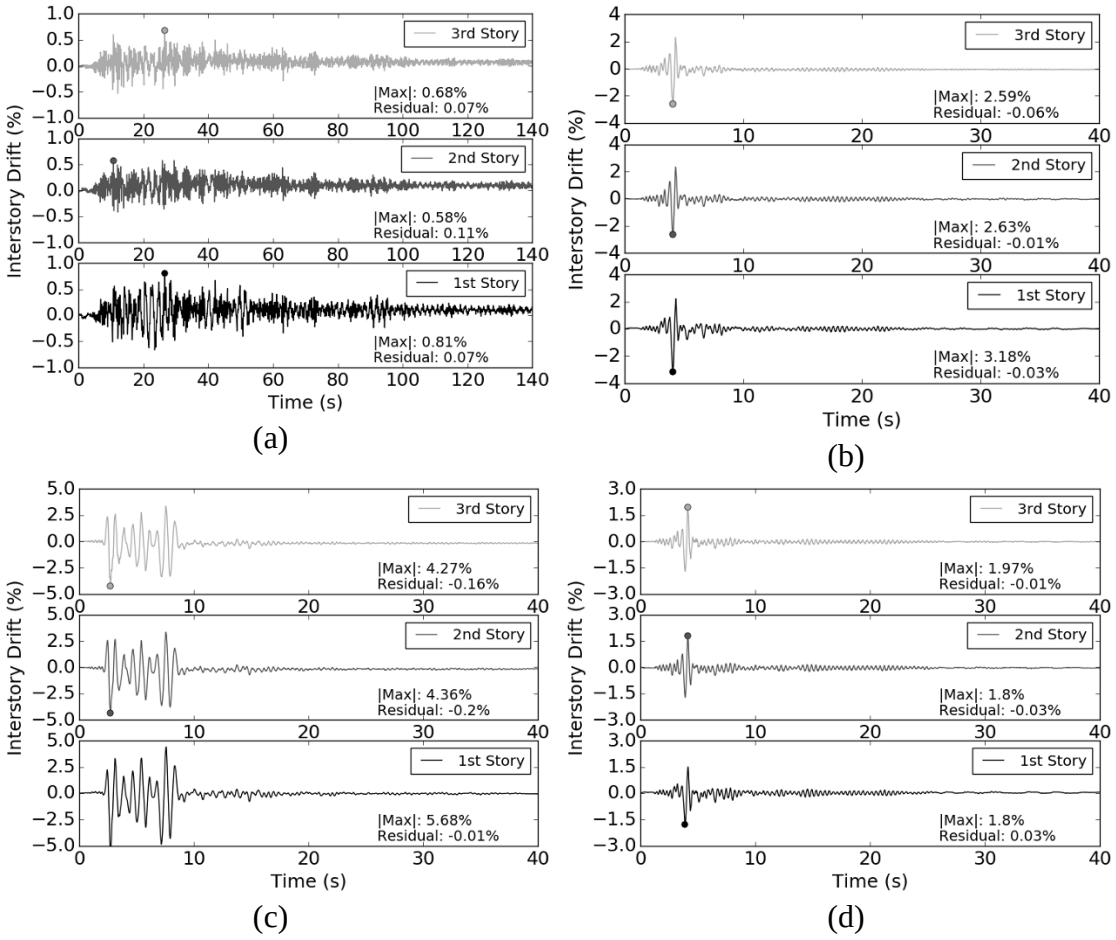

Figure 5-55: Configuration 1, interstory drifts for different motion cases: (a) Service, (b) Design, (c) Maximum, (d) Aftershock

For Configuration 1, white noise excitation was performed before and after each motion in order to:

1. Determine virgin structure mode shapes and frequencies
2. Probe changes in the dynamic properties of the system cased by damage during the strong motion runs

Smoothed transfer functions from the first white noise test performed on Configuration 1 are shown in Figure 5-56, along with picked peaks up to 30 Hz for each direction (at about 3.39Hz, 10.0Hz, 13.6Hz, 15.1 Hz, and 28.7Hz) Mode shapes associated with these frequencies were calculated using frequency domain decomposition (Brincker et al. 2001). To be used without rigorous checks of modal shape, this method requires assumptions of well-separated modes and small damping, assumptions that are met by the current structure. Mode shapes recovered using this method, then suitably post-processed and normalized are shown in Figure 5-57. The first and third modes were associated with motion in the x-direction (shaking direction). The second mode was the fundamental mode in the y-direction (transverse direction), and the fourth mode was associated with torsion. This mode shape was significantly less distinct than the others, because the structure had no intentional torsional irregularity, and therefore was not directly excited by the x-direction white noise or the incidental vibration of the structure and table in the y-direction. Although not shown in the figure, the fifth mode (around 30 Hz) was the third x-direction mode.

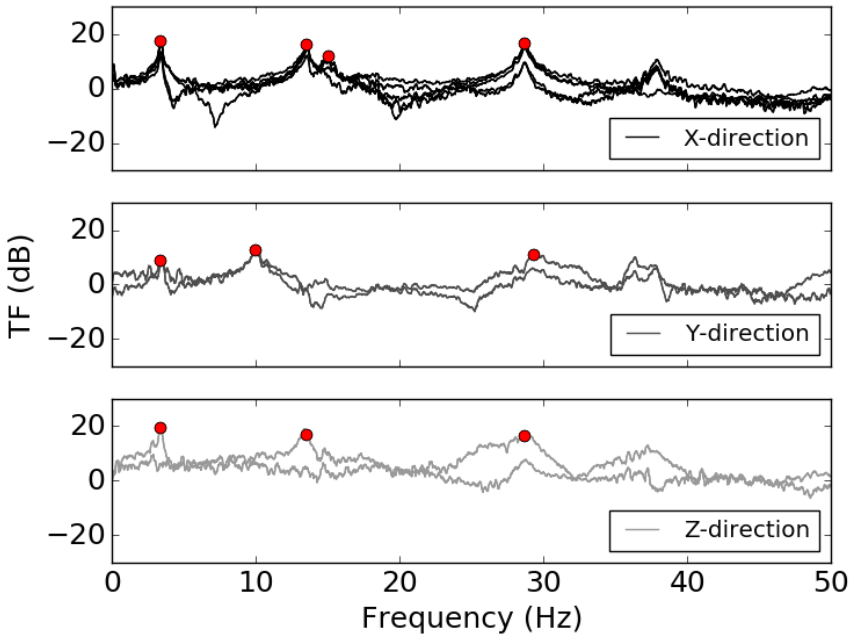

Figure 5-56: Configuration 1, transfer functions and picked peaks from all structure-mounted accelerometers for first white noise test

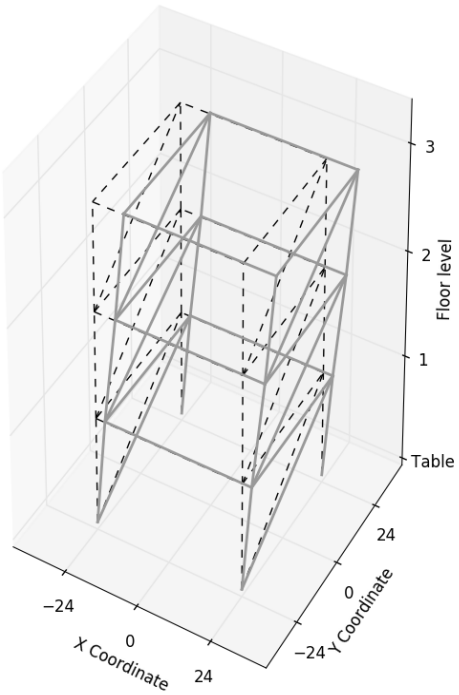

(a) Mode 1: Fundamental x-dir. (3.39Hz)

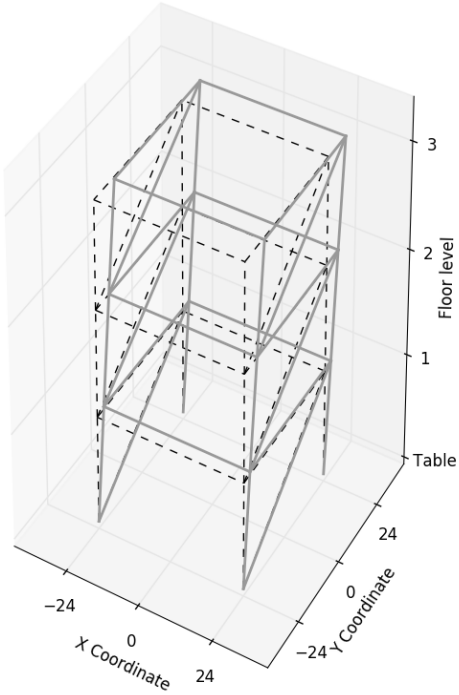

(b) Mode 2: Fundamental y-dir (10.0Hz)

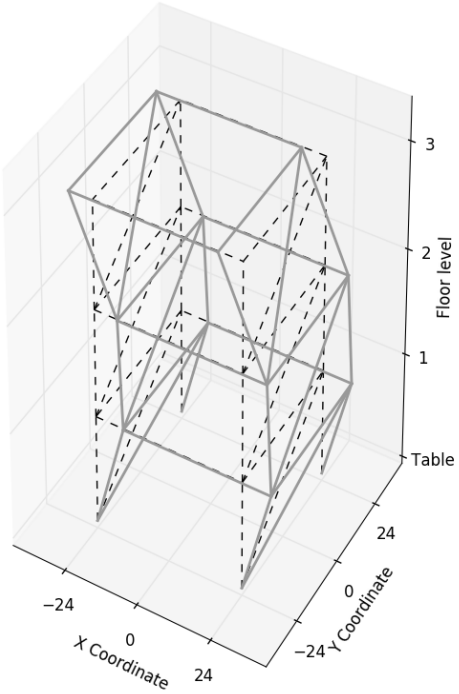

(c) Mode 3: Second x-dir (13.6Hz)

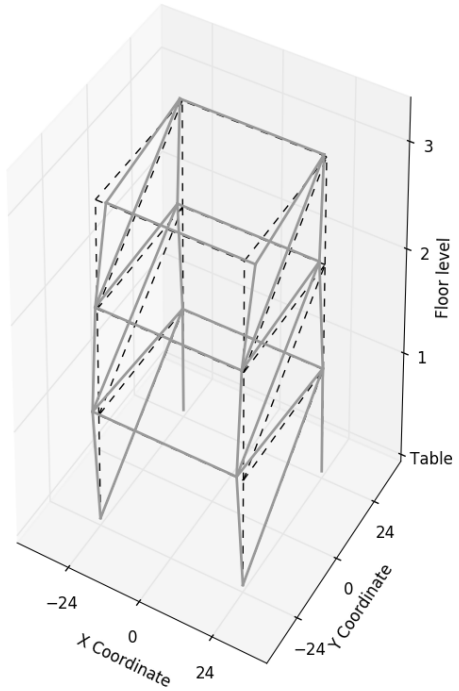

(d) Mode 4: Torsion (15.1Hz)

Figure 5-57: First four modes of Configuration 1, identified from white noise tests

The transfer function estimates from the average of the x-direction, top floor accelerometers (A3 and A7) from white noise tests conducted before and after each strong motion run are shown in Figure 5-58. There were significant drops in all three prominent modal peaks, corresponding to modes 1, 3, and 4 above (the first and second x-direction modes and the torsional mode). The average drop was about 12% for the first mode and 9% for the second mode (Table 5-13). The x-direction modal shapes ϕ_1 and ϕ_3 are reduced to only the x-direction degree of freedom in Figure 5-59. Note that the modal coordinates plotted have been normalized such that the 3rd floor coordinate, ϕ_{n3} is 1.0. The first mode shape is not significantly affected by the loss of rotational restraint caused by anchor loosening. However, the second mode shape becomes somewhat "flatter" in the anchors loose configuration. This change in mode shape is attributed to the loss of rotational restraint, which causes a change from more "whip-like" behavior to more gentle bending.

The drop in frequency associated with both modes was believed to be due to the change in boundary conditions caused by elongation of the anchors during the test. However, it is possible that loosening or slip of the double clip angle connections or other structural damage could have contributed to the change in observed frequencies. To test this, following the final strong motion test, the structure was left in the "anchors loose" configuration, and successively stronger white noise was applied to the structure (0.75%, 1.5%, 3%, and 4%g RMS, see Appendix D). If the change in frequency were due to damage or connection slip or loosening in the superstructure, it would be expected that

the TF estimates from successively more intense motion would reveal frequency drops similar to those observed in the "before and after" tests from each strong motion run. There was a drop of about 5% observed between the 0.75%g and 4.0% g test for the first mode, and about 1% for the second mode (Figure 5-60). These values are within the variability of the first mode estimates from identical structure configurations in the other white noise tests (Table 5-13). Moreover, 4.0%g RMS was the upper bound of white noise intensity that was expected not to result in plastic anchor stretch. Following testing, two anchor bolts (the SW bolt on the SW and NW baseplates) were found to be slightly loose, which probably contributed to this small frequency change. Therefore, the changes in frequencies observed from the white noise tests conducted before and after each strong motion test are ascribed predominantly to the loosening of the anchor bolts and the subsequent change in boundary conditions, and not in-structure loosening of connections. There were no significant changes to the mode shapes found in each of these tests.

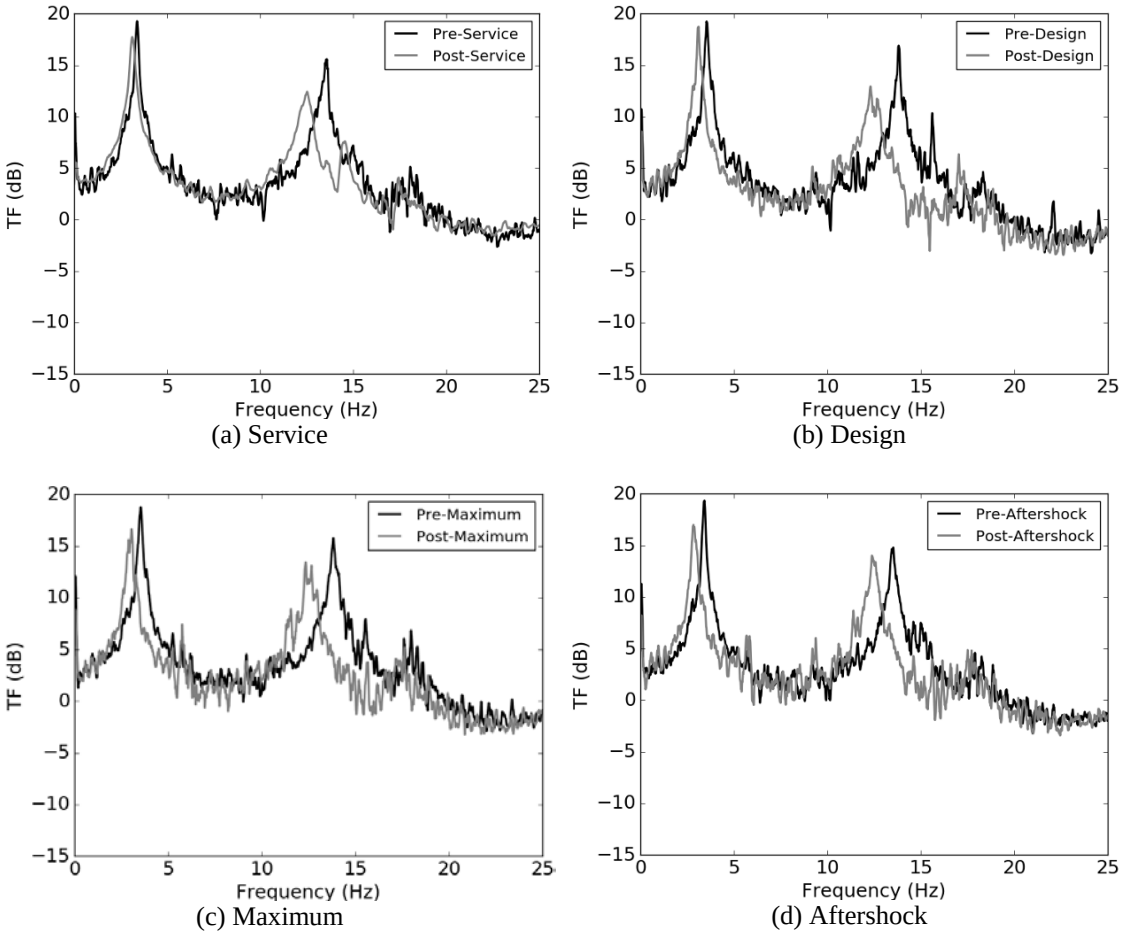

Figure 5-58: Top floor, x-direction transfer function estimates pre-and post-test

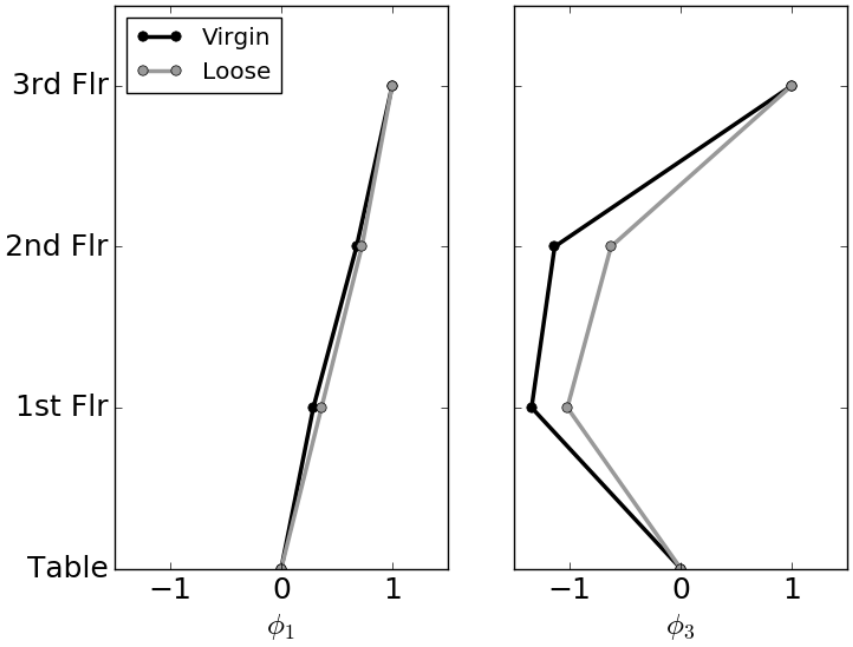

Figure 5-59: Typical virgin and "anchors loose" x-direction mode shapes for Configuration 1

Table 5-13: Change in natural frequency for first and second x-direction modes for Configuration 1

Motion	Prior f_1, Hz [T_1, s]	After f_1, Hz [T_1, s]	Prior f_3, Hz [T_2, s]	After f_3, Hz [T_2, s]
Service	3.39 [0.295]	3.13 [0.320]	13.58 [0.0736]	12.53 [0.0798]
Design	3.53 [0.283]	3.10 [0.323]	13.82 [0.0724]	12.30 [0.0813]
Maximum	3.54 [0.282]	3.05 [0.328]	13.81 [0.0724]	12.50 [0.0800]
Aftershock	3.42 [0.292]	2.88 [0.347]	13.53 [0.0739]	12.38 [0.0808]
Average:	3.47 [0.288]	3.04 [0.329] *(-12.4%)*	13.69 [0.0731]	12.43 [0.0805] *(-9.2%)*

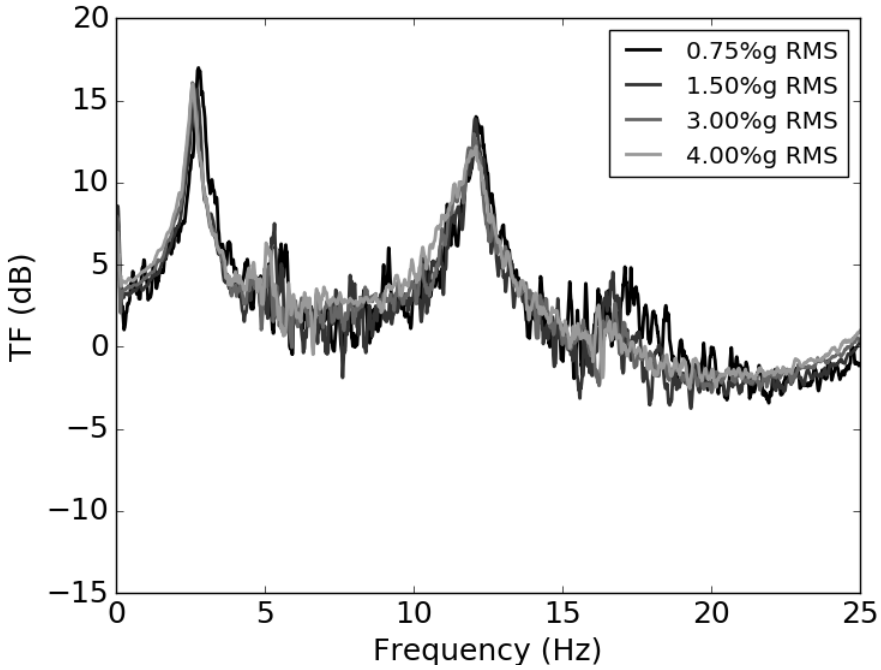

Figure 5-60: Configuration 1 transfer function estimates from Configuration 1 ("bolts loose"), white noise tests with increasing amplitude

Although damping may be estimated using the frequency domain decomposition method used to identify mode shapes, impulse tests provide an easier and more direct route to determine modal damping ratios. Impulse tests were conducted in each structural configuration prior to the white noise tests. The structure was instrumented with six auxiliary accelerometers on the north face of the structure, shown and numbered in Figure 5-61. Accelerometers were located on the north face of the columns, centered at the elevation of the beams. Note that the photograph shown was taken without the second mass, which was put into position prior to testing. The structure was excited via manual impacting with a heavy mass on the north side of the structure. The recorded acceleration

histories were then filtered to isolate the waveforms associated with each mode, and the log decrement method was used to estimate the modal damping ratio. The log decrement δ is defined as the logarithm of successive amplitude peaks, in this case acceleration in the x direction $\ddot{u}$, and may be related to the modal damping ratio ξ if the response is confined to a single mode:

$$\delta = \ln\left(\frac{\ddot{u}_i}{\ddot{u}_{i+1}}\right) = 2\pi\,\xi \qquad \text{Eq. 5-5}$$

For peaks that are j cycles apart, the damping ratio may be resolved as:

$$\xi = \frac{1}{2\pi \cdot j}\ln\left(\frac{\ddot{u}_i}{\ddot{u}_{i+j}}\right) \qquad \text{Eq. 5-6}$$

The time histories from sensors 5 and 6 were used, as these were highest on the structure and contained the clearest waveforms. The acceleration histories and points used in the log decrement calculation are shown in Figure 5-67. Note that because the amplitude of the vibration associated with the second mode first decreases, then increases. This is most likely due to a "double tap" from the imposed excitation. However, based on the points taken from the decreasing part of the response, the calculated modal damping ratios are ξ_1=1.7% and ξ_1=1.0%.

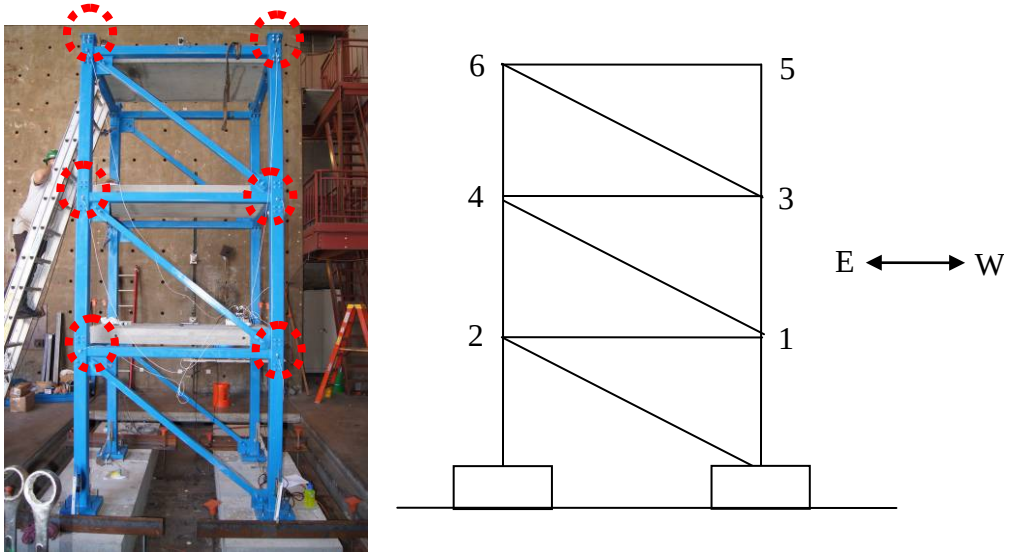

(a) Location (b) Numbering

Figure 5-61: North elevation of auxiliary accelerometers for impact tests

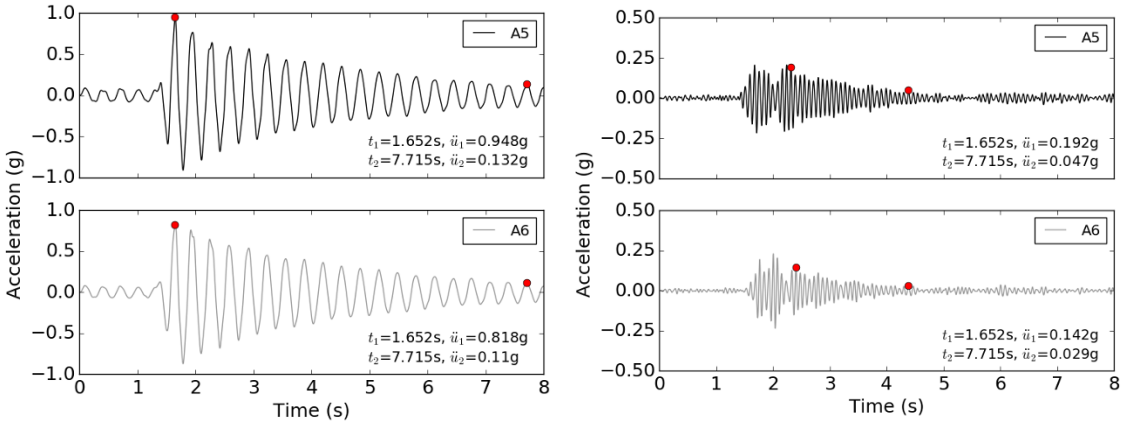

(a) First natural frequency (b) Second natural frequency

Figure 5-62: Configuration 1 - Filtered acceleration histories and points used for log decrement calculation

Configuration 2 (SD MF)

In contrast to Configuration 1, Configuration 2 was characterized by negligible baseplate connection damage and progressively increasing superstructure damage. A photograph of the condition of the SE connection following the full suite of motions,

which was typical of the condition of all connections, is shown in Figure 5-63. No grout damage or cracking occurred during any tests, and there was no visible elongation of the anchors. Anchors were checked for tightness and did not require re-tightening at any point during the test sequence. Typical time histories of the measured baseplate displacements are shown in Figure 5-64. Horizontal displacements in the shaking direction (x-direction) were less than 0.001 in., and measured vertical displacements were less than 0.01 in. Therefore, it may be concluded that the baseplates and anchors performed as intended, and neither yielded nor moved during the test sequence.

The column fuses visibly yielded during the Design and Maximum motions, but were not observed to yield during the Service and Aftershock motions. Photographs of the fuse plates following three of the motions are shown in Figure 5-65. For all cases, yielding was confined to a single side of each plate, corresponding to the region with highest stress concentration. Unfortunately, the whitewash applied to the beam fuses did not reveal any visible yielding. It is believed that no flaking of the whitewash occurred because of the lack of mill scale on the HSS sections used for this work, which prevents the white wash from scaling off. However, following the Maximum motion, residual fuse rotation was visible to the naked eye, as shown in Figure 5-66.

Figure 5-63: Configuration 2 - typical condition of baseplate connection in following all strong-motion tests

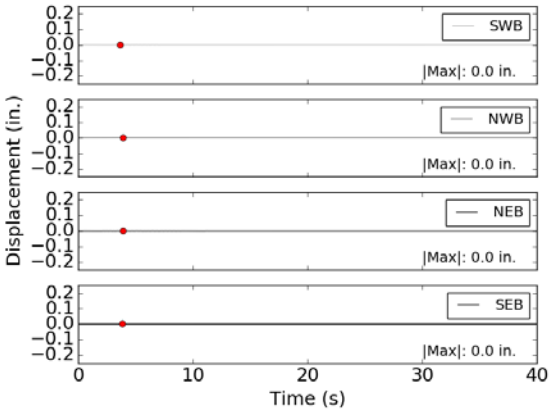

(a) Longitudinal horizontal displacement

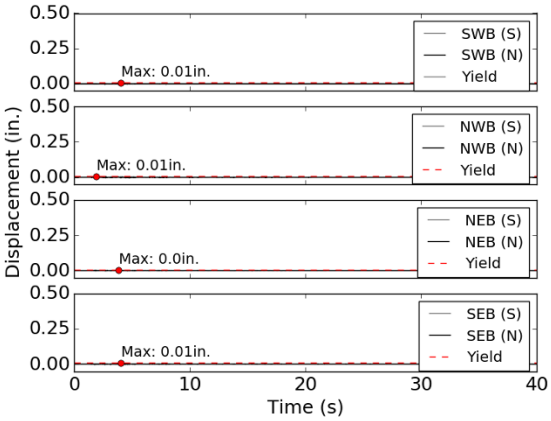

(b) Vertical displacement

Figure 5-64: Typical measured horizontal baseplate displacements for Configuration 2 [Design motion shown]

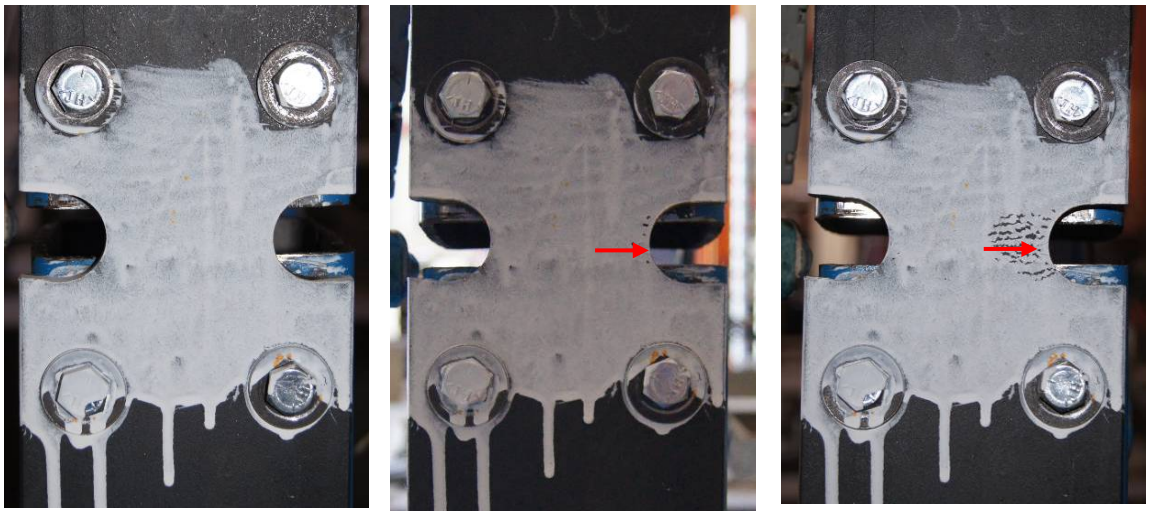

NOTE: arrow highlights regions of visible paint flaking/yielding

Figure 5-65: Configuration 2 - condition of column fuse plate following Service, Design, and Maximum motions (from left to right)

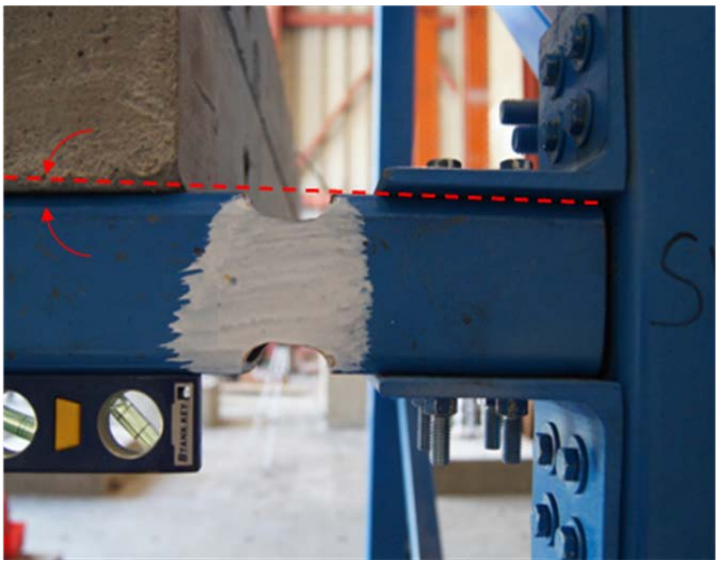

Figure 5-66: Configuration 2 - visible rotation of 1st-floor fuse in SW corner following Maximum motion

Residual structural drift was visually observed following the Design and Maximum motions, as shown in Figure 5-67. Interestingly, the maximum drift in each motion was similar to that measured in Configuration 1, however the residual interstory

drifts were on the order of 0.1% following the Service motion, 0.25% following the Design motion, and 1.75% following the Maximum motion. Note that these values are not cumulative (i.e. the sensors were re-biased prior to each motion). Residual drift due to the Aftershock motion was essentially negligible. In contrast to Configuration 1, the maximum drift in the Maximum motion was from a single, distinct cycle rather than a series of cycles associated with global rocking motion.

Time histories of the measured floor accelerations are shown in Figure 5-70. In general, maximum floor accelerations were somewhat smaller than for Configuration 1. Notably, the magnitude of accelerations immediately following the peak acceleration were significantly smaller than for Configuration 1. The ISRS, shown in Figure 5-71, were generally similar in shape to those associated with Configuration 1. The maxima of the ISRS were similar for all motions, except for the Maximum motion, which was significantly higher. The exact mechanisms responsible for the difference in behavior between Configuration 1 and Configuration 2 are discussed in a following section.

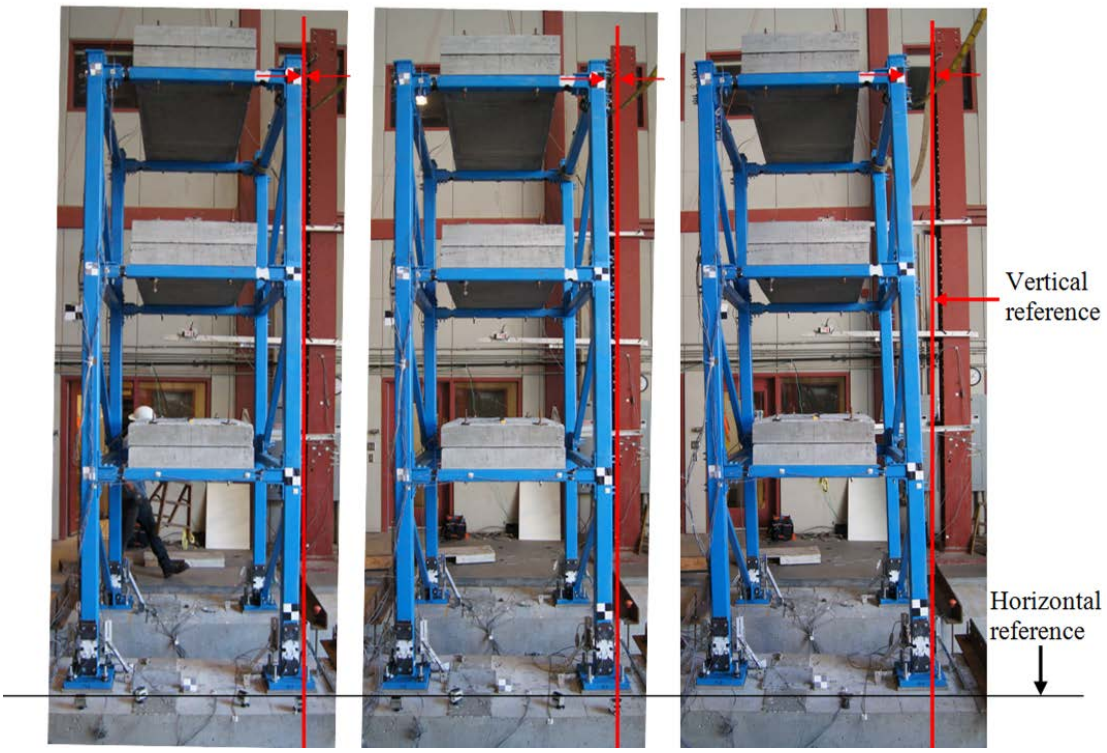

Figure 5-67: Configuration 2 - Visible residual drift following Service, Design, and Maximum motions (from left to right)

The time histories of the measured beam and column strains for the Design motion are shown in Figure 5-51. The maximum measured column strains were very near yield, while the beam strains were about 5 times yield. Shell-element modeling of the Configuration 2 beam cutout geometry, discussed in Chapter 4, indicates that the measured strains for this cases were close to the maximum strains in the cutout section. Unfortunately, the strain readings for the beam gages exceeded the maximum that could be measured by the system, due to a relatively high initial gain that was used for the expected strain range. Therefore, the maximum strain from the Design and Maximum motions is only known to be above the maximum cutoff point.

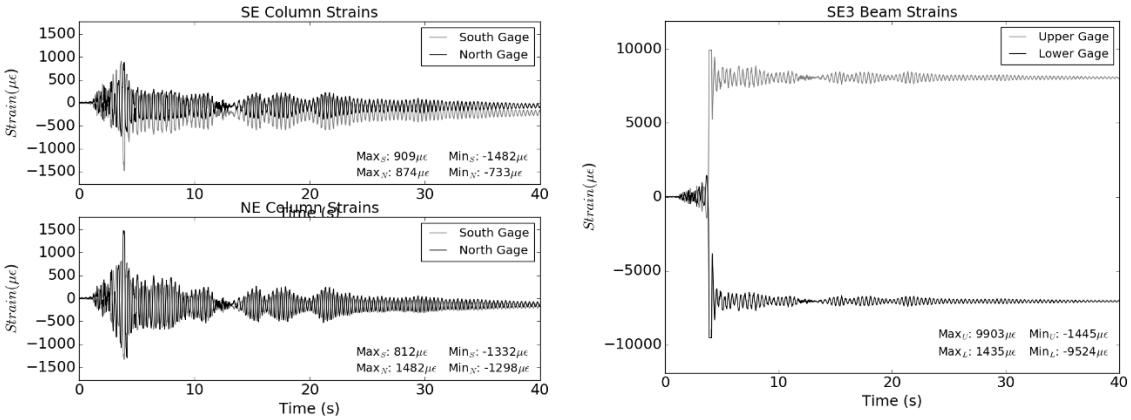

(a) SE column strains

(b) 3rd-floor beam strains (NE corner of structure)

Figure 5-68: Configuration 2, time history of strains in superstructure under design motion

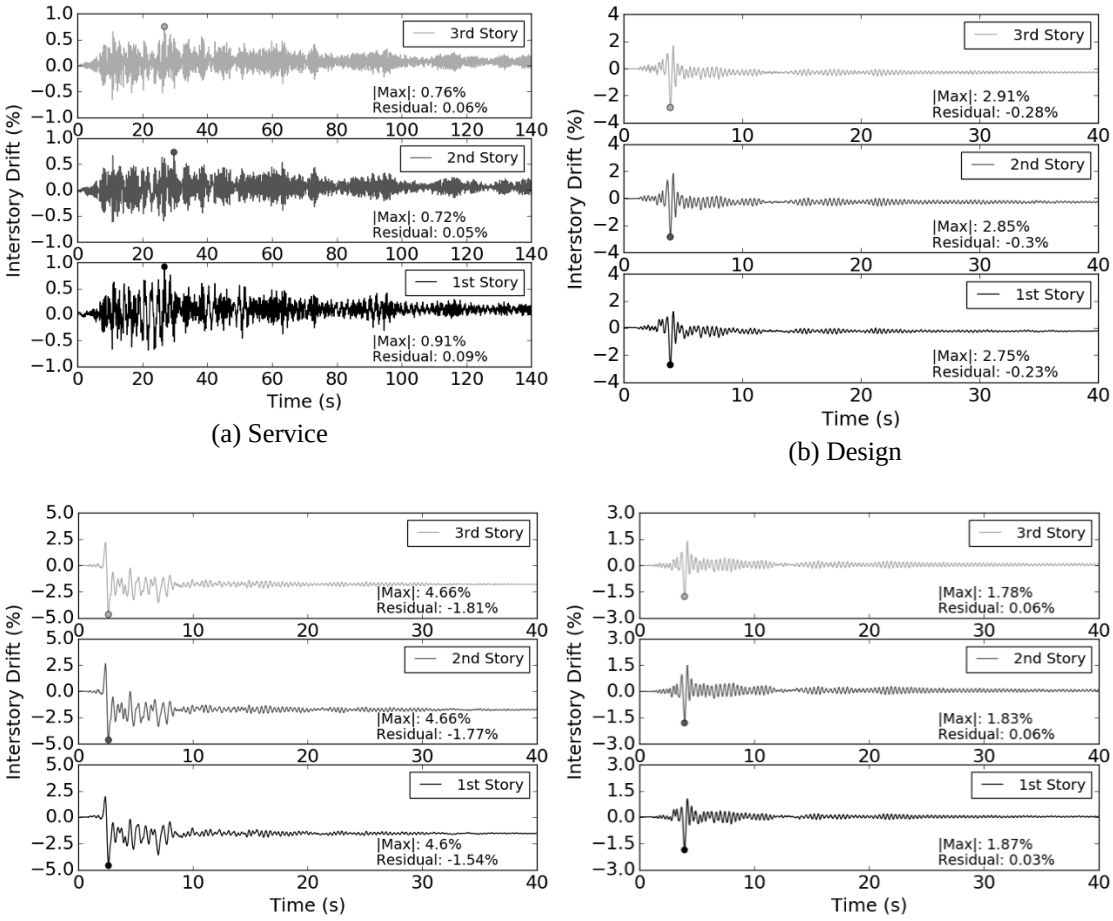

Figure 5-69: Configuration 2, interstory drifts for different motion cases

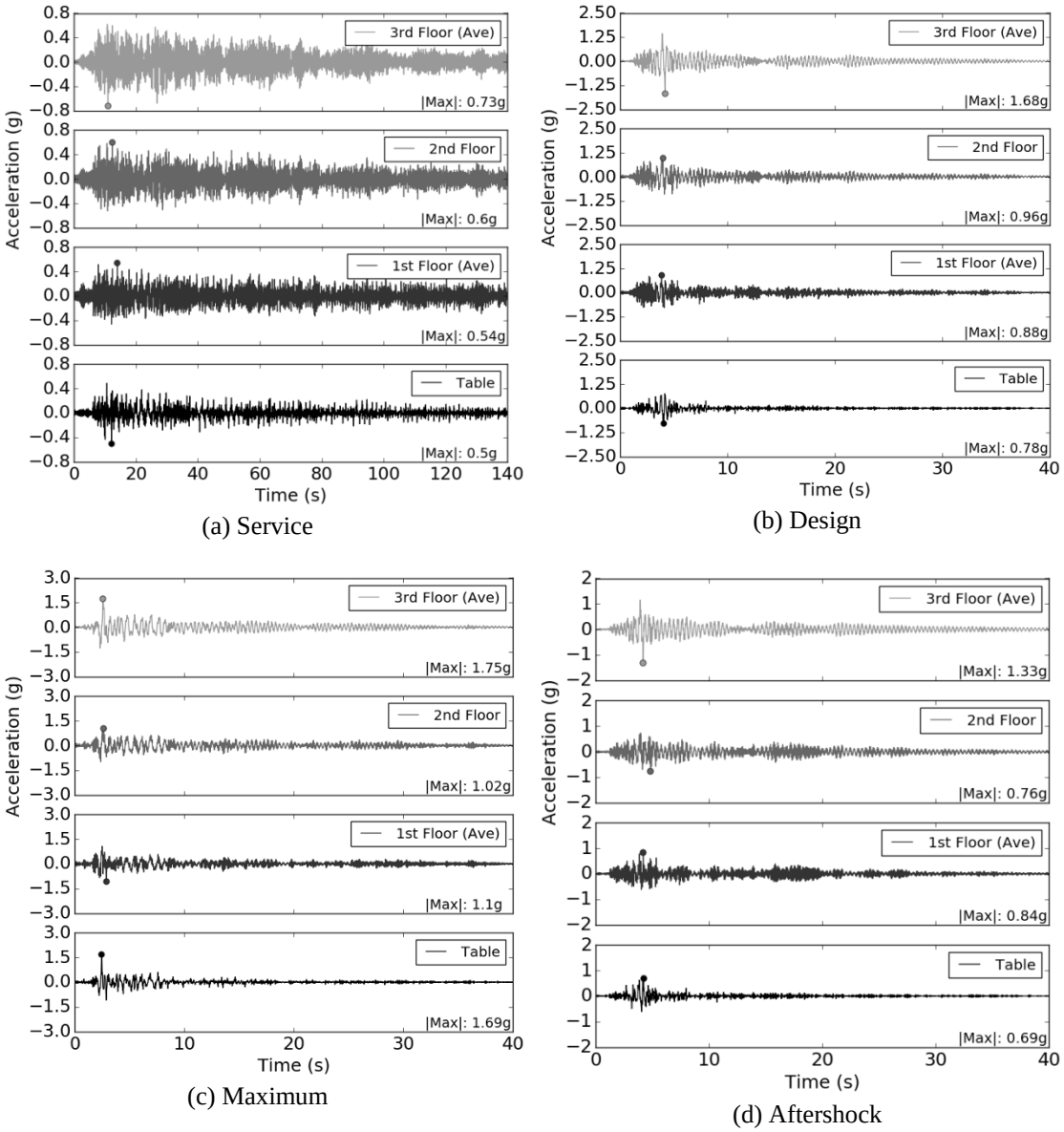

Figure 5-70: Configuration 2, ground and floor acceleration time histories for different motion cases

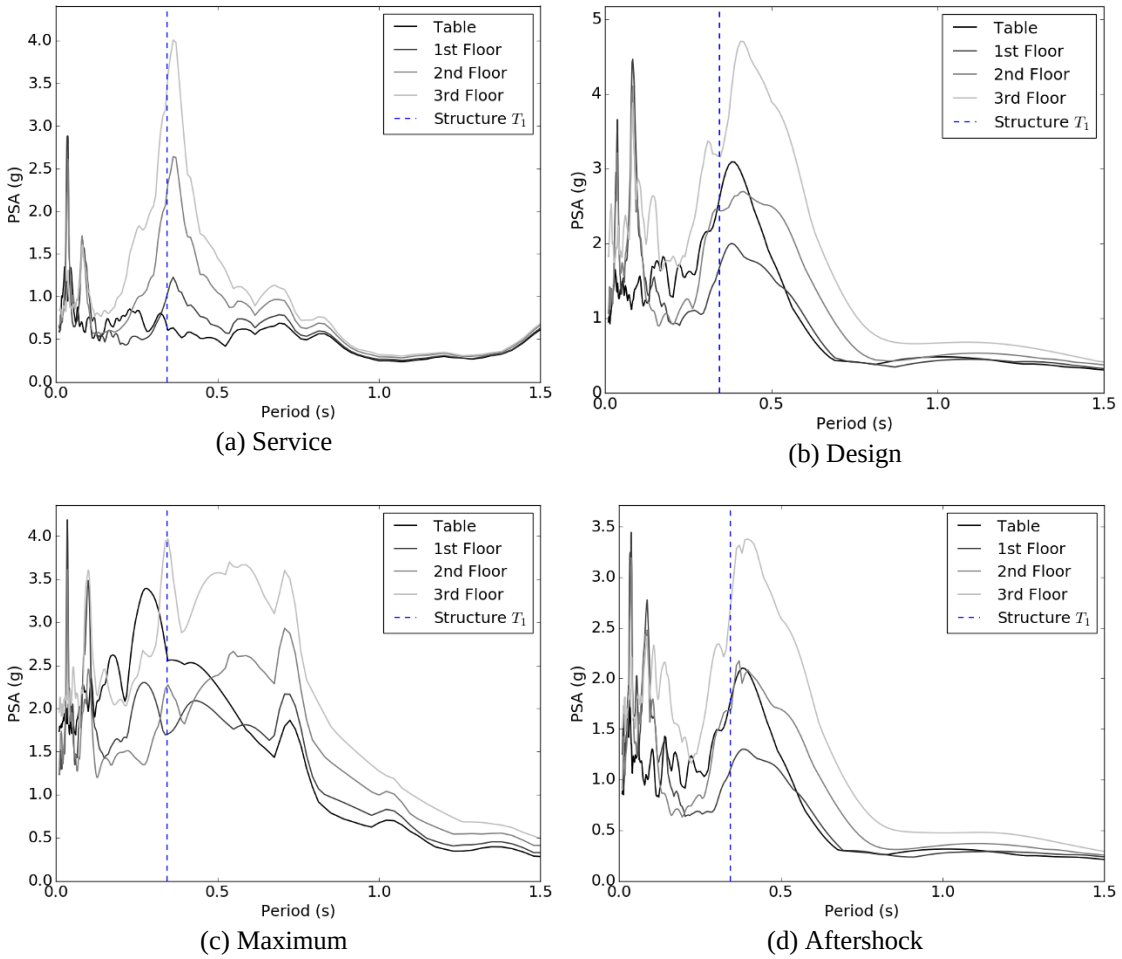

Figure 5-71: Configuration 2, 5%-damped response spectra at ground and floor levels for different motion cases

Because no loosening of the anchor bolts was observed or measured during strong-motion testing, significant changes in the dynamic properties of the system were not expected. Therefore, Configuration 2 was subjected to white noise testing at the beginning of testing, and then only once between each strong motion test. These tests are shown in Figure 5-72. The difference in transfer function peaks was less than 2% for all tests. There were no significant changes in mode shapes calculated for any of the tests. Therefore, it may be concluded that there were no appreciable changes in the dynamic

properties of the system due to anchor yielding, bolt loosening, or other superstructure connection damage.

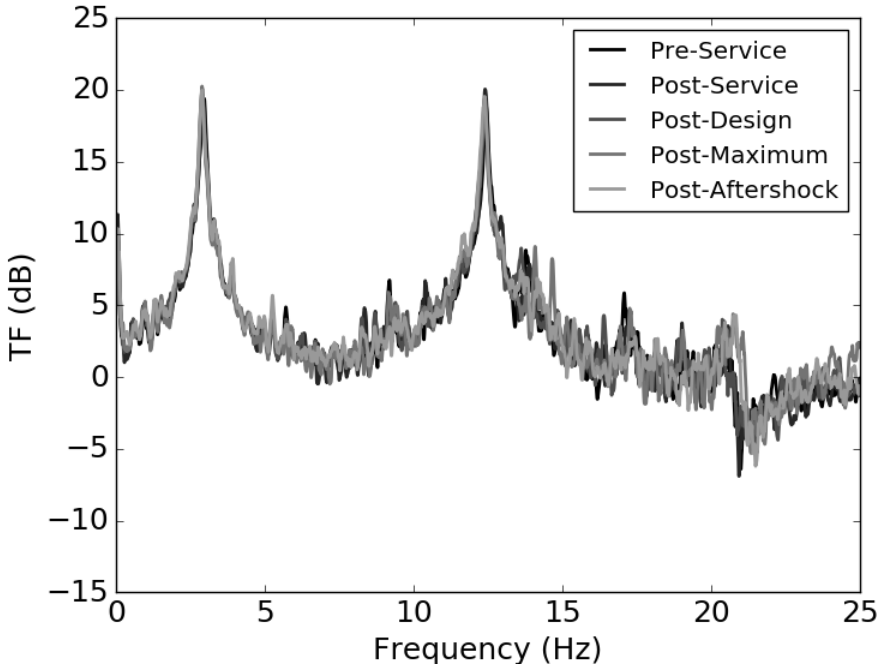

Figure 5-72: Configuration 2 white noise testing (all)

Table 5-14: Average of first and second natural frequency for Configuration 2

WN Test	f_1, Hz [T_1, s]	f_2, Hz [T_2, s]
Pre-Service	2.95 [0.339]	12.44 [0.0804]
Post-Service	2.90 [0.3448]	12.40 [0.0806]
Post-Design	2.89 [0.346]	12.39 [0.0807]
Post-Maximum	2.89 [0.346]	12.40 [0.0806]
Post-Aftershock	2.90 [0.345]	12.39 [0.0807]
Average:	2.91 [0.344]	12.40 [0.0806]

Impact testing of Configuration 2 was performed with the same instrumentation setup as for Configuration 1 (see Figure 5-62). The filtered acceleration histories used for the log decrement calculation are shown in Figure 5-73. The calculated first and second mode damping ratios were calculated to be 0.8% and 0.5%, respectively. These damping

ratios are significantly lower than those found for Configuration 1. There are several possible reasons for this, however it is likely that the relatively flexible base connection of Configuration 1 allows more motion of the baseplate relative to the foundation slab and more energy dissipation. In addition, the relatively flexible and weak beam fuse connections of Configuration 2 transmit only small moments to the clip angle connections, resulting in less connection slip (and therefore less apparent damping). The effect of the connection flexibility and damping ratio on the structure performance is discussed in the context of numerical modeling later in this chapter.

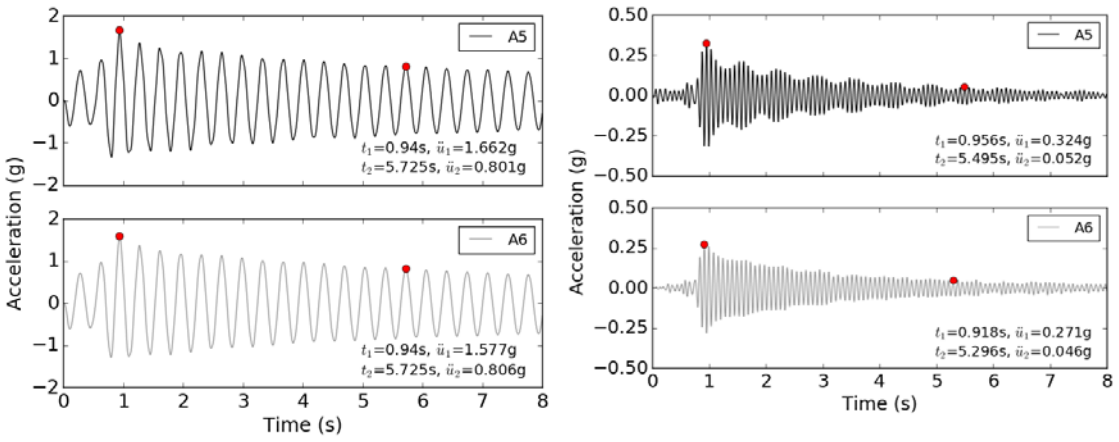

(a) First x-direction natural frequency

(b) Second x-direction natural frequency

Figure 5-73: Configuration 2 - Filtered acceleration histories and points used for log decrement calculation

Configuration 3

Configuration 3 was characterized by behavior that was generally intermediate to that of Configuration 1 and Configuration 2. Significant numbers of anchors loosened following each motion, however the magnitude of the observed anchor elongations was significantly smaller than for Configuration 1. The typical condition of the baseplate connections following the Service, Design, and Maximum motions is shown in Figure

5-74. Very limited grout cracking was observed in the SE connection following the design motion, and no other grout damage was observed. Note that in the NE connection, some significant bending of the anchor was observed (NE anchor, nearest the vertical scale in the photograph). This behavior was not observed anywhere else in the test program, and may have been due to chance placement of the anchor near the baseplate hole in this instance. This supposition is supported by measurements of the horizontal (x-direction) baseplate movement, shown in Figure 5-75. The maximum movement measured in the maximum case was approximately half that measured in Configuration 1, where no anchor bending was observed. In the vertical direction, measured baseplate displacements (corresponding to anchor elongations) were less than half that measured in Configuration 1, up to a maximum of about 0.18 in. under the Maximum motion. However, as with Configuration 1, a series of relatively high-amplitude peaks were observed. However, based on a review of video from the tests, the motion causing these peaks appeared not to be associated with global rocking, but rather a frame mode in this case.

Figure 5-74: Configuration 3 - Typical condition of baseplate connections following Service, Design, and Maximum motions (from left to right)

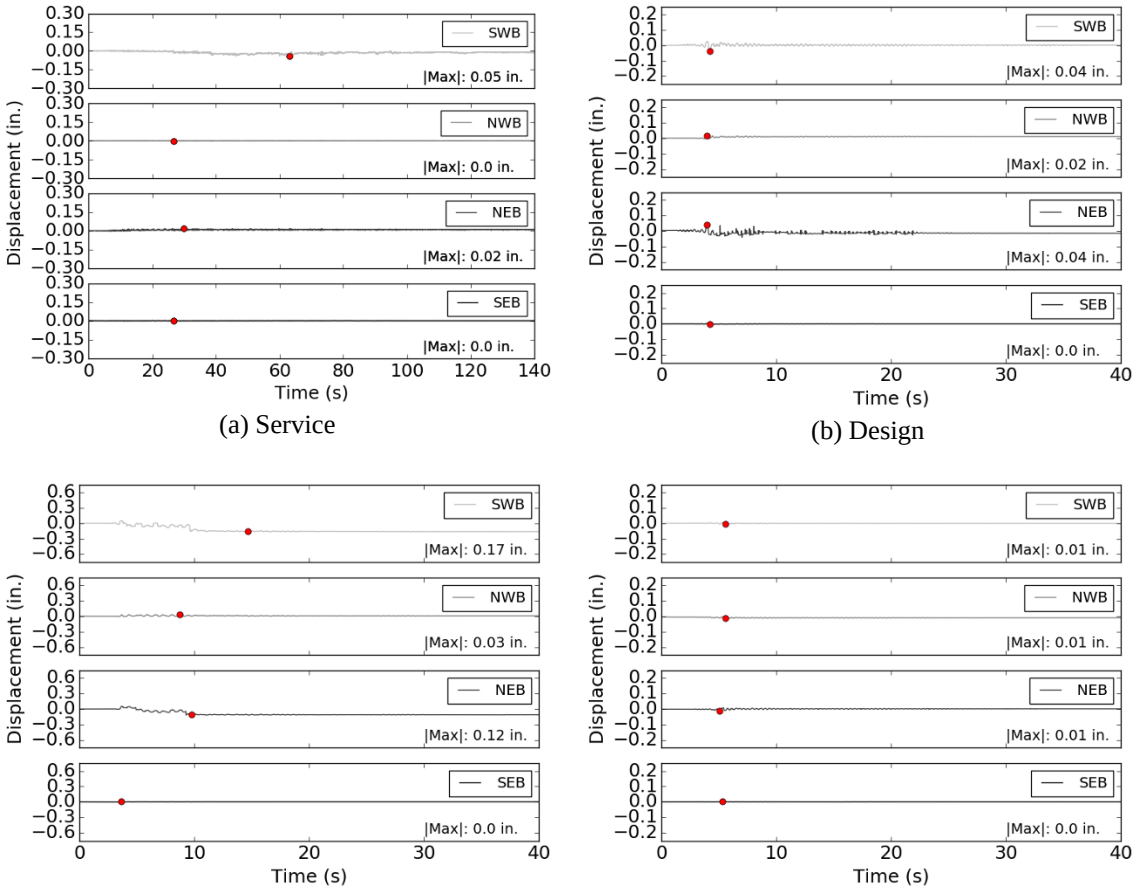

(a) Service (b) Design

(c) Maximum (d) Aftershock

Figure 5-75: Configuration 3, time history of horizontal longitudinal baseplate displacements

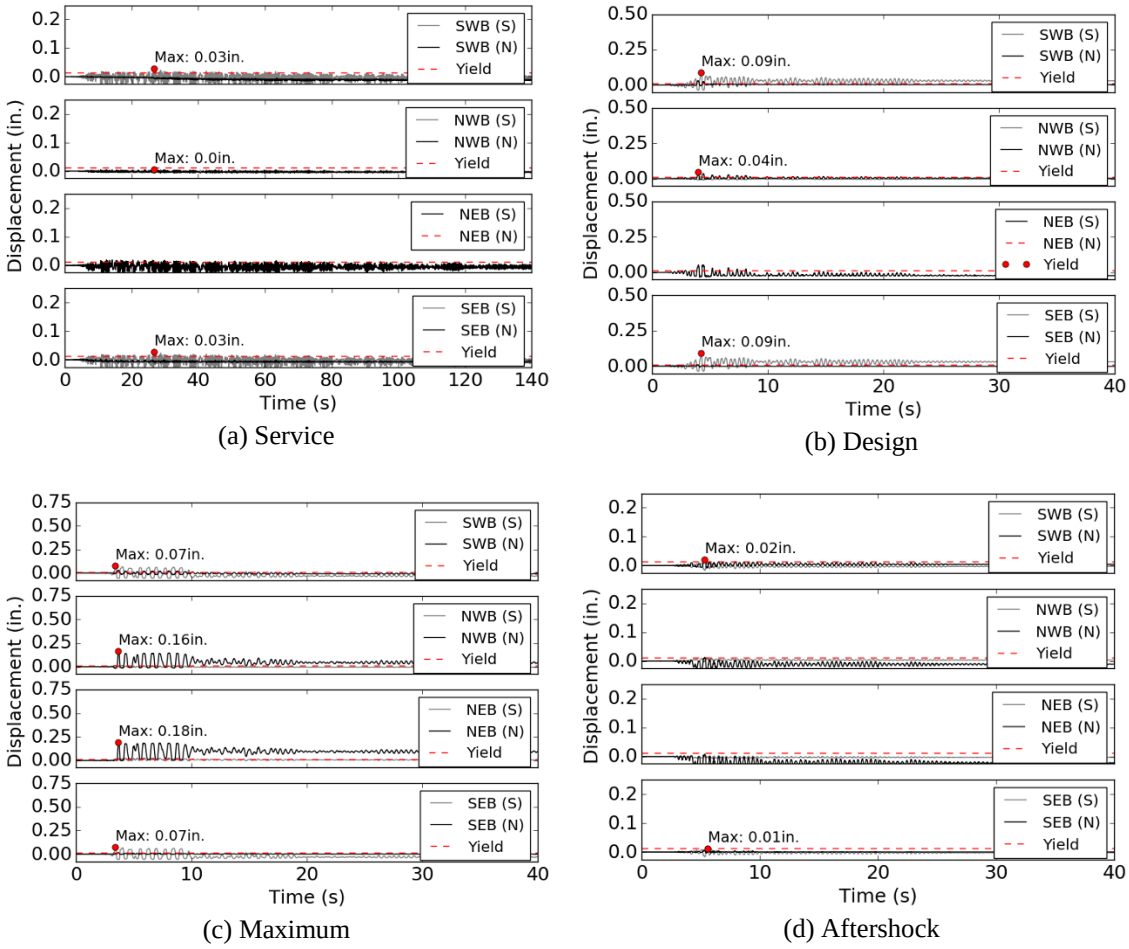

(a) Service (b) Design

(c) Maximum (d) Aftershock

Figure 5-76: Configuration 3, time history of vertical baseplate displacements

The time histories of the measured beam and column strains for the Design motion are shown in Figure 5-77. The maximum measured column strains were about 1/3 of yield, while the beam strains were a little less than half of yield. However, shell-element modeling of the Configuration 3 beam cutout geometry indicates that the measured strains for this case are about 20% of the maximum strain at the side of the cutout hole. This factor includes a contribution from the fact that the strain gages are not at the extreme fiber of the beam and a contribution from the strain concentration effect of

the hole. Therefore, the maximum strain in the beam section was approximately 2.3 times the yield. All maximum beam and column strains are tabulated later in this chapter.

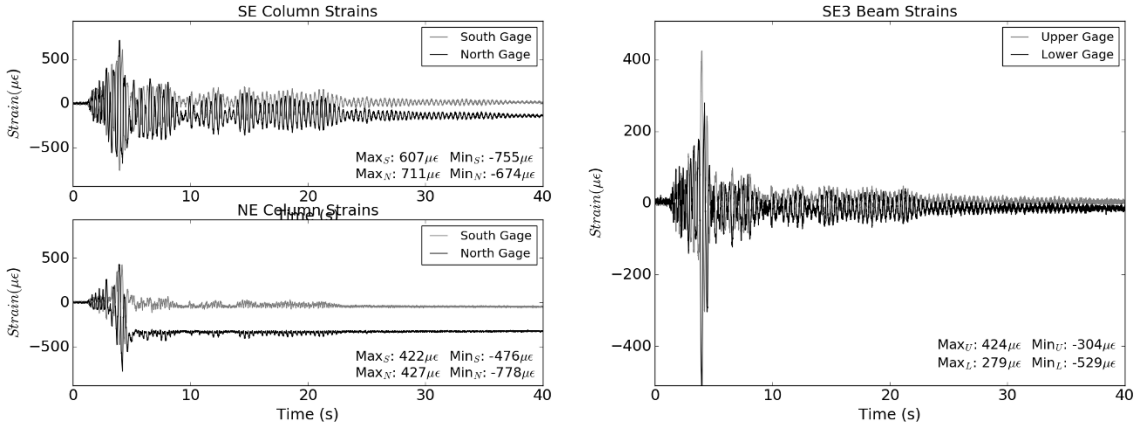

(a) SE column strains (b) 3rd-floor beam strains (NE corner of structure)

Figure 5-77: Configuration 3, time history of strains in superstructure under design motion

Acceleration time histories at the table and floor levels are shown in Figure 5-78. The maximum accelerations were generally between those measured for Configurations 1 and 2, with some important exceptions discussed in a following section. The PFA were similar to those measured for Configuration 1 in that there was no clear pattern in the direction at each floor with respect to the direction of the input maximum. The shape of the ISRS were generally similar to the other configurations, with peaks at the dominant period of the input, at the natural period of the structure, and at low period due to table noise. The peaks of the spectra were generally between those measured for Configurations 1 and 2.

The measured interstory drift also displayed similarities to both Configuration 1 and 2 (Figure 5-78). The magnitude of the maximum interstory drifts was similar to both previous configurations. As with Configuration 1, the maximum drifts were temporally aligned for all motions except Service, and the maximum drift in the lowest story was

generally larger than for the upper stories. Additionally, under the Maximum motion, the structure underwent several cycles of large drift associated with global motion due the loss of rotational and uplift restraint at the base.

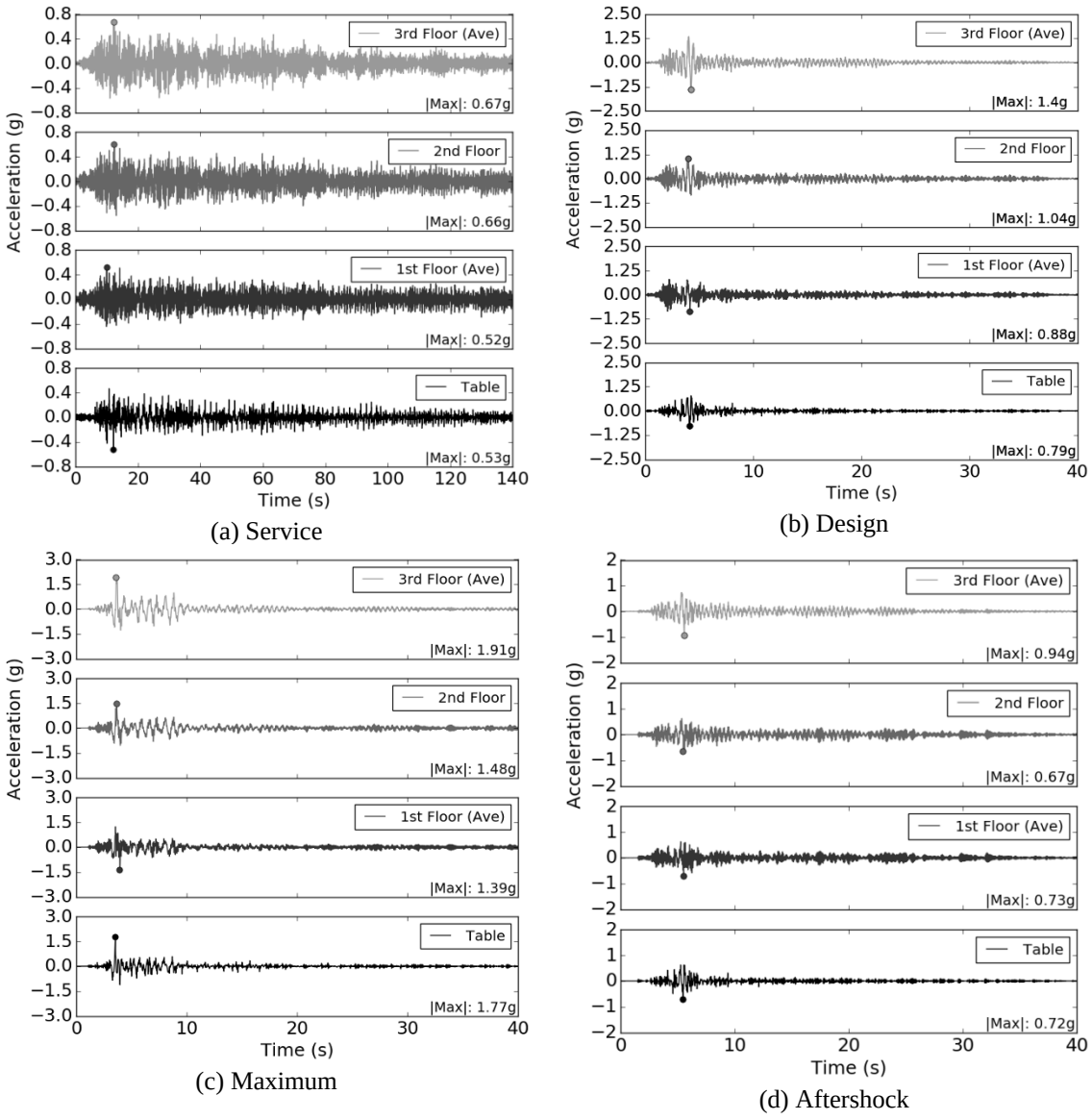

Figure 5-78: Configuration 3, ground and floor acceleration time histories for different motion cases

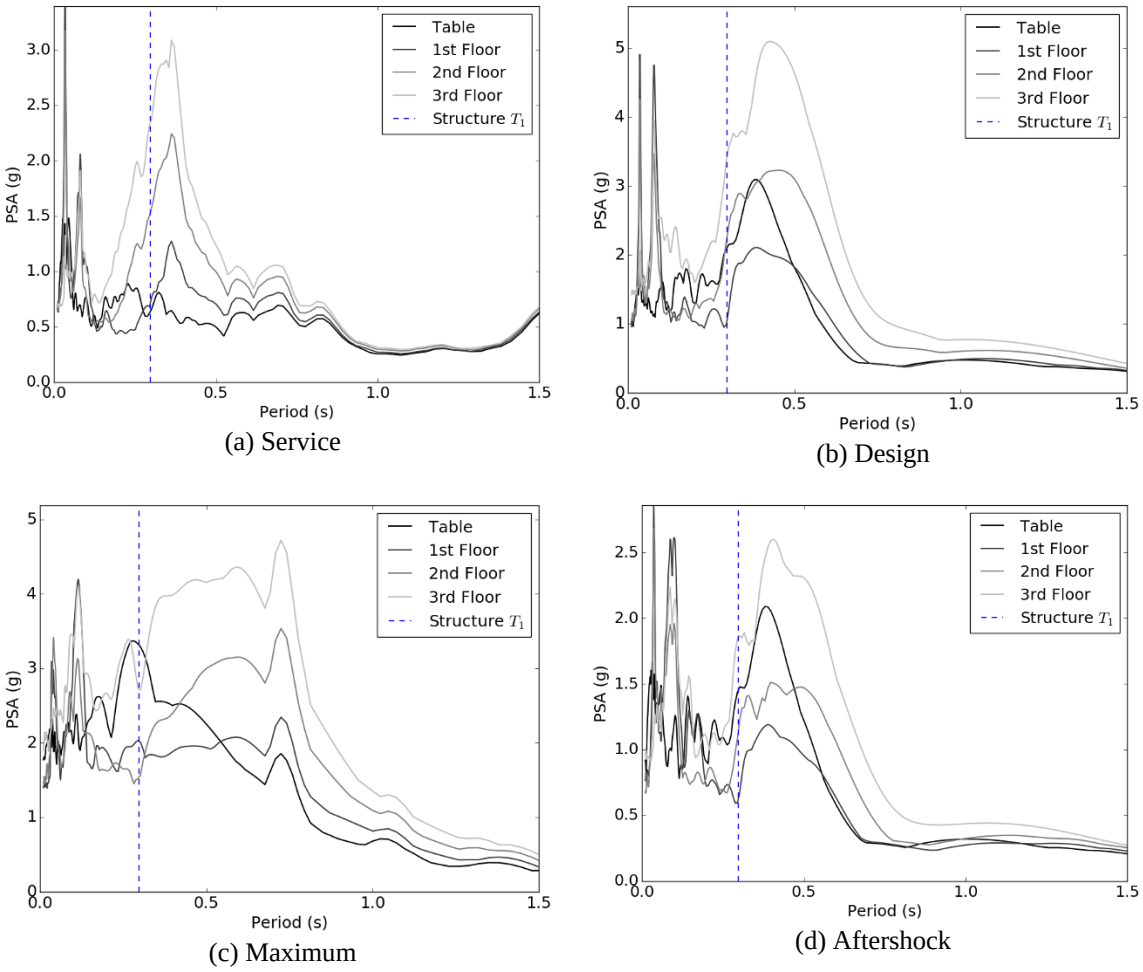

(a) Service

(b) Design

(c) Maximum

(d) Aftershock

Figure 5-79: Configuration 3, 5%-damped response spectra at ground and floor levels for different motion cases

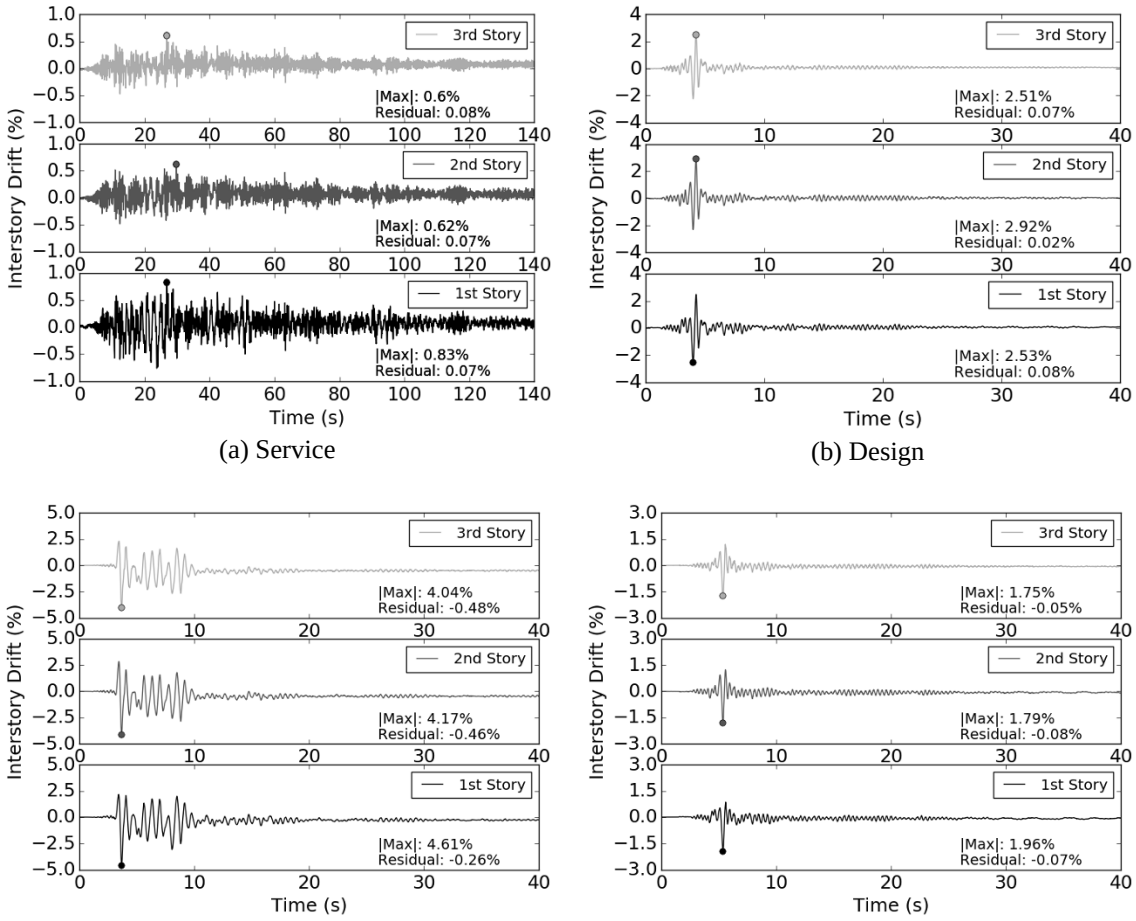

Figure 5-80: Configuration 3, interstory drifts for different motion cases

Based on the fairly small, reliable change in natural frequency observed in configuration 1, Configuration 3 was subjected to just six white-noise tests. Two pre-test (bolts tight) WN tests were run before the service motion and before the maximum motion to establish that there was no change in natural frequency due to damage in the superstructure. The other four tests were run immediately after each strong motion, to evaluate the change in natural frequency associated with bolt yielding. The results from these tests are shown in Figure 5-81. Note that the post-service service and post-design TFs are compared to the pre-service test, and the post-maximum and post-aftershock tests

are compared to the pre-maximum test. The TF peaks from each test are summarized in Table 5-15. There was a significantly smaller drop in the first natural frequency after the design and aftershock motions versus the other two motions. This result is consistent with small, sometimes incomplete, anchor bolt yielding observed during the test. However, the average magnitude of the drop in the first mode frequency was significantly larger than for Configuration 1 (about 22% versus 12%). This result is somewhat expected, given that the "loss" of elastic support provided by the 3/8 in. anchors used in this configuration is much greater than the 1/4 in. anchors used in Configuration The changes in the estimated mode shapes (Figure 5-82) were very similar to those found for Configuration 1.These results indicate that large, visible anchor elongations (such as those observed in Configuration 1) are not required to shift the natural frequency of the structure significantly -- the mere loosening of the anchors was associated with this natural frequency shift and mode shape change in Configuration 3.

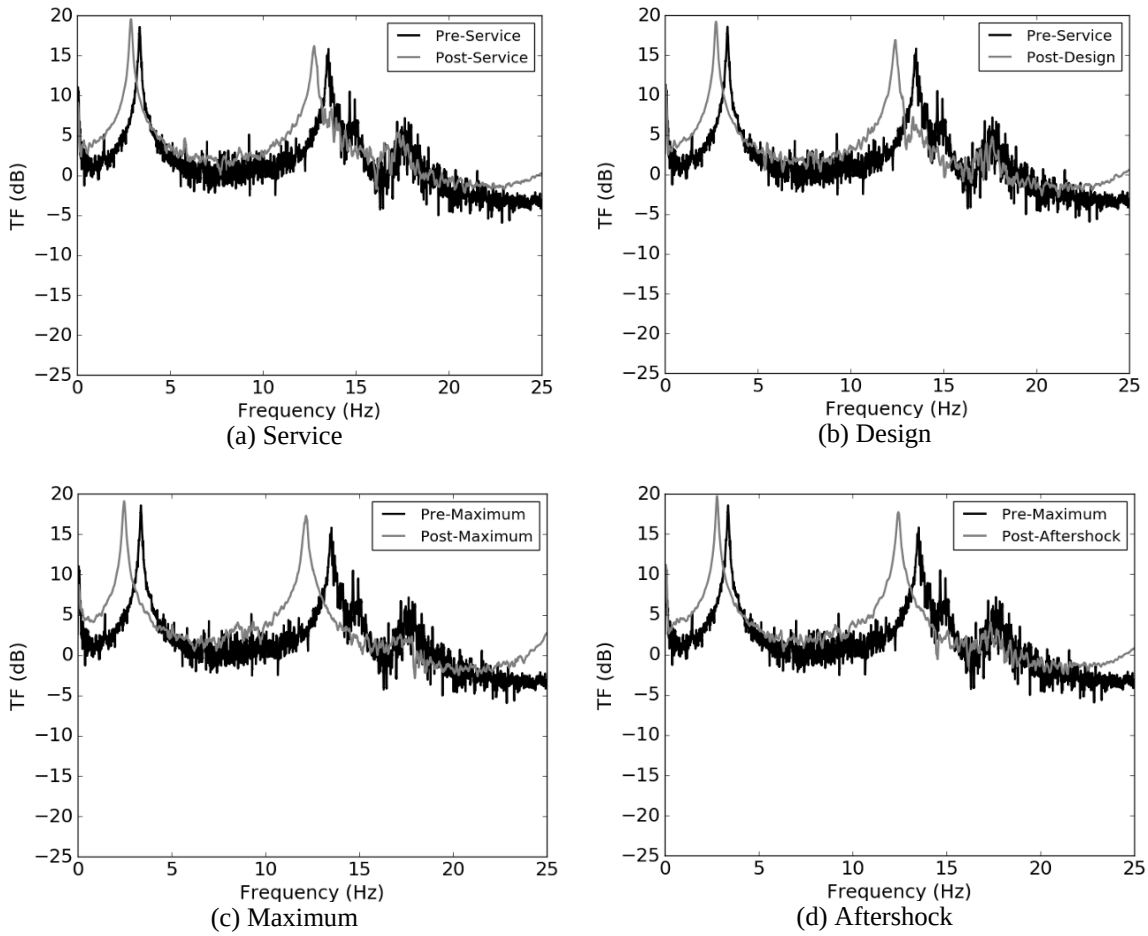

Figure 5-81: Configuration 3 transfer function estimates pre-and post-test

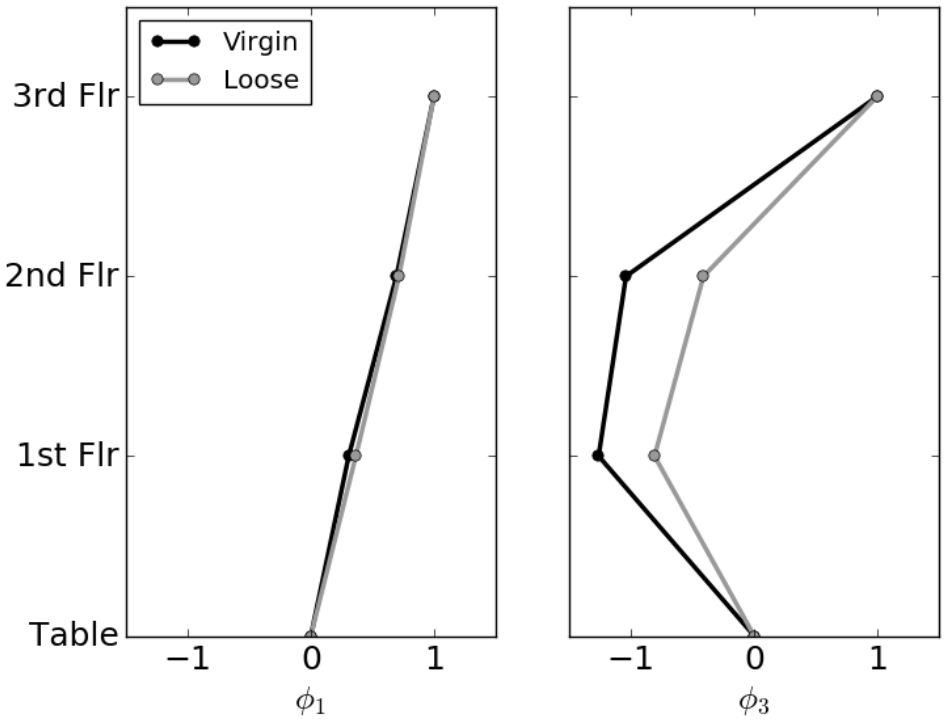

Figure 5-82: Typical virgin and "anchors loose" x-direction mode shapes for Configuration 3

Table 5-15: Change in first and second natural frequency for Configuration 3

Motion	Prior f_1, Hz [T_1, s]	After f_1, Hz [T_1, s]	Prior f_2, Hz [T_2, s]	After f_2, Hz [T_2, s]
Service	3.37 [0.297]	2.47 [0.405]	13.53 [0.0739]	12.17 [0.0822]
Design	-	2.75 [0.364]	-	12.40 [0.0806]
Maximum	3.36 [0.298]	2.49 [0.402]	13.52 [0.0740]	12.17 [0.0822]
Aftershock	-	2.78 [0.360]	-	12.44 [0.0804]
Average:	3.37 [0.297]	2.63 [0.380] *(-22.0%)*	13.53 [0.0740]	12.30 [0.0813] *(-9.1%)*

Impact testing of Configuration 3 was performed with the same instrumentation setup as for Configuration 1 and 2 (see Figure 5-62). The filtered acceleration histories used for the log decrement calculation are shown in Figure 5-83 . For an unknown reason, the second mode time series had much lower peaks and was much less distinct than for Configuration 1 and 2. The most likely explanation was that the excitation of the

structure in this case was relatively first-mode "pure" -- i.e. the frequency of the strike was very close to the first mode, and the second mode was not excited strongly. However, using the points shown, the calculated first and second mode damping ratios were both about 1.0%. The second mode damping ratio was not particularly sensitive to the particular peaks used in the calculation, with calculated ratios for any distinct peaks within the range of about 0.8% and 1.3%.

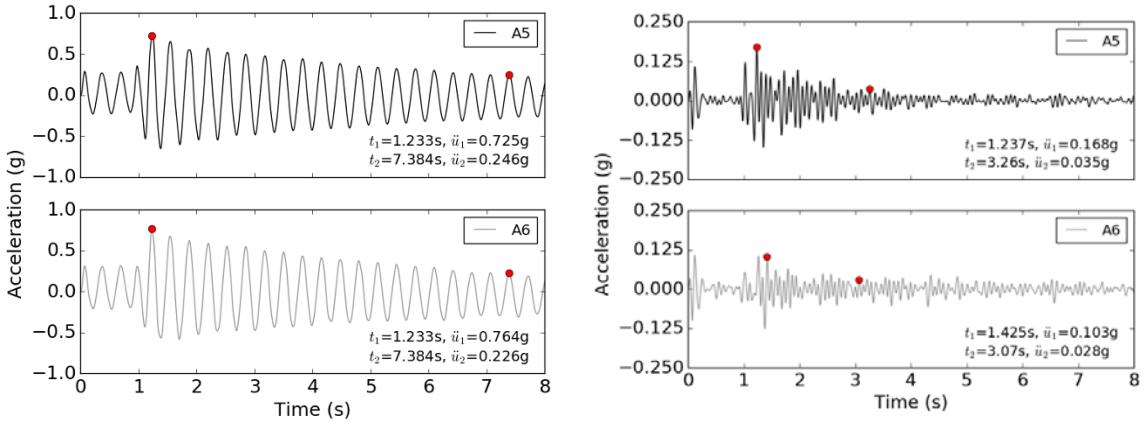

(a) First natural frequency

(b) Second natural frequency

Figure 5-83: Configuration 3 - Filtered acceleration histories and points used for log decrement calculation

Configuration 4

Configuration 4 was characterized by a very limited amount of anchor yielding and substantial structure flexibility. The anchors were found to be tight following the service motion, and a very small amount of anchor yielding was observed following the Design and Maximum motions. No grout cracking or damage was observed in any of the motions. Typical baseplate connection conditions following the Service, Design, and Maximum motions are shown in Figure 5-74. The measured baseplate vertical displacements, shown in Figure 5-85 were substantially smaller than the other two

configurations with yielding anchors (1 and 3). Measured horizontal (x-direction) baseplate displacements were negligible, as shown in Figure 5-86.

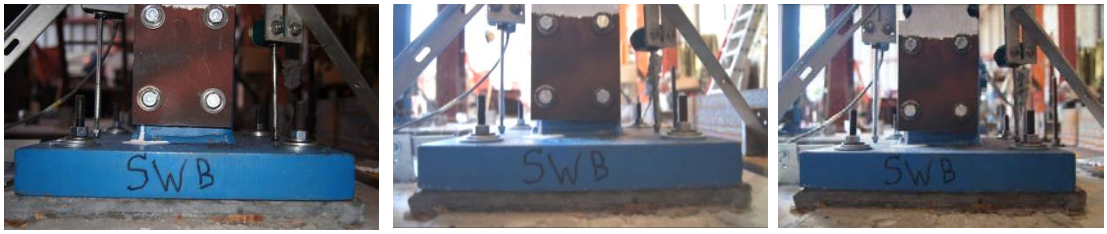

Figure 5-84: Configuration 4 - Typical condition of baseplate connections following Service, Design, and Maximum motions (from left to right)

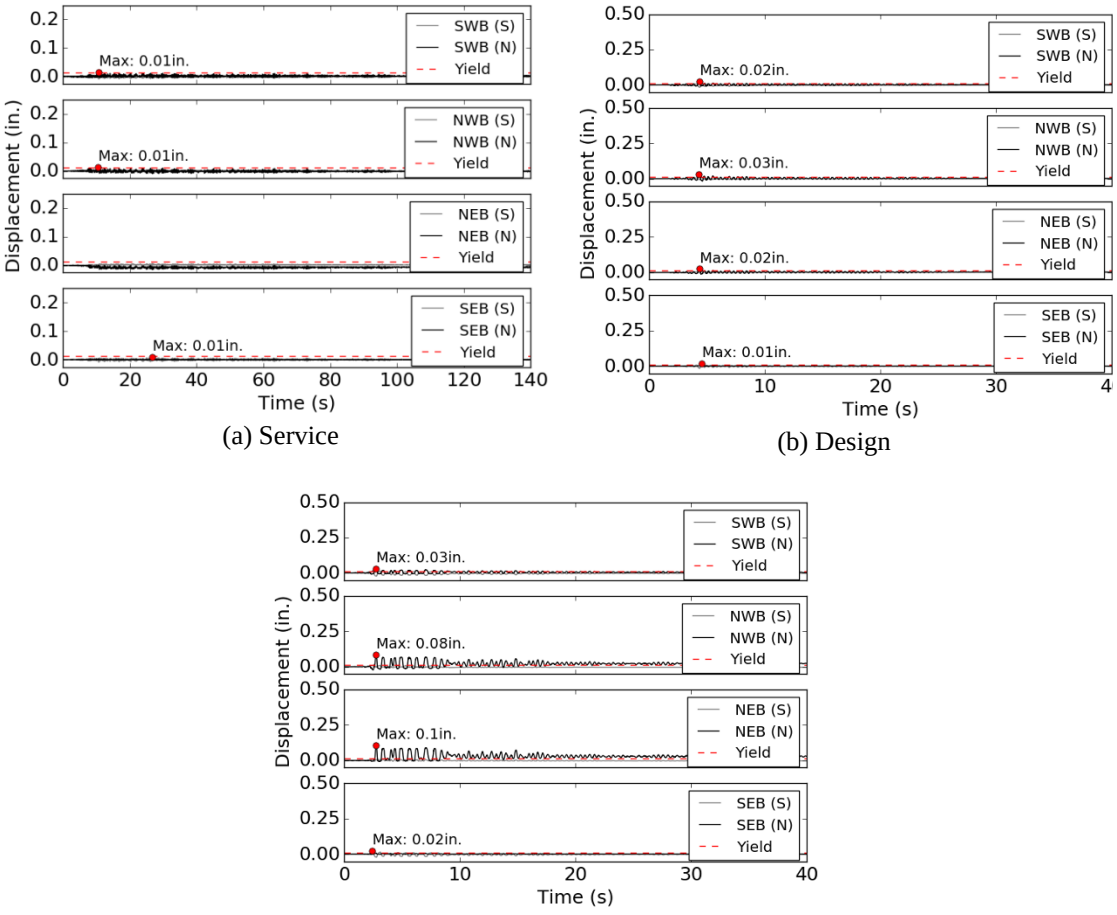

(a) Service

(b) Design

(c) Maximum

Figure 5-85: Configuration 4, time histories of vertical baseplate displacement for different motion cases

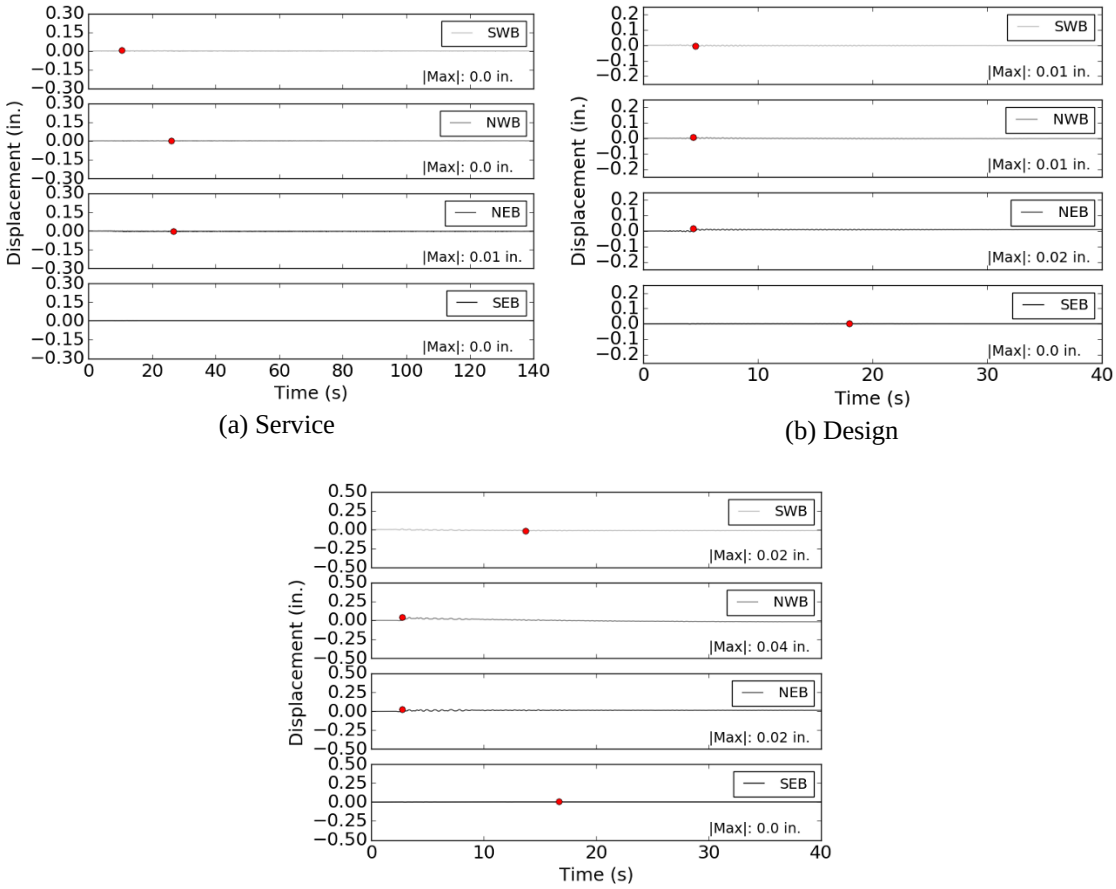

(a) Service

(b) Design

(c) Maximum

Figure 5-86: Configuration 4, time histories of horizontal longitudinal baseplate displacement for different motion cases

The acceleration histories at the roof were strongly "colored" by the natural frequency of the system regardless of motion intensity, as shown in Figure 5-87. Interestingly, for this configuration, the measured maximum acceleration at the roof level was lower than that measured at the bottom of the structure for the Service and Maximum motions. The reason for this is not entirely clear, however this phenomenon is investigated as part of the numerical analysis presented in the following chapter. The response spectra at the bottom and top of the structure are shown in Figure 5-88. Because this structure responded essentially as a SDOF, the response spectrum at the top of the

structure was significantly more peaked than for the other structural configurations. The maximum measured drift to the top of the structure ranged from a a maximum value of about 0.6% under the service level motion to a maximum of about 3.4% under the Maximum level motion (Figure 5-89). A significant residual drift of about 0.3% was recorded for the Maximum motion, while residual drifts in the other cases were negligible.

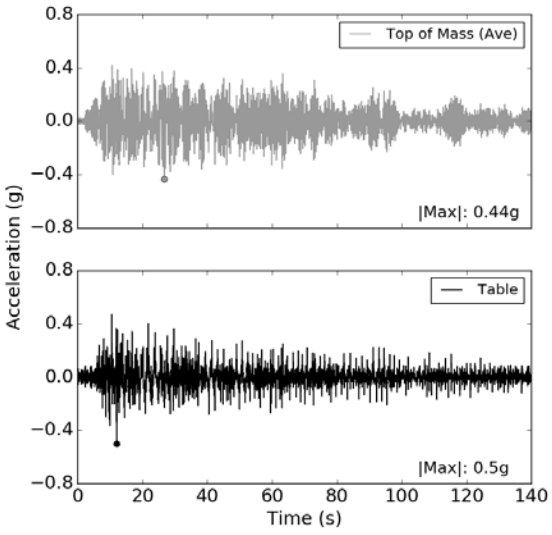

(a) Service

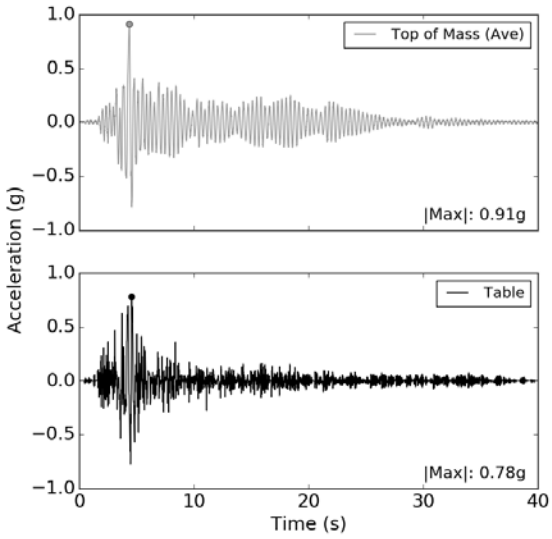

(b) Design

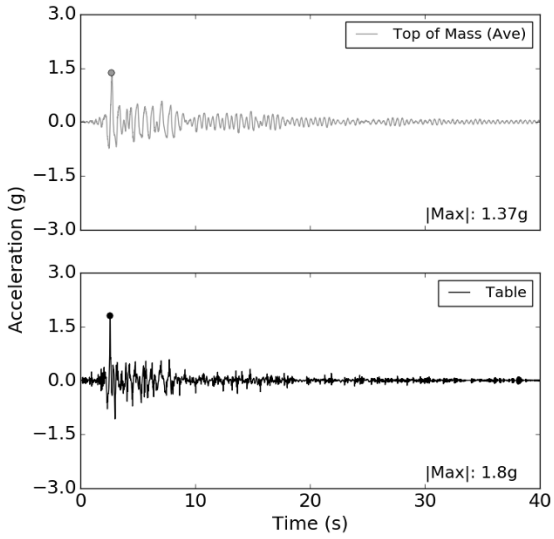

(c) Maximum

Figure 5-87: Configuration 4, ground and top floor acceleration time histories for different motion cases

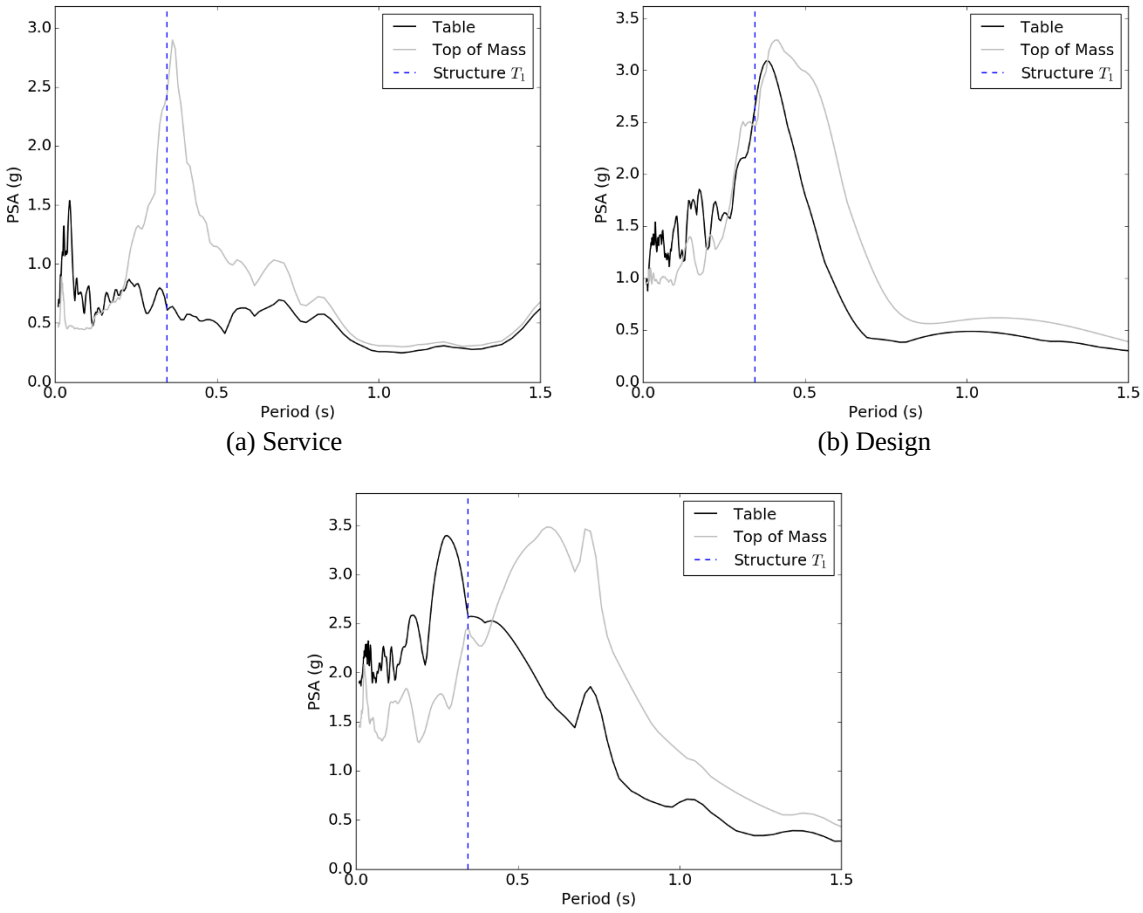

(a) Service

(b) Design

(c) Maximum

Figure 5-88: Configuration 4, 5%-damped response spectra at ground and top floor level for different motion cases

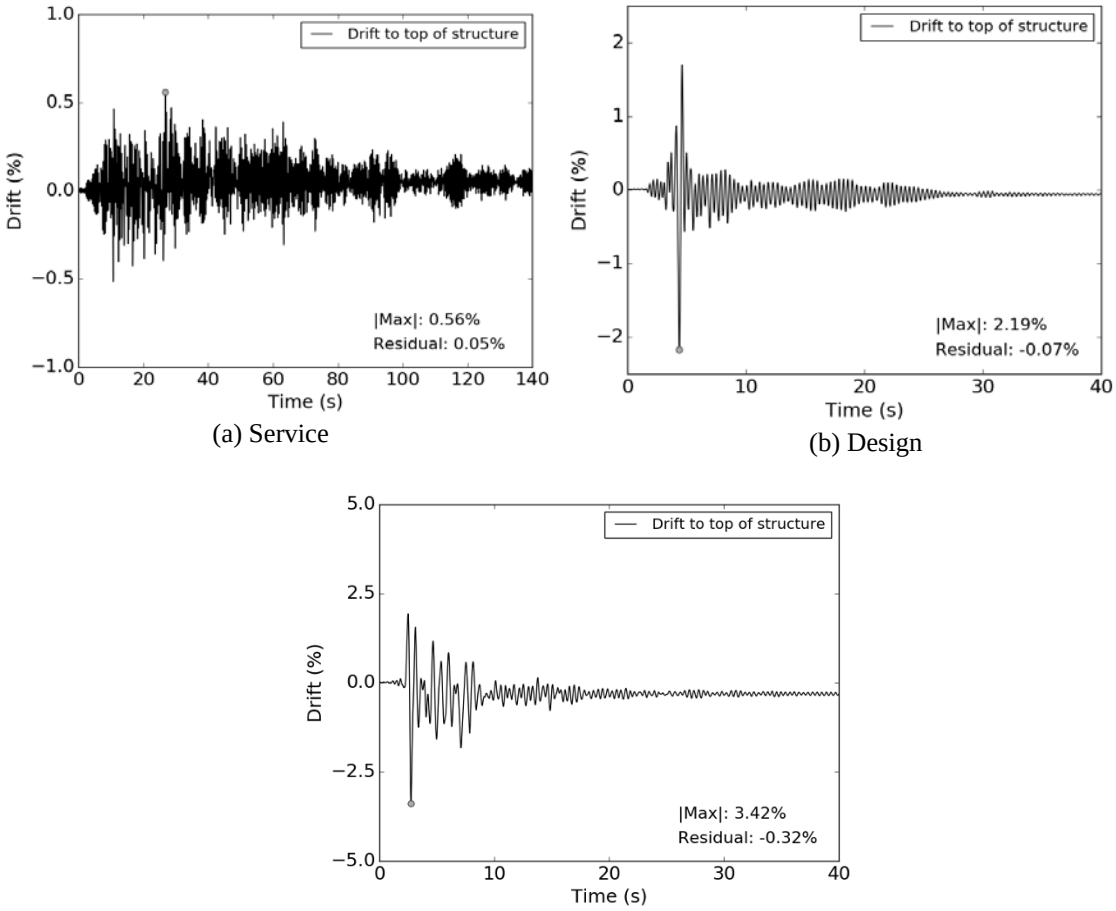

(a) Service

(b) Design

(c) Maximum

Figure 5-89: Configuration 4, structure drift for different motion cases

Configuration 4 was subjected to five white noise tests. Two were run prior to any strong motion events, in order to determine the natural frequencies of the system in the bolts-tight and bolts-loose configuration. Three were run immediately following each strong motion run for this configuration. The results from this testing are shown in Figure 5-90. Note that in each case, the transfer function post-motion is compared to the initial pre test, bolts tight test, as this was assumed to be the condition of the structure at the beginning of each test. Unlike previous tests, there was only a single natural frequency associated with an SDOF mode of the concentrated top mass. However, as with previous

tests, anchor elongation during strong motion events caused changes in the fundamental frequency. The changes in natural frequency associated with each test are summarized in Table 5-16. The mode shape was found to be similar in shape in both the virgin and anchors-loose conditions. It is possible that with denser instrumentation, mode shape changes could have been determined. In contrast to other tests, the change in natural frequency was highly dependent on the amplitude of the strong motion, and did not reach the "floor" of the natural frequency found when all anchors were loosened. This suggests that yielding of the anchor bolts was incomplete for all strong motion tests, and is consistent with observations made following each tests.

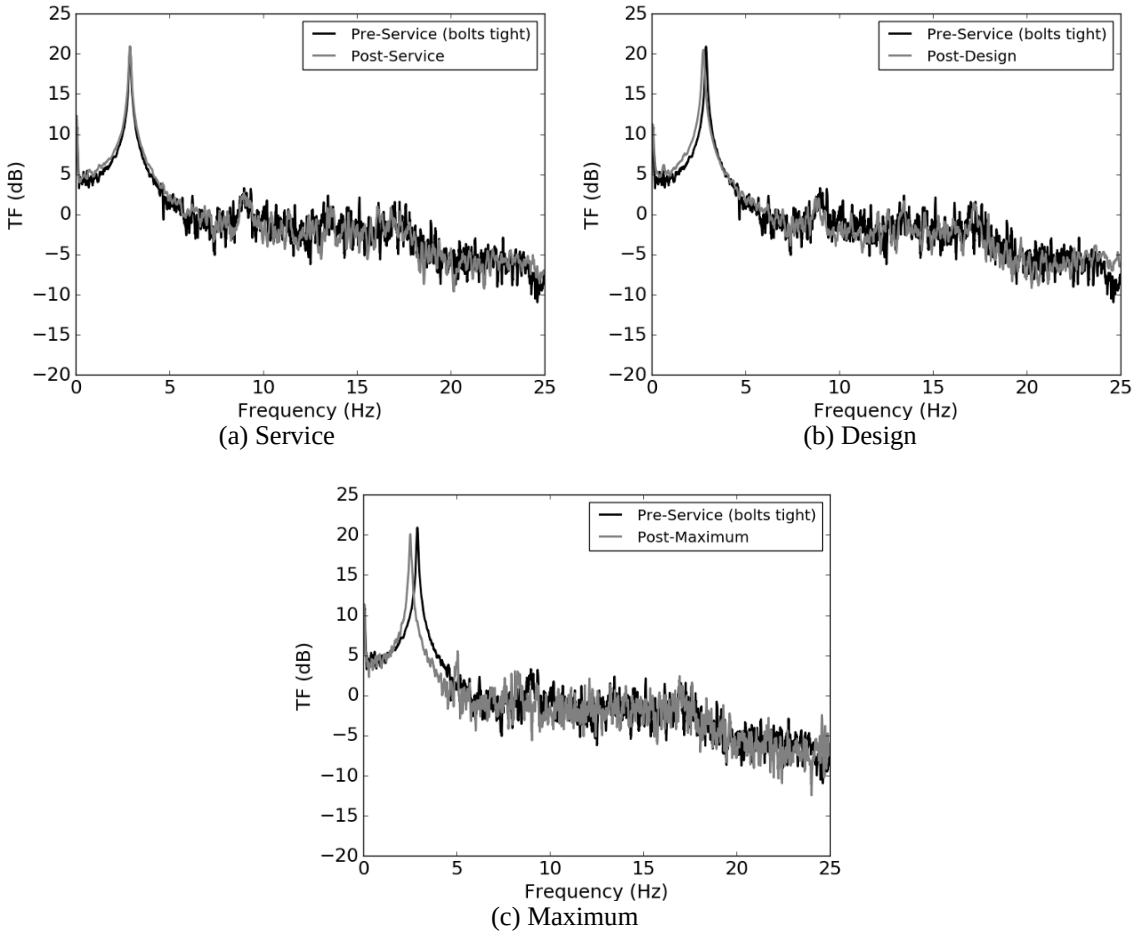

Figure 5-90: Configuration 4 transfer function estimates pre-service motion and post-test

Table 5-16: Natural frequency change, Configuration 4

	Prior	After
Motion	f_1, Hz [T_1, s]	f_1, Hz [T_1, s]
Service	2.90 [0.345]*	2.89 [0.346]
Design	-	2.76 [0.362]
Maximum	-	2.52 [0.397]
Average:	2.90 [0.345]	2.72 [0.368] *(-6.2%)*

*Note: the bolts-loose frequency was found to be 2.34Hz [T=0.427 s] from the pre-test WN evaluation

Impact testing of Configuration 4 was performed with the same instrumentation array as for all other configurations (see Figure 5-62), however only one damping ratio

corresponding to the frequency identified in Table 5-16 was recovered. The filtered acceleration histories used for the log decrement calculation are shown in Figure 5-91. The damping ratio was calculated to be about 2.0%.

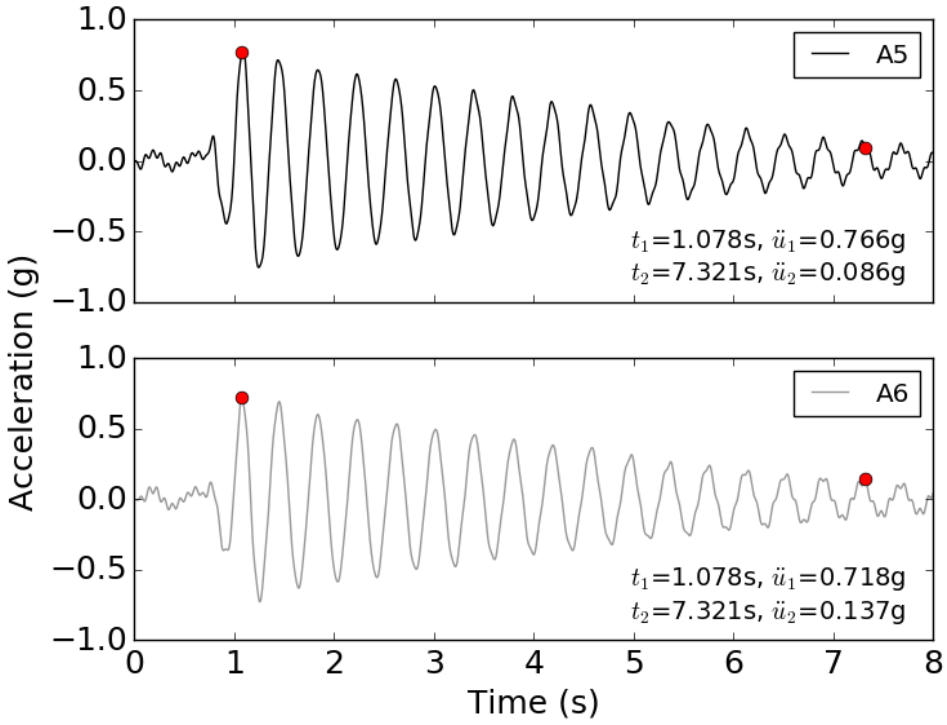

Figure 5-91: Configuration 4 - Filtered acceleration histories and points used for log decrement calculation

Configuration 5

Configuration 5 was characterized by moderate levels of anchor plasticity, particularly at more intense motion levels. The brace used on this structure was quite large relative to the demands imparted by the structure, and there was no observed superstructure plasticity. The typical condition of the baseplate connections after the Service, Design, Maximum, and Extreme motions are shown in Figure 5-92. No visible plastic elongation was observed following the Service motion, and only very slight

plastic deformation was observed following the Design motion. There was significant plastic elongation observed following the Maximum and Extreme cases, visible in (c) and (d) in the figure. In the Extreme case, the anchor threads were severely deformed on most of the anchors, and there was some grout spalling on two of the grout pads, as shown in the figure. Time histories of the measured vertical baseplate displacements are shown in Figure 5-93. In general, the maximum values were slightly less than for Configuration 1 for identical motions. However, due to the presence of the brace, anchor elongation was caused primarily by global structure rocking, rather than a combination of global rocking and frame action. Following the attainment of the maximum deformation, the response was essentially sinusoidal at the frequency of the "anchors loose" structural frequency. In contrast to the other configurations, there was significant horizontal (x-direction) baseplate displacement (Figure 5-94). Interestingly, in all cases except the Design motion case, the displacement was nearly self-centering (i.e. the structure returned to nearly its original location). It is hypothesized that this is due to the fewer number of anchors used in this configuration, which would result in less initial shear resistance. Although the anchors which were not fastened to the baseplate with nuts were left in place as shear guides, they were generally nearly centered in the holes cut in the baseplate and therefore did not provide instantaneous shear resistance.

(a) Service

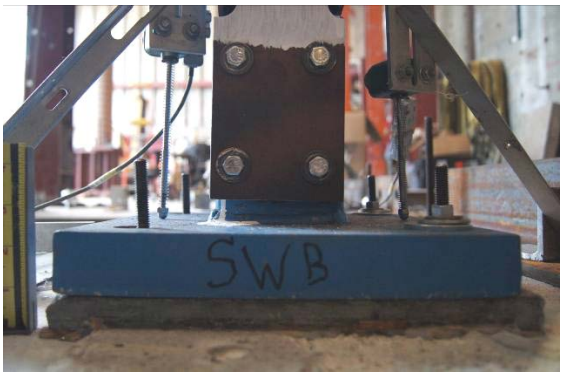

(b) Design

(c) Maximum

(d) Extreme

Figure 5-92: Configuration 5 - Typical condition of baseplate connections following motions

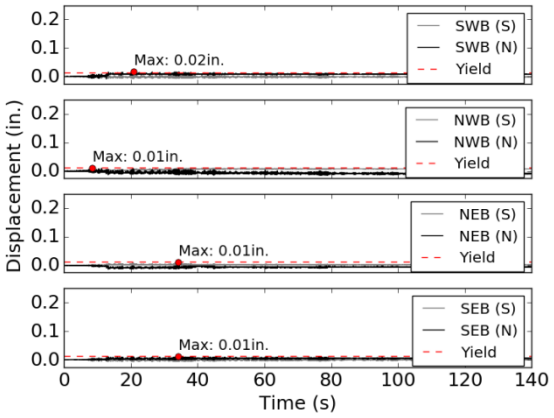

(a) Service

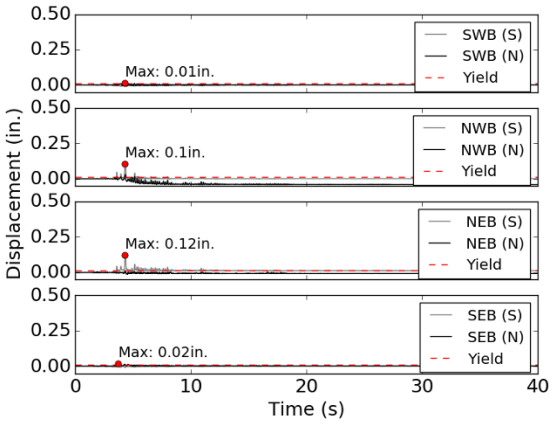

(b) Design

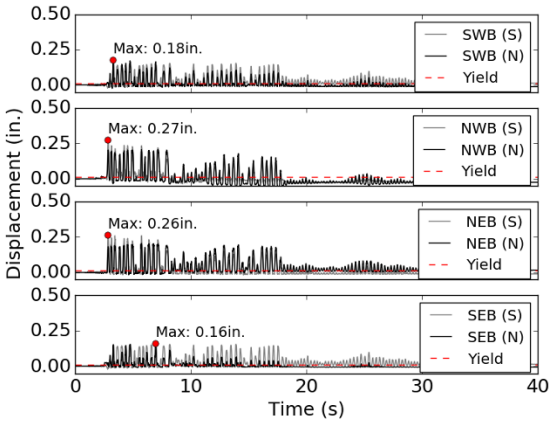

(c) Maximum

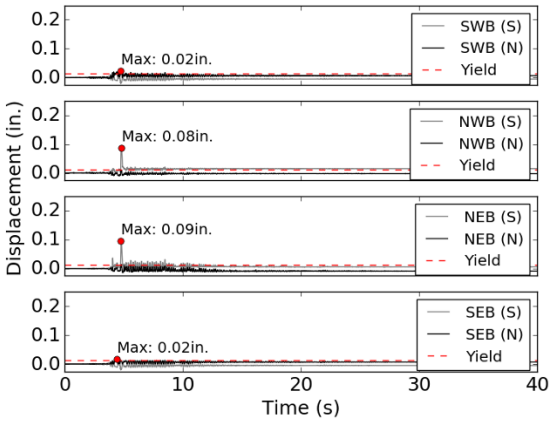

(d) Aftershock

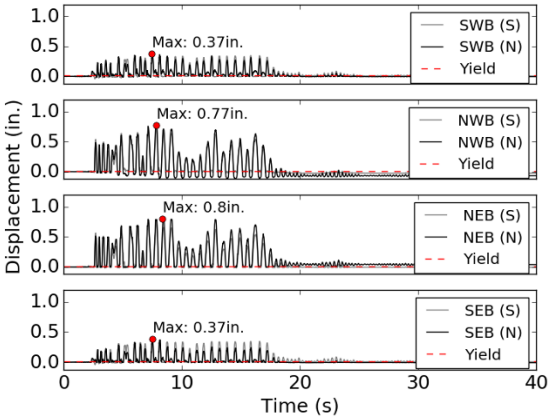

(e) Extreme

Figure 5-93: Configuration 5, time histories of vertical baseplate displacement for different motion cases

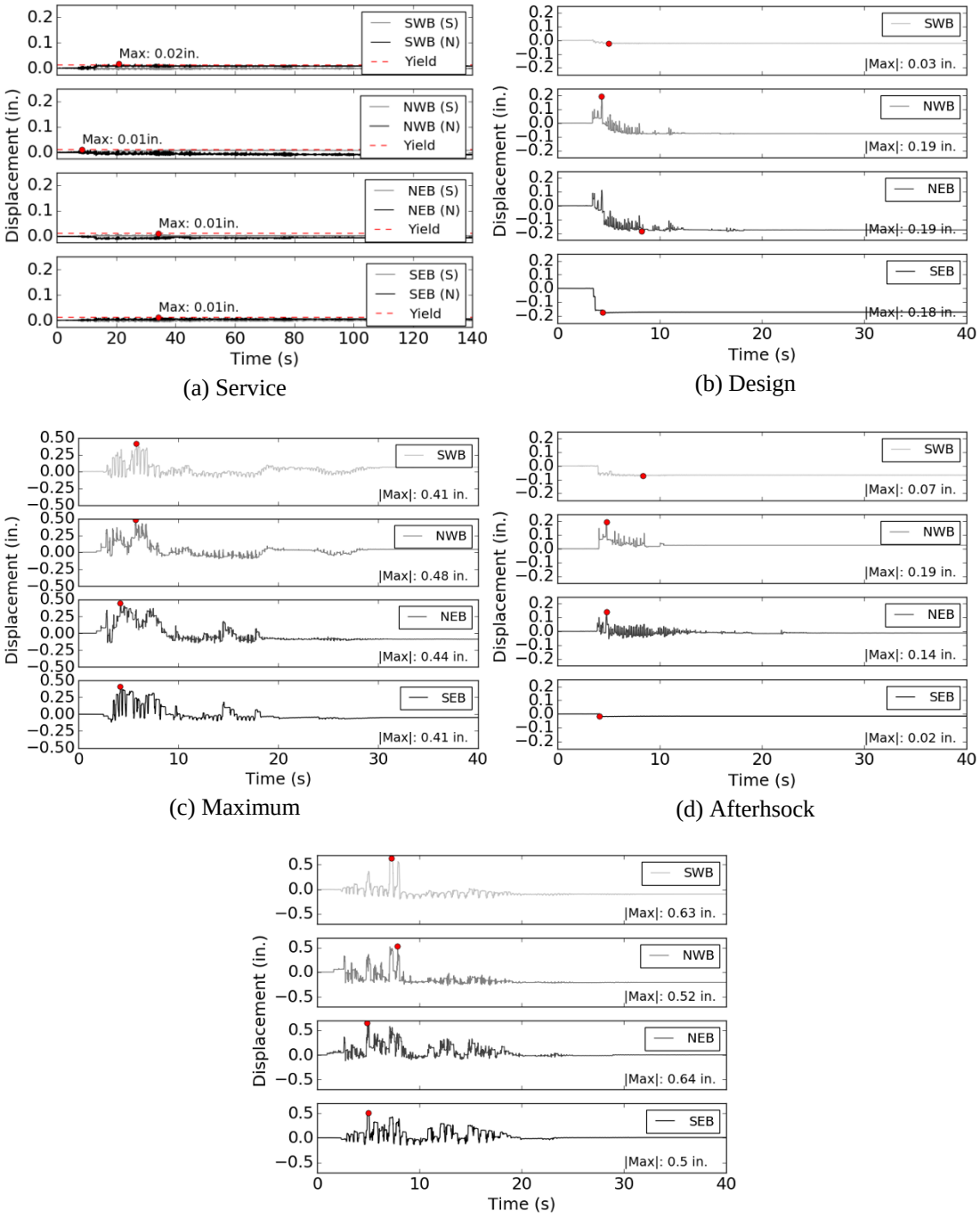

(a) Service

(b) Design

(c) Maximum

(d) Afterhsock

(e) Extreme

Figure 5-94: Configuration 5, time histories of horizontal longitudinal baseplate displacement for different motion cases

Measured top floor and achieved base acceleration time histories are shown in Figure 5-95. Maximum recorded values at the top of the structure were similar in magnitude to those recorded for Configuration 1. The amplification of maximum acceleration was highly motion-dependent, ranging from about 1.6 for the Design motion to about 0.9 for the Extreme motion. Measured acceleration response spectra are shown in Figure 5-96. As with Configuration 4, these spectra are highly peaked at the value of the single natural frequency of the structure. Measured structural drifts for each motion case are shown in Figure 5-97. Note that the measured average baseplate x-direction translation (average of the measurements shown in Figure 5-94) was removed from the measured 3rd floor relative displacement measurement prior to the calculation of drift. This was done in order to account for the significant global structural translation that occurred, particularly in the Maximum and Extreme motions, that did not contribute to structural drift. Due to the high strength and stiffness of the brace, both maximum and residual drifts were smaller than the other configurations. The maximum recorded drift was approximately 2.1% under the Extreme motion. Residual drifts were negligible in all cases.

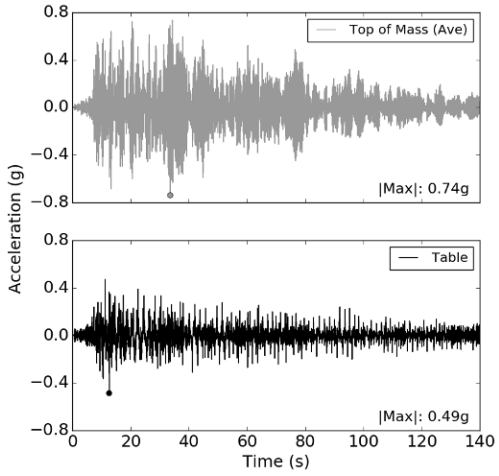

(a) Service

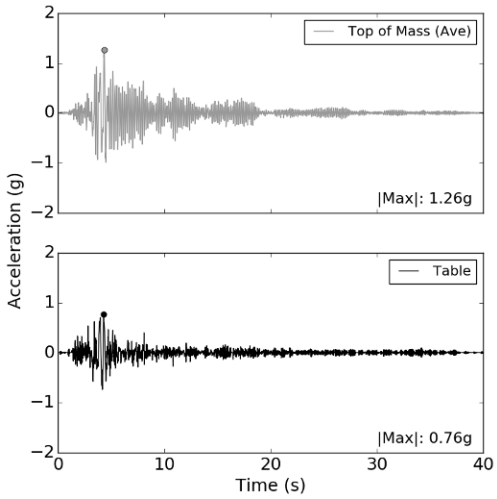

(b) Design

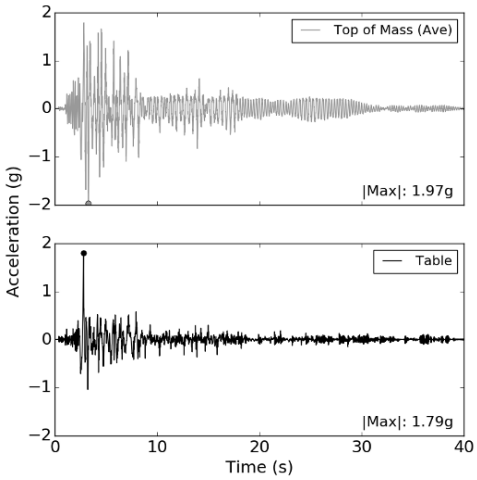

(c) Maximum

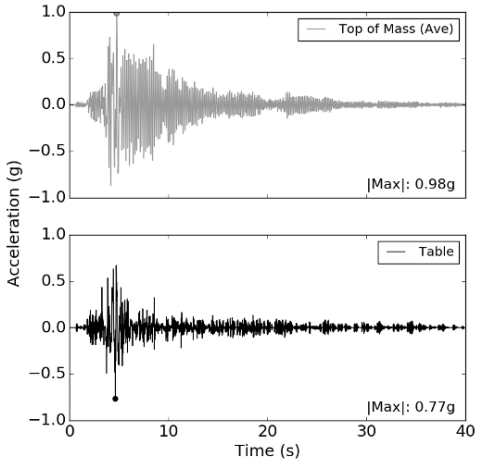

(d) Aftershock

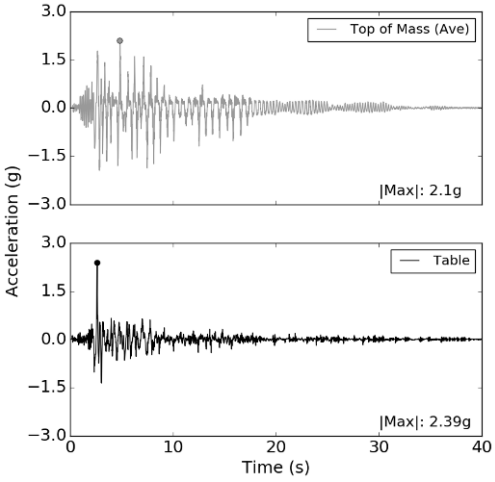

(e) Extreme

Figure 5-95: Configuration 5, ground and floor acceleration time histories for different motion cases

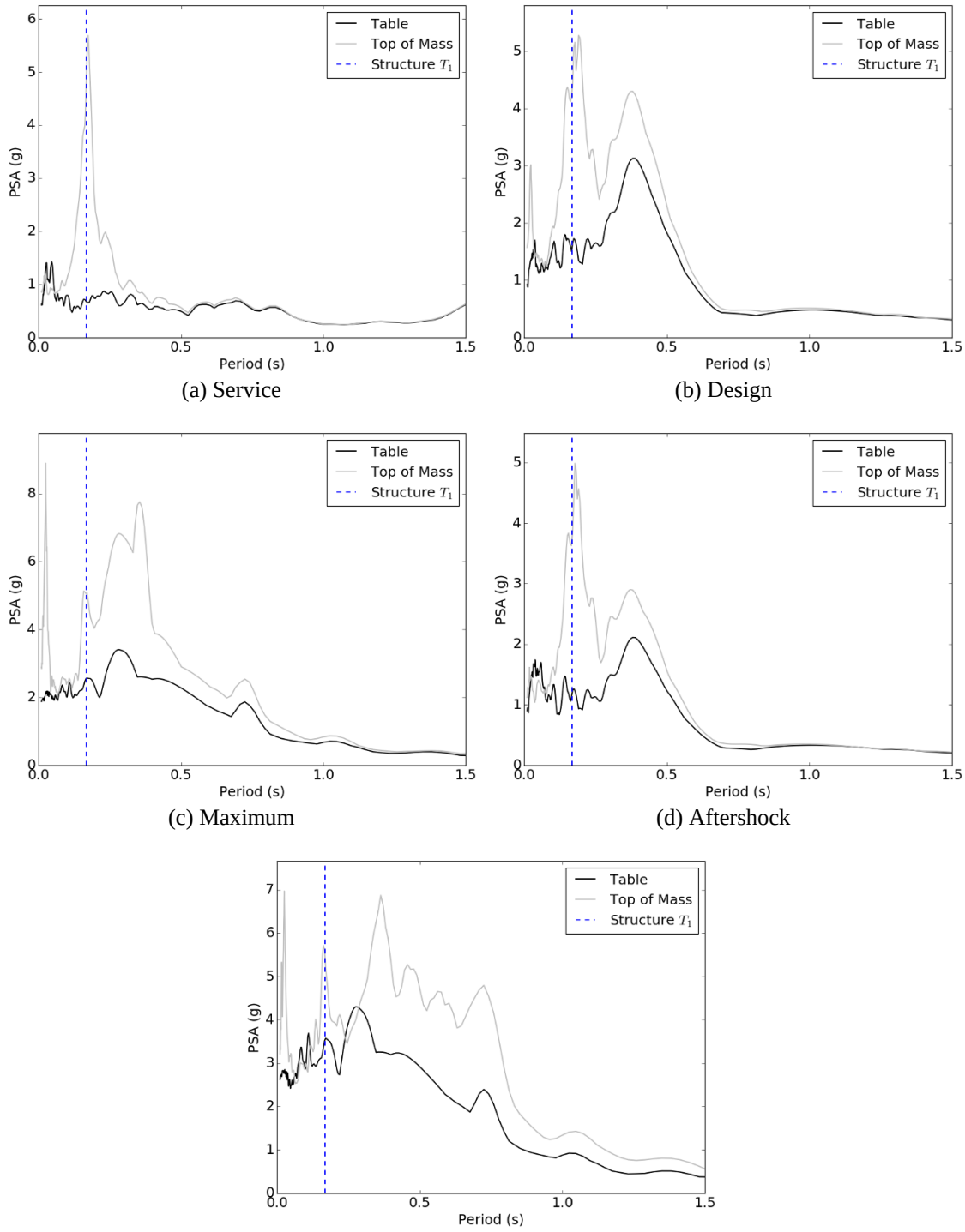

Figure 5-96: Configuration 5, 5%-damped response spectra at ground and floor levels for different motion cases

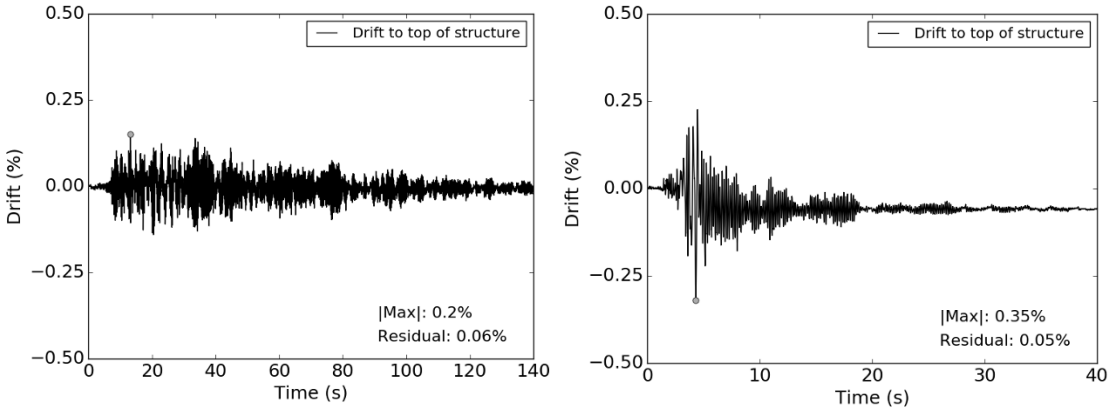

(a) Service

(b) Design

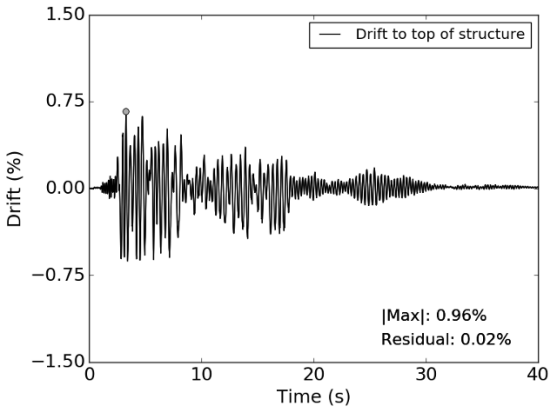

(c) Maximum

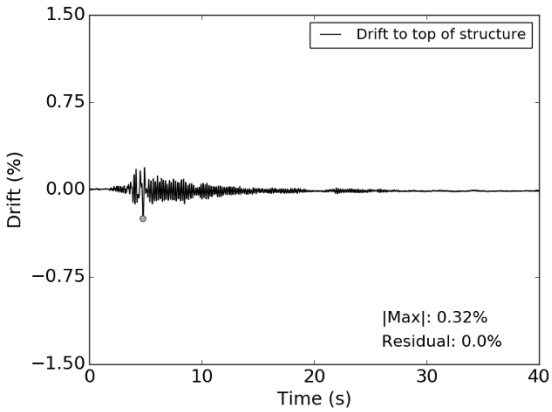

(d) Aftershock

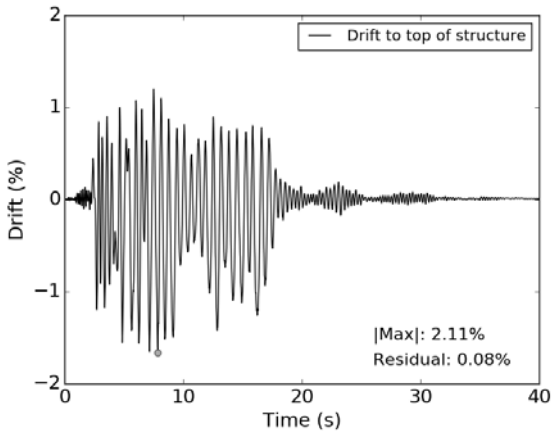

(e) Extreme

Figure 5-97: Configuration 5, interstory drifts for different motion cases

Configuration 5 was subjected to eight white noise tests. Two were performed without the structure in the final design arrangement, and are not discussed further. Two were performed prior to the initial service motion, one in the "bolts-tight" and one in the "bolts loose" configuration to determine the possible range of natural frequency for the structure. The rest of the WN tests were conducted immediately following the service, design, maximum, and aftershock events. The results of this testing are shown in Figure 5-98 and summarized in Table 5-17. Calculation of mode shapes was not performed, as the structure was dominated by only one mode of response. The TF peaks were equal to or slightly higher than the initial "bolts-tight" frequency for all cases except for the maximum motion. These results were consistent with the observed anchor bolt elongation, which was only significant under the maximum motion. WN testing was not performed following the "extreme" motion run at the end of the testing program.

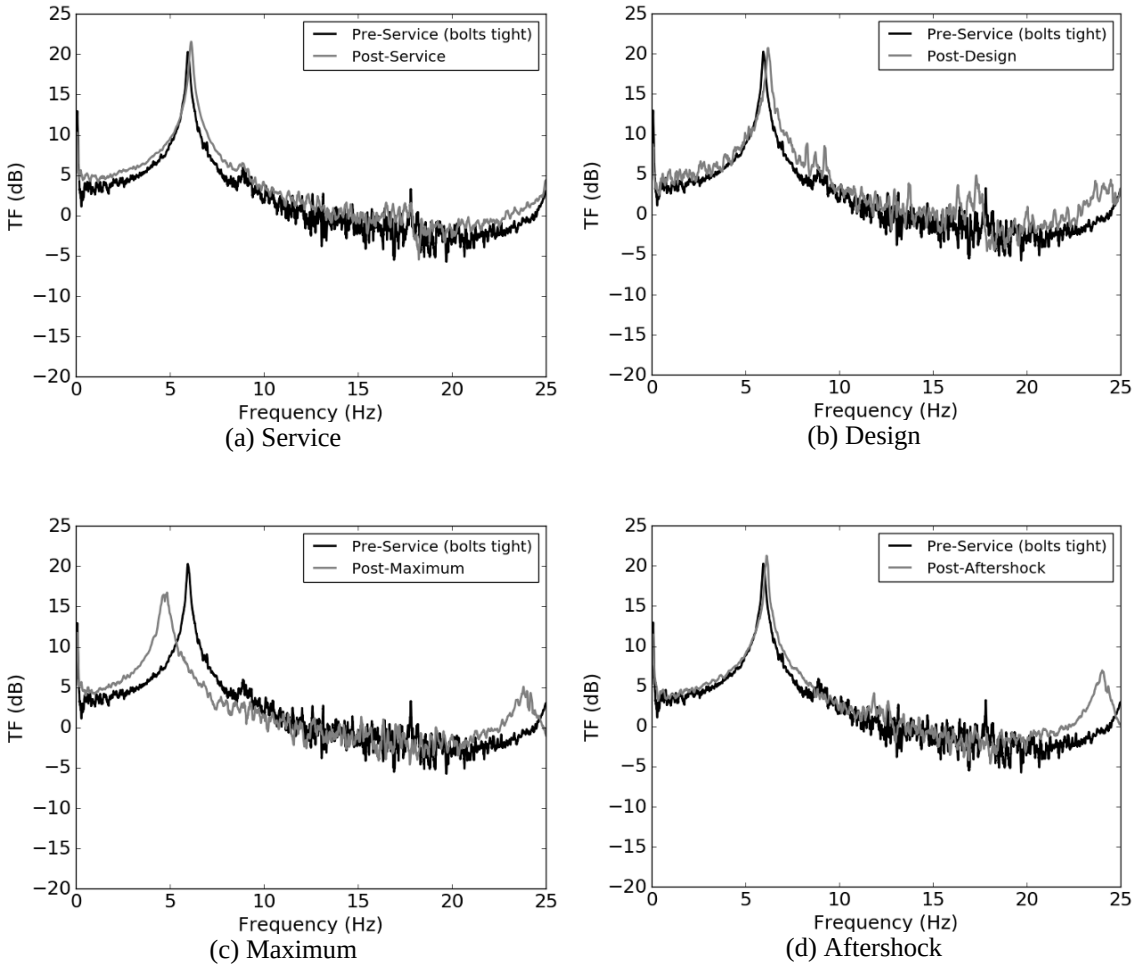

Figure 5-98: Configuration 5 transfer function estimates pre-service and post-test

Table 5-17: Change in the natural frequency for Configuration 5

	Prior	After
Motion	f_1, Hz [T_1, s]	f_1, Hz [T_1, s]
Service	5.96 [0.168][1]	6.14 [0.163]
Design	-	6.18 [0.162]
Maximum	-	4.72 [0.212][2]
Aftershock	-	6.09 [0.164]

Notes:
1) The virgin bolts-loose frequency was found to be 4.64Hz [T=0.216 s] from the pre-test WN evaluation
2) Change of 20.8% relative to previous

Due to time constraints on the table near the end of the project, Configuration 5 was not subjected to impact testing to determine damping ratios. However, Configuration 5 was subjected to a preliminary Service motion run in which the abrupt end of the input motion record caused the table control system to scramble, causing a small impulse to the system followed by free vibration. The time history of the average of the top accelerometers following this event is shown in Figure 5-99. The damping ratio calculated from this data is 1.1%.

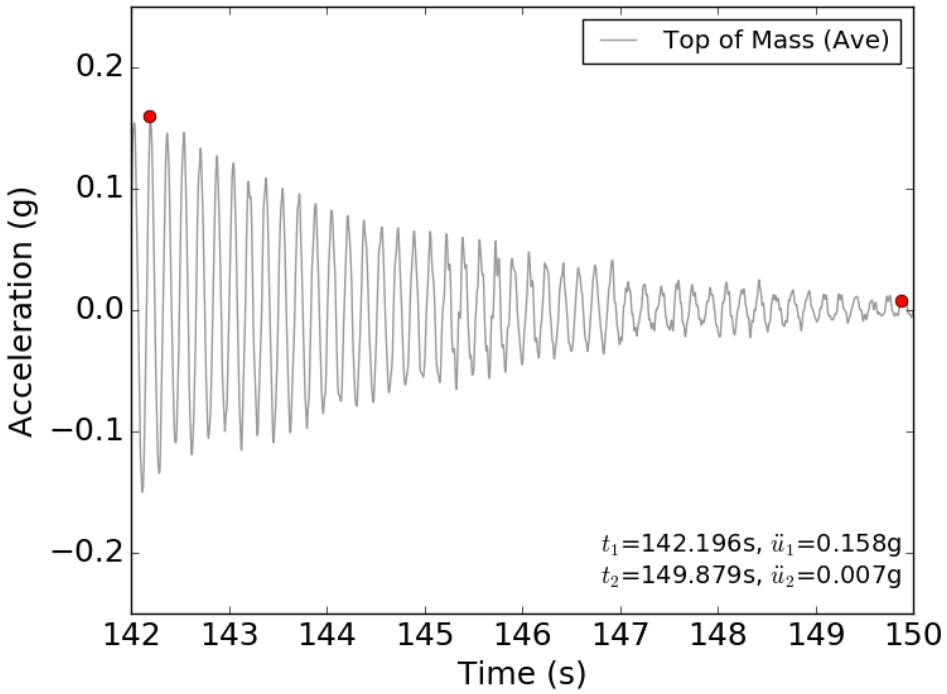

Figure 5-99: Configuration 5 - Filtered acceleration history and points used for log decrement calculation

5.4.5 Structure performance and comparative data analysis

This section presents overall comparisons between the various structural configurations. The results from Configurations 1-3 are presented and discussed together, as they have the same mass distribution and utilize a moment-frame structural system.

The results from Configuration 4 and Configuration 5 are presented separately in the following chapter, as these structures did not have corresponding "control" weak-structure configurations and must be compared to numerical models incorporating strong base connections.

The experimental program was successful in eliciting a range of superstructure and base plasticity. The maximum beam plastic hinge strain ε_b and maximum anchor elongation ΔL is reported for each configuration under each of the motions in Table 5-18. The maximum beam plastic strain was calculated on the basis of all instrumented beam locations, but generally occurred in the Floor 1 beam. The maximum strain is also expressed in terms as a fraction of the yield plastic strain measured in Chapter 2. Note that for Configuration 3-5, ε_b includes a multiplier of 5 to account for the difference between strain measured at the strain gage location and the maximum strain in the reduced section. This multiplier was established based on numerical modeling of the reduced section, as described in Chapter 4. Configurations 1 and 2 do not include a multiplier, as numerical modeling indicates that the measured strain is very close to the maximum strain. Measured beam section strains ranged from about less than 10% of yield for Configuration 1 under the Service motion to nearly nine times yield for Configuration 2 under the Maximum motion. Elongation of the anchors ranged from 0 in Configuration 2 to about 6.6% for Configuration 1 under the Maximum motion.

Table 5-18: Summary of maximum reduced-section beam strains and anchor elongations

	Maximum measured response under each motion				
Configuration	Service	Design	Maximum	Aftershock	Extreme
1 (L_s=8.5in)	ε_b = 145με (0.09ε_y) ΔL =0.04in (0.5%)	ε_b = 440με (0.26ε_y) ΔL =0.28in (3.3%)	ε_b = 760με (0.45ε_y) ΔL = 0.56in (6.6%)	ε_b = 245με (0.15ε_y) ΔL = 0.14in (1.6%)	-
2 (L_s=2.5in)	ε_b = 2030με (1.21ε_y) ΔL =0.00in (0.0%)	ε_b = 10210με (6.08ε_y) ΔL =0.00in (0.0%)	ε_b[1] = 14655με (8.72ε_y) ΔL =0.00in (0.0%)	ε_b = 3465με (2.06ε_y) ΔL =0.00in (0.0%)	-
3 (L_s=10.5in)	ε_b[2] = 975με (0.58ε_y) ΔL =0.03in (0.3%)	ε_b = 2495με (1.49ε_y) ΔL =0.09in (0.9%)	ε_b = 2730με (1.63ε_y) ΔL =0.18in (1.7%)	ε_b = 1210με (0.72ε_y) ΔL =0.02in (0.2%)	-
4 (L_s=10.5in)	ε_b = 990με (0.61ε_y) ΔL =0.01in (0.1%)	ε_b = 2020με (1.20ε_y) ΔL =0.03in (0.2%)	ε_b = 2775με *(1.65 ε_y)* ΔL =0.10in (1.0%)	-	-
5 (L_s=10.5in)	ε_b[3] = N/A ΔL =0.02in (0.2%)	ε_b = N/A ΔL = 0.12in (1.1%)	ε_b = N/A ΔL = 0.27in (2.6%)	ε_b = N/A ΔL = 0.09in (0.9%)	ε_b = N/A ΔL = 0.63in (6.0%)

NOTE:
1) Lower bound. Measurement saturated during testing.
2) Configuration 3and 4 include multiplier of 5 to account for difference between measured and maximum strain. Multiplier established based on numerical modeling.
3) Beam strain not an integral part of structural response. There was no observed superstructure plasticity.

The measured virgin natural frequency and damping ratio of the four MF-type configurations (Configurations 1-4) varied slightly due to the effects of the beam and column fuse "cuts", the initial rigidity of the base connections, and the amount of deformation that occurred in the connections. The single BF configuration was substantially stiffer, resulting in a much shorter natural period. An evaluation of comparative structure performance should therefore begin with a consideration of variations in the imposed seismic demand caused by the different natural frequencies and damping ratios of each structure. It should be noted that different natural frequencies and

damping ratios would be expected for "real" structures designed with a "base dominated" and "structure dominated" philosophy. Therefore, test results analyzed in this chapter are not strictly controlled for the different levels of demand, but are compared using the different levels of demand as a context.

The response of the structures was dominated by the first mode of response, by definition for the SDOF configurations 4 and 5 and by inspection for the other configurations. Therefore, for simplicity, only the first mode is considered in the following discussion. The virgin first natural period and damping ratio measured from the WN and impact tests are summarized in Table 5-19. The acceleration response spectra of each achieved motion corresponding to each of the measured damping levels are shown with the virgin and "anchors-loose" natural frequencies in Figure 5-100through Figure 5-103. For the Service and Maximum motions, the demand for Configurations 1 and 3 were up to about 30% lower than for Configuration 2, depending somewhat on whether the virgin or loose natural period of Configurations 1 and 3 were considered. For the Design and Aftershock motions, the spectral acceleration associated with the C3 loose natural period was substantially higher than Configuration 1 or 2, increasing almost 50% over the acceleration associated with the virgin natural period. The transition from the virgin to loose natural periods of C1 were associated with small decrease in spectral acceleration for all motions except for the Service motion.

Table 5-19: Summary of 1st mode period and damping ratio for all structural configurations

	1st Natural Period, (s)		
Configuration	Virgin	Anchors Loose	1st Modal Damping Ratio
1	0.288	0.329	1.7
2	0.344	--	0.8
3	0.297	0.380	1.0
4	0.345	0.368	2.0
5	0.168	0.212	1.1

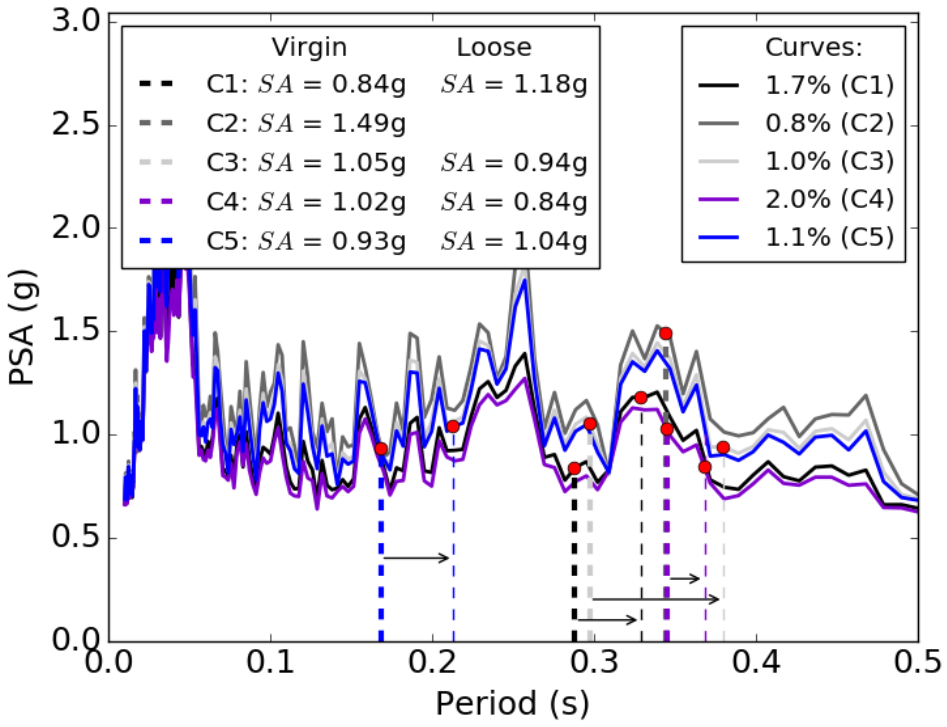

Figure 5-100: Service motion: elastic spectral accelerations associated with virgin and shifted ("anchors loose") first natural periods and measured damping ratios for all configurations

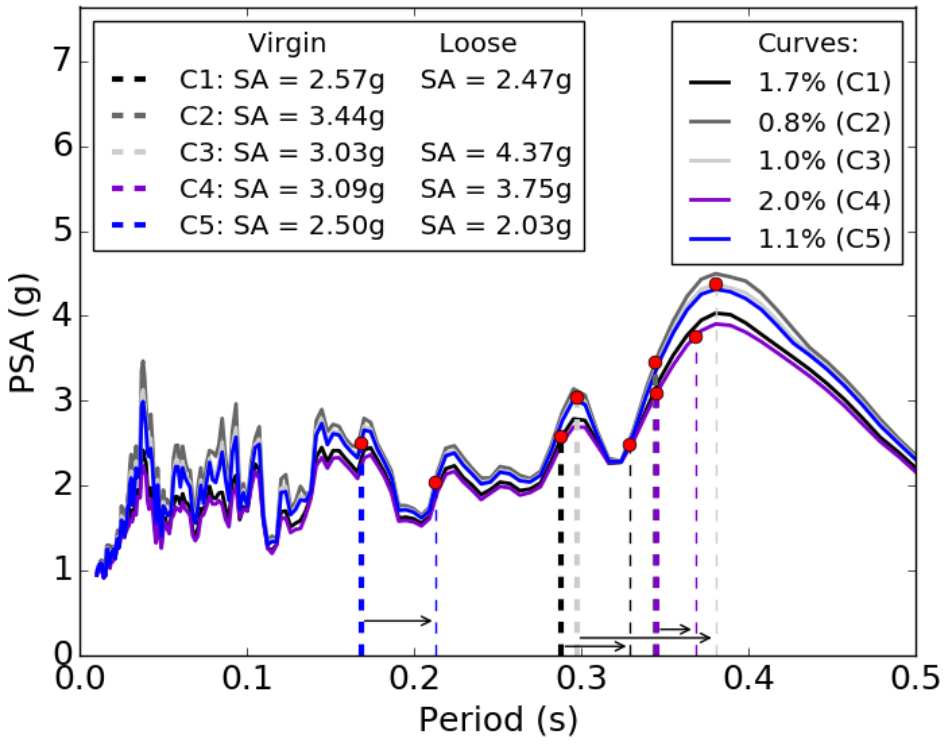

Figure 5-101: Design motion: elastic spectral accelerations associated with virgin and shifted ("anchors loose") first natural periods and measured damping ratios for all configurations

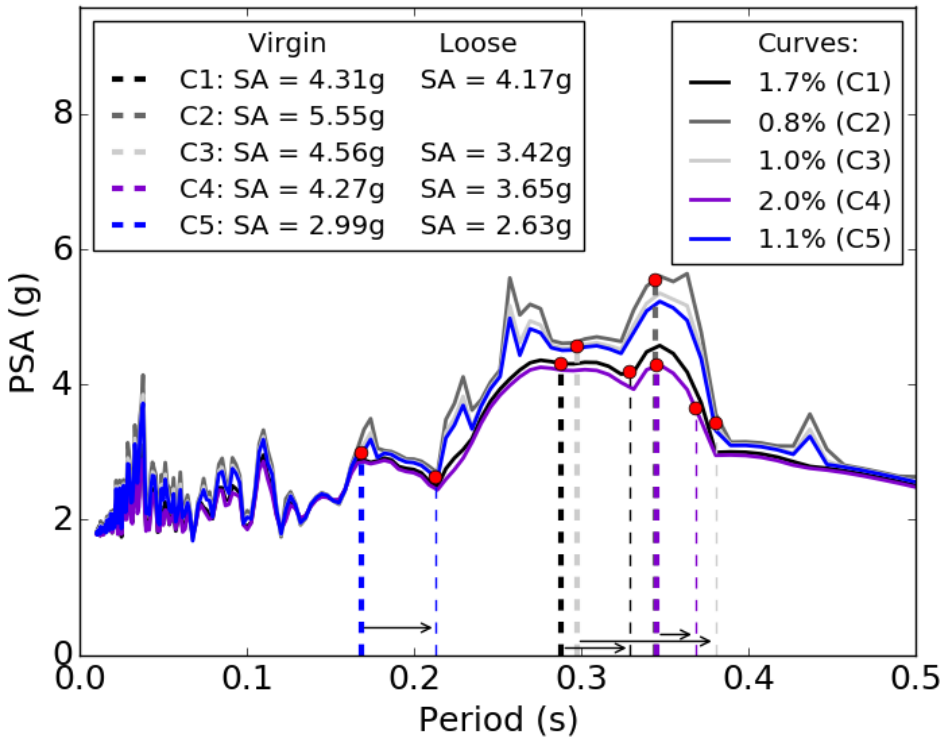

Figure 5-102: Maximum motion: spectral accelerations associated with virgin and shifted ("anchors loose") first natural periods for measured damping ratios

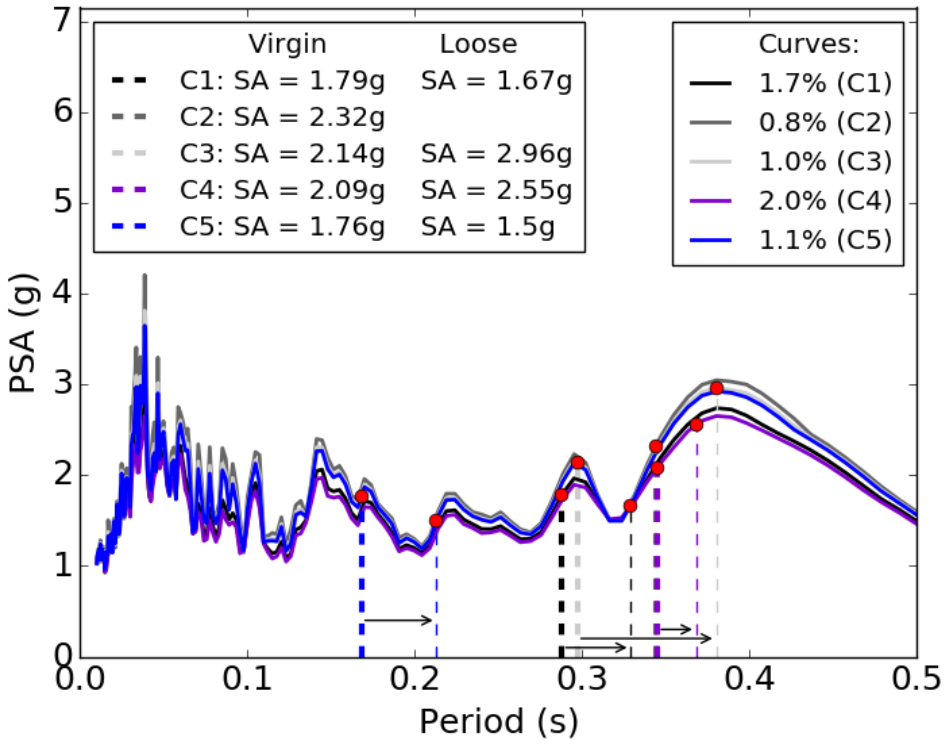

Figure 5-103: Aftershock motion: elastic spectral accelerations associated with virgin and shifted ("anchors loose") first natural periods for measured damping ratios

Story shears, particularly total base shear, are one of the most important parameters for the seismic design of structures. Larger total base shear is, in general, associated with increased required member sizes throughout the structure, more complex connections, and increased initial structural cost. In the case of the current structures, the history of the story and total base shears may be calculated using the measured acceleration history at each floor. Assuming that the structure has three lumped masses at each of the floors, as shown in Figure 5-26, the equation of motion may be idealized as:

$$\mathbf{m\ddot{u}} + \mathbf{c\dot{u}} + \mathbf{ku} = -\mathbf{m1}\ddot{u}_g$$

where **m**, **c**, and **k** are 3x3 matrices describing the mass, damping, and stiffness, 1 is the identity matrix, and **u** its derivatives are 3x1 vectors representing the relative

displacement, relative velocity, and absolute acceleration of the three floor levels. Under this idealization, the total base shear at any instant may then be calculated form dynamic equilibrium as:

$$V = \mathbf{m\ddot{u}}$$

or, expanded:

$$V = m_1\ddot{u}_1 + m_2\ddot{u}_2 + m_3\ddot{u}_3$$

where m_i and u_i are the lumped masses and accelerations at floors, numbered i=1-3. The shear in the second and third stories may be calculated as the sum of the mass times the acceleration at the levels above. The story-level shears are presented for the moment-frame configurations in Figure 5-104, Figure 5-105, Figure 5-106, and Figure 5-107 for the Service, Design, Maximum, and Aftershock motions, respectively. Note that the calculation of base shear was performed considering that a force that causes northward acceleration of masses above a free-body cut to be positive. The story shears under the service motion had several spikes of similar magnitude throughout the first third of the record. Story shears under the other motions were characterized by one or two peaks of similar magnitude corresponding to the most intense part of the motions. The story-by-story shear maxima are compared in Figure 5-108. The shears are plotted as absolute values on the bottom axis, and normalized to the total structural weight *W* on the top axis. In general, the total base shear (the lowest plotted values on the graph) is somewhat lower for Configuration 1 versus Configuration 2, the control.

Top help accentuate this difference, the total base shear of each configuration is normalized to that of Configuration 2 in Figure 5-109. Base shear in the CD

configuration is reduced over 20%, 12%, and 15% in the Service, Design, and Aftershock motions, respectively. There is less than a 5% increase under the Maximum motion. Somewhat surprisingly, there was a large increase in the total base shear under the Maximum motion for Configuration 3, while there was a small increase for the Design motion and significant decreases under the other motions. This is all the more surprising considering the elastic spectral acceleration drop associated with the period shift of Configuration 3 for the Maximum motion was significant (Figure 5-102). However, review of video from this test reveals a particularly unfortunate phasing of the structure response versus the input motion, such that the building appeared to be moving north while the largest southerly acceleration spike occurred while the anchors on the tension side were not yet yielded.

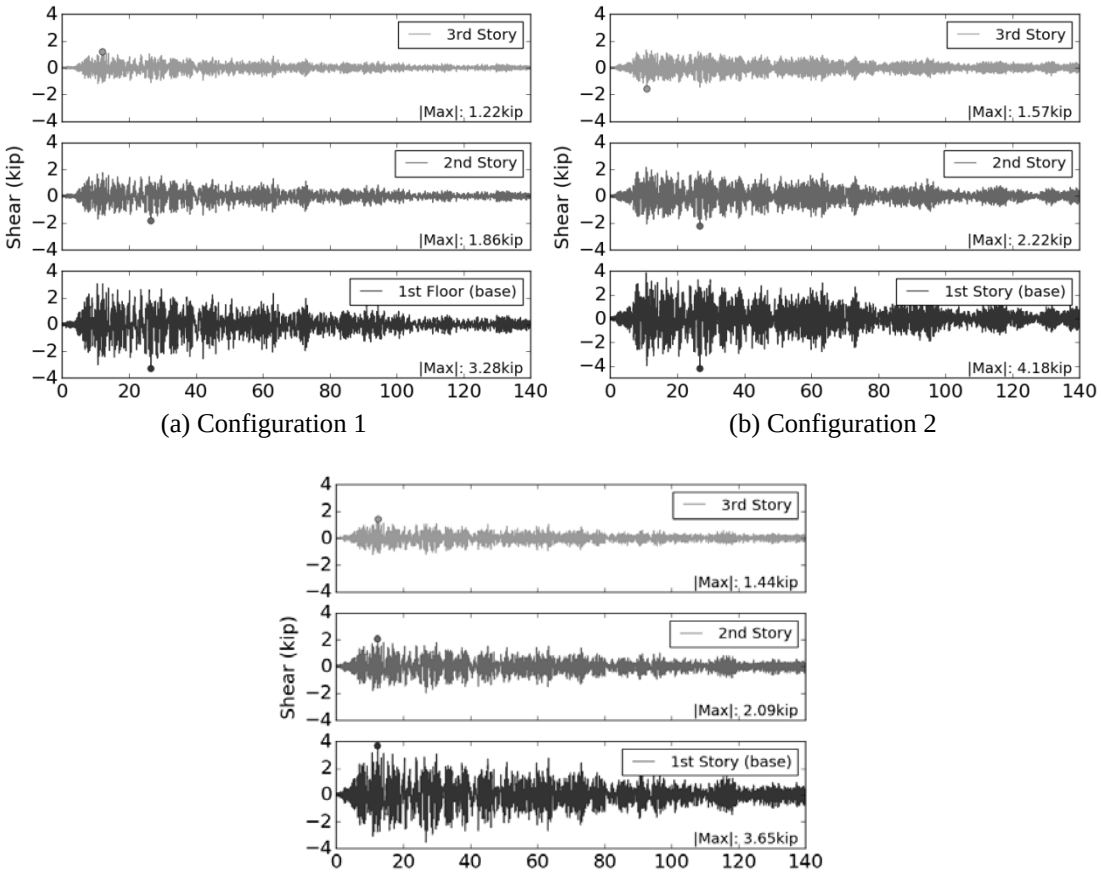

(a) Configuration 1

(b) Configuration 2

(c) Configuration 3

Figure 5-104: Story shear under Service motion, Configurations 1-3 (a-c, respectively)

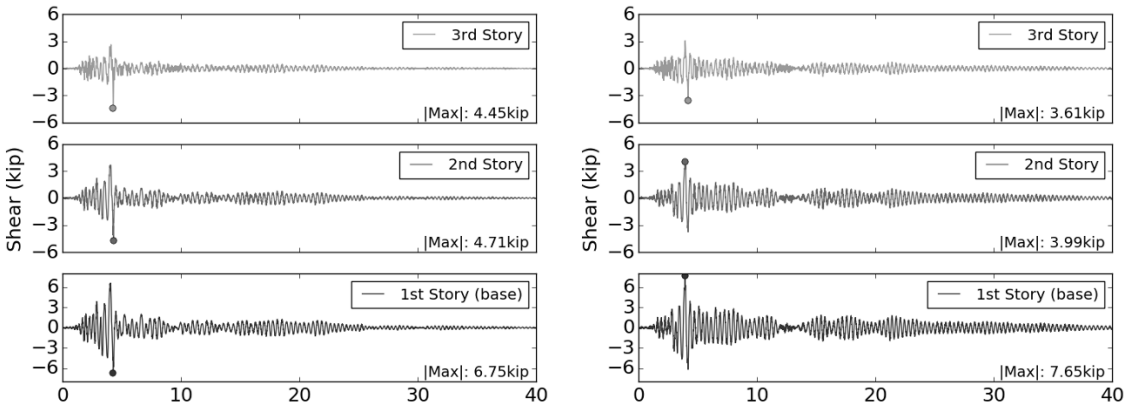

(a) Configuration 1

(b) Configuration 2

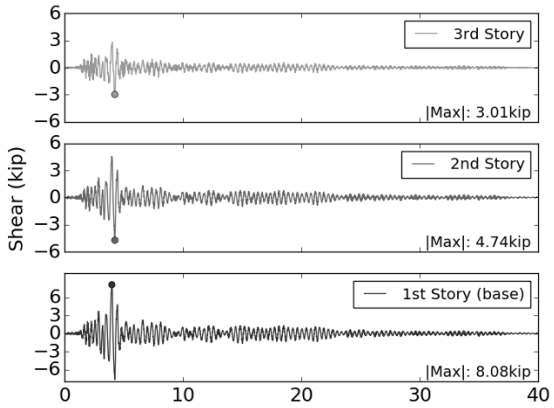

(c) Configuration 3

Figure 5-105: Story shear under Design motion, Configurations 1-3 (a-c, respectively)

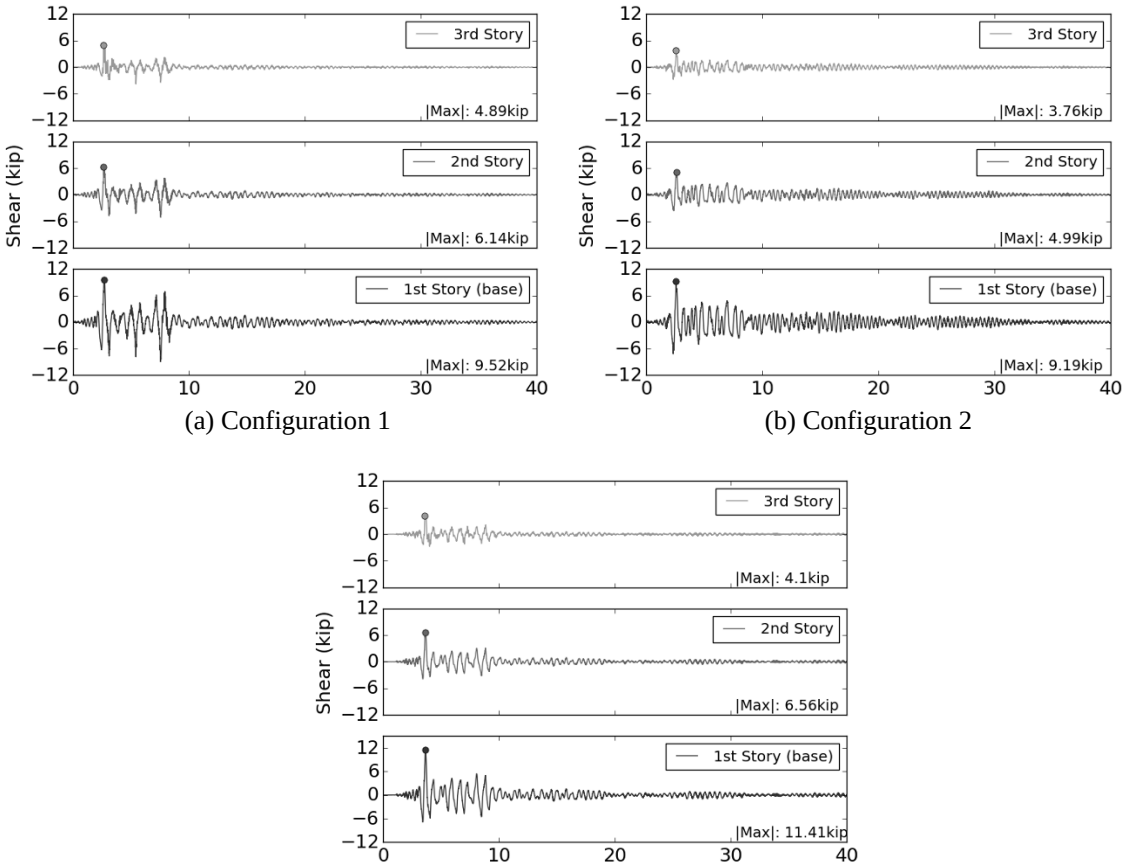

(a) Configuration 1

(b) Configuration 2

(c) Configuration 3

Figure 5-106: Story shear under Maximum motion, Configurations 1-3 (a-c, respectively)

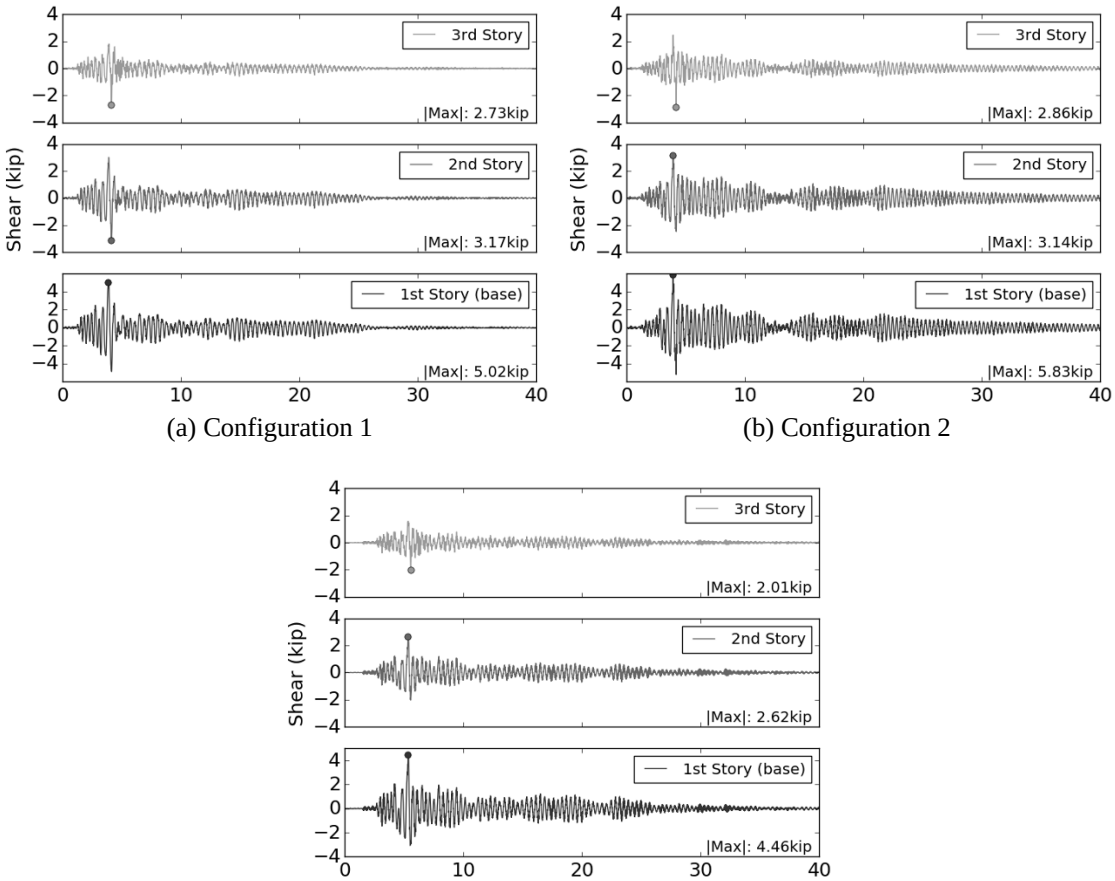

(a) Configuration 1

(b) Configuration 2

(c) Configuration 3

Figure 5-107: Story shear under Aftershock motion, Configurations 1-3 (a-c, respectively)

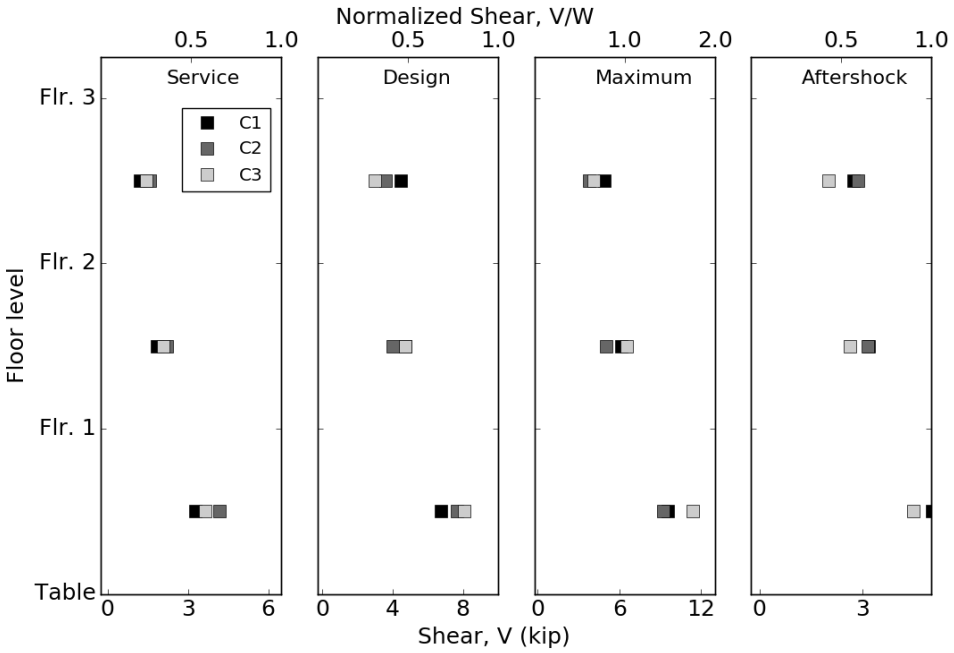

Figure 5-108: Summary of story shears under all motions, Configurations 1-3

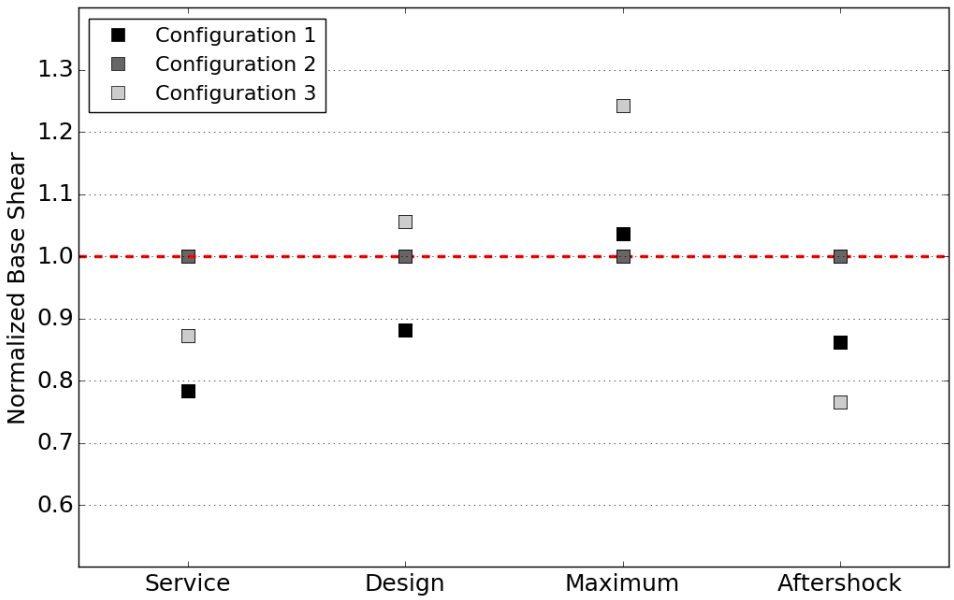

Figure 5-109: Total maximum base shear normalized to Configuration 2 base shears

The peak floor accelerations (PFAs) are a useful in-structure response to consider, as they are often used for the design of relatively rigid components attached to the structure, and may be considered as a proxy for acceleration-sensitive non-structural component damage (along with in-structure response spectra, or ISRS). PFAs in the x-direction for Configurations 1-3 are shown in Figure 5-110. Note that these peak accelerations were taken from the acceleration records filtered in accordance with Appendix D (0.05-30Hz passband). For the service and aftershock motions, there are no clear trends regarding amplification as a function of structure configuration. For the design and maximum cases, however, Configurations 1 and 3 clearly attain larger floor-level accelerations than the structure-dominated case. It is clear that the amplification of maximum acceleration is nonlinear, as the design and aftershock motions are in fact the same recording with different amplification factors, and they result in a very different distribution of in-structure maximum accelerations. The performance of the different structural configurations at the design and maximum levels may be explained partly by the presence of a very distinct, relatively high-frequency "spike" associated with the PGA in these two motions. For the SD MF configuration, this spike was associated with nearly instantaneous yielding of the column fuses. For the CD and BD configurations, this spike caused yielding of the anchors, but this did not cause instantaneous lowering of the natural frequency of the structure nor significant energy dissipation in and of itself. Therefore, although the structure remained essentially undamaged in these two cases, it also remained relatively rigid and underwent significant accelerations as the pulse travelled up the structure.

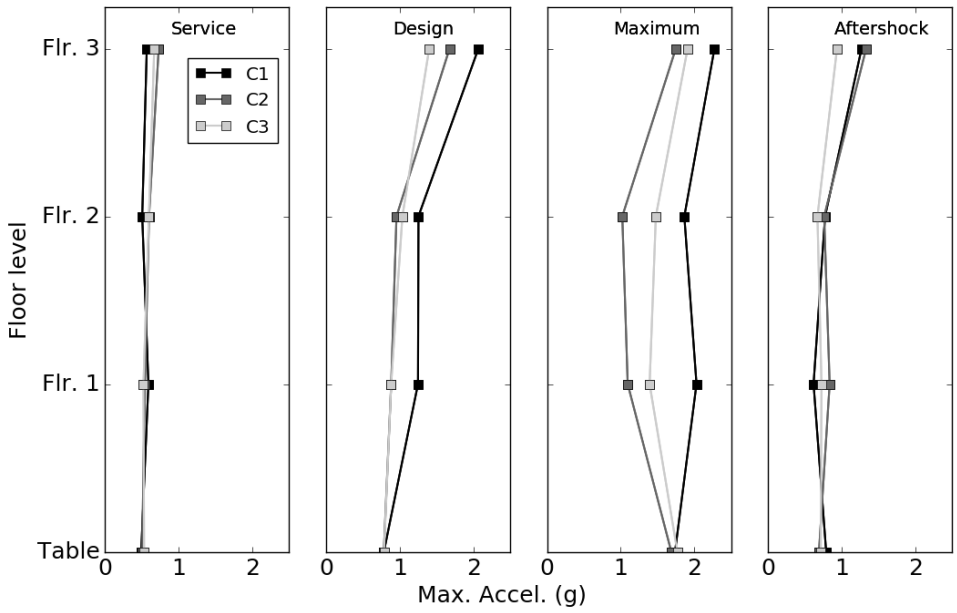

Figure 5-110: Comparison of ground and floor-level maximum accelerations for Configurations 1-3

ISRS are of interest for similar reasons to PFAs, as they indicate both design requirements and the potential for damage of flexible acceleration-sensitive nonstructural components. ISRS for each configuration and motion have been presented previously. ISRS maxima are convenient parameters for comparison, as this value represents the "worst case" acceleration for a component at a particular damping ratio, and the maximum is often used as a conservative basis for design of components of all natural frequencies. 5%-damped ISRS maxima for each configuration and motion are presented in Figure 5-111. In contrast to the maximum accelerations, the Configuration 1 values are below the Configuration 2 values in all cases but the Maximum. However, the absolute maximum of ISRS in the case of the current research program must be considered carefully, as for several of the motions, there is a narrow, high-frequency spike in the achieved response spectra due to the coupled table-foundation mode at 25 Hz (Figure 5-40). This spike propagates through the structure and is present in the overall shape of

the ISRS (e.g. Figure 5-54, Figure 5-71, etc.). Therefore, Figure 5-111 does accurately reflect the transmission of relatively high-frequency motion through the structure, but much of this motion is an artifact of the table and not present in the source motions. An alternative comparison is the ISRS maximum considering only the portions of the spectrum with periods longer than 0.25s, which is within the period range of accurate response of the table but includes the structure fundamental frequencies. This comparison is shown in Figure 5-112. In this case, the performance of the CD configuration is still superior to that of the SD configuration in all cases except the upper floors under the maximum motion. The maxima of the CD structure are between about 5 and 40% below the SD structure, except in these two cases. These exceedances are driven by relatively large peaks at the fundamental structural frequency (Figure 5-54). The reason for this peak appears to be related to the number of total number of intense motion cycles the structure undergoes. The roof drift histories for the Service, Design, and Maximum motions are shown in Figure 5-113. Under the maximum motion, the CD structure clearly undergoes several more intense cycles at the building natural frequency than the SD structure. This is due to global frame action which becomes unrestrained after the anchors have yielded, increasing the total acceleration undergone by oscillators at the building's natural frequency within the structure.

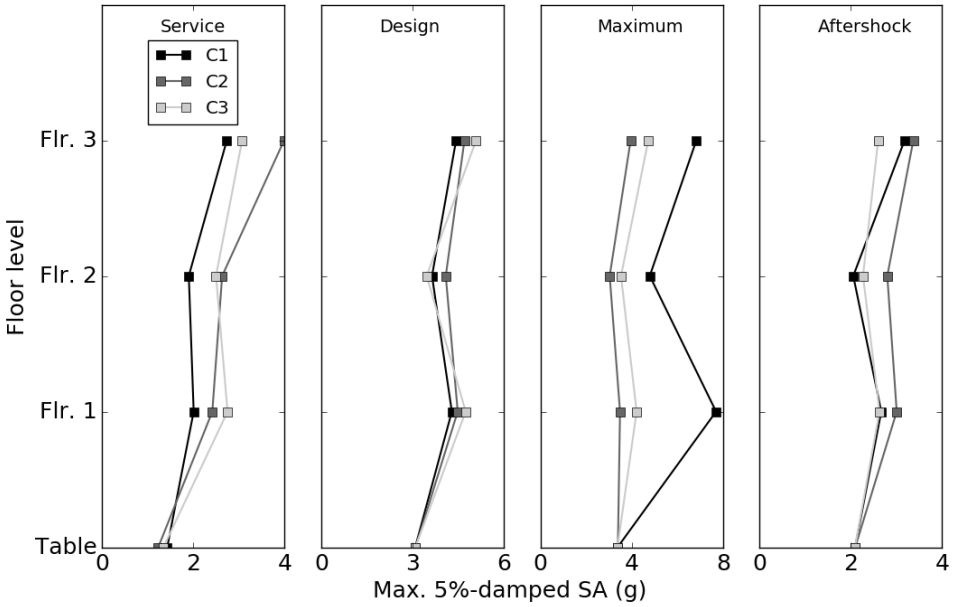

Figure 5-111: Summary of maximum 5%-damped spectral accelerations for configurations 1-3

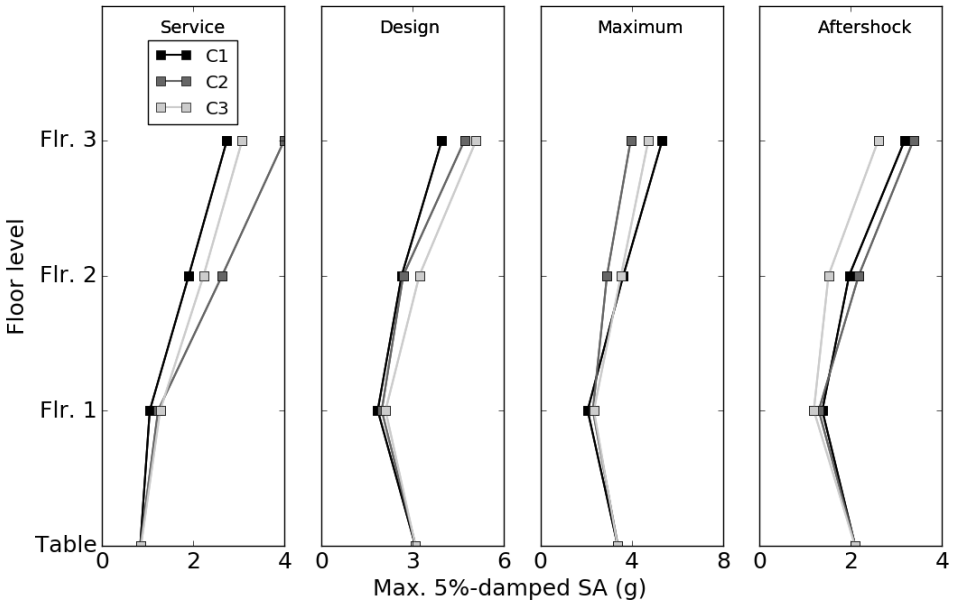

Figure 5-112: Summary of maximum 5%-damped spectral accelerations considering only periods longer than 0.25s for Configurations 1-3

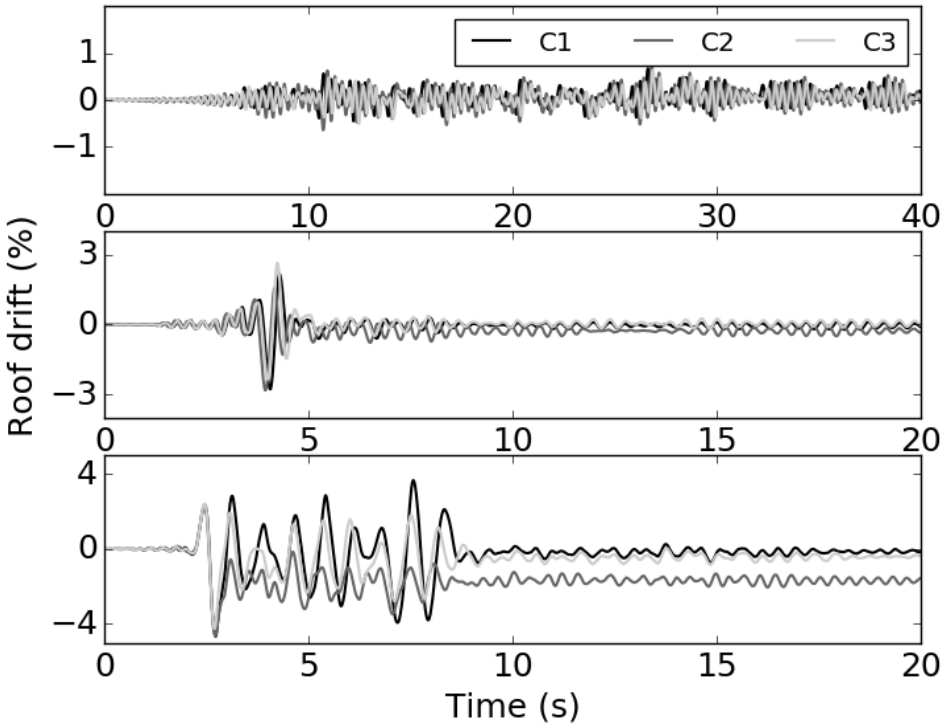

Figure 5-113: Time history of roof drift for Service, Design, and Maximum motions (top to bottom) for Configurations 1-3

A potential criticism of base-dominated structures is the possibility of the development of large vertical accelerations due to pounding, both due to connection rotation (frame action) and structural overturning (global rocking). Some previous studies on uplifting-column systems have provided specially-designed pads under the base connections to try to reduce this behavior (i.e. Hucklebridge 1977). However, in the current work, the observed column uplift did not lead to higher vertical accelerations, as shown in Figure 5-114. This figure shows the maximum absolute value from either of the two vertical accelerometers (A4 and A5), low-pass filtered at 30 Hz. Although there were slight magnitude changes, the overall pattern of the results were not sensitive to the choice of the low-pass corner frequency. For the service and aftershock motions, the vertical accelerations were nearly equal for all configurations. For the design and

maximum motions, there was a very large variation in the maximum accelerations, with the maximum from the SD case under the design motion more than double that of the BD case. It appears, therefore, that maximum vertical accelerations were more sensitive to the motion than the particular structural configuration.

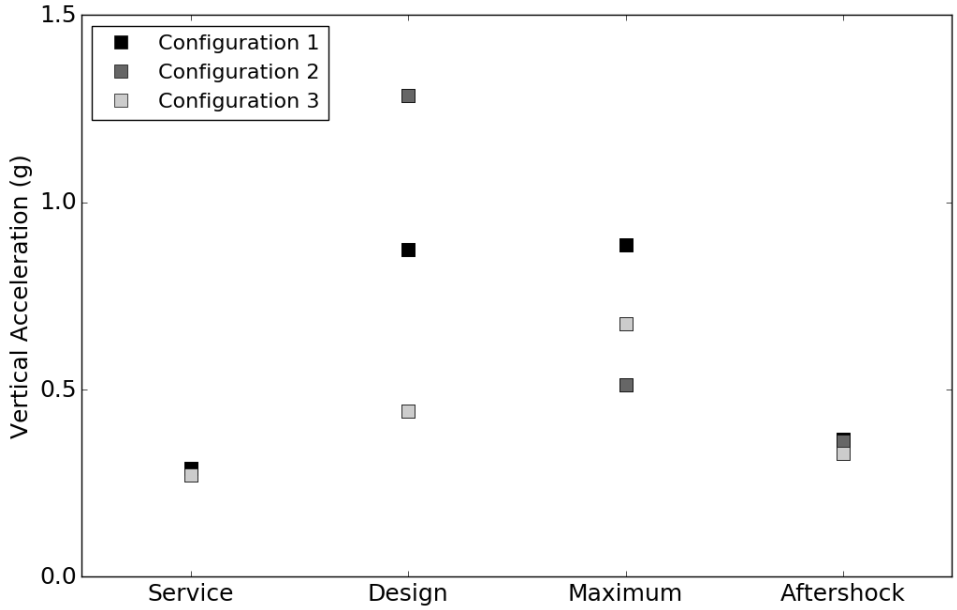

Figure 5-114: Comparison of maximum 3rd-floor vertical accelerations for Configurations 1-3

There was a large difference in both the magnitude and pattern of the measured y-direction accelerations (accelerations out of the plane of shaking). In general, the y-direction accelerations were significantly higher in the yielding-anchor cases (CD and BD) versus the SD configuration. Figure 5-115 shows a comparison between the SD and BD cases under the design motion. The maximum acceleration is over three times as high in the BD case, and there a number of relatively intense cycles during the strong-motion portion of the record. A summary of the maximum y-direction accelerations is shown in Figure 5-116. For all cases except the Service motion, the CD configuration has the

largest response. This response is due to the overall structural motion that occurs once the anchors have yielded and the structure is free to rock both in the x- and y- directions, a behavior which is clearly absent from the SD configuration. However, this behavior is not necessarily detrimental, as a real earthquake will excite the structure in both horizontal directions. The excitation of the current structure in the y-direction was due only to incidental table vibration. As shown by the data presented in Figure 5-110 through Figure 5-115, the amplification of accelerations through the structure is generally smaller for the BD and CD cases, but is highly motion-dependent. The behavior would be expected in the case of y-direction excitation as well.

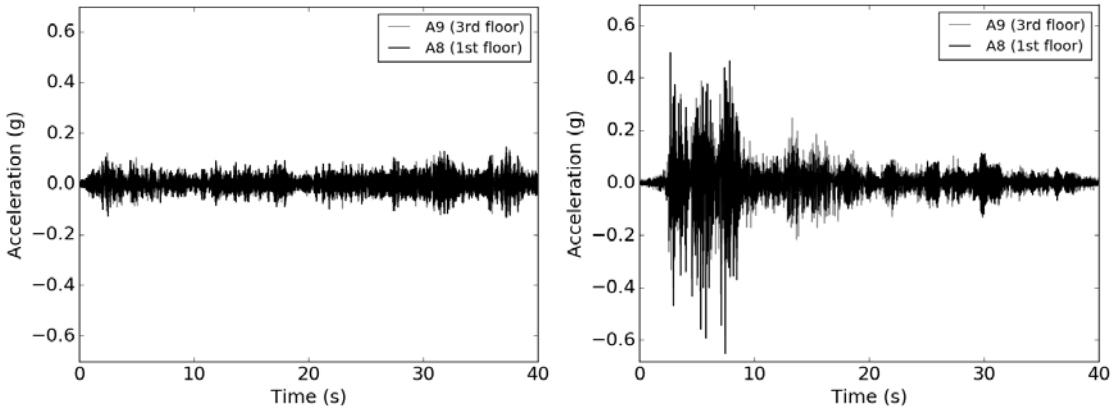

(a) Configuration 2 (b) Configuration 3

Figure 5-115: Comparison of 3rd-floor horizontal y-direction (lateral) accelerations for under Design motion

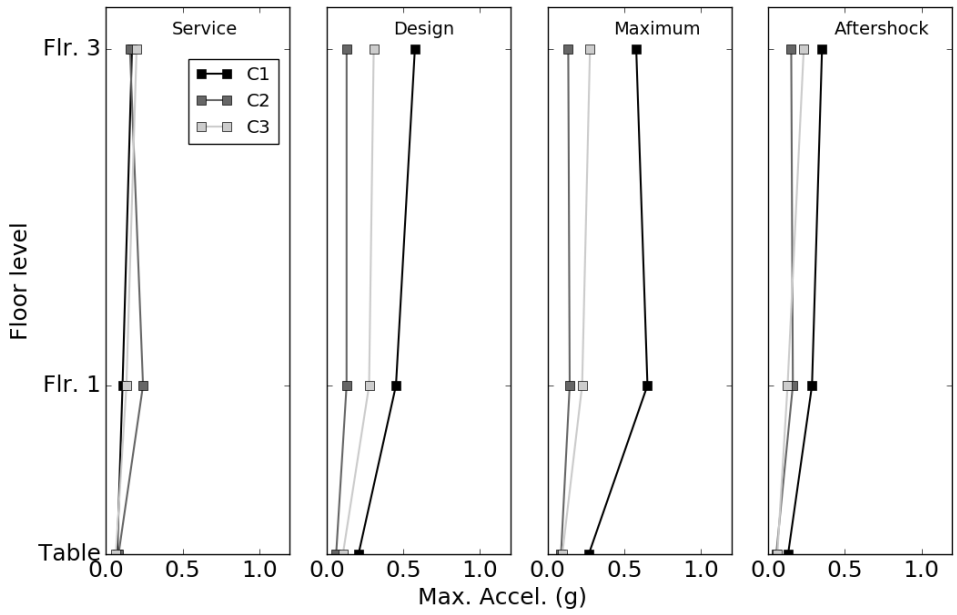

Figure 5-116: Comparison of maximum 1st- and 3rd-floor horizontal y-direction (lateral) accelerations for Configurations 1-3

Maximum interstory drift is a useful point of comparison because maximum drift may be used as a proxy for damage to floor-to-floor, displacement-sensitive components such as partition walls. Both maximum and residual interstory drift are often used to evaluate the performance of structures during earthquakes, and are make decisions about whether structural replacement or repair actions are required (SEAOC 2000). Measured maximum and residual drifts are shown in Figure 5-117 and Figure 5-118, respectively. Maximum drifts under all motions were generally very similar. The maximum interstory drifts at each level were within 30% of the smallest measured value at each level for all motions. The maximum residual drift for each configuration is reported in Table 5-20. As shown, the maximum residual interstory drifts for the Service and Aftershock motions were very small for all structural configurations, about 0.1% and below. In contrast, there were large differences in the residual drifts under the more intense motions (Design and

Maximum). Residual drifts were less than 0.2% in Configuration 1 (BD MF), regardless of motion intensity. Maximum residual drifts for Configuration 2 were about 0.3% and 1.8% under the Design and Maximum motions, respectively. Both of these levels would almost certainly require a complete structural inspection if they were found following a real earthquake. SEAOC has developed a categorization of structural limit states for typical buildings based on both maximum and residual drift (SEAOC 2016). Based on this categorization scheme, Configuration 2 was between "Operational" and "Life Safe" under the Design motion, and between Life Safe and "Near Collapse" under the Maximum motion. Configuration 1 was either "Fully Operational" or "Operational" following all motions (the SEAOC framework does not differentiate between these two limit states based on residual drift). Configuration 3 would be categorized between "Operational" and "Life Safe" following the Maximum motion, and Operational or Fully Operational for all others.

Extrapolating structural repair actions and total cost from residual drifts and/or limit state categorizations is inherently difficult, particularly considering the current buildings are miniature representations of real buildings. However, some qualitative comments can be made based on professional judgment and published damage descriptions for the preceding limit states (SEAOC 2016). Based on the damage observed during the test and the limit state categorizations discussed, Configuration 2 would likely require minor to moderate repair actions following the Design motion, such as the replacement or repair of the structural fuse locations. In a real structure, this might take the form of replacement of yielded bolts and potentially other connection

components. Following the Maximum motion, Configuration 2 would likely require complete building replacement. This assessment may be made with some certainty, as it would be difficult to envision repair actions which could restore functionality to a building with the high residual drifts measured.

In the current experiments, Configuration 1 (BD MF) was essentially damage-free, other than the anchors, which underwent significant elongation. Extrapolating to a real building, it is likely that no superstructure repairs would be necessary. The anchors, particularly if they were constructed similarly to those in the current tests, could be replaced with relative ease. The performance of Configuration 3 was intermediate of that of C1 and C2, but much closer to that of C1. Under the Maximum motion, the maximum residual interstory drift was nearly 0.5%. Therefore, the anchors would likely need replacement in this case, and some limited superstructure repairs may be necessary.

Although a detailed accounting of repair and/or replacement costs is outside the scope of the current investigation, it may nonetheless be concluded with certainty that the structural repair costs associated with Configuration 1 would be substantially less than for Configuration 2. The costs of repairing Configuration 3 would likely be intermediate. However, given that under the Maximum motion the likely outcome for Configuration 2 is complete structural replacement, while only minor or moderate repair actions would be required in the others, both of the yielding-anchor configurations hint at a sizable post-earthquake cost savings.

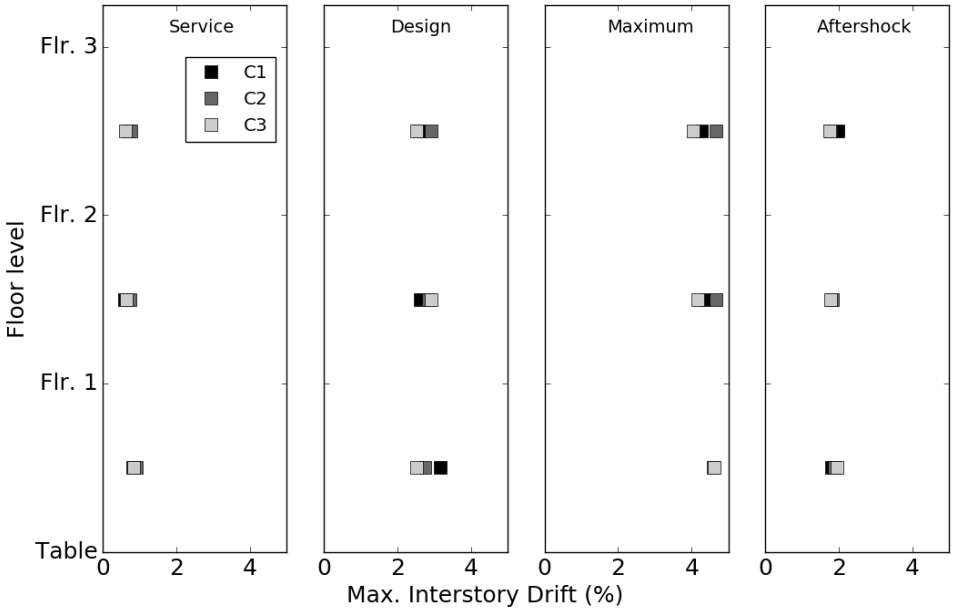

Figure 5-117: Summary of maximum interstory drift for Configurations 1-3

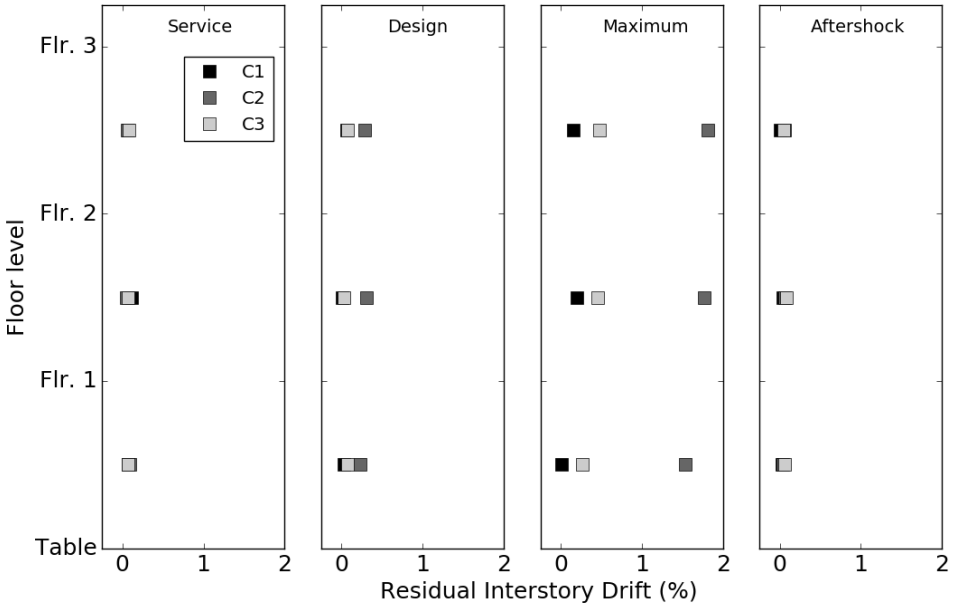

Figure 5-118: Summary of residual interstory drift for Configurations 1-3

Table 5-20: Summary of maximum residual interstory drift values

	Maximum recorded residual interstory drift (%)			
Configuration	Service	Design	Maximum	Aftershock
1	0.11	0.03	0.20	0.03
2	0.10	0.30	1.81	0.06
3	0.08	0.08	0.48	0.08

Note: values shown in table are maximum of the three stories

5.5 Numerical modeling

5.5.1 Purpose and scope

Dynamic numerical models were developed using the LS-DYNA finite element code (LSTC 2013) as part of the current work. The primary goals of the numerical modeling program were:

1) Verification of the modeling approach in terms of dynamic properties and dynamic response

2) Use of similar numerical models to evaluate the performance of the Configurations that did not have a corresponding "control" with superstructure fuses (4 and 5). In these cases, the model provides a point of comparison for behavioral changes and response improvements in the ductile anchor case.

The verified numerical models may also be used to determine forces, moments, curvatures, and other physical response measurements that were not directly available in the experimental test program. In addition, development of verified numerical modeling techniques allows the analysis of similar, but potentially larger and/or more complex structures. Both of these additional uses of the model are proposed for future work.

5.5.2 Numerical model development

Preliminary Hinge Concept Verification Models

Ideally, the frame part of the numerical models would be comprised only of beam elements. Beam elements are computationally efficient and are capable of accurately

capturing evolving cross-section plasticity if sufficient numbers of cross-section integration points are provided. However, the cross section of the beam/column cutouts utilized in Configurations 2-5 are not amenable to beam cross-section modeling for two reasons: 1) The cutouts are three-dimensional and curved in nature, meaning that there are stress concentrations in the wall of the surrounding HSS and the strain gradient in the section is nonlinear, even in the elastic range. Beam modeling cannot capture this type of behavior. 2) In the case of the column fuse, the section transitions to two truly unconnected cross-sectional elements, which cannot be easily defined using LS-DYNA without simplification.

Because of these issues, shell modeling of the cutout portions is necessary, with a transition from a shell mesh to a beam mesh at a suitable distance away from the cutout sections. The fineness of the shell mesh will be critical to accurate prediction of the response. Therefore, prior to the development of the final overall structural models, a mesh sensitivity study was conducted using the preliminary static testing of the cutout section concepts described in Section 5.4.1 as a baseline. Although the geometry of the reduced section in these tests was somewhat different than the final configuration, the overall mesh refinement needed to capture the response is expected to be similar. Two refinements were used to determine necessary mesh size, a "coarse" model with an approximately 0.5in. global mesh size in the shell region and a "fine" model with approximately 0.25in. global mesh size. A model of the beam test and column test was made using each refinement. The "coarse" beam mesh and "fine" beam mesh are shown in Figure 5-119 to give a sense of the size of the elements relative to the geometric

features in each case. In the case of the beam concept, an elastic-perfectly plastic material model was used with a hardening modulus of E_t=0 and the yield strength listed in Table 5-10 for the HSS 4x4x3/16. In the case of the column concept, an elastic-plastic material model was used with a hardening modulus of E_t=1,200ksi (~4% of the elastic modulus).

There was very little difference in the response calculated from each model, with the peak responses within about 10% of the observed values for the column hinge test and within 5% for the beam test (Figure 5-120). Therefore, it was concluded that the coarse model provides sufficiently accurate representation of the geometry and the behavior, and a mesh sizing of about 0.5 in. was used for all global structural models of the shake table specimens. The pre-peak region of the beam test was not particularly well-captured for two reasons: 1) The edges of the notches cut in the beams were beveled due to the finite diameter of the grinding wheels used. This geometry was not reflected in the model, where all shell elements had a uniform thickness throughout. 2) there was significant nonlinear behavior observed in the HSS material prior to yield (Figure 5-31a). The effect of using an elastic-plastic material model versus a more sophisticated piecewise linear model is discussed in the context of global structural response later in this chapter.

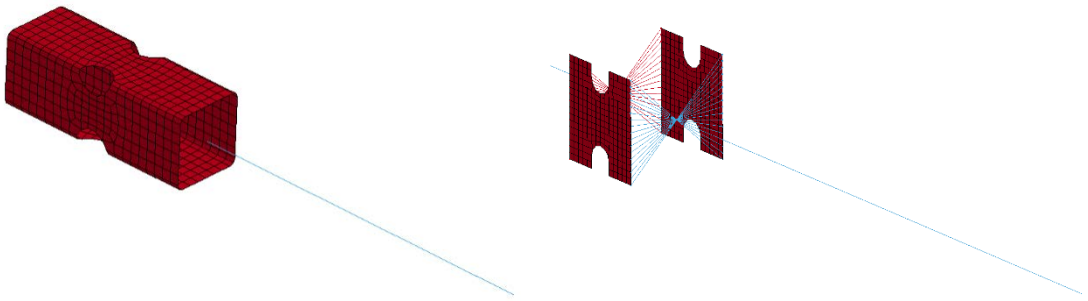

(a) Coarse beam hinge model (b) "fine" column hinge model

Figure 5-119: Models used for mesh refinement study

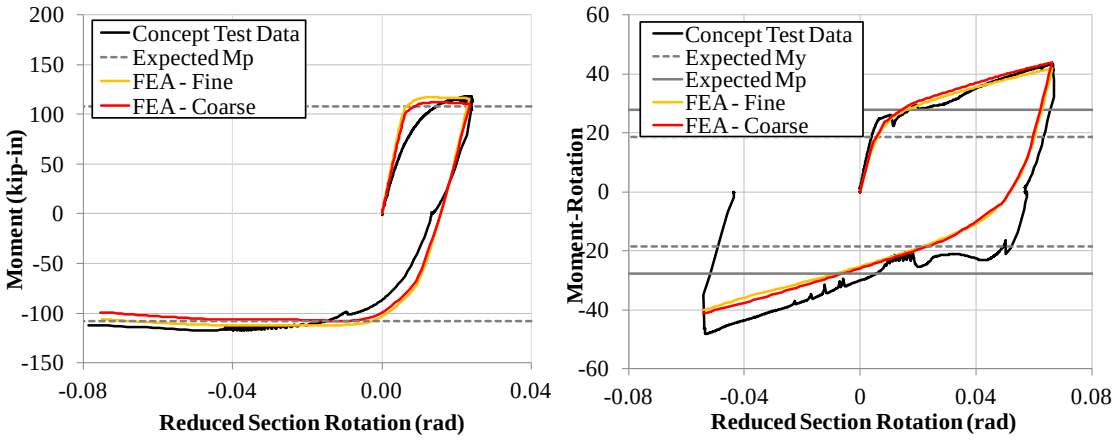

(a) Beam hinge (b) Column hinge

Figure 5-120: Concept test results with FEA calculated response

Dynamic Structural Model Geometry and Scope

Five distinct models, corresponding to each of the five test configurations, were developed as part of the numerical analysis program. The model included explicit representations of the major framing members, cross bracing, floor slabs, baseplates, anchors, and grout. The effect of the foundations, and the loading imparted by the shake table are included via boundary conditions. The models were three-dimensional and did not employ symmetry, such that they could be easily expanded to three dimensional excitation (although this was not performed in the current work). Two iterations of the model were developed. The first model iteration was used only for preliminary design and evaluation of potential structural configurations, and is referred to as the "design" model herein. This model contained an approximation of the final beam and column fuse configuration using beam elements, as described in Chapter 2. The second model iteration utilized a shell-element representation of the exact fuse configuration, and was

used for analysis of the actual dynamic testing, and is referred to as the "analysis" model. The majority of the following description is applicable to both model iterations.

The general model features and overall centerline dimensions are shown in Figure 5-121. Note that the figure is presented with the beam cross-sections rendered. In general, the major framing members were meshed using integrated cross-sections. An elastic-plastic material model with a yield stress equal to the measured yield stress reported in Table 5-10 was used for the shaking-direction beams and columns, to account for the fact that plasticity could potentially spread out of the immediate region of the beam fuse. The hardening modulus was set to zero, based on the observed behavior of the HSS tension coupons (Figure 5-30). An elastic material model was used for the cross-beams and cross-bracing, because this direction was transverse to the direction of shaking and no plastic behavior was expected or observed during testing. The baseplates were meshed using shell elements with a linear-elastic material model. The concrete floor slabs were also modeled using a linear-elastic material model and shell elements with a thickness of the two slabs, measured to be about 10.75 in. total on average. Although this modeling approach is likely too stiff (due to the fact that two slabs, rather than a single monolithic slab were present), the flexibility of the slabs appeared to contribute very little to the overall building response, and this approach was deemed acceptable.

The baseplate connection itself was modeled using a fiber-section approach that has been used successfully to model a broad range of exposed, moment-frame baseplate connections under pseudo-static, reversed cyclic loading (see Chapter 4). The anchors and grout were modeled using tension-only and compression-only nonlinear springs,

respectively. The force-displacement behavior of the anchor springs was calibrated based on the measured force-displacement response of the anchors, depending on size and grade (Figure 5-29). The force-displacement behavior of the grout springs was calibrated based on an assumed grout modulus of 500 times the average measured grout strength, which was approximately 10ksi (ACI 2013). The stiffness *k* of the springs in compression was then calculated using k=AE/L, where A was the tributary area of each spring, and L was the thickness of the grout pad. The element type used for each component of the structure, along with the material model and pertinent material characteristics are summarized in

Table 5-21.

The majority of the mesh was shared by all models; for the analysis model, the geometry of the beam and column cutouts was altered in the analysis model to reflect the particular geometry of each configuration. Based on the sensitivity study documented in the previous section, the beam and column cutout areas were meshed with shell elements with an approximate characteristic dimension of 0.5 in. The details of the beam and column hinge meshes are shown in Figure 5-122. Note that this modeling approach introduced a slight geometric inaccuracy, as the total height of the model was not changed in each case (i.e. the gap between the end of the HSS column pieces shown in Figure 5-5 was not reflected in the model). However, this error is a very small percentage of the total dimension of the structure, and is not considered to be significant.

Based on behavior observed during testing the double-clip angle connections were found believed to contribute significant flexibility to the overall structure. Therefore,

zero-length rotational spring elements were incorporated into the structure at the connection of the beam and column elements (analysis model only). The spring constant for these elements was not calculated, due to the level of detail that would be required in such a substructure analysis model. Instead, the spring constant was adjusted as part of a small sensitivity analysis to match the natural frequencies measured during testing (described below). In addition, a rotational damper element was added at these locations in an effort to model the localized energy dissipation due to connection slip. The damping coefficient for these elements was set based on matching the response histories measured during testing, as described below.

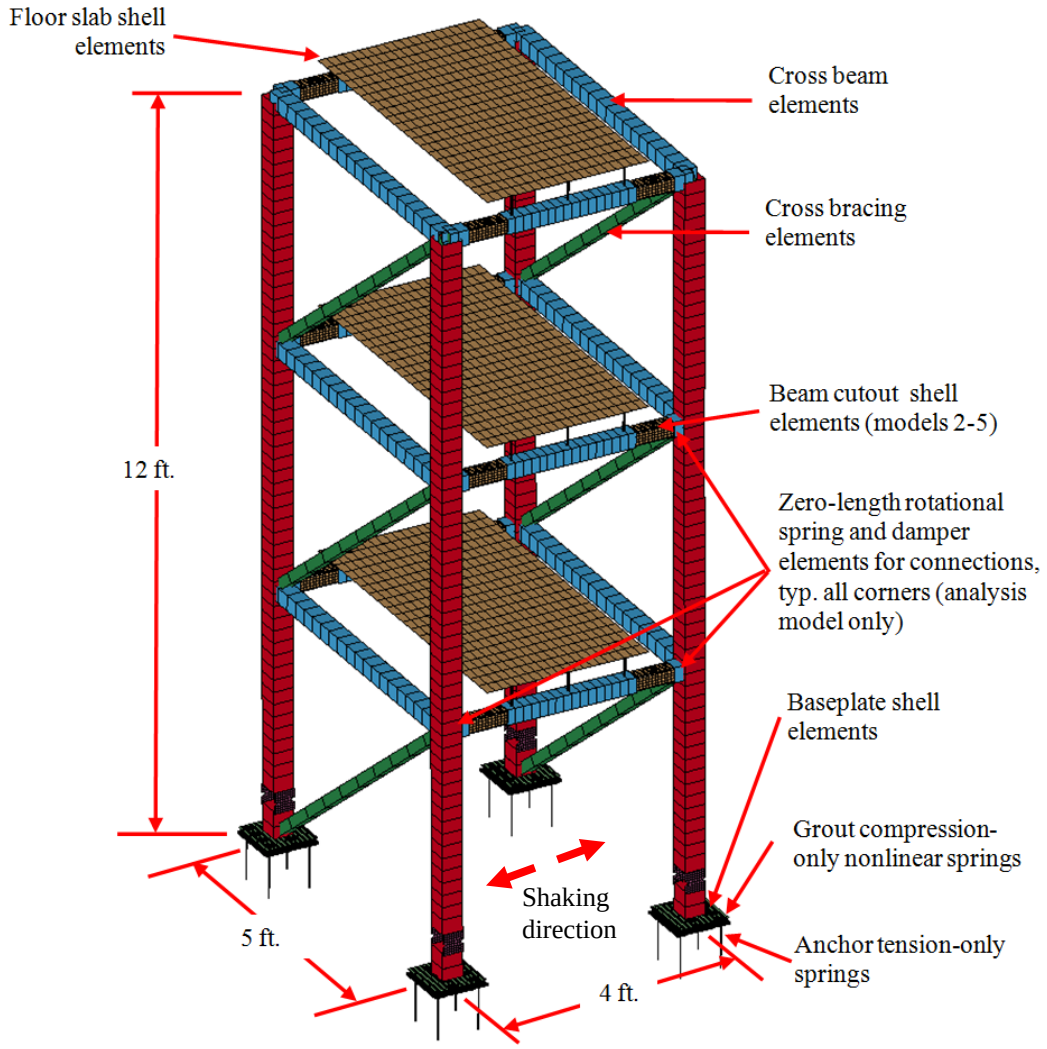

Figure 5-121: General model dimensions and features (with rendered beam element cross-sections)

Table 5-21: Element and material model type for all structure components.

Feature	Element type	Material model	Key material parameters
Beams, columns	Beam	Elastic-plastic	See Table 5-10
Braces	Beam	Elastic	E=29,000 ksi
Floor slabs	Shell	Elastic	E=4,030 ksi
Floor connections	Beam	Elastic	E=290,000 ksi (fictitious)
Baseplates	Shell	Elastic	E=29,000 ksi
Beam cutouts	Beam (design) Shell (analysis)	Elastic-plastic	See Table 5-10 and Figure 5-29
Column cutouts	Shell	Elastic-plastic	See Table 5-10
Anchors	Nonlinear spring (tension only)	Spring	See Figure 5-29
Grout	Nonlinear spring (compression only)	Spring	E_g~500$f'_{g,ave}$ =5,000 ksi

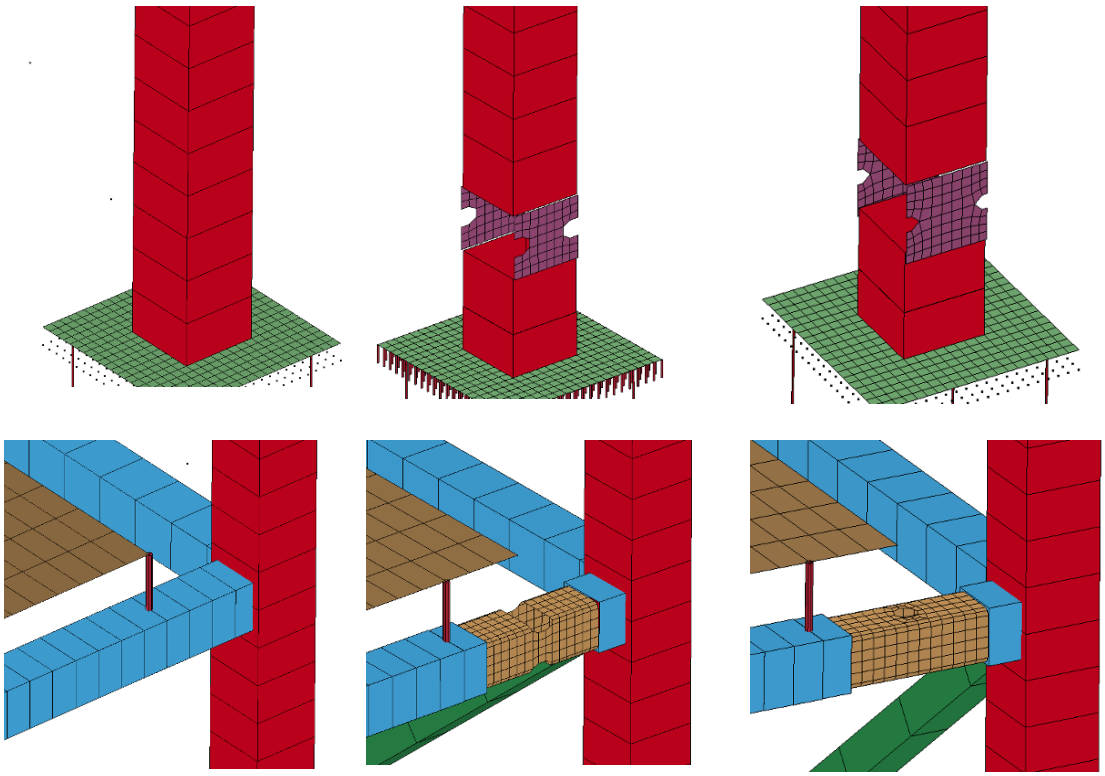

(a) Configuration 1 (b) Configuration 2 (c) Configuration 3-5

Figure 5-122: Beam and column hinge details of each analysis model

5.5.3 Analysis types, boundary conditions, and output requests

Two types of analysis were conducted as part of the current work:

- Eigenvalue analysis: used to confirm the natural frequencies and modes shapes of the model corresponded with the frequencies and mode shapes measured during white-noise excitation

- Implicit dynamic analysis: used to verify the model under the strong-motion excitation tests performed on the structure

For the implicit dynamic analysis, a prescribed x-direction displacement history was applied to all nodes at or below the baseplate. This approach approximates the movement of the foundation slab underneath the structure and allows rotation and uplift

of the baseplate, but it does not admit the possibility that the structure may slide relative to the foundation. As discussed in Chapter 3, this assumption is valid, as the translation of the structure relative to the foundation slab was very small for all motions except for the Extreme motion run for Configuration 5. This case is treated specially, as discussed later in this chapter.

For the eigenvalue analysis, the model needed to me modified slightly, as nonlinear springs are not allowed in a modal analysis in LS-DYNA. For the modal analysis of Configuration 2 (SD MF), the nonlinear grout and anchor springs were replaced with fixed boundary conditions at the base. This approach was justified considering the very large strength and rotational stiffness of the anchor/grout system compared to the column section. For all other configurations, the anchor nonlinear spring elements were replaced with linear spring elements, and a pinned boundary condition was introduced at the bottommost column node. This boundary condition was intended to represent the lateral restraint provided by friction and anchor shear, as well as the vertical restraint provided by bearing on the grout pad. Although approximate, this approach appears to have captured the boundary conditions well, as evidenced by the reasonable matches found between the calculated and measured natural frequencies discussed in the next section.

The implicit dynamic calculations were performed using the Newmark method of numerical integration, with $\gamma=0.5$ and $\beta=0.25$ (constant acceleration per step assumption). Motion was input to the structure as an acceleration time history at the level of the grout springs. For the cases where the analysis was intended to reflect an actual strong motion

run performed on the shake table, the input motion was taken as the table feedback displacement measured during the corresponding test. Global, mass-proportional and stiffness-proportional damping were introduced in all analysis, as described below. Output requests included all nodal displacement components, element-level forces, and stresses and strains at integration points. Output was requested at a spacing of 0.02s, such that the Nyquist frequency was 25Hz (above the maximum frequency of any mode of interest).

5.5.4 Design model runs and results

Prior to executing the experiments, a preliminary model known as the "design" model was used to predict the behavior of the structure in each configuration under a large suite of ground motions scaled to a variety of target intensities. The goals of this model were to:

1. Confirm that the behavioral differences between the different structural configurations would be realized for the different motion intensities, i.e. uplifting behavior of Configuration 1 would occur under the "Design" and "Maximum" motions, while significant, but reasonable superstructure plasticity would occur for Configuration 2.
2. Quantify the expected drift levels in Configuration 2 under a variety of ground motions, in order to allow selection of motions for the experimental program.

Clearly, these two goals were interrelated, in that both modifications to the structure and scaling of the ground motions could be used to elicit the desired responses from the structure. To make this problem tractable, it was decided to cap the motion scale factors

at a reasonable level, near 1.5 for the maximum motions. This way, the motions are at least plausible representations of actual motions that could occur in nature.

In general, the first goal of the modeling program was achieved: the SD analysis results were characterized by broad hysteretic response, consistent with the typical response of a moment frame with ductile detailing. In contrast, the BD model responded nearly linearly, regardless of motion intensity. As a result, the SD structure was often left with significant residual drifts driven by significant plastic rotation at the beam-column connection hinges, although this result was somewhat dependent on the individual motion characteristics. In general, the maximum drift in the BD case was also somewhat larger. A representative analysis, in this case from the motion that would eventually become the "Design" motion (150% scaled Loma Prieta-Gilroy), is shown in Figure 5-123. Although indicative of the overall shape of the hysteretic curves in most cases, this particular analysis was somewhat unusual in that the total base shear was significantly higher in the BD configuration. However, this higher transient base shear did not translate into higher maximum roof drift. More importantly, the residual roof drift was approximately 0.2% for the SD case and essentially negligible for the BD case. This behavior was found for the majority of ground motions examined in the numerical analysis suite. Although some ground motions resulted in small residual drift for the SD configuration, the majority resulted in significant residual deformation. For the BD configuration, no motions resulted in residual drifts higher than 0.05%, indicative of self-centering, damage-free behavior.

The second goal of the modeling program was somewhat more problematic. The model results for the SD case were found to be relatively sensitive to the exact details of the beam and column hinges. Therefore, motion selection for the exact parameters listed in Table 5-5 could not be carried out with confidence. The motions eventually used for the experimental program were found to elicit a wide range of behavior from the model, which was desirable. The motions designated Service, Design, and Maximum were found to elicit progressively higher maximum and residual drifts from the SD case, and were therefore selected.

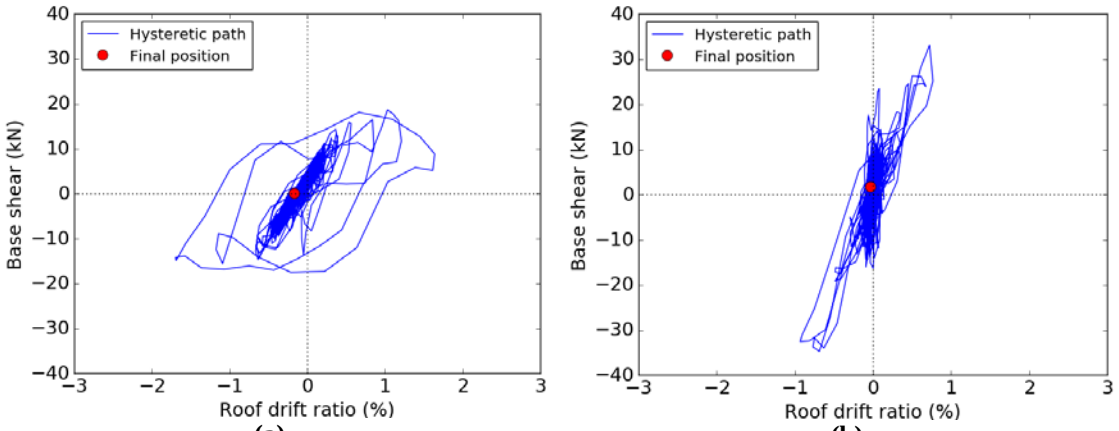

(a)
Maximum base shear: 19.8kN
Maximum drift: 1.85%
Maximum residual drift: 0.21%

(b)
Maximum base shear: 34.7kN
Maximum drift: 0.93%
Maximum residual drift: 0.04%

(a) Structure-dominated configuration [SD]

(b) BP-connection dominated configuration [BD]

Figure 5-123: − Calculated base shear versus roof drift response and maximum response parameters under Design motion

5.5.5 Analysis model verification and comparison to experimental results

Dynamic characteristic comparison: modes, mode shapes, and damping ratios

Initial verification of the model was performed by comparing the natural frequencies measured during white-noise excitation to the frequencies calculated from the

FE model. Regardless of the configuration, the first four modes consisted of 1) a moment-frame mode in the direction of shaking, 2) a braced-frame mode in the direction perpendicular to shaking, 3) a second moment-frame mode in the direction of shaking, and 4) a torsional mode. These modes are shown in Figure 5-124. Note that the x-direction shown on the triad is the shaking direction. In terms of behavior and the ordering of the modes, these correspond exactly to the modes resolved from the white-noise system ID tests (Figure 5-57).

Because the behavior in the shaking (x) direction was of primary interest, the natural frequencies associated with the first two modes in this direction were compared to the frequencies measured during the white noise tests presented previously. A small sensitivity study was performed in order to evaluate the rotational spring constant intended to model the double clip-angle connection. The objective of this study was to establish a constant value for the spring to be used in all models, while maintaining a close match between the measured and calculated frequencies. Based on the results of this study, the spring constant was set at 1,000 kip-in/rad. With this constant, the calculated first and second x-direction frequencies were within 1% and 5% of the measured values, respectively, as summarized in Table 5-22.

As described in Chapter 3, modal damping ratios were also measured for the first two x-direction modes using the measured response from low-amplitude impact testing. In contrast to some other finite-element programs, LS-DYNA does not allow for exact control over specific modal damping ratios (LSTC 2013). However, LS-DYNA has several options for applying damping, including: 1) separate, manual application of mass

and stiffness weighted damping (*DAMPING_PART_MASS and *DAMPING_PART_STIFFNESS), and 2) automatic application of stiffness- and mass-weighted damping in order to approximate the required damping ratio within a frequency range of interest (*DAMPING_FREQUENCY_RANGE). A sensitivity study was carried out using both damping application options. In this study, the model was subjected to impulses which excited the first and second x-direction modes and the log decrement method was used to calculate the damping ratio in each mode. This study indicated that the second option more reliably provided the necessary modal damping ratios without creating non-classical sharing of energy between modes. Therefore, this option was used for further dynamic verification of the models.

The damping ratios reported in Chapter 3 were measured using low-amplitude impact testing. Structure deformation, including rotation of the connections, was very small under these tests relative to the deformations measured during strong-motion testing. In addition, the strong motion testing induced strong, cyclic demands on the connection which were observed to slip a small amount, at least for configurations 1, 2, 3, and 4, as described in Chapter 3. Therefore, damping was modeled using a combination of two approaches:

1. Global structural damping was modeled using *DAMPING_FREQUENCY_RANGE as described above. The target damping ratio was selected to match the damping ratio measured for the first two x-direction modes under white-noise excitation. This approach is reasonable, as it

attempts to lump distributed damping that will be present regardless of motion intensity into a single modal-constant damping term.

2. Damping provided by deformation and slip in the connections was modeled using a zero-length rotational damper co-located with the rotational spring used to model the connection flexibility (*ELEMENT_DISCRETE with *MAT_DAMPER_VISCOUS). The damping coefficient for these elements was established based on a sensitivity analysis of the strong-motion runs for configurations 1-3, and separately for Configuration 4.

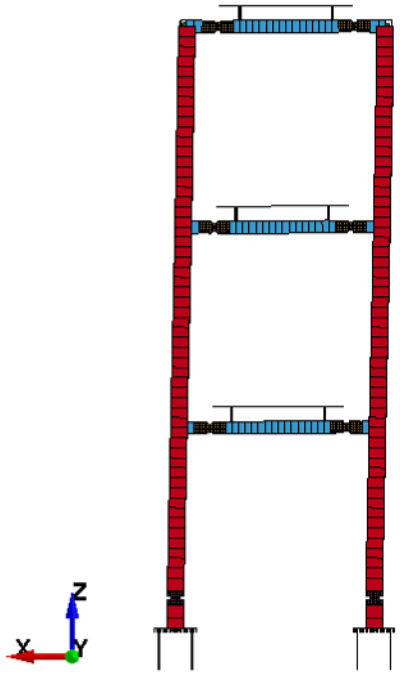

(1) First x-direction moment-frame mode

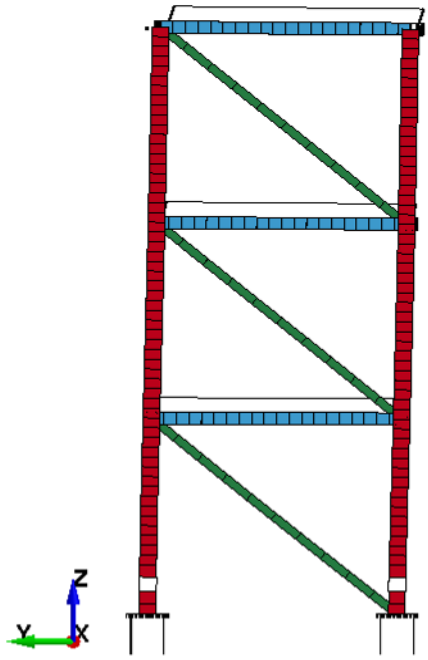

(2) Y-direction braced-frame mode

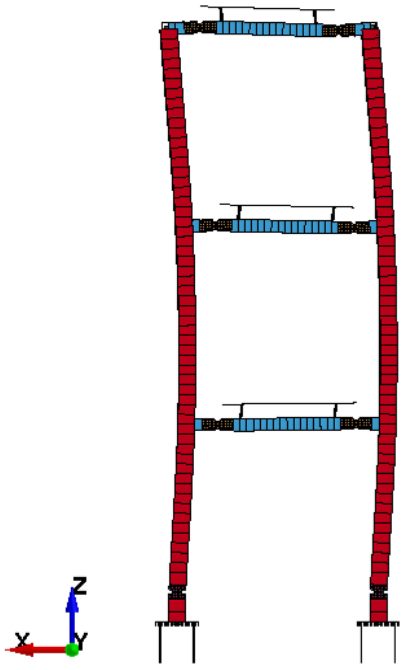

(3) second moment-frame mode

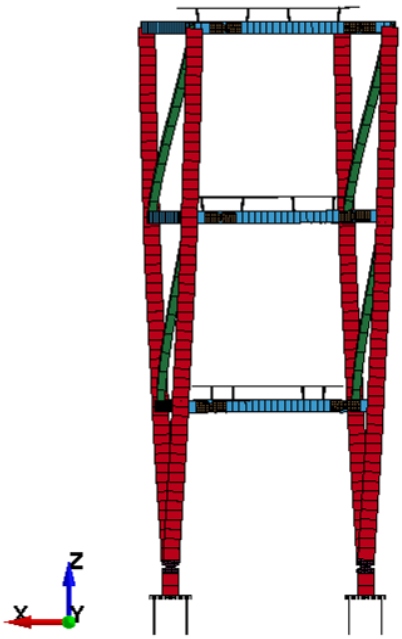

(d) Torsional mode

Figure 5-124: Typical modes from finite element analysis

Table 5-22: Comparison of measured and calculated frequencies for first two x-direction modes

		f_1			f_3		
Config.	Short name	Measured (Hz)	Calculated (Hz)	Difference (%)	Measured (Hz)	Calculated (Hz)	Difference (%)
1	CD MF	3.47	3.44	-0.86	13.69	12.81	-6.43
2	SD MF	2.91	2.91	0.00	12.40	12.12	-2.26
3	BD MF	3.37	3.34	-0.89	13.53	12.70	-6.13
4	TD MF	2.90	2.92	0.69	-	-	-
5	TD BF	6.09	6.06	-0.50	-	-	-
			Average:	-0.31		Average:	-4.94

Table 5-23: Comparison of measured and applied damping ratios for first two x-direction modes

		ξ_1		ξ_3	
Config.	Short name	Measured	Applied	Measured	Applied
1	CD MF	1.7	1.5	1.0	1.4
2	SD MF	0.8	0.9	0.5	0.9
3	BD MF	1.0	1.0	1.0	1.0
4	TD MF	2.0	2.0	-	-
5	TD BF	1.1	1.1	-	-

Dynamic test results versus model results for moment-framed buildings

The moment-frame models (from Configurations 1-3) were subjected to the achieved motions from each of the strong-motion tests (Service, Design, etc.). in order to verify the ability of the models to accurately capture the nonlinear behavior observed. LS-DYNA allows application of displacement, velocity, and acceleration time histories (LSTC 2013). However, based on the results of a small sensitivity study, the achieved table motion was applied to the model as a displacement history as this removed the need for filtering and the potential for long-period drift in the analysis.

For verification, the analysis models were compared to the test results on the basis relative displacement time histories, as these quantities were both directly-measured during the test program and easily available from the simulation. A comparison of the calculated and measured floor-level relative displacements under the design motion are

shown for Configurations 1-3 in Figure 5-125, Figure 5-126a, and Figure 5-127, respectively. The results of the Configuration 2 model under the Maximum motion are shown in Figure 5-126b to illustrate the ability of the model to accurately capture the residual deformation under this more intense motion, as well. These analyses include a rotational damping element at each beam-column connection with a coefficient of 5 kip-in-s/rad, which was found to give the best match to the test results based on the results of a small sensitivity study. The model results were found to be relatively insensitive to the selection of this coefficient. However, the inclusion of these relatively "weak" dampers was found to slightly improve the match to the experiment.

In general, the salient response characteristics were well-captured, particularly for Configuration 2. For the other configurations, the maximum response was predicted well, however the model predicts several relatively large-amplitude motion cycles following the maximum which were not observed in the test. Because this mismatch was observed only for the cases which underwent some uplift motion during the test, the cause of this is most likely due to the combination of two phenomena:

1. Radiation damping from pounding of the structure on the foundation due to both large rotation and uplift motion of the baseplate connections. This mechanism of energy loss was not included in the model.
2. Discrete slippage of connections. Although the connections were modeled using rotational springs, it is possible that the connections in the experiment slipped near the attainment of the maximum response, causing reduced response afterwards. Although no instrumentation can be used to directly verify this, a

limited amount of slippage seems to have occurred based on a review of the available video.

The model was run using the measured displacement response of the table for all tests, in order to evaluate the accuracy of the model under different motion intensities. In general, the overall fit of the curves was similar to those shown for the Design motion. The error between the maximum calculated and measured relative displacement at the third floor is reported in Table 5-24. In general, the match between the calculated and measured response was best for the Design and Maximum motions, with slightly poorer matches to the Service and Aftershock. The average misfit for Configurations 1-3 was about 12, 3, and 20%, respectively. The high misfit for Configuration 3 was driven by high error (almost 40%) in the Service level motion, in which the measured displacement was quite small. However, given the large range in motion intensity and the variety of behaviors observed, ranging from global rocking to frame-action plasticity, the overall modeling technique is considered to be adequate, and may be used in future work to reliably predict the behavior of similar structures under motions with similar intensities.

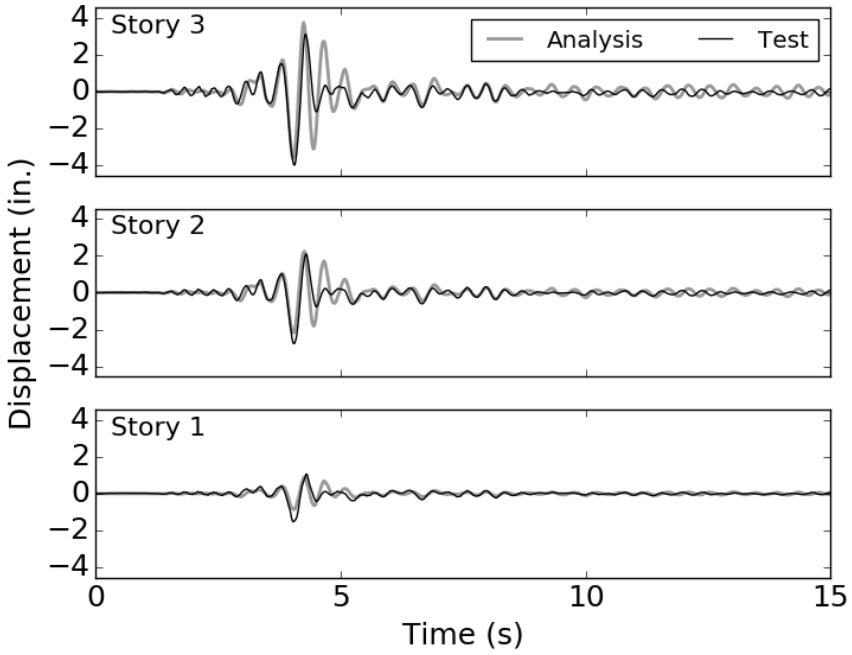

Figure 5-125: Configuration 1 (BD MF) - comparison of relative displacement and acceleration time histories (Design motion)

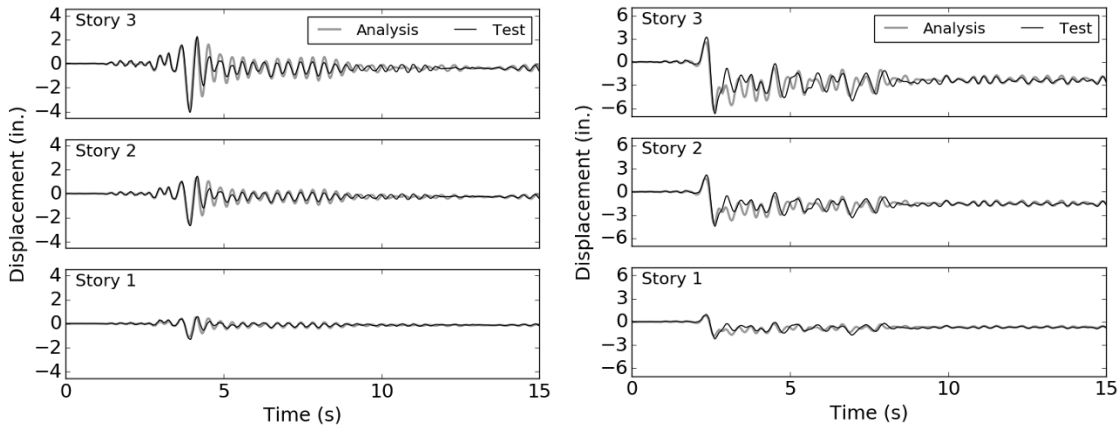

(a) Design motion (b) Maximum motion

Figure 5-126: Configuration 2 (SD MF) - comparison of top-floor displacement and acceleration time histories

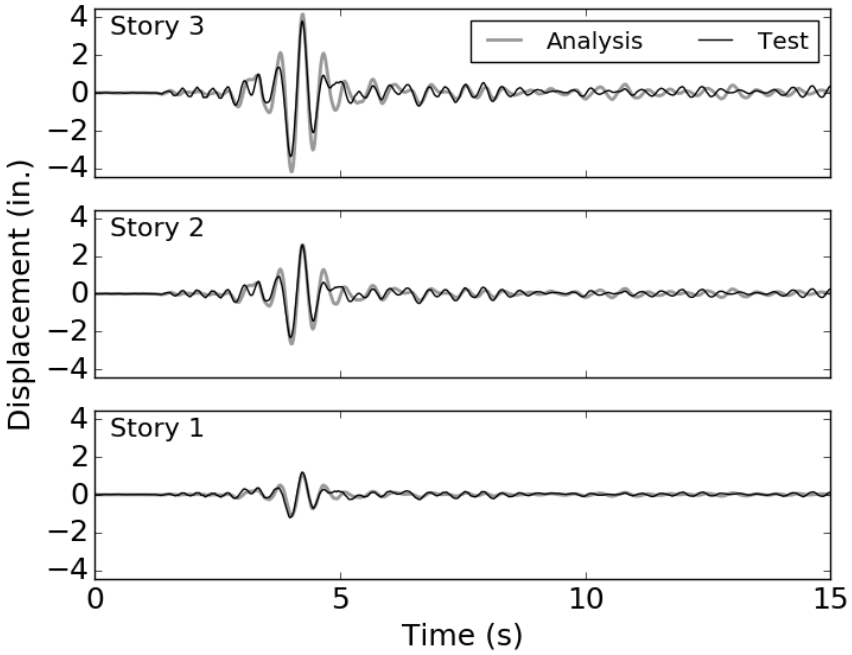

Figure 5-127: Configuration 3 (DD MF) - comparison of top-floor displacement and acceleration time histories (Design motion)

Table 5-24: Error between measured and calculated maximum 3rd-floor relative displacement (in percent)

	3rd-floor relative displacement error[1]				
Configuration	Service	Design	Maximum	Aftershock	Average
1	16.4	5.7	13.0	14.6	12.4
2	1.3	-6.9	5.9	-12.6	-3.1
3	38.5[2]	9.8	7.2	26.1	20.4
				Overall average:	9.9

NOTE: 1) Positive error indicates that simulation results were larger than observed results.
2) Large error percentage is due to small measured displacement for this case. The measured maximum displacement was 0.78 in.

Dynamic test results versus model results for SDOF buildings

The two SDOF models were modifications of the previous Configuration 3 MDOF-structure model, as all three configurations shared the same beam fuse cutout pattern. Specifically, to create the Configuration 4 model (1DD MF) the 1st- and 2nd-floor concrete shell elements were removed from the Configuration 3 model, and the top-floor concrete shell elements were doubled in thickness. The offset for the top-level mass

was also changed to reflect the new location of the center of gravity of the four-slab mass. All other model details were the same. To create the Configuration 5 model (1DD BF), a beam element was added to create the brace member shown in Figure 5-8. Only a single beam element was necessary for this modification, as this member was not subject to significant flexure. The modifications to the masses were identical to Configuration 4. The two SDOF models are shown in Figure 5-128. Note that the inside anchor elements were removed to reflect that the inside anchors were not attached during testing.

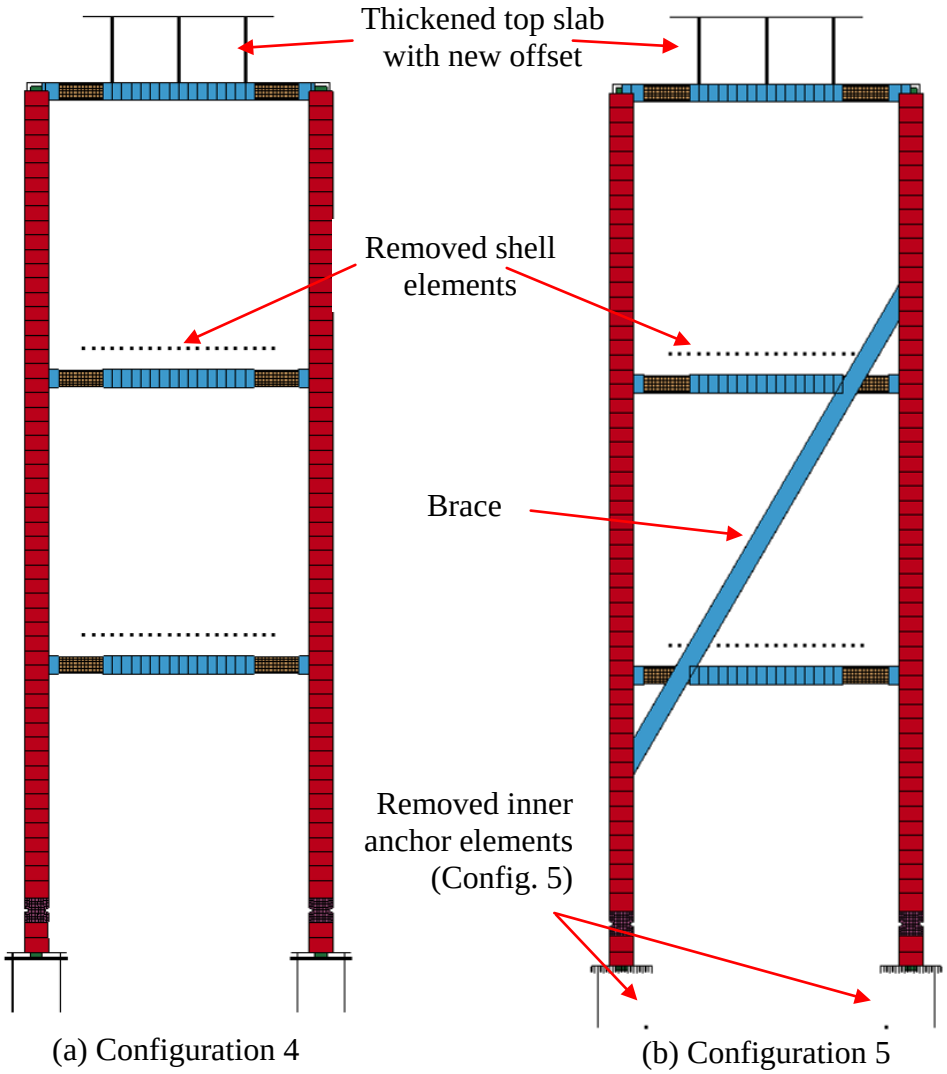

Figure 5-128: Modifications to finite element model for Configurations 4 & 5

The response of the two models to the achieved Design motion is shown in Figure 5-129. In contrast to the previous models, only the relative displacement of the top mass is shown, as this response is sufficient to judge the adequacy of the model to represent the single dominant mode of response. Although the response of the Configuration 4 model suffers from the previously-discussed problem of insufficient damping after the maximum response, the overall response of both models appears to be quite satisfactory.

In the case of Configuration 5, the relative displacements were relatively small due to the fact that this motion was not intense enough to "activate" the global overturning mode for this structure. Rigid-body translation of this model was significant for these smaller displacements. Therefore, the "test" data shown in the figure includes a correction equal to the time-coherent average of the measurements from the four longitudinal (x-direction) baseplate displacement transducers (consistent with the data presented in the previous chapter).

For the Maximum and Extreme motions, the global overturning mode was a significant component of the total response of the Configuration 5 structure. These cases included significant pounding. This behavior caused both behavioral and numerical challenges to the modeling methods used for the other configurations. The calculated response from the Configuration 5 model under the Extreme motion is shown in Figure 5-130(a). The maximum response is significantly overestimated, and there is numerical integration "noise" and unbounded behavior following the strong-motion portion of the record (shown with arrows in the figure). As noted before, uplift and pounding is associated with radiation damping that is not captured by the numerical model. The numerical noise appears to be due to the fact that the implicit solver has a difficult time converging precisely at the relatively rigid baseplate-grout interface. Due to the "gap" behavior of the nonlinear springs, this interface transitions from essentially zero stiffness to extremely high stiffness essentially instantaneously.

To combat these problems, relatively weak damper elements were added in parallel with the grout spring elements shown in Figure 5-121. The behavior of these

elements was selected to be viscous, i.e. the dissipative force in the damper is linear with respect to velocity. Although the mechanisms for energy dissipation at the baseplate interface are certainly not viscous in a physical sense, this behavior is attractive for this application for two reasons: first, the point at which energy transfer from the structure to the foundation is highest occurs at impact, the point at which the relative downward velocity of the structure and baseplate is highest. Second, because the viscous force is continuous and acts to damp out motion associated with high nodal velocity, the addition of these elements removed the integration noise and unbounded behavior observed previously.

There are several potential downsides to this approach. The response was found to be relatively sensitive to the selection of the damping coefficient. The damping coefficient itself is dependent on how much energy is dissipated, which in turn is indirectly dependent on the motion intensity. This creates a circular problem that can only be solved by comparison to test data, Secondly, the dampers dissipate energy in the uplift portion of the response, which is clearly not physical. This problem could be eliminated by the use of gap elements in series with the viscous elements, however, this approach was not taken in the current work because a satisfactory match to the test data was found with the selection of damping coefficients in a reasonable range. A last potential downside to this modeling approach is that the selection of the damping coefficient is mesh-dependent, since the number of dampers co-located with the grout springs is dependent on the mesh size of the baseplate. This problem may be overcome by using a single "master" extensional and rotational damper rigidly attached to the baseplate.

However, this approach was tried and failed in the current work due to numerical integration problems associated with high-frequency vibration of the baseplate.

For the current work, a damping coefficient of 0.00045 kip-s/in was found to give a reasonable match to the test data for both the Maximum and Extreme motion. The match to the Extreme motion test data for the model incorporating this coefficient is shown in Figure 5-130(b). The test data shown in this figure includes correction for sliding. Overall, the magnitude of the response is captured well, although there is a slight period shift due to sliding that cannot be captured by the model. However, this level of accuracy would almost certainly be sufficient for an assessment of performance for design.

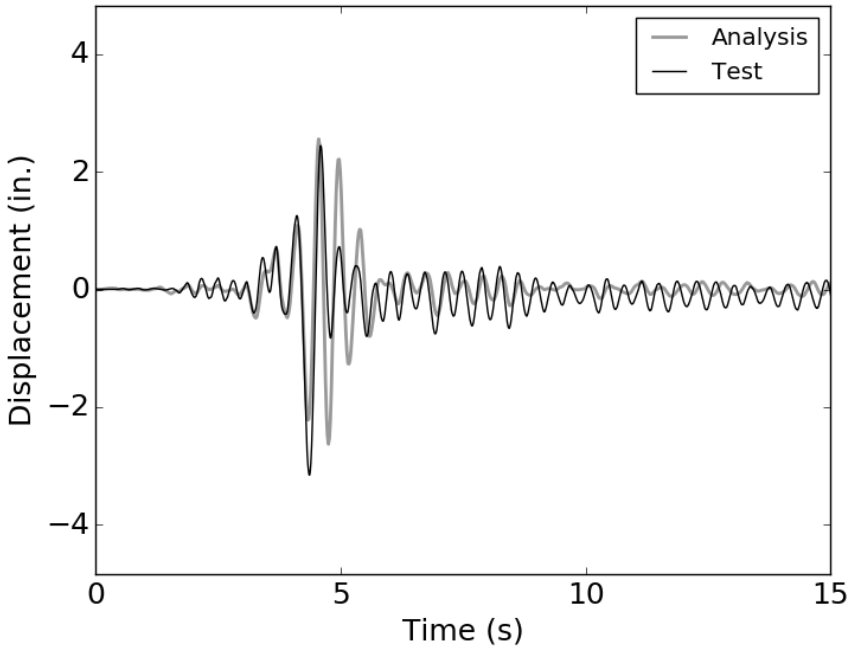

(a) Configuration 4 model

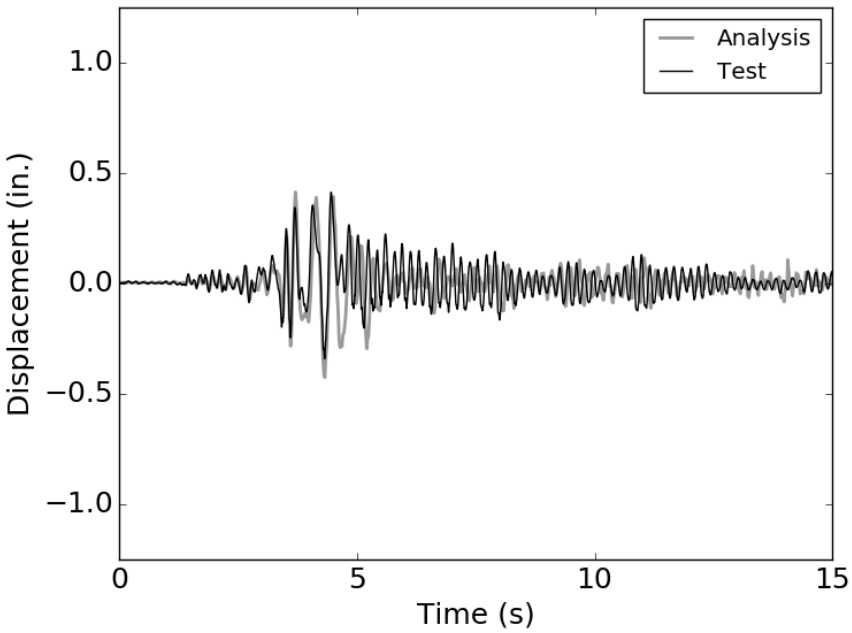

(b) Configuration 5 model

Figure 5-129: Response to Design motion: (a) Configuration 4 model (b) Configuration 5 model

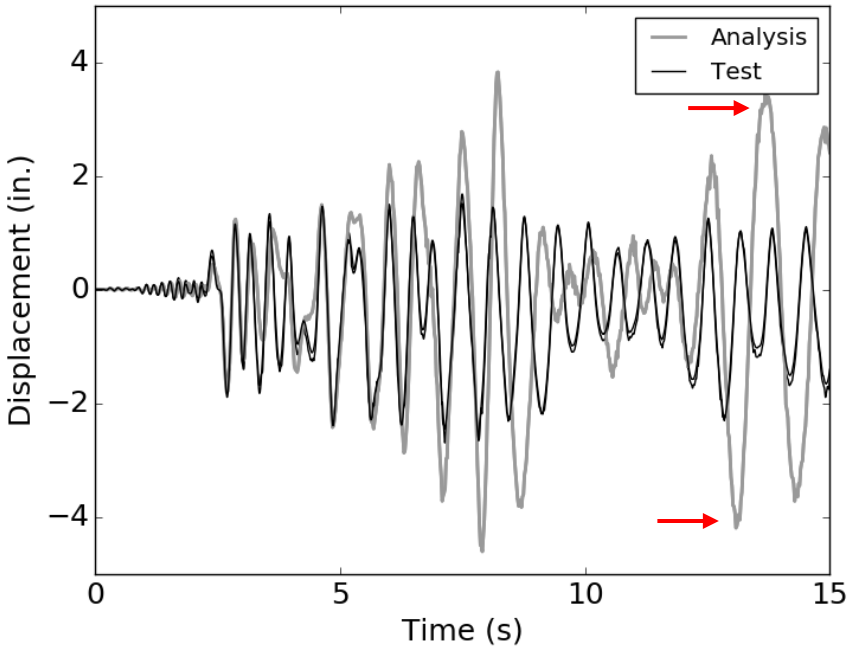

(a) Configuration 5 model without supplemental damping

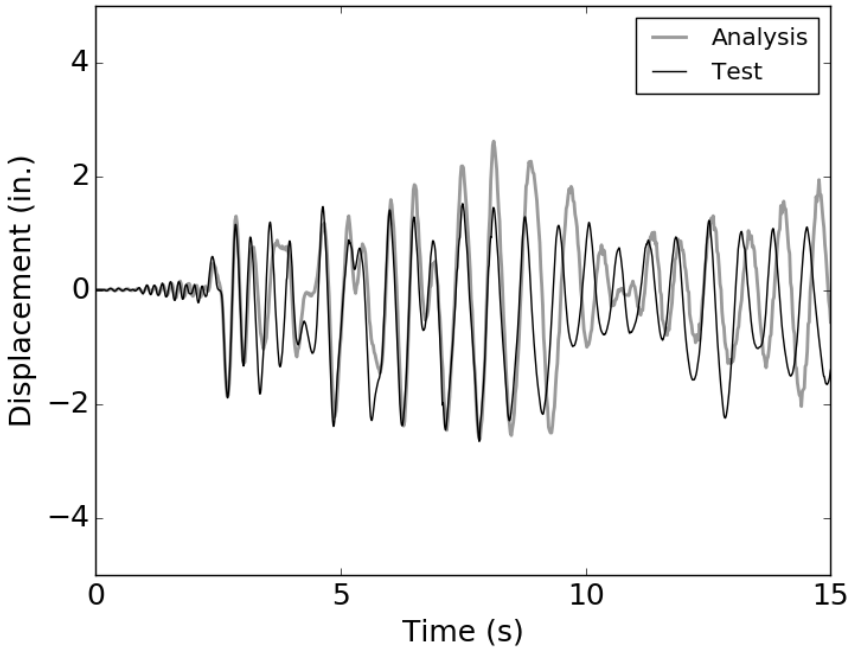

(b) Configuration 5 model with supplemental base damping

Figure 5-130: Response of Configuration 5 model to Extreme motion

Comparative analysis of ductile anchor versus strong-anchor behavior

As discussed previously, Configurations 4 and 5 did not have corresponding experimental strong-anchor configurations with which to make behavioral and performance comparisons. Therefore, comparisons were made on the basis of numerical analysis. The validated numerical model presented in the previous section was modified to create a "control" strong-anchor case by replacing the anchors used in the experiments with a linear-elastic spring with a calculated stiffness equal to that of the 3/4 in. nominal diameter, ASTM A193 B7 anchors used for Configuration 2. Anchor forces were verified to be less than yield in all analyses of the control case. The dampers used to model the energy loss from pounding, discussed previously, were also removed for the Maximum and Extreme motions for Configuration 5, as no energy loss at the base would be expected for a strong-anchor configuration. The geometry of the cutout portions was kept the same in both configurations. For Configuration 5, the configuration of the cutouts is essentially irrelevant, as the superstructure strength and stiffness is provided mainly by the brace. For Configuration 4, this approach allows the direct assessment of the impact of the anchors only. For the purposes of this comparison, the calibrated numerical models are referred to as "4" and "5", and the corresponding models with strong/stiff 3/4 in. diameter anchors are "4F" and "5F", respectively.

A comparison of the calculated relative displacement and total base shear for the Configuration 4 numerical models is shown in Figure 5-131. Important response parameters are summarized and compared in Table 5-25. Numerical results from the Service, Design, and Maximum motions are shown, corresponding to the motions

actually run for this configuration. In general, the response was insensitive to the anchor type. The relative displacement and maximum base shear were within less than 15% for all motions. The differences in the maxima of the ISRS and vertical accelerations were similarly negligible (in an absolute sense). It may be concluded that ductile-anchor uplifting connections do not improve the behavior of this structure within the motion intensities studied in this program. Configuration 4 had the lowest natural frequency of any configuration tested. The "activation" of a rocking mode is a somewhat acceleration-sensitive event, due to the fact that relatively high overturning forces must be developed to cause high column and anchor forces. Therefore, it may be also be reasonably concluded that structures with low natural frequencies which tend to experience relatively low spectral accelerations may not benefit from the ductile-anchor uplifting connection philosophy.

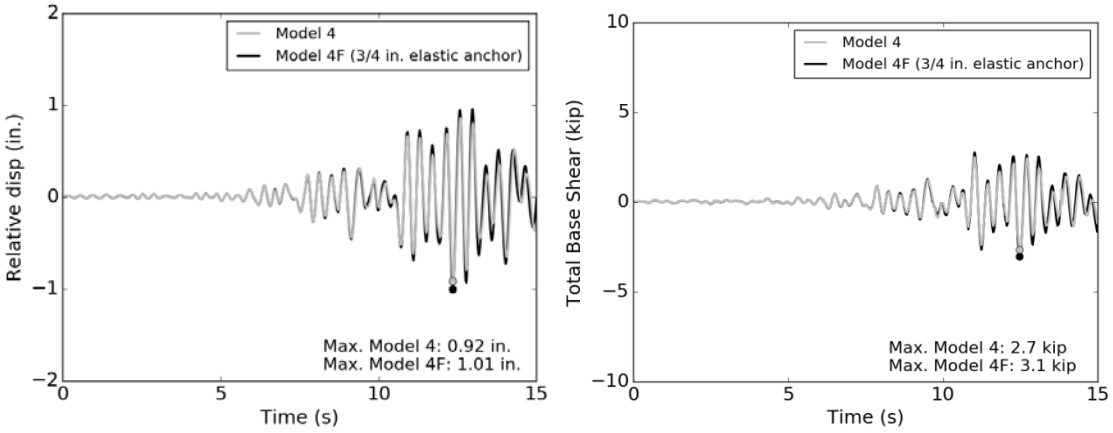

(a) Service motion

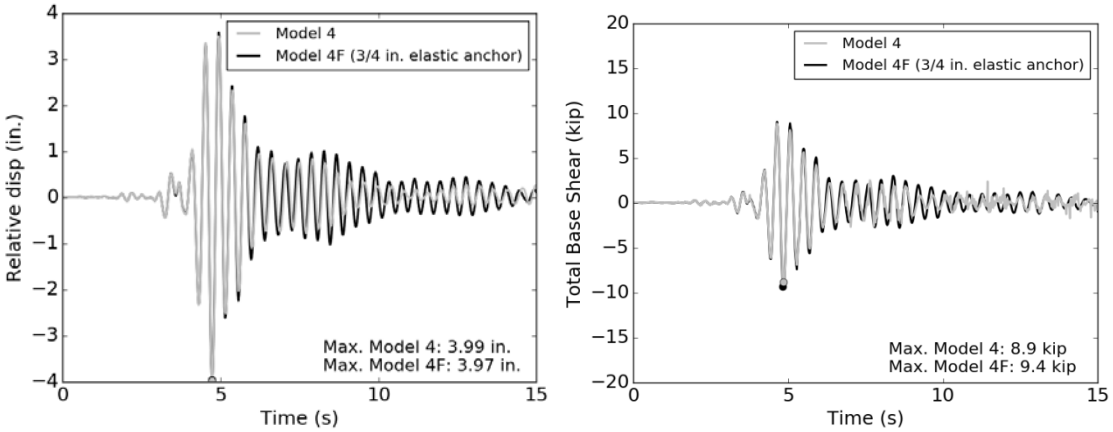

(b) Design motion

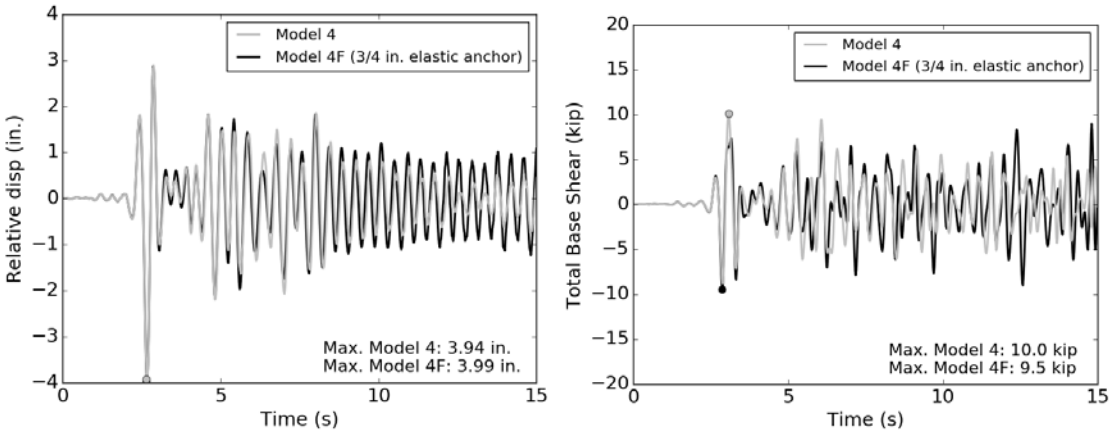

(c) Maximum motion

Figure 5-131: Comparison of calculated relative displacement and total base shear response from 4 and 4F models under several motions

Table 5-25: Comparison of calculated critical response parameters between Models 4 and 4F

	Calculated response parameters: Model 4F, *Model 4* **(% difference)**			
Motion	Relative Displacement (in.)	Peak of 5%-damped RS at mass (g)	Maximum z-direction acceleration	Maximum base shear (kip)
Service	1.01 *0.92* **(-9%)**	5.0 *4.2* **(-16%)**	0.1 *0.2* **(+50%)**	3.1 *2.7* **(-13%)**
Design	3.97 *3.99* **(+1%)**	12.8 *12.6* **(-2%)**	1.2 *0.9* **(-25%)**	9.4 *8.9* **(-5%)**
Maximum	3.99 *3.94* **(-1%)**	8.7 *8.7* **(0%)**	1.6 *1.7* **(+6%)**	9.5 *10.0* **(+5%)**
NOTE: All displacement and accelerations measured at center of top mass.				

In contrast to Configuration 4, Configuration 5 is The calculated relative displacement and total base shear for the Configuration 5 numerical models under the Service, Maximum, and Aftershock motions are shown in Figure 5-132. These three motions illustrate how different the behavior of the case where the columns are allowed to uplift may be, but the difference in behavior depends on the motion intensity. Under the Service and Aftershock motions (a-b and e-f in the figure), the global rocking mode is not activated, and the response of the structure is very similar to the fixed-base case (Model 5F). The relative displacements are slightly larger than in the fixed-base case, and the maximum base shear is slightly to moderately higher (in absolute terms). Activation of the global rocking mode, which occurred under the Design, Maximum, and Extreme motions, is associated with significantly higher relative displacements, but also significant reductions in the maximum base shear. The responses shown in c-d of the figure were typical of these three motions. In the case of the Maximum motion shown, significant column uplift and anchor yielding occurred at about 3 seconds. This point represents activation of the base "fuse" mechanism, and the total base shear is significantly smaller than the fixed-base case afterwards. A comparison of important response parameters is presented in Table 5-26. In general, the uplifting column system is

associated with significantly higher relative displacements regardless of motion intensity. Z-direction (vertical) accelerations were also significantly increased. However, both the peak of the ISRS and the maximum base shear were significantly reduced for the three strongest motions (Design, Maximum, and Extreme), an average of about 70% and 49%, respectively. These reductions were generally consistent with the experimental outcomes found for similarly-designed moment frames (i.e. the BD MF Configuration 1 and the SD MF Configuration 3). However, the magnitude of these reductions is significantly higher than for the moment frames, indicating that braced frames and/or rigid structures may benefit most from an uplifting base connection philosophy.

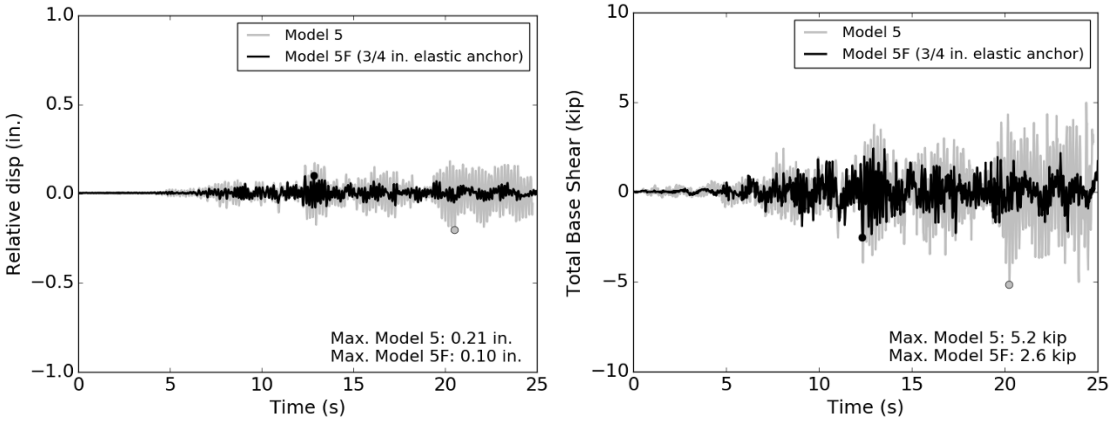

(a) Service motion

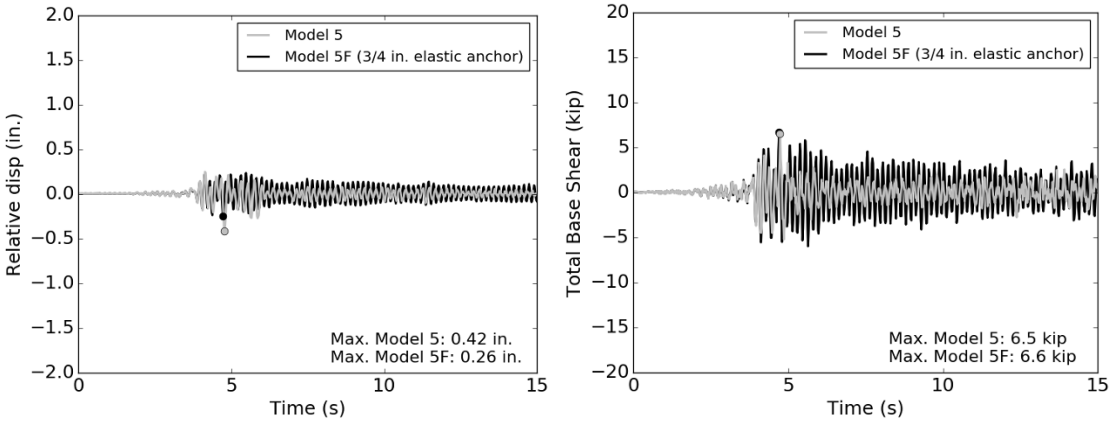

(b) Design motion

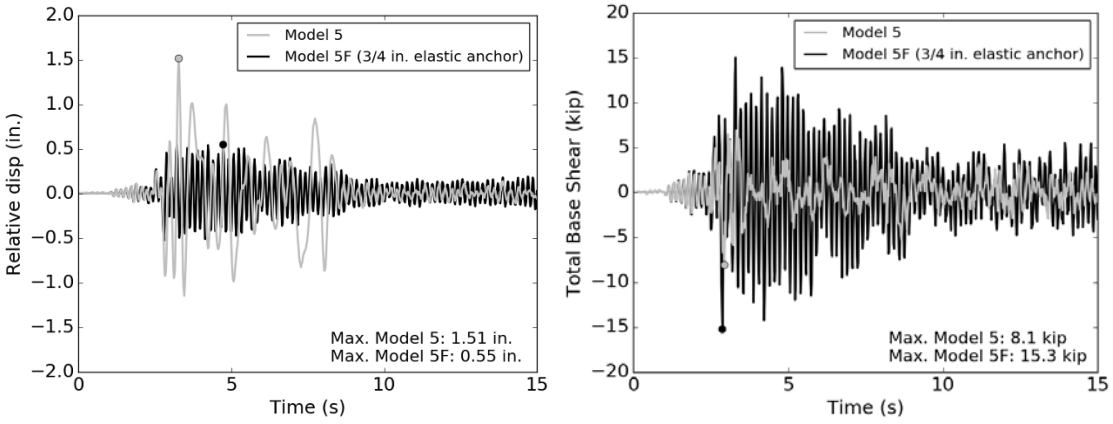

(c) Maximum motion

Figure 5-132: Comparison of calculated relative displacement and total base shear response from 5 and 5F models under (a-b) Service motion, (c-d) Maximum motion, (e-f) Aftershock motion

Table 5-26: Comparison of calculated critical response parameters between Models 5 and 5F

Calculated response parameters: Model 5F, *Model 5*, **(% difference)**

Motion	Relative x-dir. displacement (in.)	Peak of 5%-damped ISRS (g)	Maximum z-direction acceleration (g)	Maximum base shear (kip)
Service	0.10	3.8	1.5	2.6
	0.21 **(+110%)**	*6.6* **(+74%)**	*3.0* **(+100%)**	*5.2* **(+100%)**
Design	0.39	15.6	2.9	10.7
	0.43 **(+10%)**	*5.4* **(-65%)**	*4.4* **(+52%)**	5.9 **(-45%)**
Maximum	0.55	22.3	4.7	15.3
	1.51 **(+175%)**	*6.7* **(-70%)**	*6.4* **(+36%)**	*8.1* **(-47%)**
Aftershock	0.26	9.4	1.1	6.6
	0.42 **(+62%)**	*6.1* **(-35%)**	*2.4* **(+118%)**	*6.5* **(-2%)**
Extreme	0.75	23.0	4.3	19.9
	1.53 **(+104%)**	*6.2* **(-73%)**	*6.3* **(+47%)**	*8.7* **(-56%)**

NOTE: All displacement and accelerations measured at center of top mass.

Analysis using expanded suite of ground motion records

Although a statistical analysis of the potential benefits of the uplifting-column, ductile anchor design strategy is outside the scope of the current work, the Configuration 1, 2, and 5 models were subjected to a larger suite of unidirectional ground motions than were included in the experimental program to evaluate the broader applicability of this approach. In addition to the Configuration 5 (SDOF BF) model, an otherwise-identical model was run using the anchors from the Configuration 2 model, reflecting a nearly fixed-base braced frame. Therefore, in addition to the comparison of the Configuration 1 and 2 moment frame (MF) structures presented previously, three comparisons of base-dominated versus structure dominated behavior were made:

1. Comparison of the Configuration 5 BF test data to corresponding analyses of the fixed-base Configuration 5 model under the Design, Maximum, Aftershock, and Extreme ground motions

2. Comparison of the Configuration 5 and Configuration 5 fixed-base numerical models under a larger suite of ground motions

3. Comparison of the Configuration 1 and Configuration 2 numerical models under a larger suite of ground motions.

The motion suite used for comparisons (2) and (3) consisted of approximately 10 recordings from shallow crustal earthquakes with moment magnitudes exceeding 6.0. The recordings were all from sites in the western United States. These motions were scaled by factors ranging from 0.75 to 4.0 in an effort to subject the structure to demands similar to and exceeding those imposed during the test program. The base-dominated and structure-dominated base shear and residual drift from the combined test and numerical analysis program are shown in Figure 5-134.

There are several interesting trends in this figure. First, reductions in total base shear in the ductile anchor configuration are greater in magnitude and more consistent for motions of all intensities for the SDOF braced frame (BF) structural type. The structure experienced a reduction of base shear in all cases but one, and reductions of 40% or more were found in over half of the analysis cases. Reductions in residual structural drift for the BF configuration were relatively small, as the brace utilized in the current structure was strong relative to the mass and inertial loads of this structure. Interestingly, for the most intense motions, the base shear appears to "saturate" for the BD case. This is due to the development of the yield moment of the base fastening in a global sense, such that the total base shear cannot exceed M_y/h, where h is the height of the building. The development of the mechanism associated with full base plasticity has been suggested previously as a method to design the required elongation of such structures elsewhere in this dissertation.

The difference in total base shear between the SD and BD configurations of the moment frame were generally moderate. In a few cases, the base shear experienced in the BD configuration was higher. However, for the majority of cases, the base shear in the BD configuration was lower, up to almost 50%. Reductions in residual drift were substantial, with essentially damage-free performance of the BD MF regardless of motion intensity. These results were generally consistent with the results of the test program.

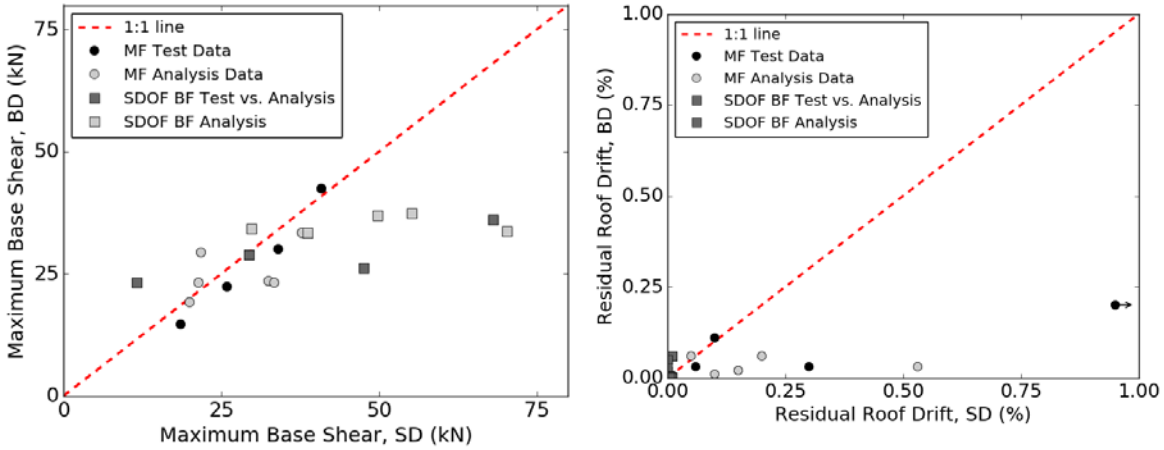

Figure 5-133: Comparison of structure dominated (SD) versus base dominated (BD) performance: (a) Total base shear, (b) Roof-level residual drift

5.6 Simplified Analytical Method for Estimating Required Anchor Elongation for Building and Nonbuilding Structures

Fracture is clearly an important ultimate limit state when designing anchors, particularly for structures allowed to uplift such as those presented previously in this chapter. Current design practice (ACI 318-14 section 17.2.3.4.3) permits the determination of the required stretch length to prevent fracture by analysis. Ideally, all connections, regardless of what they are attaching, would be designed for a consistent margin against fracture. However, generalized methods to predict the required stretch length have not been developed. The testing and numerical analysis presented in previous

chapters provides information regarding the capacity, which is uniform regardless of attached structure type. However, the anchor demand will vary depending on the behavior of the attachment under seismic loads. For example, the relationship between global demands and local anchor demands will be highly dependent on the relative strengths of the attachment and the anchors, i.e. which components behave plastically, and when. The following sections illustrate methods for calculating or bounding anchor demands for common situations encountered in practice.

Elastic Nonbuilding Structures

The 8D stretch length requirement was primarily based on observed good performance of relatively stiff industrial structures such as tanks and chimneys. For these types of structures, the required maximum anchor elongation may be estimated using the design response spectrum directly. Herein a simple derivation is presented to perform such an estimate, assuming:

1. The structure's fundamental period is within the constant-velocity portion of the design spectrum.

2. The structure weight is uniformly distributed with height or concentrated at a discrete level, such that the resultant seismic force may be assumed to act at a known height, h_r.

3. Seismic excitation is in a single direction only. It is noted that multi-direction excitation may be accommodated by expansion of the derivation presented.

4. The anchor bolts are arrayed in a circle with diameter *d* for cylindrical base connections, or a rectangular grid of dimension *d* in the direction of shaking for rectangular connections.

5. The anchors are near the edge of the structure, such that the compressive resultant can be considered co-located with the anchors on the compression side. Additionally, the elastic deformation of the anchors is small compared to the overall deformation.

6. The structure above the base remains essentially elastic, and higher-mode effects are negligible.

The total deformation of the structure will be the sum of the elastic deformation of the superstructure and plastic deformation of the anchors, as shown in Figure 8. Conceptually, the global pushover response of the structures may be idealized as elastic perfectly plastic, as shown in Figure 9. The deformation associated with elastic behavior may be related to the period at which the anchors yield through Eqs. 9-11.

$$\Delta_1 = \frac{F_y}{k} \quad \text{Eq. 5-7}$$

$$T = 2\pi\sqrt{\frac{W}{kg}} \rightarrow k = \frac{W(2\pi)^2}{T^2 g} \quad \text{Eq. 5-8}$$

$$\Delta_1 = \frac{F_y T^2 g}{W(2\pi)^2} \quad \text{Eq. 5-9}$$

The displacement of a seismically isolated structure, idealized to have an elastic perfectly plastic response, may be taken as[19]:

$$\Delta = \frac{g}{4\pi^2}\frac{S_{D1}T_T}{B} \quad \text{Eq. 5-10}$$

To compute Δ in desired length units, g is input in units of length/s^2, the spectral acceleration at the 1-s period S_{D1} is input in units of g-s, and T_T is the period in seconds associated with the secant stiffness k_T. Given that total displacement is the sum of elastic and plastic displacement, and since the elastic period and stiffness T_e and k_e may be related in a manner similar to Eq. 10, this may be written as:

$$\Delta = \frac{gS_{D1}}{2\pi B}\sqrt{\frac{W(\Delta_1+\Delta_2)}{F_y g}} \quad \text{Eq. 5-11}$$

solving for the total displacement $\Delta_1 + \Delta_2$:

$$\Delta_1 + \Delta_2 = \frac{Wg}{4\pi^2}\frac{{S_{D1}}^2}{F_y B} \quad \text{Eq. 5-12}$$

substituting Eq. 11, the base rotation component Δ_2 can then be solved for:

$$\Delta_2 = \frac{g}{4\pi^2}\left[\frac{W}{F_y}\frac{S_{D1}^2}{B} - \frac{F_y}{W}T^2\right] \quad \text{Eq. 5-13}$$

Since only Δ_2 is associated with anchor plasticity, the required anchor elongation ΔL_u can then be solved for using similar triangles.

$$\frac{\Delta L_u}{d} = \frac{\Delta_2}{h_r} \rightarrow \Delta L_u = \frac{dg}{h_r 4\pi^2}\left[\frac{W}{F_y}\frac{S_{D1}^2}{B} - \frac{F_y}{W}T^2\right] \quad \text{Eq. 5-14}$$

where the units of input are consistent with Eq. 9. The required L_s can then be selected based on stretch-length elongation relationships for the selected material type (Figure 2-6). Alternatively, if the elongation *EL* is smaller than that associated with strain localization (such as for the serviceability limit state) stretch length may then be calculated using an allowable elongation EL_{all}:

$$L_{s,min} = \frac{gd}{h_r 4\pi^2 EL_{all}}\left[\frac{W}{F_y}\frac{S_{D1}^2}{B} - \frac{F_y}{W}T^2\right] \quad \text{Eq. 5-15}$$

The application of Eq. 17 to the ultimate limit state is not appropriate, due to the inherent dependence of *EL* on L_s discussed previously. If the 5% acceptance criterion for serviceability developed in the previous section is adopted, Eq. 17 may be further simplified to give the approximate minimum stretch length for serviceability:

$$L_{s,serv} = \frac{200d}{h_r}\left[\frac{W}{F_y}\frac{S_{D1}^2}{B} - \frac{F_y}{W}T^2\right] \quad \text{Eq. 5-16}$$

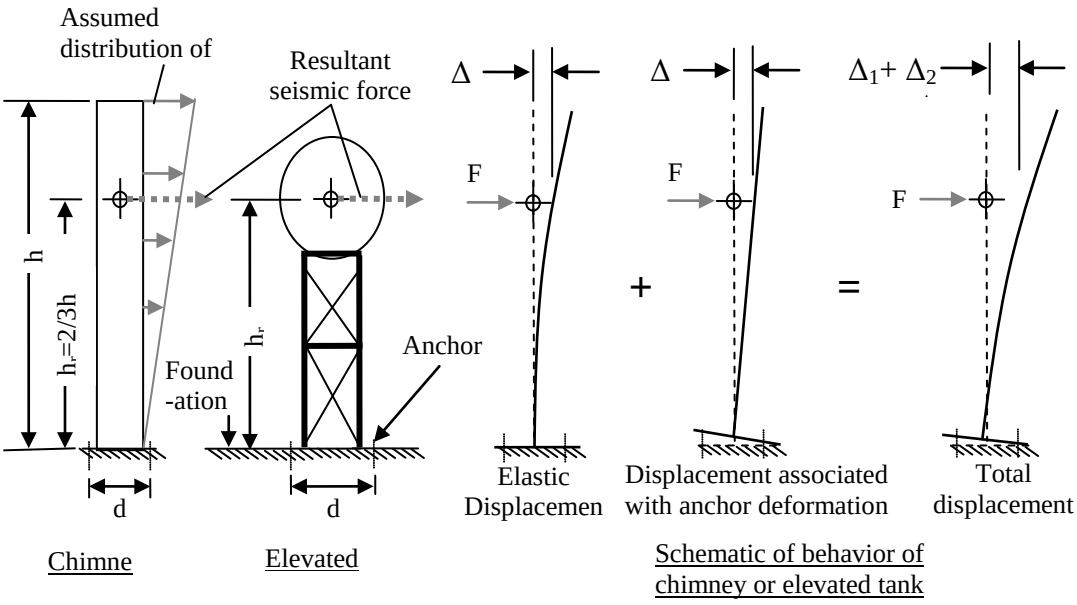

Figure 5-134: Deformations associated with seismic loading on nonbuilding structures

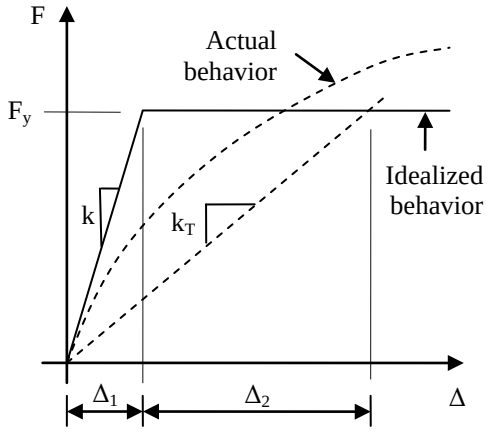

Figure 5-135: Actual and idealized pushover curves

Building Structures

Building structures with frame-type lateral force resisting systems typically have a more complex relationship between global demands and anchor demands than may be expressed by a relationship such as Eq. 16. Additionally, there is typically more variation in the types of connections utilized in these structures, ranging from thin-baseplate designs, which transmit relatively small anchor forces due to baseplate plasticity, to thick- or stiffened-baseplate configurations that may promote anchor yielding. Therefore, calculation of anchor elongation demands through simple analytical methods is generally not practical. However, it may be possible to bound the demands through appropriate assumptions of the structures response.

Herein, it is assumed that the first story drift (Δ/h) is attributed to plastic rotation at the base θ_b, which causes deformations Δ_2, and deformations within the story Δ_1 (Figure 5-136). Importantly, Δ_1 may not be strictly elastic, as was the case in the nonbuilding structure derivation presented previously. The rotation at the base can be further decomposed into components that are associated with anchor plasticity and

baseplate plasticity (see detail in Figure 5-136). Both the ratio of Δ_1 to Δ_2 and θ_{pl} to θ_{anchor} will be unknown at the onset of the design process. The ratio of θ_{pl} to θ_{anchor} is particularly problematic, as simple analytical relationships to predict the amount of connection rotation due to the baseplate and anchor deformation do not currently exist. Therefore, assumptions must be made regarding the upper bound of story drift Δ/h and the amount of rotation due to anchor deformation.

The total first story drift Δ/h may be taken relatively easily from one of two sources: 1) structural analysis, such as finite-element analysis performed under design or maximum-level events, or 2) ASCE 7 design earthquake limiting story drift ratios. If analysis results are available, the boundary conditions assumed in the structural analysis must be consistent with the eventual baseplate connection design, including the effect of the anchor stretch length on the connection stiffness. Use of code drift limits, on the other hand, can provide a first-order estimate of stretch length requirements. Table 12.12-1 of ASCE 7 provides limits on story drift under a design earthquake scenario based on structural system type and building importance[18].

Determining the amount of baseplate rotation due to anchor versus baseplate deformation (considering both elastic and inelastic deformations) is problematic unless a detailed finite element analysis is employed. However, for simplicity it may be conservatively assumed that $\theta_{anchor} = \theta_b$, i.e., that all rotation is assignable to the anchors. Additionally, assuming small rotations, such that $\tan(\Delta/h) \approx \Delta/h$, the relationship between global story drift and connection rotation is given by:

$$\theta_{anchor} = \frac{\Delta}{h} \qquad \text{Eq. 5-17}$$

Conservatively assuming that the connection rotates about the toe of the plate as shown in Figure 10, the required anchor deformation is:

$$\Delta L_u = \theta_{anchor} d_e \qquad \text{Eq. 5-18}$$

where d_e is the distance from the anchor to the extreme compressive fiber of the connection. Substituting Eq. 16 into Eq. 17, the required anchor deformation reduces to:

$$\Delta L_u = \frac{\Delta}{h} d_e \qquad \text{Eq. 5-19}$$

This equation provides an analytical expression for the minimum required anchor deformation as a function of the drift ratio Δ/h and the distance from the anchor to the extreme compression fiber. As with the previous derivation, the required minimum stretch length can then be designed based on test data or simulations such as those presented in Chapter 2, or on serviceability criteria if the anchors are desired to be re-used after the design event.

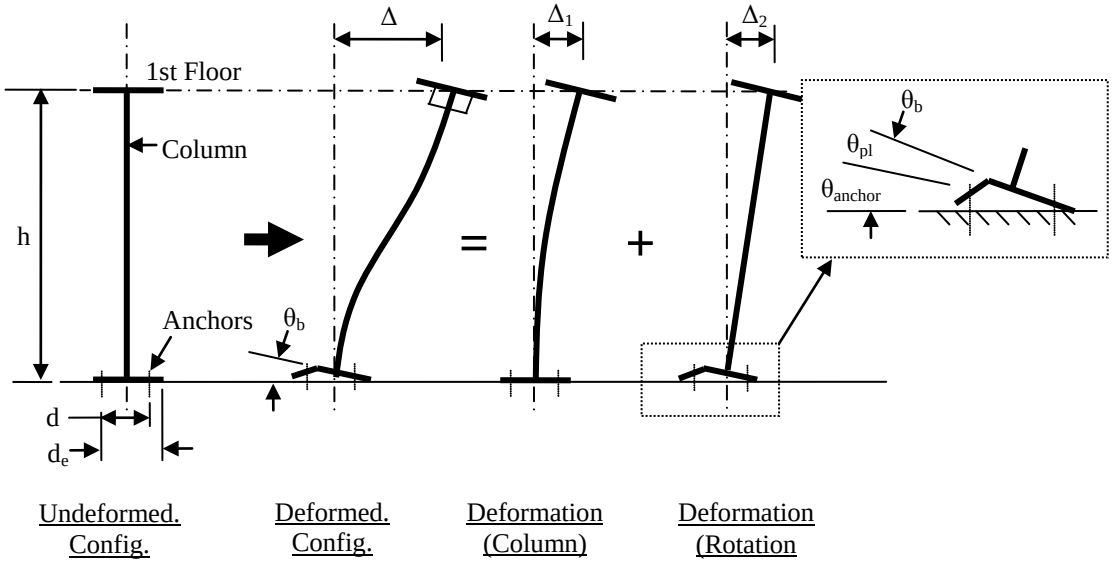

Figure 5-136: Deformations associated with seismic loading on framed-braced structures

5.7 Summary Remarks

5.7.1 Chapter Summary

This chapter describes a research program intended to probe the potential beneficial effects of uplifting base connections constructed with ductile anchor bolts. The primary goals of this work included:

1. Comparing the overall structural behavior of a building designed with uplifting baseplate connections incorporating ductile anchors to a “traditional” superstructure beam and column hinge design

2. Investigating the possible reduction of global structural demands (peak base shear, maximum drift, residual drift, maximum floor accelerations, etc.) in an uplifting-baseplate system versus a traditional design

3. Providing experimental, system-level dynamic response data documenting the distribution of demands from service to extreme earthquakes for use in numerical model validation

To these ends, a miniature steel building was built and tested on a unidirectional shake table. The building was designed to have replaceable components such that several distributions of structural stiffness and strength were possible, ranging from strong-anchor/weak-superstructure to weak-anchor/strong superstructure. In addition, the structure could be changed from a moment-frame to a braced frame configuration. In total five configurations were tested, namely:

Each configuration was tested under up to 5 different ground motions, plus white noise excitation to identify and track changes to the dynamic properties of the system. A substantial numerical analysis program was conducted in parallel with the test program. Initial numerical models were used to guide design and motion selection. Verification of more refined analysis models was performed using system identification techniques and

the results of strong motion excitation. Modeling techniques for expanding the results of the experimental program were presented and discussed.

5.7.2 Major Findings and Conclusions

The following summarize the major findings and conclusions of this Chapter:

- The moment frame structures tested had first-mode damping ratios ranging between 0.8% and about 2.0%. The variability of damping ratio was apparently tied to the strength and stiffness of the structural fuse portions relative to that of the connections, with the SD MF having the lowest measured damping ratio, and the TB MF having the highest ratio. The relatively narrow range of damping measured for the different structural types suggest that the behavior of the structures can be compared directly on the basis of measured results.
- There was a drop in the measured natural frequency of up to 22% associated with yielding of the anchors of the BD MF and DD MF configurations. The cause of this is the loss of rotational restraint due to anchor yielding, causing the boundary conditions to change from partial fixity to free (in all directions except downward movement). This phenomenon was not explicitly leveraged in the current test program, but could be used to reduce the magnitude of spectral accelerations for strategically-designed systems.
- The distribution and magnitude of peak floor accelerations (PFAs) was dependent on both the structure type and the intensity of the motion. At the highest motion level, the PFAs of the BD configuration were on the order of 125-150% higher

than in the SD MF configuration. However, at lower motion levels, the PFAs for the BD and DD were mostly lower than the SD configuration, up to about 50%.

- The peaks of the in-structure response spectra (ISRS) were generally lower for the BD and DD configurations than for the SD case, with reductions of almost 50% in some cases. An exception was for the Maximum motion, in which the in-structure response spectra were marginally higher for the BD versus the SD case. This result suggests that damage to acceleration-sensitive nonstructural components would be lessened for uplifting-base type systems under moderate motion intensities.
- Maximum inter-story drifts were very similar amongst the BD, DD, and SD moment frame configurations. Maximum drifts for the most intense motions were on the order of 4.5%. Damage to displacement-sensitive nonstructural components would likely be similar in all three types of buildings.
- Despite undergoing similar levels of maximum drifts, and despite undergoing a larger number of cycles at large displacement due to the loss of rotational restraint from the yielding anchors, the CD configuration was found to be virtually damage-free in the superstructure. Residual drift was measured to be less than 0.2%, while it was on the order of 1.5% for the SD configuration. The performance of the BD case was intermediate, with a residual drift on the order of 0.4%. This result shows that uplifting-column, ductile-anchor systems are capable of damage-free behavior, and that repair costs for these systems may be vastly smaller than their traditionally-designed counterparts.

- The base shear for the BD case was up to 22% lower than that of the SD case, with the greatest reductions occurring for the least intense, but longest duration motion. Under the most intense motion, the base shears were approximately equal. The base shear for the DD case was about 25% higher than the SD case under the most intense motion, but up to 25% lower than the SD case for other motions. This result indicates that changes in base shear are motion-dependent. However, the majority of the results indicate that the BD and DD structures were associated with a moderate reduction in base shear.
- Replacement of yielded anchor inserts was found to be both possible and practical for the design used in the current work, even for the very small diameters (1/4 in. and 3/8 in.) tested in the present program. Replacement of the anchors required no special tools or skills.
- Dynamic numerical models of all Configurations were successfully developed using LS-Dyna. A fiber-section approach, previously developed in Chapter 4 for the analysis of steel column baseplate connections under pseudo-static, reversed cyclic load, was used to model the baseplate connections in the current modeling program.
- The average misfit between the natural frequencies of the model and the experimental specimens was less than 1% for the first x-direction mode, and less than 5% for the second x-direction mode. Each of the first four mode shapes corresponded to those measured using system identification techniques.

Therefore, it may be concluded that the dynamic characteristics of the specimens were well-represented by the models.

- Models subjected to the achieved table motion showed very good correspondence to the measured structural response, as evaluated by the relative displacements at each floor. The average error between the maximum measured and calculated response for each structural type under all achieved ground motions was less than 20% in all cases, and was less than 10% for the bounding cases (Configuration 1 and Configuration 2).
- Modeling of radiation damping from pounding effects was not included for the MDOF moment-frame models (Configuration 1-3). For these configurations, the maximum response was found to be adequately captured, however pounding was found to reduce the post-maximum oscillation significantly. However, for Configuration 5 under the Maximum and Extreme motions, several cycles of global rocking were found to occur, and modeling of the energy dissipated from pounding was required. Satisfactory modeling of pounding behavior was accomplished with viscous dampers placed in series with the nonlinear grout springs.
- Configuration 4 (1DD MF) was found to be relatively insensitive to the anchor type used in the baseplate connections. This result suggests that there are limits to the beneficial effects that may be realized by uplifting connections. The reason for the relative insensitivity of this structure appears to be that the global rocking

mode is not "activated" due to the low frequency and relatively low accelerations experienced by this structure.

- The braced-frame configuration (Configuration 5) was found to benefit significantly from ductile anchors that allowed column uplift. Under the three strongest motions tested, the maximum base shear was reduced an average of about 50% compared to a similar elastic-anchor model which did not allow column uplift. While this result was consistent with the results found for the moment-frame models, the larger percentage reduction in base shear suggests that braced-frame and relatively rigid structures may benefit the most from an uplifting column/ductile anchor design philosophy.

5.8 Acknowledgement of Publications

Chapter 5 contains material submitted in the following journal papers, of which the dissertation author is the primary author: Trautner, C., Hutchinson, T., Copellini, M., Grosser, P., Bachman, R., and Silva, J. (Accepted). "Developing Ductility using Concrete Anchorage," American Concrete Institute Structural Journal. Trautner, C. and Hutchinson, T., (In Review). "Shake-Table Testing of a Miniature Steel Building with Ductile-Anchor, Uplifting-Column Base Connections for Improved Seismic Performance," Earthquake Engineering and Structural Dynamics. The dissertation author was the primary author on both papers.

Chapter 6: Conclusions and Recommendations

6.1 Summary of Research

The research presented in this dissertation was motivated by the evolving role that concrete fasteners, specifically those implemented at baseplate connections, play in the seismic performance and design of structures. Observed performance in recent earthquakes, most notably the 2010 Maule, Chile earthquake, indicates that base connections incorporating a well-defined stretch length facilitating anchor ductility promotes improved connection and system performance. In addition, previous research suggests that building frame systems with columns allowed to uplift may experience reduced seismic demands when compared to traditional designs that utilize plastic behavior in the superstructure as the primary method of providing energy dissipation and overall ductility.

The overarching hypothesis of this research is that that ductility and energy dissipation may be realized through the structural concrete fastening, and features of the design of the connection may be exploited to promote these behaviors. This dissertation presents a systematic study of connection details which permit robust performance of "traditional" steel column baseplate connections, as well as an investigation of the potential benefits of using such connections to reduce system-level seismic demands. To these ends, four primary research efforts were undertaken. These efforts are the subject of Chapters 2-5, as follows:

- Chapter 2: Anchor Reference and Anchor Material Tensile Testing – this chapter presents over 90 tension tests of headed anchors and allthread

commonly used in concrete anchors, with the primary goal of investigating the effects of material processing and stretch length on anchor strength and elongation capacity.

- Chapter 3: Component-level Testing of Steel Column Baseplate Connections – this chapter presents the results of 17 “traditional” exposed moment-frame steel column baseplate connections subjected to reversed cyclic lateral load, with the primary goal of determining how common detailing practices, including the anchor type, inclusion of stretch length, the setting method, and other details affect connection behavior and performance.
- Chapter 4: Component-Level Numerical Analysis of Steel Column Baseplate Connections – this chapter presents a systematic modeling technique for exposed, moment-frame type steel column baseplate connections. The modeling technique was verified using the test results presented in Chapter 3, as well as the results of three other test programs available in the literature. Pre-and post-processors were developed specifically to allow rapid parametric analysis.
- Chapter 5: Dynamic Testing and Numerical Analysis of Systems Incorporating Uplifting-Column, Ductile-Anchor Baseplate Connections – this chapter presents the dynamic shake table testing of a miniature steel building. The building was constructed to allow different ratios of superstructure fuse and baseplate connection stiffness and strength, in order

to determine whether uplifting-column, ductile-anchor base connections could improve system-level performance versus traditional designs with superstructure fuses and elastic base connections.

6.2 Research Significance and Uniqueness

This research has developed a large experimental database extending across anchor material, connection component, and structural system levels. At each level, the scope of the experiments performed is unique: the anchor tension test data set is, to the author's knowledge, the largest and most comprehensive available. These experiments included tests related to nut functionality, a serviceability limit state applicable not only to concrete anchors, but to all types of bolts and threaded parts. The connection test program explored issues not previously addressed in the literature but of great practical importance, including anchor type and material selection, stretch length, and setting method. The dynamic system-level test program was the first to demonstrate improvements in seismic performance of uplifting column and rocking systems incorporating ductile, replaceable base fastening versus traditional systems.

Importantly, all experiments included a focus on the elements needed for numerical modeling. Although all models were developed in a commercial finite-element code, they serve to increase the usefulness and scope of all of the experimental results. The numerical model developed to analyze the anchor material tension tests may be useful for researchers and designers interested in the force-deformation behavior of a wide range of material types, sizes, and stretch lengths of concrete anchors. The numerical modeling scheme presented in Chapter 4 related to the

connection tests is the best currently-available method for analyzing exposed moment-frame connections, both better validated and more general than any existing method or models. The validated system-level numerical models further confidence in the uplifting-column, ductile-anchor system design philosophy, and they will accelerate its implementation in design and practice in the future.

6.3 Key Results and Conclusions

The major results and conclusions from each of the research efforts are listed in the “Summary Remarks” section found at the end of each of the preceding chapters. The most important specific results and conclusions from each of the aforementioned investigations are as follows:

1. The relationship between anchor elongation at fracture and stretch length was found to be nearly linear for all of the anchor materials tested. This phenomenon has important practical implications, most notably that the elongation of an anchor at a given stretch length may be linearly interpolated or extrapolated from two other known elongation/stretch length pairs. The material type was found to have a pronounced effect on the slope of this line, essentially defining how “efficient” a material is at providing increased elongation for a given increase in stretch length. The slope of this line was found to be as low as 5% for cold-worked mild carbon steel and as high as 20% for anchors fabricated directly from hot-rolled rounds.
2. The elongation at which nuts cease to function and "bind" on threaded parts is an important serviceability limit state for bolted connections of all kinds, including concrete anchors. In the current materials testing, nuts were found

to cease function by hand-rotation between about 2 - 6% elongation for anchors between 0.75 and 1.5 in. diameter. The data suggest that 5% is a reasonable bound for serviceability failure, given that approximately 95% of the fasteners were found to be non-functional at this level.

3. Baseplate connections incorporating a variety of types of anchors, including cast in, adhesive, and undercut, are capable of broad, stable moment-rotation hysteresis under cyclic loading. The behavior and evolution of damage in these connections may be tracked using a standardized hierarchy of connection damage states developed in this research. The rotation capacity of the connections was generally very robust, with a minimum of approximately 0.04 radians for the connection incorporating adhesive anchors with relatively brittle, cold-worked all-thread, and up to about 0.15 radians or more for connections incorporating hot-rolled cast-in or annealed anchors. Very high rotation capacity, up to 0.20 radians was found for connections incorporating removable anchors with ductile inserts.
4. Existing predictive methods for ultimate strength and yield stiffness of baseplate connections were found to be reasonable and generally conservative. The methodology for calculating connection strength under large moments given by AISC Design Guide 1 predicted connection strengths that were within about 6% of observed values for both cast-in and post-installed anchors. Extension of this method to cyclically loaded connections that have multiple rows of fasteners should be performed with

care, however, because plastic strains in one direction of loading may prevent these anchors from being effective if the maximum rotation demand occurs in the other direction of loading. The methodology proposed by Kanvinde et al. (2012) to determine the secant rotational stiffness associated with first yield of the connection was found to be accurate within about 15% for the majority of the tests performed. The method was found to be less accurate for connections incorporating direct-to-steel bearing elements, such as shim packs or setting nuts on the anchors.

5. Component tests indicate that increased stretch length led to only incremental increases in baseplate connection rotation capacity. Significantly larger increases in rotation capacity were observed with the use of anchors fabricated from more ductile material. Moreover, strain penetration was found to be highly variable depending on the type of anchor. Importantly, the definition of the anchor stretch length proved to be problematic for some cases. For example, anchors bonded directly to concrete with epoxy adhesive were found to exhibit essentially no strain penetration, smooth-shank cast-in anchors were found to de-bond over their entire length at even relatively low strain levels, and cast-in anchors consisting of threaded rod with a nut and bearing plate were found to de-bond over part of their embedment. Given the limitations of the current research in terms of anchor size and material, this finding highlights the need for further work to develop guidelines to ensure the assumed stretch length is actually available to the connection. Effective

detailing (e.g., grease, taping, or sleeves) as required to ensure a reliable, well-defined stretch length, should be further investigated and should be recommended in design codes.

6. The choice of setting method (i.e., the use of baseplate shims vs. setting/leveling nuts) can have a pronounced effect on the moment-rotation behavior of baseplate connections. In cases where the setting method provides a more rigid path for compressive bearing than the grout pad under the baseplate, the secant stiffness associated with first yield of the connection is larger than that predicted by analysis methods that assume grout/concrete flexibility. The use of setting nuts in connections with anchor yielding may cause significantly degraded behavior due to "ratcheting" of the anchors as they elongate below the setting nut. This mechanism was found to lead to pinched hysteresis and premature anchor failure due to shear deformation of the anchor. Given the paucity of data regarding yielding-anchor connections assembled with setting nuts, future analyses and test programs should consider their influence, thus supporting the development of appropriate design and detailing guidance.
7. Steel column baseplate connections can be effectively and accurately modeled by a finite-element approach that uses shell and beam elements to represent the column and baseplate and a fiber-section representation of the anchors and grout. The model presented herein is unique in that a large body of experimental data is used to inform and verify the model. The mechanical

behavior of the anchors is characterized by the anchor testing presented in Chapter 2, and a total of 30 connection tests, partly from Chapter 3 and partly from previous studies, were used to verify the model. The model accuracy was evaluated on the basis of stiffness at yield, stiffness at ultimate, and area under the hysteretic curve at moderate (0.04 rad) rotation. The average misfit of the model was less than 10% on the basis of these parameters.

8. Dynamic testing indicates that moment-frame systems incorporating uplifting-column, ductile-anchor connections were found to experience nominally reduced levels of total base shear when compared to similar fixed-base systems. Measured reductions, as large as 20%, were dependent on individual structure and motion characteristics. However, the base shear was lower in the ductile-anchor configurations for the majority of tests.
9. Despite undergoing similar levels of maximum drifts and a larger number of cycles at large displacement due to the loss of rotational restraint from the yielding anchors, moment-frame, uplifting column configurations were found to be virtually damage-free in the superstructure. Under relatively intense motion, the maximum residual interstory drift was measured to be less than 0.2% for a base-connection dominated moment frame, while it was on the order of 1.8% for the “traditional” superstructure-fuse dominated configuration. This result demonstrates that uplifting-column, ductile-anchor

systems are capable of damage-free behavior, and that repair costs for these systems will be vastly smaller than their traditionally-designed counterparts.

10. A single-degree-of-freedom, braced-frame structure was found to benefit significantly from ductile anchors that allowed rocking behavior. Post-test numerical modeling indicates that the maximum base shear was reduced an average of about 50% compared to a similar model with elastically-designed anchors that did not allow column uplift under the three strongest motions in the experimental program. While this result was consistent with test results from moment-frame structures, the larger percentage reduction in base shear suggests that braced-frame and relatively rigid structures may benefit the most from an uplifting column/ductile anchor design philosophy.

6.4 Recommendations for Future Research

The current work examined several aspects of "traditional" steel column baseplate connection performance that have not been well-studied in the past, including the behavior of post-installed anchors, the role of the setting method (setting nuts or shim plates) in connection performance, systematic exploration of currently-available material properties, the role of added stretch length versus anchor material ductility in providing overall connection ductility, and the effects of strain penetration. There are several aspects of these issues which need further evaluation, including:

1. The difference between the exposed length and the stretch length for all types of anchors is an important issue for practicing engineers attempting to comply with building code requirements regarding stretch length (ACI 318-14). This issue is

of practical concern because strategically adding anchor stretch length via steel chairs on the topside of the baseplate or via an additional unbonded embedment depth is expensive and difficult to accommodate in many situations. Currently, the code tacitly suggests that stretch length should be assumed equal to the exposed length, but this delineation is not clear. Based on the reference and connection tests presented in this dissertation, this assumption appears to be appropriate for bonded anchors but likely very conservative for cast-in anchors, especially those that have smooth shanks. This conclusion is limited to a single anchor size (3/4 in.), therefore, additional research should be carried out to determine the relationship between exposed length and stretch length for common anchor types and sizes. Additionally, theoretical calculations should be carried out to determine an analytical relationship between matrix strength, matrix bond, thread geometry, and strain penetration (and resulting anchor deformation capacity).

2. Setting nuts were found to significantly degrade connection performance when compared to other leveling methods. This result is somewhat concerning, given that setting nuts are commonly used, particularly in the western United States. Additional research into this phenomenon should be conducted. In particular, connections with non-yielding or moderately yielding anchors with moderate to high axial load should be investigated in order to determine the range of connections which may be affected by this problem.

3. Efforts should be undertaken to better inform practicing engineers and designers about the tradeoff between anchor ductility and stretch length as means to prevent anchor fracture. In particular, the connection test data involving identical connections with "standard" and "8D" stretch lengths, the tensile tests of commonly-used anchor materials described in Chapter 2, and the observed significant strain penetration observed with threaded cast-in anchors all suggest that the current prescriptive requirement for an 8D stretch length may be better replaced with a more flexible requirement of using both a ductile material and a reasonable stretch length in concert to provide a reasonable anchor elongation capacity to prevent fracture.
4. The testing presented in Chapter 2 was presented to ASTM Committee F1554 and provided evidence the Committee used to change the 2015 version of the standard to disallow cold-working after product qualification tests. This change should result in much higher, more uniform elongation at fracture for anchors and allthread supplied under this common standard. However, there are several other specifications commonly used for anchor specifications, including ASTM A307 and ASTM A193. A systematic study should be undertaken to ensure that the requirements of these standards are sufficient to provide reliable minimum elongations for designers interested in preventing anchor fracture by rational analysis of anchor elongation capacity.

In addition to the more immediately-applicable issues related to traditional baseplate connections, there are several important avenues for further research on

systems incorporating uplifting-column, ductile-anchor baseplate connections. The work described in this dissertation is at least the fourth major research program into non-prestressed, uplifting, self-centering building frame systems (Clough and Huckelbridge 1973, Huckelbridge 1973, Midorikowa 2006). The systems tested in these reports, as well as the systems tested in the current work, have demonstrated significant reductions in seismic demands while requiring a minimal departure from existing construction practices. These systems have great potential to reduce the overall costs of repair and replacement for moderate-risk structures that do not justify the additional upfront costs of base isolation, viscous dampers, or other, more exotic and costly methods of seismic protection. However, in order to foster the practical application of such systems, additional research should be conducted into the following areas:

1. Limits for the applicability of such systems should be established based on modeling of building and nonbuilding structures such as tanks and chimneys. It is hypothesized that such systems have a "size" limit on their usefulness, where buildings become so large and/or tall that rocking modes cannot effectively be activated.
2. None of the research performed so far has incorporated the use of shear keys for positive shear transfer from the structure to the foundation. Although friction and anchor transfer of shear appeared to be robust and reliable in the current work, many designers may feel uncomfortable without a positive shear transfer mechanism. Additional research should address the feasibility of adding shear keys while maintaining the beneficial aspects of the current system.

3. Design criteria for such systems should be established and validated based testing of full-scale testing of prototype systems. At the very least, a comprehensive numerical modeling program should be undertaken, incorporating the modeling techniques described herein. Such a program should include a variety of prototypical buildings and a large suite of ground motions.

References

American Concrete Institute 349 Committee (1976). “Code Requirements for Nuclear Safety Related Concrete Structures and Commentary.” *ACI 349-76*, Detroit, MI.

American Concrete Institute 318 Committee (2002). “Building Code Requirements for Structural Concrete (ACI 318-02) and Commentary (ACI 318R-02).” Detroit, MI.

American Concrete Institute 318 Committee (2011). “Building Code Requirements for Structural Concrete (ACI 318-11) and Commentary (ACI 318R-11).” Detroit, MI.

American Concrete Institute 318 Committee (2014). “Building Code Requirements for Structural Concrete (ACI 318-14) and Commentary (ACI 318R-14).” Detroit, MI.

American Concrete Institute 530 Committee, (2013). “Building Code Requirements and Specification for Masonry Structures and Companion Commentaries (ACI 530-13).”, Detroit, MI.

American Institute of Steel Construction (AISC), (2005a). *Steel Construction Manual* (Including Electronic Resources), AISC, Chicago, IL.

American Institute of Steel Construction, (2005b). "Code of Standard Practice for Steel Buildings and Bridges," AISC 303, Chicago, IL.

American Institute of Steel Construction, (2005c). "Seismic Provisions for Structural Steel Buildings," ANSI/AISC 341-05, Chicago, IL.

American Institute of Steel Construction (AISC). (2010), "Seismic Provisions for Structural Steel Buildings", ANSI/AISC 341, Chicago, IL.

American Society of Civil Engineers (ASCE) Committee 7, (2010). "Minimum Design Loads for Buildings and Other Structures," ASCE, Reston, VA.

American Society of Civil Engineers, (1998). "Seismic Analysis of Safety-Related Nuclear Structures and Commentary," ASCE 4-98, ASCE, Reston, VA.

American Society of Civil Engineers, (2005). "Seismic Design Criteria for Structures, Systems, and Components in Nuclear Facilities," ASCE 43-05, American Society of Civil Engineers, Reston, VA.

American Society of Mechanical Engineers (ASME), (2003). "B1.1: Unified Inch Screw Threads," ASME, New York.

Adany, S., Calado, L., and Dunai, L. (2000). “Experimental Studies on Cyclic Behavior Modes of Base-Plate Connections,” *Proceedings of the Third International Conference on the Behavior of Steel Structures in Seismic Areas (STESSA 2000)*, Montreal, Canada, 97-104.

Akiyama, H., Kurosawa, M., Wakuni, N., and Nishinura, I. (1984). “Strength and Deformation of Exposed Type of Steel Column Bases,” *Journal of Structural and Construction Engineering*, Transactions of AIJ, 342, pp. 46-54.

Akiyama, H., Yamada, S., Takahashi, M., Katsura, D., Kumura, K., and Yahata, S. (1998). “Full Scale Shaking Test of the Exposed-Type Column Bases,” *Journal of Structural and Construction Engineering*, Transactions of AIJ, No. 514, pp. 185-192.

Astaneh, A., Bergsma, G., and Shen J. H. (1992). “Behavior and Design of Base Plates for Gravity, Wind and Seismic Loads,” *Proceedings of the National Steel Construction Conference*, Las Vegas, Nevada, AISC, Chicago, Illinois.

ASTM International, (2007). "F1554-07a,Standard Specification for Anchor Bolts, Steel, 36, 55, and 105-ksi Yield Strength," ASTM International, West Conshohocken, PA.

ASTM International, (2009). "A193-09, Standard Specification for Alloy Steel and Stainless Steel Bolting for High Temperature or High Pressure Service and Other Special Purpose Applications," ASTM International, West Conshohocken, PA.

ASTM International, (2011). "A354-11,Standard Specification for Quenched and Tempered Alloy Steel Bolts, Studs, and Other Externally Threaded Fasteners," ASTM International, West Conshohocken, PA.

ASTM International, (2011). "F606-11, Standard Test Methods for Determining the Mechanical Properties of Externally and Internally Threaded Fasteners, Washers, Direct Tension Indicators, and Rivets," ASTM International, West Conshohocken, PA.

ASTM International, (2012a). "A307-12, Standard Specification for Carbon Steel Bolts, Studs, and Threaded Rod 60000 PSI Tensile Strength," ASTM International, West Conshohocken, PA.

ASTM International, (2012b). "C39/C39M-12a, Standard Test Method for Compressive Strength of Cylindrical Concrete Specimens," ASTM International, West Conshohocken, PA.

ASTM International, (2012c). "C109/C109M-12, Standard Test Method for Compressive Strength of Hydraulic Cement Mortars (Using 2-in. or [50-mm] Cube Specimens)," ASTM International, West Conshohocken, PA.

ASTM International, (2015). "F1554-15ae1,Standard Specification for Anchor Bolts, Steel, 36, 55, and 105-ksi Yield Strength," ASTM International, West Conshohocken, PA.

Aviram, A., Stojadinovic, B., and Der Kiureghian, A., (2010). "Performance and Reliability of Exposed Column Base Plate Connections for Steel Moment-Resisting Frames," PEER Report 2010/107, University of California, Berkeley.

Blodgett, O. (1966), "Design of Welded Structures," James F. Lincoln Arc Welding Foundation, Cleveland, OH.

Brincker, R, Zhang, L, and Andersen, P, (2001). "Modal identification of output-only systems using frequency domain decomposition," Smart Materials and Structures, Institute of Physics Publishing, Bristol, UK.

Burda, J. J. and Itani, A. M. (1999). “Studies of Seismic Behavior of Steel Base Plates,” *Report No. CCEER 99-7, Center for Civil Engineering Earthquake Research, Dept. of Civil Engineering, Univ. of Nevada, Reno, Nevada.*

Clark, P., Frank, K., Krawinkler, H., and Shaw, R. (1997). "Protocol for Fabrication, Inspection, Testing, and Documentation for Beam Column Connection Tests and Other Experimental Specimens," SAC Steel Project Background Document.

Clough, R.W., Huckelbridge AA. (1977). "Preliminary Experimental Study of Seismic Uplift of a Steel Frame," Report No.UBC/EERC-77/22, EERC, University of California, Berkeley, CA.

DeWolf, J. T. (1978). “Axially Loaded Column Base Plates,” *Journal of the Structural Division,*ASCE, Vol. 104, No. ST5, May, pp. 781-794.

DeWolf, J.T. and Sarisley, E. F. (1980). “Column Base Plates with Axial Loads and Moments,” *Journal of the Structural Division*, ASCE, Vol. 106, No. ST11, November, pp. 2167-2184.

DeWolf, J.T. and Ricker D., *Steel Design Guide 1: Base Plate and Anchor Rod Design*, American Institute of Steel Construction, Inc., 1990.

European Standard EN 1993-1-8: 2005/AC (2009). " Eurocode 3: Design of steel structures - Part 1-8: Design of joints," European Commission, Brussels, Belgium.

Fahmy, M. (1999). “Seismic Behavior of Moment-resisting Steel Column Bases,” *Ph.D. Dissertation,* Department of Civil and Environmental Engineering, University of Michigan, Ann Arbor, Michigan.

European Standard EN 1993-1-8 (2009). "Eurocode 3: Design of steel structures - Part 1-8: Design of joints". Supersedes ENV 1993-1-1:1992 Incorporating Corrections and Addendums from December 2005 and July 2009.

Fisher, James M. and Kloiber, Lawrence A., *Steel Design Guide 1: Base Plate and Anchor Rod Design*, 2nd Edition, American Institute of Steel Construction, Inc., 2006.

Gomez, I., Deierlein, G., and Kanvinde, A. (2010). "Exposed column base connections subjected to axial compression and flexure," Final report to the American Institute of Steel Construction, Chicago, IL.

Grauvilardell, J., Lee, D., Hajjar, J., Dexter, R., (2005). "Synthesis of Design, Testing, and Research on Steel Column Base Connections in High-Seismic Zones," University of Minnesota Structural Engineering Report No. ST-04-02.

Hilti Corporation, North American Product Technical Guide, 2011 Edition.

Hon, K.K. and Melchers, R.E. (1988). "Experimental Behavior of Steel Column Bases" *Journal of Constructional Steel Research*, Vol. 9, Paper No. 143, pp. 35-50.

Huckelbridge, A., (1977) ."Earthquake Simulation Test of A Nine Story Steel Frame with Columns Allowed to Uplift," Report No.UBC/EERC-77/22, EERC, University of California, Berkeley, CA.

Igarashi, S., Kadoya, H., Nakashima, S., and Suzuki, M. (1992). "Behavior of Exposed-Type Fixed Column Base Connected to Riser Foundation," *Proceedings of the Tenth World Conference on Earthquake Engineering*, Madrid, Spain.

Instituto Nacional de Normalization de Chile (INN), (2003). "Official Chilean Standard NCh2369.Of2003 - Earthquake-Resistant Design of Industrial Structures and Facilities," INN, Santiago, Chile.

International Council of Building Officials (ICBO), "Uniform Building Code," ICBO, Whittier, CA, 1997.

Johnson, G.R.; Cook, W.H. (1983). "A constitutive model and data for metals subjected to large strains, high strain rates and high temperatures", Proceedings of the 7th International Symposium on Ballistics: 541–547.

Jones E., Oliphant E., Peterson P., (2015). "SciPy: Open Source Scientific Tools for Python, 2001-2015", <http://www.scipy.org/> [Online; accessed 2015-08-01].

Kanvinde, A., Grilli, D., and Zareian, F. (2012). "Rotational stiffness of exposed column base connections: Experiments and analytical models." J. Struct. Eng., 10.1061/(ASCE)ST.1943-541X.0000495, 549–560.

Kawano, A. and Matsui, C. (1998). "On the effect of restoring force characteristics of column-base on inelastic behavior of weak-beam steel frames under earthquake ground motion," *Journal of Structural Construction Engineering*, No. 507: 139-146, Architectural Institute of Japan, Tokyo.

Krawinkler, H., Gupta, A., Medina, R., and Luco, N., (2000). "*Development of Loading Histories for Testing of Steel Beam-to-Column Assemblies*," SAC Background Report SAC/BD-00/10.

Krawinkler, H (2009). "Loading Histories for Cyclic Tests in Support of Performance Assessment of Structural Components," 3rd International Conference on Advances in Experimental Earthquake Engineering, Pacific Earthquake Engineering Research Center (PEER).

Lee, D., Goel, S. C., and Stojadinovic, B. (2000), "Seismic Behavior of Column-Base Plate Connections about Weak Axis Bending," *Proceedings of the U.S.-Japan Workshop on Seismic Fracture Issues in Steel Structures*, San Francisco, California.

Li, T., Sakai, J., and Matsui, C (2000). "Seismic Behavior of Steel-Concrete Composite Column Bases," *Proceedings of the 12th World Conference on Earthquake Engineering*, Paper 1072.

Liu, W., Hutchinson, T., Kutter, B., Hakhamaneshi, M., Aschheim, M., and Kunnath, S., (2013). "Demonstration of compatible yielding between soil-foundation and superstructure components," *ASCE Journal of Structural Engineering*, 139 (8), 1408-1420.

Livermore Software Technology Corporation (LSTC), (2013). LS-DYNA Keyword User's Manual Vol I-III (Program Version 7.0.0). LSTC, LSTC, Livermore, California.

Magenes, G. (1989) "Design Analysis and Calibration of UCSD Shake Table" MS Thesis, Dept. of Structural Engineering, UCSD.

Melchers, R. E. (1992). "Column-Base Response under Applied Moment," *Journal of Constructional Steel Research*, Vol. 23, pp. 127-143.

Midorikawa, M., Azuhata, T., Ishihara, T., and Wada, A., (2006). "Shaking Table Tests on Seismic Response of Steel Braced Frames with Column Uplift," *Earthquake Engineering and Structural Dynamics*, July, pp. 1767-1785.

Midorikawa, M., Toyomaki, S., Hori, H., Asari, T., Azuhhata, T., and Ishihara, T., (2008). “Seismic Response of Six-Story Eccentrically Braced Steel Frames with Columns Partially Allowed to Uplift,” *14th World Conference on Earthquake Engineering*, October 12-17th, Beijing, China.

Miyasaka, H., Arai, S., Uchiyama, M., Yamada, T., and Hashimoto, A. (2001). “Elasto-Plastic Behavior of Structural Elements Consist in Exposure Fixed-Type Steel Column Base. Part I – Behavior to Bending Moment,” *Journal of Structural and Construction Engineering*, Transactions of AIJ, No 550, December 2001, pp.167-174.

Oppenheim, A. and Schafer, W. (2010). *Discrete Time Signal Processing*, 3rd Edition, Prentice Hall, Upper Saddle River, NJ.

Picard, A. and Beaulieu, D. (1985). “Behavior of a Simple Column Base Connection,” *Canadian Journal of Civil Engineering*, Vol. 12, pp. 126-136.

The Python Software Foundation, (2015) "Python 2.7," *<https://www.python.org/download/releases/2.7/> (Accessed June 13, 2015).*

Restrepo, J., Rodriguez, M., Kao-Stocker, G, and Carr, A. (2014). "Seismic Response of a Four-Story Miniature Building with Replaceable Plastic Hinges," Journal of Earthquake Engineering, 18:8, 1217-1240.

Risa Technologies, Inc. (2013). "Rapid Interactive Structural Analysis – Base Plate and Anchorage Analysis & Design," Version 2.1 - General Reference, *<https://risa.com/documents/risabase/RBGenRef_v210.pdf> (July 24, 2016).*

Salmon, C., Schenker, L., and Johnston, G., (1957). "Moment-rotation characteristics of column anchorage," Transactions of ASCE, Vol 122, No. 5.

Sato, K. (1987). “A Research on the Aseismic Behavior of Steel Column Base for Evaluating Its Strength Capacity and Fixity,” *Report No. 69*, Kajima Institute of Construction Technology, Tokyo, Japan.

Somiya, Y., Fukuchi, Y., and Chin, B. (2002). “Experimental Study on Elasto-Plastic Behavior and Strength Estimation of Exposed-Type Column Base with Variable Axial Force,” *Journal of Structural and Construction Engineering*, Transactions of AIJ, No. 562, pp. 137-143.

Soules, J., Bachman, R., and Silva, J. (2016). “Chile Earthquake of 2010 – Assessment of Industrial Facilities around Concepcion,” American Society of Civil Engineers, Reston, VA, 2016.

Structural Engineers Association of California (SEAOC) (2016). "Vision 2000," Accessed July 22, 2016, *<http://peer.berkeley.edu/course_modules/eqrd/index.htm?c227top.htm&227cont.htm&DesPhil/desphil5.htm>*

Targowski, R., Lamblin, D., and Guerlement, G. (1993). “Base plate Column Connection under Bending: Experimental and Numerical Study,” *Journal of Constructional Steel Research,*Vol. 27, pp. 37-54.

Trautner, C. and Hutchinson, T., (2014a). " Structural Base Plate Connection Component Testing – Phase I Part 1: Data Report," SSRP–2013/07, University of California, San Diego.

Trautner, C. and Hutchinson, T., (2014b). " Structural Base Plate Connection Component Testing – Phase I Part 2: Data Analysis, Modeling, and Conclusions," SSRP–2013/08, University of California, San Diego.

Trautner, C. and Hutchinson, T. (2015a). " Structural Base Plate Connection Component Testing – Phase II Part 1: Data Report," SSRP-2014/14, University of California, San Diego.

Trautner, C. and Hutchinson, T. (2015b). "Structural Base Plate Connection Component Testing – Phase II Part 2: Data Analysis, Modeling, and Conclusions," SSRP-2014/15, University of California, San Diego.

Trautner, C. and Hutchinson, T. (2016). "Dynamic Testing of a Miniature Building with Ductile, Uplifting Anchorage for the Reduction of Seismic Demands," SSRP-2016/06, University of California, San Diego.

Trautner, C., Copellini, M., and Hutchinson, T., (2015a) "Tension Testing of Common Threaded Rod Products Used for Anchorage to Concrete," SSRP-2014/13, University of California, San Diego.

Trautner, C., Hutchinson, T., Grosser, P., and Silva, J. (2015b). “Effects of detailing on the cyclic behavior of steel baseplate connections designed to promote anchor yielding.” ASCE Journal of Structural Engineering, *10.1061/(ASCE)ST.1943-541X.0001361*, *04015117*.

Trautner, C., Hutchinson, T., Copellini, M., Grosser, P, Bachman, R., and Silva, J, (2016a). "Developing Ductility using Concrete Anchorage," ACI Structural Journal, American Concrete Institute, Detroit, MI.

Trautner, C., Hutchinson, T.C., Grosser, P, and Silva, J. (2016b, In Review), " An Investigation of Steel Column Baseplate Connection Details Incorporating Ductile Anchors," ASCE Journal of Structural Engineering.
Trautner, C. Zheng, Y., McCartney, J., and Hutchinson, T., (2016c). "Improvements in Frictional Characteristics and Earthquake Motion Fidelity from Repairs to a Servo-Hydraulic Shake Table," In preparation for submittal to: Earthquake Engineering and Structural Dynamics, John Wiley and Sons, Hoboken, NJ.

Van der Walt, S., Colbert, C. and Varoquaux, G. (2011) "The NumPy Array: A Structure for Efficient Numerical Computation," *Computing in Science & Engineering*, 13, 22-30 (2011).

Wald, F., Simek, I., and Seifert, J. (1994). “The Tests of the Column-Base Components,” *Proceedings of the First International Conference STESSA*, Timisoara, Romania.

Wald, F. and Jaspart, J. (1998). “Stiffness Design of Column Bases,” *Journal of Constructional Steel Research*, Vol. 46, 1-3, Paper No. 135.

Wilson, E.L. (1965). "Structural analysis of axisymmetric solids", American Institute of Aeronautics and Astronautics I., 3. 2269-2274.

Appendix A: Keywords used in Axisymmetric Tension Test Model

*KEYWORD
*TITLE
*NODE
*ELEMENT_SHELL
*PART
*SECTION_SHELL
*MAT_MODIFIED_JOHNSON_COOK
*MAT_ELASTIC
*SET_NODE_LIST
*BOUNDARY_SPC_SET
*SET_NODE_LIST
*BOUNDARY_SPC_SET
*SET_NODE_LIST
*CONSTRAINED_NODAL_RIGID_BODY
*PART
*SECTION_BEAM
*ELEMENT_BEAM
*DEFINE_CURVE
*BOUNDARY_PRESCRIBED_MOTION_NODE
*CONTROL_TERMINATION
*CONTROL_IMPLICIT_GENERAL
*CONTROL_IMPLICIT_SOLVER
*CONTROL_IMPLICIT_AUTO
*DATABASE_BINARY_D3PLOT
*SET_NODE_LIST
*DATABASE_NODAL_FORCE_GROUP
*DATABASE_NODFOR
*DATABASE_SPCFORC
*END

Appendix B: Keywords used in Component FE Model

*KEYWORD
*TITLE
*NODE
*ELEMENT_SHELL
*ELEMENT_DISCRETE
*ELEMENT_BEAM_ORIENTATION
*ELEMENT_BEAM
*SET_NODE_LIST
*CONSTRAINED_NODAL_RIGID_BODY
*PART
*MAT_PLASTIC_KINEMATIC
*MAT_ELASTIC
*SECTION_SHELL
*SECTION_BEAM_AISC
*SECTION_BEAM
*MAT_SPRING_INELASTIC
*DEFINE_CURVE
*SECTION_DISCRETE
*MAT_SPRING_NONLINEAR_ELASTIC
*BOUNDARY_SPC_NODE
*LOAD_NODE
*CHANGE_CURVE_DEFINITION
*LOAD_BODY_Z
*BOUNDARY_PRESCRIBED_MOTION_NODE
*CONTROL_SOLUTION
*CONTROL_TERMINATION
*CONTROL_IMPLICIT_GENERAL
*CONTROL_IMPLICIT_AUTO
*DATABASE_BINARY_D3PLOT
*CONTROL_IMPLICIT_SOLUTION
*END

Appendix C: Keywords from Dynamic Test FE Model

*KEYWORD
*TITLE
*NODE
*ELEMENT_BEAM
*ELEMENT_DISCRETE
*ELEMENT_SHELL
*ELEMENT_BEAM_ORIENTATION
*SET_NODE_LIST
*DEFINE_SD_ORIENTATION
*PART
*SECTION_BEAM
*SECTION_SHELL
*SECTION_DISCRETE
*MAT_PLASTIC_KINEMATIC
*MAT_ELASTIC
*MAT_SPRING_INELASTIC
*DEFINE_CURVE
*MAT_SPRING_NONLINEAR_ELASTIC
*MAT_DAMPER_VISCOUS
*MAT_SPRING_ELASTIC
*MAT_DAMPER_VISCOUS
*BOUNDARY_SPC_NODE
*BOUNDARY_PRESCRIBED_MOTION_NODE
*LOAD_BODY_Z
*DAMPING_FREQUENCY_RANGE_DEFORM
*CONTROL_IMPLICIT_GENERAL
*CONTROL_IMPLICIT_DYNAMICS
*CONTROL_SOLUTION
*CONTROL_TIMESTEP
*CONTROL_IMPLICIT_AUTO
*CONTROL_TERMINATION
*DATABASE_BINARY_D3PLOT
*END

Appendix D: Integration and Filtering of Dynamic Test Results

Introduction and Purpose

This appendix describes the integration, filter design, and baseline correction processing for the strong-motion excitation experimental data. The objectives of the processing of the dynamic data are:

- Preservation of the "true" structural response
- Eliminate high-frequency artifacts (particularly in acceleration sensors)
- Reduce long-period drift in integrated displacement response

Integration scheme

Common double-integration schemes for acceleration data include the trapezoidal rule and 4th-order Runge-Kutta. If sufficient accuracy can be obtained with the trapezoidal rule, it is generally preferable because it is far more computationally efficient. In the case of the assumption of linear behavior between digitized acceleration points, the trapezoidal rule is exact (Figure D1). The current experiments and instrumentation scheme do not provide any information to suggest any interpolation scheme other than linear. Therefore, the trapezoidal rule was used for all integration in the current work.

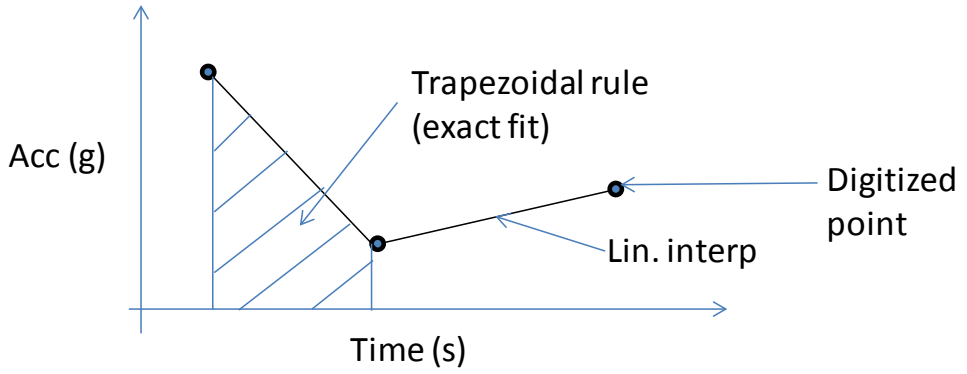

Figure D1: Trapezoidal rule integration with linearly-interpolated data

Baseline correction

Baseline correction is a method by which a double-integrated displacement history is corrected to end at a known final displacement (usually zero) to remove the effect of small errors in the measured acceleration response that result in large displacements when integrated over a relatively long time history. Several methods of baseline correcting exist. In the current work, a quartic displacement signal is added to the double-integrated displacement to result in zero ending displacement. The corresponding quadratic acceleration history is then added to the original acceleration history to create what is referred to in this report as a "baseline corrected acceleration history".

Filter Design

Filtering of acceleration data is often performed to remove high-frequency artifacts that are not important to the overall structure response. In the current work, the sampling frequency was 256Hz, which was more than ten times the highest structural mode of interest. Therefore, filtering of the acceleration data was undertaken to determine more appropriate acceleration history from the structural response. Butterworth filters are

often used in the field of earthquake engineering because they have a very flat passband response, i.e. signal distortion in the passband is very small (Oppenheim and Schafer 2010). A typical 4th-order Butterworth filter frequency response is shown in Figure D2.

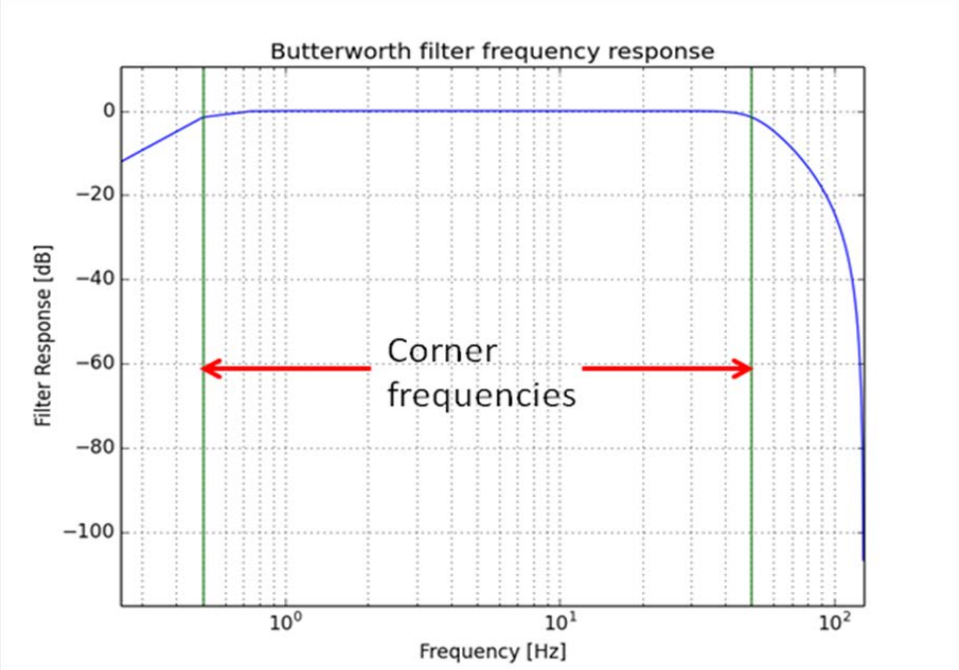

Figure D2: Frequency response for 4th-order Butterworth filter

Based on the TF estimates and analysis presented in the main body, the highest global structural frequency of interest was less than 20 Hz. Low-pass filtering of earthquake signals is often carried out at frequencies ranging from 0.05 to 0.5Hz. Therefore, several different filtering schemes were considered for the present work. To evaluate the appropriateness, reasonability, and accuracy of each filtering scheme, the maximum acceleration from each floor was compared. Additionally, the displacement history found from double-integrating the filtered acceleration history was compared to the directly-measured displacement at each floor level. The difference between the two histories was evaluated using the SRSS (square root of the sum of the squares)

procedure - the difference in displacement at each time history was squared, the differences for the entire time history was summed, and the square root of this quantity was taken. Although this result does not have physical significance, it allows for the relative accuracy of each solution to be evaluated.

Two examples of comparisons to the measured displacements at the 3rd floor level, 0.2-20Hz and 0.05-30Hz are shown in Figure D3. This isolated example is indicative of a broader trend observed in the filter evaluation process -- greater accuracy in the double-integrated displacements was realized with lower low corner (highpass) frequencies. In contrast, the integrated displacements were relatively insensitive to the value of the upper corner (lowpass) frequency. These trends are evident in the overall results, summarized in Table D1. The individual floor accelerations were relatively insensitive to the filtering scheme. The greatest accuracy of the integrated displacements was found for the 0.05-30Hz filtering scheme, therefore, these corner frequencies were used for filtering of all acceleration data presented herein, except where specifically noted otherwise.

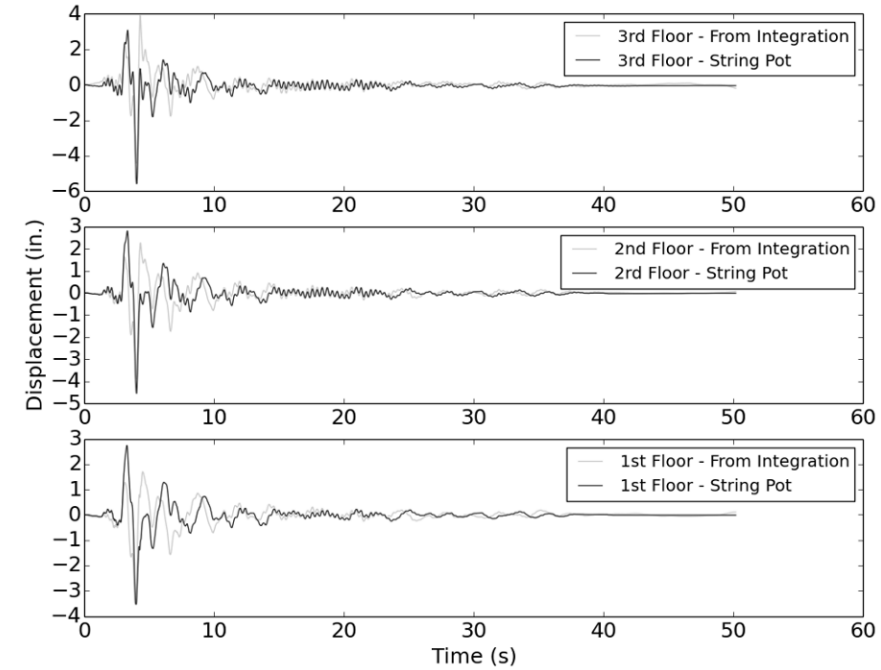

(a)

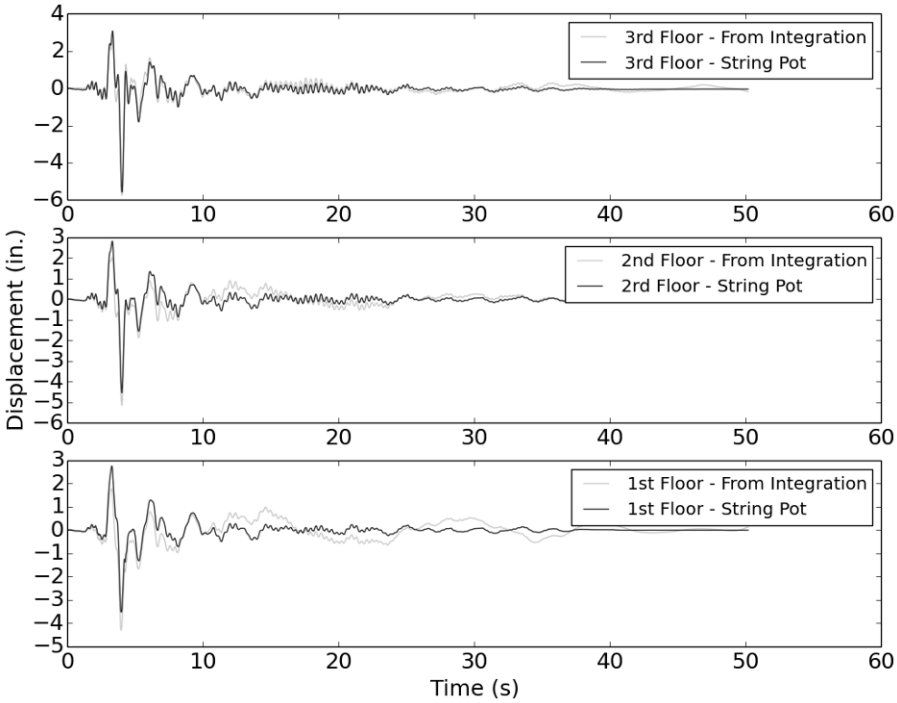

(b)

Figure D3: Trapezoidal rule integration with linearly-interpolated data, (a) 0.2-20Hz, (b) 0.05-30Hz

Table D1: Summary of floor-level maximum accelerations and integrated-displacement errors from filtering sensitivity study

Highpass (Hz)	Lowpass (Hz)	$\|AMax\|_3$ (g)	$\|AMax\|_2$ (g)	$\|AMax\|_1$ (g)	SRSS Error at Floor 3 (in.)
0.2	30.0	2.16	2.20	1.20	52.8
0.2	25.0	2.15	2.20	1.06	52.4
0.2	20.0	2.09	2.14	0.95	51.8
0.1	100.0	2.13	2.15	1.44	31.2
0.1	30.0	2.10	2.12	1.30	30.5
0.1	25.0	2.09	2.11	1.10	29.9
0.05	20.0	2.05	2.09	1.11	22.2
0.05	25.0	2.05	2.09	1.11	21.0
0.05	30.0	2.07	2.08	1.25	19.6